# Examination of Banded Iron Formation Through Petrographic, Geochemical and Iron Isotope Analyses

A Dissertation Presented for the
Doctor of Philosophy
Degree
The University of Tennessee, Knoxville

Melissa Margaret Hage
August 2015

# DEDICATION

This dissertation is dedicated to my older brother, Chris, and my younger sister, Maya, who taught me so much and who left this world far too early, with so much life left to live.

# ACKNOWLEDGEMENTS

This research was funded by NASA grant EXOB08-0063 awarded to Christopher M. Fedo and the following grants awarded to Melissa M. Hage: Geological Society of America Student Research Grant, Precambrian Institute Center Student Grant, Institute of Lake Superior Geology Student Research Grant, American Philosophical Society and NASA Astrobiology Institute's Lewis and Clark Fund for Exploration and Field Research in Astrobiology, and the Mayo Educational Foundation Scholarship. The University of Tennessee's Earth and Planetary Science Department provided additional financial support.

This dissertation would not have been possible without the continued support of my advisor, Christopher M. Fedo, over many, many, many years. His invaluable insight, support, guidance, and seemingly inexhaustible patience with me over the years will not be forgotten. What will also not be forgotten are his creative motivational sayings (e.g., "The house is on fire and the kids are inside and we only have a pail of water and spoon to fight with!"). I would also like to thank my committee members Harry Y. McSween, Linda Kah, Micah Jessup, and Steve Wilhelm for all their support and comments that improved the chapters below.

While some may say it takes a village to raise a child, I would say it takes a village to get a person through their PhD. I never would have made it with the support of all my family and friends, cheering me on from the sidelines, being a shoulder to cry on, and always having an ear for listening. You all have helped me more than you will ever know. To my parents, Marie Phillips, Robert Hage, Vince Phillips, and Odette Adrian, thank you so much for always believing in me, supporting me in whatever I chose to do or where I chose to go, and for shaping me into the person I am today. To the Tennessee crew that have been there for me over the years, Whitney Nelson (my HLP), Mike DeAngelis, Daniel Lewis, Sara Beth Cadieux, Liz Lee, David Gaines, Eric Hogan, René Lewis, Jeff Nettles, Tasha Dunn, Rhiannon Mayne, Dana Miller, Troy Dexter, and so many more, you guys rock! To my FC Posse, Melissa Thornton, Karson and Jason Beaty, Amber Crouse and Steve Blackburn, Julie Thurman, and Kate Bundren, you guys helped me get through some rough times; I hate that we all had to meet the way we did, but I love you like family. To my oldies, but goodies, Jen Scimeca, Kim Tully, Jesse Yoburn, Renee Cacciaboudo, thanks for sticking around all these years. To Oregon and Amanda Frederickson, thanks for all the wine and for being awesome. To my Boo-U peeps, Franc Auld, Bobbie Boetcher, David Armstrong, Meg Steinweg, Lauren Love, Samantha Kimball, Nellie Schmitz, and Mark Tully, thanks so much for all the laughter and booze during the final push.

# ABSTRACT

Banded iron formation (BIF) has the potential to preserve geochemical signatures critical to interpretation of early Earth because: (1) it is found within the Precambrian when fundamental changes in Earth's physical, biological and chemical evolution occurred, and (2) it may preserve a record of the depositional environment. Rare earth elements (REE) are useful for investigating BIF because they have characteristic features. One goal of this study was to evaluate the calculation of certain REE ratios to determine if the calculation affected the interpretation. It was concluded that the method for calculating certain ratios may affect the interpretation of redox conditions for a given sample. Another goal was to determine paleo-oceanic and atmospheric redox conditions. REE concentrations in BIF samples from the >3.7 Ga Isua Greenstone Belt, the ~3.0 Ga Buhwa Greenstone Belt, and the ~1.9 Ga Gunflint Iron Formation were examined and it was concluded that the ~1.9 Ga ocean was not fully ventilated, but that oxidative continental weather was occurring. A third goal was to evaluate the degree of heterogeneity in BIF mineral REE chemistry. Substantial microscale heterogeneity in mineral spot chemistry was observed and is most likely a result of inorganic, post-depositional alteration processes. Lastly, this study examined a lithology whose age and origin has been highly debated, with some arguing for a BIF protolith and others arguing for an ultramafic protolith. To investigate the unit's protolith, I analyzed mafic mineral compositions and found that they possess trace-element signatures indicative of an igneous origin, rendering a BIF protolith unnecessary. To investigate the reported age, I measured the orientation of foliations, mineral lineations and fold axes on either side of

the contact used to date the contentious lithology and concluded that the contact is tectonic and thus cannot be used to constrain the depositional age of the debated unit.

# TABLE OF CONTENTS


1. Chapter I Introduction……..... 1
   - 1.1 Introduction……..... 2
   - 1.2 Background…… 3
     - 1.2.1 Banded Iron Formation (BIF) Classification…….. 3
     - 1.2.2 Iron in Solution……... 5
     - 1.2.3 Depositional Environments and Mechanisms of BIF Deposition……..... 6
     - 1.2.4 Trace Elements…… 10
     - 1.2.5 Iron Isotopes…… 11
   - 1.3 Study Locales……. 13
     - 1.3.1 BIF Through Time…….. 13
     - 1.3.2 Isua Greenstone Belt, Greenland……. 13
     - 1.3.3 Buhwa Greenstone Belt, Zimbabwe…… 14
     - 1.3.4 Gunflint Iron Formation, Minnesota and Canada……... 15
   - 1.4 The Dissertation……. 16
   - 1.5 Significance……... 17
   - References……. 18

2. Chapter II Evidence for an Oceanic Oxycline and Oxidative Continental Weathering in the Late Paleoproterozoic Based on U-Pb-REE Systematics in Banded Iron Formation……..……. 28
   - Abstract……. 29
   - 2.1 Introduction……...……..…….. 30
   - 2.2 Geologic Background……....…….. 34
     - 2.2.1 Gunflint Formation, Minnesota and Ontario (~1.9 Ga)…….. 34
     - 2.2.2 Isua Greenstone Belt, Greenland (>3.7 Ga)……..... 37
     - 2.2.3 Buhwa Greenstone Belt, Zimbabwe (~3.0 Ga)……... 38
     - 2.2.4 Kuruman and Penge Iron Formations, South Africa (~ 2.5 Ga)……. 39
   - 2.3 Geochemical Background…….. 39
   - 2.4 Analytical Methods…… 43
     - 2.4.1 Whole Rock, Trace- and Rare Earth-Element Analysis…… 43
       - 2.4.1.1 Rock Digestion…….. 43
       - 2.4.1.2 Mass Spectrometry……..... 44
     - 2.4.2 Whole Rock Pb Isotope Analysis……..... 44
       - 2.4.2.1 Pb Purification……..... 44
       - 2.4.2.2 Mass Spectrometry…… 45
     - 2.4.3 Sample Selection……. 45
   - 2.5 Evidence for an Oceanic Oxycline…… 47
     - 2.5.1 Rare Earth Element Geochemistry…….. 47

2.5.1.1 Variability Through Time…….. 47
2.5.1.2 Gunflint Formation Variability…….. 49
2.5.2 Interpreting Rare Earth Element Geochemistry…….. 49
2.6 Oxidative Continental Weathering by ~1.9Ga…….. 51
2.6.1 Trace-Element Geochemistry…….. 51
2.6.1.1 Pb Isotope Geochemistry…….. 51
2.6.1.2 Variability in Redox Sensitive Elements Through Time……..…. 52
2.6.1.3 Gunflint Formation Variability……. 52
2.6.2 Interpretation of Trace-Element Geochemistry…..…….. 53
2.6.2.1 U-Th-Pb Geochemistry…….. 53
2.6.2.2 Molybdenum……. 55
2.6.2.3 Vanadium……..…….. 56
2.6.2.4 Cobalt……..…… 57
2.6.2.5 Chromium…..……. 58
2.6.2.6 Effects of Early Diagenesis…… 59
2.7 Oceanic Oxycline and Oxidative Continental Weathering Through Time……..... 59
2.8 Summary Points……..…….…….. 61
References……. 64
Appendix 1……..... 85

3. Chapter III Microscale Heterogeneity in the Geochemistry of Algoma and Superior Type Banded Iron Formations…….…… 105
Abstract…… 106
3.1 Introduction..…….. 107
3.2 Background…..…….…. 108
3.3 Geologic Setting and Sample Description…..……... 114
3.3.1 Isua Greenstone Belt, Greenland (> 3.7 Ga)……... 114
3.3.2 Buhwa Greenstone Belt, Zimbabwe (~ 3.0 Ga)…….. 116
3.3.3 Gunflint Iron Formation, Minnesota and Ontario (~1.9 Ga)... 117
3.4 Analytical Methods…..…….. 118
3.4.1 Whole Rock, Trace- and Rare-Earth Element Analysis……... 118
3.4.2 Mineral Specific Trace- and Rare-Earth Element Analysis… 119
3.4.3 Fe Isotope Analyses of Whole Rock and Individual Bands… 121
3.5 Results……..…… 122
3.5.1 Whole Rock Chemistry…….. 122
3.5.1.1 Major Elements…… 122
3.5.1.2 Rare Earth Elements……. 123
3.5.2 Mineral vs. Whole Rock Geochemistry – Rare Earth Elements…… 123
3.5.2.1 Isua Greenstone Belt, Greenland…….. 123
3.5.2.2. Buhwa Greenstone Belt, Zimbabwe……. 125
3.5.2.3 Gunflint Iron Formation, Minnesota and Ontario……. 127

3.5.3 REE Ratios Through Time…….. 129
3.5.2 Fe Isotopes…… 130
3.6 Discussion……. 131
3.6.1 Rare Earth Element Geochemistry……. 131
3.6.2 Iron Isotopes…… 136
3.6.2.1 Whole Rock vs. Individual Bands…… 136
3.6.2.2 Iron Isotopes Through Time……..... 137
3.7 Conclusions…… 139
References……. 141
Appendix 2…… 166

4. Chapter IV Origin of > 3.65 Ga Quartz-Amphibole-Pyroxene Rocks from Akilia, SW Greenland: An Integrated Field and Mineral Composition Investigation…… 182
Abstract……..... 183
4.1 Introduction……...……..…….. 185
4.2 Controversy Defined..……...…….. 186
4.3 Geologic Setting ……..……. 189
4.4 Analytical Methods…… 191
4.5 Field Relationships……..…….. 191
4.6 Study Samples and Petrography…… 195
4.6.1 Sample Justification……. 195
4.6.2 Akilia…….…….. 195
4.6.3 Isua Greenstone Belt (IGB)…….…… 197
4.7 Whole Rock Chemistry……. 198
4.7.1 Akilia……... 198
4.7.2 Isua Greenstone Belt……... 199
4.8 Mineral Chemistry……. 199
4.8.1 Quartz-Amphibole-Pyroxene Rock (QAP)……. 199
4.8.1.1 Pyroxene…… 199
4.8.1.2 Amphibole……. 200
4.8.2 QAP – Ultramafic Contact Zone (AK 30)…….. 200
4.8.3 Ultramafic Rock (AK 02)…… 201
4.8.4 Amphibolite (AK 47)…….. 201
4.8.5 Garnet-Bearing Rock (AK 33 and AK 48)…….. 202
4.8.6 Carbonated Mafic Rocks from Isua Greenstone Belt (IS-X and IS-Y)……... 203
4.9 Discussion…….. 204
4.9.1 Structural Evidence for Pervasive Deformation…….. 204
4.9.2 Does the Mineralogy Support a BIF Protolith?..... 205
4.9.3 Compositional Evolution – From an Ultramafic Protolith to the QAP Lithology…… 206
4.10 Conclusions…….. 210

References……. 212
Appendix 3…… 238

5. Chapter V Conclusions…….…….. 257
5.1 Major Conclusions……. 258
5.1.1 Evidence for an Oceanic Oxycline and Oxidative Continental Weathering in the Late Paleoproterozoic……... 258
5.1.2 Microscale Heterogeneity in the Geochemistry of Algoma and Superior Type Band Iron Formation……. 260
5.1.3 Origin of >3.65 Ga Quartz-Amphibole-Pyroxene Rocks from Akilia……. 261
5.2 Summary…… 263
Appendix 4 ……... 264

Vita…… 338

# LIST OF TABLES


| | | |
|---|---|---|
| Table 3.1 | Bulk rock major element compositions of samples from the IGB, BGB, and GF……. | 166 |
| Table 3.2 | Bulk rock trace and rare-earth element compositions of samples from the IGB, BGB, and GF……... | 167 |
| Table 4.1 | Trace and rare-earth element composition of Isua and Akilia samples.....…….. | 238 |
| Table 4.2 | Major element compositions of Isua and Akilia samples…….. | 239 |
| Table 4.3 | Representative microprobe analyses of pyroxenes in Akilia samples... | 240 |
| Table 4.4 | Representative microprobe analyses of amphiboles in Akilia samples. | 241 |
| Table A.1 | Major and trace element geochemistry of samples from the IGB……. | 264 |
| Table A.2 | Major and trace element geochemistry of samples from the BGB…… | 268 |
| Table A.3 | Major and trace element geochemistry of samples from the GF...…… | 272 |
| Table A.4 | Major and trace element geochemistry of samples from Akilia…… | 282 |
| Table A.5 | Lead isotope analyses from samples from the GF……. | 284 |
| Table A.6 | Iron isotope analyses from samples from the IGB, BGB, and GF…… | 285 |
| Table A.7 | LA-ICP-MS REE analyses (25μm) from samples from the IGB, BGB, and GF……. | 287 |
| Table A.8 | LA-ICP-MS REE analyses (40μm) from samples from the IGB, BGB, and GF……. | 311 |

# LIST OF FIGURES


| | | |
|---|---|---|
| Figure 2.1 | Generalized geologic maps of field areas showing sample locations…… | 85 |
| Figure 2.2 | Generalized composite stratigraphic column for the Gunflint Formation, modified from Miller et al. (1987), Fralick et al. (2002), Poulton et al. (2004), and Planavsky et al. (2009) ..... | 86 |
| Figure 2.3 | Field photographs of the Gunflint Formation..... | 88 |
| Figure 2.4 | Photomicrographs of samples from the Gunflint Formation..... | 89 |
| Figure 2.5 | Photomicrographs of samples from the Isua and Buhwa Greenstone Belts..... | 91 |
| Figure 2.6 | Average shale-normalized REY pattern for BIFs used in this study, which span a time range from 3.9 Ga to 1.9 Ga..... | 93 |
| Figure 2.7 | (A) Crossplot of Zr (ppm) vs. $Al_2O_3$ (wt. %) for BIFs from the IGB, BGB and Gunflint Formation……..... | 94 |
| Figure 2.8 | Key REE ratios through time…… | 96 |
| Figure 2.9 | The variability of REE geochemistry through Gunflint stratigraphy..... | 98 |
| Figure 2.10 | (A) Overview of the shuttle transport model of Ce and other REEs from land to deeper waters..... | 99 |
| Figure 2.11 | Crossplot of $^{238}U/^{204}Pb$ vs. $^{206}Pb/^{204}Pb$ for Gunflint BIF samples showing a strong positive correlation..... | 100 |
| Figure 2.12 | The concentration of different terrestrially sourced, redox-sensitive trace-elements in BIF through time..... | 101 |
| Figure 2.13 | The small scale heterogeneity of trace-element geochemistry through Gunflint stratigraphy..... | 102 |
| Figure 2.14 | Cross plot of $^{208}Pb/^{206}Pb$ vs. $^{232}Th/^{238}U$ for Gunflint BIF samples..... | 103 |
| Figure 2.15 | Gunflint Pb isotope data plotted on a common Pb plot, along with two isochrones emanating from the 1.9 Ga starting points for a depleted mantle source (MORB) and a sedimentary mix source (Kramers and Tolstikhin, 1997)..... | 104 |
| Figure 3.1 | Generalized geologic maps of field areas showing sample locations…… | 168 |
| Figure 3.2 | Composite photomicrographs of 1-inch polished thick sections used for laser ablation analyses…… | 169 |
| Figure 3.3 | Reflected light photomicrographs of representative laser ablation spots of study samples from the IGB, BGB, and GF…… | 170 |
| Figure 3.4 | Whole rock shale-normalized REE+Y patterns for BIFs used in this study……... | 172 |
| Figure 3.5 | Key REE ratios for the chemistry of individual mineral grains from samples IS-02-05 and IS-02-08 from the IGB……. | 173 |
| Figure 3.6 | Key REE ratios for the chemistry of individual mineral grains from samples ZB-23 and ZB-117 from the BGB……. | 175 |

| | | |
|---|---|---|
| Figure 3.7 | Key REE ratios for the chemistry of individual mineral grains from samples GF-06, GF-39, and GF-45 from the GF……. | 177 |
| Figure 3.8 | (A) Y/Ho ratios for both whole rock and individual minerals from samples from the IGB, BGB, and GF……... | 179 |
| Figure 3.9 | $\delta^{56}$Fe values for whole rock BIF samples and individual bands used in this study collected from the IGB, BGB, and GF……. | 180 |
| Figure 3.10 | $\delta^{56}$Fe values for whole rock BIF samples used in this study collected from the IGB, BGB, and GF, as well as reported $\delta^{56}$Fe values for magnetite from Dauphas et al. (2004) and whole rock or *in situ* analyses from Czaja et al. (2013)……... | 181 |
| Figure 4.1 | Generalized geologic map showing the location of Akilia, the IGB, and early Archean supracrustal rocks in the Nuuk region of SW Greenland…….. | 242 |
| Figure 4.2 | Simple structural interpretation of the geology of the southwestern end of Akilia……. | 243 |
| Figure 4.3 | (A) Oblique aerial photograph looking NW showing the main 5-m thick QAP outcrop located on the southwestern tip of Akilia……... | 243 |
| Figure 4.4 | Field photographs of the key relationship between the Akilia Association and the Amîtsoq Gneiss……. | 245 |
| Figure 4.5 | Stereographic projections of structural data collected on rocks associated with the contact between the Akilia Association and Amîtsoq Gnesiss…… | 246 |
| Figure 4.6 | Photomicrographs and back-scattered electron detection (BSE) images of samples from the QAP unit……..... | 247 |
| Figure 4.7 | Sample 92197…… | 249 |
| Figure 4.8 | (A) Field location of samples IS-X and IS-Y…… | 250 |
| Figure 4.9 | REY systematics of a sample from the QAP lithology (AK 38), ultramafic rocks adjacent to the QAP lithology (AK 02), Isua ultramafic sample with disseminated ferroan dolomite (IS- X), Isua ultramafic sample comprised almost entirely of ferroan dolomite (IS-Y), original Akilia life rock (92-197), in-place equivalent of original Akilia life rock from QAP lithology (AK 33) and an amphibolite unit adjacent to the QAP lithology (AK 47)……. | 251 |
| Figure 4.10 | (A) Composition of pyroxenes from the QAP lithology and the adjacent amphibolite and ultramafic units…… | 252 |
| Figure 4.11 | (A) Composition of amphiboles from the QAP lithology, the adjacent amphibolite and ultramafic units, and the garnet-containing shear zone that cross cuts the QAP rocks, as well as amphiboles from Isua…… | 253 |
| Figure 4.12 | Photomicrographs and back-scattered electron detection (BSE) images of ultramafic and amphibolite units on either side of the QAP outcrop……..… | 254 |

Figure 4.13 Chemistry of garnets found in sample AK 33 and AK 48 from the QAP unit indicate a consistent and homogenous almandine composition, comprised predominantly of FeO (30 wt. %) and $Al_2O_3$ (21 wt. %), with lesser amounts of CaO (8 wt. %) and MgO (2 wt.%)……. 255
Figure 4.14 Proposed protolith for QAP lithology includes two different intercalated parent rocks…… 256
Figure A4.1 Shale-normalized REY patterns for BIFs from the IGB used in this study…….. 335
Figure A4.2 Shale-normalized REY patterns for BIFs from the BGB used in this study……... 336
Figure A4.3 Shale-normalized REY patterns for BIFs from the GF used in this study…….. 337

# Chapter I

# Introduction

## 1.1 Introduction

Banded iron formation (BIF) is a chemical sedimentary rock precipitated from seawater or a combination of seawater and hydrothermal fluids. BIF has the potential to preserve geochemical signatures critical to our interpretation of early Earth history because: (1) it is found both within the oldest fragments of supracrustal material and all within the Precambrian when fundamental changes in Earth's physical, biological and chemical evolution occurred, and (2) as chemical sediments, BIF may preserve a record of the environment in which it formed (Fedo, 2000; Klein, 2005; Ohmoto et al., 2006). Despite the importance of BIF in early Earth history, and decades of study owing to its economic significance, there is still much to learn regarding BIF composition and formative mechanisms, and its environmental interpretations. As BIF genesis models have evolved, so have ways to characterize BIF geochemistry. Application of more sophisticated approaches to analyzing complete rare earth element (REE) and trace-element geochemistry (e.g., Bau and Dulski, 1996; Bau et al., 1997a; Bau and Moller, 1993; Bekker et al., 2010; Bolhar et al., 2004; Derry and Jacobsen, 1990; Frei et al., 2008; Konhauser et al., 2005; Konhauser et al., 2009; Lawrence et al., 2006a; Lawrence and Kamber, 2006; Planavsky et al., 2010; Planavsky et al., 2009) coupled with iron isotopes (e.g., Anbar, 2004; Czaja et al., 2013; Johnson and Beard, 2006; Johnson et al., 2008a; Li et al., 2013; Planavsky et al., 2012; Rouxel et al., 2005), has led to advances in the understanding of BIF that could not have been easily predicted based on previously collected data.

Beyond understanding the formative mechanisms of BIF (e.g., Bekker et al., 2010; Beukes, 2004), several studies has applied characteristics of BIF geochemistry in a

metamorphosed rock sequence to investigating the proposed oldest life on Earth and possible environments of formation (c.f., Bolhar et al., 2004; Fedo and Whitehouse, 2002; Friend et al., 2008). Central to this debate is the idea that BIF records the presence of a retained hydrosphere and could serve as a host for trapped biosphere fragments. "Fingerprinting" of BIF (e.g., Bolhar et al., 2004; Kamber, 2009) via geochemical and/or isotopic methods could lead to a powerful way of recognizing BIF even if the rock has been significantly metamorphosed or altered since the time of deposition.

## 1.2 Background

### *1.2.1 Banded Iron Formation (BIF) Classification*

An iron formation is defined as "a chemical sediment, typically thin bedded or laminated, whose principal chemical characteristic is an anomalously high content of iron, commonly, but not necessarily, containing chert" (Bekker et al., 2010; James, 1954; Klein, 2005). The quintessential feature of BIF is the presence of alternating layers of iron-rich and silica-rich layers, which is usually expressed on several scales, from fine sub-millimeter-scale varve-like laminae to meter-scale bands (Klein, 2005; Trendall and Blockey, 1970).

BIF has been classified on the basis of mineralogical composition (James, 1954), proposed tectonic setting (Gross, 1965), and depositional environment (Kimberley, 1978). James' (1954) original facies concept included oxide-, silicate-, and carbonate-facies iron formation, all thought to correspond to different water depths. Chert and recrystallized quartz is present in nearly all types of BIF. Many BIF sequences, especially those of Archean age, have been exposed to varying degrees of metamorphism

and the minerals present in these units are the metamorphic products of the minerals discussed above.

Tectonic settings have been inferred by some based on BIF size and lithologic associations (Gross, 1965). *Algoma*-type BIFs are relatively small and associated with volcanoclastic and volcanic rocks. Total primary iron content is rarely > $10^{10}$ tons and typical lateral extents are < 10 km (Appel, 1980; Goodwin, 1973; James and Trendall, 1982). The depositional environment for this type of BIF is most often interpreted to be island arc/back arc basins and intracratonic rift zones (Gross, 1983; Veizer, 1983). *Superior*-type BIFs are larger and associated with sedimentary rocks. Total primary iron content > $10^{13}$ tons and can extend over $10^5$ $km^2$ (Beukes, 1973). It is thought that these types of BIF were deposited in relatively shallow marine environments under transgressing seas, floored by continental crust (Beukes, 1973; Gross, 1965; Simonson, 1985; Simonson and Hassler, 1996). The majority of older BIFs (early- to mid-Archean) are located in greenstone belts and are *Algoma*-type. Younger BIFs (late Archean to early Proterozoic) are generally thicker and more laterally extensive and represent a transition to *Superior*-type deposition (Klein and Beukes, 1992). This transition also includes oxide-facies bands becoming more common, such as in the ~2.9-3.0 Ga BIFs from Western Australia and Canada (Fyon et al., 1984; Groves and Batt, 1984).

An understanding of the origins of BIF may provide insight into conditions of the early lithosphere, hydrosphere, and atmosphere, reflecting a potentially intimate connection with oxygen concentration. Furthermore, BIF is particularly interesting because it can reveal the conditions and environments under which life may have evolved. Iron is used as a metabolic species by numerous microorganisms, such as

specific oxygenic- and anoxygenic-photoautotrophs and chemoferrotrophs (Brown, 2006). This has been used by some (Brown, 2006; Kappler et al., 2005; Konhauser et al., 2002; Tice and Lowe, 2004) to claim that BIF deposition, at least in part, was a microbially mediated process. However, direct, unequivocal evidence for a microbial role in BIF deposition has yet to be discovered. Claims for the earliest evidence of life on Earth have been based on the presence of isotopically light C in graphite inclusions within apatite crystals from a >3.8 Ga purported BIF from the island of Akilia in southwest Greenland (Dauphas et al., 2004; Mojzsis et al., 1996), although this claim is widely disputed (Fedo and Whitehouse, 2002; Fedo et al., 2006; Lepland et al., 2002; Lepland et al., 2011; Lepland and Whitehouse, 2011; Papineau et al., 2010; Whitehouse et al., 2009).

### *1.2.2 Iron in Solution*

Large amounts of ferric-iron ($Fe^{3+}$) in solution are only stable under very acidic conditions (pH <2). The occurrence of such strongly acidic solutions during the Precambrian cannot be accounted for by physiochemical processes, even with an extremely $CO_2$-rich environment (Belevtsev et al., 1982). Acidic thermal solutions are found in hydrothermal regions; however, such waters are rich in ferrous ($Fe^{2+}$), not ferric, iron. Because ferrous iron in solution is highly susceptible to oxidation, it seems unlikely that the Fe necessary to precipitate BIF could have been transported in the presence of free oxygen. This is in agreement with calculated values for $O_2$ concentrations in the Precambrian atmosphere (Klein, 2005; Pavlov and Kasting, 2002). In contrast to ferruginous species, the solubility of silica is predominantly independent of acidity (Chigira and Watanabe, 1994).

### *1.2.3 Depositional Environments and Mechanisms of BIF Deposition*

Both continental and hydrothermal settings have been suggested as likely Fe sources for BIF (Alibert and Mcculloch, 1993; Holland, 1973; Simonson, 1985). Based on extensive studies of rare earth element (REE) patterns and Nd isotopic signatures of BIFs, it is generally accepted that the source of Fe in the BIFs was hydrothermal waters released into the deep sea in a density-stratified ocean and carried into shallower waters by upwelling currents or plumes, possibly supplemented by normal continental drainage (Holland, 1973; Isley, 1995; Jacobsen and Pimental-Klose, 1988; Klein and Beukes, 1989; Konhauser et al., 2002; Morris and Horwitz, 1983). Si isotopes suggest a hydrothermal source for some of the silica in Algoma BIF (André et al., 2006; Heck et al., 2011), while silica in Superior BIF was derived from the continents (Brengman, 2014).

It is typically thought that iron-rich mesobands formed during major episodes of hydrothermal input, whereas periods of relative hydrothermal quiescence or the temporary failure of upwelling currents to transport hydrothermal fluids to the BIF depositional basin resulted in the genesis of silica-rich bands (Konhauser et al., 2002; Morris, 1993). However, a study examining the Ge/Si ratios of BIFs (Hamade et al., 2003) postulates decoupling the iron and silica fluxes, with the latter being derived predominantly from the weathering of continental crust rather than of hydrothermal origin. In this scenario, alternating chert- and iron-rich layers may reflect competing controls through dominance of continental and hydrothermal sources respectively (Hamade et al., 2003).

The pervasiveness of finely laminated, microbanded BIF, the likely fragile nature of the original gel-like Fe-rich precipitate, and the absence of a significant epiclastic component led to the conclusion that many BIFs were deposited in basins deeper than 200 m, which is the minimum depth for modern storm wave base (Trendall, 2002). Klein and Beukes (1989) proposed a model for BIF precipitation that involves a stratified water column in which the surface waters, during a regressive stage in the depositional basin, were the location of abundant organic carbon productivity and the setting of microbial limestones. The deeper waters, during a transgressive stage, were enriched in dissolved FeO, from a hydrothermal deep ocean source, were depleted in organic C relatively to shallower waters, and were the site of iron formation deposition. This model was supported by carbon isotopic studies that concluded that the ocean was stratified with regard to total carbonate, with the deeper water where the siderite-rich BIF precipitated was depleted in $^{13}C$ (Beukes and Klein, 1990).

The stratified ocean system appears to have started to break down in the middle Paleoproterozoic based on the appearance of oolitic and granular iron formations, such as those of the Lake Superior region, the Sokoman Iron Formation in the Labrador Trough, and the Nabberu Basin, Western Australia. After around 1.9 Ga, the oceans become more mixed and slightly less reducing, and iron formations disappear from the geologic record between 1.8 and 0.8 Ga (Bekker et al., 2010; Klein, 2005). Neoproterozoic iron formations are closely associated with glaciomarine deposits and are thought to reflect low oxygen conditions resulting from stagnation in the oceans beneath a near-global ice cover. This ice cover allowed for the buildup of dissolved Fe during a glacial period and deposition during interglacial periods (Klein, 2005).

In the classic model of BIF deposition, the presence of free oxygen in shallow water derived from oxygenic microbial photosynthesis resulted in the precipitation of iron oxides. Iron carbonates were derived from the reduction of iron oxides by organic matter brought in from shallow, nearshore environments (Beukes, 2004). Another popular model for Archean ferric iron oxide deposition invokes direct photosynthetic iron oxidation, through the presence of purple and green anaerobic photosynthetic bacteria and/or chemolithoautotrophic species such as *Gallionella ferruginea* in the euphotic zone, which couples the oxidation of ferrous iron to the reduction of $CO_2$ (Beukes, 2004; Kappler and Newman, 2004; Kappler et al., 2005; Konhauser et al., 2002). Other modes for magnetite formation include anaerobic production by dissimilatory iron-reducing microorganisms (Konhauser et al., 2005; Lovley, 2004; Lovley et al., 1987; Vargas et al., 1998) and magnetite biomineralization (Chang and Kirschvink, 1989).

A study by Konhauser et al. (2002) used the concentration of iron, trace metals, and nutrients in BIFs from the Hamersley Group, Australia and total cell production of two bacterial genera that are known to oxidize $Fe^{2+}$ as an energy source (*Gallionella* sp. and *Chromatium* sp.) to establish the ecological plausibility of bacteria to oxidize sufficient iron in the water column of the depositional basin to generate the bulk, if not all, of the ferric iron in BIFs. Based on documented growth rates for both *Gallionella* and *Chromatium*, calculations show that a minimum cell density of $4.3 \times 10^4$ cells/$cm^3$ for *Gallionella* or $5.7 \times 10^4$ cells/$cm^3$ for *Chromatium* would be required throughout basin to precipitate an annual BIF layer (Konhauser et al., 2002). These calculated cell densities are much less than the modern populations of mixed bacteria and other plankton assemblages growing in the photic zone of marine coastal waters ($10^6$ cells/$cm^3$) or the

open ocean ($10^5$-$10^6$ cells/$cm^3$). Additionally, in sites where $Fe^{2+}$ is abundant, such as iron-containing groundwater seeps, *Gallionella* densities have been reported to be as high as $10^9$ cells/$cm^3$, and in anoxic lakes, *Chromatium* can comprise > 98% of the total microbial population and reach densities in excess of $10^6$ cells/$cm^3$ (Konhauser et al., 2002).

In the scenario described by Konhauser et al. (2002) the oxidation of $Fe^{2+}$ by chemolithoautotrophic species produces iron hydroxide:

$$6Fe^{2+} + 0.5O_2 + CO_2 + 16\ H_2O \rightarrow CH_2O + 6Fe(OH)_3 + 12H^+$$

Also, certain purple and green bacterial couple $Fe^{2+}$ oxidation to the reduction of $CO_2$ during anoxygenic photosynthesis, which also produces iron hydroxide (Konhauser et al., 2002):

$$4Fe^{2+} + CO^2 + 11H_2O \rightarrow CH_2O + 4Fe(OH)_2 + 8H^+$$

Once buried, the ferric hydroxide would have transformed into: (1) siderite or magnetite through microbial Fe(III) reduction; (2) clays; or (3) hematite, through dehydration of any residual $Fe(OH)_3$, after the respiratory processes consumed the labile organic carbon fraction (Konhauser, 2007). Thus, in this model, all of the iron minerals in BIF are secondary minerals that form during diagenesis.

A completely abiotic model for BIF deposition invokes photochemical oxidation of ferrous iron under anaerobic conditions, which results in the precipitation of ferric iron oxides (Braterman and Cairns-Smith, 1987; Klein, 2005). However, the reconstruction of the 3.4 Ga Buck Reef Chert (Tice and Lowe, 2004) indicates that the entire euphotic zone was depleted in iron, which suggests that light-dependent mechanisms, such as abiotic photochemical oxidation and direct photosynthetic iron oxidation, were unlikely to have

occurred. Because these two mechanisms are the only ones known to oxidize ferrous to ferric iron under anaerobic conditions, some conclude that free oxygen must have been available to produce the iron-oxide formations precipitated during the Archean. Only two known processes are thought to have been able to produce free oxygen in the Archean: UV photolysis of water vapor in the upper atmosphere, which most models indicated would have been insignificant, and bacterial photosynthesis (Beukes, 2004; Braterman and Cairns-Smith, 1987; Kappler et al., 2005).

### *1.2.4 Trace Elements*

One useful tool for the examination of BIF is trace element geochemistry. A trace element is an element that is present in a rock in concentrations of less than 0.1 wt. % (i.e., less than 1000 ppm). Several groups of trace elements that are of particular geochemical interest are found in the periodic table, including the lanthanides or rare earth elements (REE). The REE comprise the series of metals from lanthanum (La) to lutetium (Lu). In addition, the element yttrium (Y) is also sometimes included because it has an ionic radius similar to that of the REE holmium (Ho). Typically, the low-atomic-number elements of the series (La to Sm) are termed the light rare earths (LREE), those with the higher atomic numbers (Gd to Lu) the heavy rare earths (HREE). As a result of its two valences, Eu behaves anomalously, thus making it neither a LREE nor HREE and forms the break between the two series.

REE and trace-element patterns in marine sediments have characteristic features that may be used as geochemical indicators to determine origins and depositional environments of marine sediments (Bau and Moller, 1993; Bolhar et al., 2004; Kamber, 2009; Kato and Nakamura, 2003; Murray et al., 1992). Analysis of REE, even in Earth's

oldest rocks, can be valuable because it is generally thought that REE of bulk sediments may be unaffected by post-depositional processes, including diagenesis, metamorphism, and weathering (McLennan and Taylor, 1991). This may hold true for BIFs too, because there is little evidence for REE mobility during metamorphism (e.g., Bau and Moller, 1993; Kato et al., 2006a). However, work has shown that REE patterns can be mobilized as a group (Fedo et al., 2010), and high volume seawater interaction with rocks can imprint a marine signal on igneous rocks (Brengman and Fedo, 2012).

REE typically exist in a trivalent oxidation state, but Ce and Eu are different because they can also exist in a tetravalent and divalent oxidation states, respectively. Both are important elements for providing constraints on paleo-ocean chemistry (Bolhar et al., 2004; Kato et al., 2006a). The Ce anomaly in seawater corresponds to varying redox conditions because rapid reduction or oxidation reactions between $Ce^{+3}$ and $Ce^{+4}$ (Kato et al., 2006a). The presence of either a positive or negative Ce anomaly suggests that redox-related Ce fractionation took place in the ocean, although only qualitatively because there is no linear relationship between the magnitude of Ce anomalies and the concentration of dissolved $O_2$ in seawater (Kato et al., 2006a).

### *1.2.5 Iron Isotopes*

In modern oceans, dissolved Fe contents are so low that their isotopic compositions are sensitive indicators of Fe sources and pathways. Iron isotopes are exceptional indicators of Fe redox cycling, particularly in low-temperature environments where isotopic fractionations are relatively large and significant pools of $Fe^{2+}$ and $Fe^{3+}$ may coexist (Johnson and Beard, 2006). If early Earth's atmosphere had significantly lower $O_2$ contents, lower levels of oxidants for Fe would have kept Fe in solution in

seawater for much longer periods than present. In the absence of an oxidant, the range in Fe isotope compositions of the fluxes to the Archean oceans would have been more restrictive than present, where both riverine and marine hydrothermal fluxes would have had a $\delta^{56}Fe$ of ~0 ‰ (Johnson and Beard, 2006). This is not what is seen in the rock record, with a wide range of mostly negative $\delta^{56}Fe$ values preserved in Proterozoic and Archean sedimentary rocks (Johnson and Beard, 2006). This contradiction can be explained if Archean Fe cycling involved interaction between anoxic and oxic reservoirs. An oxidant is required to reconcile the occurrence of positive $\delta^{56}Fe$ values in Archean sedimentary rocks and minerals through oxidation of seawater $Fe^{2+}$ (Johnson and Beard, 2006). However, the nature of the Archean oxidant is still heavily debated, with possibilities including atmospheric oxygen, UV-photo oxidation, and anaerobic photosynthetic bacteria (Johnson and Beard, 2006).

The Fe isotopic compositions of hematite, magnetite, Fe carbonate, and pyrite measured in BIFs are interpreted to reflect a combination of the following processes: mineral specific equilibrium isotope fractionation; variations in the isotopic compositions of the fluids from which they were precipitated; and the effects of metabolic processing of Fe by bacteria (Beard et al., 1999; Johnson et al., 2003). Experiments with dissimilatory Fe-reducing bacteria of the genus *Shewanella* algae grown on a ferrihydrite substrate indicate that the $\delta^{56}Fe$ of ferrous Fe in solution is isotopically lighter than the substrate by 1.3 ‰, suggesting that the range in $\delta^{56}Fe$ of sedimentary rocks, such as BIFs, may reflect biogenic fractionation (Beard et al., 1999).

## 1.3 Study Locales

### *1.3.1 BIF Through Time*

Banded iron formation occurs throughout the Precambrian geologic record, beginning at ~3.8 Ga and temporarily disappearing at 1.8 Ga, only to reappear between 0.8 and 0.6 Ga (Bekker et al., 2010; Klein, 2005). BIF overall volume reaches a maximum around 2.5 Ga in the Hamersley Range of Western Australia (2.6-2.45 Ga) and the Transvaal Supergroup of South Africa (2.5-2.3 Ga) (Johnson et al., 2003; Klein, 2005; Konhauser et al., 2002). Samples examined in this study represent spatial and temporal variability, coming from the ~3.8 Ga Isua Greenstone Belt, Greenland (Moorbath et al., 1973; Moorbath and Whitehouse, 1996; Nutman et al., 1997), the ~3.0 Ga Buhwa Greenstone Belt, Zimbabwe (Fedo and Eriksson, 1996; Fedo et al., 1995), and the ~1.9 Ga Gunflint Iron Formation, Minnesota and Ontario (Fralick et al., 2002).

### *1.3.2 Isua Greenstone Belt, Greenland*

At ~ 3.8 Ga in age, the Algoma-type Isua Greenstone Belt (IGB) of southern West Greenland is one of the oldest known and locally well preserved successions of Eoarchean supracrustal rocks on Earth (Appel et al., 1998; Fedo, 2000; Moorbath et al., 1973; Myers, 2001). The great antiquity and repeated claims for a fossil record (Appel and Moorbath, 1999; Pflug and Jaeschke-Boyer, 1979; Rosing, 1999; Schidlowski et al., 1979) makes it one of the prime astrobiological destinations on Earth. The IGB forms an arcuate belt ~35 km long and up to 2.5 km wide that is comprised of sedimentary units, felsic volcanic rocks, metacarbonate rocks, ultramafic rocks, and mafic rocks with relict pillow lava structures. The most abundant metasedimentary rocks are chemically precipitated chert and magnetite-quartz layered BIF that are interpreted to have been

deposited in a shallow marine setting (Fedo et al., 2001). After deposition, all rocks experienced multiple episodes of amphibolite-facies metamorphism and pervasive carbonate and potassium metasomatism (Appel et al., 1998; Dymek and Klein, 1988; Fedo et al., 2001; Fedo et al., 2006; Myers and Crowley, 2000; Rollinson, 2002; Rosing, 1999), as well as ductile deformation (Komiya et al., 1999; Whitehouse and Fedo, 2007).

### *1.3.3 Buhwa Greenstone Belt, Zimbabwe*

The ~3.0 Ga Buhwa Greenstone Belt (BGB) is located along the southern margin of the Archean Zimbabwe craton and just north of the inferred thrust front of the granulite-facies Northern Marginal Zone (NMZ) of the Limpopo Belt (Fedo and Eriksson, 1995; Fedo and Eriksson, 1996; Fedo et al., 1995). Metamorphism varies across the strike of the BGB, increasing from greenschist facies (dominant metamorphic grade) in the NW to granulite facies in the SE. The cover succession of the BGB contains greenschist-facies sedimentary rocks, with lesser volcanic rocks, and can be divided into a western shelf assemblage and an eastern basinal assemblages, connected by a zone of transitional deposits (Fedo and Eriksson, 1996).

The western shelf facies, in ascending stratigraphic order, consists of quartzarenite, interbedded quartzarenite and shale, shale, and iron-formation. The Superior-type iron formation ranges in thickness from 300-500 m, and consists of laterally persistent, mm-thick, alternating bands of white chert, red chert, and hematite. Transitional deposits contain predominantly green, tan, and black shale (now phyllite), with lesser amounts of iron formation and muddy sandstone. The iron formation here has two variants. The first consists of alternating bands of iron oxide, red chert, and white chert, which represents the along-strike extension of the western shelf iron formation.

The second variant consists of mm-scale alternations of recrystallized quartz and opaque iron oxide minerals that is strikingly similar to iron formation of the eastern basinal association. The eastern assemblage consists of metamorphosed mafic-ultramafic lavas, possible carbonate, recrystallized metachert, and Algoma-type iron formation. The iron formation of the eastern assemblage has a max thickness of ~50 m and is comprised of mm-scale alternating bands of quartz and opaque iron oxides (Fedo and Eriksson, 1996).

### *1.3.4 Gunflint Iron Formation, Minnesota and Canada*

Near the NW shore of Lake Superior, along the Minnesota-Ontario border, the Gunflint Trail provides access to Archean, Paleoproterozoic, and Mesoproterozoic rocks. The Archean granite-greenstone terrane of the Wawa subprovince of the Superior Province consists of a suite of ~2,700 Ma metavolcanic rocks that were intruded at ~2689 Ma by the Saganaga Tonalite (Jirsa and Weiblen, 2007; Miller et al., 1987). These Archean units were unconformably overlain by Paleoproterozic sedimentary rocks of the Animike Group (ca. 1870-1830 Ma), which includes the Gunflint Iron Formation. Mesoproterozoic rifting is evident from a series of diabase sills and dikes (Logan intrusions) (ca. 1115 Ma), as well as anorthositic and felsic intrusions and many individual layered intrusions of tholeiitic affinity (Duluth Complex) (ca. 1100 Ma; Miller et al., 1987; Jisra and Weiblen, 2007).

Animike Group rocks crop out along a NE-SW-trending belt that extends ~175 km from Thunder Bay, Ontario to ~19 km west of the Gunflint Trail in northern Minnesota, where it is truncated by the Mesoproterozoic Duluth Complex (Floran and Papike, 1978; Jirsa and Weiblen, 2007; Miller et al., 1987). In Minnesota, the Animikie Group consists of magnetite-rich rocks of the Gunflint Iron Formation and overlying slate

and siltstone of the Rove Formation. Depositional models for the Gunflint Iron Formation show shallowing-upward, decameter-scale cycles consisting of a lower unit of laminated, Fe- and Si-rich chemical mudstone that transitions into an upper unit dominated by progradational trough cross-stratified chert grainstones (Pufahl and Fralick, 2004).

### 1.4 The Dissertation

The dissertation has three primary research objectives. The first is to investigate ancient oceanic and atmospheric redox conditions through the examination of rare earth and trace element concentrations in banded iron formation (BIF) samples from the >3.7 Ga Isua Greenstone Belt in southwest Greenland, the ~3.0 Ga Buhwa Greenstone Belt in Zimbabwe, and the ~1.9 Ga Gunflint Iron Formation in Minnesota and Ontario (Chapter 2). For this study, a two-fold approach to characterizing Paleoproterozoic ocean redox conditions is presented. First, trace-element geochemistry, including the redox-sensitive Ce, was used from the Gunflint Formation to determine paleo-ocean oxidation state. Second, the effects of atmospheric oxygenation on continental weathering were reconstructed by examining changes in redox-sensitive elements through time to determine if a change in geochemistry could be detected in BIFs deposited before and after the Great Oxidation Event.

Secondly, both whole rock geochemistry and the geochemistry of specific individual mineral grains of magnetite and hematite for samples of oxide-facies BIF ranging in age from ~3.7 Ga to ~1.9 Ga were analyzed to determine the variability and range in mineral geochemistry and to determine how well the whole rock geochemistry represents the average mineral chemistry (Chapter 3). The iron isotopic compositions of

BIFs, both at the whole rock and individual band scales, were examined to determine the degree of variability between the signature of the whole rock and of individual bands.

The third research objective is to examine the origins of controversial >3.65 Ga quartz-amphibole-pyroxene (QAP) rocks from Akilia, SW Greenland using an integrated, detailed, field and mineral composition appraisal of the critical geologic contacts and lithologies to address issues regarding the age and origin of QAP (Chapter 4). Structural data were collected to determine the nature (tectonic or igneous) of the critical contact used to date the QAP lithology. Whole rock geochemistry from a number of novel specimens relative to the protolith discussion sets the framework for determining mafic mineral (amphibole and pyroxene) and garnet composition by electron microprobe.

**1.5 Significance**

One of the goals of NASA's Astrobiology Roadmap is "*Understand how past life on Earth interacted with its changing planetary and Solar System environment. Investigate the historical relationship between Earth and its biota by integrating evidence from both the geologic and biomolecular records of ancient life and its environments.*" (Des Marais et al., 2003). Understanding the chemical and physical environment when early life evolved and covered the Earth is essential in addressing this goal, and banded iron formations provides a mechanism for preserving such environments. The biogeochemistry of iron is integral to Earth's biosphere, and its isotopic record helps us understand how the biosphere evolved. Examining the geochemistry and Fe isotopes of banded iron formation will provide a window into the composition of early Earth's atmosphere, hydrosphere, and biosphere.

**References**


Alibert, C., Mcculloch, M.T., 1993. Rare-Earth Element and Neodymium Isotopic Compositions of the Banded Iron-Formations and Associated Shales from Hamersley, Western-Australia. Geochimica et Cosmochimica Acta 57, 187-204.

Anbar, A.D., 2004. Iron stable isotopes: beyond biosignatures. Earth and Planetary Science Letters 217, 223-236.

André, L., Cardinal, D., Alleman, L., Moorbath, S., 2006. Silicon isotopes in ~3.8 Ga West Greenland rocks as clues to the Eoarchaean supracrustal Si cycle. Earth and Planetary Science Letters 245, 162-173.

Appel, P.W.U., 1980. On the Early Archean Isua Iron-Formation, West-Greenland. Precambrian Research 11, 73-87.

Appel, P.W.U., Fedo, C.M., Moorbath, S., Myers, J.S., 1998. Early Archean Isua supracrustal belt, West Greenland: pilot study of the Isua Multidisciplinary Research Project. Journal of Greenland Survey Bulletin 180, 94-99.

Bau, M., Dulski, P., 1996. Distribution of yttrium and rare-earth elements in the Penge and Kuruman iron-formations, Transvaal Supergroup, South Africa. Precambrian Research 79, 37-55.

Bau, M., Moller, P., 1993. Rare earth element systematics of the chemically precipitated component in Early Precambrain iron formations and the evolution of the terrestrial atmosphere-hydrosphere-lithosphere system. Geochimica et Cosmochimica Acta 57, 2239-2249.

Bau, M., Hohndorf, A., Dulski, P., Beukes, N.J., 1997. Sources of Precambrian rare-earth elements and iron in Paleoproterozoic iron-formations from the Transvaal Supergroup, South Africa - evidence from neodymium isotopes. J Geol 105, 121-129.

Beard, B.L., Johnson, C.M., Cox, L., Sun, H., Nealson, K.H., Aguilar, C., 1999. Iron isotope biosignatures. Science 285, 1889-1892.

Bekker, A., Slack, J.F., Planavsky, N., Krapez, B., Hofmann, A., Konhauser, K.O., Rouxel, O.J., 2010. Iron Formation: The Sedimentary Product of a Complex Interplay among Mantle, Tectonic, Oceanic, and Biospheric Processes. Econ Geol 105, 467-508.

Belevtsev, Y., Belevstev, R., Siroshtan, R., 1982. The Krivoy Rog Basin, in: Trendall, A.F., Morris, R.C. (Eds.), Iron-Formations: Facts and Problems. Elsevier, Amsterdam, pp. 211-252.

Beukes, N., 1973. Precambrian iron-formations of southern Africa. Econ Geol 68, 960-1024.

Beukes, N., 2004. Biogeochemistry - Early options in photosynthesis. Nature 431, 522-523.

Beukes, N.J., Klein, C., 1990. Geochemistry and Sedimentology of a Facies Transition - from Microbanded to Granular Iron-Formation - in the Early Proterozoic Transvaal Supergroup, South-Africa. Precambrian Research 47, 99-139.

Bolhar, R., Kamber, B.S., Moorbath, S., Fedo, C.M., Whitehouse, M.J., 2004. Characterisation of early Archaean chemical sediments by trace element signatures. Earth and Planetary Science Letters 222, 43-60.

Braterman, P.S., Cairns-Smith, A.G., 1987. Photoprecipitation and the Banded Iron-Formations - Some Quantitative Aspects. Origins of Life and Evolution of the Biosphere 17, 221-228.

Brengman, L.A., 2014. From source to sink: Silicon isotope composition of bedrock, detritial quartz arenites, chert and BIF from the ~3 Ga Buhwa Greenstone Belt, Zimbabwe, Geological Society of American Annual Meeting, Vancouver, British Columbia.

Brengman, L.A., Fedo, C.M., 2012. Origin of BIF-like jasperlite in the 2.72 Ga Hunter Mine Group. Abitibi Greenstone Belt, Quebec by metasomatic replacement of felsic volcanic rocks, Geologic Society of America Annual Meeting, Charlotte, North Carolina.

Brown, D.A., 2006. Microbial mediation of iron mobilization and deposition in iron formations since the early Precambrian, in: Kesler, S., Ohmoto, H. (Eds.), Evolution of Early Earth's Atmosphere, Hydrosphere, and Biosphere – Constraints From Ore Deposits. The Geological Soceity of America Memoir, pp. 239-256.

Chang, S.B.R., Kirschvink, J.L., 1989. Magnetofossils, the Magnetization of Sediments, and the Evolution of Magnetite Biomineralization. Annual Review of Earth and Planetary Sciences 17, 169-195.

Chigira, M., Watanabe, M., 1994. Silica precipitation behavior in a flow field with negative temperature gradients. Journal of Geophysical Research 99, 15539-15548.

Czaja, A.D., Johnson, C.M., Beard, B.L., Roden, E.E., Weiqiang, L., Moorbath, S., 2013. Biological Fe oxidation controlled deposition of banded iron formation in the ca. 3770 Ma Isua Supracrustal Belt (West Greenland). Earth and Planetary Science Letters 363, 192-203.

Dauphas, N., van Zuilen, M., Wadhwa, M., Davis, A.M., Marty, B., Janney, P.E., 2004. Clues from Fe isotope variations on the origin of early Archean BIFs from Greenland. Science 306, 2077-2080.

Derry, L.A., Jacobsen, S.B., 1990. The Chemical Evolution of Precambrian Seawater - Evidence from Rees in Banded Iron Formations. Geochimica et Cosmochimica Acta 54, 2965-2977.

Des Marais, D.J., Allamandola, L.J., Benner, S.A., Boss, A.P., Deamer, D., Falkowski, P.G., Farmer, J.D., Hedges, S.B., Jakosky, B.M., Knoll, A.H., Liskowsky, D.R., Meadows, V.S., Meyer, M.A., Pilcher, C.B., Nealson, K.H., Spormann, A.M., Trent, J.D., Turner, W.W., Woolf, N.J., Yorke, H.W., 2003. The NASA Astrobiology Roadmap. Astrobiology 3, 219-235.

Dymek, R.F., Klein, C., 1988. Chemistry, Petrology and Origin of Banded Iron-Formation Lithologies from the 3800-Ma Isua Supracrustal Belt, West Greenland. Precambrian Research 39, 247-302.

Fedo, C.M., 2000. Setting and origin for problematic rocks from the > 3.7 Ga Isua Greenstone Belt, southern west Greenland: Earth's oldest coarse elastic sediments. Precambrian Research 101, 69-78.

Fedo, C.M., Eriksson, K.A., 1995. Geologic setting and ideas concerning the origin of the iron-ore deposits at Buhwa, Zimbabwe, in: Blenkinsop, T.G., Tromp, P.L. (Eds.), Sub-Saharan Economic Geology. A.A. Balkema Publishers, Vermont, pp. 43-53.

Fedo, C.M., Eriksson, K.A., 1996. Stratigraphic framework of the similar to 3.0 Ga Buhwa greenstone belt: A unique stable-shelf succession in the Zimbabwe Archean Craton. Precambrian Research 77, 161-178.

Fedo, C.M., Whitehouse, M.J., 2002. Metasomatic origin of quartz-pyroxene rock, Akilia, Greenland, and implications for Earth's earliest life. Science 296, 1448-1452.

Fedo, C.M., Eriksson, K.A., Blenkinsop, T.G., 1995. Geologic history of the Archean Buhwa Greenstone Belt and surrounding granite-gneiss terrane, Zimbabwe, with implications for the evolution of the Limpopo Belt. Canadian Journal of Earth Sciences 32, 1977-1990.

Fedo, C., Hage, M., Schoenberg, R., Whitehouse, M., 2010. Can Fe isotopes be used to fingerprint Precambrian BIF?, Goldschmidt Knoxville, TN.

Fedo, C.M., Myers, J.S., Appel, P.W.U., 2001. Depositional setting and paleogeographic implications of earth's oldest supracrustal rocks, the > 3.7 Ga Isua Greenstone belt, West Greenland. Sediment Geol 141, 61-77.

Fedo, C.M., Whitehouse, M.J., Kamber, B.S., 2006. Geological constraints on detecting the earliest life on Earth: a perspective from the Early Archaean (older than 3.7 Gyr) of southwest Greenland. Philos Trans R Soc Lond B Biol Sci 361, 851-867.

Floran, R.J., Papike, J.J., 1978. Mineralogy and Petrology of Gunflint Iron Formation, Minnesota-Ontario - Correlation of Compositional and Assemblage Variations at Low to Moderate Grade. Journal of Petrology 19, 215-288.

Fralick, P., Davis, D.W., Kissin, S.A., 2002. The age of the Gunflint Formation, Ontario, Canada: single zircon U Pb age determinations from reworked volcanic ash. Canadian Journal of Earth Sciences 39, 1085-1091.

Frei, R., Dahl, P.S., Duke, E.F., Frei, K.M., Hansen, T.R., Frandsson, M.M., Jensen, L.A., 2008. Trace element and isotopic characterization of Neoarchean and Paleoproterozoic iron formations in the Black Hills (South Dakota, USA): Assessment of chemical change during 2.9–1.9Ga deposition bracketing the 2.4–2.2Ga first rise of atmospheric oxygen. Precambrian Research 162, 441-474.

Friend, C.R.L., Nutman, A.P., Bennett, V.C., Norman, M.D., 2008. Seawater-like trace element signatures (REE + Y) of Eoarchaean chemical sedimentary rocks from southern West Greenland, and their corruption during high-grade metamorphism. Contributions to Mineralogy and Petrology 155, 229-246.

Fyon, J., Schwarts, H., Crocket, J., 1984. Carbonization and gold mineralization in the Timmins area, Abitibi greenstone belt: Genetic links with Archean mantle CO2-degassing and lower crust granulization. Geological Association of Canada Program with Abstract 9, 65.

Goodwin, A.M., 1973. Archean volcanogenic iron-formation of the Canadian shield. Science Terra 9, 23-34.

Gross, G.A., 1965. Geology of iron deposits in Canada I. General geology and evaluation of iron deposits. Geological Survey of Canada Economic Geology Report 22.

Gross, G.A., 1983. Tectonic systems and the deposition of iron formation Precambrian Research 20, 171-187.

Groves, D.I., Batt, W., 1984. Spatial and temporal variations of Archean metallogenic association in terms of evolution of granitoid-greenstone terraines with particular emphasis on Western Australia, in: Kroner, A., Hanson, G., Goodwin, A.M. (Eds.), Archean Geochemistry. Springer-Verlag, Berlin, pp. 73-98.

Hamade, T., Konhauser, K.O., Raiswell, R., Goldsmith, S., Morris, R.C., 2003. Using Ge/Si ratios to decouple iron and silica fluxes in Precambrian banded iron formations. Geology 31, 35-38.

Heck, P.R., Huberty, J.M., Kita, N.T., Ushikubo, T., Kozdon, R., Valley, J.W., 2011. SIMS analysis of silicon and oxygen isotope ratios for quartz from Archean and Paleoproterozoic banded iron formations. Geochimica et Cosmochimica Acta 75, 5879-5891.

Holland, H.D., 1973. Ocean - possible srouce of iron in iron-formations. Econ Geol 68, 1169-1172.

Isley, A.E., 1995. Hydrothermal Plumes and the Delivery of Iron to Banded Iron-Formation. J Geol 103, 169-185.

Jacobsen, S.B., Pimental-Klose, M., 1988. A Nd isotope study of the Hamersley and Michipicoten banded iron formations: The source of REE and Fe in Archean oceans. Earth and Planetary Science Letters 87, 29-44.

James, H., 1954. Sedimentary facies of iron formations. Econ Geol 49, 235-293.

James, H., Trendall, A.F., 1982. Banded iron formation: Distribution in time and paleoenvironmental significance, in: Holland, H.D., Schidlowski, M. (Eds.), Mineral Deposits and the Evolution of the Biosphere. Spring-Verlag, NY, pp. 199-218.

Jirsa, M.A., Weiblen, P.W., 2007. Geology along the Gunflint Trail. 53rd Annual Institute on Lake Superior Geology Field Trip Guide 6.

Johnson, C.M., Beard, B.L., 2006. Fe isotopes: An emerging technique for understanding modern and ancient biogeochemical cycles. GSA Today 16, 4.

Johnson, C.M., Beard, B.L., Beukes, N.J., Klein, C., O'Leary, J.M., 2003. Ancient geochemical cycling in the Earth as inferred from Fe isotope studies of banded iron formations from the Transvaal Craton. Contributions to Mineralogy and Petrology 144, 523-547.

Johnson, C.M., Beard, B.L., Klein, C., Beukes, N.J., Roden, E.E., 2008. Iron isotopes contrain biologic and abiologic processes in banded iron formation genesis. Geochimica et Cosmochimica Acta 72, 151-169.

Kamber, B.S., 2009. Geochemical fingerprinting: 40 years of analytical development and real world applications. Applied Geochemistry 24, 1074-1086.

Kappler, A., Newman, D.K., 2004. Formation of Fe(III)-minerals by Fe(II)-oxidizing photoautotrophic bacteria 1. Geochimica et Cosmochimica Acta 68, 1217-1226.

Kappler, A., Pasquero, C., Konhauser, K.O., Newman, D.K., 2005. Deposition of banded iron formations by anoxygenic phototrophic Fe(II)-oxidizing bacteria. Geology 33, 865.

Kato, Y., Nakamura, K., 2003. Origin and global tectonic significance of Early Archean cherts from the Marble Bar greenstone belt, Pilbara Craton, Western Australia. Precambrian Research 125, 191-243.

Kato, Y., Yamaguchi, K., Ohmoto, H., 2006. Rare earth elements in Precambrian banded iron formations: Secular changes of Ce and Eu anomalies and evolution of atmospheric oxygen, in: Kesler, S., Ohmoto, H. (Eds.), Evolution of Early Earth's Atmosphere, Hydrosphere, and Biosphere - Constraints from Ore Deposits. Geological Society of America, Boulder, pp. 269-289.

Kimberley, M.M., 1978. Paleoenvironmental classification of iron formations. Econ Geol 73, 215-229.

Klein, C., 2005. Some Precambrian banded iron-formations (BIFs) from around the world: Their age, geologic setting, mineralogy, metamorphism, geochemistry, and origins. American Mineralogist 90, 1473-1499.

Klein, C., Beukes, N., 1992. Proterozoic iron-formations, in: Conder, K. (Ed.), Proterozoic Crustal Evolution. Elsevier, Amsterdam, pp. 383-418.

Klein, C., Beukes, N.J., 1989. Geochemistry and sedimentology of a facies transition from limestone to iron-formation deposition in the Early Proterozoic Transvaal Supergroup, South-Africa. Econ Geol 84.

Komiya, T., Maruyama, S., Masuda, T., Nohda, S., Hayashi, M., Okamoto, K., 1999. Plate Tectonics at 3.8-3.7 Ga: Field Evidence from the Isua Accretionary Complex, Southern West Greenland. The Journal of Geology 107, 515-554.

Konhauser, K., 2007. Introduction to Geomicrobiology. Blackwell Publishing, Massachusetts.

Konhauser, K.O., Hamade, T., Raiswell, R., Morris, R.C., Ferris, F.G., Southam, G., Canfield, D.E., 2002. Could bacteria have formed the Precambrian banded iron formations? Geology 30, 1079-1082.

Konhauser, K.O., Newman, D.K., Kappler, A., 2005. The potential significance of microbial Fe(III) reduction during deposition of Precambrian banded iron formations. Geobiology 3, 167-177.

Konhauser, K.O., Pecoits, E., Lalonde, S.V., Papineau, D., Nisbet, E.G., Barley, M.E., Arndt, N.T., Zahnle, K., Kamber, B.S., 2009. Oceanic nickel depletion and a methanogen famine before the Great Oxidation Event. Nature 458, 750-753.

Lawrence, M.G., Kamber, B.S., 2006. The behaviour of the rare earth elements during estuarine mixing—revisited. Marine Chemistry 100, 147-161.

Lawrence, M., Greig, A., Collerson, K., Kamber, B., 2006. Direct quantification of rare earth element concentrations in natural waters by ICP-MS. Applied Geochemistry 21, 839-848.

Lepland, A., Whitehouse, M.J., 2011. Metamorphic alteration, mineral paragenesis and geochemical re-equilibration of early Archean quartz-amphibole-pyroxene gneiss from Akilia, Southwest Greenland. International Journal of Earth Sciences 100, 1-22.

Lepland, A., Arrhenius, G., Cornell, D., 2002. Apatite in early Archean Isua supracrustal rocks, southern West Greenland: its origin, association with graphite and potential biomarker. Precambrian Research 119, 221-241.

Lepland, A., van Zuilen, M.A., Philippot, P., 2011. Fluid-deposited graphite and its geobiological implications in early Archean gneiss from Akilia, Greenland. Geobiology 9.

Li, W., Huberty, J.M., Beard, B.L., Kita, N.T., Valley, J.W., Johnson, C.M., 2013. Contrasting behavior of oxygen and iron isotopes in banded iron formations revealed by *in situ* isotopic analysis. Earth and Planetary Science Letters 384, 132-143.

Lovley, D.R., 2004. Potential role of dissimilatory iron reduction in the early evolution of microbial respiration, in: Seckback, J. (Ed.), Origins, Evolution and Biodiversity of Microbial Life. Kluwer, Netherlands, pp. 301-313.

Lovley, D.R., Stolz, J., Nord, G., 1987. Anaerobic production of magnetite by a dissimilatory iron-reducing microorganism. Nature 330, 252-254.

McLennan, S.M., Taylor, R., 1991. Sedimentary rocks and crustal evolution: Tectonic setting and secular trends. J Geol 99, 1-21.

Miller, J.D., Morey, G.B., Weiblen, P.W., 1987. Seagull Lake - Gunflint Lake area: A classical Precambrian stratigraphic sequence in northeastern Minnesota. America Continental Field Guide - North-Central Section, 47-51.

Mojzsis, S.J., Arrhenius, G., McKeegan, K.D., Harrison, T.M., Nutman, A.P., Friend, C.R.L., 1996. Evidence for life on Earth before 3,800 million years ago. Nature 384, 55-59.

Moorbath, S., Whitehouse, M.J., 1996. Age of the Isua supracrustal sequence of West Greenland, in: Chela-Flores, J., Raulin, F. (Eds.), Chemical Evoultion: Physics of the Origin and Evoultion of Life. Kluwer Academic Publishers, pp. 87-95.

Moorbath, S., O'Nions, R.K., Pankhurst, R.J., 1973. Early Archaean age for the Isua Iron Formation, West Greenland. Nature 245, 138-139.

Morris, R.C., 1993. Genetic modeling for banded iron formation of the Hamersley Group Pilbara craton, Western Australia. Precambrian Research 60, 243-286.

Morris, R.C., Horwitz, R., 1983. The origin of the iron-formation-rich Hamersley Group of Western Australia: Deposition on a platform. Precambrian Research 21, 273-297.

Murray, R.W., Tenbrink, M.R.B., Gerlach, D.C., Russ, G.P., Jones, D.L., 1992. Interoceanic Variation in the Rare-Earth, Major, and Trace-Element Depositional Chemistry of Chert - Perspectives Gained from the Dsdp and Odp Record. Geochimica et Cosmochimica Acta 56, 1897-1913.

Myers, J.S., 2001. Protoliths of the 3.8-3.7 Ga Isua greenstone belt, West Greenland. Precambrian Research 105, 129-141.

Myers, J.S., Crowley, J.L., 2000. Vestiges of life in the oldest Greenland rocks? A review of early Archean geology in the Godthabsfjord region, and reappraisal of field evidence for > 3850 Ma life on Akilia. Precambrian Research 103, 101-124.

Nutman, A.P., Mojzsis, S.J., Friend, C.R.L., 1997. Recognition of >3850 Ma water-lain sediments in West Greenland and their significance for the early Archean Earth. Geochimica et Cosmochimica Acta 61, 2475-2484.

Ohmoto, H., Watanabe, Y., Yamaguchi, K., Naraoka, H., Kakegawa, T., Haruna, M., Hayashi, K., Kato, Y., 2006. Chemical and biological evolution of early Earth: constraints from banded iron-formation, in: Kessler, S.E., Ohmoto, H. (Eds.), Evolution of the Atmosphere, Hydrosphere, and Biosphere on Early Earth: Constrainsts from Ore Deposits. Geological Soceity of America, Denver.

Papineau, D., De Gregorio, B.T., Stroud, R.M., Steele, A., Pecoits, E., Konhauser, K., Wang, J., Fogel, M.L., 2010. Ancient graphite in the Eoarchean quartz-pyroxene rocks from Akilia in southern West Greenland II: Isotopic and chemical compositions and comparison with Paleoproterozoic banded iron formations. Geochimica et Cosmochimica Acta 74, 5884-5905.

Pavlov, A., Kasting, J., 2002. Mass-independent fractionation of sulfur isotopes in Archean sediments: Strong evidence for an anoxic Archean atmosphere. Astrobiology 2, 27-41.

Planavsky, N., Bekker, A., Rouxel, O., Kamber, B., Hofmann, A., Knudsen, A., Lyons, T.W., 2010. Rare Earth Element and yttrium compositions of Archean and Paleoproterozic Fe formations revisited: New perspctives on the significance and mechanics of depositions. Geochimica et Cosmochimica Acta 74, 6387-6405.

Planavsky, N., Rouxel, O., Bekker, A., Shapiro, R., Fralick, P., Knudsen, A., 2009. Iron-oxidizing microbial ecosystems thrived in late Paleoproterozoic redox-stratified oceans. Earth and Planetary Science Letters 286, 230-242.

Planavsky, N., Rouxel, O.J., Bekker, A., Hofmann, A., Little, C.T.S., Lyons, T.W., 2012. Iron isotope composition of some Archean and Proterozoic iron formations. Geochimica et Cosmochimica Acta 80, 158-169.

Pufahl, P.K., Fralick, P.W., 2004. Depositional controls on Palaeoproterozoic iron formation accumulation, Gogebic Range, Lake Superior region, USA. Sedimentology 51, 791-808.

Rollinson, H., 2002. The metamorphic history of the Isua Greenstone Belt, West Greenland. Geological Society, London, Special Publications 199, 329-350.

Rosing, M.T., 1999. 13C-Depleted Carbon Microparticles in >3700-Ma Sea-Floor Sedimentary Rocks from West Greenland. Science 283, 674-676.

Rouxel, O., Bekker, A., Edwards, K., 2005. Iron isotope constraints on the Archean and Paleoproterozoic ocean redox state. Science 307, 1088-1091.

Simonson, B., 1985. Sedimentalogical constraints on the origins of the Precambrian iron-formations. Geological Society of America Bulletin 96, 244-252.

Simonson, B., Hassler, S., 1996. Was the deposition of large Precambrian iron formations linked to a major marine transgression? J Geol 104, 665-676.

Tice, M., Lowe, D.R., 2004. Photosynthetic microbial mats in the 3,416-My-old ocean. Nature 431, 549-552.

Trendall, A.F., 2002. The significance of iron-formation in the Precambrian stratigraphic record. Special Publication International Association of Sedimentalogists 33, 33-66.

Trendall, A.F., Blockey, J., 1970. The iron-formations of the Precambrian Hamersley Group, Western Australia. Geological Survey Western Australia Bulletin 119, 366.

Vargas, M., Keshefi, K., Blunt-Harris, E., Lovley, D.R., 1998. Microbiological evidence for Fe(III) reduction on early Earth. Nature 395, 65-67.

Veizer, J., 1983. Geologic evolution of the Archean - Early Proterozoic Earth, in: Schopf, J.W. (Ed.), Earth's Earliest Biosphere. Princeton University Press, NJ, pp. 240-259.

Whitehouse, M.J., Fedo, C.M., 2007. Microscale heterogeneity of Fe isotopes in >3.71 Ga banded iron formation from the Isua Greenstone Belt, southwest Greenland. Geology 35, 719.

Whitehouse, M.J., Myers, J.S., Fedo, C.M., 2009. The Akilia Controversy: field, structural and geochronological evidence questions interpretations of >3.8 Ga life in SW Greenland. Journal of the Geological Society 166, 335-348.

# Chapter II

# Evidence for an Oceanic Oxycline and Oxidative Continental Weathering in the Late Paleoproterozoic Based on U-Pb-REE Systematics in Banded Iron Formation

**Abstract**

Rare earth and trace element concentrations in banded iron formation (BIF) samples from the >3.7 Ga Isua Greenstone Belt in southwest Greenland, the ~3.0 Ga Buhwa Greenstone Belt in Zimbabwe, and the ~1.9 Ga Gunflint Iron Formation in Minnesota and Ontario were used to examine oceanic and atmospheric redox conditions. In general, Archean BIFs do not display substantial negative or positive shale-normalized Ce anomalies. After the Great Oxidation Event (GOE), however, Gunflint BIF samples display both negative and positive shale-normalized Ce anomalies. In fully ventilated oceans of the Phanerozoic, even deep water has a strong negative Ce anomaly. The co-occurrence of samples with both negative and positive Ce anomalies suggests deposition both above and below an oxycline, and supports the widely held notion that the Paleoproterozoic deep ocean was not fully ventilated. An increase in the range of the light rare earth elements to heavy rare earth elements (LREE/HREE) ratio and a decrease in the $Y_{SN}/Ho_{SN}$ ratio in post-GOE BIF provide additional support for the presence of an oxycline. Despite evidence for a persistent marine oxycline, an increase in the concentration of Mo, Co, V, Cr, and U/Pb after the GOE compared to before the GOE, indicates that oxidative continental weathering was active by 1.9 Gya.

## 2.1 Introduction

Banded iron formation (BIF), a chemical sedimentary rock primarily precipitated from seawater, has a depositional record that spans over 3 billion years of Earth's history. As such, BIFs may provide data critical to our understanding of geobiologic systems, including ocean-atmosphere oxidation through the Precambrian. Despite the importance of BIF to understanding early Earth history and decades of study driven by its economic importance, there remains much to learn about BIF, its composition and formative mechanisms, and its implication for Earth evolution (Beukes, 2004). In particular, application of more advanced analytical approaches to determining rare earth element (REE) and trace-element geochemistry (Bau and Dulski, 1996; Derry and Jacobsen, 1990; Frei et al., 2008; Konhauser et al., 2005; Konhauser et al., 2009; Lawrence et al., 2006a; Lawrence and Kamber, 2006; Planavsky et al., 2009) has led to a more sophisticated understanding of BIF than that possible from previously collected data.

The classic and most widely accepted model for BIF deposition requires the oxidation of high concentrations of dissolved ferrous iron (Cloud, 1965) that resulted from: (1) a reducing atmosphere (Bekker et al., 2004; Holland, 1984) (2) low marine sulfate concentrations (Canfield, 1998; Canfield et al., 2000; Scott et al., 2008), and (3) a hydrothermal iron flux that was not precipitated near the vent sites owing to a lack of free oxygen in deep ocean water (Kump and Seyfried, 2005). The processes of iron oxidation, however, continue to be debated.

Photo-oxidation by a high flux of ultraviolet photons that would have reached the Earth's surface prior to the rise of atmospheric oxygen and the formation of a protective ozone layer has been proposed as a possible oxidation mechanism (Anbar and Holland,

1992; Braterman and Cairns-Smith, 1987; Cairns-Smith, 1987). However, experiments conducted by Konhauser et al. (2007a) suggest that precursor sediments to oxide-facies BIF were the product of non-photochemical oxidative processes, such as direct or indirect biological oxidation. This same process of indirect biological oxidation is the second possible oxidation pathway, which occurs via bacterial oxygenic photosynthesis (Buick, 1992, 2008; Cloud, 1965, 1973; Knoll et al., 2006; Towe, 1983). While the timing of the evolution of oxygenic photosynthesis is highly contentious, the fingerprints of cyanobacteria are present as much as 2.7 Gya, and potentially as far back as 3.8 Gya (Buick, 2008). Thus, there is the potential for BIF, which dates back to 3.8 Ga (Fedo et al., 2001; Olson, 2006), to predate the onset of oxygenic photosynthesis. By contrast, direct, or metabolic, Fe oxidation, can occur via a variety of pathways, including (1) microaerophilic Fe(II) oxidizers that utilize oxygen, carbon dioxide and water (Emerson and Moyer, 2002; Holm, 1989; Sogaard et al., 2000), (2) anoxygenic photosynthesis, or photoferrotrophy, that utilizes Fe(II) rather than water as an electron donor (Ehrenreich and Widdel, 1994; Garrels and Perry, 1974; Widdel et al., 1993), and (3) carbon dioxide fixation by various purple and green bacteria that utilize Fe(II) as a reductant (Ehrenreich and Widdel, 1994; Heising and Schink, 1998; Straub et al., 1999; Widdel et al., 1993). Although the potential link between metabolic Fe-oxidation and iron formations has been known for almost a century (Harder, 1919), it has only recently been recognized as a potentially viable mechanism for the oxidation of Fe involved in BIF (Croal et al., 2009; Johnson et al., 2008b; Kappler et al., 2005; Konhauser et al., 2002; Konhauser et al., 2005; Planavsky et al., 2009).

While the transition from Earth's earliest atmosphere with $<10^{-5}$ of the present atmospheric levels of $O_2$ as diagnosed by mass-independent fractionation (MIF) of sulfur (Farquhar and Wing, 2003), to an oxygenic atmosphere is ultimately linked to the appearance and proliferation of photosynthesizing cyanobacteria, it is commonly considered that oxygen was kept at low levels in the Archean either by biological (e.g., Bjerrum and Canfield, 2002) or tectonic (e.g., Kump and Barley, 2007) buffering. The development of photosystem II, which permits direct oxidation of water using sunlight, provided early cyanobacteria the advantage of an almost endless supply of energy (Nisbet and Nisbet, 2008). This photosynthetic pathway also created the most Earth-changing waste product, molecular oxygen, which profoundly impacted every aspect of Earth. Geologic and geochemical proxies indicate that the transition from an anoxic to oxic atmosphere occurred ~2.4 billion years ago (Bekker et al., 2004; Beukes and Klein, 1990; Canfield et al., 2013; Dimroth and Kimberley, 1976; England et al., 2002; Farquhar et al., 2000; Kasting et al., 2012; MacGregor, 1927; Rasmussen and Buick, 1999; Yang and Holland, 2002) during the Great Oxidation Event (GOE), however more recent studies suggest this event may have occurred 300-400 million years earlier than originally thought (Crowe et al., 2013). This transition is defined by the disappearance of mass-independent sulfur isotope fractionation (Farquhar et al., 2000; Farquhar and Wing, 2003). Within the pre-GOE geologic record, fluvial deposits containing redox-sensitive minerals such as pyrite, uraninite and siderite, are found, which oxidize to form "red beds" in post-GOE times (Bekker et al., 2004; Canfield, 2005; Chandler, 1980; England et al., 2002; Rasmussen and Buick, 1999). The onset of oxidative continental weathering in post-GOE times resulted in increased oxidative weathering on land and the

mobilization of redox-sensitive trace metals (Anbar et al., 2007; Scott et al., 2008; Yang and Holland, 2002).

Deposition of BIF primarily occurs prior to the GOE, with the max volume of BIF occurring ~2.5 Ga and their widespread disappearance from the geologic record occurring approximately 600 million years after the GOE. Exception to the pattern of BIF deposition is the short-lived BIF reappearance in the Neoproterozoic during the Snowball Earth climatic event (Bekker et al., 2010; Klein, 2005).

Because the ~1.9 Ga Gunflint Formation (Fralick et al., 2002), Minnesota and Ontario (Fig. 2.1A), was clearly deposited after the GOE, it has the potential to preserve evidence of water column oxygenation in response to the GOE. Was the entire ocean ventilated or was a redox-chemocline present? Superior-type BIFs are well suited for trace-element studies because they precipitate within seawater, and thus may preserve seawater conditions, as long as clastic sediment and volcanic ash contamination and effects of metamorphism are taken into consideration (Bau and Dulski, 1996; Bau and Moller, 1993; Bolhar et al., 2004). The abundances of several transition elements (Mo, V, Co, Cr), as well as redox-sensitive REEs, in the oceans, and their subsequent incorporation into sedimentary rocks, are controlled by the availability of atmospheric oxygen. Prior to the GOE, redox-sensitive elements would have been largely retained in unoxidized secondary minerals during the weathering process, resulting in low oceanic concentrations. After the GOE, oxidative weathering would have resulted in an increase in the concentrations of these elements in the oceans (Anbar et al., 2007).

In this paper, we present a two-fold approach to characterizing Paleoproterozoic ocean redox conditions. First, we use trace-element geochemistry, including the redox-

sensitive Ce, from the Gunflint Formation to determine paleo-ocean oxidation state. Second, we reconstructed the effects of atmospheric oxygenation on continental weathering by examining changes in redox-sensitive elements through time. Specifically, we examined U, Mo, V, Co and Cr concentrations in BIFs from not only the ~1.9 Ga Gunflint Formation in Minnesota and Ontario (Fig. 2.1A), but also the ~3.7 Ga Isua Greenstone Belt in Greenland (Fig 2.1B; Fedo and Eriksson, 1996) and the ~3.0 Ga Buhwa Greenstone Belt in Zimbabwe (Fig. 2.1C; Fedo et al., 2001) to determine if a change in geochemistry could be detected in BIFs deposited before and after the GOE.

## 2.2 Geologic Background

### *2.2.1 Gunflint Formation, Minnesota and Ontario (~1.9 Ga)*

The ~1.9 Ga Gunflint Formation (Fralick et al., 2002) crops out along a NE-SW-trending belt that extends ~175 km from Thunder Bay, Ontario, where the unit is unmetamorphosed, to ~19 km west of the Gunflint Trail in northern Minnesota, where it is truncated and separated from the correlative Biwabik Formation in the Mesabi Range by the intrusion of the 1.1 Ga Duluth Complex (Fig. 2.1A). This intrusion developed a contact aureole, with peak metamorphism reaching upper amphibolite-facies (Floran and Papike, 1978; Jirsa and Weiblen, 2007; Miller et al., 1987). Individual units within the Gunflint Formation contain granular and banded fine-grained iron oxide (magnetite and hematite), iron-rich silicate (amphibole), carbonate (ankerite, siderite and calcite), and chert. Fining- and coarsening-upward successions document transgressive-regressive cycles (Pufahl and Fralick, 2004). Depositional models for BIF invoke upwelling of Fe(II)-rich anoxic deeper ocean water onto an oxygenated wave- and tide-dominated

shelf in water depths that did not exceed tens of meters (Poulton et al., 2004; Pufahl and Fralick, 2004).

The Gunflint Formation ranges in thickness from ~95 m in Minnesota to ~190 m in Ontario. In Minnesota, the original mineralogic character of the BIF is obscured by a thermal metamorphic overprint resulting from the emplacement of the Duluth Complex. Many of the fine-scale textural and mineralogical attributes used to subdivide the iron formation in Canada have been destroyed (Miller et al., 1987). Here we adopt the four-fold nomenclature originally proposed for the correlative Biwabik formation, which has been used to describe the Gunflint iron formation since the work of Broderick (1920). This scheme has four informal members (Lower Cherty, Lower Slaty, Upper Cherty, Upper Slaty) whose names emphasize the relative proportions of thick-bedded granular (cherty), and thin-bedded non-granular (slaty) iron formation (Miller et al., 1987; Planavsky et al., 2009). Although the boundaries of these members do not coincide with those recognized in Canada by Goodwin (1956), the two schemes have be easily equated.

These subdivisions record two upward deepening cycles (Fig. 2.2; Ojakangas et al., 2001; Planavsky et al., 2009; Pufahl and Fralick, 2004). The lowermost unit, the Lower Cherty unit, nonconformably overlies Archean basement and represents subtidal shelf to upper-slope facies, and is overlain by the Lower Slaty unit, which was deposited on a deeper-water slope. The second cycle begins with the Upper Cherty unit, which represents subtidal to upper-slope facies and is buried by deep-water-slope facies of the Upper Slaty unit. Two laterally extensive layers containing stromatolites occur at the base of the Lower and Upper Cherty units. We collected samples from all four units, and from metamorphosed sections in Minnesota (GF-4 to GF-40) and unmetamorphosed

sections in Ontario (GF-41 to GF-54) to document both the redox structure of the basin and the affects of localized contact metamorphism.

At field scale, the main lithologies of the amphibolite-facies Gunflint BIF which crops out in Minnesota and Ontario include finely and coarsely banded magnetite-quartz BIF (Fig. 2.3A, B), with less common centimeter-scale chert-dominated layers containing rip-up clasts of magnetite-rich material (Fig. 2.3C). Despite the metamorphic overprint that is present in this area, stromatolitic horizons are still preserved (Fig. 2.3D). In thin section (Fig. 2.4), metamorphosed samples alternate between Fe-silicate and oxide facies BIF, and contain varying amounts of quartz, magnetite, and amphibole. Quartz occurs as equant grains with 120º interlocking grain boundaries (Kruhl et al., 2013; Urai et al., 1986), which suggests recrystallization, and ranges in size from ~50 μm to 500 μm (Fig. 2.4A). Magnetite typically occurs as anhedral grains, ranging in size from ~10 μm to 200 μm that occur within distinct bands or as disseminated grains between quartz and amphibole. Similarly, amphibole occurs as disseminated grains and needles in between quartz and magnetite (Fig. 2.4A) or in distinct layers (Fig. 2.4B). Amphibole is found in all samples and typically occur as a clotted mass of fine (<50 μm) equant grains or needles; a few larger (~200 μm) grains are also present (Fig. 2.4A). The preservation of stromatolitic layering can also been seen in thin section (Fig. 2.4C).

Unmetamorphosed Gunflint BIF observed at Thunder Bay, Ontario represents a shallower-water facies than is recorded in the high-grade BIF of northern Minnesota. Hummocky cross-stratification (above storm wave base), silicified microbial mats, and carbonate-rich iron formation occur in these facies (Fig. 2.3E). Samples contain varying degrees of quartz, magnetite, hematite, ankerite (Fig. 2.3F), dolomite (Fig. 2.4E), and

calcite (Fig. 2.4F). However, it is likely that some of the calcite is secondary cement that formed during burial (Fig. 2.4F). Most quartz grains are anhedral and <100 μm, with some grains up to ~300 μm in size. Magnetite, hematite and carbonate grains are typically anhedral and may or may not occur in distinct bands. In some locations, hematite and magnetite oolitic facies are preserved (Fig. 2.4D).

### *2.2.2 Isua Greenstone Belt, Greenland (>3.7 Ga)*

The >3.7 Ga Isua Greenstone Belt (IGB) represents the oldest known and locally well preserved metavolcanic and metasedimentary Archean supracrustal rocks on Earth (Appel et al., 1998; Fedo, 2000; Myers, 2001). The IGB is located within the Archean high-grade gneiss complex of SW Greenland and forms an arcuate belt ~35 km long, and up to 2.5 km wide (Fig. 2.1B). The most abundant metasedimentary rocks are chemically precipitated chert and magnetite-quartz layered BIF. After their deposition, rocks were subjected to multiple episodes of regional amphibolite-facies metamorphism and pervasive carbonation and potassium metasomatism (Appel et al., 1998; Dymek and Klein, 1988; Fedo et al., 2001; Fedo et al., 2006; Myers and Crowley, 2000; Rollinson, 2002; Rosing, 1999).

Samples from the northeastern part of the IGB are dominated by mm-scale banding of quartz and iron oxide (Fig. 2.5A), which is predominantly magnetite, but contains a minor amount of hematite (Fig. 2.5B). Minor amounts of small amphibole grains (Fig. 2.5A) and trace amounts of apatite occur in most samples, however, larger amphibole grains are present in sample ISB-22 (Fig. 2.5C). All samples have experienced ductile deformation (Komiya et al., 1999; Whitehouse and Fedo, 2007). Many contain a prominent mineral stretching lineation parallel to the plunge direction of

the major synform that dominates the regional tectonic domain (Whitehouse and Fedo, 2007).

### *2.2.3 Buhwa Greenstone Belt, Zimbabwe (~ 3.0 Ga)*

The ~3.0 Ga Buhwa Greenstone Belt (BGB) is located along the southern margin of the Zimbabwe Archean craton, where metamorphism varies across-strike of the BGB, increasing from greenschist facies (dominant metamorphic grade) in the NW to granulite facies in the SE (Fig. 2.1C) (Fedo and Eriksson, 1996; Fedo et al., 1995). The cover succession of the BGB contains greenschist-facies sedimentary rocks, with minor volcanic rocks. It can be divided into the western shelf facies and the eastern deeper-water basinal assemblages, connected by a zone of transitional deposits. BIF samples were collected from all facies (Fedo and Eriksson, 1996).

In thin section, samples are dominantly mm- to cm-banded, recrystallized quartz (25 – 500 μm) and iron oxide, with minor amphibole and trace amounts of fine-grained apatite (<150 μm). Typically, the iron ore is dominated by hematite grains with magnetite cores (Fig. 2.5D), suggesting the hematite may be pseudomorphic replacement of magnetite. Only one sample contains predominantly magnetite rather than hematite (ZB-05). ZB-117 is the only granulite-facies sample and contains bands of coarser-grained recrystallized quartz (50 μm – 1 mm) and hematite replacing magnetite (Fig. 2.5E). ZB-247 and ZB-294 were collected from the Buhwa Mine and consist of bands of hematite replacing magnetite (90 %) and fine-grained recrystallized quartz (10 %) with no distinct grain boundaries (Fig. 2.5F).

### *2.2.4 Kuruman and Penge Iron Formations, South Africa (~2.5 Ga)*

Geochemical data for the Kuruman and Penge Iron Formations were compiled from a previous study by Bau and Dulski (1996). Only samples that had detailed sample descriptions were used. These two iron formations are contemporaneous and are part of the Transvaal Supergroup deposited on the Kaapvaal craton of South Africa. The Kuruman Iron Formation experienced a low degree of diagenetic-metamorphic overprint and consists of alternations of siderite, hematite and magnetite laminae, and occasionally intercalated stilpnomelane. Some of the oxide-minerals are secondary and formed from carbonate precursors. The Penge Iron Formation was modified by the intrusion of the Bushveld Complex and consists of magnetite, grunerite, quartz, biotite, ankerite, calcite, and K-feldspar, with minor amounts of sulfides, riebeckite, and ferriannite. Sampling, however, was confined to pure magnetite-quartz layers.

## 2.3 Geochemical Background

The rare earth elements (REE) comprise the lanthanides from lanthanum (La) to lutetium (Lu). Yttrium (Y) is often included in between holmium (Ho) and dysprosium (Dy) in a REE + Y (REY) plot because it has an ionic radius similar to that of adjacent Ho. REE typically exist in a trivalent oxidation state, and thus are not readily fractionated with respect to each other. Cerium (Ce) and europium (Eu) also exist in a tetravalent and a divalent oxidation state, respectively. Both Ce and Eu are important elements for providing constraints on paleo-ocean chemistry (Alibert and Mcculloch, 1993; Barrett et al., 1988; Bolhar et al., 2004; Derry and Jacobsen, 1990; Dymek and Klein, 1988; Fryer, 1977; Kato et al., 1998; Kato et al., 2006a; Liu et al., 1988) because their redox-sensitive behavior can be quantified by normalization to the geometric

average of adjacent REE elements that do not display anomalous behavior. These are referred to as Eu-anomalies ($Eu/Eu^* = Eu_{SN}/[Sm_{SN}(Sm_{SN}/Nd_{SN})^{1/3}]$) and Ce-anomalies ($Ce/Ce^* = Ce_{SN}/ [Pr_{SN}(Pr_{SN}/Nd_{SN})]$), where SN = shale-normalized (Condie, 1993; Lawrence and Kamber, 2006). Negative and positive anomalies are defined as values of less than and greater than 1, respectively. The principal requirement for calculating anomalies is that the near neighbors used in the calculation must not show any anomalous behavior themselves (Lawrence et al., 2006b; Lawrence and Kamber, 2006). Thus, La should not be used in the calculation of the Ce anomaly because it behaves anomalously and often leads to the overabundance of La, rendering unacceptable the commonly used expression for calculating cerium anomaly ($Ce/(0.5Pr + 0.5La)$). To avoid such issues, this study uses the expression ($Ce/Pr + (Pr – Nd)$), which provides a more consistent measurement of the Ce anomaly (Lawrence et al., 2006b; Lawrence and Kamber, 2006).

Regardless of age and metamorphic grade, REY patterns in BIFs have characteristic features that can be used as chemical fingerprints to determine the origin and depositional environment of marine sediments (Barrett et al., 1988; Bekker et al., 2010; Bolhar et al., 2004; Derry and Jacobsen, 1990; Dymek and Klein, 1988; Fryer, 1977; Kato et al., 1998; Klein, 2005). BIF is assumed to record minimal fractionation of REE during precipitation of ferric iron oxides and oxyhydroxides, and thus should preserve a snapshot of the REE signature of seawater at the site of Fe precipitation (Bau, 1993; Bau and Dulski, 1996; Bau and Moller, 1993; Bekker et al., 2010; Bolhar et al., 2004; Derry and Jacobsen, 1990; Kato and Nakamura, 2003; Klein, 2005; Murray et al., 1992). In oxygenated water, light REE (LREE) depletion relative to heavy REE (HREE) records preferential adsorption to, and removal by, Mn- and Fe-oxyhydroxides and other

reactive surfaces because of increased carbonate complexation (Bau and Koschinsky, 2009; Bryne and Kim, 1990; Cantrell and Byrne, 1987; Quinn et al., 2006; Sholkovitz, 1992; Sholkovitz et al., 1994). This process results in a positive slope in REY plots. Reductive dissolution then occurs as these particles settle through the water column and cross redox boundaries, resulting in an increase in the ratio of elemental light to heavy REE and thus a decrease in the positive slope of REY plots (German et al., 1991; Planavsky et al., 2010; Sholkovitz et al., 1992). In many cases, these REE shifts can be directly linked to Mn cycling (De Carlo and Green, 2002). Although both Mn- and Fe oxyhydroxides scavenge REY from the water, leaching experiments have demonstrated differences between the REY distribution in the Mn- and Fe oxyhydroxides that cannot solely be explained by the REY speciation in sweater, but requires additionally and mineral-specific REY fractionation during surface-complexation (Bau and Koschinsky, 2009). These differences include the preferential association of La, Gd, Y and Lu with Mn oxides, as well as the lack of preferential oxidative scavenging of Ce by Mn oxides as compared to hydrous Fe oxides (Bau and Koschinsky, 2009).

Other experimental work has shown that REY sorption is strongly influenced by pH. Bau (1999) showed that there is an increase in the adsorption magnitude of REY sorption with increasing pH, as well as a pH dependence in the pattern of REY fractionation. This study also showed that as a consequence of the interaction of natural waters with Fe oxyhydroxides, normalized REY patterns of the water show positive Y, La, Gd, and Lu anomalies and the W-type lanthanide tetrad effect and normalized REY patterns of the Fe oxyhydroxides precipitates show less positive or negative anomalies of the same elements, and the M-type lanthanide tetrad effect (Bau, 1999).

Chemical complexation also plays an important role in the fractionation of trace elements wherein seawater and its precipitates, such as BIF, show highly fractionated Y/Ho and Zr/Hf ratios, as well as non-redox controlled, positive La and Gd anomalies (Bau, 1996). Along with positive La and Gd anomalies, positive Eu anomalies are also found in precipitates from ancient seawater, as sampled by Archean BIF (Fig. 2.6). Europium enrichment indicates a strong influence of high temperature hydrothermal fluids on the dissolved REE composition of seawater (Derry and Jacobsen, 1990). The lack of a Eu anomaly in Neoproterozoic and Phanerozoic seawater implies deep ocean ventilation. Under these conditions, input of Fe at hydrothermal vents would precipitate rapidly at the seafloor (e.g., Fe-Mg nodules) (Bau et al., 2014). The gradual decrease in the magnitude of the Eu anomaly throughout the Archean and the Paleoproterozoic is interpreted as a decrease in hydrothermal input through time (Bau and Moller, 1993; Kamber, 2010; Klein, 2005). Cerium is the only REE with redox transformations at ambient oceanic conditions, resulting in a positive Ce anomaly in anoxic conditions and a negative Ce anomaly in oxygenated environments (Sholkovitz et al., 1994).

Rare earth element abundances in metasediments have been reported to be unaffected by post-depositional processes, including diagenesis (Webb et al., 2009), metamorphism (Bau, 1991), and weathering (Bau, 1993). For BIFs, there is no evidence for REE mobility during either diagenesis or low- to high-grade regional or contact metamorphism (Bau, 1993; Bau and Moller, 1993; Bekker et al., 2010; Kato et al., 2006a; Klein, 2005). Depending on the fluid composition and physicochemical environment, however, hydrothermal alteration may (Bau, 1991; Bau and Dulski, 1999; Brengman and Fedo, 2012; Thurston et al., 2012) have a substantial impact on REE distribution.

Similarly, weathering may also affect REE distribution, depending on source-rock mineralogy, physicochemical environment of alteration, and composition of the alteration fluid (Bau, 1993). To avoid these problems, this study specifically targeted the best-preserved BIF from settings with sound sedimentalogical background information. One iron-ore sample from the Buhwa Mine, Zimbabwe was included for comparison purposes. To test the effect of modern weathering of U and Pb in BIF, we measured Pb isotope compositions of Gunflint BIF. Both U and Pb are typically mobile under ambient weathering such as that expected U/Pb vs. Pb-isotope composition covariation breaks down.

## 2.4 Analytical Methods

### *2.4.1 Whole Rock, Trace- and Rare Earth-Element Analysis*

#### *2.4.1.1 Rock Digestion*

In a protocol adapted from Eggins et al. (1997), samples were crushed and powdered, and 100 mg aliquots were digested in capped Savillex® screw-top Teflon beakers over 72 hours at 135 °C in a 2:1 mixture of concentrated distilled HF and $HNO_3$. Following digestion, samples were evaporated to dryness and residues were redissolved twice with 1 mL of concentrated $HNO_3$ to convert and volatilize $SiF_4$ that formed during the HF digestion. Six milliliters of Milli-Q water and 2 mL of concentrated $HNO_3$ were added to all samples, and beakers were capped and refluxed at 120 °C for 48 hours. A further 2 mL of Milli-Q water was added and then the 1:100 stock solutions were homogenized and stirred using a vortex mixer and centrifuged for 10 minutes. Aliquots of the stock solutions were diluted to 1:2500 and spiked with an internal standard containing $^{6}Li$, In, Re, Bi, and $^{235}U$.

*2.4.1.2 Mass Spectrometry*

Samples were analyzed for a suite of 46 trace and rare earth elements (Li, Be, Sc, Ti, V, Cr, Co, Ni, Cu, Zn, Ga, As, Rb, Sr, Y, Zr, Nb, Mo, Ag, Cd, In, Sn, Sb, Cs, Ba, La, Ce, Pr, Nd, Sm, Eu, Gd, Tb, Dy, Ho, Er, Tm, Yb, Lu, Gf, Ta, W, Tl, Pb, Th, U) using a quadrupole Thermo X II Series inductively coupled plasma-mass spectrometer (ICP-MS) at Laurentian University, Sudbury, Ontario. The instrument was tuned to 1.5% $CeO^+/Ce^+$, and all isobaric interferences were corrected using oxide formation rates determined for pure elemental solutions measured immediately following sample analysis. Multiple digestions of the USGS reference material W-2 were used for instrumental calibration. USGS standards BHVO-1 and BIR-1 were analyzed as unknowns and compared to the long-term reproducibility reported in Kamber (2009) to serve as an external quality control. The majority of elements were reproduced to better than 1 % relative standard deviation and were found to be accurate within 2 % (Tables A.1, A.2 and A.3).

***2.4.2 Whole Rock Pb Isotope Analysis***

*2.4.2.1 Pb Purification*

Following the protocol for the "HCl method" reported in Kamber and Gladu (2009), the remaining solution from whole rock digestion was evaporated to dryness and the residue was converted to bromide through two additions of 1 mL $H_2O$ and one drop of concentrated HBr. Samples were allowed to equilibrate with 0.5 mL of 0.5 M HBr prior to being centrifuged and purified with a single-stage anion exchange method eluting with HBr–HCl. Once loaded onto the columns, samples were washed into the resin bed with 0.08 mL of 0.5 M HBr, followed by 2 mL of 0.5 mol/L HBr, and elution using 0.9

mL of 2 M HCl. Finally, the Pb was removed from the resin using 0.4 mL of 10.8 M HCl.

*2.4.2.2 Mass Spectrometry*

Purified Pb was diluted with 2% v/v $HNO_3$ to an optimum concentration based on the known abundance from trace element experiments. Once diluted, samples were analyzed by a quadrupole Thermo X II Series ICP-MS (Table A.5) at Laurentian University, Sudbury, Ontario according to the protocol of Ulrich et al. (2010).

***2.4.3 Sample Selection***

Before interpretation of BIF geochemistry, samples were assessed for contamination by clastic material, which carries its own trace-element signature (Condie, 1993) and may affect the trace-element signature of BIF. Samples with an elevated detrital siliciclastic content were considered contaminated and were assigned a different symbol in all graphs. To estimate an upper acceptable limit of contamination, siliciclastic indicators such as the concentration of $Al_2O_3$ and Zr and the LREE/HREE ratio were evaluated and cut-off values established through mixing calculations of relatively pure BIF samples and Post-Archean Australian Average Shale (PAAS), which was used to approximate clastic input. The basic requirement was that samples retain positive La, Eu, Gd, and Y anomalies. At a mixture of 80 % BIF and 20 % PAAS for Gunflint and Zimbabwe samples, and 85 % BIF and 15 % PAAS for Isua samples, the first fingerprint of BIF (i.e. positive La anomaly) disappeared. These values were used as a primary cut-off to screen for contamination. In addition, cut-off values for $Al_2O_3$ and Zr were determined to prevent the inclusion of samples with siliciclastic contamination. Here, the concentration of $Al_2O_3$ is used as a proxy for clay and the concentration of Zr is used as a

proxy for zircon (Fig. 2.7A). A natural break in the distribution of Gunflint and Zimbabwe samples occurred at $Al_2O_3$ = 1.7 wt. % and Zr = 19 ppm, which corresponds to 6.5 % and 10 % PAAS contamination, respectively. For Isua samples, the natural break occurred at $Al_2O_3$ = 0.8 wt. % and Zr = 4 ppm, which corresponds to 3 % and 2 % PAAS contamination, respectively. The natural breaks in the samples were used simply as a guide in the selection of specific values that corresponded to less than 20 % PAAS for Gunflint and Zimbabwe samples and less than 15 % PASS for Isua samples. Thus, any sample from Zimbabwe and Gunflint that had a concentration of Zr (ppm) >27 or $Al_2O_3$ (wt. %) >1.67, and any sample from Isua that had a concentration of Zr (ppm) >5 or $Al_2O_3$ (wt. %) >0.8, was considered contaminated. Note, these samples did not appear to have a large component of siliciclastic contamination based on observations in the field and in thin section. Thus, this additional step of screening samples for siliciclastic contamination based on geochemistry allows us to include only the most pristine samples in the study.

BIF not contaminated with siliciclastic debris is depleted in LREE relative to HREE resulting in a positively sloped REE pattern and a $Pr_{SN}/Yb_{SN}$ ratio of less than 1 (Planavsky et al., 2010; Sholkovitz et al., 1994). Admixtures of siliciclastic detritus have a tendency to flatten the shale-normalized Pr/Yb slope because shale, by definition, has a value of unity. To investigate whether this mixing caused the observed variability in BIF chemistry, indicators of siliciclastic contamination were plotted against $Pr_{SN}/Yb_{SN}$ ratios. By comparison with BIF, shale is greatly enriched in $Al_2O_3$, which is associated with clay minerals, and Zr, an element directly associated with detrital zircon in sedimentary rocks. The results for $Pr_{SN}/Yb_{SN}$ vs. $Al_2O_3$ (wt. %) and $Pr_{SN}/Yb_{SN}$ vs. Zr (ppm) are shown in

Figure 2.7B, C, respectively. Samples with a $Pr_{SN}/Yb_{SN}$ ratio of greater than one are depleted in HREE relative to LREE and have a negatively sloped REE pattern, indicative of siliciclastic contamination. All samples considered contaminated have been assigned an open circle symbol. Results for $Pr_{SN}/Yb_{SN}$ vs. Sc (ppm), Th (ppm) and Y/Ho are not presented here, but are consistent with the findings for $Al_2O_3$ and Zr. This additional test for detrital contamination acts as a novel screening filter. Its application here resulted in the rejection of a number of samples that otherwise would have been used if only screened by assessing the more conventional concentrations of $Al_2O_3$ and Zr (Konhauser et al., 2009; Planavsky et al., 2010).

Samples that lack a positive La anomaly (i.e., La/La* <1, where La/La* = $La_{SN}/[Pr_{SN} (Pr_{SN}/Nd_{SN})^2]$) were given a separate symbol because a positive La anomaly is a commonly used diagnostic fingerprint of seawater and hydrogenous sediment, such as BIF (Bolhar et al., 2004). These samples, however, contain no evidence of siliciclastic contamination and their data plots with other BIF samples that do posses a positive La anomaly.

## 2.5 Evidence For An Oceanic Oxycline

### *2.5.1 Rare Earth Element Geochemistry*

#### *2.5.1.1 Variability Through Time*

The majority of Archean BIF samples lack Ce anomalies or have slightly positive anomalies (Table 2.1; Fig. 2.8A). Data reported in this study for samples from the IGB plot within the range previously reported (Bolhar et al., 2004). The average Ce anomaly for BIF from the IGB is 1.1, 1.0 from the BGB, 1.1 from Kuruman, and 1.0 from Penge. Sample ZB-117 contains evidence for the likely metamorphic replacement of magnetite

with hematite, suggesting that not only is this sample of higher metamorphic grade (granulite-facies), it has also experienced more severe, likely supergene, alteration than other Zimbabwe samples. This sample has an unusually large positive Ce anomaly (1.6). Sample ZB-18, a chert from BGB, has an unusually negative Ce anomaly (0.5; Table 2.1; Fig. 2.8A). In GF BIF samples, more strongly positive Ce anomalies are recorded, up to 1.9, with the average Ce anomaly being 1.2. Negative Ce anomalies, however, are found in samples GF-4, GF-38, GF-39, GF-40 (Table 2.1; Fig. 2.8A).

The range of LREE/HREE ratios in non-contaminated, oxide-facies BIF, calculated as $Pr_{SN}/Yb_{SN}$, increases in late Paleoproterozoic BIF compared to Archean BIF (Fig. 2.3, 2.8B). In the Archean, ratios range from 0.0 to 0.6 for IGB BIF, 0.3-0.9 for BGB BIF, and 0.2 to 0.6 for Kuruman and Penge BIF. Sample ZB-247 has an anomalously positive ratio (1.5). This sample, however, was collected from the Buhwa Mine and may have later alteration resulting from hydrothermal ore-forming processes (Fedo and Eriksson, 1995). In the GF BIF of the late Paleoproterozoic, ratios range from 0.3 to 2.2.

We also observe a change in the $Y_{SN}/Ho_{SN}$ ratio through time when Archean and Paleoproterozoic BIFs are compared (Fig. 2.3, 2.8C). The average $Y_{SN}/Ho_{SN}$ ratios for Archean BIF are all greater than the shale composite ratio of ~27 (IGB = 45, BGB = 34, Kuruman and Penge = 47). This is in contrast to the $Y_{SN}/Ho_{SN}$ ratios of the Paleoproterozoic GF BIF, that have values above and below the shale composite ratio, ranging from 21 to 40 (average = 31).

*2.5.1.2 Gunflint Formation Variability*

In order to determine if there was stratigraphic control on the distribution of REE geochemistry, samples were analyzed throughout the ~200 m of Gunflint stratigraphy. No relationship was found between the chemistry and stratigraphic position or depositional environment (Fig. 2.9). Negative Ce anomalies are found in 4 samples that represent a cross section of Gunflint stratigraphy from both shallow and deep water facies. There is no consistent trend in the REE ratios up stratigraphic section, or between the different subenvironments. Samples GF9 through GF23 were collected from a 7.5 m outcrop of the Lower Slaty unit that was measured in detail. No relationship is evident between rare earth element chemistry and stratigraphy even at this fine scale of observation.

***2.5.2 Interpreting Rare Earth Element Geochemistry***

In modern oxygen-stratified ocean basins, oxygenated water displays a strong negative $Ce_{SN}$ anomaly, whereas deeper, anoxic water displays a preferential enrichment of Ce and a corresponding positive $Ce_{SN}$ anomaly (German and Elderfield, 1990). These distributions can be attributed to the oxidative precipitation of insoluble Ce(IV) above the oxycline and reductive dissolution to soluble Ce(III) in reducing deep waters (Bau, 1999; Bryne and Sholkovitz, 1996; German and Elderfield, 1990; German et al., 1991). In this scenario (Fig. 2.10), some of the Ce released is Ce(IV) and is transported to the oceans via rivers during oxidative weathering releases Ce. Ce remains in the tetravalent form in the oxidized well-mixed shallow waters (Fig. 2.10B). Because the oxidation of Ce(III) to Ce(IV) greatly reduces the solubility of Ce, Ce (IV) is more permanently attached onto particulate matter compared to trivalent REE, which easily adsorbs and desorbs from the

surface of particles (Fig. 2.10B). When this particulate matter sinks below the oxycline, Ce(IV) is reduced to Ce(III), which increases its solubility and desorbtion from particulate matter (Fig. 2.10C; Brookins, 1989; Sholkovitz et al., 1994). This results in an increased concentration of Ce in deep anoxic water, which in turn results in positive Ce anomalies within minerals precipitated from these waters (Fig. 2.8A, 2.10D).

For the majority of Archean samples, there is very little deviation in trivalent Ce behavior (Fig. 2.8A), indicating that reducing conditions prevailed over a significant enough portion of the water column that Ce oxidation was insignificant. By contrast, the existence of both positive and negative Ce anomalies in Gunflint samples indicates deposition above and below an oxycline, clearly suggesting that deep water in the Gunflint basin was not well ventilated (Fig. 2.10A). The presence of strongly positive Ce anomalies in Gunflint samples (Fig. 2.8A) further suggests a substantial release of Ce in deep anoxic waters. The upper water column, however, had to be oxic in order to shuttle enough Ce to deeper waters to result in positive anomalies. It was also necessary for iron oxide to precipitate in different parts of the water column to preserve the changing Ce anomaly (Fig. 2.10).

In oxygenated water, LREE preferentially adsorb to and are removed by Mn- and Fe-oxyhydroxides and other reactive surfaces, resulting in light REE depletion relative to HREE. As these LREE-enriched particles cross a redox boundary, reductive dissolution occurs, LREE are released, and the ratio of light to heavy REE increases (German et al., 1991; Planavsky et al., 2010; Sholkovitz, 1992). An increase in the light to heavy REE ratios, which can be seen in the lowering of the $Pr_{SN}/Yb_{SN}$ ratio, in the Paleoproterozoic

Gunflint BIF relative, to Archean BIF, further supports the presence of an oxycline (Fig. 2.8B).

Additional evidence for an oxycline in the Gunflint ocean basin comes from the decrease in the average $Y_{SN}/Ho_{SN}$ ratio of Gunflint BIF relative to BIF deposited in the Archean (Fig. 2.8C). Differences in particle reactivity result in differential scavenging and Y and Ho fractionation within Mn- and Fe-oxyhydroxides (Bau et al., 1997b; Nozaki et al., 1997). The lower stability of surface complexes of Y relative to its REE neighbor result in Y having a lower marine particle reactivity than Ho, thus making it is less effectively scavenged from seawater (Nozaki et al., 1997). Increased uptake of Ho results in an increase in Ho in anoxic waters as Mn- and Fe-oxyhydroxides dissolve, thus decreasing the dissolved seawater Y/Ho ratio and leaving a signature that would be passed on to precipitating BIF (Bau et al., 1997b; Nozaki et al., 1997; Planavsky et al., 2010).

## 2.6. Oxidative Continental Weathering By ~1.9 Ga

### *2.6.1 Trace-Element Geochemistry*

#### *2.6.1.1 Pb Isotope Geochemistry*

The isotopic ratios ranged from 35.7 to 43.4 (avg. = 38.6) for $^{208}Pb/^{204}Pb$, 15.5 to 23.5 (avg. = 16.4) for $^{207}Pb/^{204}Pb$, 17.2 to 100.1 (avg. = 26.8) for $^{206}Pb/^{204}Pb$, and 1.7 to 348.9 (avg. = 47.6) for $^{238}U/^{204}Pb$ (Table 2.1). A positive correlation exists between $^{238}U/^{204}Pb$ and $^{206}Pb/^{204}Pb$ (Fig. 2.11). Given that $^{238}U$ decays to $^{206}Pb$, the linearity of the data indicates that the $^{238}U/^{206}Pb$ ratio is constant, and that the measured U/Pb ratio today for the Gunflint samples is the same as the original ratio rather than an artifact of modern weathering or later U mobilization (Pollack et al., 2009). Determining if the U/Pb ratio is

a primary signature is an important step that is often overlooked and should become the standard when using iron formation as paleoceanographic archives to ensure that interpretations are not being made using data that reflects modern weathering and U mobilization.

*2.6.1.2 Variability In Redox Sensitive Elements Through Time*

A number of terrestrially sourced, redox-sensitive elements and ratios show an increase in concentration in post-GOE BIF compared to pre-GOE BIF (Table 2.1; Fig. 2.12). We present trace-metal data as molar ratios normalized to Fe (e.g., Konhauser et al., 2009) because of different speciation with Fe colloids versus Si colloids. When the median U/Pb ratios are compared in pre- and post-GOE BIFs, with Archean ratios ranging from 0.0 to 0.1 and Gunflint BIFs being 0.3 (Fig. 2.12A). The Mo/Fe ratio ranges from 0.0 to 0.005 in the Archean, whereas in the Paleoproterozoic, Mo/Fe ratios range from 0.0 to 0.015 (Fig. 2.12B). V/Fe ratios range from 0.003 to 0.079 in the Archean and increase to 0.03 to 0.382 in the Paleoproterozoic (Fig. 2.12C). For Co/Fe, ratios range from 0.005 to 0.03 in the Archean and increases to 0.007 to 0.116 in the Paleoproterozoic (Fig. 2.12D). For Cr/Fe, ratios range from 0.019 to 0.202 in the Archean, whereas in the Paleoproterozoic, Cr/Fe ratios range from 0.001 to 0.183 (Fig. 2.12E).

*2.6.1.3 Gunflint Formation Variability*

Similar to the more detailed examination of REE geochemistry conducted throughout the Gunflint Iron formation, trace metal geochemistry was analyzed throughout the full Gunflint stratigraphy to determine if variability in chemistry was controlled by stratigraphy or depositional environment. No relationship is evident

between the trace element geochemistry and stratigraphy or depositional environment of the Gunflint BIF (Fig. 2.13). The range in chemistry that is found in the 7.5 m thick detailed measured section of the Lower Slaty unit is close to the full range in chemistry that is found throughout the entire ~200 m thick Gunflint stratigraphy and shows no stratigraphic variability.

### *2.6.2 Interpretation of Trace-Element Geochemistry*

#### *2.6.2.1 U-Th-Pb Geochemistry*

Uranium (U) has two common oxidation states (+4 and +6) that are geochemically relevant to this study. The chemical behavior of U(IV) and U(VI) is influenced by dissolution, precipitation, complexation, and sorption reactions, which are affected by redox conditions, pH, water composition, and water-rock interaction (Duff et al., 2002; Tribovillard et al., 2006). Tetravalent U is insoluble under surface conditions and hexavalent U is highly soluble and forms very stable U hydr(oxides), $UO_2^{2+}$ and uranyl carbonate ionic complexes, which are stable enough to contain considerable concentrations of U under slightly reducing conditions (Duff et al., 2002; Hostetler and Garrels, 1962; Pollack et al., 2009). Under reducing atmospheric conditions, insoluble U has a strong tendency to hydrolyze and form colloids. The only solid phase, however, expected to occur and be stable in the presence of water and variable oxygen concentrations is uraninite, in which U would be transported to the oceans with detrital material (Hostetler and Garrels, 1962).

The redox-sensitive geochemical nature of U permits the use of the U-Th couple as a geochemical proxy for atmospheric oxidation state during deposition. The U-Th couple is also useful at constraining paleoredox conditions because $^{238}U$, $^{235}U$, and $^{232}Th$

are long-lived radionuclides that decay to $^{206}Pb$, $^{207}Pb$, and $^{208}Pb$, respectively, making it possible to determine time-integrated U/Pb and Th/U ratios (Faure, 1986; Pollack et al., 2009). Under reducing conditions, U(IV) and Th, which only has one common oxidation state (+4), are largely insoluble and would be transported to the oceans with detrital materials, resulting in BIF having Th/U ratios close to the average upper continental crust ratio of 3.8 (Pollack et al., 2009; Taylor and McLennan, 1985). In post-GOE times when the atmosphere was oxidizing, uranium should have been released during oxidative weathering of continental crust and delivered to the oceans as water-soluble uranyl ions, which would result in BIF being enriched in U relative to pre-GOE BIFs, as well as being more radiogenic with regards to Pb (i.e., have a much higher time-integrated U/Pb ratio than pre-GOE, Archean aged BIF) (Pollack et al., 2009). This post-GOE enrichment in U is seen in Figure 2.13E. The positive slope on the $^{238}U/^{204}Pb$ vs. $^{206}Pb/^{204}Pb$ plot (Fig. 2.11) and the lack of evidence for recent gain or loss of U or Pb suggests that the high U in the Gunflint samples is not an artifact of modern weathering. Rather, the very radiogenic Pb compositions of the samples indicate preferential flux of U, not Th, in response to oxidative weathering at 1.9 Ga (Fig. 2.14). Most bulk-rock $^{208}Pb/^{206}Pb$ ratios on Earth are ~ 2 and most bulk-rock $^{232}Th/^{238}U$ ratios are ~ 4 (Faure, 1986). If there was preferential addition of U to the system, the $^{232}Th/^{238}U$ ratios would decrease, and given time decay, $^{206}Pb$ accumulation would be enhanced relative to $^{208}Pb$ in the low Th/U rocks, resulting in a decrease in the $^{208}Pb/^{206}Pb$ ratio. Samples from the Gunflint Iron Formation analyzed here have predominately $^{208}Pb/^{206}Pb$ ratios less than 2 and $^{232}Th/^{238}U$ ratios greater than 4, suggesting the preferential addition of U.

To test whether Pb in the Gunflint was derived from a single source, the Pb isotope data from the Gunflint samples were plotted on a common Pb plot (Fig. 2.15). The data plot between two 1.9 Ga isochrons, one that represents a depleted mantle source (MORB) and the other that represents a mix of sedimentary sources (Kramers and Tolstikhin, 1997). Samples were coded according to stratigraphic position and depositional environment (Fig. 2.15A), $Y_{SN}/Ho_{SN}$ ratio (Fig. 15B), $Al_2O_3$ content (Fig. 2.15C), and Zr content (Fig. 2.15D) to attempt to determine whether the samples with a more crustal isotope signature had lower Y/Ho and higher Al. There is no clear correlation, however, between trace elements and Pb-isotope ratios and it is not clear what was controlling the distribution of the samples between these two sources. Other potential correlative factors, including $Pr_{SN}/Yb_{SN}$ ratio, Ce anomaly, Eu anomaly, and metamorphism were also examined, but no trends were found. The lack of a single source for the Pb in the Gunflint basin suggests that both hydrothermal (mantle-like) and crustal sources contributed metals to the basin.

*2.6.2.2 Molybdenum*

Similar to U, Mo has two oxidation states, Mo(VI) and Mo(IV). Its solubility decreases under reducing conditions, making its presence or absence in sedimentary deposits a proxy for oxygen concentration (Anbar, 2004; Anbar et al., 2007; Emerson and Huested, 1991; McManus et al., 2006; Tribovillard et al., 2006). In modern oxygenated systems, Mo is released during oxidative continental weathering of Mo-bearing sulfide minerals. It is then strongly hydrolyzed and exists in rivers (the dominant source of Mo) and in oceans (the dominant sink of Mo) as the unreactive molybdate ion ($MoO_4^{-2}$) (Anbar, 2004; Anbar and Rouxel, 2007; Emerson and Huested, 1991; Tribovillard et al.,

2006). In the presence of anoxia, Mo remains in unoxidized crustal minerals during weathering, resulting in lower concentrations of Mo in the oceans, and in BIF (Anbar et al., 2007). Thus, the increase in Mo concentration in BIF across the GOE boundary (Fig. 2.12A) can best be explained by Mo release during oxidative continental weathering.

The concentration of Mo in the water column of anoxic basins, however, are typically lower than in oxic seawater because of preferential uptake into highly anoxic sediments as a result of reduction to Mo(IV), followed by coprecipitation of reduced Mo(IV) with iron sulfides and complexation by sediment and pore-water organic matter (Emerson and Huested, 1991). Mo burial in anoxic settings is tied to the conversion of molybdate to thiomolybdates ($MoO_nS_4^{-2}{}_n$) by dissolved sulfide, transforming the geochemically inert form of dissolved Mo into a form that is readily scavenged by particles (Helz et al., 2011; Tribovillard et al., 2006). Although a Mo-Fe association in nature is common and thiomolybdates can be removed by pyrite, the strong correlation of Mo with organic carbon in sediments is observed and cannot be ignored (Anbar et al., 2007; Helz et al., 2011; Volkov and Fomina, 1974). Another likely scavenger is a nanoscale Fe(II) – Mo(VI) sulfide mineral discovered by Helz et al. (2011). Additionally, in iron formations, much of the Mo is removed with oxides, with the amount of sorption being dependent on the amount of Si in solution (Konhauser et al., 2007b).

*2.6.2.3 Vanadium*

The aqueous geochemistry of V is dominated by V(IV) and V(V), where there is a decrease in solubility from its oxidized to reduced form. In oxic water, the primary V species are the phosphate-like anions $H_2VO_4^-$ and $HVO_4^{-2}$. In reducing conditions, the

vanadyl cation $VO^{+2}$ dominates, which has a tendency to hydrolyze, is insoluble in the pH range of natural waters and is strongly adsorbed onto particles and forms stable complexes with organic ligands, as well as humic and fulvic acids (Emerson and Huested, 1991; Shiller and Mao, 2000; Tribovillard et al., 2006; Wehrli and Stumm, 1989). The reduction of V occurs in two steps. First, V(V) converts to V(IV), which will be particle reactive, but further reduction to V(III) is likely needed for the large (100's of ppm) V enrichment observed in black shales (Morford and Emerson, 1999). While sorption to oxides is not the most efficient way to get large V enrichments, it is likely the most important mechanism in the formation of iron formations, rather than through mineral formation or complexation with dissolved organic ligands (Wehrli and Stumm, 1989). Similar to Mo, V is preferentially concentrated in sediments overlain by anoxic water, however, the mechanism for this incorporation is different (Emerson and Huested, 1991). Although fluvial input is an important source of V to the oceans, it is also important to recognize that V is consistently enriched in hydrothermal fluids with respect to seawater (German and Von Damm, 2006). Because V is only soluble and mobile in its oxidized form, and a main source of V to oceans is fluvial input; Concentrations in seawater, and thus in BIF, should be low before the GOE and increase after the onset of oxidative continental weathering, (Fig. 2.12B).

*2.6.2.4 Cobalt*

Cobalt exists in two oxidation states in terrestrial minerals, Co(II) and Co(III) (Burns, 1976). Rivers deposit Co that is adsorbed onto particles into the oceans where Co is efficiently desorbed and scavenged by hydrous iron oxides (Aston and Chester, 1973). This allows seawater Co concentration to be preserved by BIF. In previous

studies, Co shows the same type of systematics as V and Cr (Dymek and Klein, 1988). Similar to V, Co is consistently enriched in hydrothermal fluids with respect to seawater (German and Von Damm, 2006). Based on their redox chemistry, concentrations of both V and Cr are expected to increase after the GOE, thus we can also expect the same for Co. Our data show an increase in Co in post GOE samples (Fig. 2.12C), which we interpret to support the presence of oxidative continental weathering.

*2.6.2.5 Chromium*

Cr is sensitive to the redox state of the surface environment because oxidative continental weathering oxidizes reduced Cr(III) to Cr(VI), which is catalyzed by $MnO_2$. Hexavalent Cr is highly soluble and mobile as either chromate ($CrO_4^{-2}$) in alkaline conditions or bichromate ($HCrO_4^-$) in acidic conditions. Trivalent Cr is chemically similar to $Fe^{3+}$ and $Al^{3+}$, is insoluble and immobile, and accumulates in secondary oxides and clays (Frei et al., 2009; Johnson and Bullen, 2004; Tribovillard et al., 2006). While Cr, likely as Cr(III), can be delivered to the oceans via hydrothermal fluids, this contribution is considered small seawater Cr(VI) concentrations are thought to be directly linked to riverine input and thus can preserve evidence for atmospheric oxidation. This evidence is passed on to BIF because, in the presence of Fe(II), Cr(IV) is efficiently reduced to Cr(III), which is subsequently scavenged by Fe-oxyhydroxides as a result of the very low solubility of $FeCr(OH)_3$ solids (Frei et al., 2009; Tribovillard et al., 2006). We see evidence for this preservation of atmospheric oxidation in our samples, where there is a clear increase in the Cr/Fe ratios in post-GOE BIFs relative to pre-GOE BIFs (Fig. 2.12D).

*2.6.2.6 Effects of Early Diagenesis*

Because trace elements respond in largely predictable ways to redox variations, they are useful in the analysis of environmental redox conditions. However, some elements may be more mobile than others post deposition. Thus, redox studies are best centered on elements least vulnerable to primary and secondary complications, such as U, V, Mo, Ni, and Cu (Tribovillard et al., 2006). The net effect on any influx (ex. hydrothermal, riverine, etc.) to the oceans of particle reactive elements (i.e., Cr, Co, V, Mo) is in least partly dependent on the extent to which metal/Fe ratio are preserved during sedimentary diagenesis. The early diagenetic alteration of Fe oxyhydroxides, on which many transition metals are adsorbed, is dominated by the transformation of ferrihydrite to goethite (Dunk and Mills, 2006). However, the rate of this alteration is slow, with the time to half conversion of ferrihydrite being on the order of ~100 Ka. The stabilization of the ferrihydrite in deep-sea sediments has been attributed to both the presence of adsorbed and/or co-precipitated divalent transition metal species, as well as to the presence of bacteria (Dunk and Mills, 2006). A recent study by Dunk and Mills (2006) on hydrothermal plume sediments where metal adsorption onto Fe and Mn oxides are prevalent, indicate that there is minimal redox disturbance during early diagenesis and that these sediments represent a relatively permanent sink.

## 2.7 Oceanic Oxycline and Oxidative Continental Weathering Through Time

The presence of predominately positive Ce anomalies in the Gunflint Iron Formation compared to pre-GOE Archean-aged BIF (Fig. 2.8A) supports the presence of an oxycline in the ~1.9 Ga Gunflint ocean basin. This suggests that the redox structure of the depositional basins in which BIF formed has changed relative to BIF deposited prior

to the GOE. An increase in the concentration of U and other redox-sensitive elements (Mo, V, Co, Cr) that have multiple oxidation states, where the reduced form is less soluble and mobile than the oxidized form, in post-GOE BIFs relative to pre-GOE BIFs (Fig. 2.12) also suggests that oxidative continental weathering was active by ~1.9 Ga. The Pb isotope composition of the Gunflint samples (Fig. 2.11) indicates that this increase in U was a result of oxidative weathering and not an artifact of modern weathering. By proxy it can be concluded that the concentrations of the other redox-sensitive elements are not a result of modern oxidative weather because U is mobilized under smaller quantities of oxygen compared to other trace elements, such as V, Cr, and Mo (Tribovillard et al., 2006).

Prior to the GOE, there was very little ($<10^{-5}$ PAL) free atmospheric oxygen, therefore oxidative continental weathering was suppressed and U and other redox-sensitive elements were not readily released and transported to the oceans by the same means. Because continental run-off is the primary source for these elements, their concentrations in BIFs at this time were very low. There was also little free oxygen anywhere in the ocean column at this time, resulting in no Ce anomalies, or slightly positive anomalies, in BIF.

It has been suggested that there may have been a slight increase in the oxygenation state of the upper ocean immediately before the start of the GOE (Anbar et al., 2007; Bekker and Holland, 2012; Beukes et al., 2010; Crowe et al., 2013; Kamber and Whitehouse, 2007), which would have resulted in the oxidation of Ce(III) to Ce(IV) and the production of negative Ce anomalies. The deeper ocean, however, would still

have been anoxic, Ce(III) would not have been oxidized and absent or slightly positive Ce anomalies would be produced.

After the GOE, free oxygen in the atmosphere resulted in increased oxygen concentrations in the upper water column and oxidative continental weathering resulted in the increased transport of redox-sensitive elements to the oceans via rivers, with the contribution from hydrothermal fluids becoming relatively less important. BIFs precipitated from the oceans at this time have increased concentrations of many of these elements (Mo, Co, V, Cr, U/Pb,) relative to their concentrations in BIFs deposited before the GOE. There is evidence (i.e. the presence of both negative and positive Ce anomalies in post-GOE BIFs), however, that the entire ocean column was not fully ventilated.

**2.8 Summary Points**

Banded iron formation has the potential of preserving important changes in the redox condition of the Earth's early oceans and atmosphere. The shift from an anoxic to oxic atmosphere occurred at approximately 2.3 Ga during the Great Oxidation Event. At 1.9 Ga, the Gunflint Iron Formation was deposited and preserves evidence for the evolving oxidization state of the oceans and atmosphere. In order to explore any changes in the redox state of the Gunflint ocean basin and atmosphere at 1.9 Ga, Gunflint BIF geochemistry was compared to the geochemistry of Archean-aged BIF samples. Taken together, the shift in these data from pre- to post-Archean aged samples support the presence of an oxycline and oxidative continental weathering at 1.9 Ga.

1. To determine if samples from the Gunflint Iron Formation preserved primary trace-element signatures or were altered by siliciclastic contamination and/or by modern weathering, we measured a variety of siliciclastic indictors and Pb isotope compositions,

respectively. Gunflint and Zimbabwe samples with greater than 1.7 wt% $Al_2O_3$ and 30 ppm Zr were considered contaminated. Isua samples with greater than 0.8 wt% $Al_2O_3$ and 5 ppm Zr were considered contaminated. All samples with a $Pr_{SN}/Yb_{SN}$ ratio of greater than 1 were also considered contaminated.

2. In general, pre-GOE BIFs from the >3.7 Ga Isua Greenstone Belt and the 3.0 Buhwa Greenstone Belt do not display negative or positive shale-normalized Ce anomalies, averaging 1.07 and 1.00, respectively. The lack of a positive anomaly indicates trivalent Ce behavior and a reducing depositional basin. In contrast, post-GOE BIF from the 1.9 Gunflint Iron Formation record more strongly positive Ce anomalies (up to 1.9), with an average value of 1.2, as well as negative Ce anomalies. This is a result of oxidative precipitation of insoluble Ce(IV) above an oxycline in oxygenated shallow water and reductive dissolution to soluble Ce(III) below an oxycline in reducing deep water.

3. LREE preferentially adsorb to, and are removed by, Mn- and Fe-oxyhydroxides and other reactive surfaces in oxygenated waters. Reductive dissolution occurs as these particles cross a redox boundary into deep, anoxic waters, where the LREE are released and the ratio of light to heavy REE increases. Thus, the increase in the range of LREE/HREE, calculated as $Pr_{SN}/Yb_{SN}$, in post-GOE GF BIF when compared to Archean BIF from the IGB and BGB is consistent with the presence of an oxycline in the Gunflint ocean basin.

4. Because Y is less effectively scavenged than Ho from seawater by Mn- and Fe-oxyhydroxides, there is increased adsorption of Ho. This results in increased Ho in deep anoxic waters as Mn- and Fe-oxyhydroxides dissolve when they cross an oxycline, which

in turn results in a decrease in the dissolved seawater $Y_{SN}/Ho_{SN}$ ratio. The average $Y_{SN}/Ho_{SN}$ ratio decreases in BIFs from the Archean (IGB = 45, BGB = 34, Kuruman and Penge = 47) to the Paleoproterozoic (GF = 31), which provides additional evidence for an oxycline in the Gunflint ocean basin.

5. To determine if samples from the Gunflint Iron Formation preserved primary geochemical signatures, Pb isotopes were measured. The positive correlation between $^{238}U/^{204}Pb$ and $^{206}Pb/^{204}Pb$ indicates that the U/Pb ratios measured today for the Gunflint samples are the same as the original ratios and are not an artifact of modern weathering. The U-Pb work in this study provides strong support that rather odd REE patterns seen in the Animikie Basin, relative to Archean BIF REE patterns, are not diagenetic artifacts. Therefore, the REEs provide evidence for fundamental differences in the redox structure of the basins in which pre- and post-GOE BIFs were formed. It was also determined that the Pb was derived from two sources, depleted mantle and continental sediments, suggesting that the Gunflint samples were derived from a complex oceanic geochemical reservoir.

6. Mo, V, Co, Cr and U/Pb are all terrestrially-sourced, redox-sensitive elements and ratios that show an increase in their concentration in post-GOE BIFs relative to pre-GOE BIF. All of these elements are more mobile and soluble in their oxidized forms and would have been released during oxidative continental weathering and transported to the oceans via rivers.

**References**


Alibert, C., Mcculloch, M.T., 1993. Rare-Earth Element and Neodymium Isotopic Compositions of the Banded Iron-Formations and Associated Shales from Hamersley, Western-Australia. Geochimica et Cosmochimica Acta 57, 187-204.

Anbar, A.D., 2004. Iron stable isotopes: beyond biosignatures. Earth and Planetary Science Letters 217, 223-236.

Anbar, A.D., Duan, Y., Lyons, T.W., Arnold, G.L., Kendall, B., Creaser, R.A., Kaufman, A.J., Gordon, G.W., Scott, C., Garvin, J., Buick, R., 2007. A whiff of oxygen before the great oxidation event? Science 317, 1903-1906.

Anbar, A.D., Holland, H.D., 1992. The Photochemistry of Manganese and the Origin of Banded Iron Formations. Geochimica et Cosmochimica Acta 56, 2595-2603.

Anbar, A.D., Zahnle, K.J., Arnold, G.L., Mojzsis, S.J., 2001. Extraterrestrial iridium, sediment accumulation and the habitability of the early Earth's surface. Journal of Geophysical Research 106, 3219-3236.

André, L., Cardinal, D., Alleman, L., Moorbath, S., 2006. Silicon isotopes in ~3.8 Ga West Greenland rocks as clues to the Eoarchaean supracrustal Si cycle. Earth and Planetary Science Letters 245, 162-173.

Appel, P.W.U., 1980. On the Early Archean Isua Iron-Formation, West-Greenland. Precambrian Research 11, 73-87.

Appel, P.W.U., Fedo, C.M., Moorbath, S., Myers, J.S., 1998. Early Archean Isua supracrustal belt, West Greenland: pilot study of the Isua Multidisciplinary Research Project. Journal of Greenland Survey Bulletin 180, 94-99.

Aston, S.R., Chester, R., 1973. The influence of suspended particles on the precipitation of iron in natural waters. Estuarine and Coastal Marine Science I, 225-231.

Baadsgaard, H., Lambert, R., Krupicka, J., 1976. Mineral isotopic age relationships in the polymetamorphic Amitsoq gneisses, Godthaab District, West Greenland. Geochimica et Cosmochimica Acta 40, 513-527.

Barrett, T.J., Fralick, P., Jarvis, I., 1988. Rare-earth-element geochemistry of some Archean iron formations north of Lake Superior, Ontario. Canadian Journal of Earth Sciences 25, 570-580.

Bau, M., 1991. Rare-earth element mobility during hydrothermal and metamorphic fluid-rock interaction and the significance of the oxidation state of eruopium. Chemical Geology 93, 219-230.

Bau, M., 1993. Effects of syn- and post-depositional processes on the rare-earth element distribution in Precambrian iron-formations. European Journal of Mineralogy 5, 257-267.

Bau, M., 1996. Controls on the fractionation of isovalent trace elements in magmatic and aqueous systems: Evidence from Y/Ho, Zr/Hf, and lanthanide tetrad effect. Contributions to Mineralogy and Petrology 123, 323-333.

Bau, M., 1999. Scavenging of dissolved yttrium and rare earths by precipitating iron oxyhydroxide: Experimental evidence for Ce oxidation, Y-Ho fractionation, and lanthanide tetrad effect. Geochimica et Cosmochimica Acta 63, 67-77.

Bau, M., Dulski, P., 1996. Distribution of yttrium and rare-earth elements in the Penge and Kuruman iron-formations, Transvaal Supergroup, South Africa. Precambrian Research 79, 37-55.

Bau, M., Dulski, P., 1999. Comparing yttrium and rare earths in hydrothermal fluids from the Mid-Atlantic Ridge: implications for Y and REE behaviour during near-vent mixing and for the YrHo ratio of Proterozoic seawater. Chemical Geology 155, 77-90.

Bau, M., Koschinsky, A., 2009. Oxidative scavenging of cerium on hydrous Fe oxide: Evidence from the distribution of rare earth elements and yttrium between Fe oxides and Mn oxides in hydrogenetic ferromanganese crusts. Geochemical Journal 43, 37-47.

Bau, M., Moller, P., 1993. Rare earth element systematics of the chemically precipitated component in Early Precambrain iron formations and the evolution of the terrestrial atmosphere-hydrosphere-lithosphere system. Geochimica et Cosmochimica Acta 57, 2239-2249.

Bau, M., Hohndorf, A., Dulski, P., Beukes, N.J., 1997a. Sources of Precambrian rare-earth elements and iron in Paleoproterozoic iron-formations from the Transvaal Supergroup, South Africa - evidence from neodymium isotopes. J Geol 105, 121-129.

Bau, M., Moller, P., Dulski, P., 1997b. Yttrium and lanthanides in eastern Mediterranean seawater and their factionation during redox-cycling. Marine Chemistry 56, 123-131.

Beard, B.L., Johnson, C.M., Cox, L., Sun, H., Nealson, K.H., Aguilar, C., 1999. Iron isotope biosignatures. Science 285, 1889-1892.

Bekker, A., Holland, H.D., Wang, P.L., Rumble, D., Stein, H.J., Hannah, J.L., Coetzee, L.L., Beukes, N.J., 2004. Dating the rise of atmospheric oxygen. Nature 427, 117-120.

Bekker, A., Slack, J.F., Planavsky, N., Krapez, B., Hofmann, A., Konhauser, K.O., Rouxel, O.J., 2010. Iron Formation: The Sedimentary Product of a Complex Interplay among Mantle, Tectonic, Oceanic, and Biospheric Processes. Econ Geol 105, 467-508.

Belevtsev, Y., Belevstev, R., Siroshtan, R., 1982. The Krivoy Rog Basin, in: Trendall, A.F., Morris, R.C. (Eds.), Iron-Formations: Facts and Problems. Elsevier, Amsterdam, pp. 211-252.

Beukes, N., 1973. Precambrian iron-formations of southern Africa. Econ Geol 68, 960-1024.

Beukes, N., 2004. Biogeochemistry - Early options in photosynthesis. Nature 431, 522-523.

Beukes, N.J., Klein, C., 1990. Geochemistry and Sedimentology of a Facies Transition - from Microbanded to Granular Iron-Formation - in the Early Proterozoic Transvaal Supergroup, South-Africa. Precambrian Research 47, 99-139.

Beukes, N.J., Gutzmer, J., Nel, B.P., 2010. Ce anomalies in ~2.4 Ga iron and managnese formations as proxy for early oxygenation of oceanic environments. Goldschmidt Conference Abstracts.

Bjerrum, C.J., Canfield, D.E., 2002. Ocean productivity before about 1.9 Gyr ago limited by phosphorus adsorption onto iron oxides. Nature 417, 159-162.

Bolhar, R., Kamber, B.S., Moorbath, S., Fedo, C.M., Whitehouse, M.J., 2004. Characterisation of early Archaean chemical sediments by trace element signatures. Earth and Planetary Science Letters 222, 43-60.

Bonnichsen, B., 1975. Geology of the Biwabik iron formation, Dunka River area, Minnesota. Econ Geol 70, 319-340.

Braterman, P.S., Cairns-Smith, A.G., 1987. Photoprecipitation and the Banded Iron-Formations - Some Quantitative Aspects. Origins of Life and Evolution of the Biosphere 17, 221-228.

Brengman, L.A., 2014. From source to sink: Silicon isotope composition of bedrock, detritial quartz arenites, chert and BIF from the ~3 Ga Buhwa Greenstone Belt, Zimbabwe, Geological Society of American Annual Meeting, Vancouver, British Columbia.

Brengman, L.A., Fedo, C.M., 2012. Origin of BIF-like jasperlite in the 2.72 Ga Hunter Mine Group. Abitibi Greenstone Belt, Quebec by metasomatic replacement of felsic volcanic rocks, Geologic Society of America Annual Meeting, Charlotte, North Carolina.

Brocks, J.J., Logan, G.A., Buick, R., Summons, R.E., 1999. Archean Molecular Fossils and the Early Rise of Eukaryotes. Science 285, 1033-1036.

Broderick, T.M., 1920. Economic geology and stratigraphy of the Gunflint Iron District, Minnesota. Econ Geol 15, 422-452.

Brookins, D.G., 1989. Aqueous geochemistry of rare earth elements, in: Lipin, B.R., McKay, G.A. (Eds.), Reviews in Mineralogy: Geochemistry and Mineralogy of Rare Earth Elements. Mineralogical Society of America, Washington, D.C., pp. 201-225.

Brown, D.A., 2006. Microbial mediation of iron mobilization and deposition in iron formations since the early Precambrian, in: Kesler, S., Ohmoto, H. (Eds.), Evolution of Early Earth's Atmosphere, Hydrosphere, and Biosphere – Constraints From Ore Deposits. The Geological Soceity of America Memoir, pp. 239-256.

Bryne, R.H., Kim, K.H., 1990. Rare earth element scavenging in seawater. Geochimica et Cosmochimica Acta 54, 2645-2656.

Bryne, R.H., Sholkovitz, E.R., 1996. Marine chemistry and geochemistry of the lanthanides, in: Gschneider, K.A., Eyring, L. (Eds.), Handbook on the Physics and Chemistry of the Rare Earths. Elsevier, Amsterdam, pp. 497-593.

Buick, R., 1992. The Antiquity of Oxygenic Photosynthesis - Evidence from Stromatolites in Sulfate-Deficient Archean Lakes. Science 255, 74-77.

Buick, R., 2008. When did oxygenic photosynthesis evolve? Philos Trans R Soc Lond B Biol Sci 363, 2731-2743.

Burns, R.G., 1976. Uptake of Cobalt into Ferromanganese Nodules, Soils, and Synthetic Manganese(Iv) Oxides. Geochimica et Cosmochimica Acta 40, 95-102.

Cairns-Smith, A.G., 1987. Precambrian solution photochemistry, inverse segregation, and banded iron formations. Nature 76.

Canfield, D.E., 1998. A new model for Proterozoic ocean chemistry. Nature 396, 450-453.

Canfield, D.E., 2005. The early history of atmospheric oxygen: Homage to Robert A. Garrels. Annual Review of Earth and Planetary Sciences 33, 1-36.

Canfield, D.E., Habicht, K.S., Thamdrup, B., 2000. The Archean Sulfur Cycle and the Early History of Atmospheric Oxygen. Science 288, 658-661.

Cantrell, K.J., Byrne, R.H., 1987. Rare-Earth Element Complexation by Carbonate and Oxalate Ions. Geochimica et Cosmochimica Acta 51, 597-605.

Chandler, F.W., 1980. Proterozoic redbed sequences of Canada. Canadian Geological Survey Bulletin 311.

Chang, S.B.R., Kirschvink, J.L., 1989. Magnetofossils, the Magnetization of Sediments, and the Evolution of Magnetite Biomineralization. Annual Review of Earth and Planetary Sciences 17, 169-195.

Chigira, M., Watanabe, M., 1994. Silica precipitation behavior in a flow field with negative temperature gradients. Journal of Geophysical Research 99, 15539-15548.

Cloud, P.E., 1965. Significance of Gunflint (Precambrian) microflora-photosynthetic oxygen may have had important local effects before becoming a major atmospheric gas. Science 148, 1135-1143.

Cloud, P.E., 1973. Paleoecological significance of banded iron-formation. Econ Geol 68, 1135-1143.

Condie, K.C., 1993. Chemical-Composition and Evolution of the Upper Continental-Crust - Contrasting Results from Surface Samples and Shales. Chemical Geology 104, 1-37.

Croal, L.R., Jiao, Y., Kappler, A., Newman, D.K., 2009. Phototrophic Fe(II) oxidation in an atmosphere of H2: implications for Archean banded iron formations. Geobiology 7, 21-24.

Czaja, A.D., Johnson, C.M., Beard, B.L., Roden, E.E., Weiqiang, L., Moorbath, S., 2013. Biological Fe oxidation controlled deposition of banded iron formation in the ca. 3770 Ma Isua Supracrustal Belt (West Greenland). Earth and Planetary Science Letters 363, 192-203.

Dauphas, N., van Zuilen, M., Wadhwa, M., Davis, A.M., Marty, B., Janney, P.E., 2004. Clues from Fe isotope variations on the origin of early Archean BIFs from Greenland. Science 306, 2077-2080.

Dauphas, N., Vanzuilen, M., Busigny, V., Lepland, A., Wadhwa, M., Janney, P., 2007. Iron isotope, major and trace element characterization of early Archean supracrustal rocks from SW Greenland: Protolith identification and metamorphic overprint. Geochimica et Cosmochimica Acta 71, 4745-4770.

De Carlo, E.H., Green, W.J., 2002. Rare earth elements in the water column of Lake Vanda, McMurdo Dry Valleys, Antarctica. Geochimica et Cosmochimica Acta 66, 1323-1333.

Derry, L.A., Jacobsen, S.B., 1990. The Chemical Evolution of Precambrian Seawater - Evidence from Rees in Banded Iron Formations. Geochimica et Cosmochimica Acta 54, 2965-2977.

Des Marais, D.J., Allamandola, L.J., Benner, S.A., Boss, A.P., Deamer, D., Falkowski, P.G., Farmer, J.D., Hedges, S.B., Jakosky, B.M., Knoll, A.H., Liskowsky, D.R., Meadows, V.S., Meyer, M.A., Pilcher, C.B., Nealson, K.H., Spormann, A.M., Trent, J.D., Turner, W.W., Woolf, N.J., Yorke, H.W., 2003. The NASA Astrobiology Roadmap. Astrobiology 3, 219-235.

Dimroth, E., Kimberley, M.M., 1976. Precambrian atmosphereic oxygen: Evidence in the sedimentary distribution of carbon, sulfur, uranium, and iron. Canadian Journal of Earth Sciences 13, 1161-1185.

Duff, M.C., Coughlin, J.U., Hunter, D.B., 2002. Uranium co-precipitation with iron oxide minerals. Geochimica et Cosmochimica Acta 66, 3533-3547.

Dunk, R.M., Mills, R.A., 2006. The impact of oxic alteration on plume-derived transition metals in ridge flank sediments from the East Pacific Rise. Marine Geology 229, 133-157.

Dymek, R.F., Klein, C., 1988. Chemistry, Petrology and Origin of Banded Iron-Formation Lithologies from the 3800-Ma Isua Supracrustal Belt, West Greenland. Precambrian Research 39, 247-302.

Eggins, S.M., Woodhead, J.D., Kinsley, L.P.J., Mortimer, G.E., Sylvester, P., McCulloch, M.T., Hergt, J.M., Handler, M.R., 1997. A simple method for the precise determination of >=40 trace elements in geological samples by ICPMS using enriched isotope internal standardisation. Chemical Geology 134, 311-326.

Ehrenreich, A., Widdel, F., 1994. Anaerobic Oxidation of Ferrous Iron by Purple Bacteria, a New-Type of Phototrophic Metabolism. Appl Environ Microb 60, 4517-4526.

Emerson, D., Moyer, C.L., 2002. Neutrophilic Fe-Oxidizing bacteria are abundant at the Loihi Seamount hydrothermal vents and play a major role in Fe oxide deposition. Appl Environ Microb 68, 3085-3093.

Emerson, S.R., Huested, S.S., 1991. Ocean Anoxia and the Concentrations of Molybdenum and Vanadium in Seawater. Marine Chemistry 34, 177-196.

England, G.L., Rasmussen, B., Krapez, B., Groves, D.I., 2002. Paleoenvironmental significance of rounded pyrite in siliciclastic sequences of the Late Archean Witwaterstand Basin: Oxygen-deficient atmosphere or hydrothermal alteration? Sedimentology 49, 1133-1156.

Farquhar, J., Bao, H.M., Thiemens, M., 2000. Atmospheric influence of Earth's earliest sulfur cycle. Science 289, 756-758.

Farquhar, J., Wing, B.A., 2003. Multiple sulfur isotopes and the evolution of the atmosphere. Earth and Planetary Science Letters 213, 1-13.

Faure, G., 1986. Principles of Isotope Geolog. John Wiley & Sons, Inc., New Jersey.

Fedo, C.M., 2000. Setting and origin for problematic rocks from the > 3.7 Ga Isua Greenstone Belt, southern west Greenland: Earth's oldest coarse elastic sediments. Precambrian Research 101, 69-78.

Fedo, C.M., Eriksson, K.A., 1995. Geologic setting and ideas concerning the origin of the iron-ore deposits at Buhwa, Zimbabwe, in: Blenkinsop, T.G., Tromp, P.L. (Eds.), Sub-Saharan Economic Geology. A.A. Balkema Publishers, Vermont, pp. 43-53.

Fedo, C.M., Eriksson, K.A., 1996. Stratigraphic framework of the similar to 3.0 Ga Buhwa greenstone belt: A unique stable-shelf succession in the Zimbabwe Archean Craton. Precambrian Research 77, 161-178.

Fedo, C.M., Whitehouse, M.J., 2002. Metasomatic origin of quartz-pyroxene rock, Akilia, Greenland, and implications for Earth's earliest life. Science 296, 1448-1452.

Fedo, C.M., Eriksson, K.A., Blenkinsop, T.G., 1995. Geologic history of the Archean Buhwa Greenstone Belt and surrounding granite-gneiss terrane, Zimbabwe, with implications for the evolution of the Limpopo Belt. Canadian Journal of Earth Sciences 32, 1977-1990.

Fedo, C., Hage, M., Schoenberg, R., Whitehouse, M., 2010. Can Fe isotopes be used to fingerprint Precambrian BIF?, Goldschmidt Knoxville, TN.

Fedo, C.M., Myers, J.S., Appel, P.W.U., 2001. Depositional setting and paleogeographic implications of earth's oldest supracrustal rocks, the > 3.7 Ga Isua Greenstone belt, West Greenland. Sediment Geol 141, 61-77.

Fedo, C.M., Whitehouse, M.J., Kamber, B.S., 2006. Geological constraints on detecting the earliest life on Earth: a perspective from the Early Archaean (older than 3.7 Gyr) of southwest Greenland. Philos Trans R Soc Lond B Biol Sci 361, 851-867.

Floran, R.J., Papike, J.J., 1978. Mineralogy and Petrology of Gunflint Iron Formation, Minnesota-Ontario - Correlation of Compositional and Assemblage Variations at Low to Moderate Grade. Journal of Petrology 19, 215-288.

Fralick, P., Davis, D.W., Kissin, S.A., 2002. The age of the Gunflint Formation, Ontario, Canada: single zircon U Pb age determinations from reworked volcanic ash. Canadian Journal of Earth Sciences 39, 1085-1091.

Frei, R., Dahl, P.S., Duke, E.F., Frei, K.M., Hansen, T.R., Frandsson, M.M., Jensen, L.A., 2008. Trace element and isotopic characterization of Neoarchean and Paleoproterozoic iron formations in the Black Hills (South Dakota, USA): Assessment of chemical change during 2.9–1.9Ga deposition bracketing the 2.4–2.2Ga first rise of atmospheric oxygen. Precambrian Research 162, 441-474.

Frei, R., Gaucher, C., Poulton, S.W., Canfield, D.E., 2009. Fluctuations in Precambrian atmospheric oxygenation recorded by chromium isotopes. Nature 461, 250-253.

French, B.M., 1971. Stability relations of siderite ($FeCO_3$) in the system Fe-C-O. American Journal of Science 271, 37-78.

Friend, C.R.L., Nutman, A.P., 2005. Complex 3670-3500 Ma orogenic episodes superimposed on juvenile crust accreted between 3850 and 3690 Ma, Itsaq Gneiss Complex, Southern West Greenland. J Geol 113, 375-397.

Friend, C.R.L., Nutman, A.P., Bennett, V.C., Norman, M.D., 2008. Seawater-like trace element signatures (REE + Y) of Eoarchaean chemical sedimentary rocks from southern West Greenland, and their corruption during high-grade metamorphism. Contributions to Mineralogy and Petrology 155, 229-246.

Frost, B.R., 1979. Metamorphism of iron-formation: paragenesis in the systems Fe-Si-C-O-H. Econ Geol 74, 775-785.

Fryer, B.J., 1977. Rare earth evidence in iron-formations for changing Precambrian oxidation states. Geochimica et Cosmochimica Acta 41, 361-367.

Fyon, J., Schwarts, H., Crocket, J., 1984. Carbonization and gold mineralization in the Timmins area, Abitibi greenstone belt: Genetic links with Archean mantle CO2-degassing and lower crust granulization. Geological Association of Canada Program with Abstract 9, 65.

Garrels, R.M., Perry, E.A.J., 1974. Cycling of carbon, sulfur, and oxygen through geologic time, in: Goldberg, E.A. (Ed.), The Sea. Wiley, New York, pp. 303-336.

German, C.R., Elderfield, H., 1990. Application of the Ce anomaly as a paleoredox indicator: The ground rules. Paleoceanography 5, 823-833.

German, C.R., Holliday, B.P., Elderfield, H., 1991. Redox cycling of rare earth elemtns in the suboxic zone of the Black Sea. Geochimica et Cosmochimica Acta 55, 3553-3558.

German, C.R., Von Damm, K.L., 2006. Hydrothermal Processes, in: Elderfield, H. (Ed.), The oceans and marine geochemistry. Elsevier, Oxford, UK, pp. 181-222.

Goodwin, A.M., 1956. Facies relations in the Gunflint Iron Formation. Econ Geol 51, 565-595.

Goodwin, A.M., 1973. Archean volcanogenic iron-formation of the Canadian shield. Science Terra 9, 23-34.

Griffin, W.L., McGregor, V.R., Nutman, A.P., Taylor, P.N., Bridgwater, D., 1980. Early Archean granulite-facies metamorphism south of Ameralik, West Greenland. Earth and Planetary Science Letters 50, 59-74.

Gross, G.A., 1965. Geology of iron deposits in Canada I. General geology and evaluation of iron deposits. Geological Survey of Canada Economic Geology Report 22.

Gross, G.A., 1983. Tectonic systems and the deposition of iron formation Precambrian Research 20, 171-187.

Groves, D.I., Batt, W., 1984. Spatial and temporal variations of Archean metallogenic association in terms of evolution of granitoid-greenstone terraines with particular emphasis on Western Australia, in: Kroner, A., Hanson, G., Goodwin, A.M. (Eds.), Archean Geochemistry. Springer-Verlag, Berlin, pp. 73-98.

Hamade, T., Konhauser, K.O., Raiswell, R., Goldsmith, S., Morris, R.C., 2003. Using Ge/Si ratios to decouple iron and silica fluxes in Precambrian banded iron formations. Geology 31, 35-38.

Harder, E.C., 1919. Iron depositing bacteria and their geological relations. The Journal of Geology 30, 506-509.

Heck, P.R., Huberty, J.M., Kita, N.T., Ushikubo, T., Kozdon, R., Valley, J.W., 2011. SIMS analysis of silicon and oxygen isotope ratios for quartz from Archean and Paleoproterozoic banded iron formations. Geochimica et Cosmochimica Acta 75, 5879-5891.

Heising, S., Schink, B., 1998. Phototrophic oxidation of ferrous iron by a Rhodomicrobium vannielii strain. Microbiol-Uk 144, 2263-2269.

Helz, G.E., Bura-Nakic, E., Mikac, N., Ciglenecki, I., 2011. New model for molybdenum behavior in euxinic waters. Chemical Geology 284, 323-332.

Holland, H.D., 1973. Ocean - possible srouce of iron in iron-formations. Econ Geol 68, 1169-1172.

Holland, H.D., 1984. The chemical evoultion of the atmosphere and oceans. Princeton University Press, New York.

Holm, N.G., 1989. The 13C/12C ratios of siderite and organic matter of a modern metalliferous hydrothermal sediment and their implications for banded iron formations. Chemical Geology 77, 41-45.

Holm, N.G., Charlou, J.L., 2001. Initial indications of abiotic formation of hydrocarbons in the Rainbow ultramafic hydrothermal system, Mid-Atlantic Ridge. Earth and Planetary Science Letters 191, 1-8.

Hostetler, P.B., Garrels, R.M., 1962. Transportation and precipitation of uranium and vanadium at low temperatures, with special reference to sandstone-type uranium deposits. Econ Geol 57, 137-167.

Isley, A.E., 1995. Hydrothermal Plumes and the Delivery of Iron to Banded Iron-Formation. J Geol 103, 169-185.

Jacobsen, S.B., Pimental-Klose, M., 1988. A Nd isotope study of the Hamersley and Michipicoten banded iron formations: The source of REE and Fe in Archean oceans. Earth and Planetary Science Letters 87, 29-44.

James, H., 1954. Sedimentary facies of iron formations. Econ Geol 49, 235-293.

James, H., Trendall, A.F., 1982. Banded iron formation: Distribution in time and paleoenvironmental significance, in: Holland, H.D., Schidlowski, M. (Eds.), Mineral Deposits and the Evolution of the Biosphere. Spring-Verlag, NY, pp. 199-218.

Jirsa, M.A., Weiblen, P.W., 2007. Geology along the Gunflint Trail. 53rd Annual Institute on Lake Superior Geology Field Trip Guide 6.

Johnson, C.M., Beard, B.L., 2006. Fe isotopes: An emerging technique for understanding modern and ancient biogeochemical cycles. GSA Today 16, 4.

Johnson, C.M., Beard, B.L., Beukes, N.J., Klein, C., O'Leary, J.M., 2003. Ancient geochemical cycling in the Earth as inferred from Fe isotope studies of banded iron formations from the Transvaal Craton. Contributions to Mineralogy and Petrology 144, 523-547.

Johnson, C.M., Beard, B.L., Klein, C., Beukes, N.J., Roden, E.E., 2008a. Iron isotopes contrain biologic and abiologic processes in banded iron formation genesis. Geochimica et Cosmochimica Acta 72, 151-169.

Johnson, C.M., Beard, B.L., Roden, E.E., 2008b. The Iron Isotope Fingerprints of Redox and Biogeochemical Cycling in Modern and Ancient Earth. Annual Review of Earth and Planetary Sciences 36, 457-493.

Johnson, T.M., Bullen, T.D., 2004. Mass-dependent fractionation of selenium and chromium isotopes in low-temperature environments, in: Johnson, C.M., Beard, B.L., Albarede, F. (Eds.), Rev Mineral Geochem. Mineralogical Society of America, Washington, pp. 289-317.

Kamber, B.S., 2009. Geochemical fingerprinting: 40 years of analytical development and real world applications. Applied Geochemistry 24, 1074-1086.

Kamber, B.S., 2010. Archean mafic–ultramafic volcanic landmasses and their effect on ocean–atmosphere chemistry. Chemical Geology 274, 19-28.

Kamber, B.S., Gladu, A.H., 2009. Comparison of Pb Purification by Anion-Exchange Resin Methods and Assessment of Long-Term Reproducibility of Th/U/Pb Ratio Measurements by Quadrupole ICP-MS. Geostand Geoanal Res 33, 169-181.

Kamber, B.S., Moorbath, S., 1998. Initial Pb of the Amitsoq gneiss revisited: implications for the timing of early Archean crustal evolution in West Greenland. Chemical Geology 150, 19-41.

Kamber, B.S., Whitehouse, M.J., 2007. Micro-scale sulphur isotope evidence for sulphur cycling in the late Archean shallow ocean. Geobiology 5, 5-17.

Kappler, A., Newman, D.K., 2004. Formation of Fe(III)-minerals by Fe(II)-oxidizing photoautotrophic bacteria 1. Geochimica et Cosmochimica Acta 68, 1217-1226.

Kappler, A., Pasquero, C., Konhauser, K.O., Newman, D.K., 2005. Deposition of banded iron formations by anoxygenic phototrophic Fe(II)-oxidizing bacteria. Geology 33, 865.

Kato, Y., Nakamura, K., 2003. Origin and global tectonic significance of Early Archean cherts from the Marble Bar greenstone belt, Pilbara Craton, Western Australia. Precambrian Research 125, 191-243.

Kato, Y., Ohta, I., Tsunematsu, T., Watanabe, Y., Isozaki, Y., Maruyama, S., Imai, N., 1998. Rare earth element variations in mid-Archean banded iron formations: Implications for the chemistry of ocean and continent and plate tectonics. Geochimica et Cosmochimica Acta 62, 3475-3497.

Kato, Y., Yamaguchi, K., Ohmoto, H., 2006. Rare earth elements in Precambrian banded iron formations: Secular changes of Ce and Eu anomalies and evolution of atmospheric oxygen, in: Kesler, S., Ohmoto, H. (Eds.), Evolution of Early Earth's Atmosphere, Hydrosphere, and Biosphere - Constraints from Ore Deposits. Geological Society of America, Boulder, pp. 269-289.

Kimberley, M.M., 1978. Paleoenvironmental classification of iron formations. Econ Geol 73, 215-229.

Klein, C., 2005. Some Precambrian banded iron-formations (BIFs) from around the world: Their age, geologic setting, mineralogy, metamorphism, geochemistry, and origins. American Mineralogist 90, 1473-1499.

Klein, C., Beukes, N., 1992. Proterozoic iron-formations, in: Conder, K. (Ed.), Proterozoic Crustal Evolution. Elsevier, Amsterdam, pp. 383-418.

Klein, C., Beukes, N.J., 1989. Geochemistry and sedimentology of a facies transition from limestone to iron-formation deposition in the Early Proterozoic Transvaal Supergroup, South-Africa. Econ Geol 84.

Knoll, A.H., Javaux, E.J., Hewitt, D., Cohen, P., 2006. Eukaryotic organisms in Proterozoic oceans. Philos T R Soc B 361, 1023-1038.

Komiya, T., Maruyama, S., Masuda, T., Nohda, S., Hayashi, M., Okamoto, K., 1999. Plate Tectonics at 3.8-3.7 Ga: Field Evidence from the Isua Accretionary Complex, Southern West Greenland. The Journal of Geology 107, 515-554.

Konhauser, K., 2007. Introduction to Geomicrobiology. Blackwell Publishing, Massachusetts.

Konhauser, K., Amskold, L., Lalonde, S., Posth, N., Kappler, A., Anbar, A., 2007a. Decoupling photochemical Fe(II) oxidation from shallow-water BIF deposition. Earth and Planetary Science Letters 258, 87-100.

Konhauser, K.O., Hamade, T., Raiswell, R., Morris, R.C., Ferris, F.G., Southam, G., Canfield, D.E., 2002. Could bacteria have formed the Precambrian banded iron formations? Geology 30, 1079-1082.

Konhauser, K.O., Lalonde, S.V., Amskold, L., Holland, H.D., 2007b. Was there really an Archean phosphate crisis? Science 315, 1234-1234.

Konhauser, K.O., Newman, D.K., Kappler, A., 2005. The potential significance of microbial Fe(III) reduction during deposition of Precambrian banded iron formations. Geobiology 3, 167-177.

Konhauser, K.O., Pecoits, E., Lalonde, S.V., Papineau, D., Nisbet, E.G., Barley, M.E., Arndt, N.T., Zahnle, K., Kamber, B.S., 2009. Oceanic nickel depletion and a methanogen famine before the Great Oxidation Event. Nature 458, 750-753.

Kramers, J.D., Tolstikhin, I.N., 1997. Two terrestrial lead isotope paradoxes, forward transport modelling, core formation and the history of the continental crust. Chemical Geology 139, 75-110.

Kump, L., Seyfried, W., 2005. Hydrothermal Fe fluxes during the Precambrian: Effect of low oceanic sulfate concentrations and low hydrostatic pressure on the composition of black smokers. Earth and Planetary Science Letters 235, 654-662.

Kump, L.R., Barley, M.E., 2007. Increased subaerial volcanism and the rise of atmospheric oxygen 2.5 billion years ago. Nature 448, 1033-1036.

Lawrence, M.G., Kamber, B.S., 2006. The behaviour of the rare earth elements during estuarine mixing—revisited. Marine Chemistry 100, 147-161.

Lawrence, M., Greig, A., Collerson, K., Kamber, B., 2006a. Direct quantification of rare earth element concentrations in natural waters by ICP-MS. Applied Geochemistry 21, 839-848.

Lawrence, M.G., Greig, A., Collerson, K.D., Kamber, B.S., 2006b. Rare Earth Element and Yttrium Variability in South East Queensland Waterways. Aquatic Geochemistry 12, 39-72.

Lepland, A., Whitehouse, M.J., 2010. Metamorphic alteration, mineral paragenesis and geochemical re-equilibration of early Archean quartz–amphibole–pyroxene gneiss from Akilia, Southwest Greenland. International Journal of Earth Sciences.

Lepland, A., Whitehouse, M.J., 2011. Metamorphic alteration, mineral paragenesis and geochemical re-equilibration of early Archean quartz-amphibole-pyroxene gneiss from Akilia, Southwest Greenland. International Journal of Earth Sciences 100, 1-22.

Lepland, A., Arrhenius, G., Cornell, D., 2002. Apatite in early Archean Isua supracrustal rocks, southern West Greenland: its origin, association with graphite and potential biomarker. Precambrian Research 119, 221-241.

Lepland, A., van Zuilen, M.A., Arrhenius, G., Whitehouse, M.J., Fedo, C.M., 2005. Questioning the evidence for Earth's earliest life—Akilia revisited. Geology 33, 77.

Lepland, A., van Zuilen, M.A., Philippot, P., 2011. Fluid-deposited graphite and its geobiological implications in early Archean gneiss from Akilia, Greenland. Geobiology 9.

Li, W., Huberty, J.M., Beard, B.L., Kita, N.T., Valley, J.W., Johnson, C.M., 2013. Contrasting behavior of oxygen and iron isotopes in banded iron formations revealed by *in situ* isotopic analysis. Earth and Planetary Science Letters 384, 132-143.

Liu, Y.G., Miah, M.R.U., Schmitt, R.A., 1988. Cerium: A chemical tracer for paleo-oceanic redox conditions. Geochimica et Cosmochimica Acta 52, 1361-1371.

Lovley, D.R., 2004. Potential role of dissimilatory iron reduction in the early evolution of microbial respiration, in: Seckback, J. (Ed.), Origins, Evolution and Biodiversity of Microbial Life. Kluwer, Netherlands, pp. 301-313.

Lovley, D.R., Stolz, J., Nord, G., 1987. Anaerobic production of magnetite by a dissimilatory iron-reducing microorganism. Nature 330, 252-254.

MacGregor, A.M., 1927. The problem of the Precambrian atmosphere. South African Journal of Science 23, 155-172.

Manning, C.E., Mojzsis, S.J., Harrison, T.M., 2006. Geology, Age and Origin of Supracrustal Rocks at Akilia, West Greenland. American Journal of Science 306, 303-366.

McGregor, V.R., Mason, B.J., 1977. Petrogenesis and geochemistry of metabasic and metasedimentary enclaves in the Amitsoq gneisses, West Greenland. American Mineralogist 62, 887-904.

McKeegan, K.D., Kudryavtsev, A.B., Schopf, J.W., 2007. Raman and ion microscopic imagery of graphitic inclusions in apatite from older than 3830 Ma Akilia supracrustal rocks, west Greenland. Geology 35, 591.

McLennan, S.M., Taylor, R., 1991. Sedimentary rocks and crustal evolution: Tectonic setting and secular trends. J Geol 99, 1-21.

McManus, J., Berelson, W., Severmann, S., Poulson, R., Hammond, D., Klinkhammer, G., Holm, C., 2006. Molybdenum and uranium geochemistry in continental margin sediments: Paleoproxy potential. Geochimica et Cosmochimica Acta 70, 4643-4662.

Miller, J.D., Morey, G.B., Weiblen, P.W., 1987. Seagull Lake - Gunflint Lake area: A classical Precambrian stratigraphic sequence in northeastern Minnesota. America Continental Field Guide - North-Central Section, 47-51.

Mojzsis, S.J., Harrison, T.M., 1999. Geochronological studies of the oldest known marine sediments. 9th Annual V.M. Goldschmidt Conference Abstract 7602.

Mojzsis, S.J., Harrison, T.M., 2002. Origin and significance of Archean quartzose rocks at Akilia, Greenland. Science 298, 917a - 917a.

Mojzsis, S.J., Arrhenius, G., McKeegan, K.D., Harrison, T.M., Nutman, A.P., Friend, C.R.L., 1996. Evidence for life on Earth before 3,800 million years ago. Nature 384, 55-59.

Mojzsis, S.J., Coath, C.D., Greenwood, J.P., McKeegan, K.D., Harrison, T.M., 2003. Mass-independent isotope effects in Archean (2.5 to 3.8 Ga) sedimentary sulfides

determined by ion microprobe analysis. Geochimica et Cosmochimica Acta 67, 1635-1658.

Moorbath, S., Whitehouse, M.J., 1996. Age of the Isua supracrustal sequence of West Greenland, in: Chela-Flores, J., Raulin, F. (Eds.), Chemical Evoultion: Physics of the Origin and Evoultion of Life. Kluwer Academic Publishers, pp. 87-95.

Moorbath, S., O'Nions, R.K., Pankhurst, R.J., 1973. Early Archaean age for the Isua Iron Formation, West Greenland. Nature 245, 138-139.

Morford, J.L., Emerson, S., 1999. The geochemistry of redox sensitive trace metals in sediments. Geochimica et Cosmochimica Acta 63, 1735-1750.

Morris, R.C., 1993. Genetic modeling for banded iron formation of the Hamersley Group Pilbara craton, Western Australia. Precambrian Research 60, 243-286.

Morris, R.C., Horwitz, R., 1983. The origin of the iron-formation-rich Hamersley Group of Western Australia: Deposition on a platform. Precambrian Research 21, 273-297.

Murray, R.W., Tenbrink, M.R.B., Gerlach, D.C., Russ, G.P., Jones, D.L., 1992. Interoceanic Variation in the Rare-Earth, Major, and Trace-Element Depositional Chemistry of Chert - Perspectives Gained from the Dsdp and Odp Record. Geochimica et Cosmochimica Acta 56, 1897-1913.

Myers, J.S., 2001. Protoliths of the 3.8-3.7 Ga Isua greenstone belt, West Greenland. Precambrian Research 105, 129-141.

Myers, J.S., Crowley, J.L., 2000. Vestiges of life in the oldest Greenland rocks? A review of early Archean geology in the Godthabsfjord region, and reappraisal of field evidence for > 3850 Ma life on Akilia. Precambrian Research 103, 101-124.

Nisbet, E.G., Nisbet, R.E.R., 2008. Methane, oxygen, photosynthesis, rubisco and the regulation of the air through time. Philos T R Soc B 363, 2745-2754.

Nozaki, Y., Zhang, J., Amakawa, H., 1997. The fractionation between Y and Ho in the marine environment. Earth and Planetary Science Letters 148, 329-340.

Nutman, A.P., Friend, C.R.L., 2006. Petrography and geochemistry of apatites in banded iron formation, Akilia, W. Greenland: Consequences for oldest life evidence. Precambrian Research 147, 100-106.

Nutman, A.P., Friend, C.R.L., 2007. Adjacent terranes with c. 2715 and 2650 Ma high-pressure metamorphic assemblages in the Nuuk region of the North Atlantic Craton, souther West Greenland: complexities of Neoarchean collisional orogeny. Precambrian Research 155, 159-203.

Nutman, A.P., Dawes, P.R., Kalsbeek, F., Hamilton, M.A., 2008. Palaeoproterozoic and Archaean gneiss complexes in northern Greenland: Palaeoproterozoic terrane assembly in the High Arctic. Precambrian Research 161, 419-451.

Nutman, A.P., Friend, C.R.L., Bennett, V.C., McGregor, V.R., 2004. Dating of the Ameralik dyke swarms of the Nuuk district, souther West Greenland: mafic intrusion events starting from c. 3510 Ma. Journal of the Geological Society of London 161, 421-430.

Nutman, A.P., McGregor, V.R., Friend, C.R.L., Bennett, V.C., Kinny, P.D., 1996. The Itsaq Gneiss Complex of southern West Greenland; the world's most extensive record of early crustal evolution (3900 - 3600 Ma). Precambrian Research 78, 1-39.

Nutman, A.P., Mojzsis, S.J., Friend, C.R.L., 1997. Recognition of >3850 Ma water-lain sediments in West Greenland and their significance for the early Archean Earth. Geochimica et Cosmochimica Acta 61, 2475-2484.

Ohmoto, H., Watanabe, Y., Yamaguchi, K., Naraoka, H., Kakegawa, T., Haruna, M., Hayashi, K., Kato, Y., 2006. Chemical and biological evolution of early Earth: constraints from banded iron-formation, in: Kessler, S.E., Ohmoto, H. (Eds.), Evolution of the Atmosphere, Hydrosphere, and Biosphere on Early Earth: Constrainsts from Ore Deposits. Geological Soceity of America, Denver.

Ojakangas, R.W., Morey, G.B., Southwick, D.L., 2001. Paleoproterozoic basin development and sedimentation in the Lake Superior region, North America. Sediment Geol 141, 319-341.

Olson, J.M., 2006. Photosynthesis in the Archean era. Photosynth Res 88, 109-117.

Pankhurst, R.J., Moorbath, S., McGregor, V.R., 1973. Late event in the geological evolution of the Godthaab District, West Greenland. Nature 243, 24-26.

Papineau, D., De Gregorio, B.T., Stroud, R.M., Steele, A., Pecoits, E., Konhauser, K., Wang, J., Fogel, M.L., 2010. Ancient graphite in the Eoarchean quartz-pyroxene rocks from Akilia in southern West Greenland II: Isotopic and chemical compositions and comparison with Paleoproterozoic banded iron formations. Geochimica et Cosmochimica Acta 74, 5884-5905.

Papineau, D., Fogel, M.L., Cody, G.D., DeGregorio, B.T., Fries, M.D., Mojzsis, S.J., Steele, A., Stroud, R.M., Wang, J., 2008. Graphite associated with apatite in the ~3.8 Ga quartz-pyroxene rock from Akilia, Southwest Greenland. Astrobiology 8, 412.

Pavlov, A., Kasting, J., 2002. Mass-independent fractionation of sulfur isotopes in Archean sediments: Strong evidence for an anoxic Archean atmosphere. Astrobiology 2, 27-41.

Perry, E.C., Ahmad, S.N., 1977. Carbon isotope composition of graphite and carbonate minerals from 3.8-AE metamorphosed sediments, Isukasia, Greenland. Earth and Planetary Science Letters 36, 280-284.

Planavsky, N., Bekker, A., Rouxel, O., Kamber, B., Hofmann, A., Knudsen, A., Lyons, T.W., 2010. Rare Earth Element and yttrium compositions of Archean and Paleoproterozic Fe formations revisited: New perspctives on the significance and mechanics of depositions. Geochimica et Cosmochimica Acta 74, 6387-6405.

Planavsky, N., Rouxel, O., Bekker, A., Shapiro, R., Fralick, P., Knudsen, A., 2009. Iron-oxidizing microbial ecosystems thrived in late Paleoproterozoic redox-stratified oceans. Earth and Planetary Science Letters 286, 230-242.

Planavsky, N., Rouxel, O.J., Bekker, A., Hofmann, A., Little, C.T.S., Lyons, T.W., 2012. Iron isotope composition of some Archean and Proterozoic iron formations. Geochimica et Cosmochimica Acta 80, 158-169.

Planavsky, N.J., Rouxel, O.J., Bekker, A., Lalonde, S.V., Konhauser, K.O., Reinhard, C.T., Lyons, T.W., 2010c. The evolution of the marine phosphate reservoir. Nature 467, 1088-1090.

Pollack, G.D., Krogstad, E.J., Bekker, A., 2009. U–Th–Pb–REE systematics of organic-rich shales from the ca. 2.15 Ga Sengoma Argillite Formation, Botswana: Evidence for oxidative continental weathering during the Great Oxidation Event. Chemical Geology 260, 172-185.

Poulton, S.W., Fralick, P.W., Canfield, D.E., 2004. The transition to a sulphidic ocean similar to 1.84 billion years ago. Nature 431, 173-177.

Pufahl, P.K., Fralick, P.W., 2004. Depositional controls on Palaeoproterozoic iron formation accumulation, Gogebic Range, Lake Superior region, USA. Sedimentology 51, 791-808.

Quinn, K.A., Byrne, R.H., Schijf, J., 2006. Sorption of yttrium and rare earth elements by amorphous ferric hydroxide: Influence of solution complexation with carbonate. Geochimica et Cosmochimica Acta 70, 4151-4165.

Rasmussen, B., Buick, R., 1999. Redox state of the Archean atmosphere: Evidence from detrital heavy minerals in ca. 3250-2750 Ma sandstones from the Pilbara Craton, Australia. Geology 27, 115-118.

Rollinson, H., 2002. The metamorphic history of the Isua Greenstone Belt, West Greenland. Geological Society, London, Special Publications 199, 329-350.

Rose, N.M., Rosing, M.T., Bridgwater, D., 1996. The origin of metacarbonate rocks in the Archaean Isua Supracrustal Belt, West Greenland. American Journal of Science 296, 1004-1044.

Rosing, M.T., 1999. 13C-Depleted Carbon Microparticles in >3700-Ma Sea-Floor Sedimentary Rocks from West Greenland. Science 283, 674-676.

Rosing, M.T., Rose, N.M., Bridgwater, D., Thomsen, H.S., 1996. Earliest part of Earth's stratigraphic record: A reappraisal of the > 3.7 Ga Isua (Greenland) supracrustal sequence. Geology 24, 43-46.

Rouxel, O., Bekker, A., Edwards, K., 2005. Iron isotope constraints on the Archean and Paleoproterozoic ocean redox state. Science 307, 1088-1091.

Schidlowski, M., Appel, P.W.U., Eichmann, R., Junge, C.E., 1979. Carbon isotope geochemistry of the 3.7 x 109 yr. old Isua sediments, West Greenland: Implications for the Archean carbon and oxygen cycles. Geochimica et Cosmochimica Acta 43, 189-199.

Schmidt, P., 2003. Reversal asymmetry in Mesoproterozoic overprinting of the 1.88-Ga Gunflint Formation, Ontario, Canada: non-dipole effects or apparent polar wander? Tectonophysics 377, 7-32.

Schopf, J.W., 1993. Microfossils of the early Archean Apex chert: new evidnce of the antiquity of life. Science 260, 640-646.

Schopf, J.W., 2006. Fossil evidence of Archaean life. Philos Trans R Soc Lond B Biol Sci 361, 869-885.

Scott, C., Lyons, T.W., Bekker, A., Shen, Y., Poulton, S.W., Chu, X., Anbar, A.D., 2008. Tracing the stepwise oxygenation of the Proterozoic ocean. Nature 452, 456-459.

Shiller, A.M., Mao, L., 2000. Dissolved vanadium in rivers: effects of silicate weathering. Chemical Geology 165, 13-22.

Sholkovitz, E.R., 1992. Chemical evolution of rare earth elements: fractionation between colloidal and solution phases of filtered river water. Earth and Planetary Science Letters 114, 77-84.

Sholkovitz, E.R., Landing, W.M., Lewis, B.L., 1994. Ocean Particle Chemistry - the Fractionation of Rare-Earth Elements between Suspended Particles and Seawater. Geochimica et Cosmochimica Acta 58, 1567-1579.

Sholkovitz, E.R., Shaw, T.J., Schneider, D.L., 1992. The Geochemistry of Rare-Earth Elements in the Seasonally Anoxic Water Column and Porewaters of Chesapeake Bay. Geochimica et Cosmochimica Acta 56, 3389-3402.

Simonson, B., 1985. Sedimentalogical constraints on the origins of the Precambrian iron-formations. Geological Society of America Bulletin 96, 244-252.

Simonson, B., Hassler, S., 1996. Was the deposition of large Precambrian iron formations linked to a major marine transgression? J Geol 104, 665-676.

Sogaard, E.G., Medenwaldt, R., Abraham-Peskir, J.V., 2000. Conditions and rates of biotic and abiotic iron precipitation in selected Danish freshwater plants and microscopic analysis of precipitate morphology. Water Res 34, 2675-2682.

Straub, K.L., Rainey, F.A., Widdel, F., 1999. Rhodovulum iodosum sp. nov, and Rhodovulum robiginosum sp. nov., two new marine phototrophic ferrous-iron-oxidizing purple bacteria. Int J Syst Bacteriol 49, 729-735.

Taylor, S.R., McLennan, S.M., 1985. The Continental Crust: Its Compostion and Evolution. Blackwell, Oxford.

Thurston, P.C., Kamber, B.S., Whitehouse, M., 2012. Archean cherts in banded iron formation: Insight into Neoarchean ocean chemistry and depositional processes. Precambrian Research 214-215, 227-257.

Tice, M., Lowe, D.R., 2004. Photosynthetic microbial mats in the 3,416-My-old ocean. Nature 431, 549-552.

Towe, K.M., 1983. Precambrian Atmospheric Oxygen and Banded Iron Formations - a Delayed Ocean Model. Precambrian Research 20, 161-170.

Trendall, A.F., 2002. The significance of iron-formation in the Precambrian stratigraphic record. Special Publication International Association of Sedimentalogists 33, 33-66.

Trendall, A.F., Blockey, J., 1970. The iron-formations of the Precambrian Hamersley Group, Western Australia. Geological Survey Western Australia Bulletin 119, 366.

Ulrich, T., Kamber, B.S., Woodhead, J.D., Spencer, L.A., 2010. Long-Term Observations of Isotope Ratio Accuracy and Reproducibility Using Quadrupole ICP-MS. Geostand Geoanal Res 34, 161-174.

van Zuilen, M.A., Lepland, A., Arrhenius, G., 2002. Reassessing the evidence for the earliest traces of life. Nature 418, 627-630.

van Zuilen, M.A., Lepland, A., Teranes, J., Finarelli, J., Wahlen, M., Arrhenius, G., 2003. Graphite and carbonates in the 3.8 Ga old Isua Supracrustal Belt, southern West Greenland. Precambrian Research 126, 331-348.

Vargas, M., Keshefi, K., Blunt-Harris, E., Lovley, D.R., 1998. Microbiological evidence for Fe(III) reduction on early Earth. Nature 395, 65-67.

Veizer, J., 1983. Geologic evolution of the Archean - Early Proterozoic Earth, in: Schopf, J.W. (Ed.), Earth's Earliest Biosphere. Princeton University Press, NJ, pp. 240-259.

Volkov, I.I., Fomina, L.S., 1974. Influence of organic material and processes of sulfide formation on distribution of some trace elements in deep-water sediments of the Black Sea, in: Degens, E.T., Ross, D.A. (Eds.), The Black Sea - Geology, Chemistry and Biology, American Association of Petroleum Geologists Memoir 20, Tulsa, OK, pp. 456-476.

Webb, G.E., Northdurft, L.D., Kamber, B.S., Kloprogge, J.T., Zhao, J., 2009. Rare earth element geochemistry of scleractinian coral skeleton during meteroic diagenesis: a sequence through neomorphism and aragonite to calcite. Sedimentology 56.

Wehrli, B., Stumm, W., 1989. Vanadyl in natural waters: Adsportion and hydrolysis promote oxygenation. Geochimica et Cosmochimica Acta 53, 69-77.

Whitehouse, M., Kamber, B., Fedo, C., Lepland, A., 2005. Integrated Pb- and S-isotope investigation of sulphide minerals from the early Archaean of southwest Greenland. Chemical Geology 222, 112-131.

Whitehouse, M.J., Fedo, C.M., 2003. Deformation features and critical field relationships of early Archean rocks, Akilia, southwest Greenland. Precambrian Research 126, 259-271.

Whitehouse, M.J., Fedo, C.M., 2007. Microscale heterogeneity of Fe isotopes in >3.71 Ga banded iron formation from the Isua Greenstone Belt, southwest Greenland. Geology 35, 719.

Whitehouse, M.J., Kamber, B.S., 2005. Assigning dates to thin gneissic veins in high-grade metamorphic terranes: a cautionary tale from Akilia, southwest Greenland. Journal of Petrology 46, 291-318.

Whitehouse, M.J., Kamber, B.S., Moorbath, S., 1999. Age significance of U-Th-Pb zircon data from early Archean rocks of west Greenland: a reassessment based on combined ion-microprobe and imaging studies. Chemical Geology 160, 201-224.

Whitehouse, M.J., Myers, J.S., Fedo, C.M., 2009. The Akilia Controversy: field, structural and geochronological evidence questions interpretations of >3.8 Ga life in SW Greenland. Journal of the Geological Society 166, 335-348.

Widdel, F., Schnell, S., Heising, S., Ehrenreich, A., Assmus, B., Schink, B., 1993. Ferrous Iron Oxidation by Anoxygenic Phototrophic Bacteria. Nature 362, 834-836.

Yang, W., Holland, H.D., 2002. The redox-sensitive trace elements, Mo, U, and Re in Precambrian carbonaceous shales: Indicators of the Great Oxidation Event. Geological Society of America Bulletin 34, 381.

**Appendix 1**

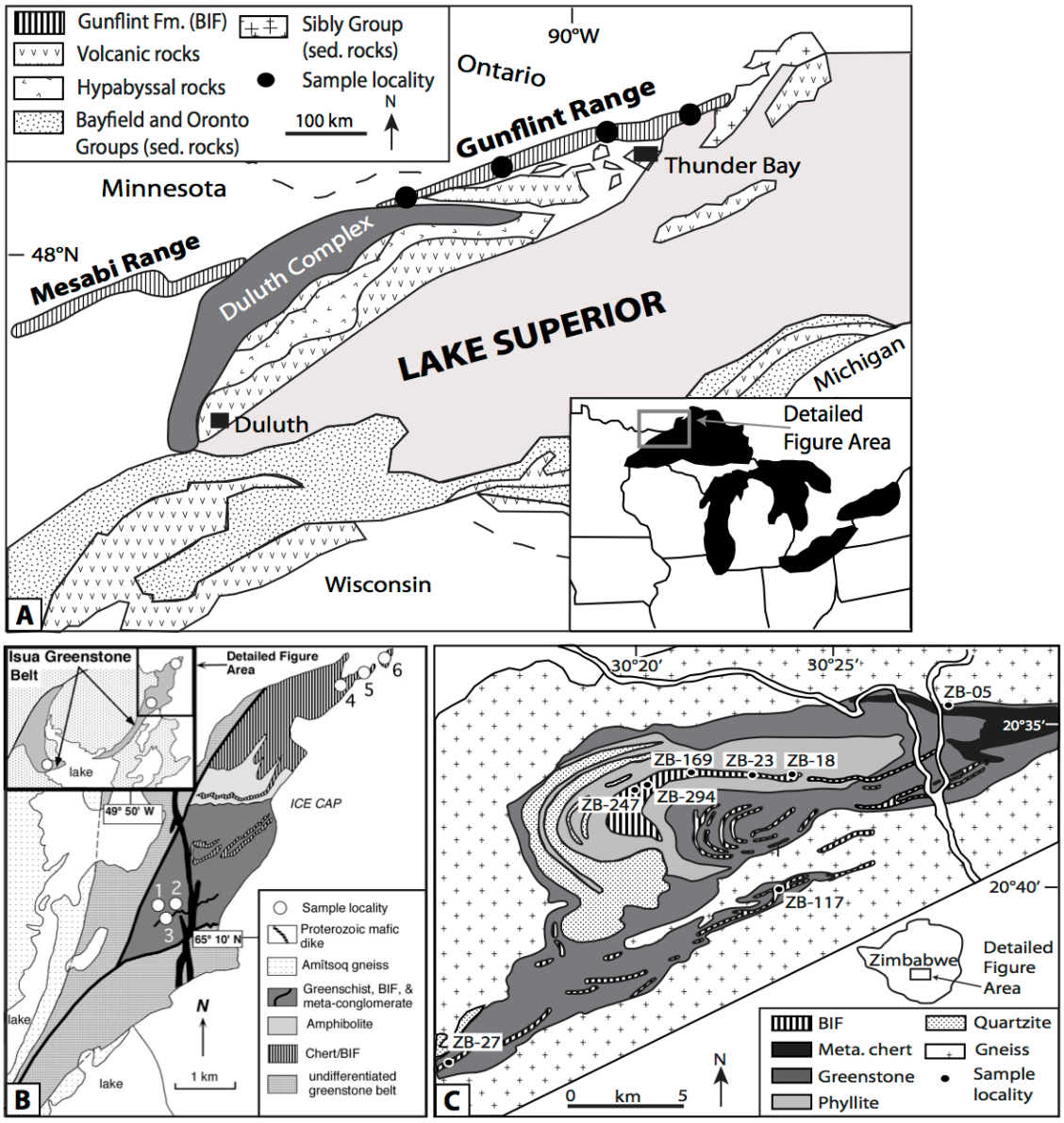



Figure 2.1. Generalized geologic maps of field areas showing sample locations. (A) Gunflint Formation, Minnesota and Ontario. Map modified from Schmidt and Williams (2003). (B) Isua Greenstone Belt, SW Greenland. Map modified from Fedo (2000). Sample localities used in this study are numbered 1-7, where 1 = IS-02-05, 2 = IS-02-06, 3 = ISB22, 4 = IS-02-08, 5 = ISB55, 6 = 462604, and 7 = 462610. (C) Buhwa Greenstone Belt, Zimbabwe. Map modified from Fedo and Eriksson (1995).

Figure 2.2. Generalized composite stratigraphic column for the Gunflint Formation, modified from Miller et al. (1987), Fralick et al. (2002), Poulton et al. (2004), and Planavsky et al. (2009). Also included are sample locations, unit thickness and descriptions, and depositional environments. Samples 4-40 were collected from metamorphosed outcrops in Minnesota and samples 41-54 were collected from unmetamorphosed sections in Ontario. Sample locations are based on correlation to this composite section. Exact stratigraphic position for samples 4, 5, and 40 cannot be determined because sample locations are in areas with extensive intrusions of the Middle Proterozoic Logan diabase (Miller et al., 1987) and lack stratigraphic continuity. Samples 9-23 were collected from a 7.5 m thick section of the Lower Slaty member in MN that was measured in detail. Black square marks the location of the volcaniclastic layer from which a zircon population has yielded an 1878.3 ± 1 Ma U-Pb age, believed to be synchronous with deposition (Fralick et al., 2002). Interpretation of depositional environments based on Planavsky et al. (2009) and Ojakangas et al. (2001).

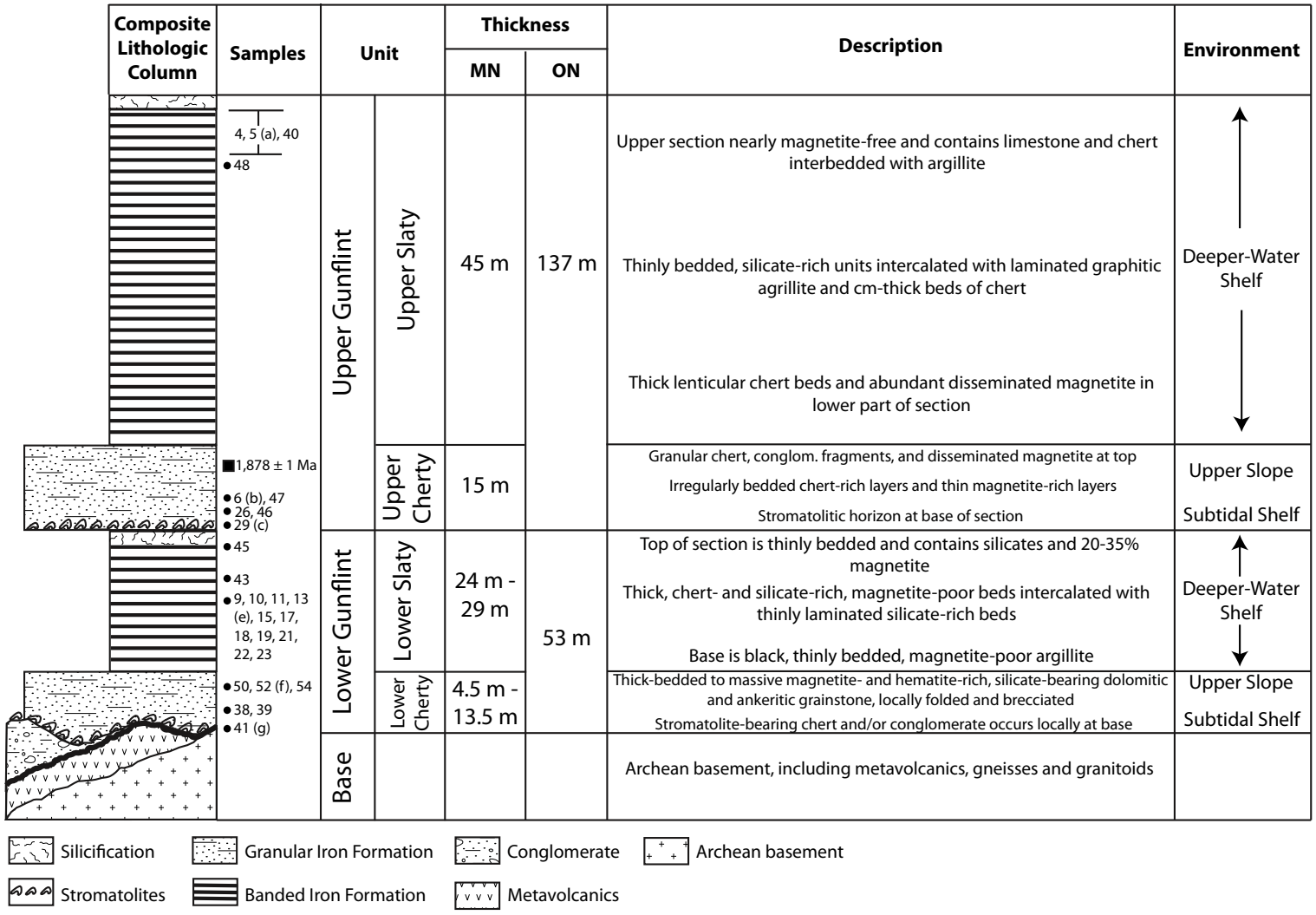



Figure 2.2 cont.

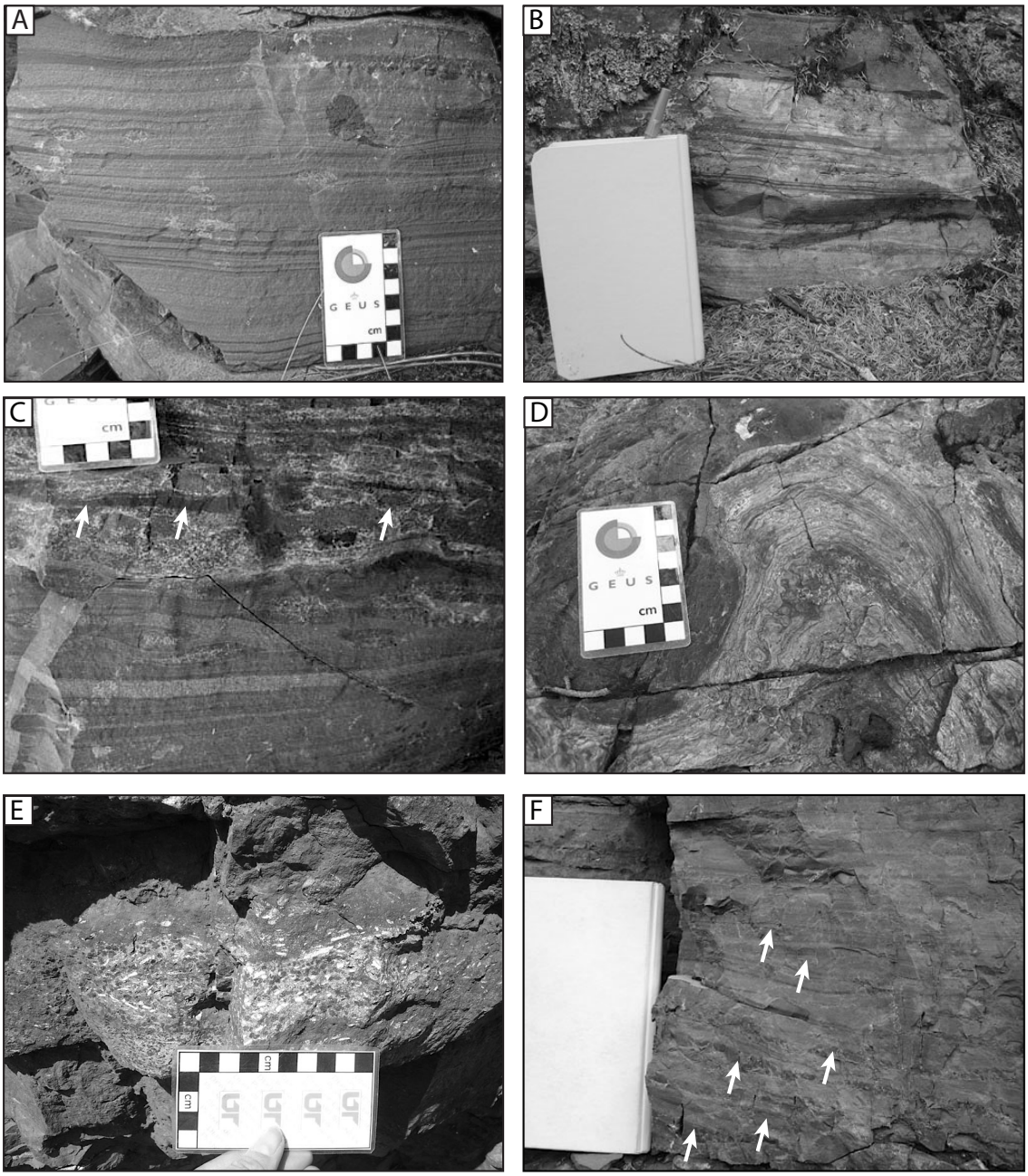



Figure 2.3. Field photographs of the Gunflint Formation. (A) Finely banded magnetite-quartz BIF (GF-13) from the Lower Slaty unit in MN. (B) Coarsely banded magnetite-quartz BIF (GF-10) from the Lower Slaty unit in MN. Field book for scale. (C) Chert-dominated layer containing rip-up clasts of magnetite-rich layers (GF-17) from Lower Slaty in MN. White arrows point to magnetite clasts. (D) Stromatolite horizon in lower section of Upper Cherty Unit in MN. (E) BIF showing alternating bands of chert (dark) and ankerite (light) from the Lower Cherty Unity in ON. Arrows pointing out chert layers. Carbonate layers are found in between. (F) Sample GF-52 from the red, hematite- and dolomite-rich, brecciated section of the Lower Cherty Unit in ON.

Figure 2.4. Photomicrographs of samples from the Gunflint Formation. (A) Cross-polarized light image of sample GF-10 from the Lower Slaty in MN. Sample dominated by quartz (qtz), which is present as equant grains with 120° interlocking grains and disseminated amphiboles (amph), with only minor amounts of magnetite (mt). (B) Cross-polarized light image of sample GF-22 from the Lower Slaty in MN, which contains thick bands of magnetite (black layers; mt) and thin bands of amphibole (white layers; amph). (C) Plane-polarized light image of sample GF-29 from the stromatolite horizon in the Upper Cherty in MN, containing quartz (qtz) and magnetite (mt). (D) Reflected-light image of sample GF-4 from the Upper Cherty in ON. Example of magnetite-rich granular iron formation. (E) Cross-polarized image of hematite (hem), dolomite (dol), and quartz (qtz) in sample GF-54 from the Lower Cherty in ON. (F) Cross-polarized image of magnetite (mt), calcite (cal), quartz (qtz) and amphibole (amph) in sample GF-43 from the Lower Slaty in ON.

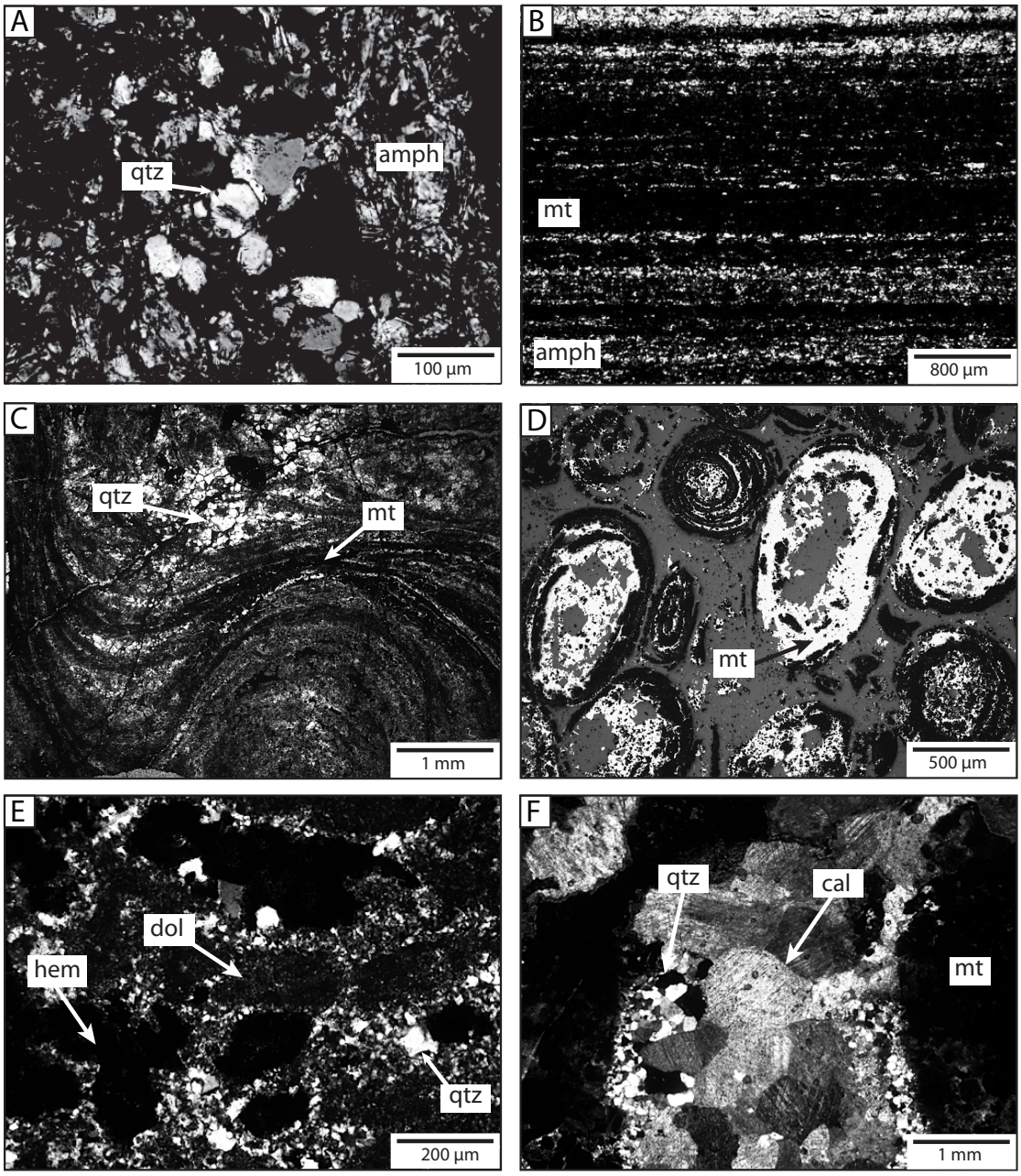



Figure 2.4 continued

Figure 2.5. Photomicrographs of samples from the Isua and Buhwa Greenstone Belts. (A) Plane-polarized light image of alternations of quartz (qtz) and iron oxide (hematite and magnetite), with minor amount of amphibole (amph) present from sample ISB-55 from IGB. (B) Reflected-light image of predominately magnetite (mt), with lesser amount of hematite (hem) from sample IS-02-08, IGB. (C) Plane-polarized light image of larger amphibole (amph) grains with quartz (qtz) and magnetite (mt) in sample ISB-22 from IGB. (D) Reflected-light image of sample ZB-247 from BGB showing typical hematite (hem) as a pseudomorphic replacement of magnetite (mt). (E) Plane-polarized light image of alternations of course-grained quartz (qtz) and iron oxide (hematite replacing magnetite) from the granulite-facies ZB-117 from BGB. (F) Reflected-light image of alternations of finer-grained and coarser-grained iron oxides (hematite replacing magnetite) and quartz from sample ZB-169 from BGB.

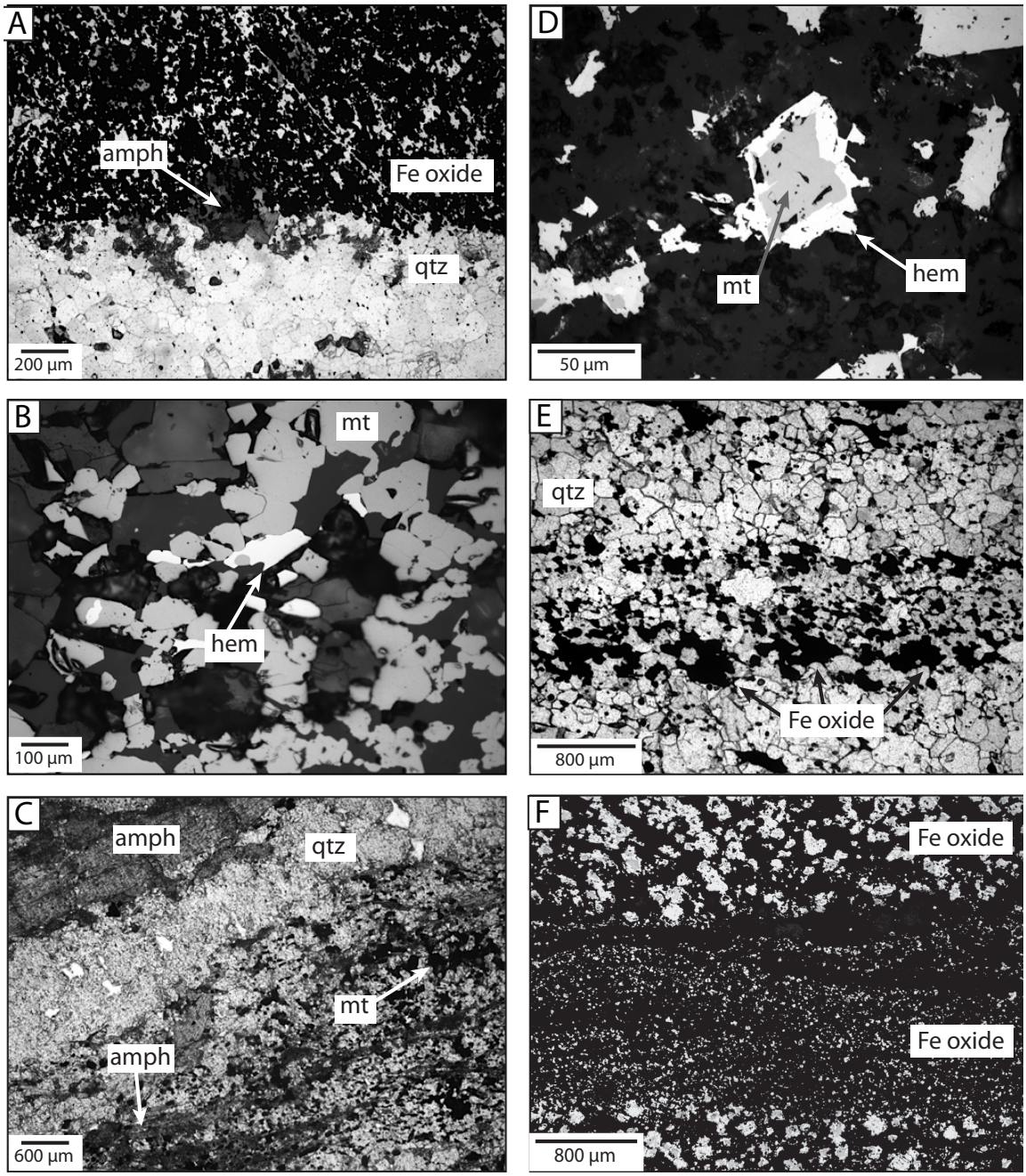



Figure 2.5 continued

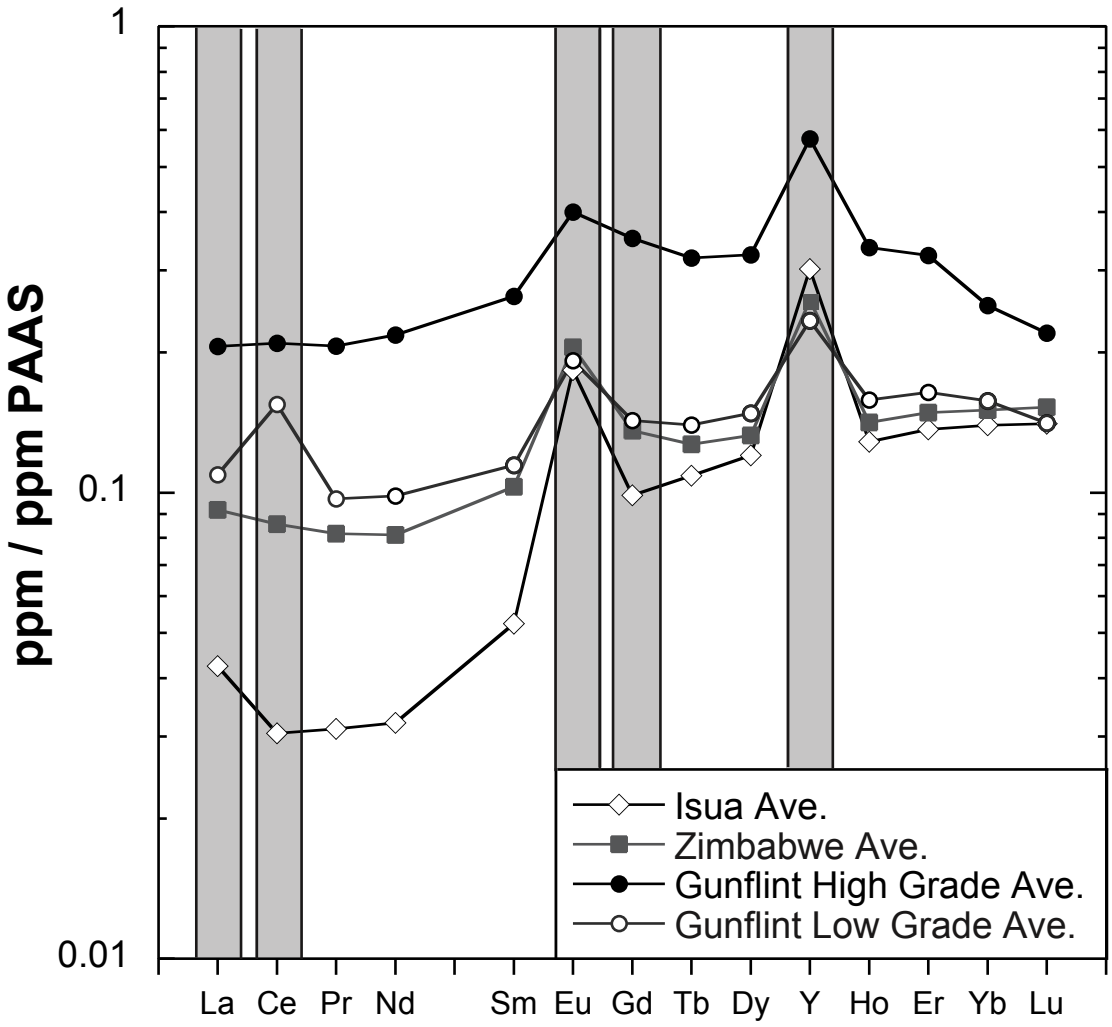



Figure 2.6. Average shale-normalized REY patterns for BIFs used in this study, which span a time range from 3.9 Ga to 1.9 Ga. Patterns display overall LREE depletion relative to HREE, positive La, Gd, Eu, and Y anomalies (highlighted by gray bars), and variable Ce anomalies. It is important to note that regardless of age or metamorphic grade, all patterns look similar, confirming the ability of BIF to retain primary seawater signatures. The REY plots for each sample at each location can be seen in Figures A4.1 – A4.3.

Figure 2.7. (A) Crossplot of Zr (ppm) vs. $Al_2O_3$ (wt. %) for BIFs from the IGB, BGB and Gunflint Formation. The dotted lines mark the natural break in sample distribution at 30 ppm Zr and 1.7 wt. % $Al_2O_3$ for Gunflint and Zimbabwe samples and at 5 ppm Zr and 0.8 wt. % $Al_2O_3$ for Isua. Samples that have concentrations greater than these cut-off values have been labeled "other" and their data may be questionable. (B) Crossplot of $Pr_{SN}/Yb_{SN}$ vs $Al_2O_3$ (wt. %) and (C) $Pr_{SN}/Yb_{SN}$ vs Zr (ppm) for BIFs from IGB, BGB and Gunflint Formation. The dotted lines mark the same cut-off values for $Al_2O_3$ and Zr determined in (A). Samples with a $Pr_{SN}/Yb_{SN}$ ratio of greater than one are depleted in HREE relative to LREE and have a negatively sloped REE pattern, indicative of siliciclastic contamination. These samples have been labeled "other" in subsequent graphs.

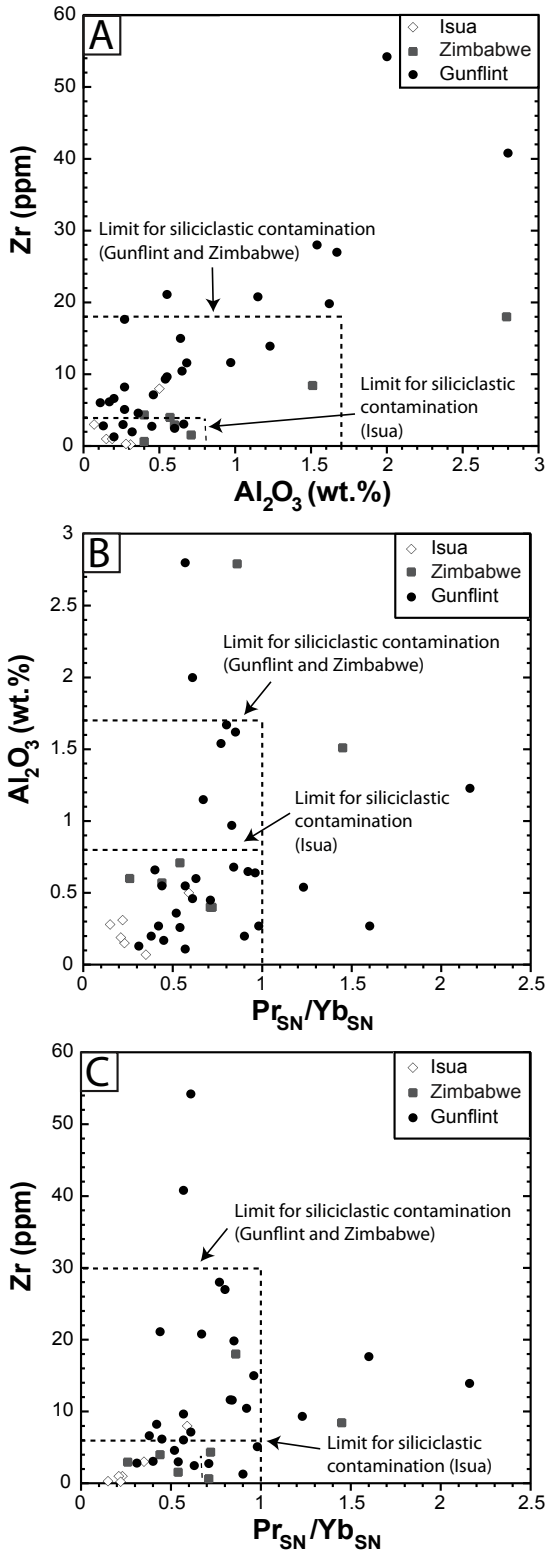



Figure 2.7 continued

Figure 2.8. Key REE ratios through time. (A) Shale-normalized Ce anomalies in BIFs through time, where $Ce/Ce^* = Ce_{SN} / [Pr_{SN} (Pr_{SN} / Nd_{SN})]$. Previously reported data from the Penge Formation acquired from Bolhar et al. (2004) and Kuruman Formation from Bau and Dulski (1996). (B) PAAS-normalized $Pr_{SN}/Yb_{SN}$ ratios through time showing an increase in the light to heavy REE ratios in the post-GOE Paleoproterozoic Gunflint BIF relative to Archean BIF. The dotted line represents the switch from a positively-sloped REY plot ($Pr_{SN}/Yb_{SN} < 1$) to a negatively-sloped REY plot ($Pr_{SN}/Yb_{SN} > 1$). Samples with a $Pr_{SN}/Yb_{SN}$ ratio of > 1 are considered contaminated. (C) PAAS-normalized $Y_{SN}/Ho_{SN}$ through time showing a decrease in the average $Y_{SN}/Ho_{SN}$ ratio in the post-GOE Paleoproterozoic Gunflint BIF relative to BIF deposited in the Archean.

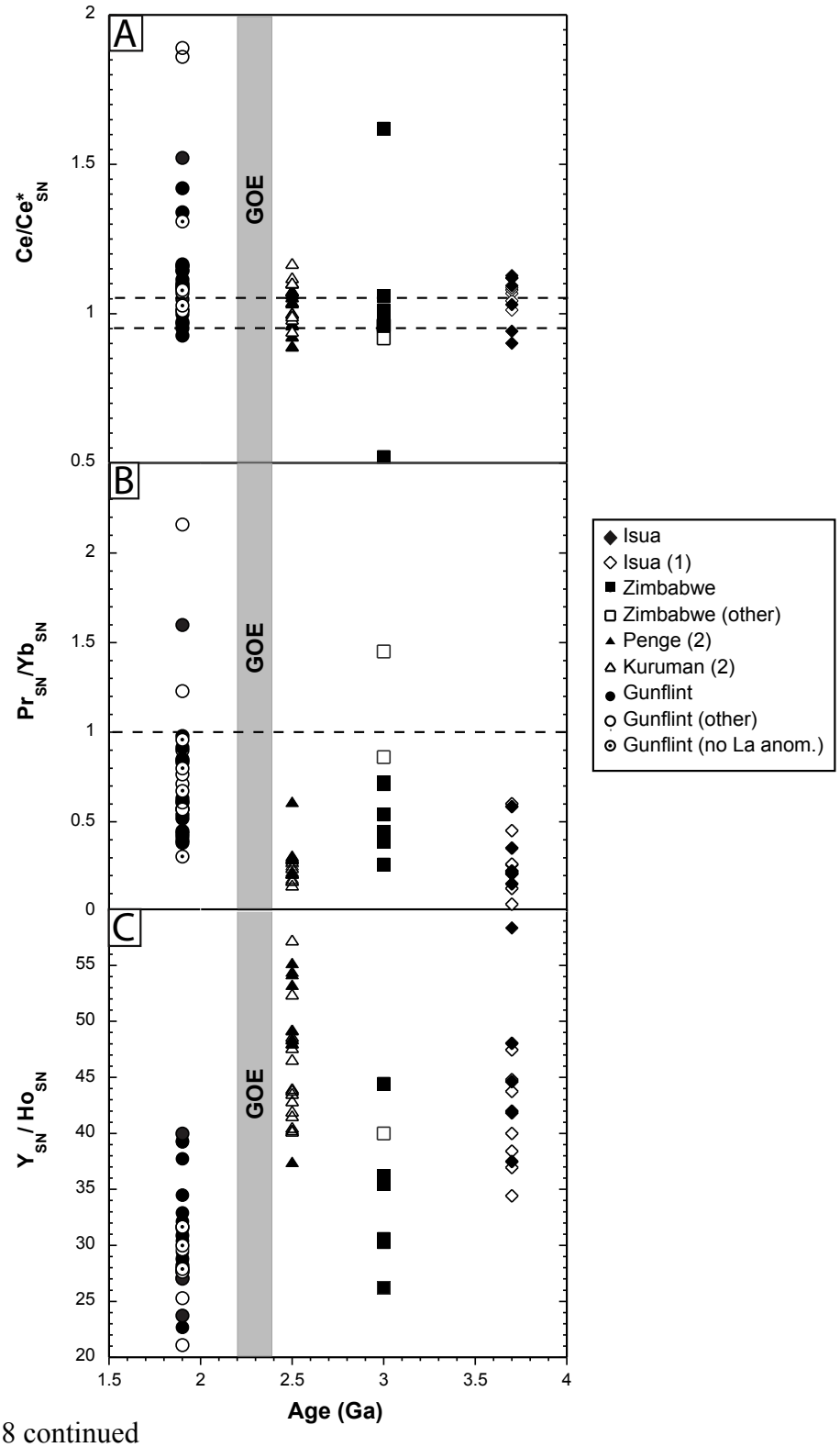



Figure 2.8 continued

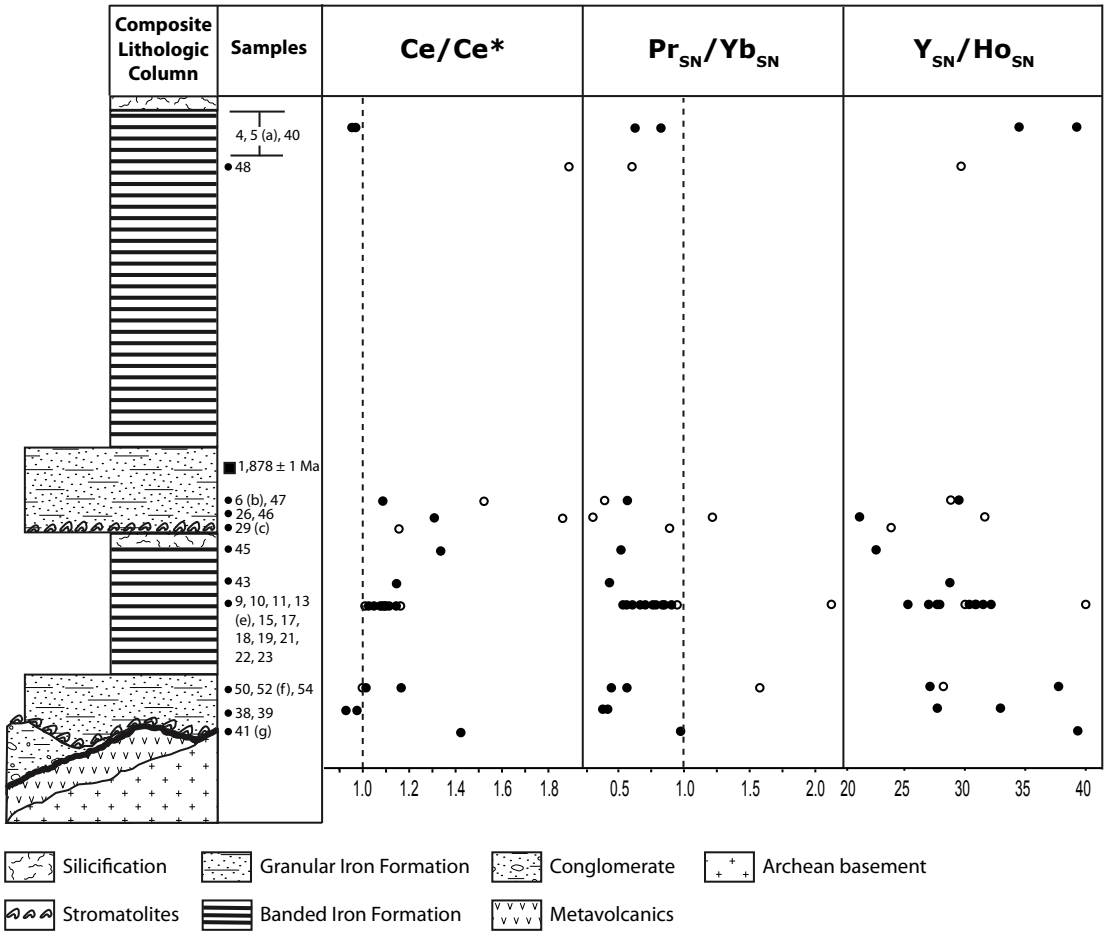



Figure 2.9. The variability of REE geochemistry through Gunflint stratigraphy. See Figure 1 for estimates of unit thickness. No relationship is evident between the chemistry and stratigraphic position or depositional environment. Open circles represent samples that are either contaminated with siliciclastic material or lack a positive La anomaly. The dashed line on Ce/Ce* plot distinguishes between a positive (Ce/Ce* >1) and negative (Ce/Ce* <1) Ce anomaly. The dashed line on $Pr_{SN}/Yb_{SN}$ plot distinguishes between a positively sloped ($Pr_{SN}/Yb_{SN}$ <1) and negatively sloped ($Pr_{SN}/Yb_{SN}$ >1) REY pattern.

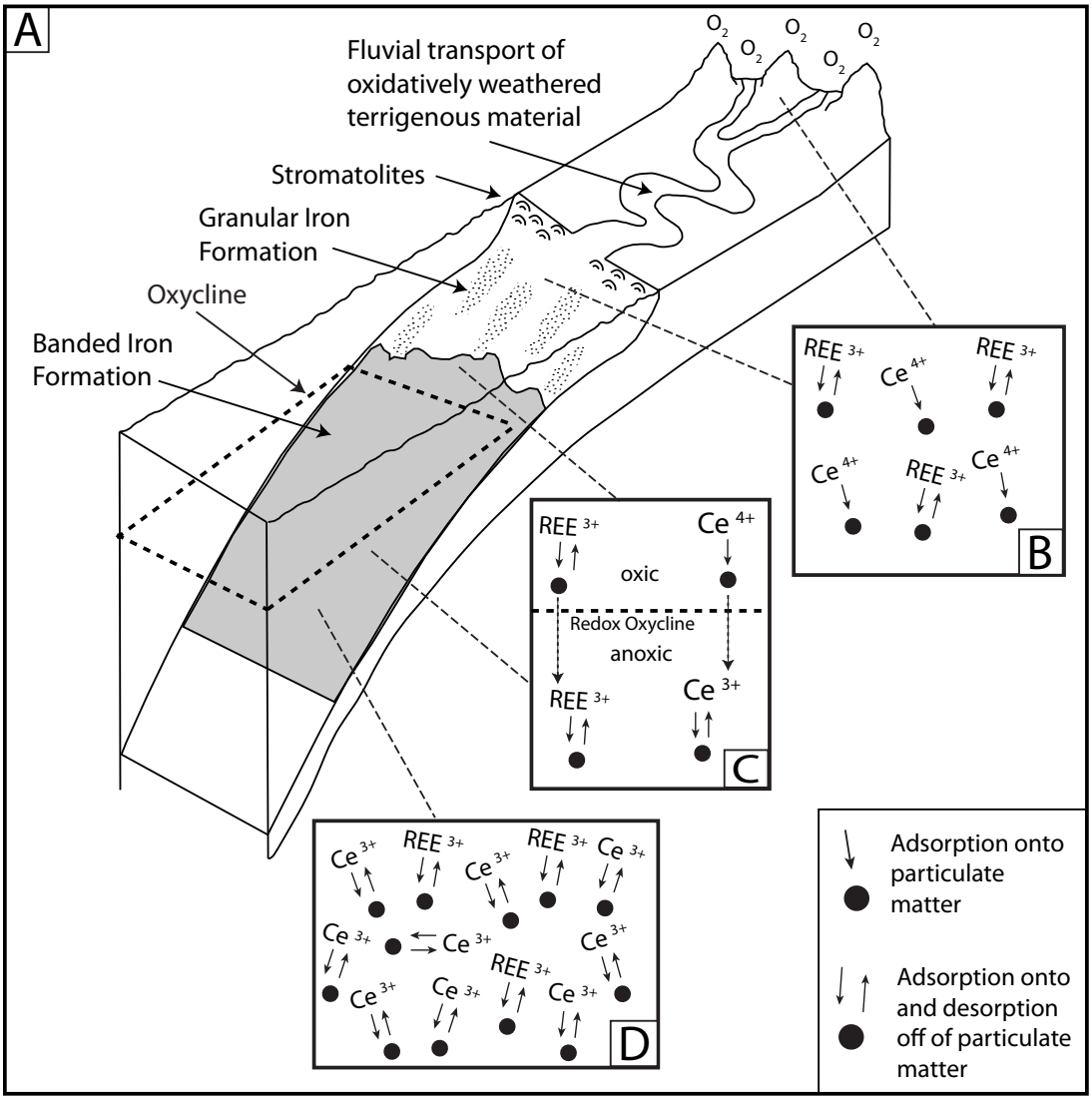



Figure 2.10. (A) Overview of the shuttle transport model of Ce and other REEs from land to deeper waters. Ce other REEs are transported from the continents to the oceans via rivers. (B) In oxygenated shallow waters, Ce(III) to oxidized to Ce(IV), resulting in the more permanent attachment onto sinking particulate matter than other trivalent REEs. (C) Once the particulate matter crosses over the oxycline, Ce(IV) is reduce back to Ce(III). (D) Ce(III) is more easily removed from the particulate matter, along with other trivalent REEs, and become dissolved in deeper waters, resulting in a Ce(III) enrichment.

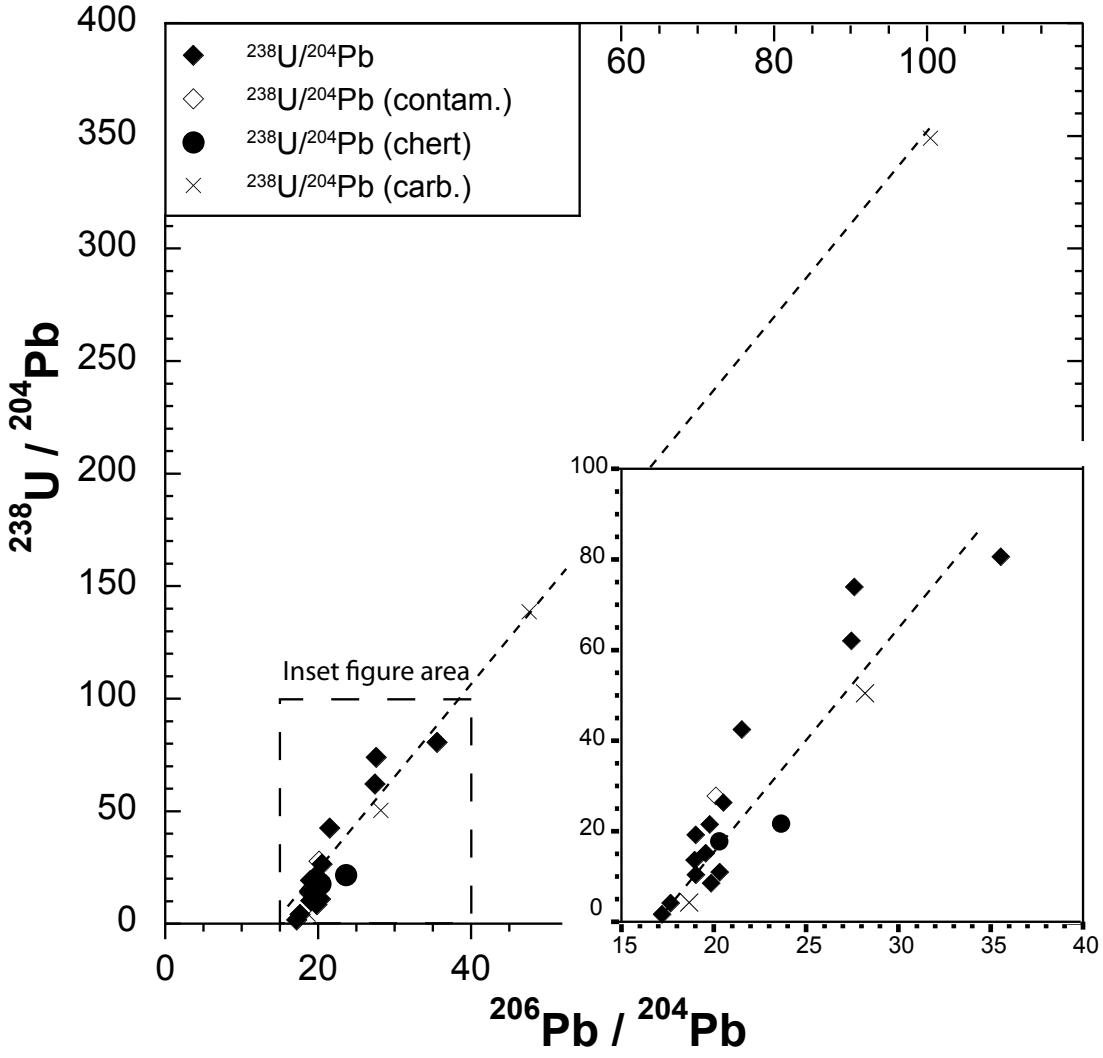



Figure 2.11. Crossplot of $^{238}U/^{204}Pb$ vs. $^{206}Pb/^{204}Pb$ for Gunflint BIF samples showing a strong positive correlation. Given that $^{238}U$ decays to $^{206}Pb$, the linearity of the data indicates that the $^{238}U/^{206}Pb$ ratio is constant, and that the measured U/Pb ratio today for the Gunflint samples is the same as the original ratio rather than an artifact of modern weathering. Inset plot is a magnification of the majority of the data points.

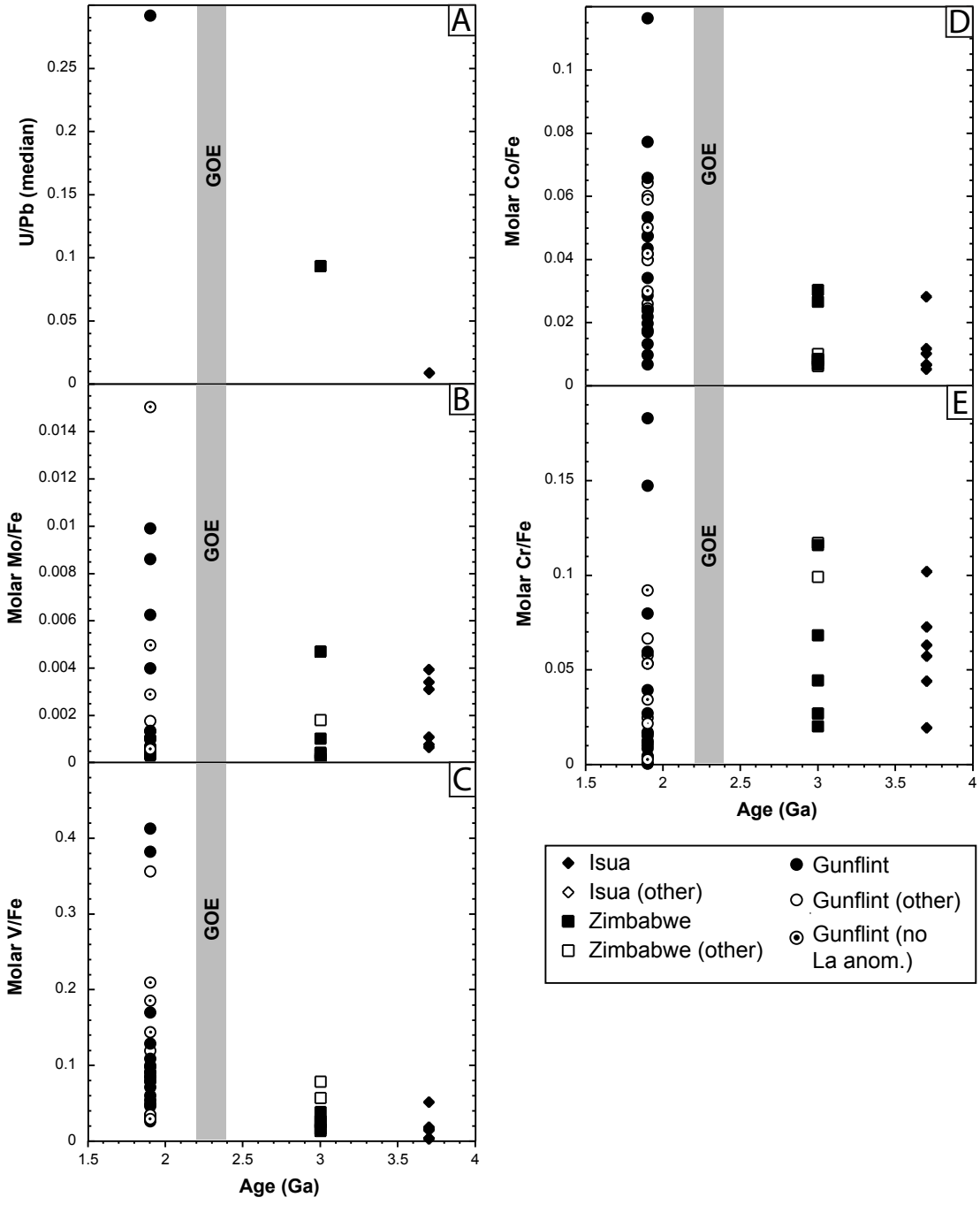



Figure 2.12. The concentration of terrestrially sourced, redox-sensitive trace elements in BIF through time. Plots show variation of (A) median U/Pb, (B) molar Mo/Fe, (C) molar V/Fe, (D) molar Co/Fe, and (E) molar Cr/Fe. All ratios show a jump through time, with a major jump occurring in post-GOE samples, supporting the onset of oxidative continental weathering by 1.9 Ga.

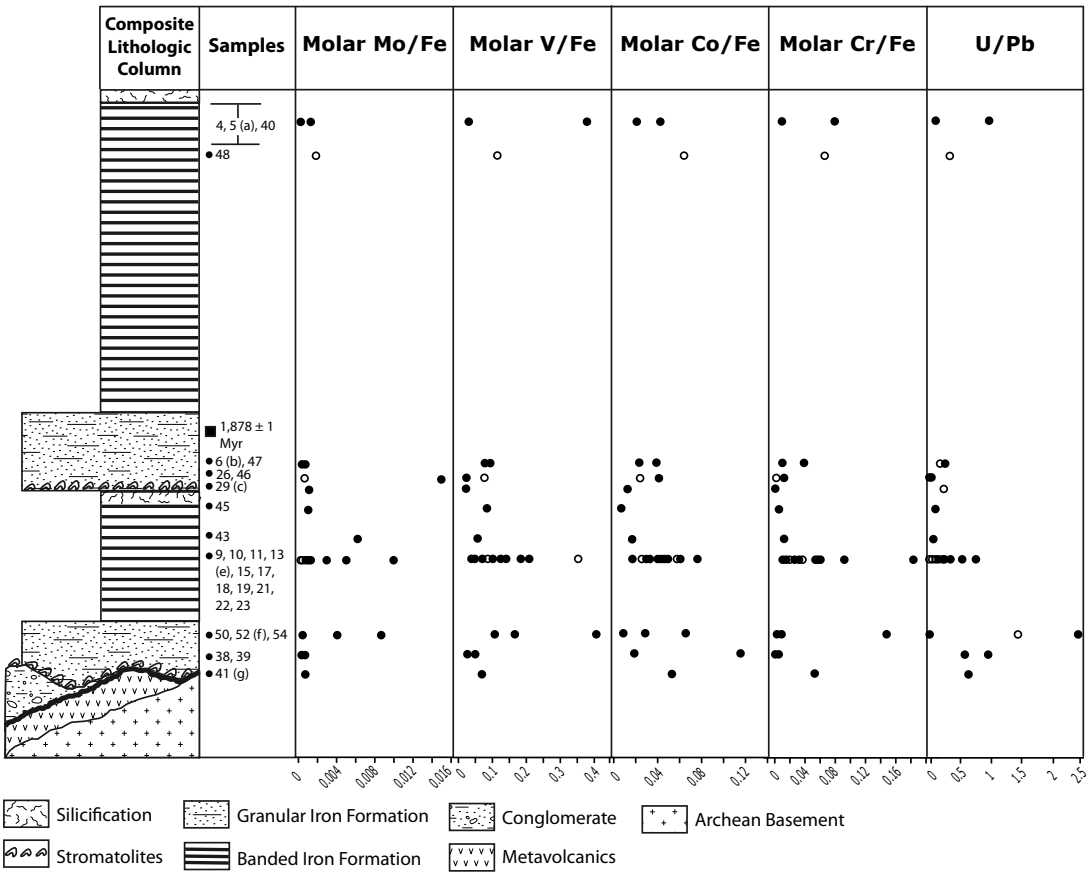



Figure 2.13. The small scale heterogeneity of trace element geochemistry through Gunflint stratigraphy. No relationship is evident between the chemistry and stratigraphic position or depositional environment. Open circle represent samples that are either contaminated or lack a positive La anomaly.

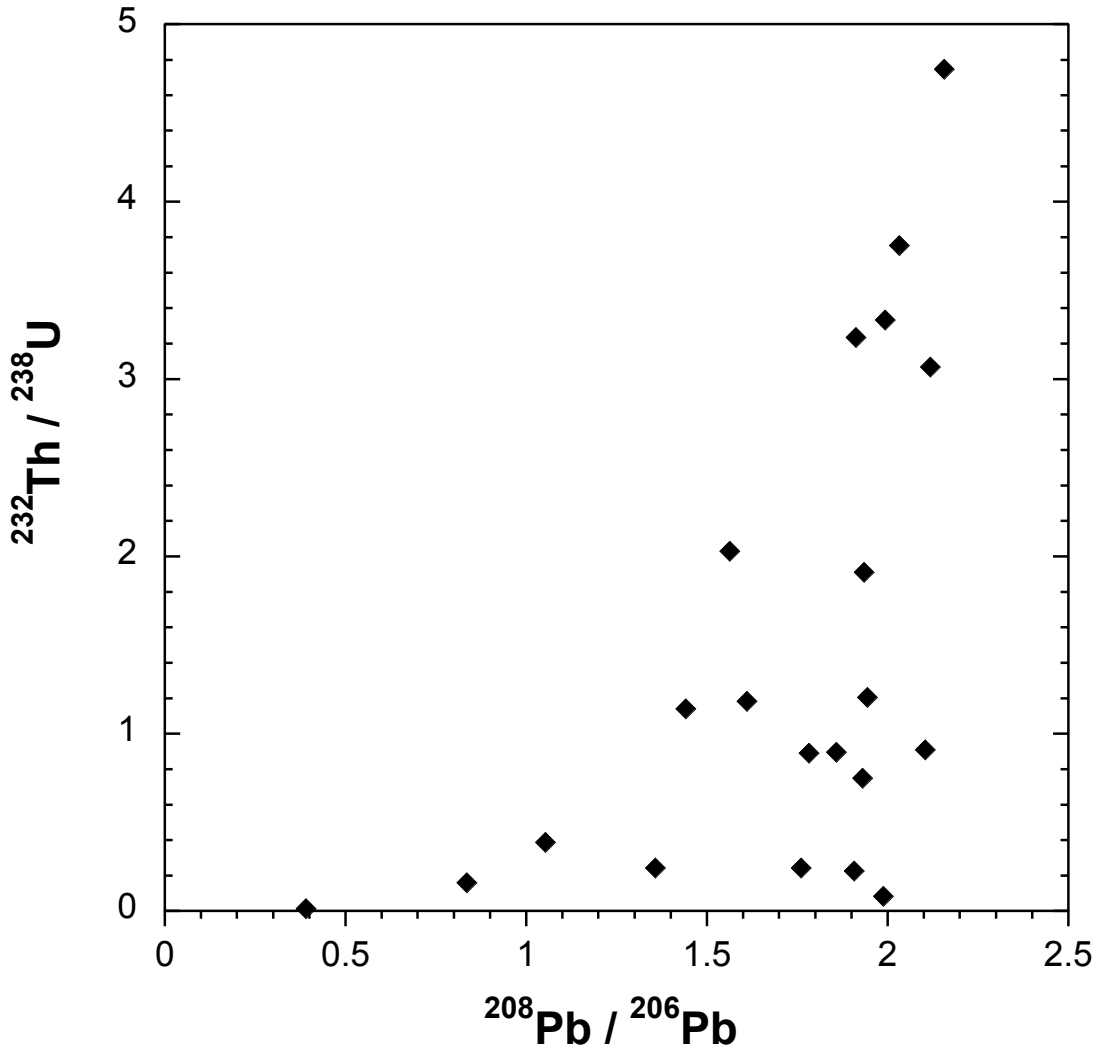



Figure 2.14. Cross plot of $^{208}Pb/^{206}Pb$ vs. $^{232}Th/^{238}U$ for Gunflint BIF samples. (1) The positive correlation, (2) samples having $^{208}Pb/^{206}Pb$ ratios less than 2 and (3) samples having $^{232}Th/^{238}U$ ratios less than 4 all indicate very radiogenic Pb compositions and suggest the preferential addition of U, rather than Th, in response to oxidative continental weathering.

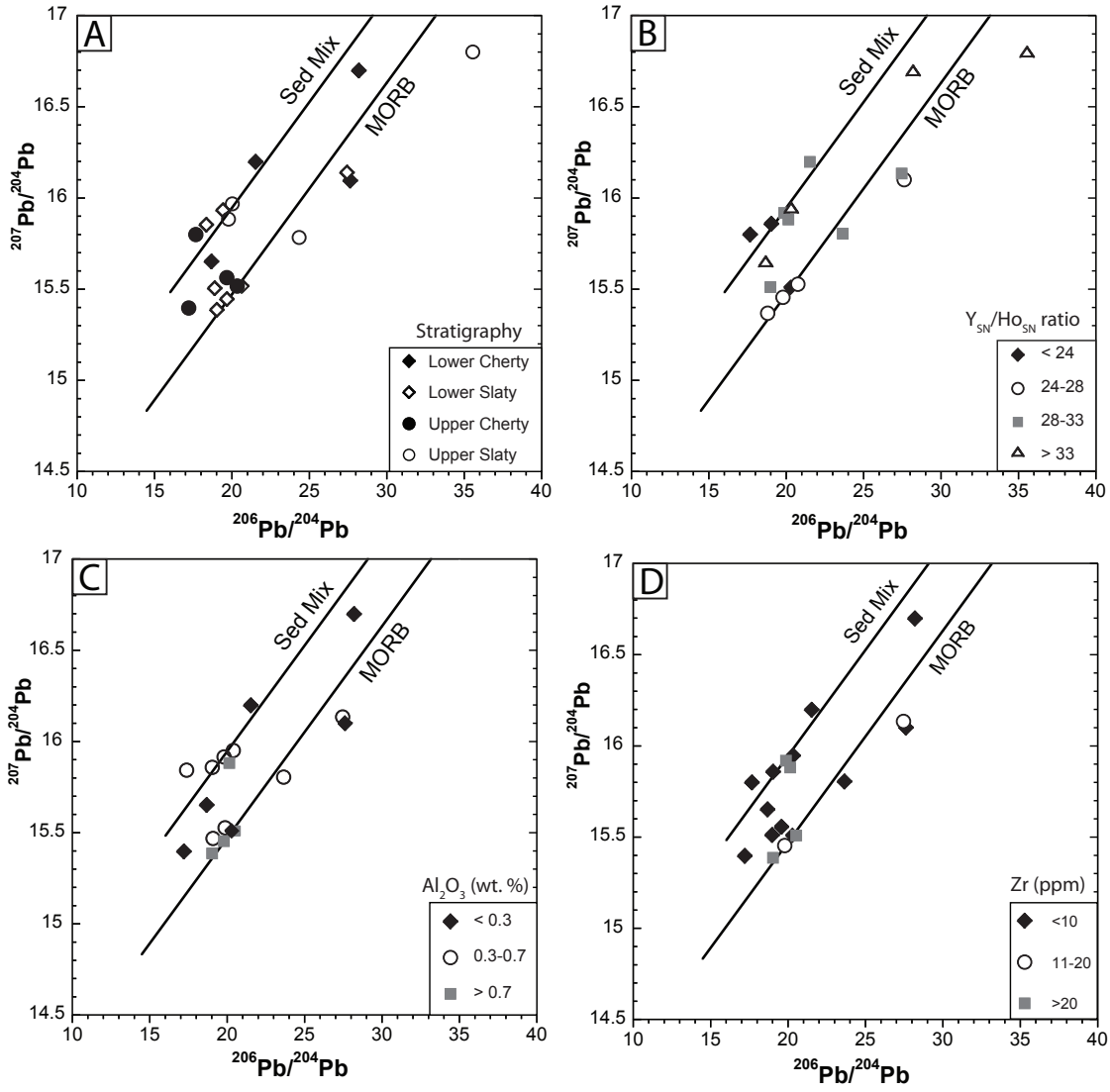



Figure 2.15. Gunflint Pb isotope data plotted on a common Pb plot, along with two isochrons emanating from the 1.9 Ga starting points for a depleted mantle source (MORB) and a mix of sedimentary sources (Kramers and Tolstikhin, 1997). Samples were coded according to stratigraphic position and depositional environment (A), $Y_{SN}/Ho_{SN}$ ratio (B), $Al_2O_3$ content (C) and Zr content (D) to attempt to determine why samples plot more crustal or more like mantle. Lead in the Gunflint samples was sourced from both the depleted mantle via hydrothermal vents and the continent (i.e. sedimentary mix). It is not clear, however, as to what is controlling the distribution of the samples between these two sources.

# Chapter III

# Microscale Heterogeneity in the Geochemistry of Algoma- and Superior-Type Banded Iron Formations

**Abstract**

In this study, we analyzed both bulk rock geochemistry and the geochemistry of individual mineral grains of magnetite and hematite from oxide-facies BIF ranging in age from ~3.7 Ga to ~1.9 Ga to determine the variability and range in mineral geochemistry and to determine how well bulk chemistry represents the average mineral chemistry. We also examined the iron isotope compositions of BIFs, both of the bulk-rock and of individual mm-scale bands, to determine the degree of variability between the isotopic signature of the bulk rock and of individual bands. Mineral chemistry data were collected using a laser-ablation microprobe coupled to an inductively coupled plasma-mass spectrometer (LA-ICP-MS). All samples had the bulk geochemical BIF REE fingerprint, having an overall light rare earth element (LREE) depletion relative to heavy rare earth elements (HREE), positive La, Gd, Eu, and Y anomalies and either positive, negative or absent Ce anomalies. However, there was substantial variability with regard to these key REE signatures at the mineral scale. Microscale heterogeneity observed in this study was ubiquitous, regardless of sample age, location, metamorphic grade, BIF type (Algoma vs. Superior), mineralogy (magnetite vs. hematite) and element. It is extremely unlikely that this variability is a reflection of the ocean chemistry conditions during Fe oxyhydroxides precipitation, but rather may result from inorganic, post-depositional alteration processes. Fine-scale heterogeneity is also seen in $\delta^{56}Fe$ values in study samples. This heterogeneity may also represent post-depositional processes, but rather than being controlled uniquely by inorganic processes, the heterogeneity may also reflect dissimilatory iron reduction (DIR) processes in the sediment porewater prior to lithification.

## 3.1 Introduction

Banded iron formation (BIF) is a chemical sedimentary rock that has the potential to address a variety of questions about the early evolution of Earth because: (1) it is found within the oldest fragments of supracrustal material, and (2) the geochemistry of BIF may preserve a record of the environment in which it formed (Bekker et al., 2010; Bolhar et al., 2004; Klein, 2005). Previous studies (e.g., Bekker et al., 2010; Heimann et al., 2010; Johnson et al., 2008b; Konhauser et al., 2009; Planavsky et al., 2010) have examined the geochemistry of BIF through time to look for changes in the paleoenvironmental conditions of early Earth, however these studies have focused primarily on whole rock geochemical and iron-isotopic analyses. A potential concern with examining whole rock geochemistry is that this approach may homogenize any heterogeneity present in the sample.

This study takes a novel approach to examining BIF by analyzing both whole rock geochemistry and the geochemistry of individual mineral grains of magnetite and hematite in BIF from the ~3.7 Ga Isua Greenstone Belt, Greenland, (Fig. 3.1A; Moorbath et al., 1973; Moorbath and Whitehouse, 1996; Nutman et al., 1997) ~3.0 Ga Buhwa Greenstone Belt, Zimbabwe 3, and the ~1.9 Ga Gunflint Iron Formation, Minnesota and Ontario (Fig. 3.1B; Fedo and Eriksson, 1996; Fedo et al., 1995), to determine the variability and range in mineral geochemistry. Specifically we address whether key pieces of information regarding BIF is being missed by simply examining the average composition of a large number of grains rather than examining the individual grains. We also address whether whole rock values are accurately reflecting the average composition of all the minerals.

Fine-scale variation in mineralogy and petrography of BIFs suggest that *in situ* geochemical analytical approaches on individual mineral grains could provide a more complete understanding of BIF genesis compared to whole-rock methods (Fig. 3.1C; Fralick et al., 2002). Laser-ablation inductively coupled plasma-mass spectrometry (LA-ICP-MS) provides the opportunity to determine a number of trace elements with precision approaching that of conventional bulk-rock analysis, but with high spatial resolution. Using this approach, this study analyses individual magnetite and hematite grains along both single layers, and across multiple layers, within BIF. This allows us to see the degree of variability in mineral chemistry between individual grains on a range of scales. The mineral chemistries of individual grains from a single sample were then compared to the whole rock chemistry of the same sample. If the whole rock geochemistry of a sample represents the chemistry of the sample's comprising minerals, there should be little variation in mineral versus whole geochemistry. If there is a difference between whole rock and individual mineral data, we may be able to use these differences to better understand the processes associated with BIF formation. This study also examines iron isotopic composition of the sample samples BIFs, both at the whole rock and individual band scales, to determine the degree of variability between the signature of the bulk rock and of individual bands to investigate BIF genesis and the preservation of Fe isotope signatures.

**3.2 Background**

BIF is a chemical sedimentary rock, precipitated from seawater, comprised of alternating mm- to cm-thick, iron- and silica-rich layers, with 20-40 wt. % of $Fe_{total}$ and 43-56 wt. % of $SiO_2$ (Li et al., 2013). BIF are generally classified into two types based

on their formation age, size, proposed tectonic setting, depositional environment and associated lithologies (Klein, 2005). Algoma-type BIF formed during the Archean in association with volcanic sequences. These deposits are relatively small, with lateral extents <10 km and thicknesses 10-100 m (Gross, 1965, 1980; Kimberley, 1978), and are interpreted to have formed within island arc/back arc basins and intracratonic rift zones (Appel, 1980; Condie, 1981; Goodwin, 1973; Gross, 1965; Isley and Abbott, 1999). Superior-type BIF primarily formed during the Late Archean and Paleoproterozoic in association with both clastic sedimentary rocks and volcanic rocks. Superior-type BIFs are typically very large deposits, with some being hundreds of meters thick and extending over $10^5$ $km^2$ (Gross, 1983; Veizer, 1983); they are the dominant iron resource in the world (Beukes, 1973; Trendall and Blockey, 1970). Superior BIF has been interpreted to originate in relatively shallow marine environments under transgressing seas, possibly on the continental shelves of tectonically passive margins (Kato et al., 2006b). For both Algoma- and Superior-type BIFs, we must consider both the source of iron and oxidation mechanism.

The dominant Algoma-type BIF-formation mechanism involves the upwelling of hydrothermally sourced reduced iron from deep water, which is oxidized in the oxygenated photic zone of a predominately anoxic ocean, resulting in the formation of ferric oxyhydroxides ($Fe(OH)_3$), the precursor to Fe(III) oxide layers (Beukes, 1973; Gross, 1965; Simonson, 1985; Simonson and Hassler, 1996). The hydrothermal origin for the Fe is supported by rare earth element (REE) patterns with positive Eu anomalies and mantle-like Nd isotopic signatures (Beukes and Gutzmer, 2008; Isley, 1995; Konhauser et al., 2002; Steinhoefel et al., 2010). During times of hydrothermal quiescence,

deposition of Fe-rich layers was replaced with deposition of Si-rich layers, with the Si either precipitated directly from Si-saturated waters in the form of an amorphous silica gel or coprecipitated with Fe by adsorption of dissolved Si onto ferric oxyhydroxides (Alibert and Mcculloch, 1993; Bau and Dulski, 1996; Bau et al., 1997a; Derry and Jacobsen, 1990). Si isotopes suggest a hydrothermal source for the silica in Algoma-type BIF (Fischer and Knoll, 2009; Konhauser et al., 2007b; Siever, 1992). The formation mechanism for Superior-type BIF is similar in that it still involves the oxidization of reduced iron in the oxygenated photic zone of a predominately anoxic ocean, resulting in the formation of ferric oxyhydroxides ($Fe(OH)_3$). However, the hydrothermally sourced Fe is supplemented more by continental drainage (André et al., 2006; Heck et al., 2011) and Si isotopes suggest that the silica was derived predominantly from the continents (Holland, 1973; Isley, 1995; Jacobsen and Pimental-Klose, 1988; Klein and Beukes, 1989; Konhauser et al., 2002; Morris and Horwitz, 1983).

The oxidation mechanism for reduced iron is uncertain, and may have varied throughout Earth's history (Brengman, 2014). The oxidation of $Fe(II)_{aq}$ to $Fe(III)_{aq}$, which later precipitated as $Fe(OH)_3$, could have been caused by (1) the interaction with free $O_2$ produced by oxygenic photosynthesis (Braterman and Cairns-Smith, 1987; Czaja et al., 2013; Kappler et al., 2005; Koehler et al., 2010; Konhauser et al., 2002), (2) anoxygenic photosynthetic Fe(II) oxidation (Widdel et al., 1993; Konhauser et al., 2002; Kappler et al., 2005; Konhauser et al., 2005; Croal et al., 2009; Planavsky et al., 2009), or (3) UV photooxidation (Buick, 1992, 2008; Cloud, 1965, 1973; Knoll et al., 2006; Towe, 1983). The third possibility seems unlikely, however, based on experimental studies by Konhauser et al. (Anbar and Holland, 1992; Braterman and Cairns-Smith, 1987; Cairns-

Smith, 1987), which suggest that UV photooxidation is too inefficient of a process to be a significant source of Fe oxides.

An initial oxidation stage is followed by sediment digenesis where $Fe(II)_{aq}$ reacts with deposited Fe(III) oxides to produce magnetite, or with carbonate or dissolved silica to produce siderite or Fe(II)-bearing silicate phases, respectively (2007a). Oxidation of $Fe(II)_{aq}$ in the upper water column followed by settling of particles through Fe(II)-rich anoxic bottom water results in the formation of ferric oxyhydroxides, which, when dehydrated during early diagenesis, produces hematite in unmetamorphosed BIF (Beukes and Gutzmer, 2008; Klein, 2005).

Regardless of age and metamorphic grade, BIF has been shown to have rare earth element patterns that carry features of having interacted with marine water (Steinhoefel et al., 2010). BIF is assumed to record minimal fractionation of REE during precipitation of ferric iron oxides and oxyhydroxides, and thus may preserve a snapshot of the REE signature of seawater at the site of Fe precipitation (Barrett et al., 1988; Bekker et al., 2010; Bolhar et al., 2004; Derry and Jacobsen, 1990; Dymek and Klein, 1988; Fryer, 1977; Kato et al., 1998; Klein, 2005). A typical shale-normalized bulk rock BIF REE pattern consists of an overall light rare earth element (LREE) depletion relative to heavy rare earth elements (HREE), positive La, Gd, Eu, and Y anomalies, and positive, negative, or absent Ce anomalies (Bau, 1993; Bau and Dulski, 1996; Bau and Moller, 1993; Bekker et al., 2010; Bolhar et al., 2004; Derry and Jacobsen, 1990; Kato and Nakamura, 2003; Klein, 2005; Murray et al., 1992). Negative and positive anomalies are defined as values of less than and greater than 1, respectively. Europium enrichment indicates an influence of high-temperature hydrothermal fluids on the dissolved REE

composition of seawater (Bau, 1996; Bau and Koschinsky, 2009; Bryne and Kim, 1990; Derry and Jacobsen, 1990; Quinn et al., 2006; Sholkovitz, 1992; Sholkovitz et al., 1994). The gradual decrease in the magnitude of the Eu anomaly throughout the Archean and the Paleoproterozoic is interpreted as a decrease in hydrothermal input through time (Derry and Jacobsen, 1990).

Our understanding of BIF genesis has been aided by research developments using iron isotopes (Bau and Moller, 1993; Kamber, 2010; Klein, 2005). Some interpret the Fe isotope compositions of BIF to directly reflect those of ancient seawater and invoke extensive abiotic precipitation of iron oxides to produce the observed negative $\delta^{56}$Fe excursion in Neoarchean to Paleoproterozoic rocks (e.g., Craddock and Dauphas, 2011; Czaja et al., 2013; Heimann et al., 2010; Johnson et al., 2003; Johnson et al., 2008b; Planavsky et al., 2012; Rouxel et al., 2005; Steinhoefel et al., 2010). Others do not consider BIF Fe isotope compositions to be a direct seawater proxy and explain Fe isotope variability through microbial iron cycling in the soft sediment prior to lithification (Anbar and Rouxel, 2007; Rouxel et al., 2005).

Both positive and negative $\delta^{56}$Fe values have been recorded in Fe oxide phases in BIF, with an observed 5 ‰ range, from -3 ‰ to +2 ‰ (Johnson et al., 2008a; Johnson et al., 2008b; Percak-Dennett et al., 2011). If BIF deposition involves the oxidation of hydrothermally sourced Fe(II)-rich fluids, it should record a $\delta^{56}$Fe value at or slightly below 0 ‰ (Anbar, 2004; Beard et al., 2004; Johnson et al., 2008b; Rouxel et al., 2005). Both proposed methods for the oxidation of $Fe(II)_{aq}$ (i.e., by anaerobic photosynthesis and by dissolved oxygen in the upper water column) precipitate ferric hydroxide with a Fe isotope composition that is ~ 1.5 ‰ heavier than Fe(II) in seawater (Johnson et al.,

2008a). When complete oxidation of the iron reservoir has occurred, the $\delta^{56}Fe$ values in the precipitates match those of the source Fe(II), producing an apparent $\Delta^{56}Fe_{Fe(OH)3\text{-}Fe(II)}$ fractionation of zero (Anbar et al., 2005; Croal et al., 2004; Welch et al., 2003). By contrast, partial oxidation of hydrothermal $Fe(II)_{aq}$ will produce positive $\delta^{56}Fe$ values for the precipitated Fe(III) oxide and carbonate phases (Bullen et al., 2001; Johnson et al., 2004; Li et al., 2013; Rouxel, 2003; Rouxel et al., 2008). In this case, only part of the reservoir of dissolved Fe(II) in the upper water column was oxidized suggesting that the oxidant was the limiting factor (Dauphas et al., 2004; Johnson et al., 2003; Johnson et al., 2008b; Li et al., 2013; Rouxel, 2003; Rouxel et al., 2005; Whitehouse and Fedo, 2007).

Negative $\delta^{56}Fe$ values in Fe oxides and carbonates are thus attributed to the complete oxidation of $Fe(II)_{aq}$ that was already depleted in heavy Fe isotopes relative to hydrothermal sourced fluids through the activity of microbial dissimilatory iron reduction (DIR) during diagenesis (Johnson et al., 2003; Johnson et al., 2008b; Steinhoefel et al., 2010). During DIR, microbes use organic carbon as an electron donor to reduce Fe(III), releasing $Fe(II)_{aq}$ that has $\delta^{56}Fe$ values as much as 3 ‰ lower than the initial Fe(III) hydroxides (Craddock and Dauphas, 2011; Johnson et al., 2003; Johnson et al., 2008b; Li et al., 2013; Percak-Dennett et al., 2011; Tangalos et al., 2010). The extent of fractionation during DIR is dependent on the proportions of aqueous Fe(II), adsorbed Fe(II) and reactive Fe(III) on particle surfaces (Bergquist and Boyle, 2006; Crosby et al., 2005; Crosby et al., 2007; Homoky et al., 2009; Severmann et al., 2006; Severmann et al., 2008; Wu et al., 2009). Negative $\delta^{56}Fe$ values in Fe oxide phases can be produced during precipitation from seawater that had previously undergone extensive oxidation,

leaving behind an aqueous reservoir with depleted $\delta^{56}Fe$ values (Crosby et al., 2005; Crosby et al., 2007).

The use of iron isotopes in BIF as a proxy for the ancient oceans may further be complicated by the extended diagenetic and metamorphic histories of BIF. However, consistent $\delta^{56}Fe$ values measured for bulk rocks in the >3.7 Ga Isua Supracrustal Belt of SW Greenland (Anbar and Rouxel, 2007; Li et al., 2013; Rouxel et al., 2005; Tsikos et al., 2010) and in the >3.75 Ga Nuvvuagittuq Supracrustal Belt of Canada (Czaja et al., 2013; Dauphas et al., 2007b) suggest that metamorphism did not affect the bulk Fe isotope compositions (Dauphas et al., 2007a). In addition, Fe isotopes from both low grade and high grade rocks from the ~1.9 Ga Biwabik Iron Formation in Minnesota were found to be characteristic of chemical sedimentation processes, confirming that Fe isotopes can be used to identify sedimentary processes in the Precambrian rock record (Czaja et al., 2013; Dauphas et al., 2007a; Dauphas and Rouxel, 2006).

## 3.3. Geologic Setting And Sample Description

### *3.3.1 Isua Greenstone Belt, Greenland ( > 3.7 Ga)*

The > 3.7 Algoma-type Ga Isua Greenstone Belt (IGB) of southern West Greenland is one of the oldest known and locally well preserved successions of metavolcanic and metasedimentary rocks on Earth (Frost et al., 2006; Hyslop et al., 2007). The IGB forms an arcuate belt ~35 km long and up to 2.5 km wide (Fig. 3.1A). The most abundant metasedimentary rocks are BIF, which have been interpreted to have been deposited in a shallow marine setting (Appel et al., 1998; Fedo, 2000; Moorbath et al., 1973; Myers, 2001). After deposition, all rocks experienced multiple episodes of ductile deformation (Fedo et al., 2001), amphibolite-facies metamorphism and pervasive

carbonate and potassium metasomatism (Komiya et al., 1999; Whitehouse and Fedo, 2007). The IGB is divided into five tectonic domains (Appel et al., 1998; Dymek and Klein, 1988; Fedo et al., 2001; Fedo et al., 2006; Myers and Crowley, 2000; Rollinson, 2002; Rosing, 1999), including a domain of comparatively low strain (Myers, 2001; Rollinson, 2002, 2003) where the majority of samples for this study were collected (Fig. 3.1A).

Samples for this study are dominated by mm-scale banding of quartz and iron oxide (predominantly magnetite), although some sample also contain a minor amount of hematite (Appel et al., 1998; Myers, 2001). Quartz occurs as equant to semi-equant grains with 120º interlocking grain boundaries and ranges in size from ~50 μm to 200 μm. Magnetite and hematite typically occurs as anhedral grains, ranging in size from ~ 20 μm to 200 μm.

Two samples (IS-02-05, IS-02-08) were analysed for mineral specific trace element geochemistry. These represent variants of typical "quartz - magnetite" BIF from the northeastern part of the IGB (Dymek and Klein, 1988; Whitehouse and Fedo, 2003). Sample IS-02-08 consists of mm-scale magnetite and quartz alternations, and sample IS-02-05 consists of alternating mm-scale bands of oriented beige amphibole needles + quartz and magnetite (Dymek and Klein, 1988; Whitehouse and Fedo, 2007). For IS-02-05, 26 different grains were analyzed (17 magnetite + 9 hematite grains) in 5 distinct bands (Fig. 3.2A). For IS-02-08, 25 different grains were analyzed (14 magnetite + 11 hematite). However, instead of several distant bands being present in the sample, it appears as though it may be a single band that has been folded, which is consistent with the pervasive ductal deformation in the area and is an example of the high-strain rootless

folds found in the region (Whitehouse and Fedo, 2007).

### *3.3.2 Buhwa Greenstone Belt, Zimbabwe (~ 3.0 Ga)*

The ~3.0 Ga Buhwa Greenstone Belt (BGB) is located along the southern margin of the Zimbabwe Archean craton, where it comes in contact with the granulites of the Northern Marginal zone of the Limpopo Belt (Fig. 3.2B; Whitehouse and Fedo, 2007). The outcrops form an east-plunging syncline, and metamorphism increases from the north to south, and west to east (Fedo and Eriksson, 1995; Fedo et al., 1995; Fedo et al., 1996). The BGB is divided into a western shelf facies and an eastern basinal facies, connected by a zone of transitional deposits (Fig. 3.1B; Fedo and Eriksson, 1996; Fedo et al., 1995). BIF samples studied here are representative of all the aspects of the BGB and are predominantly Superior-type.

In thin section, samples dominantly consist of alternating mm- to cm-bands of recrystallized quartz (25 – 500 μm) and iron oxide, with minor amounts of amphibole and trace amounts of fine-grained apatite (<150 μm) in the some of the iron oxide bands. Typically, the iron ore is dominated by hematite grains with magnetite cores, suggesting the hematite is recrystallized and may be pseudomorphic replacement of magnetite. Only one sample (ZB-05), an Algoma-type BIF, contains predominantly magnetite rather than hematite. The only granulite-facies sample (ZB-117) contains bands of coarser-grained recrystallized quartz (50 μm – 1 mm) and hematite replacing magnetite. Samples ZB-247 and ZB-294 were collected from the Buhwa Mine and consist of bands of hematite replacing magnetite (90 %) and microcyrstalline quartz (10 %). Sample ZB-117 and ZB-23 were analyzed for mineral specific trace element compositions. For ZB-23, 16

magnetite grains were analyzed in 4 different bands (Fig. 3.2C), and for ZB-117, 19 magnetite grains where analyzed in 4 different bands (Fig. 3.2D).

### *3.3.3 Gunflint Iron Formation, Minnesota and Ontario (~1.9 Ga)*

The ~1.9 Ga Superior-type Gunflint Formation (GF) outcrops along a 175 km NE-SW trending belt from Thunder Bay, Ontario, where the unit is ~190 m thick and unmetamorphosed, to the Gunflint Trail in northern Minnesota, where the unit is ~95 m thick and has been subjected to amphibolite facies contact metamorphism by the intrusion of the 1.1 Ga Duluth Complex (Fedo and Eriksson, 1996). The GF is commonly subdivided into four units that record two upward transgressive cycles: the Lower Cherty, Lower Slaty, Upper Cherty and Upper Slaty units (Fig. 3.1C; Floran and Papike, 1978; Fralick et al., 2002; Jirsa and Weiblen, 2007; Miller et al., 1987; Planavsky et al., 2009). We collected BIF samples from all four units and from both metamorphosed and unmetamorphosed sections.

In thin section, metamorphosed BIF samples are comprised of mm- to cm-thick alternating bands of Fe-silicate and Fe-oxide, and contain varying amounts of quartz, magnetite, and amphibole. Quartz occurs as equant grains with 120º interlocking grain boundaries, which suggests recrystallization, and ranges in size from ~50 μm to 500 μm. Magnetite typically occurs as anhedral grains, ranging in size from ~ 10 μm to 200 μm that occurs within distinct bands or as disseminated grains between quartz and amphibole. Unmetamorphosed samples contain varying degrees of quartz, magnetite, hematite, ankerite, dolomite, and calcite. However, it is likely that some of the calcite is secondary cement that formed during burial. Most quartz grains are anhedral and <100 μm, with some grains up to ~300 μm in size. Magnetite, hematite and carbonate grains

are typically anhedral and may or may not occur in distinct bands. In some locations, hematite and magnetite oolite is preserved.

Three samples were analyzed for mineral chemistry. Samples GF-6 and GF-39 were collected from the metamorphosed section in Minnesota; sample GF-45, a granular iron formation, was collected from the unmetamorphosed section in Ontario. For GF-6, twenty magnetite grains were analyzed in 4 different bands (Fig. 3.2E). Sample GF-39 and GF-45 are examples of oolitic granular iron formation and thus no distinct banding is present; the magnetite grains are rounded rather than anhedral. For both samples, 7 magnetite grains were analyzed throughout the sample (Fig. 3.2F).

## *3.4 Analytical Methods*

### *3.4.1 Whole Rock, Trace- and Rare-Earth Element Analysis*

In a protocol adapted from Eggins et al. (Broderick, 1920; Miller et al., 1987; Ojakangas et al., 2001; Planavsky et al., 2009; Pufahl and Fralick, 2004), samples were crushed and powdered, and 100 mg aliquots were digested in capped Savillex® screw-top Teflon beakers over 72 hours at 130 °C in a 2:1 mixture of concentrated distilled HF and $HNO_3$. Following digestion, samples were evaporated to dryness and the residues were redissolved twice with 1 mL of concentrated $HNO_3$ to convert and volatilize any fluorides that formed during the HF digestion. Six milliliters of Milli-Q water and 2 mL of concentrated $HNO_3$ were added to all samples, and beakers were capped and heated at 120 °C for 48 hours. Samples were homogenized and stirred using a vortex mixer and centrifuged for 10 minutes. Aliquots of the samples were diluted and spiked with an internal standard (SNOWY) containing $^{6}Li$, In, Re, Bi, and $^{235}U$.

Samples were analysed for a suite of 46 trace and rare earth elements (Li, Be, Sc, Ti, V, Cr, Co, Ni, Cu, Zn, Ga, As, Rb, Sr, Y, Zr, Nb, Mo, Ag, Cd, In, Sn, Sb, Cs, Ba, La, Ce, Pr, Nd, Sm, Eu, Gd, Tb, Dy, Ho, Er, Tm, Yb, Lu, Gf, Ta, W, Tl, Pb, Th, U) using a quadrupole Thermo X II Series inductively coupled plasma-mass spectrometer (ICP-MS) at Laurentian University, Sudbury, Ontario (Tables A.1, A.2, and A.3). The instrument was tuned to 1.5 % $CeO^+/Ce^+$, and all isobaric interferences were corrected using oxide formation rates determined for pure elemental solutions measured immediately following sample analysis. Multiple digestions of the USGS reference material W-2 were used for instrumental calibration. USGS standards BHVO-1 and BIR-1 were analysed as unknowns and compared to the long-term reproducibility reported in Kamber (1997) to serve as an external standard control, with reproducibility at better than 1 % rsd using a quartz spray chamber.

*3.4.2 Mineral Specific Trace- and Rare-Earth Element Analysis*

A laser-ablation microprobe coupled to an inductively coupled plasma-mass spectrometer (LA-ICP-MS) has produced a relatively simple and inexpensive instrument capable of *in situ*, high-sensitivity multi-element and isotopic ratio analysis (2009). Methods of calibration use both internal and external (NIST trace-element glasses) reference materials.

Extra thick polished mounts were prepared for *in situ* geochemical analysis of magnetite (mt) and hematite (hem) grains using a New Wave Nd: YAG 213 nm laser ablation system coupled to the quadrupole Thermo X II Series ICP-MS (LA-ICP-MS) operated under conditions similar to those reported in Kamber and Web (Arrowsmith, 1987; Eggins et al., 1997; Fryer et al., 1995; Gray, 1985; Halliday et al., 1998; Jackson et

al., 1992; Jenner and O'Neill, 2012; Moenke-Blankenburg, 1993; Muller et al., 2003; Steinhoefel et al., 2009). Similar to the method described in Baldwin et al. (2007), either a 25 μm or 40 μm laser beam diameter, depending on sample grain size, at a repetition of 10 Hz and energy density of 13 J/cm$^2$, was used to analyze multiple grains of each mineral per band per sample. A total analytical time of 50-55 seconds was used, including a background washout time of 30 seconds. All spots were pre-ablated with a beam diameter greater than what was used to analyze the grain in order to remove any possible surface contamination. Instrumental calibration was conducted using the synthetic glass standards NIST 610 (mt and hem), which were analyzed using the same parameters as the samples at the beginning and end of each run, as well as after every 5-10 spots to ensure that the machine was maintaining analytical consistency. Because only ~20 elements per spot could be analyzed, 2 spots per grain, if the grain was large enough, or 2 grains close to each other had to be selected so that all 41 elements could be analyzed (Tables A.7 and A.8):

Spot 1: Sr, Y, Zr, Ba, La, Ce, Pr, Nd, Sm, Eu, Gd, Tb, Dy, Ho, Er, Tm, Yb, Lu, Hf, Pb, Th, U

Spot 2: Li, Be, Sc, Ti, V, Cr, Mn, Co, Ni, Cu, Zn, Ga, Nb, Mo, Sn, Sb, Ta, W, Bi

Photomicrographs of laser ablation pits were examined afterwards to assure that spots were contained within the boundaries of the desired grain. We used only mineral data from when the laser ablation pit was completely within the boundary of the grain of interest for analysis (Fig. 3.3). All other points were excluded from the study.

*3.4.3 Fe Isotope Analyses of Whole Rock and Individual Bands*

Fe was extracted from the samples using the procedures described in detail in Schoenberg and von Blanckenburg (2011). Samples were digested in HF-$HNO_3$ in closed Savillex® screw-top PFA containers on a hot plate at 150 ºC. Full oxidation of Fe to its trivalent state was achieved by repeated cycles of dissolution in concentrated $HNO_3$, heating to 150 ºC and drying. Digested samples were dissolved in 1-2 mL of 6 mol $L^{-1}$ HCl for anion-exchange chromatographic Fe separation.

Anion-exchange chromatography was executed in a 7.5 mL Spectrum® polypropylene column using 1 mL of BioRad AG®, 100-200 mesh resin. The resin was pre-cleaned and pre-conditioned with 2 mL of $H_2O$, 5 mL of 5 mol $L^{-1}$ $HNO_3$, 2 mL of $H_2O$ and 8 mL of 6 mol $L^{-1}$ $HNO_3$. Once the sample was loaded on the resin matrix, elements were eluded with 6 mL of 6 mol $L^{-1}$ HCl. The Fe was then eluded with 2 mL $H_2O$ and 5 mL of 5 mol $L^{-1}$ $HNO_3$. It was essential for there to be complete Fe recovery otherwise substantial isotope fractionation can occur. To avoid oxide interferences on the ThermoFinnigan Neptune multi collector inductively coupled mass spectrometer (MC-ICP-MS), 200 μL of 14 mol $L^{-1}$ $HNO_3$ were added to the samples to convert from the chloride to the nitric form. Dried Fe samples were then dissolved in2 mL of 0.3 mol $L^{-1}$ $HNO_3$ and diluted to adequate concentrations for matrix check by inductively coupled plasma optical emission spectrometry (ICP-OES) and isotope ratio determination by mass spectrometry.

Fe isotope compositions were measured on a ThermoFinnigan Neptune MC-ICP-MS in medium-resolution mode, according to the methods established in Frost et al. (2005). Fe isotopes were detected simultaneously in a first integration cycle together

with $^{52}Cr$ and $^{60}Ni$ as monitors for the correction of isobaric interferences of $^{52}Cr$ and $^{60}Ni$ on $^{58}Fe$. Instrumental mass discrimination was corrected by standard-sample-bracketing using the reference material IRMM-014. Fe isotope data are expressed in the δ notation as the ‰ deviation of the Fe isotope ratios of samples from the average of the respective ratios of their immediately preceding and following IRMM-014 standards, e.g., for $\delta^{56}Fe$ (Table A.6):

$$\delta^{56}Fe_{Sample} = [(^{56}Fe / {}^{54}Fe_{Sample}) / (^{56}Fe / {}^{54}Fe_{IRMM\text{-}014})] - 1 \times 1000$$

## 3.5 Results

### *3.5.1 Whole Rock Geochemistry*

#### *3.5.1.1 Major Elements*

$SiO_2$ and $Fe_2O_3$ dominated all samples at all three locations (Table 3.1). The relative abundance of $SiO_2$ for IGB samples range from 55.03 to 60.98 wt. %, with a median value of 55.03 wt. %, and for $Fe_2O_3$, range from 36.57 to 48.63 wt. %, with a median value of 42.29 wt. %. Excluding the ore sample (ZB 294), samples from the BGB range from 40.13 to 61.90 wt. % (median = 49.68 wt. %) for $SiO_2$ and 30.34 to 57.30 wt. % (median = 51.32 wt. %) for $Fe_2O_3$. Sample ZB 294 contains 3.70 wt. % $SiO_2$ and 91.71 wt. % $Fe_2O_3$. For samples from the GF, $SiO_2$ range from 36.10 to 78.23 wt. %, with a median value of 43.11 wt. %, and $Fe_2O_3$ range from 20.17 to 57.67 wt. %, with a median value of 52.21 wt. %. The third dominant major element for samples from the IGB and GF is MgO, ranging from 1.06 to 4.14 wt. % (median = 1.15 wt. %) and 0.19 to 4.93 wt. % (median = 2.17 wt. %), respectively. For samples from the BGB, $Al_2O_3$ is the third dominate major element, ranging from 0.4 to 1.51 wt. % (median = 0.71 wt. %), followed closely by MgO, which ranges from 0.07 to 0.68 wt. % (median = 0.57 wt. %).

The rest of the major elements (MnO, CaO, $Na_2O$, $K_2O$, $TiO_2$ and $P_2O_5$) all have a relative abundance of less than 0.8 wt. % for all samples from all three locales.

*3.5.1.2 Rare Earth Elements*

Samples used in this study from all three locations have REE characteristics common to BIF, having an overall light rare earth element (LREE) depletion relative to heavy rare earth elements (HREE), positive La, Gd, Eu, and Y shale-normalized anomalies and either positive, negative or absent Ce anomalies, with only a few minor exceptions (Table 3.2 and Fig. 3.4). Sample ZB 247 does not display an overall LREE depletion relative to HREE, having a $La/Yb_{SN}$ value of 1.48, where SN = shale normalized. The LREE depletion relative to HREE is very minor in sample ZB 294, which has a $La/Yb_{SN}$ value of 0.94. This sample also lacks a positive La anomaly, having a $La_{SN}/(La_{SN} \times (Pr_{SN}/Nd_{SN})^2)$ value of 0.88. Sample GF 22 also lacks a positive La anomaly, having a $La_{SN}/(La_{SN} \times (Pr_{SN}/Nd_{SN})^2)$ value of 0.77. There are no temporal changes in the whole rock REE patterns, except for with the size of the Eu anomaly ($Eu/Eu^* = Eu_{SN}/[(Sm_{SN})^2 \times (Tb)^{1/3}]$) (2006), which decreases through time. Samples from the 3.7 Ga IGB have Eu/Eu* values that range from 2.74 to 3.50, while samples from the 3.0 BGB range from 1.87 to 2.03 and those from the 1.9 Ga GF range from 1.16 to 1.41.

***3.5.2 Mineral vs. Whole Rock Geochemistry – Rare Earth Elements***

*3.5.2.1 Isua Greenstone Belt, Greenland*

For all IGB spot data, there was no evidence of zircon inclusions or siliclastic contamination, based on the low concentration of Zr in each grain and the LREE/HREE (i.e., Pr/Yb) of <1 (Lawrence and Kamber, 2006). There was also no evidence of apatite

inclusions, based on low Sr concentration in each grain; Sr is one of the most common substituents in the apatite structure (Planavsky et al., 2010; Sholkovitz et al., 1994). However, one grain (IS5_1_2) was excluded from the study based on its anomalously high sum REE value (133.8).

When examining specific geochemical relationships that are important in BIF, such as the LREE/HREE ratio ($Pr_{SN}/Yb_{SN}$), the La anomaly (La/La*), the Ce anomaly (Ce/Ce*), the Eu anomaly (Eu/Eu*) and the Y anomaly (Y/Y*), the variability in spot data and the difference between spot values and the whole rock value is evident. In addition, there was no observable trend in the data with regards to mineralogy (mt vs. hem), stratigraphy (i.e., between different bands) or band thickness. The positive Y anomalies (Y/Y* > 26) and positive La anomalies (La/La* > 1) found in whole rock BIF samples was also seen in the whole rock geochemistry of IS-05 and IS-08, as well as in all of the mineral spot data from IS-08 and the majority of the mineral spot data from IS-05 (Fig. 3.5A, B). The whole rock Y/Y* values for IS-05 (44.62) and IS-08 (58.76) indicated anomalously high Y abundances relative to terrestrial rocks (~26). However, these whole rock values do not represent the wide range in Y anomalies that can be found in each sample, with values ranging from 30.46 to 103.28 in IS-05 and from 50.78 to 108.65 in IS-08 (Fig. 3.5A, B). The whole rock La anomaly for IS-05 (1.01) plots more in the middle of the range of mineral La/La* data, which ranges from 0.59 to 5.24 (Fig. 3.5A). However, the whole rock La anomaly for IS-08 (1.23) does not represent the wider range seen in the La anomalies of the mineral spot data, which ranges from 2.12 to 13.94 (Fig. 3.5B).

Depletion of LREE relative to HREE (as represented by $Pr/Yb_{SN} < 1$) and the positive Eu anomaly ($Eu/Eu^* > 1$) in whole rock BIF samples was also seen in the whole rock geochemistries of IS-05 and IS-08, as well as in all of the mineral spot data from IS-08 and the majority of the mineral spot data from IS-05 (Fig. 3.5C, D). The whole rock $Pr_{SN}/Yb_{SN}$ value (0.35) and Eu anomaly (3.05) plots more in the middle of the range of the mineral $Pr_{SN}/Yb_{SN}$ data (0.07 – 0.36) and mineral Eu anomaly data (1.09 – 3.16) for IS-08 than it does for IS-05 (Fig. 3.5C, D). For IS-05, the whole rock $Pr_{SN}/Yb_{SN}$ values is 0.15, but the range in mineral data is 0.06 to 2.39, and the whole rock Eu anomaly is 3.72, but the mineral spot data ranges from 0.57 to 5.30 (Fig. 3.5C).

The whole rock geochemistry for samples IS-05 and IS-05 lack any Ce anomaly, either positive or negative; Both Ce/Ce* and Pr/Pr* values are around 1 (Fig. 3.5E, F). However, these whole rock "averages" hide the presence of predominately positive Ce anomalies found in the individual minerals from both samples, as well as two negative Ce anomalies found in IS-05 (Fig. 3.5E, F). Ce/Ce* and Pr/Pr* values in mineral data from IS-05 range from 0.5 to 4.73 and from 0.46 to 1.41, respectively (Fig. 3.5E). For IS-08, Ce/Ce* values for mineral data range from 1.23 to 5.69 and 0.42 to 0.88 for Pr/Pr* (Fig. 3.5F).

*3.5.2.2 Buhwa Greenstone Belt, Zimbabwe*

For all BGB spot data, there was no evidence of zircon inclusions or siliclastic contamination, based on the low concentration of Zr in each grain and the LREE/HREE (i.e., Pr/Yb) of < 1 (Rakovan and Huges, 2000). There was evidence of apatite inclusions in three of the grains, based on high sum REE and Sr concentrations in those grains; these

three grains were removed from the study. The rest of the mineral data showed no signs of apatite inclusions.

Similar to the samples from the IGB, there was substantial variability in mineral chemistry data in samples from the BGB with regards to the key BIF REE signatures. The differences between spot values and the whole rock values are also present in BGB samples and again, there was no observable trend in any of the data with regards to mineralogy (mt vs. hem), stratigraphy (i.e., between different bands) or band thickness.

The whole rock values for samples ZB-23 and ZB-117 exhibit the traditional bulk BIF signature of having positive Y (30.28 and 26.3, respectively) and La anomalies (1.08 and 0.98, respectively) (Fig. 3.6A, B). However, neither of these whole rock values plot even close to the center of the range of mineral data for both Y/Y* and La/La*, with Y/Y* values for ZB-23 ranging from 22.0 to 34.08 and 21.65 to 31.85 for ZB-117, and La/La* values for ZB-23 ranging from 1.25 to 3.28 and 0.98 to 2.54 for ZB-117 (Fig. 3.6A, B). The depletion of LREE relative to HREE and the positive Eu anomaly typically seen in whole rock BIF samples was also seen in the whole rock geochemistry of ZB-23 ($Pr/Yb_{SN}$ = 0.23; Eu/Eu* = 2.10) and ZB-117 ($Pr/Yb_{SN}$ = 0.2; Eu/Eu* = 2.12), as well as in all of the mineral data from ZB-117 and the majority of the mineral data from ZB-23 (Fig. 3.6C, D). Spot data for $Pr/Yb_{SN}$ range from 0.04 to 1.09 for ZB-23 and from 0.15 to 0.69 for ZB-117 (Fig. 3.6C, D). For Eu/Eu*, spot data for ZB-23 range from 0.89 to 2.91 and from 1.41 to 2.29 fro ZB-117 (Fig. 3.6C, D). When looking for the presence or absence of true Ce anomalies, the whole values for both ZB-23 and ZB-117 do a poor job of representing the full range in Ce chemistry preserved in the individual minerals. The whole rock chemistry of ZB-23 records a lack of any Ce anomaly, with

Ce/Ce* and Pr/Pr* both being ~1, however the mineral chemistry indicates the presence of both positive and negative Ce anomalies, with Ce/Ce* ranging from 0.45 to 1.32 and Pr/Pr* ranging from 0.64 to 1.32 (Fig. 3.6E). The whole rock geochemistry of ZB-117 records a positive Ce anomaly, with Ce/Ce* = 1.62 and Pr/Pr* = 0.76, however the mineral chemistry indicates the presence of both positive and negative Ce anomalies, with Ce/Ce* ranging from 0.07 to 0.99 and Pr/Pr* ranging from 0.94 to 1.63 (Fig. 3.6F).

*3.5.2.3 Gunflint Iron Formation, Minnesota and Ontario*

For all GF spot data, there was no evidence of zircon inclusions or siliclastic contamination, based on the low concentration of Zr in each grain and the LREE/HREE (i.e., Pr/Yb) of < 1 (Sholkovitz et al., 1994). There was evidence of apatite inclusions in two of the grains, based on high sum REE and Sr concentrations in those grains; these two grains were removed from the study. The rest of the mineral data showed no signs of apatite inclusions. Overall, the concentrations of Zr, Sr and sum REE were greater in the GF samples compared to samples from the IGB and BGB.

There is a great deal of variability in mineral chemistry data in samples from the GF with regards to the key BIF REE ratios. The differences between spot values and the whole rock values are again present and there was no observable trend in any of the data with regards to mineralogy (mt vs. hem), stratigraphy (i.e., between different bands) or band thickness.

The whole rock Y anomaly for GF-06 is positive (Y/Y* = 29.45), however, the mineral data show both positive and negative Y anomalies, with Y/Y* ranging from 20.73 to 36.47 (Fig. 3.7A). The whole rock La anomaly for GF-06 does not show the typical whole rock BIF positive anomaly, as it is slightly negative (La/La* = 0.89).

However, this is a good average of the mineral data, whose La/La* ranges from 0.49 to 1.75 (Fig. 3.7A). Similarly, the whole rock Y anomaly for GF-39 is positive (Y/Y* = 27.70), while the mineral data show both positive and negative Y anomalies, with Y/Y* ranging from 22.84 to 30.40 (Fig. 3.7B). GF-39 does show the typical whole rock BIF positive La anomaly (La/La* = 1.39); however the mineral data includes both positive and negative La anomalies, with La/La* ranging from 0.85 to 2.90, with one sample having an anomalously positive La anomaly of 10.72 (Fig. 3.7B). The whole rock geochemistry for GF-45 shows a negative Y anomaly (Y/Y* = 22.68) and a positive La anomaly (La/La* = 1.07), while the mineral data show only negative anomalies for Y, with Y/Y* ranging from 19.42 to 24. 68, and both negative and positive anomalies fro L, with La/La* ranging from 0.83 to 2.06 (Fig. 3.7B).

The whole rock geochemistry of GF-06 and GF-39, as well as the majority of the mineral data, all show enrichment in LREE over HREE and a positive Eu anomaly. For GF-06, the whole rock $Pr_{SN}/Yb_{SN}$ value was 0.57, with mineral data ranging from 0.29 to 3.23, and the whole rock $Pr_{SN}/Yb_{SN}$ value for GF-39 was 0.38, with mineral data ranging from 0.06 to 0.51 (Fig. 3.7C, D). GF-45 whole rock chemistry is enriched in HREE over LREE ($Pr_{SN}/Yb_{SN}$ = 1.37), however all of the mineral data show the typical LREE over HREE enrichment, with $Pr/Yb_{SN}$ ranging from 0.13 to 0.74 (Fig. 3.7D). The whole rock geochemistry for GF-45 shows a positive Eu anomaly (Eu/Eu* = 1.22), but half of the mineral data lacks this positive anomaly, with Eu/Eu* values ranging from 0.57 to 1.61 (Fig. 3.7D).

Whole rock geochemical data for GF-06 and GF-39 shows a lack of anomalous Ce behavior, with both Ce/Ce* and Pr/Pr* being around 1 for both samples. Mineral data

for GF-06 records the presence of both positive and negative Ce anomalies, with Ce/Ce* ranging from 0.64 to 1.54 and Pr/Pr* ranging from 0.81 to 1.24 (Fig. 3.7E). Mineral data for GF-39 is a bit anomalous, in that the majority of the samples plot in the field that indicates the lack of either a positive or negative Ce anomaly, with Ce/Ce* ranging from 1.18 to 1.93 and Pr/Pr* ranging from 0.72 to 0.91 (Fig. 3.7F). Only positive Ce anomalies are recorded in the mineral data from sample GF-45 (Fig. 3.7F).

### *3.5.3 REE Ratios Through Time*

When Y/Ho (i.e., Y/Y*) ratios from magnetite and hematite grains from samples collected from the IGB, BGB, and GF are compared, two trends are evident. First, the heterogeneity of Y/Ho decreases from ~3.8 Ga to ~1.9 Ga (Fig. 3.8A). Second, the difference between whole rock Y/Ho values and the median individual mineral Y/Ho values decreases from ~3.8 Ga to ~1.9 Ga. The whole rock Y/Ho ratio for IS-05 is 44.62 and the median of all the individual mineral spots measured in the sample is 55.83. For IS-08, the whole rock value is 58.33 while the mineral spot median is 63.08. When the Y/Ho ratios for whole rock and individual mineral spots are compared for samples from the BGB, values that are more similar. For ZB-23, the whole rock value is 30.28 and the mineral spot median 27.27. For ZB-117, the whole rock value is 26.23 and the mineral spot median is 26.69. The Y/Ho ratios for whole rock and individual mineral spots are even more similar when examined in samples from the GF. For GF-06, the whole rock value is 29.45 and the mineral spot median is 27.94. For GF-39, the bulk value is 27.70 and the mineral spot median is 26.68. And lastly, for GF-45, the whole rock value is 22.68 and the mineral spot median is 23.36.

When LREE/HREE (i.e., $Pr_{SN}/Yb_{SN}$) ratios from magnetite and hematite grains from samples collected from the IGB, BGB, and GF are compared, the degree of variability in the values between locations is small (Fig. 3.8B). Overall, the LREE/HREE for samples from the IGB vary from 0.02 to 2.16, a range of 2.14. For samples from the BGB, the range is a smaller (1.16), with LREE/HREE ratios varying between 0.04 and 1.20. The degree of variability increases for samples from the GF (3.22), ranging from 0.01 to 3.23. Unlike with Y/Ho, there is no trend between whole rock values and the median of individual mineral spots between the different sample locations.

When the Eu anomaly (i.e., Eu/Eu*) from magnetite and hematite grains from samples collected from the IGB, BGB, and GF are compared, the expected trend of decreasing Eu anomaly through time is seen (Fig. 3.8C). Focus on only whole rock values hides the variability of the Eu anomaly, which is clearly seen in mineral spot data. Both positive and negative Eu anomalies are found in samples from each time period. The other trend that is evident is that the range in the mineral Eu anomalies decreases through time (Fig. 3.8C).

### *3.5.4 Fe Isotopes*

We analyzed individual iron-oxide-rich bands of BIF from samples from each of the three study locales (IGB, BGB, GF). $\delta^{56}Fe$ values from individual bands were always within 0.132 ‰ of the bulk sample, but on average, were only 0.061 ‰ from the bulk composition (Fig. 3.9). In some instances, the band $\delta^{56}Fe$ value and the bulk rock $\delta^{56}Fe$ value were even closer. Band 3 from sample IS-02-06 had the exact sample $\delta^{56}Fe$ value as the bulk rock (+1.046 ‰). Band 1 from sample ISB-55 (+0.549 ‰) was only 0.004 % heavier than the bulk sample (+0.545 ‰).

We found a wide range of $\delta^{56}Fe$ values when comparing whole rock BIF samples through time (Fig. 3.10). BIF from the ~3.8 Ga IGB have values ranging from -0.239 ‰ to +1.046 ‰, with a mean of +0.449 ‰ and a median of +0.545 ‰. Only one sample, IS-02-08, has a negative $\delta^{56}Fe$ value. BIF from the 3.0 Ga BGB has a much small range in values than those from the IGB, ranging from +0.197 ‰ to +0.491 ‰, with a mean of +0.361 ‰ and a median of 0.341 ‰. While both formations were deposited prior to the rise of atmospheric oxygen at ~2.4 Ga, samples from the IGB are Algoma-type BIF and samples from the BGB are Superior-type BIF. After the Great Oxidation Event, the oceans were still anoxic and the last pulse of BIF until the Mesoproterozoic was deposited ~1.9 Gya. BIF from the 1.9 Ga GF records a return to a wider range of $\delta^{56}Fe$ values, ranging from -0.127 ‰ to +0.871 ‰, with a mean of +0.464 ‰ and a median of +0.559 ‰. The wide range is more similar to that of the Archean aged IGB, however samples from the GF are Superior-type BIF. If sample IS-02-08 were excluded from the IGB dataset, our data indicates an increase in the overall range in $\delta^{56}Fe$ values from the Archean to the late Paleoproterozoic.

## 3.6 Discussion

### *3.6.1 Rare Earth Element Geochemistry*

Analyses of rare earth element geochemistry indicate that the compositions of individual grains of magnetite and hematite in all samples are extremely variable. The microscale heterogeneity observed in this study is ubiquitous, regardless of sample age, location, metamorphic grade, BIF type (Algoma vs. Superior), mineralogy (magnetite vs. hematite), and analyzed elements.

The precursor material to the magnetite and hematite grains observed in BIF precipitates directly from the seawater and thus possibility records ocean chemistry. Heterogeneities in the modern ocean result from a mixing of sources (i.e., hydrothermal, continental, atmospheric) (Planavsky et al., 2010; Sholkovitz et al., 1994) and it is therefore not surprising that heterogeneity may have been passed onto individual BIF minerals. However, if we assume that all of the minerals in a single band of BIF formed around the same time and under similar ocean chemistry conditions, it seems unlikely for ocean water heterogeneity alone to explain the extreme variability observed in the mineral chemistry seen in a single band, as well as in a single sample. If the heterogeneity in mineral chemistry is not a primary signature of the depositional environment, then possible post-depositional changes need to be investigated as possible causes for the variability in mineral chemistry. Other studies have demonstrated and noted that the iron-rich bands in BIF are susceptible to diagenetic modification and alteration, particularly if $Fe^{2+}$ minerals such as magnetite dominated the primary iron mineralogy. Reduced ferrous mineral phases are highly vulnerable to post-depositional oxidation, potentially resulting in the mobility of trace elements. (Craddock and Bach, 2010; Gibbs, 1970).

The deviation from trivalent Ce behavior in Archean and early Paleoproterozoic seawater seen in this study (Fig. 3.6C) has also been observed in several other studies (Baldwin et al., 2011; Bau, 1993) and other studies have questioned the validity of these measurements (Kato et al., 2002; Kato et al., 2006b; Klein and Beukes, 1989; Ohmoto et al., 2006; Spier et al., 2007). However, we are not concluding that the deviation from trivalent Ce behavior indicates early oxidation of Earth's atmosphere, as the other studies

have concluded. Rather, we conclude that the wide range in Ce/Ce* is a result of post-depositional alteration. It has been proposed that at least some of the reported negative Ce anomalies reflect metamorphic or recent weathering-related redistribution of REEs (Planavsky et al., 2010). This might be a valid conclusion for this study if we only saw anomalous behavior and wide variability with Ce or other redox sensitive elements. However, microscale heterogeneity occurs in all REEs in all samples, so it seems unlikely that the responsible process solely reflects redox reactions.

There are several possible post-depositional processes to explain the microscale heterogeneity seen in the study samples. There may be even finer-grained scale heterogeneity at the individual grain level (i.e., mineral zonation) or there may be micro-inclusions of other REE-rich mineral phases, such as apatite or zircon (Baldwin et al., 2011). However, the fine-grained nature of many of the samples makes such analyses difficult. Other techniques, such as secondary ion mass spectrometry (SIMS) or nanoSIMS, would need to be employed for this type of investigation. Another possibility is post-depositional fluid interactions, either near the sediment-water interface before for the amorphous Fe oxyhydroxide gel forms magnetite grains, or afterwards as a result of microfractures within the sample or within individual grains. In both of these scenarios, local effects of surface sorption need to be considered. The large specific surface area of Fe oxyhydroxides results in Fe-oxide mineral phases being very effective scavengers of trace and rare earth elements, with specific interactions, such as adsorption, surface precipitation, and oxidation/scavenging between the elements and Fe oxyhydroxides, being dependent on a variety of processes (Planavsky et al., 2010).

The high degree of variability in the REE chemistry of individual mineral grains is difficult to imagine if the whole rock chemical signature is representative of all the processes involved in the formation and alteration of BIF. When whole rock values are compared to the values of all the individual mineral grains from that same sample, the whole rock values tell a very different story. The whole rock values rarely plot in the center of the spread of mineral chemistry data, suggesting that whole rock geochemistry does a poor job of being a good representation of the mineral chemistry. However, one thing to keep in mind when thinking about the whole rock value is that it represents an average of all the minerals present in the sample, including the Fe-rich mineral phases, quartz, and any accessory minerals present, not just the Fe-rich minerals that were analyzed in this study. Additionally, more grains need to be analyzed in each sample to ensure that the full spectrum of mineral geochemistry is being captured. This is particularly true for samples where the whole rock chemistry does not appear to be a good average of the mineral geochemistry. If the whole rock value is an average of the chemistries of the sample's constituent minerals, there must be minerals with geochemical concentrations +/- the whole rock value. However, if this is the case, then the heterogeneity in the mineral geochemistry is greater than it currently appears with the number of analyzed mineral grains in this study.

The focus of this paper is not to define temporal trends. However, we can use temporal trends in REE patterns as an example of where important details may be lost by only examining whole rock data. Planavsky et al. (2010) conducted a geochemical study of 18 iron formations and found key trends in REE patterns. First, they concluded that Archean and early Paleoproterozoic samples have positive $Y_{(SN)}$ anomalies, with average

Y/Ho values well above the shale composite ratio of ~27, whereas late Paleoproterozoic samples have a wider range in Y/Ho ratios. If just the bulk data for the samples in our study were examined, this same trend would be evident, with Y/Ho values from the Archean IGB being 44.62 and 58.33, Y/Ho values from the Archean BGB being 30.28 and 26.23, and Y/Ho values from the late Paleoproterozoic GF being 22.68, 27.70, and 29.4. However, when the Y/Ho ratios of individual grains from all three locales are examined, a much wider range of ratios is seen from all time periods (Fig. 3.8A).

Planavsky et al. (2010) also concluded that late Paleoproterozoic iron formation samples exhibit a greater range of LREE/HREE ratios than older Fe formations. Similar to the Y/Ho ratios, such a trend is seen if only the bulk data for samples from our study are examined, but a different pattern appears when spot data are inspected. Samples from the Archean, early Protopaleozoic, and late Protopaleozoic all have a more similar range in LREE/HREE ratios than seen in Planavsky et al. (2010).

It has been argued that high Y/Ho ratios and light REE depletion in Archean and early Paleoproterozoic Fe formations are inconsistent with the assumption that Fe oxide precipitation occurred in the transitions zone between oxic and anoxic waters, as these conditions would produce greater variability in LREE/HREE and Y/Ho ratios due to oxidative scavenging and reductive dissolution above and below a redoxcline (Fig. 3.8B; Planavsky et al., 2010). This assumption holds true for the late Paleoproterozoic, but it does not hold true if just bulk samples are analyzed from the Archean and early Paleoproterozoic. Together this suggests that there was an absence of an oxide shuttle in the Archean and early Paleoproterozoic (Planavsky et al., 2010). However, when the REE patterns from individual mineral grains are taken into consideration, the data do not

necessarily preclude the presence of an oxycline. The greater variability in LREE/HREE and Y/Ho seen in the individual grain samples from the Archean-aged IGB and BGB in this study argue that the assumption of oxide precipitation in a transition zone may also hold true for these older samples. We recognize that this is a preliminary conclusion, as only 124 grains between 7 samples were analyzed. However, the focus should be that completing a mineral-scale REE analysis of Fe formations potentially paints a very different picture from only examining bulk geochemical REE analyses.

### *3.6.2 Iron Isotopes*

#### 3.6.2.1 Whole Rock vs. Individual Bands

The $\delta^{56}$Fe values of individual bands do not typically match whole rock $\delta^{56}$Fe values exactly, as seen in this study (Fig. 3.9). This may be a result of fine-scale Fe isotope heterogeneity found in BIFs. Several *in situ* studies of magnetite grains document a wide range in $\delta^{56}$Fe values, with variations up to 2.3 ‰ (Planavsky et al., 2010). Individual magnetite crystals have also been shown to be internally heterogeneous in their Fe isotope composition, with the cores being up to 0.3 ‰ lighter than the rims (Craddock and Dauphas, 2011; Johnson et al., 2008a; Li et al., 2013). In Neoarchean and Paleoproterozoic BIFs, DIR within the porewater and soft sediments prior to lithification may have played a significant role in producing this heterogeneity, as such variations would be difficult to explain solely by direct precipitation from seawater (Steinhoefel et al., 2009). Experimental work conducted by Percak-Dennett et al. (Czaja et al., 2013; Percak-Dennett et al., 2011; Planavsky et al., 2012) found that solid Fe(II) and Fe(III) components produced during DIR may have very different iron isotope compositions, depending on the specific oxidation/reduction pathway taken by the

component. The end result of these processes would be a section of sediment that contained a larger range in iron isotope compositions for Fe-rich minerals over relatively small spatial scales and thickness (Percak-Dennett 2011). It is also not surprising that individual bands in the same sample have different Fe isotopic compositions because the Fe-rich bands are separated from each other by quartz bands, which would be an effective barrier to Fe diffusion (2011).

3.6.2.2 Iron Isotopes Through Time

An interesting finding of this study is the presence of isotopically lighter BIF samples from the IGB than have been previously reported (Fig. 3.10). Reported $\delta^{56}$Fe values for magnetite from bulk samples by Dauphas et al. (Czaja et al., 2013) and bulk or *in situ* analyses from Czaja et al. (2004) range from 0.46 ‰ to 1.17 ‰, with the majority of samples falling between 0.7 ‰ and 1.2 ‰. In this study, we have 2 samples that fall far below this range, at 0.273 ‰ and -0.239 ‰. The negative $\delta^{56}$Fe value comes from sample IS-02-08, which is an almost idealized oxide-facies BIF sample. It contains 49.28 wt.% $SiO_2$ and 48.63 wt.‰ Fe and mm-thick alternations of magnetite and quartz, with minor amounts of hematite and amphibole. The presence of light $\delta^{56}$Fe values in the IGB may indicate the presence of DIR earlier than previously suggested (2013). It may also indicate the precipitation of BIF from an aqueous reservoir with depleted $\delta^{56}$Fe values (Craddock and Dauphas, 2011; Czaja et al., 2013; Johnson et al., 2003; Johnson et al., 2008b; Li et al., 2013; Percak-Dennett et al., 2011; Tangalos et al., 2010).

When examining $\delta^{56}$Fe values from the 3.0 Ga BGB, there is a much smaller range in compositions compared to those reported for the similarly aged Pongolo

Supergroup iron formation (ca. 2.95 Ga), Witwatersrand Supergroup iron formation (ca. 2.95 Ga), and Fig Tree Group iron formation (3.24 Ga) (Anbar and Rouxel, 2007; Li et al., 2013; Rouxel et al., 2005; Tsikos et al., 2010). While all four locales are in South Africa and dominantly comprised of Superior-type BIFs (sample ZB-05 is Algoma-type BIF), the BGB is located in the Zimbabwe craton, which is separated from the other sites in the Kaapvaal Craton by the Limpopo Belt. In the BGB, the $\delta^{56}$Fe values only vary 0.29 ‰ and are all positive, which indicates partial oxidation of hydrothermal $Fe(II)_{aq}$ (Fig. 3.10; Czaja et al., 2013; Dauphas et al., 2004) rather than the involvement of DIR. It may be that DIR was not widespread at this time and might have only been found in specific basins, like those found in the Kaapvaal Craton where negative $\delta^{56}$Fe values have been recorded.

The $\delta^{56}$Fe values for BIFs from the GF analysed in this study are comparable to values previously reported (Fig. 3.10). The presence of both positive and negative $\delta^{56}$Fe values indicate a combination of a variety of processes, including partial oxidation of hydrothermally derived aqueous Fe(II) (Dauphas et al., 2004; Johnson et al., 2003; Johnson et al., 2008b; Li et al., 2013; Rouxel, 2003; Rouxel et al., 2005; Whitehouse and Fedo, 2007) and the complete oxidation of $Fe(II)_{aq}$ that was already depleted in heavy Fe isotopes relative to hydrothermal sourced fluids through the activity of microbial dissimilatory iron reduction (DIR) during diagenesis (Dauphas et al., 2004; Johnson et al., 2003; Johnson et al., 2008b; Li et al., 2013; Rouxel, 2003; Rouxel et al., 2005; Whitehouse and Fedo, 2007). While many processes are at work during BIF formation, water-column processing of hydrothermally delivered Fe is most likely the strongest

influence on the whole iron isotope composition of Archean and Paleoproterozoic BIF (Craddock and Dauphas, 2011; Johnson et al., 2003; Johnson et al., 2008b; Li et al., 2013; Percak-Dennett et al., 2011; Tangalos et al., 2010).

## 3.7 Conclusions

Microscale heterogeneity of REEs is ubiquitous within BIFs, regardless of sample age, location, metamorphic grade, BIF type (Algoma vs. Superior), mineralogy (magnetite vs. hematite) and element. The range of values observed in individual grains millimeters apart represents the full range in chemistry we can observe in BIFs through time. It is extremely unlikely that this variability is a reflection of the ocean chemistry conditions during Fe oxyhydroxides precipitation, but rather a result of inorganic, post-depositional alteration processes. An important implication of this degree of heterogeneity is the possibility that solely examining the whole rock geochemistry of BIF may not provide a complete picture of the paleoenvironmental and/or post-depositional processes being recorded in the sample. When whole rock and mineral geochemistry from the same sample are compared, the whole rock values rarely plot in the center of the spread of mineral chemistry data, suggesting that whole rock geochemistry does not provide a good representation of the full range of mineral chemistry.

Fine-scale heterogeneity is also seen in $\delta^{56}Fe$ values in study samples. This heterogeneity is also likely to do post-depositional processes, but rather than likely being controlled by inorganic processes, it is likely connected to DIR processes in the sediment porewater prior to lithification. Looking at the range in $\delta^{56}Fe$ values through time may also provide interesting insight with regards to the timing and extent of DIR. The presence of light $\delta^{56}Fe$ values in the IGB possibly indicate the presence of DIR earlier

than previously suggested and the much smaller range in $\delta^{56}Fe$ values for the 3.0 Ga BGB compared to those reported for similarly aged iron formations possibly indicate that DIR was not widespread at this time and might have only been found in specific basins.

**References**


Alibert, C., Mcculloch, M.T., 1993. Rare-Earth Element and Neodymium Isotopic Compositions of the Banded Iron-Formations and Associated Shales from Hamersley, Western-Australia. Geochimica et Cosmochimica Acta 57, 187-204.

Anbar, A.D., 2004. Iron stable isotopes: beyond biosignatures. Earth and Planetary Science Letters 217, 223-236.

Anbar, A.D., Holland, H.D., 1992. The Photochemistry of Manganese and the Origin of Banded Iron Formations. Geochimica et Cosmochimica Acta 56, 2595-2603.

Anbar, A.D., Rouxel, O., 2007. Metal stable isotopes in paleoceanography. Annual Review of Earth and Planetary Sciences 35, 717-746.

Anbar, A.D., Duan, Y., Lyons, T.W., Arnold, G.L., Kendall, B., Creaser, R.A., Kaufman, A.J., Gordon, G.W., Scott, C., Garvin, J., Buick, R., 2007. A whiff of oxygen before the great oxidation event? Science 317, 1903-1906.

Anbar, A.D., Jarzecki, A.A., Spiro, T.G., 2005. Theoretical investigation of iron isotope fractionation between $Fe(H_2O)_6^{3+}$ and $Fe(H_2O)_6^{2+}$: implications for iron stable isotope geochemistry. Geochimica et Cosmochimica Acta 69, 825-837.

Anbar, A.D., Zahnle, K.J., Arnold, G.L., Mojzsis, S.J., 2001. Extraterrestrial iridium, sediment accumulation and the habitability of the early Earth's surface. Journal of Geophysical Research 106, 3219-3236.

André, L., Cardinal, D., Alleman, L., Moorbath, S., 2006. Silicon isotopes in ~3.8 Ga West Greenland rocks as clues to the Eoarchaean supracrustal Si cycle. Earth and Planetary Science Letters 245, 162-173.

Appel, P.W.U., 1980. On the Early Archean Isua Iron-Formation, West-Greenland. Precambrian Research 11, 73-87.

Appel, P.W.U., Moorbath, S., 1999. Exploring Earth's oldest geologic record in Greenland. EOS 80, 257-264.

Appel, P.W.U., Fedo, C.M., Moorbath, S., Myers, J.S., 1998. Early Archean Isua supracrustal belt, West Greenland: pilot study of the Isua Multidisciplinary Research Project. Journal of Greenland Survey Bulletin 180, 94-99.

Arrowsmith, P., 1987. Laser Ablation of Solids for Elemental Analysis by Inductively Coupled Plasma Mass-Spectrometry. Anal Chem 59, 1437-1444.

Aston, S.R., Chester, R., 1973. The influence of suspended particles on the precipitation of iron in natural waters. Estuarine and Coastal Marine Science I, 225-231.

Baadsgaard, H., Lambert, R., Krupicka, J., 1976. Mineral isotopic age relationships in the polymetamorphic Amitsoq gneisses, Godthaab District, West Greenland. Geochimica et Cosmochimica Acta 40, 513-527.

Baldwin, G.J., Thurston, P.C., Kamber, B.S., 2011. High-precision rare earth element, nickel, and chromium chemistry of chert microbands pre-screened with in-situ analysis. Chemical Geology 285, 133-143.

Barrett, T.J., Fralick, P., Jarvis, I., 1988. Rare-earth-element geochemistry of some Archean iron formations north of Lake Superior, Ontario. Canadian Journal of Earth Sciences 25, 570-580.

Bau, M., 1991. Rare-earth element mobility during hydrothermal and metamorphic fluid-rock interaction and the significance of the oxidation state of eruopium. Chemical Geology 93, 219-230.

Bau, M., 1993. Effects of syn- and post-depositional processes on the rare-earth element distribution in Precambrian iron-formations. European Journal of Mineralogy 5, 257-267.

Bau, M., 1996. Controls on the fractionation of isovalent trace elements in magmatic and aqueous systems: Evidence from Y/Ho, Zr/Hf, and lanthanide tetrad effect. Contributions to Mineralogy and Petrology 123, 323-333.

Bau, M., 1999. Scavenging of dissolved yttrium and rare earths by precipitating iron oxyhydroxide: Experimental evidence for Ce oxidation, Y-Ho fractionation, and lanthanide tetrad effect. Geochimica et Cosmochimica Acta 63, 67-77.

Bau, M., Dulski, P., 1996. Distribution of yttrium and rare-earth elements in the Penge and Kuruman iron-formations, Transvaal Supergroup, South Africa. Precambrian Research 79, 37-55.

Bau, M., Dulski, P., 1999. Comparing yttrium and rare earths in hydrothermal fluids from the Mid-Atlantic Ridge: implications for Y and REE behaviour during near-vent mixing and for the YrHo ratio of Proterozoic seawater. Chemical Geology 155, 77-90.

Bau, M., Koschinsky, A., 2009. Oxidative scavenging of cerium on hydrous Fe oxide: Evidence from the distribution of rare earth elements and yttrium between Fe oxides and Mn oxides in hydrogenetic ferromanganese crusts. Geochemical Journal 43, 37-47.

Bau, M., Moller, P., 1993. Rare earth element systematics of the chemically precipitated component in Early Precambrain iron formations and the evolution of the terrestrial atmosphere-hydrosphere-lithosphere system. Geochimica et Cosmochimica Acta 57, 2239-2249.

Bau, M., Hohndorf, A., Dulski, P., Beukes, N.J., 1997a. Sources of Precambrian rare-earth elements and iron in Paleoproterozoic iron-formations from the Transvaal Supergroup, South Africa - evidence from neodymium isotopes. J Geol 105, 121-129.

Bau, M., Moller, P., Dulski, P., 1997b. Yttrium and lanthanides in eastern Mediterranean seawater and their factionation during redox-cycling. Marine Chemistry 56, 123-131.

Beard, B.L., Johnson, C.M., Albarede, F., 2004. Fe isotope variations in the modern and ancient earth and other planetary bodies, Reviews in Mineralogy: Geochemistry of non-traditional stable isotopes. Mineralogical Society of America, Washington, pp. 319-357.

Beard, B.L., Johnson, C.M., Cox, L., Sun, H., Nealson, K.H., Aguilar, C., 1999. Iron isotope biosignatures. Science 285, 1889-1892.

Bekker, A., Holland, H.D., Wang, P.L., Rumble, D., Stein, H.J., Hannah, J.L., Coetzee, L.L., Beukes, N.J., 2004. Dating the rise of atmospheric oxygen. Nature 427, 117-120.

Bekker, A., Slack, J.F., Planavsky, N., Krapez, B., Hofmann, A., Konhauser, K.O., Rouxel, O.J., 2010. Iron Formation: The Sedimentary Product of a Complex Interplay among Mantle, Tectonic, Oceanic, and Biospheric Processes. Econ Geol 105, 467-508.

Belevtsev, Y., Belevstev, R., Siroshtan, R., 1982. The Krivoy Rog Basin, in: Trendall, A.F., Morris, R.C. (Eds.), Iron-Formations: Facts and Problems. Elsevier, Amsterdam, pp. 211-252.

Bergquist, B.A., Boyle, E.A., 2006. Iron isotopes in the Amazon River system: Weathering and transport signatures. Earth and Planetary Science Letters 248, 54-68.

Beukes, N., 1973. Precambrian iron-formations of southern Africa. Econ Geol 68, 960-1024.

Beukes, N., 2004. Biogeochemistry - Early options in photosynthesis. Nature 431, 522-523.

Beukes, N.J., Gutzmer, J., 2008. Origin and paleoenvironmental significance of major iron formations at the Archean-Paleoproterozoic boundary. Reviews in Economic Geology Series 15, 5-47.

Beukes, N.J., Klein, C., 1990. Geochemistry and Sedimentology of a Facies Transition - from Microbanded to Granular Iron-Formation - in the Early Proterozoic Transvaal Supergroup, South-Africa. Precambrian Research 47, 99-139.

Beukes, N.J., Gutzmer, J., Nel, B.P., 2010. Ce anomalies in ~2.4 Ga iron and managnese formations as proxy for early oxygenation of oceanic environments. Goldschmidt Conference Abstracts.

Bjerrum, C.J., Canfield, D.E., 2002. Ocean productivity before about 1.9 Gyr ago limited by phosphorus adsorption onto iron oxides. Nature 417, 159-162.

Bolhar, R., Kamber, B.S., Moorbath, S., Fedo, C.M., Whitehouse, M.J., 2004. Characterisation of early Archaean chemical sediments by trace element signatures. Earth and Planetary Science Letters 222, 43-60.

Bonnichsen, B., 1975. Geology of the Biwabik iron formation, Dunka River area, Minnesota. Econ Geol 70, 319-340.

Braterman, P.S., Cairns-Smith, A.G., 1987. Photoprecipitation and the Banded Iron-Formations - Some Quantitative Aspects. Origins of Life and Evolution of the Biosphere 17, 221-228.

Brengman, L.A., 2014. From source to sink: Silicon isotope composition of bedrock, detritial quartz arenites, chert and BIF from the ~3 Ga Buhwa Greenstone Belt, Zimbabwe, Geological Society of American Annual Meeting, Vancouver, British Columbia.

Brengman, L.A., Fedo, C.M., 2012. Origin of BIF-like jasperlite in the 2.72 Ga Hunter Mine Group. Abitibi Greenstone Belt, Quebec by metasomatic replacement of felsic volcanic rocks, Geologic Society of America Annual Meeting, Charlotte, North Carolina.

Brocks, J.J., Logan, G.A., Buick, R., Summons, R.E., 1999. Archean Molecular Fossils and the Early Rise of Eukaryotes. Science 285, 1033-1036.

Broderick, T.M., 1920. Economic geology and stratigraphy of the Gunflint Iron District, Minnesota. Econ Geol 15, 422-452.

Brookins, D.G., 1989. Aqueous geochemistry of rare earth elements, in: Lipin, B.R., McKay, G.A. (Eds.), Reviews in Mineralogy: Geochemistry and Mineralogy of Rare Earth Elements. Mineralogical Society of America, Washington, D.C., pp. 201-225.

Brown, D.A., 2006. Microbial mediation of iron mobilization and deposition in iron formations since the early Precambrian, in: Kesler, S., Ohmoto, H. (Eds.), Evolution of Early Earth's Atmosphere, Hydrosphere, and Biosphere –

Constraints From Ore Deposits. The Geological Soceity of America Memoir, pp. 239-256.

Bryne, R.H., Kim, K.H., 1990. Rare earth element scavenging in seawater. Geochimica et Cosmochimica Acta 54, 2645-2656.

Bryne, R.H., Sholkovitz, E.R., 1996. Marine chemistry and geochemistry of the lanthanides, in: Gschneider, K.A., Eyring, L. (Eds.), Handbook on the Physics and Chemistry of the Rare Earths. Elsevier, Amsterdam, pp. 497-593.

Buick, R., 1992. The Antiquity of Oxygenic Photosynthesis - Evidence from Stromatolites in Sulfate-Deficient Archean Lakes. Science 255, 74-77.

Buick, R., 2008. When did oxygenic photosynthesis evolve? Philos Trans R Soc Lond B Biol Sci 363, 2731-2743.

Bullen, T.D., White, A.F., Childs, C.W., Vivit, D.V., Schulz, M.S., 2001. Demonstration of significant abiotic iron isotope fractionation in nature. Geology 29, 699-702.

Burns, R.G., 1976. Uptake of Cobalt into Ferromanganese Nodules, Soils, and Synthetic Manganese(Iv) Oxides. Geochimica et Cosmochimica Acta 40, 95-102.

Cairns-Smith, A.G., 1987. Precambrian solution photochemistry, inverse segregation, and banded iron formations. Nature 76.

Canfield, D.E., 1998. A new model for Proterozoic ocean chemistry. Nature 396, 450-453.

Canfield, D.E., 2005. The early history of atmospheric oxygen: Homage to Robert A. Garrels. Annual Review of Earth and Planetary Sciences 33, 1-36.

Canfield, D.E., Habicht, K.S., Thamdrup, B., 2000. The Archean Sulfur Cycle and the Early History of Atmospheric Oxygen. Science 288, 658-661.

Cantrell, K.J., Byrne, R.H., 1987. Rare-Earth Element Complexation by Carbonate and Oxalate Ions. Geochimica et Cosmochimica Acta 51, 597-605.

Chandler, F.W., 1980. Proterozoic redbed sequences of Canada. Canadian Geological Survey Bulletin 311.

Chang, S.B.R., Kirschvink, J.L., 1989. Magnetofossils, the Magnetization of Sediments, and the Evolution of Magnetite Biomineralization. Annual Review of Earth and Planetary Sciences 17, 169-195.

Chigira, M., Watanabe, M., 1994. Silica precipitation behavior in a flow field with negative temperature gradients. Journal of Geophysical Research 99, 15539-15548.

Cloud, P.E., 1965. Significance of Gunflint (Precambrian) microflora-photosynthetic oxygen may have had important local effects before becoming a major atmospheric gas. Science 148, 1135-1143.

Cloud, P.E., 1973. Paleoecological significance of banded iron-formation. Econ Geol 68, 1135-1143.

Condie, K.C., 1981. Archean Greenstone Belts. Elsevier, Amsterdam.

Condie, K.C., 1993. Chemical-Composition and Evolution of the Upper Continental-Crust - Contrasting Results from Surface Samples and Shales. Chemical Geology 104, 1-37.

Craddock, P.R., Bach, W., 2010. Trace element and isotopic compositions of anhydrite sampled in the Manus Basin, Papua New Guinea. Geochimica et Cosmochimica Acta 74, 5514-5536.

Craddock, P.R., Dauphas, N., 2011. Iron and carbon isotope evidence for microbial iron respiration throughout the Archean. Earth and Planetary Science Letters 303, 121-132.

Croal, L.R., Jiao, Y., Kappler, A., Newman, D.K., 2009. Phototrophic Fe(II) oxidation in an atmosphere of H2: implications for Archean banded iron formations. Geobiology 7, 21-24.

Croal, L.R., Johnson, C.M., Beard, B.L., Newman, D.K., 2004. Iron isotope fractionation by Fe(II)-oxidizing photoautotrophic bacteria 1. Geochimica et Cosmochimica Acta 68, 1227-1242.

Crosby, H.A., Johnson, C.M., Roden, E.E., Beard, B.L., 2005. Coupled Fe(II)-Fe(III) electron and atom exchange as a mechanism for Fe isotope fractionation during dissimilatory iron oxide reduction. Environ Sci Technol 39, 6698-6704.

Crosby, H.A., Roden, E.E., Johnson, C.M., Beard, B.L., 2007. The mechanisms of iron isotope fractionation produced during dissimilatory Fe(III) reduction by Shewanella putrefaciens and Geobacter sulfurreducens. Geobiology 5, 169-189.

Czaja, A.D., Johnson, C.M., Beard, B.L., Roden, E.E., Weiqiang, L., Moorbath, S., 2013. Biological Fe oxidation controlled deposition of banded iron formation in the ca. 3770 Ma Isua Supracrustal Belt (West Greenland). Earth and Planetary Science Letters 363, 192-203.

Dauphas, N., Rouxel, O., 2006. Mass spectrometry and natural variations of iron isotopes. Mass Spectrom Rev 25, 515-550.

Dauphas, N., Cates, N., Mojzsis, S., Busigny, V., 2007a. Identification of chemical sedimentary protoliths using iron isotopes in the >3750 Ma Nuvvuagittuq supracrustal belt, Canada. Earth and Planetary Science Letters 254, 358-376.

Dauphas, N., van Zuilen, M., Wadhwa, M., Davis, A.M., Marty, B., Janney, P.E., 2004. Clues from Fe isotope variations on the origin of early Archean BIFs from Greenland. Science 306, 2077-2080.

Dauphas, N., van Zuilen, M., Busigny, V., Lepland, A., Wadhwa, M., Janney, P., 2007c. Iron isotope, major and trace element characterization of early Archean supracrustal rocks from SW Greenland: Protolith identification and metamorphic overprint. Geochimica et Cosmochimica Acta 71, 4745-4770.

Davranche, M., Pourret, O., Grauau, G., Dia, A., 2004. Impact of humate complexation on the adsoprtion of REE onto Fe oxyhydroxide. Journal of Colloid and Interface Science 277, 271-279.

De Carlo, E.H., Green, W.J., 2002. Rare earth elements in the water column of Lake Vanda, McMurdo Dry Valleys, Antarctica. Geochimica et Cosmochimica Acta 66, 1323-1333.

Derry, L.A., Jacobsen, S.B., 1990. The Chemical Evolution of Precambrian Seawater - Evidence from Rees in Banded Iron Formations. Geochimica et Cosmochimica Acta 54, 2965-2977.

Des Marais, D.J., Allamandola, L.J., Benner, S.A., Boss, A.P., Deamer, D., Falkowski, P.G., Farmer, J.D., Hedges, S.B., Jakosky, B.M., Knoll, A.H., Liskowsky, D.R., Meadows, V.S., Meyer, M.A., Pilcher, C.B., Nealson, K.H., Spormann, A.M., Trent, J.D., Turner, W.W., Woolf, N.J., Yorke, H.W., 2003. The NASA Astrobiology Roadmap. Astrobiology 3, 219-235.

Dimroth, E., Kimberley, M.M., 1976. Precambrian atmosphereic oxygen: Evidence in the sedimentary distribution of carbon, sulfur, uranium, and iron. Canadian Journal of Earth Sciences 13, 1161-1185.

Duff, M.C., Coughlin, J.U., Hunter, D.B., 2002. Uranium co-precipitation with iron oxide minerals. Geochimica et Cosmochimica Acta 66, 3533-3547.

Dunk, R.M., Mills, R.A., 2006. The impact of oxic alteration on plume-derived transition metals in ridge flank sediments from the East Pacific Rise. Marine Geology 229, 133-157.

Dymek, R.F., Klein, C., 1988. Chemistry, Petrology and Origin of Banded Iron-Formation Lithologies from the 3800-Ma Isua Supracrustal Belt, West Greenland. Precambrian Research 39, 247-302.

Eggins, S.M., Woodhead, J.D., Kinsley, L.P.J., Mortimer, G.E., Sylvester, P., McCulloch, M.T., Hergt, J.M., Handler, M.R., 1997. A simple method for the precise determination of >=40 trace elements in geological samples by ICPMS using enriched isotope internal standardisation. Chemical Geology 134, 311-326.

Ehrenreich, A., Widdel, F., 1994. Anaerobic Oxidation of Ferrous Iron by Purple Bacteria, a New-Type of Phototrophic Metabolism. Appl Environ Microb 60, 4517-4526.

Emerson, D., Moyer, C.L., 2002. Neutrophilic Fe-Oxidizing bacteria are abundant at the Loihi Seamount hydrothermal vents and play a major role in Fe oxide deposition. Appl Environ Microb 68, 3085-3093.

Emerson, S.R., Huested, S.S., 1991. Ocean Anoxia and the Concentrations of Molybdenum and Vanadium in Seawater. Marine Chemistry 34, 177-196.

England, G.L., Rasmussen, B., Krapez, B., Groves, D.I., 2002. Paleoenvironmental significance of rounded pyrite in siliciclastic sequences of the Late Archean Witwaterstand Basin: Oxygen-deficient atmosphere or hydrothermal alteration? Sedimentology 49, 1133-1156.

Farquhar, J., Bao, H.M., Thiemens, M., 2000. Atmospheric influence of Earth's earliest sulfur cycle. Science 289, 756-758.

Farquhar, J., Wing, B.A., 2003. Multiple sulfur isotopes and the evolution of the atmosphere. Earth and Planetary Science Letters 213, 1-13.

Faure, G., 1986. Principles of Isotope Geolog. John Wiley & Sons, Inc., New Jersey.

Fedo, C.M., 2000. Setting and origin for problematic rocks from the > 3.7 Ga Isua Greenstone Belt, southern west Greenland: Earth's oldest coarse elastic sediments. Precambrian Research 101, 69-78.

Fedo, C.M., Eriksson, K.A., 1995. Geologic setting and ideas concerning the origin of the iron-ore deposits at Buhwa, Zimbabwe, in: Blenkinsop, T.G., Tromp, P.L. (Eds.), Sub-Saharan Economic Geology. A.A. Balkema Publishers, Vermont, pp. 43-53.

Fedo, C.M., Eriksson, K.A., 1996. Stratigraphic framework of the similar to 3.0 Ga Buhwa greenstone belt: A unique stable-shelf succession in the Zimbabwe Archean Craton. Precambrian Research 77, 161-178.

Fedo, C.M., Whitehouse, M.J., 2002. Metasomatic origin of quartz-pyroxene rock, Akilia, Greenland, and implications for Earth's earliest life. Science 296, 1448-1452.

Fedo, C.M., Eriksson, K.A., Blenkinsop, T.G., 1995. Geologic history of the Archean Buhwa Greenstone Belt and surrounding granite-gneiss terrane, Zimbabwe, with implications for the evolution of the Limpopo Belt. Canadian Journal of Earth Sciences 32, 1977-1990.

Fedo, C.M., Eriksson, K.A., Krogstad, E.J., 1996. Geochemistry of shales from the Archean (similar to 3.0 Ga) Buhwa greenstone belt, Zimbabwe: Implications for provenance and source-area weathering. Geochimica et Cosmochimica Acta 60, 1751-1763.

Fedo, C., Hage, M., Schoenberg, R., Whitehouse, M., 2010. Can Fe isotopes be used to fingerprint Precambrian BIF?, Goldschmidt Knoxville, TN.

Fedo, C.M., Myers, J.S., Appel, P.W.U., 2001. Depositional setting and paleogeographic implications of earth's oldest supracrustal rocks, the > 3.7 Ga Isua Greenstone belt, West Greenland. Sediment Geol 141, 61-77.

Fedo, C.M., Whitehouse, M.J., Kamber, B.S., 2006. Geological constraints on detecting the earliest life on Earth: a perspective from the Early Archaean (older than 3.7 Gyr) of southwest Greenland. Philos Trans R Soc Lond B Biol Sci 361, 851-867.

Fischer, W.W., Knoll, A.H., 2009. An iron shuttle for deepwater silica in Late Archean and early Paleoproterozoic iron formations. GSA Bulletin 121, 222-235.

Floran, R.J., Papike, J.J., 1978. Mineralogy and Petrology of Gunflint Iron Formation, Minnesota-Ontario - Correlation of Compositional and Assemblage Variations at Low to Moderate Grade. Journal of Petrology 19, 215-288.

Fralick, P., Davis, D.W., Kissin, S.A., 2002. The age of the Gunflint Formation, Ontario, Canada: single zircon U Pb age determinations from reworked volcanic ash. Canadian Journal of Earth Sciences 39, 1085-1091.

Frei, R., Dahl, P.S., Duke, E.F., Frei, K.M., Hansen, T.R., Frandsson, M.M., Jensen, L.A., 2008. Trace element and isotopic characterization of Neoarchean and Paleoproterozoic iron formations in the Black Hills (South Dakota, USA): Assessment of chemical change during 2.9–1.9Ga deposition bracketing the 2.4–2.2Ga first rise of atmospheric oxygen. Precambrian Research 162, 441-474.

Frei, R., Gaucher, C., Poulton, S.W., Canfield, D.E., 2009. Fluctuations in Precambrian atmospheric oxygenation recorded by chromium isotopes. Nature 461, 250-253.

French, B.M., 1971. Stability relations of siderite ($FeCO_3$) in the system Fe-C-O. American Journal of Science 271, 37-78.

Friend, C.R.L., Nutman, A.P., 2005. Complex 3670-3500 Ma orogenic episodes superimposed on juvenile crust accreted between 3850 and 3690 Ma, Itsaq Gneiss Complex, Southern West Greenland. J Geol 113, 375-397.

Friend, C.R.L., Nutman, A.P., Bennett, V.C., Norman, M.D., 2008. Seawater-like trace element signatures (REE + Y) of Eoarchaean chemical sedimentary rocks from southern West Greenland, and their corruption during high-grade metamorphism. Contributions to Mineralogy and Petrology 155, 229-246.

Frost, B.R., 1979. Metamorphism of iron-formation: paragenesis in the systems Fe-Si-C-O-H. Econ Geol 74, 775-785.

Frost, C.D., Blanckenburg, F., Schoenberg, R., Frost, B.R., Swapp, S.M., 2006. Preservation of Fe isotope heterogeneities during diagenesis and metamorphism of banded iron formation. Contributions to Mineralogy and Petrology 153, 211-235.

Fryer, B.J., 1977. Rare earth evidence in iron-formations for changing Precambrian oxidation states. Geochimica et Cosmochimica Acta 41, 361-367.

Fryer, B.J., Jackson, S.E., Longerich, H.P., 1995. Design, Operation and Role of the Laser-Ablation Microprobe Coupled with an Inductively-Coupled Plasma - Mass-Spectrometer (Lam-Icp-Ms) in the Earth-Sciences. Can Mineral 33, 303-312.

Fyon, J., Schwarts, H., Crocket, J., 1984. Carbonization and gold mineralization in the Timmins area, Abitibi greenstone belt: Genetic links with Archean mantle CO2-degassing and lower crust granulization. Geological Association of Canada Program with Abstract 9, 65.

Garrels, R.M., Perry, E.A.J., 1974. Cycling of carbon, sulfur, and oxygen through geologic time, in: Goldberg, E.A. (Ed.), The Sea. Wiley, New York, pp. 303-336.

German, C.R., Elderfield, H., 1990. Application of the Ce anomaly as a paleoredox indicator: The ground rules. Paleoceanography 5, 823-833.

German, C.R., Holliday, B.P., Elderfield, H., 1991. Redox cycling of rare earth elemtns in the suboxic zone of the Black Sea. Geochimica et Cosmochimica Acta 55, 3553-3558.

German, C.R., Von Damm, K.L., 2006. Hydrothermal Processes, in: Elderfield, H. (Ed.), The oceans and marine geochemistry. Elsevier, Oxford, UK, pp. 181-222.

Gibbs, R.J., 1970. Mechanisms Controlling World Water Chemistry. Science 170, 1088-1090.

Goodwin, A.M., 1956. Facies relations in the Gunflint Iron Formation. Econ Geol 51, 565-595.

Goodwin, A.M., 1973. Archean volcanogenic iron-formation of the Canadian shield. Science Terra 9, 23-34.

Gray, A.L., 1985. Solid Sample Introduction by Laser Ablation for Inductively Coupled Plasma Source-Mass Spectrometry. Analyst 110, 551-556.

Griffin, W.L., McGregor, V.R., Nutman, A.P., Taylor, P.N., Bridgwater, D., 1980. Early Archean granulite-facies metamorphism south of Ameralik, West Greenland. Earth and Planetary Science Letters 50, 59-74.

Gross, G.A., 1965. Geology of iron deposits in Canada I. General geology and evaluation of iron deposits. Geological Survey of Canada Economic Geology Report 22.

Gross, G.A., 1980. A classification of iron formations based on depositional environments. Can Mineral 18, 215-222.

Gross, G.A., 1983. Tectonic systems and the deposition of iron formation Precambrian Research 20, 171-187.

Groves, D.I., Batt, W., 1984. Spatial and temporal variations of Archean metallogenic association in terms of evolution of granitoid-greenstone terraines with particular emphasis on Western Australia, in: Kroner, A., Hanson, G., Goodwin, A.M. (Eds.), Archean Geochemistry. Springer-Verlag, Berlin, pp. 73-98.

Halliday, A.N., Lee, D.C., Christensen, J.N., Rehkamper, M., Yi, W., Luo, X.Z., Hall, C.M., Ballentine, C.J., Pettke, T., Stirling, C., 1998. Applications of multiple collector-ICPMS to cosmochemistry, geochemistry, and paleoceanography. Geochimica et Cosmochimica Acta 62, 919-940.

Hamade, T., Konhauser, K.O., Raiswell, R., Goldsmith, S., Morris, R.C., 2003. Using Ge/Si ratios to decouple iron and silica fluxes in Precambrian banded iron formations. Geology 31, 35-38.

Harder, E.C., 1919. Iron depositing bacteria and their geological relations. The Journal of Geology 30, 506-509.

Heck, P.R., Huberty, J.M., Kita, N.T., Ushikubo, T., Kozdon, R., Valley, J.W., 2011. SIMS analysis of silicon and oxygen isotope ratios for quartz from Archean and Paleoproterozoic banded iron formations. Geochimica et Cosmochimica Acta 75, 5879-5891.

Heimann, A., Johnson, C.M., Beard, B.L., Valley, J.W., Roden, E.E., Spicuzza, M.J., Beukes, N.J., 2010. Fe, C, and O isotope compositions of banded iron formation

carbonates demonstrate a major role for dissimilatory iron reduction in ~2.5Ga marine environments. Earth and Planetary Science Letters 294, 8-18.

Heising, S., Schink, B., 1998. Phototrophic oxidation of ferrous iron by a Rhodomicrobium vannielii strain. Microbiol-Uk 144, 2263-2269.

Helz, G.E., Bura-Nakic, E., Mikac, N., Ciglenecki, I., 2011. New model for molybdenum behavior in euxinic waters. Chemical Geology 284, 323-332.

Holland, H.D., 1973. Ocean - possible srouce of iron in iron-formations. Econ Geol 68, 1169-1172.

Holland, H.D., 1984. The chemical evoultion of the atmosphere and oceans. Princeton University Press, New York.

Holm, N.G., 1989. The 13C/12C ratios of siderite and organic matter of a modern metalliferous hydrothermal sediment and their implications for banded iron formations. Chemical Geology 77, 41-45.

Holm, N.G., Charlou, J.L., 2001. Initial indications of abiotic formation of hydrocarbons in the Rainbow ultramafic hydrothermal system, Mid-Atlantic Ridge. Earth and Planetary Science Letters 191, 1-8.

Homoky, W.B., Severmann, S., Mills, R.A., Statham, P.J., Fones, G.R., 2009. Pore-fluid Fe isotopes reflect the extent of benthic Fe redox recycling: Evidence from continental shelf and deep-sea sediments. Geology 37, 751-754.

Hostetler, P.B., Garrels, R.M., 1962. Transportation and precipitation of uranium and vanadium at low temperatures, with special reference to sandstone-type uranium deposits. Econ Geol 57, 137-167.

Hyslop, E.V., Valley, J.W., Johnson, C.M., Beard, B.L., 2007. The effects of metamorphism on O and Fe isotope compositions in the Biwabik Iron Formation, northern Minnesota. Contributions to Mineralogy and Petrology 155, 313-328.

Isley, A.E., 1995. Hydrothermal Plumes and the Delivery of Iron to Banded Iron-Formation. J Geol 103, 169-185.

Isley, A.E., Abbott, D.H., 1999. Plume-related mafic volcanism and the deposition of banded iron formation. Journal of Geophysical Research 104, 15461-15477.

Jackson, S.E., Longerich, H.P., Dunning, G.R., Fryer, B.J., 1992. The application of laser-ablation microprobe-inductively coupled plasma-mass spectrometry (LAM-ICP-MS) to in situ trace-element determinations in minerals. Can Mineral 30, 1049-1064.

Jacobsen, S.B., Pimental-Klose, M., 1988. A Nd isotope study of the Hamersley and Michipicoten banded iron formations: The source of REE and Fe in Archean oceans. Earth and Planetary Science Letters 87, 29-44.

James, H., 1954. Sedimentary facies of iron formations. Econ Geol 49, 235-293.

James, H., Trendall, A.F., 1982. Banded iron formation: Distribution in time and paleoenvironmental significance, in: Holland, H.D., Schidlowski, M. (Eds.), Mineral Deposits and the Evolution of the Biosphere. Spring-Verlag, NY, pp. 199-218.

Jenner, F., O'Neill, H.S.C., 2012. Major and trace analyses of basaltic glasses by laser-ablation ICP-MS. Geochemistry, Geophysics, Geosystems 13, Q03003.

Jirsa, M.A., Weiblen, P.W., 2007. Geology along the Gunflint Trail. 53rd Annual Institute on Lake Superior Geology Field Trip Guide 6.

Johnson, C.M., Beard, B.L., 2006. Fe isotopes: An emerging technique for understanding modern and ancient biogeochemical cycles. GSA Today 16, 4.

Johnson, C.M., Beard, B.L., Albarede, F., 2004. Overview and general concepts, Rev Mineral Geochem. The Mineralogical Society of America, Washington, DC, pp. 1-22.

Johnson, C.M., Beard, B.L., Beukes, N.J., Klein, C., O'Leary, J.M., 2003. Ancient geochemical cycling in the Earth as inferred from Fe isotope studies of banded iron formations from the Transvaal Craton. Contributions to Mineralogy and Petrology 144, 523-547.

Johnson, C.M., Beard, B.L., Klein, C., Beukes, N.J., Roden, E.E., 2008a. Iron isotopes contrain biologic and abiologic processes in banded iron formation genesis. Geochimica et Cosmochimica Acta 72, 151-169.

Johnson, C.M., Beard, B.L., Roden, E.E., 2008b. The Iron Isotope Fingerprints of Redox and Biogeochemical Cycling in Modern and Ancient Earth. Annual Review of Earth and Planetary Sciences 36, 457-493.

Johnson, T.M., Bullen, T.D., 2004. Mass-dependent fractionation of selenium and chromium isotopes in low-temperature environments, in: Johnson, C.M., Beard, B.L., Albarede, F. (Eds.), Rev Mineral Geochem. Mineralogical Society of America, Washington, pp. 289-317.

Kamber, B.S., 2009. Geochemical fingerprinting: 40 years of analytical development and real world applications. Applied Geochemistry 24, 1074-1086.

Kamber, B.S., 2010. Archean mafic–ultramafic volcanic landmasses and their effect on ocean–atmosphere chemistry. Chemical Geology 274, 19-28.

Kamber, B.S., Gladu, A.H., 2009. Comparison of Pb Purification by Anion-Exchange Resin Methods and Assessment of Long-Term Reproducibility of Th/U/Pb Ratio Measurements by Quadrupole ICP-MS. Geostand Geoanal Res 33, 169-181.

Kamber, B.S., Moorbath, S., 1998. Initial Pb of the Amitsoq gneiss revisited: implications for the timing of early Archean crustal evolution in West Greenland. Chemical Geology 150, 19-41.

Kamber, B.S., Webb, G.E., 2007. Transition metal abundances in microbial carbonate: a pilot study based on in situ La-ICP-MS analysis. Geobiology 5, 375-389.

Kamber, B.S., Whitehouse, M.J., 2007. Micro-scale sulphur isotope evidence for sulphur cycling in the late Archean shallow ocean. Geobiology 5, 5-17.

Kappler, A., Newman, D.K., 2004. Formation of Fe(III)-minerals by Fe(II)-oxidizing photoautotrophic bacteria 1. Geochimica et Cosmochimica Acta 68, 1217-1226.

Kappler, A., Pasquero, C., Konhauser, K.O., Newman, D.K., 2005. Deposition of banded iron formations by anoxygenic phototrophic Fe(II)-oxidizing bacteria. Geology 33, 865.

Kato, Y., Kano, T., Kunugiza, K., 2002. Negative Ce anomaly in the Indian banded iron formations: Evidence for the emergence of oxygenated deep-sea at 2.9 similar to 2.7 Ga. Resour Geol 52, 101-110.

Kato, Y., Nakamura, K., 2003. Origin and global tectonic significance of Early Archean cherts from the Marble Bar greenstone belt, Pilbara Craton, Western Australia. Precambrian Research 125, 191-243.

Kato, Y., Ohta, I., Tsunematsu, T., Watanabe, Y., Isozaki, Y., Maruyama, S., Imai, N., 1998. Rare earth element variations in mid-Archean banded iron formations: Implications for the chemistry of ocean and continent and plate tectonics. Geochimica et Cosmochimica Acta 62, 3475-3497.

Kato, Y., Yamaguchi, K., Ohmoto, H., 2006a. Rare earth elements in Precambrian banded iron formations: Secular changes of Ce and Eu anomalies and evolution of atmospheric oxygen, in: Kesler, S., Ohmoto, H. (Eds.), Evolution of Early Earth's Atmosphere, Hydrosphere, and Biosphere - Constraints from Ore Deposits. Geological Society of America, Boulder, pp. 269-289.

Kimberley, M.M., 1978. Paleoenvironmental classification of iron formations. Econ Geol 73, 215-229.

Klein, C., 2005. Some Precambrian banded iron-formations (BIFs) from around the world: Their age, geologic setting, mineralogy, metamorphism, geochemistry, and origins. American Mineralogist 90, 1473-1499.

Klein, C., Beukes, N., 1992. Proterozoic iron-formations, in: Conder, K. (Ed.), Proterozoic Crustal Evolution. Elsevier, Amsterdam, pp. 383-418.

Klein, C., Beukes, N.J., 1989. Geochemistry and sedimentology of a facies transition from limestone to iron-formation deposition in the Early Proterozoic Transvaal Supergroup, South-Africa. Econ Geol 84.

Knoll, A.H., Javaux, E.J., Hewitt, D., Cohen, P., 2006. Eukaryotic organisms in Proterozoic oceans. Philos T R Soc B 361, 1023-1038.

Koehler, I., Konhauser, K., Kappler, A., 2010. Role of Microorganisms in Banded Iron Formations. 309-324.

Komiya, T., Maruyama, S., Masuda, T., Nohda, S., Hayashi, M., Okamoto, K., 1999. Plate Tectonics at 3.8-3.7 Ga: Field Evidence from the Isua Accretionary Complex, Southern West Greenland. The Journal of Geology 107, 515-554.

Konhauser, K., 2007. Introduction to Geomicrobiology. Blackwell Publishing, Massachusetts.

Konhauser, K., Amskold, L., Lalonde, S., Posth, N., Kappler, A., Anbar, A., 2007a. Decoupling photochemical Fe(II) oxidation from shallow-water BIF deposition. Earth and Planetary Science Letters 258, 87-100.

Konhauser, K.O., Hamade, T., Raiswell, R., Morris, R.C., Ferris, F.G., Southam, G., Canfield, D.E., 2002. Could bacteria have formed the Precambrian banded iron formations? Geology 30, 1079-1082.

Konhauser, K.O., Lalonde, S.V., Amskold, L., Holland, H.D., 2007c. Was there really an Archean phosphate crisis? Science 315, 1234-1234.

Konhauser, K.O., Newman, D.K., Kappler, A., 2005. The potential significance of microbial Fe(III) reduction during deposition of Precambrian banded iron formations. Geobiology 3, 167-177.

Konhauser, K.O., Pecoits, E., Lalonde, S.V., Papineau, D., Nisbet, E.G., Barley, M.E., Arndt, N.T., Zahnle, K., Kamber, B.S., 2009. Oceanic nickel depletion and a methanogen famine before the Great Oxidation Event. Nature 458, 750-753.

Kramers, J.D., Tolstikhin, I.N., 1997. Two terrestrial lead isotope paradoxes, forward transport modelling, core formation and the history of the continental crust. Chemical Geology 139, 75-110.

Kump, L., Seyfried, W., 2005. Hydrothermal Fe fluxes during the Precambrian: Effect of low oceanic sulfate concentrations and low hydrostatic pressure on the composition of black smokers. Earth and Planetary Science Letters 235, 654-662.

Kump, L.R., Barley, M.E., 2007. Increased subaerial volcanism and the rise of atmospheric oxygen 2.5 billion years ago. Nature 448, 1033-1036.

Lawrence, M.G., Kamber, B.S., 2006. The behaviour of the rare earth elements during estuarine mixing—revisited. Marine Chemistry 100, 147-161.

Lawrence, M., Greig, A., Collerson, K., Kamber, B., 2006a. Direct quantification of rare earth element concentrations in natural waters by ICP-MS. Applied Geochemistry 21, 839-848.

Lawrence, M., Greig, A., Collerson, K., Kamber, B., 2006b. Rare Earth Element and Yttrium Variability in South East Queensland Waterways. Aquatic Geochemistry 12, 39-72.

Lepland, A., Whitehouse, M.J., 2010. Metamorphic alteration, mineral paragenesis and geochemical re-equilibration of early Archean quartz–amphibole–pyroxene gneiss from Akilia, Southwest Greenland. International Journal of Earth Sciences.

Lepland, A., Whitehouse, M.J., 2011. Metamorphic alteration, mineral paragenesis and geochemical re-equilibration of early Archean quartz-amphibole-pyroxene gneiss from Akilia, Southwest Greenland. International Journal of Earth Sciences 100, 1-22.

Lepland, A., Arrhenius, G., Cornell, D., 2002. Apatite in early Archean Isua supracrustal rocks, southern West Greenland: its origin, association with graphite and potential biomarker. Precambrian Research 119, 221-241.

Lepland, A., van Zuilen, M.A., Arrhenius, G., Whitehouse, M.J., Fedo, C.M., 2005. Questioning the evidence for Earth's earliest life—Akilia revisited. Geology 33, 77.

Lepland, A., van Zuilen, M.A., Philippot, P., 2011. Fluid-deposited graphite and its geobiological implications in early Archean gneiss from Akilia, Greenland. Geobiology 9.

Li, W., Huberty, J.M., Beard, B.L., Kita, N.T., Valley, J.W., Johnson, C.M., 2013. Contrasting behavior of oxygen and iron isotopes in banded iron formations revealed by *in situ* isotopic analysis. Earth and Planetary Science Letters 384, 132-143.

Liu, Y.G., Miah, M.R.U., Schmitt, R.A., 1988. Cerium: A chemical tracer for paleo-oceanic redox conditions. Geochimica et Cosmochimica Acta 52, 1361-1371.

Lovley, D.R., 2004. Potential role of dissimilatory iron reduction in the early evolution of microbial respiration, in: Seckback, J. (Ed.), Origins, Evolution and Biodiversity of Microbial Life. Kluwer, Netherlands, pp. 301-313.

Lovley, D.R., Stolz, J., Nord, G., 1987. Anaerobic production of magnetite by a dissimilatory iron-reducing microorganism. Nature 330, 252-254.

MacGregor, A.M., 1927. The problem of the Precambrian atmosphere. South African Journal of Science 23, 155-172.

Manning, C.E., Mojzsis, S.J., Harrison, T.M., 2006. Geology, Age and Origin of Supracrustal Rocks at Akilia, West Greenland. American Journal of Science 306, 303-366.

McGregor, V.R., Mason, B.J., 1977. Petrogenesis and geochemistry of metabasic and metasedimentary enclaves in the Amitsoq gneisses, West Greenland. American Mineralogist 62, 887-904.

McKeegan, K.D., Kudryavtsev, A.B., Schopf, J.W., 2007. Raman and ion microscopic imagery of graphitic inclusions in apatite from older than 3830 Ma Akilia supracrustal rocks, west Greenland. Geology 35, 591.

McLennan, S.M., Taylor, R., 1991. Sedimentary rocks and crustal evolution: Tectonic setting and secular trends. J Geol 99, 1-21.

McManus, J., Berelson, W., Severmann, S., Poulson, R., Hammond, D., Klinkhammer, G., Holm, C., 2006. Molybdenum and uranium geochemistry in continental margin sediments: Paleoproxy potential. Geochimica et Cosmochimica Acta 70, 4643-4662.

Miller, J.D., Morey, G.B., Weiblen, P.W., 1987. Seagull Lake - Gunflint Lake area: A classical Precambrian stratigraphic sequence in northeastern Minnesota. America Continental Field Guide - North-Central Section, 47-51.

Moenke-Blankenburg, L., 1993. Laser-ICP-spectrometry. Spectrochimica Acta Review 15, 1-37.

Mojzsis, S.J., Harrison, T.M., 1999. Geochronological studies of the oldest known marine sediments. 9th Annual V.M. Goldschmidt Conference Abstract 7602.

Mojzsis, S.J., Harrison, T.M., 2002. Origin and significance of Archean quartzose rocks at Akilia, Greenland. Science 298, 917a - 917a.

Mojzsis, S.J., Arrhenius, G., McKeegan, K.D., Harrison, T.M., Nutman, A.P., Friend, C.R.L., 1996. Evidence for life on Earth before 3,800 million years ago. Nature 384, 55-59.

Mojzsis, S.J., Coath, C.D., Greenwood, J.P., McKeegan, K.D., Harrison, T.M., 2003. Mass-independent isotope effects in Archean (2.5 to 3.8 Ga) sedimentary sulfides determined by ion microprobe analysis. Geochimica et Cosmochimica Acta 67, 1635-1658.

Moorbath, S., O'Nions, R.K., Pankhurst, R.J., 1973. Early Archaean age for the Isua Iron Formation, West Greenland. Nature 245, 138-139.

Moorbath, S., Whitehouse, M.J., 1996. Age of the Isua supracrustal sequence of West Greenland, in: Chela-Flores, J., Raulin, F. (Eds.), Chemical Evoultion: Physics of the Origin and Evoultion of Life. Kluwer Academic Publishers, pp. 87-95.

Morford, J.L., Emerson, S., 1999. The geochemistry of redox sensitive trace metals in sediments. Geochimica et Cosmochimica Acta 63, 1735-1750.

Morris, R.C., 1993. Genetic modeling for banded iron formation of the Hamersley Group Pilbara craton, Western Australia. Precambrian Research 60, 243-286.

Morris, R.C., Horwitz, R., 1983. The origin of the iron-formation-rich Hamersley Group of Western Australia: Deposition on a platform. Precambrian Research 21, 273-297.

Muller, B., Axelsson, M.D., Ohlander, B., 2003. Trace elements in magnetite from Kiruna, northern Sweden, as determined by LA-ICP-MS. Gff 125, 1-5.

Murray, R.W., Tenbrink, M.R.B., Gerlach, D.C., Russ, G.P., Jones, D.L., 1992. Interoceanic Variation in the Rare-Earth, Major, and Trace-Element Depositional Chemistry of Chert - Perspectives Gained from the Dsdp and Odp Record. Geochimica et Cosmochimica Acta 56, 1897-1913.

Myers, J.S., 2001. Protoliths of the 3.8-3.7 Ga Isua greenstone belt, West Greenland. Precambrian Research 105, 129-141.

Myers, J.S., Crowley, J.L., 2000. Vestiges of life in the oldest Greenland rocks? A review of early Archean geology in the Godthabsfjord region, and reappraisal of field evidence for > 3850 Ma life on Akilia. Precambrian Research 103, 101-124.

Nisbet, E.G., Nisbet, R.E.R., 2008. Methane, oxygen, photosynthesis, rubisco and the regulation of the air through time. Philos T R Soc B 363, 2745-2754.

Nozaki, Y., Zhang, J., Amakawa, H., 1997. The fractionation between Y and Ho in the marine environment. Earth and Planetary Science Letters 148, 329-340.

Nutman, A.P., Dawes, P.R., Kalsbeek, F., Hamilton, M.A., 2008. Palaeoproterozoic and Archaean gneiss complexes in northern Greenland: Palaeoproterozoic terrane assembly in the High Arctic. Precambrian Research 161, 419-451.

Nutman, A.P., Friend, C.R.L., 2006. Petrography and geochemistry of apatites in banded iron formation, Akilia, W. Greenland: Consequences for oldest life evidence. Precambrian Research 147, 100-106.

Nutman, A.P., Friend, C.R.L., 2007. Adjacent terranes with c. 2715 and 2650 Ma high-pressure metamorphic assemblages in the Nuuk region of the North Atlantic Craton, souther West Greenland: complexities of Neoarchean collisional orogeny. Precambrian Research 155, 159-203.

Nutman, A.P., Friend, C.R.L., Bennett, V.C., McGregor, V.R., 2004. Dating of the Ameralik dyke swarms of the Nuuk district, souther West Greenland: mafic intrusion events starting from c. 3510 Ma. Journal of the Geological Society of London 161, 421-430.

Nutman, A.P., McGregor, V.R., Friend, C.R.L., Bennett, V.C., Kinny, P.D., 1996. The Itsaq Gneiss Complex of southern West Greenland; the world's most extensive record of early crustal evolution (3900 - 3600 Ma). Precambrian Research 78, 1-39.

Nutman, A.P., Mojzsis, S.J., Friend, C.R.L., 1997. Recognition of >3850 Ma water-lain sediments in West Greenland and their significance for the early Archean Earth. Geochimica et Cosmochimica Acta 61, 2475-2484.

Ohmoto, H., Watanabe, Y., Yamaguchi, K., Naraoka, H., Kakegawa, T., Haruna, M., Hayashi, K., Kato, Y., 2006. Chemical and biological evolution of early Earth: constraints from banded iron-formation, in: Kessler, S.E., Ohmoto, H. (Eds.), Evolution of the Atmosphere, Hydrosphere, and Biosphere on Early Earth: Constrainsts from Ore Deposits. Geological Soceity of America, Denver.

Ojakangas, R.W., Morey, G.B., Southwick, D.L., 2001. Paleoproterozoic basin development and sedimentation in the Lake Superior region, North America. Sediment Geol 141, 319-341.

Olson, J.M., 2006. Photosynthesis in the Archean era. Photosynth Res 88, 109-117.

Pankhurst, R.J., Moorbath, S., McGregor, V.R., 1973. Late event in the geological evolution of the Godthaab District, West Greenland. Nature 243, 24-26.

Papineau, D., De Gregorio, B.T., Stroud, R.M., Steele, A., Pecoits, E., Konhauser, K., Wang, J., Fogel, M.L., 2010. Ancient graphite in the Eoarchean quartz-pyroxene rocks from Akilia in southern West Greenland II: Isotopic and chemical compositions and comparison with Paleoproterozoic banded iron formations. Geochimica et Cosmochimica Acta 74, 5884-5905.

Papineau, D., Fogel, M.L., Cody, G.D., DeGregorio, B.T., Fries, M.D., Mojzsis, S.J., Steele, A., Stroud, R.M., Wang, J., 2008. Graphite associated with apatite in the

~3.8 Ga quartz-pyroxene rock from Akilia, Southwest Greenland. Astrobiology 8, 412.

Pavlov, A., Kasting, J., 2002. Mass-independent fractionation of sulfur isotopes in Archean sediments: Strong evidence for an anoxic Archean atmosphere. Astrobiology 2, 27-41.

Percak-Dennett, E.M., Beard, B.L., Xu, H., Konishi, H., Johnson, C.M., Roden, E.E., 2011. Iron isotopic fractionation during microbial dissimilatory iron oxide reduction in simulated Archean seawater. Geobiology 9, 205-220.

Perry, E.C., Ahmad, S.N., 1977. Carbon isotope composition of graphite and carbonate minerals from 3.8-AE metamorphosed sediments, Isukasia, Greenland. Earth and Planetary Science Letters 36, 280-284.

Pflug, H.D., Jaeschke-Boyer, H., 1979. Combined structural and chemical analysis of 3,800-Myr-old microfossils. Nature 280, 4830486.

Planavsky, N., Bekker, A., Rouxel, O., Kamber, B., Hofmann, A., Knudsen, A., Lyons, T.W., 2010a. Rare Earth Element and yttrium compositions of Archean and Paleoproterozic Fe formations revisited: New perspctives on the significance and mechanics of depositions. Geochimica et Cosmochimica Acta 74, 6387-6405.

Planavsky, N., Bekker, A., Rouxel, O.J., Kamber, B., Hofmann, A., Knudsen, A., Lyons, T.W., 2010. Rare Earth Element and yttrium compositions of Archean and Paleoproterozoic Fe formations revisited: New perspectives on the significance and mechanisms of deposition. Geochimica et Cosmochimica Acta 74, 6387-6405.

Planavsky, N., Rouxel, O., Bekker, A., Shapiro, R., Fralick, P., Knudsen, A., 2009. Iron-oxidizing microbial ecosystems thrived in late Paleoproterozoic redox-stratified oceans. Earth and Planetary Science Letters 286, 230-242.

Planavsky, N., Rouxel, O.J., Bekker, A., Hofmann, A., Little, C.T.S., Lyons, T.W., 2012. Iron isotope composition of some Archean and Proterozoic iron formations. Geochimica et Cosmochimica Acta 80, 158-169.

Planavsky, N.J., Rouxel, O.J., Bekker, A., Lalonde, S.V., Konhauser, K.O., Reinhard, C.T., Lyons, T.W., 2010b. The evolution of the marine phosphate reservoir. Nature 467, 1088-1090.

Pollack, G.D., Krogstad, E.J., Bekker, A., 2009. U–Th–Pb–REE systematics of organic-rich shales from the ca. 2.15 Ga Sengoma Argillite Formation, Botswana: Evidence for oxidative continental weathering during the Great Oxidation Event. Chemical Geology 260, 172-185.

Poulton, S.W., Fralick, P.W., Canfield, D.E., 2004. The transition to a sulphidic ocean similar to 1.84 billion years ago. Nature 431, 173-177.

Pufahl, P.K., Fralick, P.W., 2004. Depositional controls on Palaeoproterozoic iron formation accumulation, Gogebic Range, Lake Superior region, USA. Sedimentology 51, 791-808.

Quinn, K.A., Byrne, R.H., Schijf, J., 2006. Sorption of yttrium and rare earth elements by amorphous ferric hydroxide: Influence of solution complexation with carbonate. Geochimica et Cosmochimica Acta 70, 4151-4165.

Rakovan, J.F., Huges, J.M., 2000. Strontium in the Apatite Structure: Strongian Fluoroapatite and Belovite-(Ce). The Canadian Minerologist 38, 839-845.

Rasmussen, B., Buick, R., 1999. Redox state of the Archean atmosphere: Evidence from detrital heavy minerals in ca. 3250-2750 Ma sandstones from the Pilbara Craton, Australia. Geology 27, 115-118.

Rollinson, H., 2002. The metamorphic history of the Isua Greenstone Belt, West Greenland. Geological Society, London, Special Publications 199, 329-350.

Rollinson, H., 2003. Metamorphic history suggested by garnet-growth chronologies in the Isua Greenstone Belt, West Greenland. Precambrian Research 126, 181-196.

Rose, N.M., Rosing, M.T., Bridgwater, D., 1996. The origin of metacarbonate rocks in the Archaean Isua Supracrustal Belt, West Greenland. American Journal of Science 296, 1004-1044.

Rosing, M.T., 1999. 13C-Depleted Carbon Microparticles in >3700-Ma Sea-Floor Sedimentary Rocks from West Greenland. Science 283, 674-676.

Rosing, M.T., Rose, N.M., Bridgwater, D., Thomsen, H.S., 1996. Earliest part of Earth's stratigraphic record: A reappraisal of the > 3.7 Ga Isua (Greenland) supracrustal sequence. Geology 24, 43-46.

Rouxel, O., 2003. Iron isotope fractionation during oceanic crust alteration. Chemical Geology 202, 155-182.

Rouxel, O., Bekker, A., Edwards, K., 2005. Iron isotope constraints on the Archean and Paleoproterozoic ocean redox state. Science 307, 1088-1091.

Rouxel, O.J., Sholkovitz, E.R., Charette, M., Edwards, K.J., 2008. Iron isotope fractionation in subterranean estuaries. Geochimica et Cosmochimica Acta 72, 3413-3430.

Schidlowski, M., Appel, P.W.U., Eichmann, R., Junge, C.E., 1979. Carbon isotope geochemistry of the 3.7 x 109 yr. old Isua sediments, West Greenland:

Implications for the Archean carbon and oxygen cycles. Geochimica et Cosmochimica Acta 43, 189-199.

Schmidt, P., 2003. Reversal asymmetry in Mesoproterozoic overprinting of the 1.88-Ga Gunflint Formation, Ontario, Canada: non-dipole effects or apparent polar wander? Tectonophysics 377, 7-32.

Schoenberg, R., von Blanckenburg, F., 2005. An assessment of the accuracy of stable Fe isotope ratio measurements on samples with organic and inorganic matrices by high-resolution multicollector ICP-MS. International Journal of Mass Spectrometry 242, 257-272.

Schopf, J.W., 1993. Microfossils of the early Archean Apex chert: new evidnce of the antiquity of life. Science 260, 640-646.

Schopf, J.W., 2006. Fossil evidence of Archaean life. Philos Trans R Soc Lond B Biol Sci 361, 869-885.

Scott, C., Lyons, T.W., Bekker, A., Shen, Y., Poulton, S.W., Chu, X., Anbar, A.D., 2008. Tracing the stepwise oxygenation of the Proterozoic ocean. Nature 452, 456-459.

Severmann, S., Johnson, C.M., Beard, B.L., McManus, J., 2006. The effect of early diagenesis on the Fe isotope compositions of porewaters and authigenic minerals in continental margin sediments. Geochimica et Cosmochimica Acta 70, 2006-2022.

Severmann, S., Lyons, T.W., Anbar, A., McManus, J., Gordon, G.W., 2008. Modern iron isotope perspective on benthic iron shuttle and the redox evolution of ancient oceans. Geology 36, 487-490.

Shiller, A.M., Mao, L., 2000. Dissolved vanadium in rivers: effects of silicate weathering. Chemical Geology 165, 13-22.

Sholkovitz, E.R., 1992. Chemical evolution of rare earth elements: fractionation between colloidal and solution phases of filtered river water. Earth and Planetary Science Letters 114, 77-84.

Sholkovitz, E.R., Landing, W.M., Lewis, B.L., 1994. Ocean Particle Chemistry - the Fractionation of Rare-Earth Elements between Suspended Particles and Seawater. Geochimica et Cosmochimica Acta 58, 1567-1579.

Sholkovitz, E.R., Shaw, T.J., Schneider, D.L., 1992. The Geochemistry of Rare-Earth Elements in the Seasonally Anoxic Water Column and Porewaters of Chesapeake Bay. Geochimica et Cosmochimica Acta 56, 3389-3402.

Siever, R., 1992. The silica cycyle in the Precambrian. Geochimica et Cosmochimica Acta 56, 3265-3272.

Simonson, B., 1985. Sedimentalogical constraints on the origins of the Precambrian iron-formations. Geological Society of America Bulletin 96, 244-252.

Simonson, B., Hassler, S., 1996. Was the deposition of large Precambrian iron formations linked to a major marine transgression? J Geol 104, 665-676.

Sogaard, E.G., Medenwaldt, R., Abraham-Peskir, J.V., 2000. Conditions and rates of biotic and abiotic iron precipitation in selected Danish freshwater plants and microscopic analysis of precipitate morphology. Water Res 34, 2675-2682.

Spier, C., de Oliveira, S.M.B., Sial, A.N., Rios, F.J., 2007. Geochemistry and genesis of the banded Fe formations of the Caue Formation, Quadriletero Ferrifero, Minas Gerais, Brazil. Precambrian Research 152, 170-206.

Steinhoefel, G., Horn, I., von Blanckenburg, F., 2009. Micro-scale tracing of Fe and Si isotopic signatures in banded iron formation using femtosecond laser ablation. Geochimica et Cosmochimica Acta 73, 5343-5360.

Steinhoefel, G., von Blanckenburg, F., Horn, I., Konhauser, K.O., Beukes, N.J., Gutzmer, J., 2010. Deciphering formation processes of banded iron formations from the Transvaal and the Hamersley successions by combined Si and Fe isotope analysis using UV femtosecond laser ablation. Geochimica et Cosmochimica Acta 74, 2677-2696.

Straub, K.L., Rainey, F.A., Widdel, F., 1999. Rhodovulum iodosum sp. nov, and Rhodovulum robiginosum sp. nov., two new marine phototrophic ferrous-iron-oxidizing purple bacteria. Int J Syst Bacteriol 49, 729-735.

Tangalos, G.E., Beard, B.L., Johnson, C.M., Alpers, C.N., Shelobolina, E.S., Xu, H., Konishi, H., Roden, E.E., 2010. Microbial production of isotopically light iron(II) in a modern chemically precipitated sediment and implications for isotopic variations in ancient rocks. Geobiology 8, 197-208.

Taylor, S.R., McLennan, S.M., 1985. The Continental Crust: Its Compostion and Evolution. Blackwell, Oxford.

Thurston, P.C., Kamber, B.S., Whitehouse, M., 2012. Archean cherts in banded iron formation: Insight into Neoarchean ocean chemistry and depositional processes. Precambrian Research 214-215, 227-257.

Tice, M., Lowe, D.R., 2004. Photosynthetic microbial mats in the 3,416-My-old ocean. Nature 431, 549-552.

Towe, K.M., 1983. Precambrian Atmospheric Oxygen and Banded Iron Formations - a Delayed Ocean Model. Precambrian Research 20, 161-170.

Trendall, A.F., 2002. The significance of iron-formation in the Precambrian stratigraphic record. Special Publication International Association of Sedimentalogists 33, 33-66.

Trendall, A.F., Blockey, J., 1970. The iron-formations of the Precambrian Hamersley Group, Western Australia. Geological Survey Western Australia Bulletin 119, 366.

Tsikos, H., Matthews, A., Erel, Y., Moore, J.M., 2010. Iron isotopes constrain biogeochemial redox cycling of iron and manganese in a Paleoproterozoic stratified basin. Earth and Planetary Science Letters 298, 125-143.

Ulrich, T., Kamber, B.S., Woodhead, J.D., Spencer, L.A., 2010. Long-Term Observations of Isotope Ratio Accuracy and Reproducibility Using Quadrupole ICP-MS. Geostand Geoanal Res 34, 161-174.

van Zuilen, M.A., Lepland, A., Arrhenius, G., 2002. Reassessing the evidence for the earliest traces of life. Nature 418, 627-630.

van Zuilen, M.A., Lepland, A., Teranes, J., Finarelli, J., Wahlen, M., Arrhenius, G., 2003. Graphite and carbonates in the 3.8 Ga old Isua Supracrustal Belt, southern West Greenland. Precambrian Research 126, 331-348.

Vargas, M., Keshefi, K., Blunt-Harris, E., Lovley, D.R., 1998. Microbiological evidence for Fe(III) reduction on early Earth. Nature 395, 65-67.

Veizer, J., 1983. Geologic evolution of the Archean - Early Proterozoic Earth, in: Schopf, J.W. (Ed.), Earth's Earliest Biosphere. Princeton University Press, NJ, pp. 240-259.

Volkov, I.I., Fomina, L.S., 1974. Influence of organic material and processes of sulfide formation on distribution of some trace elements in deep-water sediments of the Black Sea, in: Degens, E.T., Ross, D.A. (Eds.), The Black Sea - Geology, Chemistry and Biology, American Association of Petroleum Geologists Memoir 20, Tulsa, OK, pp. 456-476.

Webb, G.E., Northdurft, L.D., Kamber, B.S., Kloprogge, J.T., Zhao, J., 2009. Rare earth element geochemistry of scleractinian coral skeleton during meteroic diagenesis: a sequence through neomorphism and aragonite to calcite. Sedimentology 56.

Wehrli, B., Stumm, W., 1989. Vanadyl in natural waters: Adsportion and hydrolysis promote oxygenation. Geochimica et Cosmochimica Acta 53, 69-77.

Welch, S.A., Beard, B.L., Johnson, C.M., Braterman, P.S., 2003. Kinetic and equilibrium Fe isotope fractionation between aqueous Fe(II) and Fe(III). Geochimica et Cosmochimica Acta 67, 4231-4250.

Whitehouse, M.J., Fedo, C.M., 2003. Deformation features and critical field relationships of early Archean rocks, Akilia, southwest Greenland. Precambrian Research 126, 259-271.

Whitehouse, M.J., Fedo, C.M., 2007. Microscale heterogeneity of Fe isotopes in >3.71 Ga banded iron formation from the Isua Greenstone Belt, southwest Greenland. Geology 35, 719.

Whitehouse, M.J., Kamber, B.S., 2005. Assigning dates to thin gneissic veins in high-grade metamorphic terranes: a cautionary tale from Akilia, southwest Greenland. Journal of Petrology 46, 291-318.

Whitehouse, M.J., Kamber, B.S., Moorbath, S., 1999. Age significance of U-Th-Pb zircon data from early Archean rocks of west Greenland: a reassessment based on combined ion-microprobe and imaging studies. Chemical Geology 160, 201-224.

Whitehouse, M., Kamber, B., Fedo, C., Lepland, A., 2005. Integrated Pb- and S-isotope investigation of sulphide minerals from the early Archaean of southwest Greenland. Chemical Geology 222, 112-131.

Whitehouse, M.J., Myers, J.S., Fedo, C.M., 2009. The Akilia Controversy: field, structural and geochronological evidence questions interpretations of >3.8 Ga life in SW Greenland. Journal of the Geological Society 166, 335-348.

Widdel, F., Schnell, S., Heising, S., Ehrenreich, A., Assmus, B., Schink, B., 1993. Ferrous Iron Oxidation by Anoxygenic Phototrophic Bacteria. Nature 362, 834-836.

Wu, L., Beard, B.L., Roden, E.E., Johnson, C.M., 2009. Influence of pH and dissolved Si on Fe isotope fractionation during dissimilatory microbial reduction of hematite. Geochimica et Cosmochimica Acta 73, 5584-5599.

Yang, W., Holland, H.D., 2002. The redox-sensitive trace elements, Mo, U, and Re in Precambrian carbonaceous shales: Indicators of the Great Oxidation Event. Geological Society of America Bulletin 34, 381.

# Appendix 2

Table 3.1
Bulk rock major element compositions of samples from the IGB, BGB, and GF

| Sample | Age (Ga) | $SiO_2$ (wt. %) | $Al_2O_3$ (wt. %) | $Fe_2O_{3(T)}$ (wt.%) | MnO (wt. %) | MgO (wt. %) | CaO (wt. %) | $Na_2O$ (wt. %) | $K_2O$ (wt. %) | $TiO_2$ (wt. %) | $P_2O_5$ (wt. %) |
|---|---|---|---|---|---|---|---|---|---|---|---|
| ***Isua*** | | | | | | | | | | | |
| IS-02-05 | 3.7 | 55.03 | 0.19 | 42.29 | 0.04 | 4.14 | 0.06 | 0.06 | 0.05 | 0.00 | 0.04 |
| IS-02-08 | 3.7 | 49.28 | 0.07 | 48.63 | 0.03 | 1.06 | 0.81 | 0.04 | 0.01 | 0.00 | 0.08 |
| ISB-55 | 3.7 | 60.98 | 0.31 | 36.57 | 0.10 | 1.15 | 0.61 | 0.00 | 0.00 | 0.02 | 0.04 |
| Average | | 55.10 | 0.19 | 42.50 | 0.05 | 2.12 | 0.49 | 0.03 | 0.02 | 0.01 | 0.05 |
| Median | | 55.03 | 0.19 | 42.29 | 0.04 | 1.15 | 0.61 | 0.04 | 0.01 | 0.00 | 0.04 |
| ***Zimbabwe*** | | | | | | | | | | | |
| ZB-23 | 3.0 | | | | | | | | | | |
| ZB-18 | 3.0 | 61.90 | 0.40 | 30.34 | 0.47 | 0.57 | 0.03 | 0.01 | 0.01 | 0.01 | 0.04 |
| ZB-117 | 3.0 | 40.13 | 0.71 | 57.30 | 0.55 | 0.68 | 0.07 | 0.01 | 0.02 | 0.01 | 0.07 |
| ZB-247 | 3.0 | 47.00 | 1.51 | 51.32 | 0.01 | 0.07 | 0.03 | 0.01 | 0.03 | 0.06 | 0.03 |
| ZB-294 | 3.0 | 3.70 | 2.79 | 91.71 | 0.03 | 0.02 | 0.03 | 0.16 | 0.15 | 0.12 | 0.12 |
| Average | | 38.18 | 1.35 | 57.67 | 0.27 | 0.34 | 0.04 | 0.05 | 0.05 | 0.05 | 0.07 |
| Median | | 47.00 | 0.71 | 51.32 | 0.47 | 0.57 | 0.03 | 0.01 | 0.02 | 0.01 | 0.04 |
| ***Gunflint*** | | | | | | | | | | | |
| GF-07-6 | 1.9 | 46.11 | 0.55 | 47.03 | 0.67 | 3.80 | 1.89 | 0.01 | 0.03 | 0.08 | 0.07 |
| GF-07-22 | 1.9 | 36.10 | 1.67 | 57.38 | 0.27 | 4.93 | 0.88 | 0.17 | 0.33 | 0.18 | 0.07 |
| GF-09-39 | 1.9 | 40.10 | 0.20 | 57.67 | 2.06 | 0.54 | 0.72 | 0.01 | 0.01 | 0.01 | 0.03 |
| GF-09-45 | 1.9 | 78.23 | 0.36 | 20.17 | 0.09 | 0.19 | 0.37 | 0.01 | 0.01 | 0.01 | 0.01 |
| Average | | 50.14 | 0.70 | 45.56 | 0.77 | 2.37 | 0.97 | 0.05 | 0.10 | 0.07 | 0.05 |
| Median | | 43.11 | 0.46 | 52.21 | 0.47 | 2.17 | 0.80 | 0.01 | 0.02 | 0.05 | 0.05 |

Table 3.2.
Bulk rock trace and rare-earth element compositions of samples from the IGB, BGB, and GF

| Element (ppm) | IS-02-05 | IS-02-08 | ISB-55 | ZB-23 | ZB-18 | ZB-117 | ZB-247 | ZB-294 | GF-07-6 | GF-07-22 | GF-09-39 | GF-09-45 |
|---|---|---|---|---|---|---|---|---|---|---|---|---|
| Sc | 1 | 1 | 0.15 | 0.311 | 0.532 | 0.572 | 2.15 | 3 | 1.161 | 3 | 1.091 | 0.394 |
| Be | 1 | 3 | 0.85 | 0.336 | 1.208 | 0.629 | 0.81 | < 1 | 0.942 | 2 | 2.642 | 0.881 |
| V | 5 | 5 | 0.94 | 6.869 | 2.633 | 5.846 | 18.67 | 46 | 25.373 | 68 | 11.160 | 11.093 |
| Cr | 20 | 20 | 10.49 | 6.521 | 5.359 | 7.568 | 33.16 | 70 | 3.164 | 20 | 0.273 | 0.607 |
| Co | 2 | 4 | 2.61 | 1.983 | 6.453 | 2.737 | 3.62 | 4 | 7.849 | 16 | 7.989 | 0.964 |
| Ni | 20 | 20 | 14.93 | 5.138 | 27.607 | 14.898 | 26.90 | 20 | 2.674 | 20 | 2.200 | 0.964 |
| Cu | 10 | 10 | 0.58 | 1.381 | 15.978 | 3.930 | 2.65 | 10 | 0.744 | 10 | 2.680 | 5.687 |
| Zn | 30 | 30 | 14.38 | 5.387 | 97.479 | 7.311 | 9.35 | 30 | 20.890 | 30 | 47.050 | 3.040 |
| Ga | 1 | 1 | 0.33 | 1.043 | 0.344 | 0.841 | 2.30 | 3 | 1.213 | 4 | 1.801 | 0.980 |
| Ge | 5.2 | 15.8 | 0.00 | n/d | 0.000 | 0.000 | 0.00 | 3.6 | n/d | 15.8 | n/d | n/d |
| As | 5 | 5 | 0.69 | 1.044 | 0.193 | 0.441 | 0.65 | < 5 | 5.861 | 5 | 0.373 | 1.930 |
| Rb | 1 | < 1 | 0.09 | 0.226 | 0.060 | 1.320 | 0.83 | 4 | 1.194 | 35 | 0.169 | 2.411 |
| Sr | 2 | 4 | 0.98 | 0.403 | 1.278 | 4.681 | 3.65 | 6 | 37.374 | 141 | 12.409 | 8.765 |
| Zr | 1 | 3 | 0.23 | 1.500 | 0.638 | 1.547 | 8.44 | 18 | 9.671 | 27 | 6.654 | 4.597 |
| Nb | 0.2 | 0.2 | 0.04 | 0.253 | 0.056 | 0.276 | 0.68 | 2.1 | 2.041 | 5.8 | 2.675 | 1.157 |
| Mo | 2 | 2 | 0.34 | 0.183 | 0.065 | 0.300 | 0.24 | 2 | 0.379 | 2 | 0.191 | 0.240 |
| Ag | < 0.5 | 0.5 | 0.02 | 0.075 | 0.030 | 0.023 | 0.05 | < 0.5 | 0.004 | 0.5 | 0.007 | 0.005 |
| In | 0.1 | 0.1 | 0.00 | 0.002 | 0.004 | 0.004 | 0.01 | < 0.1 | 0.008 | 0.1 | 0.014 | 0.002 |
| Sn | < 1 | 1 | 0.00 | 0.069 | 0.426 | 0.489 | 0.07 | < 1 | 0.698 | 1 | 1.090 | 0.112 |
| Sb | 0.8 | 3.9 | 0.36 | 0.580 | 0.116 | 0.214 | 0.54 | 1.1 | 2.690 | 6.4 | 0.321 | 0.082 |
| Cs | < 0.1 | < 0.1 | 0.02 | 0.020 | 0.008 | 0.045 | 0.05 | < 0.1 | 0.224 | 11.6 | 0.101 | 0.578 |
| Ba | 5 | < 3 | 2.23 | 3.110 | 19.502 | 510.209 | 7.65 | 9 | 6.659 | 111 | 139.845 | 7.431 |
| La | 1.45 | 3.63 | 0.99 | 1.157 | 2.220 | 5.351 | 5.89 | 21.8 | 2.429 | 5.42 | 5.662 | 1.550 |
| Ce | 2.5 | 5.28 | 1.45 | 2.227 | 2.306 | 16.050 | 11.27 | 42.7 | 6.348 | 15.7 | 9.190 | 4.220 |
| Pr | 0.27 | 0.62 | 0.16 | 0.253 | 0.501 | 1.077 | 1.33 | 4.64 | 0.738 | 1.6 | 1.285 | 0.363 |
| Nd | 1.04 | 2.27 | 0.67 | 1.010 | 1.963 | 4.051 | 5.22 | 16 | 3.221 | 6.09 | 5.769 | 1.442 |
| Sm | 0.26 | 0.5 | 0.15 | 0.229 | 0.386 | 0.819 | 1.01 | 3.14 | 0.725 | 1.25 | 1.376 | 0.273 |
| Eu | 0.245 | 0.365 | 0.15 | 0.106 | 0.154 | 0.370 | 0.33 | 1.07 | 0.233 | 0.337 | 0.394 | 0.071 |
| Gd | 0.4 | 0.79 | 0.26 | 0.286 | 0.396 | 0.907 | 0.78 | 2.2 | 0.836 | 1.15 | 1.870 | 0.282 |
| Tb | 0.08 | 0.13 | 0.04 | 0.047 | 0.050 | 0.151 | 0.09 | 0.37 | 0.129 | 0.19 | 0.309 | 0.049 |
| Dy | 0.56 | 0.83 | 0.31 | 0.311 | 0.276 | 0.968 | 0.46 | 2.37 | 0.815 | 1.15 | 2.038 | 0.332 |
| Y | 5.8 | 10.5 | 3.91 | 2.206 | 2.228 | 5.772 | 2.47 | 22 | 5.329 | 6.7 | 13.062 | 1.692 |
| Ho | 0.13 | 0.18 | 0.08 | 0.073 | 0.063 | 0.220 | 0.09 | 0.55 | 0.181 | 0.24 | 0.472 | 0.075 |
| Er | 0.41 | 0.54 | 0.25 | 0.218 | 0.187 | 0.650 | 0.27 | 1.83 | 0.515 | 0.71 | 1.350 | 0.230 |
| Yb | 0.41 | 0.56 | 0.23 | 0.208 | 0.225 | 0.640 | 0.29 | 1.72 | 0.410 | 0.64 | 1.071 | 0.221 |
| Lu | 0.061 | 0.097 | 0.04 | 0.031 | 0.039 | 0.094 | 0.05 | 0.251 | 0.054 | 0.086 | 0.139 | 0.029 |
| Tm | 0.064 | 0.084 | 0.04 | 0.033 | 0.031 | 0.100 | 0.04 | 0.278 | 0.072 | 0.105 | 0.193 | 0.037 |
| Hf | 0.1 | 0.1 | 0.01 | 0.040 | 0.016 | 0.040 | 0.23 | 0.6 | 0.182 | 0.7 | 0.032 | 0.026 |
| Ta | 0.02 | < 0.01 | 0.00 | 0.017 | 0.003 | 0.025 | 0.06 | 0.2 | 0.062 | 0.25 | 0.007 | 0.003 |
| W | < 0.5 | 2.2 | 0.22 | 0.312 | 0.005 | 0.098 | 0.96 | 3.7 | 0.646 | 0.8 | 0.058 | 0.210 |
| Tl | 0.05 | 0.05 | 0.00 | 0.001 | 0.006 | 0.046 | 0.01 | < 0.05 | 0.004 | 0.2 | 0.001 | 0.004 |
| Pb | 8 | 5 | 5.97 | 3.743 | 0.696 | 0.155 | 2.58 | 5 | 0.569 | 5 | 0.103 | 0.864 |
| Th | 0.05 | 0.07 | 0.03 | 0.269 | 0.045 | 0.053 | 0.91 | 3.1 | 0.258 | 1.03 | 0.119 | 0.033 |
| U | 0.07 | 0.08 | 0.03 | 0.124 | 0.329 | 0.207 | 0.24 | 0.88 | 0.135 | 0.26 | 0.104 | 0.144 |

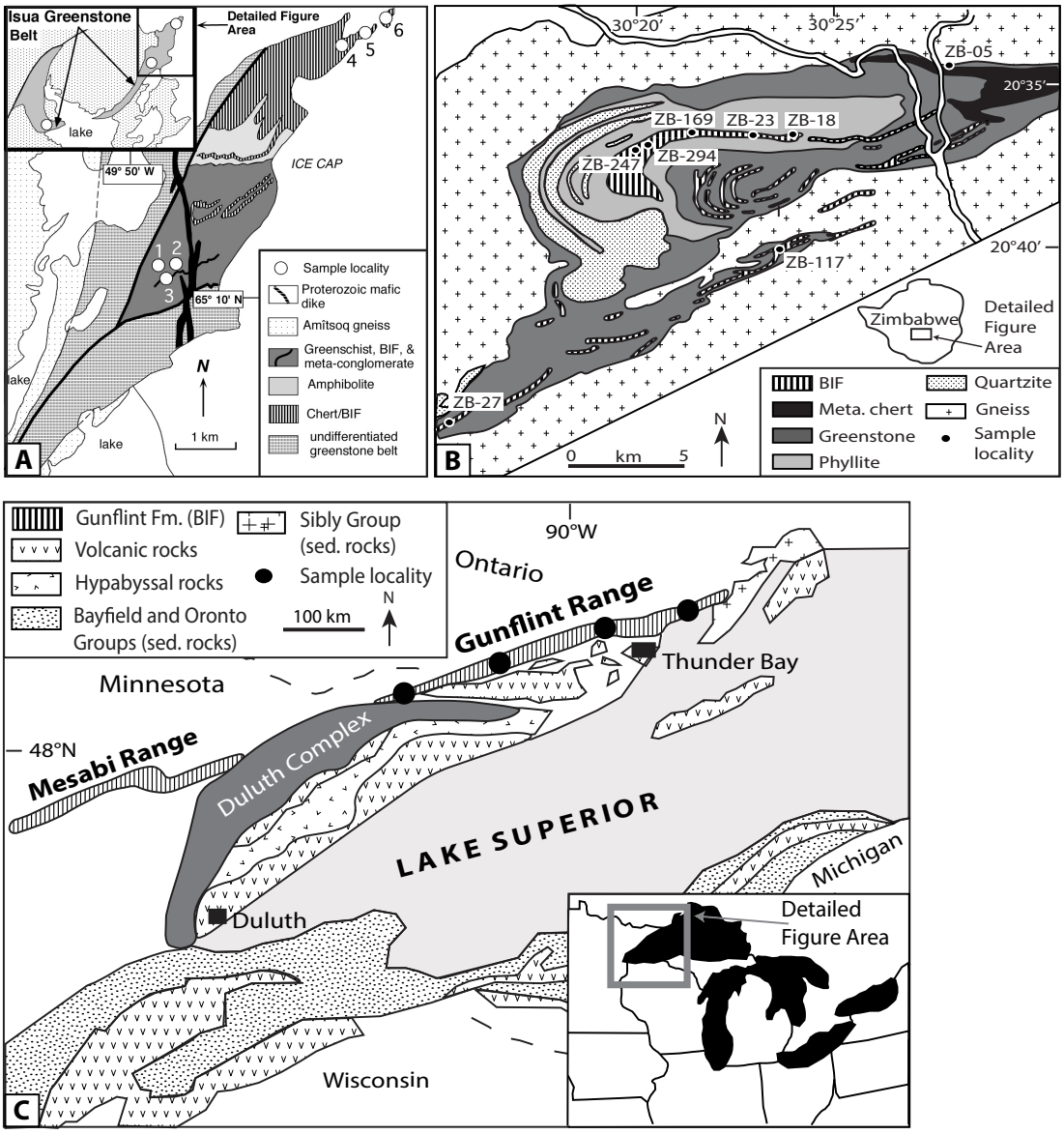



Figure 3.1. Generalized geologic maps of field areas showing sample locations. (A) Isua Greenstone Belt, SW Greenland. Map modified from Fedo . (B) Buhwa Greenstone Belt, Zimbabwe. Map modified from Fedo and Eriksson (2000). (C) Gunflint Formation, Minnesota and Ontario. Map modified from Schmidt and Williams (1995).

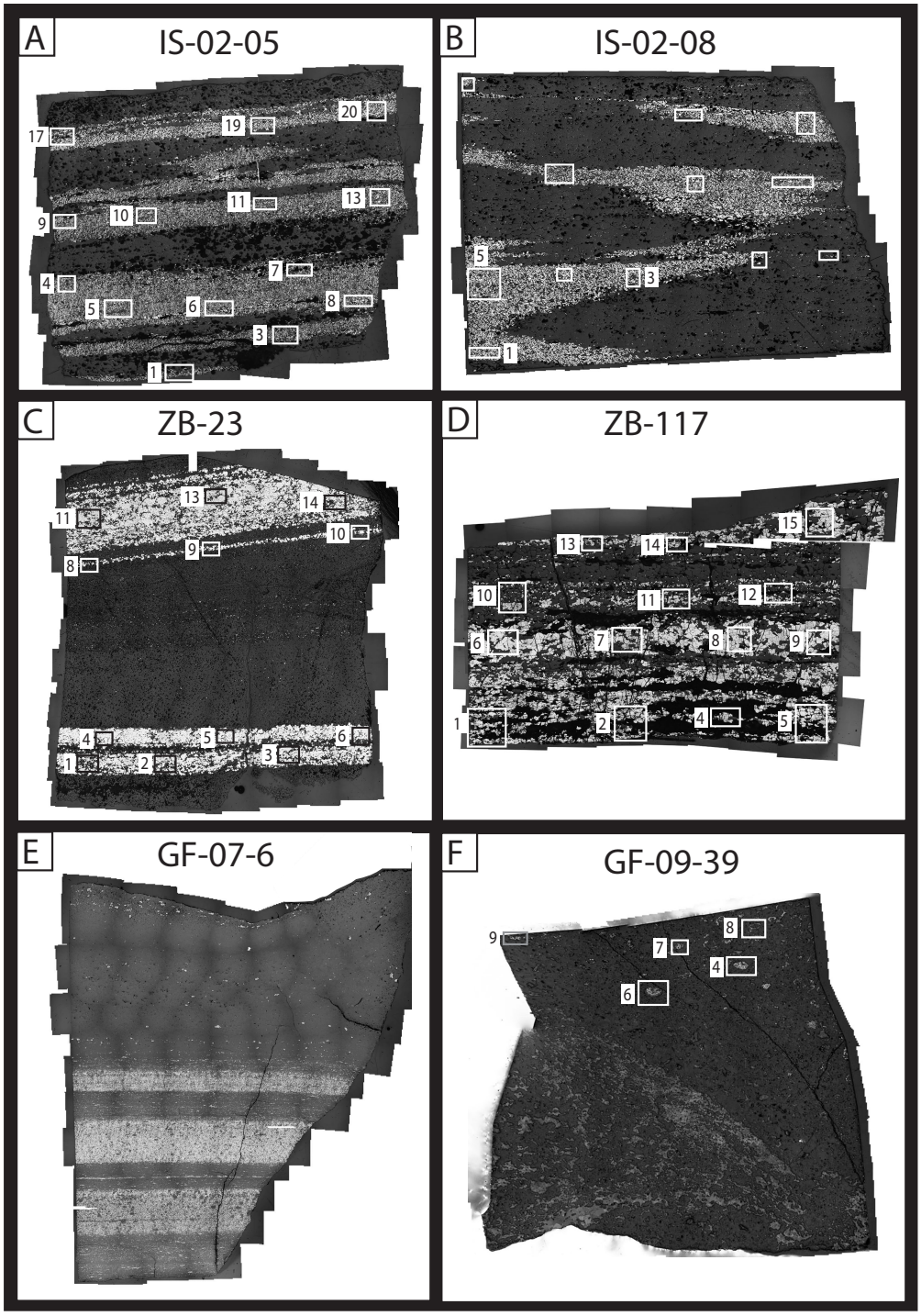



Figure 3.2. Composite photomicrographs of 1-inch polished thick sections used for laser ablation analyses. Boxes outline the region where each individual mineral grains analyzed in the study are located. (A) IS-02-05. (B) IS-02-08. (C) ZB-23. (D) ZB-117. (E) GF-06. (F) GF-39.

Figure 3.3. Reflected light photomicrographs of representative laser ablation spots of study samples from the IGB, BGB, and GF. (A) Spots 1 and 2 from Band 13 from sample IS-02-05. Both magnetite and hematite grains are present. An example of a good laser ablation spot can be seen, as well as a laser ablation pit that was not confined within the boundaries of the desired grain, resulting in the data being discarded. (B) Spot 2 from Band 15 from sample IS-02-08. Both magnetite and hematite grains are present. A good example of a laser ablation pit confined within a single hematite grain. (C) Spots 1 and 2 from Band 11 from sample ZB-23. (D) Spots 1 and 2 from Band 9 from sample ZB-23, where the mixed iron-oxide mineralogy (both magnetite and hematite) can be more easily seen. (E) Spot 1 and 2 from Band 9 from sample ZB-117, where the mixed iron-oxide mineralogy (both magnetite and hematite) can be easily seen. (F) Spots 1 and 2 from Band 13 from sample GF-06. (G) Spots 1, 2, 3 and 4 from area 4 from the granular iron formation sample GF-39. (H) Spots 1, 2, 3 and 4 from area 4 from the granular iron formation sample GF-45.

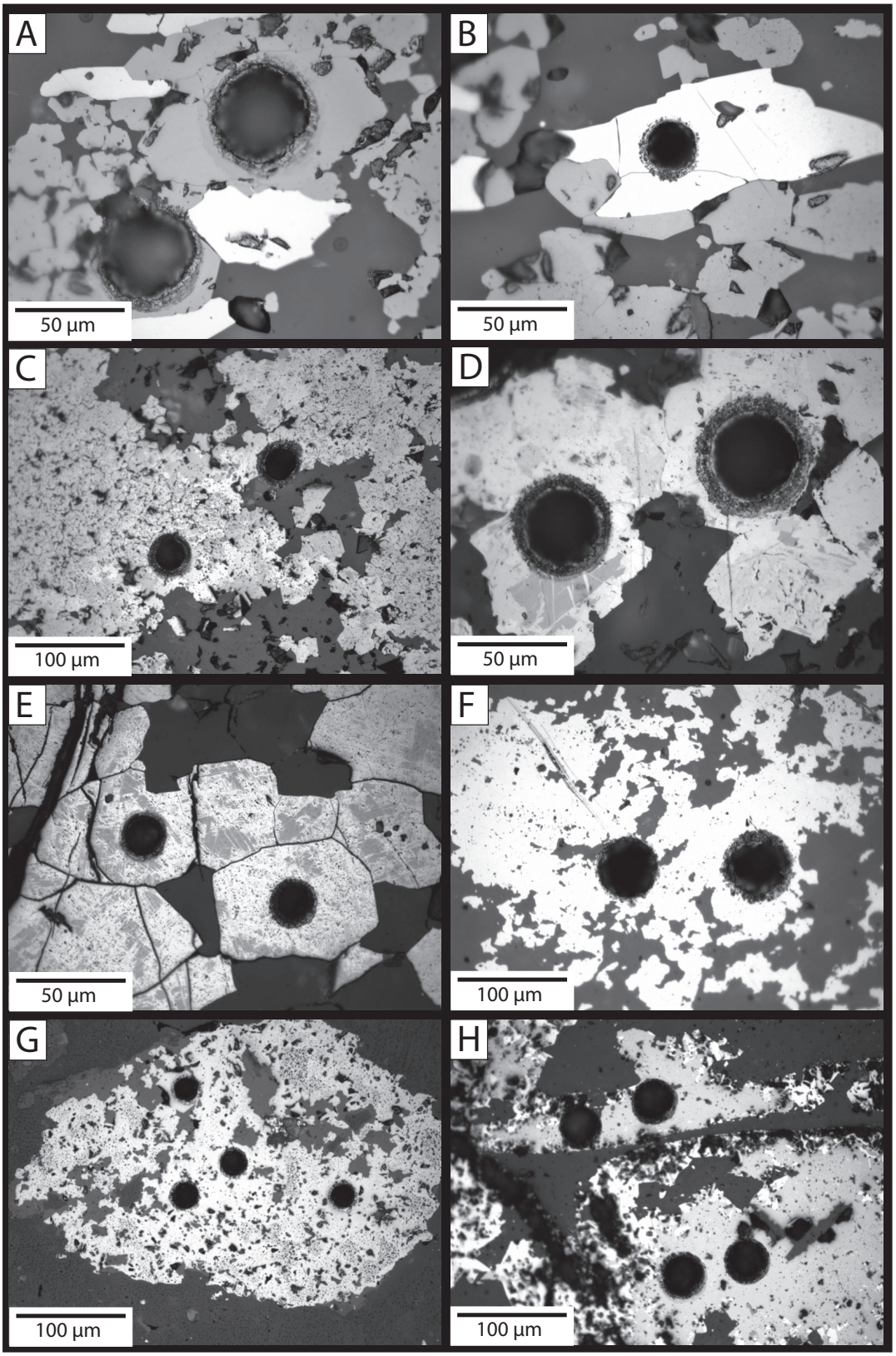


Figure 3.3. continued

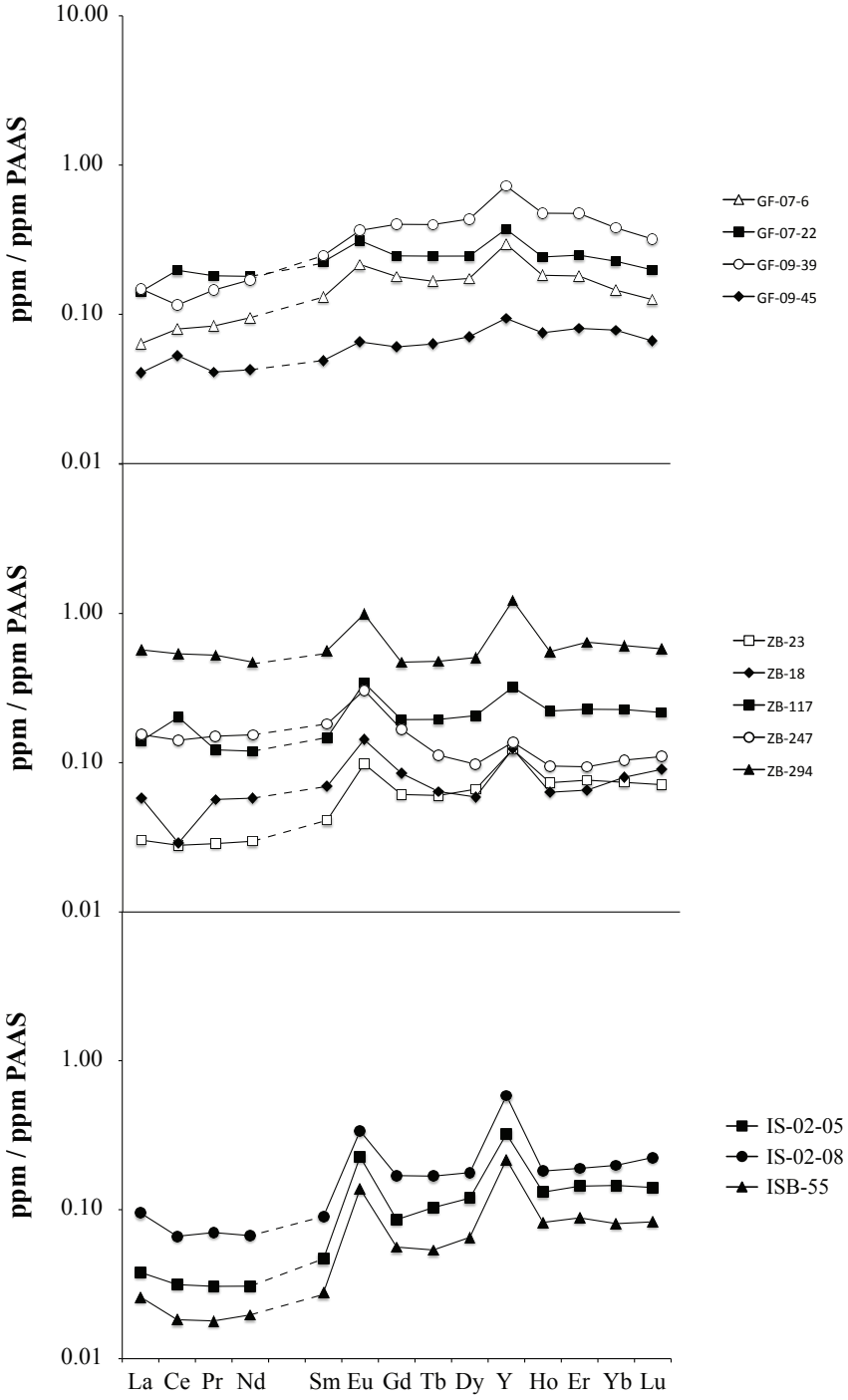



Figure 3.4. Whole rock shale-normalized REE +Y patterns for BIFs used in this study. Patterns display overall LREE depletion relative to HREE, positive La, Gd, Eu, and Y anomalies, and variable Ce anomalies. It is important to note that regardless of age or metamorphic grade, all patterns look similar, confirming the ability of BIF to retain primary seawater signatures.

Figure 3.5. Key REE ratios for the chemistry of individual mineral grains from samples IS-02-05 and IS-02-08 from the IGB. Open symbols represent magnetite grains, gray symbols represent hematite grains, and black symbols represent whole rock values. Dotted lines represent the cutoff between positive (>1) and negative (<1) anomalies for each ratio, except for the horizontal dotted line for Y/Y*, which represents the average Y/Y* value for terrestrial rocks (A) Cross plot of La/La* vs. Y/Y* for sample IS-02-05. (B) Cross plot of La/La* vs. Y/Y* for sample IS-02-08. (C) Cross plot of $Pr/Yb_{SN}$ vs. Eu/Eu* for sample IS-02-05. (D) Cross plot of $Pr/Yb_{SN}$ vs. Eu/Eu* for sample IS-02-08. (E). Cross plot of Pr/Pr* vs. Ce/Ce* for sample IS-02-05, which indicates the presence of a true positive or negative Ce anomaly. (F). Cross plot of Pr/Pr* vs. Ce/Ce* for sample IS-02-08, which indicates the presence of a true positive or negative Ce anomaly.

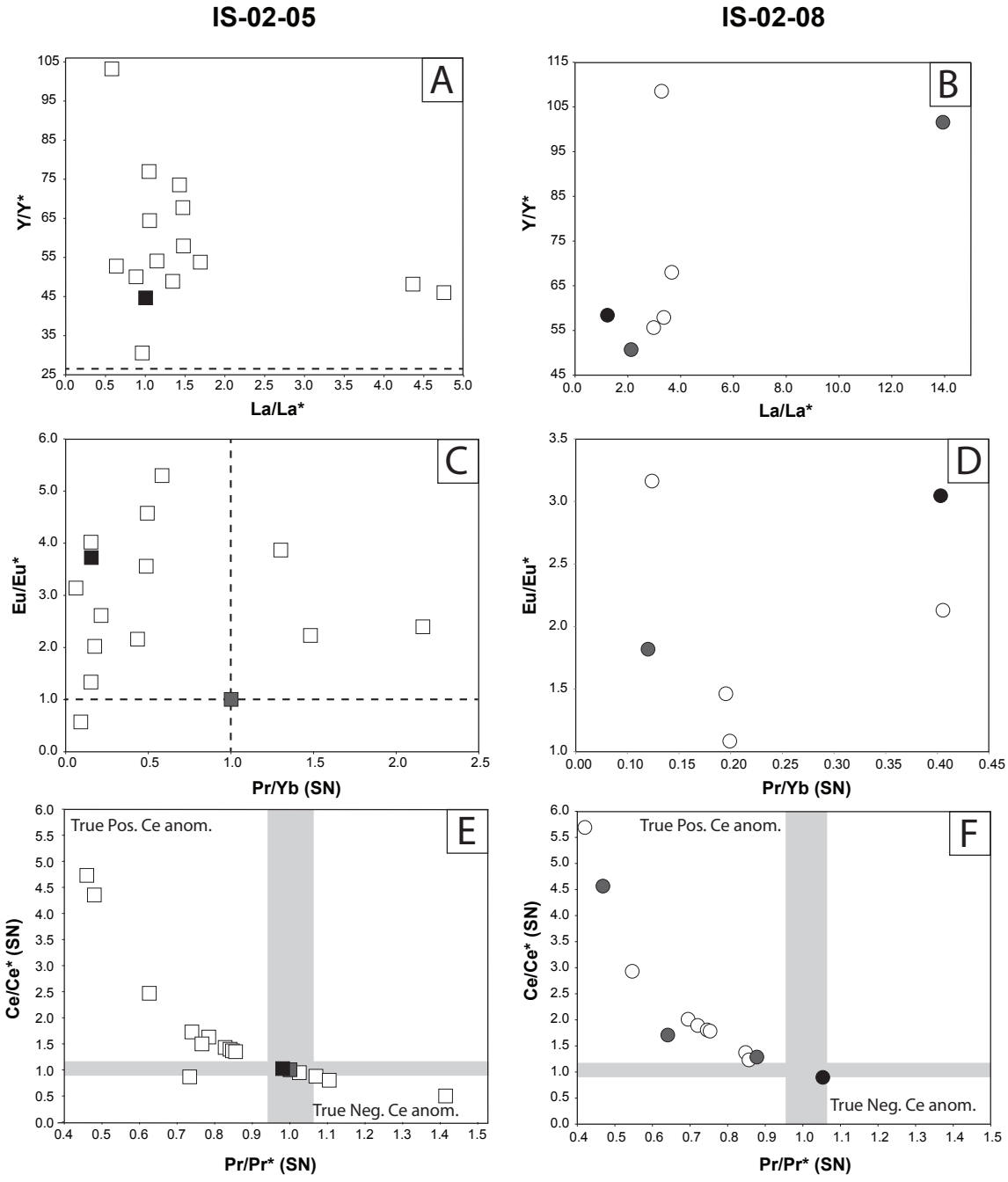



Figure 3.5 continued

Figure 3.6. Key REE ratios for the chemistry of individual mineral grains from samples ZB-23 and ZB-117 from the BGB. Open symbols represent iron oxide (intergrown magnetite and hematite) grains and black symbols represent whole rock values. Dotted lines represent the cutoff between positive (>1) and negative (<1) anomalies for each ratio, except for the horizontal dotted line for Y/Y*, which represents the average Y/Y* value for terrestrial rocks (A) Cross plot of La/La* vs. Y/Y* for sample ZB-23. (B) Cross plot of La/La* vs. Y/Y* for sample ZB-117. (C) Cross plot of $Pr/Yb_{SN}$ vs. Eu/Eu* for sample ZB-23. (D) Cross plot of $Pr/Yb_{SN}$ vs. Eu/Eu* for sample ZB-117. (E). Cross plot of Pr/Pr* vs. Ce/Ce* for sample ZB-23, which indicates the presence of a true positive or negative Ce anomaly. (F). Cross plot of Pr/Pr* vs. Ce/Ce* for sample ZB-117, which indicates the presence of a true positive or negative Ce anomaly.

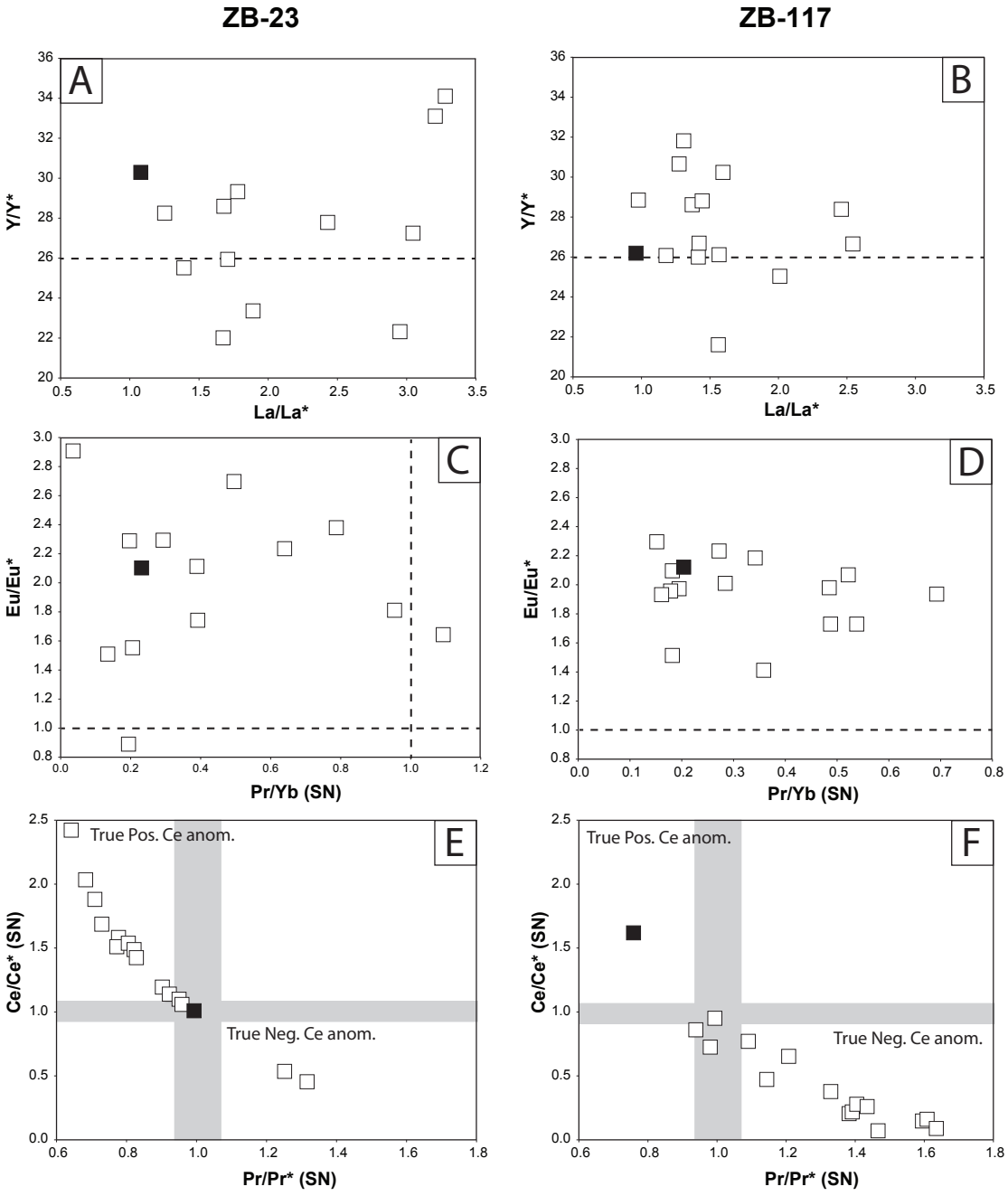



Figure. 3.6 continued

Figure 3.7 Key REE ratios for the chemistry of individual mineral grains from samples GF-06, GF-39, and GF-45 from the GF. GF-39 (circles) and GF-45 (squares) are plotted together because they are both samples of granular iron formation as opposed to GF-06, which is banded iron formation. Open symbols represent magnetite grains, gray symbols represent hematite grains, and black symbols represent whole rock values. Dotted lines represent the cutoff between positive (>1) and negative (<1) anomalies for each ratio, except for the horizontal dotted line for Y/Y*, which represents the average Y/Y* value for terrestrial rocks (A) Cross plot of La/La* vs. Y/Y* for sample GF-06. (B) Cross plot of La/La* vs. Y/Y* for samples GF-39 (circles) and GF-45 (squares). (C) Cross plot of $Pr/Yb_{SN}$ vs. Eu/Eu* for sample GF-06. (D) Cross plot of $Pr/Yb_{SN}$ vs. Eu/Eu* for samples GF-39 (circles) and GF-45 (squares) (E). Cross plot of Pr/Pr* vs. Ce/Ce* for sample GF-06, which indicates the presence of a true positive or negative Ce anomaly. (F). Cross plot of Pr/Pr* vs. Ce/Ce* for samples GF-39 (circles) and GF-45 (squares), which indicates the presence of a true positive or negative Ce anomaly.

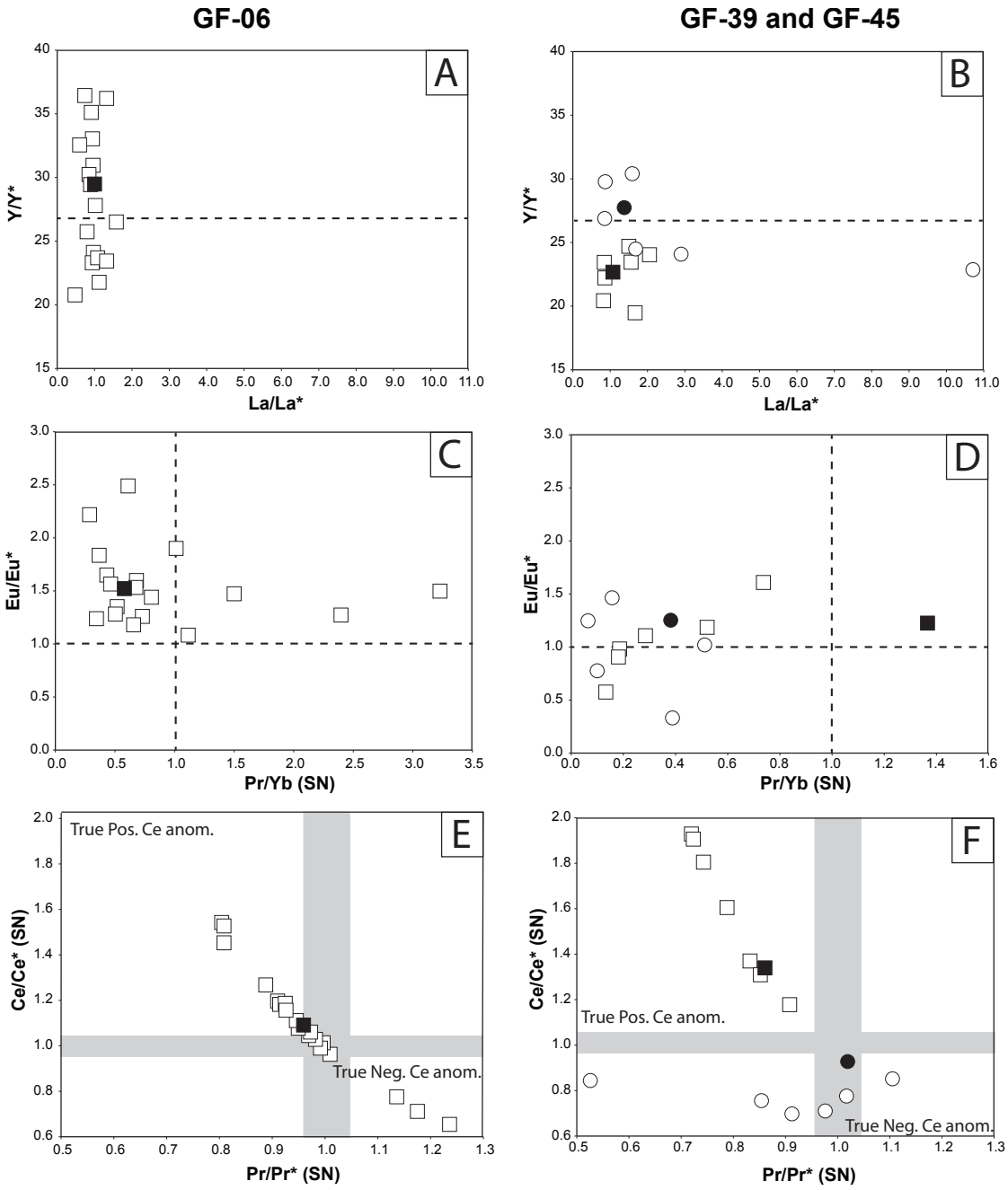



Figure. 3.7 continued

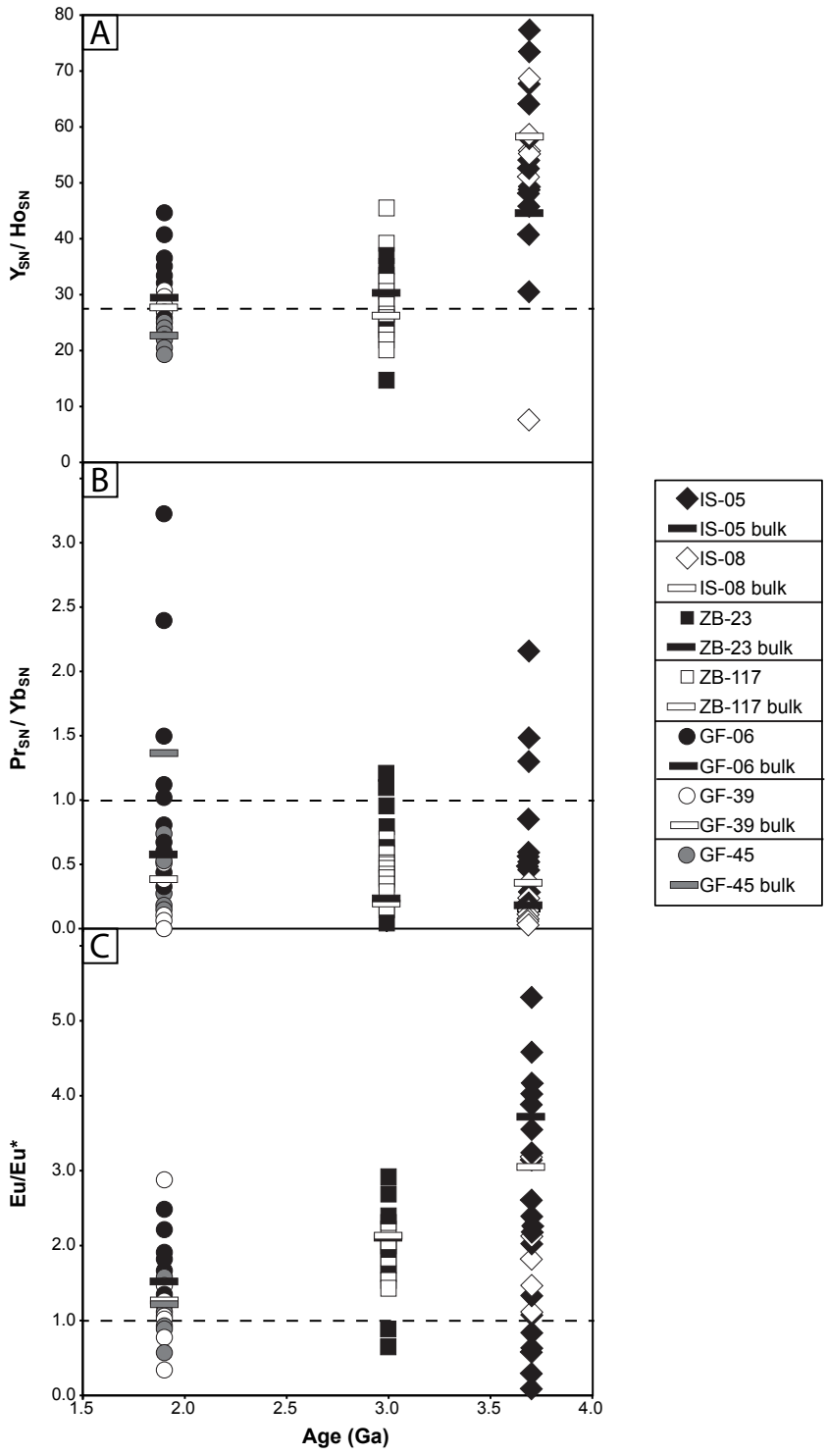



Figure 3.8. (A) Y/Ho ratios for both whole rock and individual minerals from samples from the IGB, BGB, and GF. (B) Pr/Yb ratios for both whole rock and individual minerals from samples from the IGB, BGB, and GF. (C) Eu anomalies for both whole rock and individual minerals from samples from the IGB, BGB, and GF.

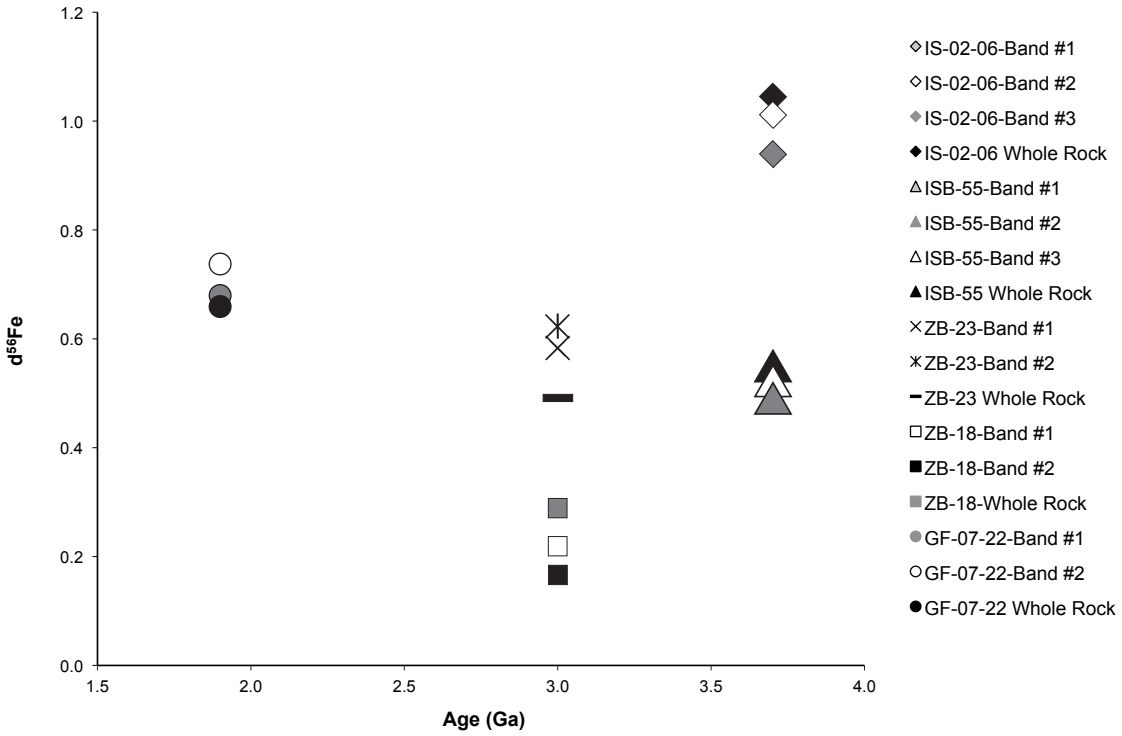



Figure 3.9. $\delta^{56}$Fe values for whole rock BIF samples and individual bands used in this study collected from the IGB, BGB, and GF.

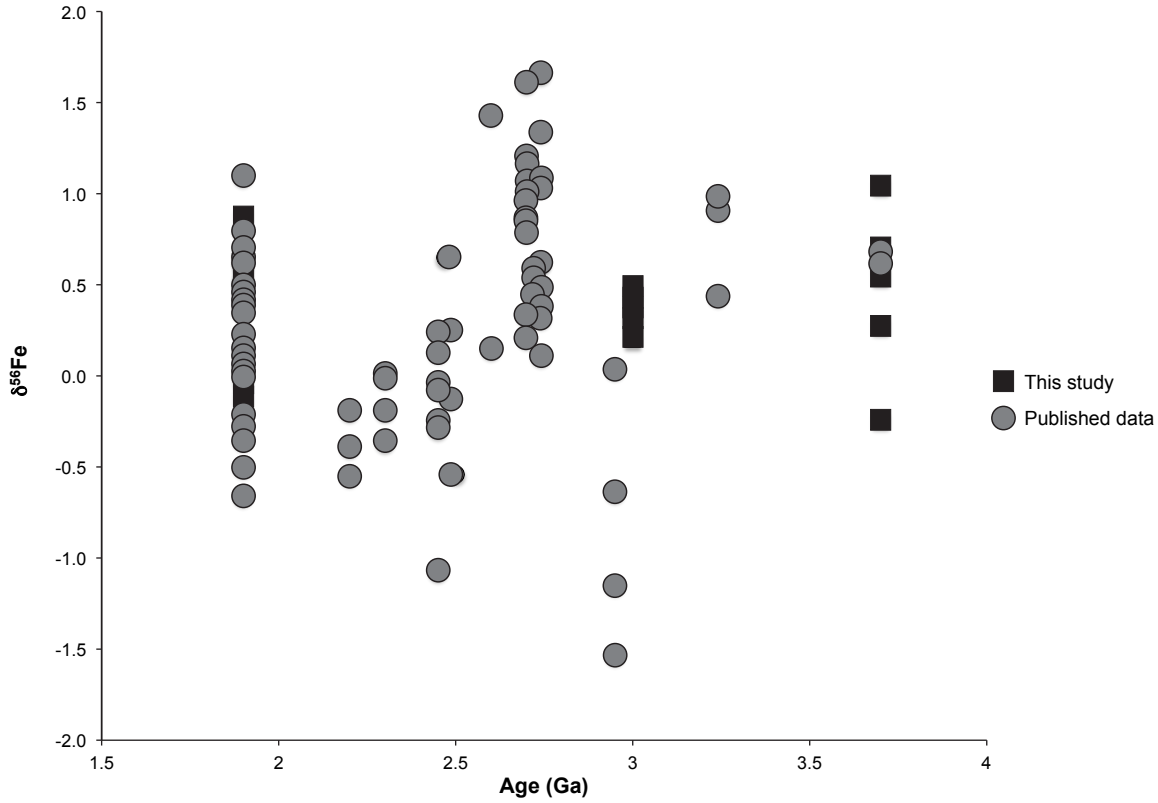



Figure 3.10. $\delta^{56}$Fe values for whole rock BIF samples used in this study collected from the IGB, BGB, and GF, as well as reported $\delta^{56}$Fe values for magnetite from Dauphas et al. (2003) and whole rock or *in situ* analyses from Czaja et al. (2004).

# Chapter IV

# Origin of >3.65 Ga Quartz-Amphibole-Pyroxene Rocks from Akilia, SW Greenland: An Integrated Field and Mineral Composition Investigation

**Abstract**

Earth's oldest (~3.8 Ga) known supracrustal rocks are exposed in SW Greenland and are composed dominantly of mafic igneous rocks, with less common sedimentary units, including banded iron formation (BIF). Unfortunately, many primary characteristics of these rocks have been overprinted during multiple high-grade metamorphic events. One example of this concerns an ~5 m thick lithology on Akilia, that is dominated by bands of quartz, amphibole, and pyroxene, interpreted by some as BIF. Correct identification of these rocks is important because they are reported to contain evidence for the oldest life on Earth. Both the age and the protolith of these rocks, however, remain uncertain. Because the quartz-amphibole-pyroxene (QAP) lithology cannot be dated directly, crosscutting relationships have been used to establish its antiquity. In the field, we observed intense foliation involving the key contact between tonalitic Amîtsoq Gneiss and mafic and ultramafic rocks of the Akilia Association used to establish the age of the QAP unit. After measuring the orientation of the foliations, mineral lineations and fold axes, data indicate that the contact in question is tectonic in nature. To investigate the possible protolith of purported BIF, we analyzed mafic mineral compositions. Ultramafic rocks from outside the QAP lithology are dominated by enstatite, anthophyllite, and hornblende and possess whole rock trace-element signatures indicative of an igneous origin. Sample AK 38, a band of mixed pyroxene and amphibole that occurs within the QAP unit, also has a whole rock trace-element composition consistent with an ultramafic protolith, but contains Fe-rich clinopyroxene. AK 38 amphiboles are dominated by actinolite, although a few analyses of anthophyllite point towards an original Mg-rich protolith. Other QAP samples contain

Fe-rich clino- and orthopyroxenes, actinolite and hornblende. A protolith consisting of ultramafic rocks with disseminated carbonate combined with a Fe-rich carbonate band, brought to granulite facies metamorphism, can produce the observed pyroxene and amphibole compositions in the QAP lithology, rendering a BIF protolith unnecessary.

## 4.1 Introduction

Sedimentary rocks have the potential to reveal conditions of the paleoenviromental settings in which they were deposited. Banded iron formation (BIF), a marine chemical precipitate, is among the oldest sedimentary rocks on Earth and have been linked to Earth's early biosphere (Cloud, 1973; Klein, 2005; Moorbath et al., 1973). Due to their age, many primary physical and chemical characteristics of Archean supracrustal rocks, of which BIF is a common component, have been hydrothermally and metamorphically overprinted. This overprinting may result in ambiguities in protolith interpretation, which may lead to the questioning of the biogenecity of any material found in the rocks.

Eoarchean rocks whose protolith identification has been particularly controversial occur on the island of Akilia, in the outer Gothåbsfjord region of SW Greenland. Rocks on Akilia (Figs. 4.1, 4.2) have experienced granulite-facies metamorphism (Brocks et al., 1999; Cloud, 1965; Mojzsis et al., 1996; Schidlowski et al., 1979; Schopf, 1993, 2006) and intense deformation (Griffin et al., 1980; Nutman et al., 1996). Within this succession, there is an ~5 m-thick banded lithology comprised mostly of quartz, amphibole, and pyroxene (QAP) interleaved between amphibolite and ultramafic rocks (Figs. 4.2, 4.3) that has been interpreted by some as BIF (Fedo and Whitehouse, 2002; Myers and Crowley, 2000; Whitehouse and Fedo, 2003; Whitehouse et al., 2009). Others have interpreted the same rocks to be mafic and ultramafic igneous rocks that have experienced repeated metasomatism, thus only superficially resembling BIF (Dauphas et al., 2007b; Dauphas et al., 2004; Friend et al., 2008; Manning et al., 2006; Mojzsis et al., 1996; Nutman et al., 2008; Nutman et al., 1997). Correct identification of the QAP

lithology is important because it locally contains grains of apatite with $^{13}C$-depleted graphite inclusions (Fedo and Whitehouse, 2002; Fedo et al., 2006; Lepland et al., 2005; Lepland and Whitehouse, 2010; Whitehouse and Fedo, 2003) that have been claimed as evidence for the oldest (> 3800 Mya) life on Earth (McKeegan et al., 2007; Mojzsis et al., 1996), despite persistent concerns about the biogenecity of the graphite (Dauphas et al., 2007b; Dauphas et al., 2004; Mojzsis et al., 1996; Nutman et al., 1997) and its age (Lepland et al., 2005; Lepland et al., 2011; Nutman and Friend, 2006; Papineau et al., 2010).

In this paper, we address the QAP protolith problem from a perspective different from past works. Namely, we integrate field and mineral compositional data along the critical geologic contacts and lithologies to address issues regarding the age and origin of the QAP unit. Structural data were collected to determine the nature (tectonic or igneous) of the critical contact used to date the QAP lithology. Whole rock geochemistry from a number of novel specimens relative to the protolith discussion sets the framework for determining mafic mineral (amphibole and pyroxene) and garnet composition by electron microprobe. The goal is for the geologic field data to be able to provide critical context for understanding mineral compositions and rock evolution.

**4.2 Controversy Defined**

The controversy about the age and protolith of rocks on Akilia has lasted more than a decade, and has resulted in extensive examination of the different lithologies with multiple approaches. Previous work on the QAP lithology includes whole-rock major- and trace-element geochemistry (Kamber and Moorbath, 1998; Whitehouse and Kamber, 2005; Whitehouse et al., 1999; Whitehouse et al., 2009), as well as use of iron and sulfur

isotopes (Bolhar et al., 2004; Dauphas et al., 2007b; Fedo and Whitehouse, 2002; Fedo et al., 2006; Friend et al., 2008), carbon isotopes (Dauphas et al., 2007b; Dauphas et al., 2004; Fedo et al., 2006; Mojzsis et al., 2003; Whitehouse et al., 2005) and geochronology (Mojzsis et al., 1996; Nutman et al., 1997; Papineau et al., 2010; Papineau et al., 2008). Despite extensive analyses, determination of the protolith and its the potential role in hosting evidence of the earliest life on Earth continues to garner considerable attention (Fedo et al., 2006; Manning et al., 2006; Mojzsis and Harrison, 1999; Nutman et al., 1997; Whitehouse et al., 1999). A fundamental aspect to understanding the protolith is to recognize that the rocks on Akilia have been repeatedly metamorphosed and deformed at high temperatures and pressures, reaching granulite facies (Lepland et al., 2011; Lepland and Whitehouse, 2011; McKeegan et al., 2007; Papineau et al., 2010; Papineau et al., 2008) (T = 650-700 ºC, P = 8-10 kb; Griffin et al., 1980). Consequently, all Eoarchean lithologies in this area are strongly foliated (Fig. 3.1; Myers and Crowley, 2000; Whitehouse and Fedo, 2003) and mineral phases have been coarsely recrystallized.

Several lines of evidence have been used to infer a BIF origin for the QAP lithology, all of which have been debated. A BIF protolith has been inferred from the occurrence of fine-scale banding, which has been interpreted as depositional layering (e.g., Fedo and Whitehouse, 2002; Myers and Crowley, 2000). Alternatively, this banding has been interpreted as a high-strain foliation (Anbar et al., 2001; Friend et al., 2008; Mojzsis et al., 1996; Mojzsis and Harrison, 1999; Nutman et al., 1997). Although BIFs may have equant crystals of quartz and iron oxides, the rocks on Akilia display a coarse granoblastic texture, with abundant, mm-scale, clear quartz crystals that display 120º triple junctions consistent with strong recrystallization and reequilibration during later

metamorphic events (Fedo and Whitehouse, 2002; Myers and Crowley, 2000; Whitehouse and Fedo, 2003; Whitehouse et al., 2009). Whole rock rare earth element (REE) patterns have been variously interpreted as supporting (Fedo et al., 2006) and not supporting (Manning et al., 2006; Mojzsis and Harrison, 2002) a BIF protolith. Adding to the debate has been whether specific sulfide minerals carry a mass independent fractionation (MIF) S signature (Bolhar et al., 2004; Fedo and Whitehouse, 2002) or not (Mojzsis et al., 2003), and when the sulfide minerals were formed (Whitehouse et al., 2005).

Different isotopic systems have also been used to investigate the origin of the QAP rocks, with one system ($\delta^{56}Fe$) providing data favoring a BIF protolith, another system ($\delta^{30}Si$) providing data favoring an ultramafic protolith, and a third system ($\delta^{18}O$) remaining inconclusive. Dauphas et al. (Fedo et al., 2006) suggested that fractionated Fe isotopes ($\delta^{56}Fe$ >0 ‰) in Akilia samples were consistent with a BIF origin based on the near-constant $\delta^{56}Fe$ = 0 ‰ of igneous rocks formed at different times, locations and tectonic settings. However, silicon isotopes of quartz from QAP rocks ($\delta^{30}Si$ = -0.36 ‰) are more similar to metamorphic-derived quartz ($\delta^{30}Si$ = -0.50 ‰), supporting tectonic reworking and silica metasomatism of an ultramafic protolith rather than a primary chemical sedimentary origin (2004). Oxygen isotope compositions of quartz crystals from the QAP lithology had a consistent $\delta^{18}O_{SMOW}$ = +12 ‰, which is significantly lower than uncontested BIF found at Isua and are more similar to those found in granites and pegmatites (André et al., 2006), and so provides no specific QAP protolith answers.

In another argument, the incorporation of carbonate minerals has been used to explain the appearance of Fe-Mg minerals in the purported BIF. Following the work of Rosing et al. (Fedo et al., 2006; van Zuilen et al., 2002), Dauphas et al. (1996) suggested that the supracrustal rocks on Akilia had been modified by carbonate metasomatism, which resulted in QAP and other lithologies integrating dolomite and calcite. Dauphas et al. (2004) used this processes to explain the presence of Fe-Mg minerals, suggesting that progressive granulite-facies metamorphism under low oxygen fugacity of such mineral assemblages would lead to pyroxene formation. However, in the absence of compositional constraints on amphiboles and pyroxenes on Akilia, specific reactions were not reported. As a result, many aspects about the QAP rock remain poorly resolved.

**4.3 Geologic Setting**

The complex tectonothermal history of the Eoarchean rocks of the outer Gothåbsfjord, southwest Greenland has been well documented. Granulite and amphibolite facies metamorphism and intense deformation occurred at ca. 3.6 Ga (2004) and 2.7 Ga (Friend and Nutman, 2005; Griffin et al., 1980), respectively. Archean rocks in this area have also been affected by the intrusion of doleritic Ameralik dykes at ca. 3.3-3.5 Ga (Nutman and Friend, 2007) and Qôrqut granite at ca. 2.55 Ga (Nutman et al., 2004). In addition, there was a thermal event disturbing some isotopic systems at ca. 1.6-1.7 Ga (Baadsgaard et al., 1976).

This complex history has resulted in complex lithologic relationships that are difficult to unravel. Rocks on Akilia include two main lithologic assemblages. The most abundant is the ~3.65-3.85 Ga tonalitic Amîtsoq Gneisses (Fig. 4.2; Pankhurst et al., 1973; Whitehouse et al., 2009). The second assemblage, termed the Akilia Association

(Whitehouse et al., 2009), consists of predominantly coarse-grained mafic and ultramafic supracrustal rocks (Fig. 4.2), which is generally assumed to be older than the Amîtsoq Gneisses, but could be younger (McGregor and Mason, 1977). The contact between the Amîtsoq Gneisses and the Akilia Association remains intact (Fig. 4.2) and is crucial for the determination of the age of QAP unit.

Regionally, both uncontested BIF and volcanic rocks are present within the Akilia Association. The banded, 5 m thick QAP lithology that lies within the Akilia Association occurs sandwiched between homogeneous amphibolite to the southwest and ultramafic rocks to the northeast (Figs. 4.2, 4.3). Gneissic banding within QAP is parallel with adjacent schistosity (Whitehouse et al., 2009) and intense deformation has resulted in segmentation, stretching and boudinage of the bands (Fedo and Whitehouse, 2002; Myers and Crowley, 2000; Whitehouse and Fedo, 2003). The QAP lithology has magnetite abundances of 10 % within a few amphibole- and pyroxene-rich bands, but most parts of the unit contain magnetite only in trace amounts (Fedo and Whitehouse, 2002).

Evidence of alteration is present in a variety of different locations on Akilia. Younger veins of quartz ± amphibole ± garnet are found within shear-zones that crosscut banding within the QAP unit (Fedo and Whitehouse, 2002; Lepland and Whitehouse, 2010) and alteration is present on both sides of these veins where they crosscut the QAP lithology. Alteration can also be seen north and south of the QAP unit (Lepland and Whitehouse, 2010). In places where bodies of interleaved Akilia Association and Amîtsoq Gneiss are crosscut by younger, 2.5 Gya Qôrqut granite (Fig. 4.3A), reaction rims are present, with rocks in the QAP until being coarser grained and preserving an increase in the amount of potassium feldspar (Fig. 4.3A; Whitehouse et al., 2009).

## 4.4 Analytical Methods

Polished thin sections of field samples were examined to study petrographic characteristics (textures and compositions) using reflected-, incident-, and transmitted-light microscopy and using an electron probe microanalyzer (EPMA, Cameca SX50 and SX100) at the University of Tennessee, Knoxville. Mineral compositions were determined using wavelength dispersive spectrometry (WDS), with an accelerating potential of 15 kV, a 20 nA beam current, 2 μm beam size, and standard ZAF (PAP) correction procedures for all silicate minerals. Peak and background counting times were 20-30 s, and data quality was maintained by analyzing a combination of synthetic oxide and natural mineral standards. Drift was within counting error throughout every analytical session. Analytical errors (1σ) are due to counting statistics. Detection limits (3σ background) are typically <0.03 wt. % for $SiO_2$, $TiO_2$, $Al_2O_3$, MgO, CaO, $Na_2O$, $K_2O$ and $P_2O_5$, and <0.05-0.1 wt. % for FeO, MnO, $Cr_2O_3$, NiO and $V_2O_5$.

X-Ray diffraction (XRD) data were collected from $2^o$ to $82^o$ 2θ with a step size of $0.02^o$ and scanning speed of $10^o$ per minute using a Rigaku Rotaflex diffractometer operating at 45 kV accelerating voltage and 160 mA beam current, with a rotating-anode Co source (Co Kα, λ=1.7902 Å) at the University of Western Ontario. Diffractograms were analyzed using BrukerAXS EVA software and the International Center for Diffraction Data Powder Diffraction File (ICDD-PDF).

## 4.5 Field Relationships

A critical component to the claim that the QAP unit houses the oldest evidence of life on Earth is the age of the rocks, which has proved difficult to determine given the polyphase high-grade metamorphism that has reset zircon ages (Whitehouse et al., 2009).

An assumption used in earlier attempts to date these rocks was that the QAP unit was an integral part of a volcano-sedimentary succession with adjacent mafic and ultramafic rocks, whose minimum age could be determined from the age of cross-cutting tonalitic gneiss (Fedo et al., 2006; Whitehouse et al., 2009). After detailed mapping, Manning et al. (Manning et al., 2006; Mojzsis et al., 1996; Nutman et al., 1997) described the cross-cutting unit as heterogeneous quartzfeldspathic orthogneisses (*Ogn*) of the Amîtsoq Gneisses. Myers and Crowley (2006), who investigated the geology and structure of the QAP until and their regional context, demonstrated that both the age and origin of these rocks were in doubt. Understanding the contact between the tonalitic Amîtsoq Gneisses and the mafic and ultramafic rocks of the Akilia Association (Fig. 4.2) is critical to constrain the geology, age and origin of the QAP lithology. If the contact is not cross cutting, the Amîtsoq Gneisses provide no constraint on the age of supracrustal formation, leaving the age of the QAP unit unresolved.

The contact between the tonalitic Amîtsoq Gneisses and the mafic and ultramafic rocks of the Akilia Association is difficult to interpret. Fedo et al. (2006) highlighted that much of this debate centered on a single exposure where a clear example of the key crosscutting relationship was unmistakably tectonic in nature (Fig. 4.2). Myers and Crowley (2000) mapped the outcrop of this contact at a scale of 1:12 (see their Fig. 9, p. 116) and observed that the compositional layers in the *Ogn* parallels foliation in the tonalitic Amîtsoq Gneisses and the gneissosity in the adjacent mafic and ultramafic units. Whitehouse et al. (2009) supported this conclusion by considering the contact between the tonalitic gneiss and mafic and ultramafic rocks to most likely represent a deformed fault or unconformity rather than an intrusive contact. A strong co-axial deformation

resulting in penetrative tectonic fabric dominates the regional geology and most rocks on Akilia preserve evidence for repeated intense ductile deformation, making it difficult to establish true cross-cutting relationships (2000).

This study aims to shed additional light on the tectonic nature of the contact by examining the strike and dip of foliations and fold axial planes, and the trend and plunge of mineral lineations and fold axes within the Amîtsoq Gneisses (*Ogn*) and the Akilia Association (Fig. 4.2). The key discordance between the tonalitic Amîtsoq Gneisses (*Ogn*) and mafic and ultramafic gneiss that contains the QAP rocks is a fold, thus making it a tectonic contact (Fig. 4.4A, B). The rocks surrounding the key cross-cutting contact are comprised of structurally interleaved amphibolites of the Akilia Association and Amîtsoq gneiss, as well as vein quartz, all which show evidence of intense deformation (folding, mineral elongation lineations; Fig. 4.4C, D).

Structural data for both the Amîtsoq Gneisses and Akilia Association on both sides of the key contact show the same orientations. Foliation planes in both units consistently strike NNW-SSE and dip towards the W (Fig. 4.5A). Axial-surface data of cm-scale folds in both the Amîtsoq Gneisses and Akilia Association indicate folds that strike NE-SW and dip SE (Fig. 4.5B). Fold axes in both the Amîtsoq Gneisses and Akilia Association plunge gently to the SW (Fig. 4.5B). Because all 43 fold axes data points plot very close to each other, it can be assumed that these folds were parallel. Mineral lineations in both the Amîtsoq Gneisses and Akilia Association trend SW and plunge gently to moderately in the same direction as the fold axes (i.e., towards the SSW; Fig. 4.5A, B). The lineations correspond directly with the fold axes data, which implies that either the mineral lineations are linked to the same deformation event that created the

folding or that the two formed during different events and then rotated towards parallel during a later event. The parallel deformation between the Amîtsoq Gneisses and Akilia Association indicates that the relationship seen today between the two units is tectonic. Any previous relationships have been erased during high temperature and pressure deformation and metamorphism, which strongly affected both the Amîtsoq Gneisses and Akilia Association. As a result, no original relationships between the two units can be determined. The data presented here corresponds best with the tight asymmetrical refolding (F3) event that refolded the large isoclinal fold (Fig. 4.2; Fedo et al., 2006; Myers and Crowley, 2000; Whitehouse and Fedo, 2003; Whitehouse et al., 2009). A strong strain gradient is present across the F3 fold hinge, allowing for the better preservation of geometric relations in the western part of Akilia where strain is comparably low (Manning et al., 2006; Whitehouse et al., 2009). As there is no clear cross-cutting relationship and because the contacts between the Amîtsoq Gneisses and Akilia Association are tectonic, there is very little field evidence for understanding the age or potential protolith of the QAP lithology. The tectonic nature of the crucial contact also suggests a broader tectonic overprint on all of the rocks in the area, including the QAP lithology, which adds to the controversy over the unit's origins. Examination of the mineral composition of samples from the QAP outcrop and surrounding rocks, relative to the composition of BIF and ultramafic rocks from elsewhere in the Isua Greenstone Belt (IGB), may shed light on the protolith of QAP.

## 4.6 Study Samples and Petrography

### *4.6.1 Sample Justification*

The samples analyzed for this study come from both the island of Akilia and the mainland Isua Greenstone Belt (IGB). Akilia samples were collected from throughout the 5-m thick QAP lithology, as well as from the adjacent ultramafic and amphibolite layers (Fig. 4.3). Samples from the IGB were included as analogues for the potential protolith of the debated QAP rocks.

### *4.6.2 Akilia*

The QAP unit exhibits layering consisting typically of mm- to cm-thick mixed bands of clinopyroxene (cpx), ± orthopyroxene (opx), and amphibole (hornblende (hbl), actinolite (act), and cummingtonite (cum)) alternating with cm-thick bands of coarse-grained clear quartz (Manning et al., 2006). Samples contain 60-80 % quartz and 20-40 % pyroxenes and amphiboles. Magnetite is typically only found in trace amounts (<1 %), except in two sub-units (AK 33 and AK 43) where the magnetite (5-10 %) occurs as thin bands within the amphibole-pyroxene bands (Fig. 4.6A, E, F). Also present are trace amounts of apatite, calcite, garnet (AK 33 and AK 48), and pyrrhotite. QAP rocks possess a coarse granoblastic texture, with polygonal interlocking grains that commonly intersect at 120º triple junctions (Fig. 4.6A, C, D, E, F). Exsolution lamellae are present in both some of the opx and cpx grains; however the lamellae were too narrow to analyze separately. No zonation was observed in either the pyroxenes or amphiboles, suggesting probable homogenization during one of the episodes of granulite facies metamorphism known to have affected the unit.

Sample 92-197 (Fig. 4.7A) correlates with the widely publicized G91-26 (Fig. 4.3; Fedo and Whitehouse, 2002; Lepland and Whitehouse, 2010). Based on whole rock major-element and REE geochemistry (Table 4.1, 2; Fig. 4.5), the closest *in situ* equivalent of 92-197 is AK 33 of Fedo and Whitehouse (Mojzsis et al., 1996). Sample 92-197 contains approximately quartz (60 %), pyroxene (orthopyroxene and clinopyroxene) (25 %), amphibole (high- and low-Ca) (15 %) and magnetite (1 %). Minor (<1 %) components include pyrite, calcite, and apatite. Half of the sample is coarsely crystalline, magnetite poor, and dominated by clinopyroxene (cpx) and quartz (Variant 1; Fig. 4.7B). The other half is more fine-grained, magnetite is present, and orthopyroxene (opx), quartz, and amphibole is dominant (Variant 2; Fig. 4.7C). Quartz and pyroxene grains are aligned in bands. Both clinopyroxene and orthopyroxene contain exsolution lamella and twinning.

Across the 5-m thickness of QAP, sample AK 33 is one of the few samples that contains modal magnetite (5-10 % of the sample). The sample comes from 0.5 m from the contact with the ultramafic schist (Fig. 4.3) and is composed predominantly of amphibole (high- and low-Ca) (30 %), clinopyroxene (30 %) and quartz (40 %), with lesser amounts of magnetite (5 %) and garnet (1 %) (Fig. 4.6A, B). A reaction rim of amphibole occurs around the garnet (Fig. 4.6B), suggesting it formed at the same time as the pyroxene and amphibole (Fig. 4.6B).

Sample AK 38 was collected from the least structurally compromised subunit within the QAP lithology (Fig. 4.3B). This sample comes from an ~5 cm thick layer that is concordant with local foliation and consists mainly of amphibole originating during retrograde metamorphism (Fedo and Whitehouse, 2002). It is comprised predominately

of amphibole (high- and low-Ca) (70%) and clinopyroxene (25%), with a lower concentration of quartz (5%) than is seen in other samples from the QAP unit.

Sample AK 02 was collected from ultramafic rocks several meters north of the QAP lithology (Fig. 4.3A) and is dominated by amphibole and pyroxene, with minor (<1 %) amounts of magnetite, pyrrhotite, olivine, chlorite and titanite. The banding in the QAP lithology is concordant with schistosity developed in the ultramafic unit from which AK 02 was collected. While the presence of magnetite bands at some levels in the QAP rock has been cited as evidence of a sedimentary origin, it is important to note that magnetite also occurs in AK 02 and represents a potential product of the metamorphic breakdown of siderite (Lepland and Whitehouse, 2010) or from serpentinization of olivine-rich precursors (Perry and Ahmad, 1977).

### *4.6.3 Isua Greenstone Belt (IGB)*

The >3.7 Ga IGB is located within the Archean high-grade gneiss complex of SW Greenland and forms an arcuate belt ~35 km long by several km wide (Fig. 4.1). A large lake separates the western and eastern parts of this belt. Two samples (IS-X and IS-Y) were collected from an island located within this lake. Samples consist of buff dolomite intercalated with green amphibole. Large lenses of ferroan dolomite and carbonate veins, lenses, and mm-scale disseminations are pervasive. Sample IS-X consists of high- and low-Ca amphibole (50 %) mixed with disseminated ferroan dolomite (45 %), and lesser amounts of quartz, plagioclase feldspar, and micas (Fig. 4.8A), whereas IS-Y is comprised almost entirely of ferroan dolomite (90 %), with minor amounts of high-Ca amphibole (10 %), quartz, and plagioclase feldspar (Fig. 4.8B).

## 4.7 Whole Rock Chemistry

### *4.7.1 Akilia*

Whole rock chemical trends for major and trace elements, as well as the rare earth elements (REE), for the QAP unit have been discussed elsewhere (Holm and Charlou, 2001). We summarize this work to provide context for new mineral composition data reported here. Lepland and Whitehouse (2010) suggested sample AK 38 to be the most retrogressed sample among all they analyzed, consisting almost entirely of hornblende, which had a higher Ti and Cr content (Table 4.1) than other samples with a retrograde mineral assemblage. Sample AK 38, which has been considered a proxy for the QAP protolith (Bolhar et al., 2004; Fedo and Whitehouse, 2002; Fedo et al., 2006), has trace-element geochemistry similar to that of the surrounding ultramafic rocks (i.e., AK 02; Table 4.1). The Th/Sc, Cr/Th, and Cr ratios are all very different from BIFs in the Isua Greenstone Belt. Conversely, Mojzsis and Harrison (Fedo and Whitehouse, 2002) considered AK 38 to be a secondary pyroxenite vein because of its concave downward PAAS-normalized REE pattern (Fig. 4.9), and thus petrogenetically unrelated to the rest of the QAP lithology. This includes sample 92-197, even though there is a distinct concave down pattern for QAP rocks 92-197 and AK 33. Whole rock geochemistry for AK 33 (Table 4.2) shows a roughly equal amount of Mg (5.53 wt. %) and Ca (7.33 wt. %). Other whole rock geochemistry that has been previously reported includes that of AK 02, a sample from the ultramafic layer adjacent to the QAP lithology, which shows a high Mg (22.35 wt. %) and Al (7.35 wt. %) content (Table 4.2). These ultramafic rocks have enriched LREE abundances (Fig. 4.9) and are considered a sink for LREE

remobilized from the QAP unit during retrograde alteration and metasomatism (Fedo and Whitehouse, 2002).

### *4.7.2 Isua Greenstone Belt*

Sample IS-X is amphibole schist with disseminated ferroan dolomite (Fig. 4.8A), whereas IS-Y is comprised almost entirely of ferroan dolomite (Fig. 4.8B). Sample IS-X has a considerably greater Si content than IS-Y because of the increased presence of silicate minerals, but both samples have similar Mg and Ca abundances (Table 4.2). While their trace-element concentrations are similar to 92-197 (Table 4.1), both IS-X and IS-Y REY profiles vary, with more prominent Eu and Y anomalies and HREE enrichment compared to 92-197 and other QAP samples (Fig. 4.9). REE data were normalized to Post-Archean Australian Average Shale (PAAS) because it is a reference standard that has an average crustal composition that is most compatible with the samples. Ferroan dolomite compositions were determined by both XRD and EMPA.

## 4.8 Mineral Chemistry

### *4.8.1 Quartz-Amphibole-Pyroxene Rock (QAP)*

#### *4.8.1.1 Pyroxene*

Clinopyroxene is the dominant pyroxene composition found in the QAP samples, being present in all samples (Figs. 4.10A-E); orthopyroxene only occurs in two samples (92-197 and AK 43; Fig. 4.10D, E). Except for AK 38, clinopyroxenes in the QAP suite have similar compositions of $En_{25}Wo_{47}Fs_{28}$ to $En_{27}Wo_{37}Fs_{36}$ (Fig. 4.10A). XRD analysis was used to confirm the composition of clinopyroxene in sample AK 33, where augite was the dominant form. Minor elements ($Al_2O_3$, $Cr_2O_3$, and $Na_2O$) are typically low (<0.5 wt. %) in the QAP pyroxene (Table 4.3). Orthopyroxene has a composition near

$En_{30}Wo_1Fs_{69}$ (Fig. 4.10A, C, D, and E). Clinopyroxene in AK 38 exhibits slightly higher En component ($En_{32}Wo_{47}Fs_{21}$) than those in the other QAP samples (AK 33, 92-197, 42, and 33).

*4.8.1.2 Amphibole*

Both high- and low-Ca amphibole is found in all QAP samples except AK 43, which only contains low-Ca amphibole (Fig. 4.11). All the iron in amphibole is calculated as ferrous in this study, although ferric iron can be dominant in high-Ca amphiboles. Actinolite and hornblende are present as high-Ca amphiboles in the QAP suite. Cummingtonite is present as the low-Ca amphibole, as confirmed by XRD analysis in sample AK 33 Similar to the pyroxene, each of the low- and high-Ca amphibole in AK 38 is generally more magnesian than those in the other QAP samples (Fig. 4.11A-D, F-G and Table 4.4). Actinolite shows variable compositions, with a higher Mg# (43-62) compared to other QAP samples (Mg# = 30-45) and Cummingtonite has Mg# = 47 (molar ratio of $Mg/[Mg+Fe^{2+}]*100$), while those in the other QAP samples have Mg# of 33-36.

***4.8.2 QAP – Ultramafic Contact Zone (AK 30)***

Sample AK 30 was collected across the contact between the distinct hornblendite unit and the QAP unit (Fig. 4.3). The ultramafic component is dominated by amphibole (80 %) and quartz (20 %), with trace amounts of titanite, while the QAP portion of the sample is predominantly quartz (80 %) with a few thin bands of amphibole (20 %). All of the amphibole found in this sample is Ca-rich (Fig. 4.11B), where hornblende is the most common (Table 4.4) and has an average $Mg_{50}$. The next most common amphibole

is actinolite, a low-Al, high Ca variety, comprised of $SiO_2$, FeO, MgO, CaO, but only 4 wt. % $Al_2O_3$ (Fig. 4.11B; Table 4.4). The actinolite has a greater $Mg_{49\text{-}65}$.

### *4.8.3 Ultramafic Rock (AK 02)*

Ultramafic rocks (represented here by sample AK 02) are located north of QAP (Fig. 4.3) and are predominantly comprised of amphibole and pyroxene (orthopyroxene, ~ 95 %), with lesser amounts of quartz (5 %) and magnetite (1 %) (Fig. 4.12A). Trace amounts (< 1 %) of pyrrhotite, titanite, mica, and sulfides are also present in the sample (Fig. 4.12B). No distinct banding is observed at either the field or thin-section scale. Both low- and high-Ca amphibole (hornblende and cummingtonite) is present in the ultramafic suite. The minerals have a homogeneous composition in terms of both major and minor elements (Fig. 4.11A; Table 4.4) and show similar $Mg_{80}$, which is distinctly more magnesian than those in the other suites. Orthopyroxene (Fig. 4.10A; Table 4.3) also has a homogeneous composition in terms of both major and minor elements, a composition near $En_{77}Wo_{<1}Fs_{23}$, and ~1.5 wt. % $Al_2O_3$, which is distinctly higher than those in pyroxene from the QAP and amphibolite suites (Table 4.3). Low-Ca pyroxene is rare in the sample (Fig. 4.10A).

### *4.8.4 Amphibolite (AK 47)*

Amphibolite facies occur southwest of the QAP unit (Fig. 4.3) and are composed of amphibole (hornblende, 70 %), with lesser amounts of plagioclase (20 %), pyroxene (5 %), and quartz (5 %) (Fig. 4.12E, F). Trace amounts (< 1 %) of apatite, magnetite, and pyrrhotite are also present. Only Ca-rich amphiboles are present (Fig. 4.11A, I). The hornblende is similar to hornblende found in samples from the QAP lithology (Table 4.4), however the actinolite has a higher Ca component and Mg# than those in the QAP

samples (Table 4.4). Only clinopyroxene is present in the sample (AK 47; Fig. 4.10A, F) and has a homogeneous composition $En_{25}Wo_{45}Fs_{30}$, which is similar to the clinopyroxene in the QAP suite (except AK 38) (Table 4.3). $Al_2O_3$ content in clinopyroxene from this sample is higher than those in the QAP suite, but lower than those in the ultramafic unit (AK 02).

### *4.8.5 Garnet-Bearing Rock (AK 33 and AK 48)*

Garnets are comprised predominantly of FeO (30 wt. %) and $Al_2O_3$ (21 wt.%), with lesser amounts of CaO (8 wt. %) and MgO (2 wt.%) (Fig. 4.13; Table 4.5). They have an almandine composition and several occurrences in the studied area; one locale within sample AK 33 from the primary QAP unit and another in a shear zone that cross cuts the QAP unit. Sample AK 33 is one of the QAP samples that contain a modal amount of magnetite and is comprised of approximately 50 % quartz, 25 % amphibole, 20 % clinopyroxene, 5 % magnetite and <1 % garnet. Only clinopyroxene is found in AK 33. They have a homogenous composition of $En_{25}Wo_{47}Fs_{29}$ (Fig. 4.10A, B; Table 4.3), which is most similar to the clinopyroxenes found in the adjoining amphibolite unit ($En_{25}Wo_{45}Fs_{30}$) and other layers in the QAP unit, except for AK 38 (Table 4.3). Both high- and low-Ca amphibole phases are present in AK 33, with the former having $Mg_{30-47}$ and the latter having a homogenous $Mg_{37}$. The reaction rim present around the garnet (Fig. 4.7B) contains high-Ca amphibole rich in $Al_2O_3$, ranging from 6-10 wt. %; the rest of the amphibole phases (both high- and low-Ca) have an $Al_2O_3$ content of <2 wt. %.

Sample AK 48 comes from one of the N-striking, steeply dipping, apparent right-lateral, centimeter-wide shear zones with a very small amount of displacement that cross-cut the amphibolite, ultramafic and QAP units (Fedo and Whitehouse, 2002; Lepland and

Whitehouse, 2010; Manning et al., 2006). The sample was collected from where the shear zone cuts across the QAP lithology (Fig. 4.3), as this is the only place where millimeter-scale garnets are present in the shear zone. Sample AK 48 is dominated by quartz (70 %), amphibole (15 %) and garnet (15 %). The amphiboles are predominately high-Ca (hornblende), however some low-Ca grains (cummingtonite) are present (Fig. 4.10I). Garnets have a homogeneous almandine composition, dominated by FeO (29 wt. %), $Al_2O_3$ (21 wt. %), with lesser amounts of CaO (6 wt. %), MgO (3 wt. %) and MnO (2 wt. %) (Fig. 4.13).

### *4.8.6 Carbonated Mafic Rocks from Isua Greenstone Belt (IS-X and IS-Y)*

Two samples from the IGB that contain varying degrees of carbonate were examined in the study to be used as a potential protolith analog for the QAP unit. Sample IS-X is comprised of magnesiohornblende (60 %), with ferroan dolomite (40 %) disseminated throughout the sample (Fig. 4.8A). Sample IS-Y is dominantly ferroan dolomite (90 %), with the amphibole component being significantly less (10 %) (Fig. 4.8B). Amphiboles form the only Fe-Mg minerals found in both samples. Sample IS-X contains only Ca-rich amphiboles, which are dominated by $SiO_2$, MgO, CaO, FeO and $Al_2O_3$ and have an average $Mg_{78}$. Sample IS-Y contains both Ca- and Mg-rich amphiboles (Fig. 4.11), with the Ca-amphiboles having the same elemental distribution as those in IS-X, but having a slightly lower $Mg_{75}$. The Mg-amphiboles are comprised of $SiO_2$, FeO, MgO, and CaO, with a lesser amount (<1 wt. %) of $Al_2O_3$ and a lower $Mg_{59}$. Along with identifying the magnesiohornblende and ferroan dolomite in both sample, the XRD data also identified trace amounts of magnesium calcite and quartz.

## 4.9 Discussion

### *4.9.1 Structural Evidence for Pervasive Deformation*

A sedimentary protolith interpretation for the QAP lithology has been partially based on apparent well preserved layering of QAP (Fig. 4.3; Fedo et al., 2006). Upon closer inspection, the ubiquitous banding of all rocks older than 2.7 Ga on Akilia represents foliation rather than sedimentary layering. In addition, there are abundant small-scale deformational features (penetrative foliations, pinch-and-swell structures, boudinage, shear zones, mineral filled brittle fractures) found throughout QAP (Fedo and Whitehouse, 2002), which suggests that visible banding is unlikely to represent primary sedimentary layers.

Previously reports of a clear cross-cutting intrusive relationship used to establish the minimum age of the QAP lithology also contrasts starkly with the pervasive and intense deformation that is evident from structural analysis. The critical "cross-cutting" contact is clearly tectonic in nature with no apparent igneous precursor, and thus provides no constraint on the depositional age of the QAP unit. On either side of the crucial contact, both the Amîtsoq Gneisses and the Akilia Association show the same intense deformation structures, with parallel foliation planes, fold axes, and mineral lineations regardless of their position relative to the contact. There is such a heavy structural overprint that the only contact features that can be seen today are those generated after the rocks came together. This structural data permit an interpretation that the rocks were previously in contact, but then deformed together, or perhaps brought together by that deformation. Intense deformation in the area would also permit the transformation of a

unit of ultramafic rocks into a lithology with mm-scale layering that superficially resembles BIF.

### *4.9.2 Does the Mineralogy Support a BIF Protolith?*

It has been argued that the QAP unit contains metamorphosed BIF that was originally composed only of quartz and magnetite (Dauphas et al., 2007b; Dauphas et al., 2004; Friend et al., 2008; Manning et al., 2006; Mojzsis et al., 1996; Nutman et al., 2008; Nutman et al., 1997). Starting with this original mineralogy, it would be expected that the composition of the pyroxene in the now present metamorphosed QAP rock would be ferrosilite following equation 1 (Mojzsis et al., 1996):

(eq. 1) $2Fe_3O_4$ (magnetite) + $6SiO_2$ (quartz) = $3Fe_2Si_2O_6$ (ferrosilite) + $O_2$

Based on the results of the present study, it is not possible for the protolith of QAP to have contained only quartz and magnetite because samples do not contain ferrosilite. Furthermore, high-Ca pyroxene are abundant, and there is a distinct enstatite component to the mafic minerals. Nutman et al. (1997) did observe and analyze ferrosilite in samples from the QAP lithology, suggesting potential variability across the QAP unit, but they also observed and analyzed orthopyroxene (eulite) and amphibole (grunerite), which were not observed in this study. Another possible result of the original protolith being comprised of only quartz and magnetite could be the product of metamorphic fayalite, based on the following equation 2 (Nutman et al., 1997):

(eq. 2) $2Fe_3O_4$ (magnetite) + $3SiO_2$ (quartz) = $3Fe_2SiO_4$ (fayalite) + $O_2$

However, after thorough petrographic and mineral chemistry analyses, no olivine was found in any sample of QAP.

Dauphas et al. (2007a) recognized that the supracrustal rocks in Isua have been influenced by carbonate metasomatism, which resulted in the BIF incorporating dolomite and calcite. They suggested that progressive granulite-facies metamorphism under low oxygen fugacity, such as the conditions experienced by the QAP rocks on Akilia, of carbonate metasomatized BIF would lead to the formation of pyroxene. However, the specific compositions of such pyroxene was not discussed in their study, thus making it hard to compare the pyroxene formation mechanism presented in Dauphas et al. (2004) with the pyroxene compositions examined in this study. Other studies have also suggested the pervasive carbonate metasomatism in the lower grade IGB (Dauphas et al., 2004), lending support to the idea of post-formational compositional change.

### *4.9.3 Compositional Evolution – From an Ultramafic Protolith to the QAP Lithology*

Based on the current research and available scientific literature, there are two possible protoliths for the QAP lithology: BIF or ultramafic rocks. In order to produce the current QAP mineralogical composition from a BIF protolith, a great deal of magnetite would have to be removed and both Ca and Mg would need to be added. The addition of Ca and Mg could be accomplished through the addition of dolomite during carbonate metasomatism. However, if BIF from the IGB is used as reference protolith, BIF and carbonate are not typically found together. The thickest BIF accumulation within the IGB occurs as prominent outcrops at the far NE terminus of the IGB, where very little carbonate is preserved (Rose et al., 1996; Rosing et al., 1996; van Zuilen et al., 2003). Carbonate is most commonly associated with ultramafic lithologies in the IGB (Fig. 4.1; Myers and Crowley, 2000).

In order to produce the current QAP mineralogical composition from an ultramafic protolith, both Ca and Fe would need to be added. The presence of almandine garnet in samples AK 33 and AK 48 (Fig. 4.13) provides evidence for post-depositional Fe mobility and enrichment. If there were a later Mg mobility and enrichment, as would be necessary if the QAP protolith was BIF, garnets with a pyrope composition might be expected. Additional support for later Fe mobility comes from the comparison of whole rock Mg/Fe ratios. The ultramafic AK 02 sample, as expected, has a higher Mg/Fe ratio compared to QAP samples (Table 4.2). If the QAP protolith was ultramafic, this decrease in the Mg/Fe ratio could be explained by the addition of Fe. Minor amounts of magnetite are found in samples 92-197, AK 33, and AK 43, which could have formed through the decarbonation of siderite (Rose et al., 1996; Rosing et al., 1996; van Zuilen et al., 2003):

(eq. 3) $6FeCO_3 \rightarrow 2Fe_3O_4 + 5CO_2 + C$

A minor amount of magnetite has been found in AK 02, providing evidence that this reaction may have taken place in ultramafic rocks on Akilia.

Sample AK 38 appears to be the critical sample that links a possible ultramafic protolith to the rest of the QAP rocks. The layer from which this sample was collected is the thickest (5 cm), most structurally intact layer of the QAP outcrop, and lacks evidence for boudinage, pinch-and-swell structures, or quartz infiltration. This may explain why this layer is less affected by reactions with disseminated carbonate and fluids moving through the rock. Geochemically, AK 38 looks more like an ultramafic rock (AK 02) than any other subunit of the QAP outcrop (French, 1971; Lepland et al., 2002; Lepland and Whitehouse, 2011; Perry and Ahmad, 1977; van Zuilen et al., 2002). When REY

patterns are compared, samples AK 02 and AK 38 are nearly identical (Fig. 4.9). When compatible element (Cr, Sc, Sr, Co, V, and Zn) concentrations are compared, AK 38 is more similar to AK 02 than other QAP subunits (Table 4.1). Others have observed this trend as well, specifically when ratios of compatible to incompatible elements are compared. Fedo and Whitehouse (2002; see their Fig. 3B) plotted Th/Sc vs. Cr/Th and found AK 38 to plot with Akilia ultramafic rocks and Archean komatiite; IGB BIF samples plotted in a different field. When the whole rock Mg/Fe ratios are examined more closely, AK 38 again sits in between the ratio of AK 02 and the other QAP samples (Table 4.2). Lastly, when the whole rock Al contents of the samples are compared, AK02 is the most enriched, followed closely by AK 38, and then the other QAP samples (Table 4.2). High Al content in Archean ultramafic komatiites is well documented (Fedo and Whitehouse, 2002). Rocks with a BIF protolith would be expected to have a low Al content. However, Isua rocks with a clear non-BIF protolith (i.e., IS-X and IS-Y) also have a low whole rock Al content, as well as low-Al amphiboles and pyroxenes (Table 4.2, 4.3 and 4.4; Figs. 4.6, 4.10). The lower Al content in AK 38 compared to AK 02 suggests Al mobility, which is also supported by garnet formation.

Here we propose two different, but interrelated protolith variants: (1) ultramafic rocks with disseminated carbonate and (2) pure iron-rich carbonate exposed to granulite facies metamorphism. Together, these two variants can produce the observed pyroxene and amphibole compositions observed in the QAP lithology (Fig. 4.14). Additionally, each of these starting lithologies is known from exposures from the lower metamorphic grade Isua Greenstone Belt (e.g., IS-X and IS-Y).

Both of these variants are represented in sample 92-197. Half of the sample is coarsely crystalline and magnetite-poor, and contains pyroxenes dominated by hedenbergite (Variant 1; Fig. 4.7). This calcium-rich pyroxene (i.e. clinopyroxene) will form during metamorphism from an original Mg-rich ultramafic protolith that contained disseminated secondary Ca-bearing carbonate (similar to IS-Y; Fig. 4.14). The other half of sample 92-197 is finer-grained and contains magnetite and low-calcium pyroxene and amphibole phases (Variant 2; Fig. 4.7). Low-calcium pyroxene and amphibole phases could have been derived from an Fe-rich metasomatic carbonate band located within an ultramafic protolith (similar to sample IS-X; Fig. 4.14), based on the following reactions (Condie, 1993):

(eq. 2) $7FeCO_3$ (siderite) + $8SiO_2$ (quartz) + $H_2O \rightarrow Fe_7Si_8O_{22}(OH)_2$ + (cummingtonite + grunerite) + $7CO_2$

(eq. 3) $Fe_7Si_8O_{22}(OH)_2$ (cummingtonite-grunerite) $\rightarrow$ $7FeSiO_3$ (opx) + $SiO_2$ (quartz) + $H_2O$

Examples of ultramafic rocks with disseminated carbonate and iron-rich carbonate bands and abundant quartz veins within ultramafic rocks occur in the amphibolite-facies metamorphosed Isua Greenstone Belt (Bonnichsen, 1975), rendering a BIF protolith for the QAP unit technically possible, yet less parsimonious relative to known lithology and processes that have affected the region and unnecessary. The two carbonate metasomatized mafic samples from Isua (IS-X and IS-Y) no longer exhibit a typical mafic major, trace, or rare earth element geochemical signature (Table 4.1, 4.2; Fig. 4.9), suggesting that the metasomatic fluids flowing through the original mafic protolith has removed all of the compatible elements. Even though IS-Y and IS-X have an uncontested

mafic protolith, these samples are geochemically (i.e., trace element, rare-earth element and amphibole compositions) more similar to the Akilia QAP unit (excluding AK 38) than to the Akilia ultramafic unit. Our conclusion here is that carbonate- and silica-metasomatized ultramafics represents a plausible explanation to account for the composition of most of the QAP lithology and is based on known, highly relevant geology.

## 4.10 Conclusions

Both the age and protolith of the QAP lithology have been hotly debated for over a decade. All of the rocks on Akilia, including the QAP unit, have been affected by granulite and amphibolite facies metamorphism and intense deformation, resulting in complex field relationships. Evidence of this deformation can be seen when examining the critical cross-cutting relationship of the Amîtsoq Gneiss (*Ogn*) and Akilia Association and the structural orientations of the observed intense foliations, mineral lineations, and fold axes point that are now parallel to each other to a tectonic, rather than igneous relationship. These structural relationships highlight the intense regional deformation and suggest that the apparent contact between the Amîtsoq Gneiss and Akilia Association cannot be used for determining the minimum age of the QAP lithology. Intense deformation within QAP and related rocks may have been the origin of mm-scale layering that has been used to support a sedimentary BIF origin. If sedimentary BIF was the protolith to the QAP lithology, the Fe-Mg minerals within in the unit should reflect this Fe-rich protolith. However, amphibole in the samples consists dominantly of actinolite, hornblende and cummingtonite, not grunerite, and the pyroxene is dominantly diopside, hedenbergite and augite, not ferrosilite. We argue that such amphibole and

pyroxene compositions are more likely to be derived from an original protolith consisting of ultramafic rocks with disseminated carbonate combined with a Fe-rich carbonate band brought to granulite facies metamorphism, analogous to rocks on Isua (IS-X and IS-Y), and rendering a BIF protolith unnecessary.

## References


Alibert, C. and Mcculloch, M.T. (1993) Rare-earth element and neodymium isotopic compositions of the banded iron-formations and associated shales from Hamersley, Western-Australia. Geochimica et Cosmochimica Acta 57, 187-204.

Anbar, A.D. (2004) Iron stable isotopes: beyond biosignatures. Earth and Planetary Science Letters 217, 223-236.

Anbar, A.D. and Holland, H.D. (1992) The Photochemistry of Manganese and the Origin of Banded Iron Formations. Geochimica et Cosmochimica Acta 56, 2595-2603.

Anbar, A.D. and Rouxel, O. (2007) Metal stable isotopes in paleoceanography. Annual Review of Earth and Planetary Sciences 35, 717-746.

Anbar, A.D., Duan, Y., Lyons, T.W., Arnold, G.L., Kendall, B., Creaser, R.A., Kaufman, A.J., Gordon, G.W., Scott, C., Garvin, J. and Buick, R. (2007) A whiff of oxygen before the great oxidation event? Science 317, 1903-1906.

Anbar, A.D., Jarzecki, A.A. and Spiro, T.G. (2005) Theoretical investigation of iron isotope fractionation between $Fe(H_2O)_6^{3+}$ and $Fe(H_2O)_6^{2+}$: implications for iron stable isotope geochemistry. Geochimica et Cosmochimica Acta 69, 825-837.

Anbar, A.D., Zahnle, K.J., Arnold, G.L. and Mojzsis, S.J. (2001) Extraterrestrial iridium, sediment accumulation and the habitability of the early Earth's surface. Journal of Geophysical Research 106, 3219-3236.

André, L., Cardinal, D., Alleman, L. and Moorbath, S. (2006) Silicon isotopes in ~3.8 Ga West Greenland rocks as clues to the Eoarchaean supracrustal Si cycle. Earth and Planetary Science Letters 245, 162-173.

Appel, P.W.U. (1980) On the Early Archean Isua Iron-Formation, West-Greenland. Precambrian Research 11, 73-87.

Appel, P.W.U. and Moorbath, S. (1999) Exploring Earth's oldest geologic record in Greenland. EOS 80, 257-264.

Appel, P.W.U., Fedo, C.M., Moorbath, S. and Myers, J.S. (1998) Early Archean Isua supracrustal belt, West Greenland: pilot study of the Isua Multidisciplinary Research Project. Journal of Greenland Survey Bulletin 180, 94-99.

Arrowsmith, P. (1987) Laser Ablation of Solids for Elemental Analysis by Inductively Coupled Plasma Mass-Spectrometry. Anal Chem 59, 1437-1444.

Aston, S.R. and Chester, R. (1973) The influence of suspended particles on the precipitation of iron in natural waters. Estuarine and Coastal Marine Science I, 225-231.

Baadsgaard, H., Lambert, R. and Krupicka, J. (1976) Mineral isotopic age relationships in the polymetamorphic Amitsoq gneisses, Godthaab District, West Greenland. Geochimica et Cosmochimica Acta 40, 513-527.

Baldwin, G.J., Thurston, P.C. and Kamber, B.S. (2011) High-precision rare earth element, nickel, and chromium chemistry of chert microbands pre-screened with in-situ analysis. Chemical Geology 285, 133-143.

Barrett, T.J., Fralick, P. and Jarvis, I. (1988) Rare-earth-element geochemistry of some Archean iron formations north of Lake Superior, Ontario. Canadian Journal of Earth Sciences 25, 570-580.

Bau, M. (1991) Rare-earth element mobility during hydrothermal and metamorphic fluid-rock interaction and the significance of the oxidation state of eruopium. Chemical Geology 93, 219-230.

Bau, M. (1993) Effects of syn- and post-depositional processes on the rare-earth element distribution in Precambrian iron-formations. European Journal of Mineralogy 5, 257-267.

Bau, M. (1996) Controls on the fractionation of isovalent trace elements in magmatic and aqueous systems: Evidence from Y/Ho, Zr/Hf, and lanthanide tetrad effect. Contributions to Mineralogy and Petrology 123, 323-333.

Bau, M. (1999) Scavenging of dissolved yttrium and rare earths by precipitating iron oxyhydroxide: Experimental evidence for Ce oxidation, Y-Ho fractionation, and lanthanide tetrad effect. Geochimica et Cosmochimica Acta 63, 67-77.

Bau, M. and Dulski, P. (1996) Distribution of yttrium and rare-earth elements in the Penge and Kuruman iron-formations, Transvaal Supergroup, South Africa. Precambrian Research 79, 37-55.

Bau, M. and Dulski, P. (1999) Comparing yttrium and rare earths in hydrothermal fluids from the Mid-Atlantic Ridge: implications for Y and REE behaviour during near-vent mixing and for the YrHo ratio of Proterozoic seawater. Chemical Geology 155, 77-90.

Bau, M. and Koschinsky, A. (2009) Oxidative scavenging of cerium on hydrous Fe oxide: Evidence from the distribution of rare earth elements and yttrium between Fe oxides and Mn oxides in hydrogenetic ferromanganese crusts. Geochemical Journal 43, 37-47.

Bau, M. and Moller, P. (1993) Rare earth element systematics of the chemically precipitated component in Early Precambrain iron formations and the evolution of the terrestrial atmosphere-hydrosphere-lithosphere system. Geochimica et Cosmochimica Acta 57, 2239-2249.

Bau, M., Hohndorf, A., Dulski, P. and Beukes, N.J. (1997a) Sources of Precambrian rare-earth elements and iron in Paleoproterozoic iron-formations from the Transvaal Supergroup, South Africa - evidence from neodymium isotopes. J Geol 105, 121-129.

Bau, M., Moller, P. and Dulski, P. (1997b) Yttrium and lanthanides in eastern Mediterranean seawater and their factionation during redox-cycling. Marine Chemistry 56, 123-131.

Bau, M., Schmidt, K., Koschinsky, A., Hein, J.R., Kuhn, T. and Usui, A. (2014) Discriminating between different genetic types of marine ferro-manganese crusts and nodules based on rare earth elements and yttrium. Chemical Geology 381, 1-9.

Beard, B.L., Johnson, C.M. and Albarede, F. (2004) Fe isotope variations in the modern and ancient earth and other planetary bodies, Reviews in Mineralogy: Geochemistry of non-traditional stable isotopes. Mineralogical Society of America, Washington, pp. 319-357.

Beard, B.L., Johnson, C.M., Cox, L., Sun, H., Nealson, K.H. and Aguilar, C. (1999) Iron isotope biosignatures. Science 285, 1889-1892.

Bekker, A. and Holland, H.D. (2012) Oxygen overshoot and recovery during the early Paleoproterozoic. Earth and Planetary Science Letters 317-318, 295-304.

Bekker, A., Holland, H.D., Wang, P.L., Rumble, D., Stein, H.J., Hannah, J.L., Coetzee, L.L. and Beukes, N.J. (2004) Dating the rise of atmospheric oxygen. Nature 427, 117-120.

Bekker, A., Slack, J.F., Planavsky, N., Krapez, B., Hofmann, A., Konhauser, K.O. and Rouxel, O.J. (2010) Iron Formation: The Sedimentary Product of a Complex Interplay among Mantle, Tectonic, Oceanic, and Biospheric Processes. Econ Geol 105, 467-508.

Belevtsev, Y., Belevstev, R. and Siroshtan, R. (1982) The Krivoy Rog Basin, in: Trendall, A.F., Morris, R.C. (Eds.), Iron-Formations: Facts and Problems. Elsevier, Amsterdam, pp. 211-252.

Bergquist, B.A. and Boyle, E.A. (2006) Iron isotopes in the Amazon River system: Weathering and transport signatures. Earth and Planetary Science Letters 248, 54-68.

Beukes, N. (1973) Precambrian iron-formations of southern Africa. Econ Geol 68, 960-1024.

Beukes, N. (2004) Biogeochemistry - Early options in photosynthesis. Nature 431, 522-523.

Beukes, N.J. and Gutzmer, J. (2008) Origin and paleoenvironmental significance of major iron formations at the Archean-Paleoproterozoic boundary. Reviews in Economic Geology Series 15, 5-47.

Beukes, N.J. and Klein, C. (1990) Geochemistry and sedimentology of a facies transition - from microbanded to granular iron-formation - in the early Proterozoic Transvaal Supergroup, South-Africa. Precambrian Research 47, 99-139.

Beukes, N.J., Gutzmer, J. and Nel, B.P. (2010) Ce anomalies in ~2.4 Ga iron and managnese formations as proxy for early oxygenation of oceanic environments. Goldschmidt Conference Abstracts.

Bjerrum, C.J. and Canfield, D.E. (2002) Ocean productivity before about 1.9 Gyr ago limited by phosphorus adsorption onto iron oxides. Nature 417, 159-162.

Bolhar, R., Kamber, B.S., Moorbath, S., Fedo, C.M. and Whitehouse, M.J. (2004) Characterisation of early Archaean chemical sediments by trace element signatures. Earth and Planetary Science Letters 222, 43-60.

Bonnichsen, B. (1975) Geology of the Biwabik iron formation, Dunka River area, Minnesota. Econ Geol 70, 319-340.

Braterman, P.S. and Cairns-Smith, A.G. (1987) Photoprecipitation and the Banded Iron-Formations - Some Quantitative Aspects. Origins of Life and Evolution of the Biosphere 17, 221-228.

Brengman, L.A. (2014) From source to sink: Silicon isotope composition of bedrock, detritial quartz arenites, chert and BIF from the ~3 Ga Buhwa Greenstone Belt, Zimbabwe, Geological Society of American Annual Meeting, Vancouver, British Columbia.

Brengman, L.A. and Fedo, C.M. (2012) Origin of BIF-like jasperlite in the 2.72 Ga Hunter Mine Group. Abitibi Greenstone Belt, Quebec by metasomatic replacement of felsic volcanic rocks, Geologic Society of America Annual Meeting, Charlotte, North Carolina.

Brocks, J.J., Logan, G.A., Buick, R. and Summons, R.E. (1999) Archean Molecular Fossils and the Early Rise of Eukaryotes. Science 285, 1033-1036.

Broderick, T.M. (1920) Economic geology and stratigraphy of the Gunflint Iron District, Minnesota. Econ Geol 15, 422-452.

Brookins, D.G. (1989) Aqueous geochemistry of rare earth elements, in: Lipin, B.R., McKay, G.A. (Eds.), Reviews in Mineralogy: Geochemistry and Mineralogy of Rare Earth Elements. Mineralogical Society of America, Washington, D.C., pp. 201-225.

Brown, D.A. (2006) Microbial mediation of iron mobilization and deposition in iron formations since the early Precambrian, in: Kesler, S., Ohmoto, H. (Eds.), Evolution of Early Earth's Atmosphere, Hydrosphere, and Biosphere – Constraints From Ore Deposits. The Geological Soceity of America Memoir, pp. 239-256.

Bryne, R.H. and Kim, K.H. (1990) Rare earth element scavenging in seawater. Geochimica et Cosmochimica Acta 54, 2645-2656.

Bryne, R.H. and Sholkovitz, E.R. (1996) Marine chemistry and geochemistry of the lanthanides, in: Gschneider, K.A., Eyring, L. (Eds.), Handbook on the Physics and Chemistry of the Rare Earths. Elsevier, Amsterdam, pp. 497-593.

Buick, R. (1992) The Antiquity of Oxygenic Photosynthesis - Evidence from Stromatolites in Sulfate-Deficient Archean Lakes. Science 255, 74-77.

Buick, R. (2008) When did oxygenic photosynthesis evolve? Philos Trans R Soc Lond B Biol Sci 363, 2731-2743.

Bullen, T.D., White, A.F., Childs, C.W., Vivit, D.V. and Schulz, M.S. (2001) Demonstration of significant abiotic iron isotope fractionation in nature. Geology 29, 699-702.

Burns, R.G. (1976) Uptake of Cobalt into Ferromanganese Nodules, Soils, and Synthetic Manganese(Iv) Oxides. Geochimica et Cosmochimica Acta 40, 95-102.

Cairns-Smith, A.G. (1987) Precambrian solution photochemistry, inverse segregation, and banded iron formations. Nature 76.

Canfield, D., Ngombi-Pemba, L., Hammarlund, E., Bengston, S., Chaussidon, M., Gauthier-Lafaye, F., Meunier, A., Riboulleau, A., Rollion-Bard, C., Rouxel, O., Asael, D., Pierson-Wickmann, A. and Albani, A. (2013) Oxygen dynamics in the aftermath of the Great Oxidation of Earth's atmosphere. PNAS 110, 16736-16741.

Canfield, D.E. (1998) A new model for Proterozoic ocean chemistry. Nature 396, 450-453.

Canfield, D.E. (2005) The early history of atmospheric oxygen: Homage to Robert A. Garrels. Annual Review of Earth and Planetary Sciences 33, 1-36.

Canfield, D.E., Habicht, K.S. and Thamdrup, B. (2000) The Archean Sulfur Cycle and the Early History of Atmospheric Oxygen. Science 288, 658-661.

Cantrell, K.J. and Byrne, R.H. (1987) Rare-Earth Element Complexation by Carbonate and Oxalate Ions. Geochimica et Cosmochimica Acta 51, 597-605.

Chandler, F.W. (1980) Proterozoic redbed sequences of Canada. Canadian Geological Survey Bulletin 311.

Chang, S.B.R. and Kirschvink, J.L. (1989) Magnetofossils, the Magnetization of Sediments, and the Evolution of Magnetite Biomineralization. Annual Review of Earth and Planetary Sciences 17, 169-195.

Chigira, M. and Watanabe, M. (1994) Silica precipitation behavior in a flow field with negative temperature gradients. Journal of Geophysical Research 99, 15539-15548.

Cloud, P.E. (1965) Significance of Gunflint (Precambrian) microflora-photosynthetic oxygen may have had important local effects before becoming a major atmospheric gas. Science 148, 1135-1143.

Cloud, P.E. (1973) Paleoecological significance of banded iron-formation. Econ Geol 68, 1135-1143.

Condie, K.C. (1981) Archean Greenstone Belts. Elsevier, Amsterdam.

Condie, K.C. (1993) Chemical-Composition and Evolution of the Upper Continental-Crust - Contrasting Results from Surface Samples and Shales. Chemical Geology 104, 1-37.

Craddock, P.R. and Bach, W. (2010) Trace element and isotopic compositions of anhydrite sampled in the Manus Basin, Papua New Guinea. Geochimica et Cosmochimica Acta 74, 5514-5536.

Craddock, P.R. and Dauphas, N. (2011) Iron and carbon isotope evidence for microbial iron respiration throughout the Archean. Earth and Planetary Science Letters 303, 121-132.

Croal, L.R., Jiao, Y., Kappler, A. and Newman, D.K. (2009) Phototrophic Fe(II) oxidation in an atmosphere of H2: implications for Archean banded iron formations. Geobiology 7, 21-24.

Croal, L.R., Johnson, C.M., Beard, B.L. and Newman, D.K. (2004) Iron isotope fractionation by Fe(II)-oxidizing photoautotrophic bacteria 1. Geochimica et Cosmochimica Acta 68, 1227-1242.

Crosby, H.A., Johnson, C.M., Roden, E.E. and Beard, B.L. (2005) Coupled Fe(II)-Fe(III) electron and atom exchange as a mechanism for Fe isotope fractionation during dissimilatory iron oxide reduction. Environ Sci Technol 39, 6698-6704.

Crosby, H.A., Roden, E.E., Johnson, C.M. and Beard, B.L. (2007) The mechanisms of iron isotope fractionation produced during dissimilatory Fe(III) reduction by Shewanella putrefaciens and Geobacter sulfurreducens. Geobiology 5, 169-189.

Crowe, S., Dossing, L., Beukes, N., Bau, M., Kruger, S., Frei, R. and Canfield, D. (2013) Atmospheric oxygenation three billion years ago. Nature 501, 535-538.

Czaja, A.D., Johnson, C.M., Beard, B.L., Roden, E.E., Weiqiang, L. and Moorbath, S. (2013) Biological Fe oxidation controlled deposition of banded iron formation in the ca. 3770 Ma Isua Supracrustal Belt (West Greenland). Earth and Planetary Science Letters 363, 192-203.

Dauphas, N. and Rouxel, O. (2006) Mass spectrometry and natural variations of iron isotopes. Mass Spectrom Rev 25, 515-550.

Dauphas, N., Cates, N., Mojzsis, S. and Busigny, V. (2007a) Identification of chemical sedimentary protoliths using iron isotopes in the >3750 Ma Nuvvuagittuq supracrustal belt, Canada. Earth and Planetary Science Letters 254, 358-376.

Dauphas, N., van Zuilen, M., Busigny, V., Lepland, A., Wadhwa, M. and Janney, P. (2007b) Iron isotope, major and trace element characterization of early Archean supracrustal rocks from SW Greenland: Protolith identification and metamorphic overprint. Geochimica et Cosmochimica Acta 71, 4745-4770.

Dauphas, N., van Zuilen, M., Wadhwa, M., Davis, A.M., Marty, B. and Janney, P.E. (2004) Clues from Fe isotope variations on the origin of early Archean BIFs from Greenland. Science 306, 2077-2080.

De Carlo, E.H. and Green, W.J. (2002) Rare earth elements in the water column of Lake Vanda, McMurdo Dry Valleys, Antarctica. Geochimica et Cosmochimica Acta 66, 1323-1333.

Derry, L.A. and Jacobsen, S.B. (1990) The Chemical Evolution of Precambrian Seawater - Evidence from Rees in Banded Iron Formations. Geochimica et Cosmochimica Acta 54, 2965-2977.

Des Marais, D.J., Allamandola, L.J., Benner, S.A., Boss, A.P., Deamer, D., Falkowski, P.G., Farmer, J.D., Hedges, S.B., Jakosky, B.M., Knoll, A.H., Liskowsky, D.R.,

Meadows, V.S., Meyer, M.A., Pilcher, C.B., Nealson, K.H., Spormann, A.M., Trent, J.D., Turner, W.W., Woolf, N.J. and Yorke, H.W. (2003) The NASA Astrobiology Roadmap. Astrobiology 3, 219-235.

Dimroth, E. and Kimberley, M.M. (1976) Precambrian atmosphereic oxygen: Evidence in the sedimentary distribution of carbon, sulfur, uranium, and iron. Canadian Journal of Earth Sciences 13, 1161-1185.

Duff, M.C., Coughlin, J.U. and Hunter, D.B. (2002) Uranium co-precipitation with iron oxide minerals. Geochimica et Cosmochimica Acta 66, 3533-3547.

Dunk, R.M. and Mills, R.A. (2006) The impact of oxic alteration on plume-derived transition metals in ridge flank sediments from the East Pacific Rise. Marine Geology 229, 133-157.

Dymek, R.F. and Klein, C. (1988) Chemistry, petrology and origin of banded iron-formation lithologies from the 3800-Ma Isua Supracrustal Belt, West Greenland. Precambrian Research 39, 247-302.

Eggins, S.M., Woodhead, J.D., Kinsley, L.P.J., Mortimer, G.E., Sylvester, P., McCulloch, M.T., Hergt, J.M. and Handler, M.R. (1997) A simple method for the precise determination of >=40 trace elements in geological samples by ICPMS using enriched isotope internal standardisation. Chemical Geology 134, 311-326.

Ehrenreich, A. and Widdel, F. (1994) Anaerobic Oxidation of Ferrous Iron by Purple Bacteria, a New-Type of Phototrophic Metabolism. Appl Environ Microb 60, 4517-4526.

Emerson, D. and Moyer, C.L. (2002) Neutrophilic Fe-Oxidizing bacteria are abundant at the Loihi Seamount hydrothermal vents and play a major role in Fe oxide deposition. Appl Environ Microb 68, 3085-3093.

Emerson, S.R. and Huested, S.S. (1991) Ocean Anoxia and the Concentrations of Molybdenum and Vanadium in Seawater. Marine Chemistry 34, 177-196.

England, G.L., Rasmussen, B., Krapez, B. and Groves, D.I. (2002) Paleoenvironmental significance of rounded pyrite in siliciclastic sequences of the Late Archean Witwaterstand Basin: Oxygen-deficient atmosphere or hydrothermal alteration? Sedimentology 49, 1133-1156.

Farquhar, J. and Wing, B.A. (2003) Multiple sulfur isotopes and the evolution of the atmosphere. Earth and Planetary Science Letters 213, 1-13.

Farquhar, J., Bao, H.M. and Thiemens, M. (2000) Atmospheric influence of Earth's earliest sulfur cycle. Science 289, 756-758.

Faure, G. (1986) Principles of Isotope Geolog. John Wiley & Sons, Inc., New Jersey.

Fedo, C.M. (2000) Setting and origin for problematic rocks from the > 3.7 Ga Isua Greenstone Belt, southern west Greenland: Earth's oldest coarse elastic sediments. Precambrian Research 101, 69-78.

Fedo, C.M. and Eriksson, K.A. (1995) Geologic setting and ideas concerning the origin of the iron-ore deposits at Buhwa, Zimbabwe, in: Blenkinsop, T.G., Tromp, P.L. (Eds.), Sub-Saharan Economic Geology. A.A. Balkema Publishers, Vermont, pp. 43-53.

Fedo, C.M. and Eriksson, K.A. (1996) Stratigraphic framework of the similar to 3.0 Ga Buhwa greenstone belt: A unique stable-shelf succession in the Zimbabwe Archean Craton. Precambrian Research 77, 161-178.

Fedo, C.M. and Whitehouse, M.J. (2002) Metasomatic origin of quartz-pyroxene rock, Akilia, Greenland, and implications for Earth's earliest life. Science 296, 1448-1452.

Fedo, C.M., Eriksson, K.A. and Blenkinsop, T.G. (1995) Geologic history of the Archean Buhwa Greenstone Belt and surrounding granite-gneiss terrane, Zimbabwe, with implications for the evolution of the Limpopo Belt. Canadian Journal of Earth Sciences 32, 1977-1990.

Fedo, C.M., Eriksson, K.A. and Krogstad, E.J. (1996) Geochemistry of shales from the Archean (similar to 3.0 Ga) Buhwa greenstone belt, Zimbabwe: Implications for provenance and source-area weathering. Geochimica et Cosmochimica Acta 60, 1751-1763.

Fedo, C., Hage, M., Schoenberg, R. and Whitehouse, M. (2010) Can Fe isotopes be used to fingerprint Precambrian BIF?, Goldschmidt Knoxville, TN.

Fedo, C.M., Myers, J.S. and Appel, P.W.U. (2001) Depositional setting and paleogeographic implications of earth's oldest supracrustal rocks, the > 3.7 Ga Isua Greenstone belt, West Greenland. Sediment Geol 141, 61-77.

Fedo, C.M., Whitehouse, M.J. and Kamber, B.S. (2006) Geological constraints on detecting the earliest life on Earth: a perspective from the Early Archaean (older than 3.7 Gyr) of southwest Greenland. Philos Trans R Soc Lond B Biol Sci 361, 851-867.

Fischer, W.W. and Knoll, A.H. (2009) An iron shuttle for deepwater silica in Late Archean and early Paleoproterozoic iron formations. GSA Bulletin 121, 222-235.

Floran, R.J. and Papike, J.J. (1978) Mineralogy and Petrology of Gunflint Iron Formation, Minnesota-Ontario - Correlation of Compositional and Assemblage Variations at Low to Moderate Grade. Journal of Petrology 19, 215-288.

Fralick, P., Davis, D.W. and Kissin, S.A. (2002) The age of the Gunflint Formation, Ontario, Canada: single zircon U Pb age determinations from reworked volcanic ash. Canadian Journal of Earth Sciences 39, 1085-1091.

Frei, R., Dahl, P.S., Duke, E.F., Frei, K.M., Hansen, T.R., Frandsson, M.M. and Jensen, L.A. (2008) Trace element and isotopic characterization of Neoarchean and Paleoproterozoic iron formations in the Black Hills (South Dakota, USA): Assessment of chemical change during 2.9–1.9Ga deposition bracketing the 2.4–2.2Ga first rise of atmospheric oxygen. Precambrian Research 162, 441-474.

Frei, R., Gaucher, C., Poulton, S.W. and Canfield, D.E. (2009) Fluctuations in Precambrian atmospheric oxygenation recorded by chromium isotopes. Nature 461, 250-253.

French, B.M. (1971) Stability relations of siderite ($FeCO_3$) in the system Fe-C-O. American Journal of Science 271, 37-78.

Friend, C.R.L. and Nutman, A.P. (2005) Complex 3670-3500 Ma orogenic episodes superimposed on juvenile crust accreted between 3850 and 3690 Ma, Itsaq Gneiss Complex, Southern West Greenland. J Geol 113, 375-397.

Friend, C.R.L., Nutman, A.P., Bennett, V.C. and Norman, M.D. (2008) Seawater-like trace element signatures (REE + Y) of Eoarchaean chemical sedimentary rocks from southern West Greenland, and their corruption during high-grade metamorphism. Contributions to Mineralogy and Petrology 155, 229-246.

Frost, C.D., Blanckenburg, F., Schoenberg, R., Frost, B.R. and Swapp, S.M. (2006) Preservation of Fe isotope heterogeneities during diagenesis and metamorphism of banded iron formation. Contributions to Mineralogy and Petrology 153, 211-235.

Fryer, B.J. (1977) Rare earth evidence in iron-formations for changing Precambrian oxidation states. Geochimica et Cosmochimica Acta 41, 361-367.

Fryer, B.J., Jackson, S.E. and Longerich, H.P. (1995) Design, Operation and Role of the Laser-Ablation Microprobe Coupled with an Inductively-Coupled Plasma - Mass-Spectrometer (Lam-Icp-Ms) in the Earth-Sciences. Can Mineral 33, 303-312.

Fyon, J., Schwarts, H. and Crocket, J. (1984) Carbonization and gold mineralization in the Timmins area, Abitibi greenstone belt: Genetic links with Archean mantle CO2-degassing and lower crust granulization. Geological Association of Canada Program with Abstract 9, 65.

Garrels, R.M. and Perry, E.A.J. (1974) Cycling of carbon, sulfur, and oxygen through geologic time, in: Goldberg, E.A. (Ed.), The Sea. Wiley, New York, pp. 303-336.

German, C.R. and Elderfield, H. (1990) Application of the Ce anomaly as a paleoredox indicator: The ground rules. Paleoceanography 5, 823-833.

German, C.R. and Von Damm, K.L. (2006) Hydrothermal Processes, in: Elderfield, H. (Ed.), The oceans and marine geochemistry. Elsevier, Oxford, UK, pp. 181-222.

German, C.R., Holliday, B.P. and Elderfield, H. (1991) Redox cycling of rare earth elemtns in the suboxic zone of the Black Sea. Geochimica et Cosmochimica Acta 55, 3553-3558.

Gibbs, R.J. (1970) Mechanisms Controlling World Water Chemistry. Science 170, 1088-1090.

Goodwin, A.M. (1956) Facies relations in the Gunflint Iron Formation. Econ Geol 51, 565-595.

Goodwin, A.M. (1973) Archean volcanogenic iron-formation of the Canadian shield. Science Terra 9, 23-34.

Gray, A.L. (1985) Solid Sample Introduction by Laser Ablation for Inductively Coupled Plasma Source-Mass Spectrometry. Analyst 110, 551-556.

Griffin, W.L., McGregor, V.R., Nutman, A.P., Taylor, P.N. and Bridgwater, D. (1980) Early Archean granulite-facies metamorphism south of Ameralik, West Greenland. Earth and Planetary Science Letters 50, 59-74.

Gross, G.A. (1965) Geology of iron deposits in Canada I. General geology and evaluation of iron deposits. Geological Survey of Canada Economic Geology Report 22.

Gross, G.A. (1980) A classification of iron formations based on depositional environments. Can Mineral 18, 215-222.

Gross, G.A. (1983) Tectonic systems and the deposition of iron formation Precambrian Research 20, 171-187.

Groves, D.I. and Batt, W. (1984) Spatial and temporal variations of Archean metallogenic association in terms of evolution of granitoid-greenstone terraines with particular emphasis on Western Australia, in: Kroner, A., Hanson, G., Goodwin, A.M. (Eds.), Archean Geochemistry. Springer-Verlag, Berlin, pp. 73-98.

Halliday, A.N., Lee, D.C., Christensen, J.N., Rehkamper, M., Yi, W., Luo, X.Z., Hall, C.M., Ballentine, C.J., Pettke, T. and Stirling, C. (1998) Applications of multiple

collector-ICPMS to cosmochemistry, geochemistry, and paleoceanography. Geochimica et Cosmochimica Acta 62, 919-940.

Hamade, T., Konhauser, K.O., Raiswell, R., Goldsmith, S. and Morris, R.C. (2003) Using Ge/Si ratios to decouple iron and silica fluxes in Precambrian banded iron formations. Geology 31, 35-38.

Harder, E.C. (1919) Iron depositing bacteria and their geological relations. The Journal of Geology 30, 506-509.

Heck, P.R., Huberty, J.M., Kita, N.T., Ushikubo, T., Kozdon, R. and Valley, J.W. (2011) SIMS analysis of silicon and oxygen isotope ratios for quartz from Archean and Paleoproterozoic banded iron formations. Geochimica et Cosmochimica Acta 75, 5879-5891.

Heimann, A., Johnson, C.M., Beard, B.L., Valley, J.W., Roden, E.E., Spicuzza, M.J. and Beukes, N.J. (2010) Fe, C, and O isotope compositions of banded iron formation carbonates demonstrate a major role for dissimilatory iron reduction in ~2.5Ga marine environments. Earth and Planetary Science Letters 294, 8-18.

Heising, S. and Schink, B. (1998) Phototrophic oxidation of ferrous iron by a Rhodomicrobium vannielii strain. Microbiol-Uk 144, 2263-2269.

Helz, G.E., Bura-Nakic, E., Mikac, N. and Ciglenecki, I. (2011) New model for molybdenum behavior in euxinic waters. Chemical Geology 284, 323-332.

Holland, H.D. (1973) Ocean - possible srouce of iron in iron-formations. Econ Geol 68, 1169-1172.

Holland, H.D. (1984) The chemical evoultion of the atmosphere and oceans. Princeton University Press, New York.

Holm, N.G. (1989) The 13C/12C ratios of siderite and organic matter of a modern metalliferous hydrothermal sediment and their implications for banded iron formations. Chemical Geology 77, 41-45.

Holm, N.G. and Charlou, J.L. (2001) Initial indications of abiotic formation of hydrocarbons in the Rainbow ultramafic hydrothermal system, Mid-Atlantic Ridge. Earth and Planetary Science Letters 191, 1-8.

Homoky, W.B., Severmann, S., Mills, R.A., Statham, P.J. and Fones, G.R. (2009) Pore-fluid Fe isotopes reflect the extent of benthic Fe redox recycling: Evidence from continental shelf and deep-sea sediments. Geology 37, 751-754.

Hostetler, P.B. and Garrels, R.M. (1962) Transportation and precipitation of uranium and vanadium at low temperatures, with special reference to sandstone-type uranium deposits. Econ Geol 57, 137-167.

Hyslop, E.V., Valley, J.W., Johnson, C.M. and Beard, B.L. (2007) The effects of metamorphism on O and Fe isotope compositions in the Biwabik Iron Formation, northern Minnesota. Contributions to Mineralogy and Petrology 155, 313-328.

Isley, A.E. (1995) Hydrothermal Plumes and the Delivery of Iron to Banded Iron-Formation. J Geol 103, 169-185.

Isley, A.E. and Abbott, D.H. (1999) Plume-related mafic volcanism and the deposition of banded iron formation. Journal of Geophysical Research 104, 15461-15477.

Jackson, S.E., Longerich, H.P., Dunning, G.R. and Fryer, B.J. (1992) The application of laser-ablation microprobe-inductively coupled plasma-mass spectrometry (LAM-ICP-MS) to in situ trace-element determinations in minerals. Can Mineral 30, 1049-1064.

Jacobsen, S.B. and Pimental-Klose, M. (1988) A Nd isotope study of the Hamersley and Michipicoten banded iron formations: The source of REE and Fe in Archean oceans. Earth and Planetary Science Letters 87, 29-44.

James, H. (1954) Sedimentary facies of iron formations. Econ Geol 49, 235-293.

James, H. and Trendall, A.F. (1982) Banded iron formation: Distribution in time and paleoenvironmental significance, in: Holland, H.D., Schidlowski, M. (Eds.), Mineral Deposits and the Evolution of the Biosphere. Spring-Verlag, NY, pp. 199-218.

Jenner, F. and O'Neill, H.S.C. (2012) Major and trace analyses of basaltic glasses by laser-ablation ICP-MS. Geochemistry, Geophysics, Geosystems 13, Q03003.

Jirsa, M.A. and Weiblen, P.W. (2007) Geology along the Gunflint Trail. 53rd Annual Institute on Lake Superior Geology Field Trip Guide 6.

Johnson, C.M. and Beard, B.L. (2006) Fe isotopes: An emerging technique for understanding modern and ancient biogeochemical cycles. GSA Today 16, 4.

Johnson, T.M. and Bullen, T.D. (2004) Mass-dependent fractionation of selenium and chromium isotopes in low-temperature environments, in: Johnson, C.M., Beard, B.L., Albarede, F. (Eds.), Rev Mineral Geochem. Mineralogical Society of America, Washington, pp. 289-317.

Johnson, C.M., Beard, B.L. and Albarede, F. (2004) Overview and general concepts, Rev Mineral Geochem. The Mineralogical Society of America, Washington, DC, pp. 1-22.

Johnson, C.M., Beard, B.L., Beukes, N.J., Klein, C. and O'Leary, J.M. (2003) Ancient geochemical cycling in the Earth as inferred from Fe isotope studies of banded iron formations from the Transvaal Craton. Contributions to Mineralogy and Petrology 144, 523-547.

Johnson, C.M., Beard, B.L., Klein, C., Beukes, N.J. and Roden, E.E. (2008a) Iron isotopes contrain biologic and abiologic processes in banded iron formation genesis. Geochimica et Cosmochimica Acta 72, 151-169.

Johnson, C.M., Beard, B.L. and Roden, E.E. (2008b) The Iron Isotope Fingerprints of Redox and Biogeochemical Cycling in Modern and Ancient Earth. Annual Review of Earth and Planetary Sciences 36, 457-493.

Kamber, B.S. (2009) Geochemical fingerprinting: 40 years of analytical development and real world applications. Applied Geochemistry 24, 1074-1086.

Kamber, B.S. (2010) Archean mafic–ultramafic volcanic landmasses and their effect on ocean–atmosphere chemistry. Chemical Geology 274, 19-28.

Kamber, B.S. and Gladu, A.H. (2009) Comparison of Pb Purification by Anion-Exchange Resin Methods and Assessment of Long-Term Reproducibility of Th/U/Pb Ratio Measurements by Quadrupole ICP-MS. Geostand Geoanal Res 33, 169-181.

Kamber, B.S. and Moorbath, S. (1998) Initial Pb of the Amitsoq gneiss revisited: implications for the timing of early Archean crustal evolution in West Greenland. Chemical Geology 150, 19-41.

Kamber, B.S. and Webb, G.E. (2007) Transition metal abundances in microbial carbonate: a pilot study based on in situ La-ICP-MS analysis. Geobiology 5, 375-389.

Kamber, B.S. and Whitehouse, M.J. (2007) Micro-scale sulphur isotope evidence for sulphur cycling in the late Archean shallow ocean. Geobiology 5, 5-17.

Kappler, A. and Newman, D.K. (2004) Formation of Fe(III)-minerals by Fe(II)-oxidizing photoautotrophic bacteria 1. Geochimica et Cosmochimica Acta 68, 1217-1226.

Kappler, A., Pasquero, C., Konhauser, K.O. and Newman, D.K. (2005) Deposition of banded iron formations by anoxygenic phototrophic Fe(II)-oxidizing bacteria. Geology 33, 865.

Kasting, J., Catling, D. and Zahnle, K. (2012) Atmospheric oxygenation and volcanism. Nature 487, E1.

Kato, Y. and Nakamura, K. (2003) Origin and global tectonic significance of Early Archean cherts from the Marble Bar greenstone belt, Pilbara Craton, Western Australia. Precambrian Research 125, 191-243.

Kato, Y., Kano, T. and Kunugiza, K. (2002) Negative Ce anomaly in the Indian banded iron formations: Evidence for the emergence of oxygenated deep-sea at 2.9 similar to 2.7 Ga. Resour Geol 52, 101-110.

Kato, Y., Ohta, I., Tsunematsu, T., Watanabe, Y., Isozaki, Y., Maruyama, S. and Imai, N. (1998) Rare earth element variations in mid-Archean banded iron formations: Implications for the chemistry of ocean and continent and plate tectonics. Geochimica et Cosmochimica Acta 62, 3475-3497.

Kato, Y., Yamaguchi, K. and Ohmoto, H. (2006) Rare earth elements in Precambrian banded iron formations: Secular changes of Ce and Eu anomalies and evolution of atmospheric oxygen, in: Kesler, S., Ohmoto, H. (Eds.), Evolution of Early Earth's Atmosphere, Hydrosphere, and Biosphere - Constraints from Ore Deposits. Geological Society of America, Boulder, pp. 269-289.

Kimberley, M.M. (1978) Paleoenvironmental classification of iron formations. Econ Geol 73, 215-229.

Klein, C. (2005) Some Precambrian banded iron-formations (BIFs) from around the world: Their age, geologic setting, mineralogy, metamorphism, geochemistry, and origins. American Mineralogist 90, 1473-1499.

Klein, C. and Beukes, N. (1992) Proterozoic iron-formations, in: Conder, K. (Ed.), Proterozoic Crustal Evolution. Elsevier, Amsterdam, pp. 383-418.

Klein, C. and Beukes, N.J. (1989) Geochemistry and sedimentology of a facies transition from limestone to iron-formation deposition in the Early Proterozoic Transvaal Supergroup, South-Africa. Econ Geol 84.

Knoll, A.H., Javaux, E.J., Hewitt, D. and Cohen, P. (2006) Eukaryotic organisms in Proterozoic oceans. Philos T R Soc B 361, 1023-1038.

Koehler, I., Konhauser, K. and Kappler, A. (2010) Role of Microorganisms in Banded Iron Formations. 309-324.

Komiya, T., Maruyama, S., Masuda, T., Nohda, S., Hayashi, M. and Okamoto, K. (1999) Plate Tectonics at 3.8-3.7 Ga: Field Evidence from the Isua Accretionary Complex, Southern West Greenland. The Journal of Geology 107, 515-554.

Konhauser, K. (2007) Introduction to Geomicrobiology. Blackwell Publishing, Massachusetts.

Konhauser, K., Amskold, L., Lalonde, S., Posth, N., Kappler, A. and Anbar, A. (2007a) Decoupling photochemical Fe(II) oxidation from shallow-water BIF deposition. Earth and Planetary Science Letters 258, 87-100.

Konhauser, K.O., Hamade, T., Raiswell, R., Morris, R.C., Ferris, F.G., Southam, G. and Canfield, D.E. (2002) Could bacteria have formed the Precambrian banded iron formations? Geology 30, 1079-1082.

Konhauser, K.O., Lalonde, S.V., Amskold, L. and Holland, H.D. (2007b) Was there really an Archean phosphate crisis? Science 315, 1234-1234.

Konhauser, K.O., Newman, D.K. and Kappler, A. (2005) The potential significance of microbial Fe(III) reduction during deposition of Precambrian banded iron formations. Geobiology 3, 167-177.

Konhauser, K.O., Pecoits, E., Lalonde, S.V., Papineau, D., Nisbet, E.G., Barley, M.E., Arndt, N.T., Zahnle, K. and Kamber, B.S. (2009) Oceanic nickel depletion and a methanogen famine before the Great Oxidation Event. Nature 458, 750-753.

Kramers, J.D. and Tolstikhin, I.N. (1997) Two terrestrial lead isotope paradoxes, forward transport modelling, core formation and the history of the continental crust. Chemical Geology 139, 75-110.

Kruhl, J., Wirth, R. and Morales, L. (2013) Quartz grain boundaries as fluid pathways in metamorphic rocks. Journal of Geophysical Research 118, 1957-1967.

Kump, L. and Seyfried, W. (2005) Hydrothermal Fe fluxes during the Precambrian: Effect of low oceanic sulfate concentrations and low hydrostatic pressure on the composition of black smokers. Earth and Planetary Science Letters 235, 654-662.

Kump, L.R. and Barley, M.E. (2007) Increased subaerial volcanism and the rise of atmospheric oxygen 2.5 billion years ago. Nature 448, 1033-1036.

Lawrence, M.G. and Kamber, B.S. (2006) The behaviour of the rare earth elements during estuarine mixing—revisited. Marine Chemistry 100, 147-161.

Lawrence, M., Greig, A., Collerson, K. and Kamber, B. (2006a) Direct quantification of rare earth element concentrations in natural waters by ICP-MS. Applied Geochemistry 21, 839-848.

Lawrence, M.G., Greig, A., Collerson, K.D. and Kamber, B.S. (2006b) Rare earth element and yttrium variability in South East Queensland waterways. Aquatic Geochemistry 12, 39-72.

Lepland, A. and Whitehouse, M.J. (2010) Metamorphic alteration, mineral paragenesis and geochemical re-equilibration of early Archean quartz–amphibole–pyroxene gneiss from Akilia, Southwest Greenland. International Journal of Earth Sciences.

Lepland, A. and Whitehouse, M.J. (2011) Metamorphic alteration, mineral paragenesis and geochemical re-equilibration of early Archean quartz-amphibole-pyroxene gneiss from Akilia, Southwest Greenland. International Journal of Earth Sciences 100, 1-22.

Lepland, A., Arrhenius, G. and Cornell, D. (2002) Apatite in early Archean Isua supracrustal rocks, southern West Greenland: its origin, association with graphite and potential biomarker. Precambrian Research 119, 221-241.

Lepland, A., van Zuilen, M.A., Arrhenius, G., Whitehouse, M.J. and Fedo, C.M. (2005) Questioning the evidence for Earth's earliest life—Akilia revisited. Geology 33, 77.

Lepland, A., van Zuilen, M.A. and Philippot, P. (2011) Fluid-deposited graphite and its geobiological implications in early Archean gneiss from Akilia, Greenland. Geobiology 9.

Li, W., Huberty, J.M., Beard, B.L., Kita, N.T., Valley, J.W. and Johnson, C.M. (2013) Contrasting behavior of oxygen and iron isotopes in banded iron formations revealed by *in situ* isotopic analysis. Earth and Planetary Science Letters 384, 132-143.

Liu, Y.G., Miah, M.R.U. and Schmitt, R.A. (1988) Cerium: A chemical tracer for paleo-oceanic redox conditions. Geochimica et Cosmochimica Acta 52, 1361-1371.

Lovley, D.R. (2004) Potential role of dissimilatory iron reduction in the early evolution of microbial respiration, in: Seckback, J. (Ed.), Origins, Evolution and Biodiversity of Microbial Life. Kluwer, Netherlands, pp. 301-313.

Lovley, D.R., Stolz, J. and Nord, G. (1987) Anaerobic production of magnetite by a dissimilatory iron-reducing microorganism. Nature 330, 252-254.

MacGregor, A.M. (1927) The problem of the Precambrian atmosphere. South African Journal of Science 23, 155-172.

Manning, C.E., Mojzsis, S.J. and Harrison, T.M. (2006) Geology, Age and Origin of Supracrustal Rocks at Akilia, West Greenland. American Journal of Science 306, 303-366.

McGregor, V.R. and Mason, B.J. (1977) Petrogenesis and geochemistry of metabasic and metasedimentary enclaves in the Amitsoq gneisses, West Greenland. American Mineralogist 62, 887-904.

McKeegan, K.D., Kudryavtsev, A.B. and Schopf, J.W. (2007) Raman and ion microscopic imagery of graphitic inclusions in apatite from older than 3830 Ma Akilia supracrustal rocks, west Greenland. Geology 35, 591.

McLennan, S.M. and Taylor, R. (1991) Sedimentary rocks and crustal evolution: Tectonic setting and secular trends. J Geol 99, 1-21.

McManus, J., Berelson, W., Severmann, S., Poulson, R., Hammond, D., Klinkhammer, G. and Holm, C. (2006) Molybdenum and uranium geochemistry in continental margin sediments: Paleoproxy potential. Geochimica et Cosmochimica Acta 70, 4643-4662.

Miller, J.D., Morey, G.B. and Weiblen, P.W. (1987) Seagull Lake - Gunflint Lake area: A classical Precambrian stratigraphic sequence in northeastern Minnesota. America Continental Field Guide - North-Central Section, 47-51.

Moenke-Blankenburg, L. (1993) Laser-ICP-spectrometry. Spectrochimica Acta Review 15, 1-37.

Mojzsis, S.J. and Harrison, T.M. (1999) Geochronological studies of the oldest known marine sediments. 9th Annual V.M. Goldschmidt Conference Abstract 7602.

Mojzsis, S.J. and Harrison, T.M. (2002) Origin and significance of Archean quartzose rocks at Akilia, Greenland. Science 298, 917a - 917a.

Mojzsis, S.J., Arrhenius, G., McKeegan, K.D., Harrison, T.M., Nutman, A.P. and Friend, C.R.L. (1996) Evidence for life on Earth before 3,800 million years ago. Nature 384, 55-59.

Mojzsis, S.J., Coath, C.D., Greenwood, J.P., McKeegan, K.D. and Harrison, T.M. (2003) Mass-independent isotope effects in Archean (2.5 to 3.8 Ga) sedimentary sulfides determined by ion microprobe analysis. Geochimica et Cosmochimica Acta 67, 1635-1658.

Moorbath, S., O'Nions, R.K. and Pankhurst, R.J. (1973) Early Archaean age for the Isua Iron Formation, West Greenland. Nature 245, 138-139.

Moorbath, S. and Whitehouse, M.J. (1996) Age of the Isua supracrustal sequence of West Greenland, in: Chela-Flores, J., Raulin, F. (Eds.), Chemical Evoultion: Physics of the Origin and Evoultion of Life. Kluwer Academic Publishers, pp. 87-95.

Morford, J.L. and Emerson, S. (1999) The geochemistry of redox sensitive trace metals in sediments. Geochimica et Cosmochimica Acta 63, 1735-1750.

Morris, R.C. (1993) Genetic modeling for banded iron formation of the Hamersley Group Pilbara craton, Western Australia. Precambrian Research 60, 243-286.

Morris, R.C. and Horwitz, R. (1983) The origin of the iron-formation-rich Hamersley Group of Western Australia: Deposition on a platform. Precambrian Research 21, 273-297.

Muller, B., Axelsson, M.D. and Ohlander, B. (2003) Trace elements in magnetite from Kiruna, northern Sweden, as determined by LA-ICP-MS. Gff 125, 1-5.

Murray, R.W., Tenbrink, M.R.B., Gerlach, D.C., Russ, G.P. and Jones, D.L. (1992) Interoceanic Variation in the Rare-Earth, Major, and Trace-Element Depositional Chemistry of Chert - Perspectives Gained from the Dsdp and Odp Record. Geochimica et Cosmochimica Acta 56, 1897-1913.

Myers, J.S. (2001) Protoliths of the 3.8-3.7 Ga Isua greenstone belt, West Greenland. Precambrian Research 105, 129-141.

Myers, J.S. and Crowley, J.L. (2000) Vestiges of life in the oldest Greenland rocks? A review of early Archean geology in the Godthabsfjord region, and reappraisal of field evidence for > 3850 Ma life on Akilia. Precambrian Research 103, 101-124.

Nisbet, E.G. and Nisbet, R.E.R. (2008) Methane, oxygen, photosynthesis, rubisco and the regulation of the air through time. Philos T R Soc B 363, 2745-2754.

Nozaki, Y., Zhang, J. and Amakawa, H. (1997) The fractionation between Y and Ho in the marine environment. Earth and Planetary Science Letters 148, 329-340.

Nutman, A.P., Dawes, P.R., Kalsbeek, F. and Hamilton, M.A. (2008) Palaeoproterozoic and Archaean gneiss complexes in northern Greenland: Palaeoproterozoic terrane assembly in the High Arctic. Precambrian Research 161, 419-451.

Nutman, A.P. and Friend, C.R.L. (2006) Petrography and geochemistry of apatites in banded iron formation, Akilia, W. Greenland: Consequences for oldest life evidence. Precambrian Research 147, 100-106.

Nutman, A.P. and Friend, C.R.L. (2007) Adjacent terranes with c. 2715 and 2650 Ma high-pressure metamorphic assemblages in the Nuuk region of the North Atlantic Craton, souther West Greenland: complexities of Neoarchean collisional orogeny. Precambrian Research 155, 159-203.

Nutman, A.P., Friend, C.R.L., Bennett, V.C. and McGregor, V.R. (2004) Dating of the Ameralik dyke swarms of the Nuuk district, souther West Greenland: mafic intrusion events starting from c. 3510 Ma. Journal of the Geological Society of London 161, 421-430.

Nutman, A.P., McGregor, V.R., Friend, C.R.L., Bennett, V.C. and Kinny, P.D. (1996) The Itsaq Gneiss Complex of southern West Greenland; the world's most

extensive record of early crustal evolution (3900 - 3600 Ma). Precambrian Research 78, 1-39.

Nutman, A.P., Mojzsis, S.J. and Friend, C.R.L. (1997) Recognition of >3850 Ma water-lain sediments in West Greenland and their significance for the early Archean Earth. Geochimica et Cosmochimica Acta 61, 2475-2484.

Ohmoto, H., Watanabe, Y., Yamaguchi, K., Naraoka, H., Kakegawa, T., Haruna, M., Hayashi, K. and Kato, Y. (2006) Chemical and biological evolution of early Earth: constraints from banded iron-formation, in: Kessler, S.E., Ohmoto, H. (Eds.), Evolution of the Atmosphere, Hydrosphere, and Biosphere on Early Earth: Constrainsts from Ore Deposits. Geological Soceity of America, Denver.

Ojakangas, R.W., Morey, G.B. and Southwick, D.L. (2001) Paleoproterozoic basin development and sedimentation in the Lake Superior region, North America. Sediment Geol 141, 319-341.

Olson, J.M. (2006) Photosynthesis in the Archean era. Photosynth Res 88, 109-117.

Pankhurst, R.J., Moorbath, S. and McGregor, V.R. (1973) Late event in the geological evolution of the Godthaab District, West Greenland. Nature 243, 24-26.

Papineau, D., De Gregorio, B.T., Stroud, R.M., Steele, A., Pecoits, E., Konhauser, K., Wang, J. and Fogel, M.L. (2010) Ancient graphite in the Eoarchean quartz-pyroxene rocks from Akilia in southern West Greenland II: Isotopic and chemical compositions and comparison with Paleoproterozoic banded iron formations. Geochimica et Cosmochimica Acta 74, 5884-5905.

Papineau, D., Fogel, M.L., Cody, G.D., DeGregorio, B.T., Fries, M.D., Mojzsis, S.J., Steele, A., Stroud, R.M. and Wang, J. (2008) Graphite associated with apatite in the ~3.8 Ga quartz-pyroxene rock from Akilia, Southwest Greenland. Astrobiology 8, 412.

Pavlov, A. and Kasting, J. (2002) Mass-independent fractionation of sulfur isotopes in Archean sediments: Strong evidence for an anoxic Archean atmosphere. Astrobiology 2, 27-41.

Percak-Dennett, E.M., Beard, B.L., Xu, H., Konishi, H., Johnson, C.M. and Roden, E.E. (2011) Iron isotopic fractionation during microbial dissimilatory iron oxide reduction in simulated Archean seawater. Geobiology 9, 205-220.

Perry, E.C. and Ahmad, S.N. (1977) Carbon isotope composition of graphite and carbonate minerals from 3.8-AE metamorphosed sediments, Isukasia, Greenland. Earth and Planetary Science Letters 36, 280-284.

Pflug, H.D. and Jaeschke-Boyer, H. (1979) Combined structural and chemical analysis of 3,800-Myr-old microfossils. Nature 280, 4830486.

Planavsky, N., Bekker, A., Rouxel, O.J., Kamber, B., Hofmann, A., Knudsen, A. and Lyons, T.W. (2010) Rare Earth Element and yttrium compositions of Archean and Paleoproterozoic Fe formations revisited: New perspectives on the significance and mechanisms of deposition. Geochimica et Cosmochimica Acta 74, 6387-6405.

Planavsky, N., Rouxel, O., Bekker, A., Shapiro, R., Fralick, P. and Knudsen, A. (2009) Iron-oxidizing microbial ecosystems thrived in late Paleoproterozoic redox-stratified oceans. Earth and Planetary Science Letters 286, 230-242.

Planavsky, N., Rouxel, O.J., Bekker, A., Hofmann, A., Little, C.T.S. and Lyons, T.W. (2012) Iron isotope composition of some Archean and Proterozoic iron formations. Geochimica et Cosmochimica Acta 80, 158-169.

Pollack, G.D., Krogstad, E.J. and Bekker, A. (2009) U–Th–Pb–REE systematics of organic-rich shales from the ca. 2.15 Ga Sengoma Argillite Formation, Botswana: Evidence for oxidative continental weathering during the Great Oxidation Event. Chemical Geology 260, 172-185.

Poulton, S.W., Fralick, P.W. and Canfield, D.E. (2004) The transition to a sulphidic ocean similar to 1.84 billion years ago. Nature 431, 173-177.

Pufahl, P.K. and Fralick, P.W. (2004) Depositional controls on Palaeoproterozoic iron formation accumulation, Gogebic Range, Lake Superior region, USA. Sedimentology 51, 791-808.

Quinn, K.A., Byrne, R.H. and Schijf, J. (2006) Sorption of yttrium and rare earth elements by amorphous ferric hydroxide: Influence of solution complexation with carbonate. Geochimica et Cosmochimica Acta 70, 4151-4165.

Rakovan, J.F. and Huges, J.M. (2000) Strontium in the Apatite Structure: Strongian Fluoroapatite and Belovite-(Ce). The Canadian Minerologist 38, 839-845.

Rasmussen, B. and Buick, R. (1999) Redox state of the Archean atmosphere: Evidence from detrital heavy minerals in ca. 3250-2750 Ma sandstones from the Pilbara Craton, Australia. Geology 27, 115-118.

Rollinson, H. (2002) The metamorphic history of the Isua Greenstone Belt, West Greenland. Geological Society, London, Special Publications 199, 329-350.

Rollinson, H. (2003) Metamorphic history suggested by garnet-growth chronologies in the Isua Greenstone Belt, West Greenland. Precambrian Research 126, 181-196.

Rose, N.M., Rosing, M.T. and Bridgwater, D. (1996) The origin of metacarbonate rocks in the Archaean Isua Supracrustal Belt, West Greenland. American Journal of Science 296, 1004-1044.

Rosing, M.T. (1999) 13C-Depleted Carbon Microparticles in 3700-Ma Sea-Floor Sedimentary Rocks from West Greenland. Science 283, 674-676.

Rosing, M.T., Rose, N.M., Bridgwater, D. and Thomsen, H.S. (1996) Earliest part of Earth's stratigraphic record: A reappraisal of the > 3.7 Ga Isua (Greenland) supracrustal sequence. Geology 24, 43-46.

Rouxel, O. (2003) Iron isotope fractionation during oceanic crust alteration. Chemical Geology 202, 155-182.

Rouxel, O., Bekker, A. and Edwards, K. (2005) Iron isotope constraints on the Archean and Paleoproterozoic ocean redox state. Science 307, 1088-1091.

Rouxel, O.J., Sholkovitz, E.R., Charette, M. and Edwards, K.J. (2008) Iron isotope fractionation in subterranean estuaries. Geochimica et Cosmochimica Acta 72, 3413-3430.

Schidlowski, M., Appel, P.W.U., Eichmann, R. and Junge, C.E. (1979) Carbon isotope geochemistry of the 3.7 x 109 yr. old Isua sediments, West Greenland: Implications for the Archean carbon and oxygen cycles. Geochimica et Cosmochimica Acta 43, 189-199.

Schmidt, P. (2003) Reversal asymmetry in Mesoproterozoic overprinting of the 1.88-Ga Gunflint Formation, Ontario, Canada: non-dipole effects or apparent polar wander? Tectonophysics 377, 7-32.

Schoenberg, R. and von Blanckenburg, F. (2005) An assessment of the accuracy of stable Fe isotope ratio measurements on samples with organic and inorganic matrices by high-resolution multicollector ICP-MS. International Journal of Mass Spectrometry 242, 257-272.

Schopf, J.W. (1993) Microfossils of the early Archean Apex chert: new evidnce of the antiquity of life. Science 260, 640-646.

Schopf, J.W. (2006) Fossil evidence of Archaean life. Philos Trans R Soc Lond B Biol Sci 361, 869-885.

Scott, C., Lyons, T.W., Bekker, A., Shen, Y., Poulton, S.W., Chu, X. and Anbar, A.D. (2008) Tracing the stepwise oxygenation of the Proterozoic ocean. Nature 452, 456-459.

Severmann, S., Johnson, C.M., Beard, B.L. and McManus, J. (2006) The effect of early diagenesis on the Fe isotope compositions of porewaters and authigenic minerals in continental margin sediments. Geochimica et Cosmochimica Acta 70, 2006-2022.

Severmann, S., Lyons, T.W., Anbar, A., McManus, J. and Gordon, G.W. (2008) Modern iron isotope perspective on benthic iron shuttle and the redox evolution of ancient oceans. Geology 36, 487-490.

Shiller, A.M. and Mao, L. (2000) Dissolved vanadium in rivers: effects of silicate weathering. Chemical Geology 165, 13-22.

Sholkovitz, E.R. (1992) Chemical evolution of rare earth elements: fractionation between colloidal and solution phases of filtered river water. Earth and Planetary Science Letters 114, 77-84.

Sholkovitz, E.R., Landing, W.M. and Lewis, B.L. (1994) Ocean Particle Chemistry - the Fractionation of Rare-Earth Elements between Suspended Particles and Seawater. Geochimica et Cosmochimica Acta 58, 1567-1579.

Sholkovitz, E.R., Shaw, T.J. and Schneider, D.L. (1992) The Geochemistry of Rare-Earth Elements in the Seasonally Anoxic Water Column and Porewaters of Chesapeake Bay. Geochimica et Cosmochimica Acta 56, 3389-3402.

Siever, R. (1992) The silica cycyle in the Precambrian. Geochimica et Cosmochimica Acta 56, 3265-3272.

Simonson, B. (1985) Sedimentalogical constraints on the origins of the Precambrian iron-formations. Geological Society of America Bulletin 96, 244-252.

Simonson, B. and Hassler, S. (1996) Was the deposition of large Precambrian iron formations linked to a major marine transgression? J Geol 104, 665-676.

Simpson, S. (2003) Questioning the oldest signs of life. Scientific American, 70-77.

Sogaard, E.G., Medenwaldt, R. and Abraham-Peskir, J.V. (2000) Conditions and rates of biotic and abiotic iron precipitation in selected Danish freshwater plants and microscopic analysis of precipitate morphology. Water Res 34, 2675-2682.

Spier, C., de Oliveira, S.M.B., Sial, A.N. and Rios, F.J. (2007) Geochemistry and genesis of the banded Fe formations of the Caue Formation, Quadriletero Ferrifero, Minas Gerais, Brazil. Precambrian Research 152, 170-206.

Steinhoefel, G., Horn, I. and von Blanckenburg, F. (2009) Micro-scale tracing of Fe and Si isotopic signatures in banded iron formation using femtosecond laser ablation. Geochimica et Cosmochimica Acta 73, 5343-5360.

Steinhoefel, G., von Blanckenburg, F., Horn, I., Konhauser, K.O., Beukes, N.J. and Gutzmer, J. (2010) Deciphering formation processes of banded iron formations from the Transvaal and the Hamersley successions by combined Si and Fe isotope analysis using UV femtosecond laser ablation. Geochimica et Cosmochimica Acta 74, 2677-2696.

Straub, K.L., Rainey, F.A. and Widdel, F. (1999) Rhodovulum iodosum sp. nov, and Rhodovulum robiginosum sp. nov., two new marine phototrophic ferrous-iron-oxidizing purple bacteria. Int J Syst Bacteriol 49, 729-735.

Tangalos, G.E., Beard, B.L., Johnson, C.M., Alpers, C.N., Shelobolina, E.S., Xu, H., Konishi, H. and Roden, E.E. (2010) Microbial production of isotopically light iron(II) in a modern chemically precipitated sediment and implications for isotopic variations in ancient rocks. Geobiology 8, 197-208.

Taylor, S.R. and McLennan, S.M. (1985) The Continental Crust: Its Compostion and Evolution. Blackwell, Oxford.

Thurston, P.C., Kamber, B.S. and Whitehouse, M. (2012) Archean cherts in banded iron formation: Insight into Neoarchean ocean chemistry and depositional processes. Precambrian Research 214-215, 227-257.

Tice, M. and Lowe, D.R. (2004) Photosynthetic microbial mats in the 3,416-My-old ocean. Nature 431, 549-552.

Towe, K.M. (1983) Precambrian Atmospheric Oxygen and Banded Iron Formations - a Delayed Ocean Model. Precambrian Research 20, 161-170.

Trendall, A.F. (2002) The significance of iron-formation in the Precambrian stratigraphic record. Special Publication International Association of Sedimentalogists 33, 33-66.

Trendall, A.F. and Blockey, J. (1970) The iron-formations of the Precambrian Hamersley Group, Western Australia. Geological Survey Western Australia Bulletin 119, 366.

Tribovillard, N., Algeo, T., Lyons, T.W. and Riboulleau, A. (2006) Trace metals as paleoredox and paleoproductivity proxies: An update. Chemical Geology 232, 12-32.

Tsikos, H., Matthews, A., Erel, Y. and Moore, J.M. (2010) Iron isotopes constrain biogeochemial redox cycling of iron and manganese in a Paleoproterozoic stratified basin. Earth and Planetary Science Letters 298, 125-143.

Ulrich, T., Kamber, B.S., Woodhead, J.D. and Spencer, L.A. (2010) Long-Term Observations of Isotope Ratio Accuracy and Reproducibility Using Quadrupole ICP-MS. Geostand Geoanal Res 34, 161-174.

Urai, J., Means, W. and Lister, G. (1986) Dynamic Recrystallization of Minerals, in: Hobbs, B., Heard, H. (Eds.), Mineral and Rock Deformation: Laboratory Studies. American Geophysical Union, pp. 161-199.

van Zuilen, M.A., Lepland, A. and Arrhenius, G. (2002) Reassessing the evidence for the earliest traces of life. Nature 418, 627-630.

van Zuilen, M.A., Lepland, A., Teranes, J., Finarelli, J., Wahlen, M. and Arrhenius, G. (2003) Graphite and carbonates in the 3.8 Ga old Isua Supracrustal Belt, southern West Greenland. Precambrian Research 126, 331-348.

Vargas, M., Keshefi, K., Blunt-Harris, E. and Lovley, D.R. (1998) Microbiological evidence for Fe(III) reduction on early Earth. Nature 395, 65-67.

Veizer, J. (1983) Geologic evolution of the Archean - Early Proterozoic Earth, in: Schopf, J.W. (Ed.), Earth's Earliest Biosphere. Princeton University Press, NJ, pp. 240-259.

Volkov, I.I. and Fomina, L.S. (1974) Influence of organic material and processes of sulfide formation on distribution of some trace elements in deep-water sediments of the Black Sea, in: Degens, E.T., Ross, D.A. (Eds.), The Black Sea - Geology, Chemistry and Biology, American Association of Petroleum Geologists Memoir 20, Tulsa, OK, pp. 456-476.

Webb, G.E., Northdurft, L.D., Kamber, B.S., Kloprogge, J.T. and Zhao, J. (2009) Rare earth element geochemistry of scleractinian coral skeleton during meteroic diagenesis: a sequence through neomorphism and aragonite to calcite. Sedimentology 56.

Wehrli, B. and Stumm, W. (1989) Vanadyl in natural waters: Adsportion and hydrolysis promote oxygenation. Geochimica et Cosmochimica Acta 53, 69-77.

Welch, S.A., Beard, B.L., Johnson, C.M. and Braterman, P.S. (2003) Kinetic and equilibrium Fe isotope fractionation between aqueous Fe(II) and Fe(III). Geochimica et Cosmochimica Acta 67, 4231-4250.

Whitehouse, M.J. and Fedo, C.M. (2003) Deformation features and critical field relationships of early Archean rocks, Akilia, southwest Greenland. Precambrian Research 126, 259-271.

Whitehouse, M.J. and Fedo, C.M. (2007) Microscale heterogeneity of Fe isotopes in >3.71 Ga banded iron formation from the Isua Greenstone Belt, southwest Greenland. Geology 35, 719.

Whitehouse, M.J. and Kamber, B.S. (2005) Assigning dates to thin gneissic veins in high-grade metamorphic terranes: a cautionary tale from Akilia, southwest Greenland. Journal of Petrology 46, 291-318.

Whitehouse, M., Kamber, B., Fedo, C. and Lepland, A. (2005) Integrated Pb- and S-isotope investigation of sulphide minerals from the early Archaean of southwest Greenland. Chemical Geology 222, 112-131.

Whitehouse, M.J., Kamber, B.S. and Moorbath, S. (1999) Age significance of U-Th-Pb zircon data from early Archean rocks of west Greenland: a reassessment based on combined ion-microprobe and imaging studies. Chemical Geology 160, 201-224.

Whitehouse, M.J., Myers, J.S. and Fedo, C.M. (2009) The Akilia Controversy: field, structural and geochronological evidence questions interpretations of >3.8 Ga life in SW Greenland. Journal of the Geological Society 166, 335-348.

Widdel, F., Schnell, S., Heising, S., Ehrenreich, A., Assmus, B. and Schink, B. (1993) Ferrous Iron Oxidation by Anoxygenic Phototrophic Bacteria. Nature 362, 834-836.

Wu, L., Beard, B.L., Roden, E.E. and Johnson, C.M. (2009) Influence of pH and dissolved Si on Fe isotope fractionation during dissimilatory microbial reduction of hematite. Geochimica et Cosmochimica Acta 73, 5584-5599.

Yang, W. and Holland, H.D. (2002) The redox-sensitive trace elements, Mo, U, and Re in Precambrian carbonaceous shales: Indicators of the Great Oxidation Event. Geological Society of America Bulletin 34, 381.

# Appendix 3

Table 4.1.
Trace and rare-earth element compositions of Isua and Akilia samples

| Element | IS-Y | IS-X | 92-197 | AK-33 | AK-38[1] | AK-02[1] |
|---|---|---|---|---|---|---|
| Sc (ppm) | < 1 | < 1 | 1 | < 1 | 20.1 | 25.7 |
| Be | < 1 | < 1 | < 1 | < 1 | n.d. | n.d. |
| V | 6 | < 5 | 10 | < 5 | 118 | 131.17 |
| Cr | < 20 | < 20 | < 20 | < 20 | 2200 | 3600 |
| Co | 1 | < 1 | 8 | 7 | 35 | 93 |
| Ni | < 20 | < 20 | 130 | 90 | 108 | 758.00 |
| Cu | 10 | 10 | 210 | 240 | 848 | 106.63 |
| Zn | 50 | 40 | 50 | 40 | 131 | 113.95 |
| Ga | 1 | 2 | 2 | 3 | 10.17 | 7.73 |
| Ge | < 0.5 | 1 | 3.2 | 3.6 | 8.18 | 1.32 |
| As | < 5 | < 5 | 11 | 13 | n.d. | n.d. |
| Rb | < 1 | 1 | 3 | 2 | 3.82 | 2.06 |
| Sr | 30 | 20 | 14 | 7 | 17.69 | 20.84 |
| Y | 4.5 | 6.6 | 2.2 | 4.7 | 17.07 | 9.65 |
| Zr | 3 | 40 | 3 | 2 | 16.02 | 19.17 |
| Nb | 0.4 | 1.1 | 2.3 | 1.1 | 4.49 | 1.17 |
| Mo | < 2 | < 2 | 3 | 3 | 4.38 | b.d. |
| Ag | < 0.5 | < 0.5 | 1.9 | 1 | n.d. | n.d. |
| In | < 0.1 | < 0.1 | 0.1 | 0.1 | 0.11 | b.d. |
| Sn | < 1 | < 1 | 1 | < 1 | 3.67 | b.d. |
| Sb | < 0.2 | < 0.2 | 0.3 | 0.3 | b.d. | b.d. |
| Cs | 0.5 | 0.3 | 0.2 | 0.3 | b.d. | b.d. |
| Ba | 95 | 106 | 36 | 4 | 4.37 | 6.13 |
| La | 3.57 | 4.48 | 3 | 2.16 | 4.06 | 1.08 |
| Ce | 3.47 | 5.4 | 3.65 | 3.62 | 14.82 | 2.86 |
| Pr | 0.36 | 0.6 | 0.5 | 0.75 | 2.08 | 0.44 |
| Nd | 1.15 | 2.02 | 2.49 | 4.08 | 9.44 | 2.41 |
| Pm | n.d. | n.d. | n.d. | n.d. | n.d. | n.d. |
| Sm | 0.21 | 0.38 | 0.76 | 1.34 | 2.47 | 0.88 |
| Eu | 0.205 | 0.274 | 0.254 | 0.359 | 1.07 | 0.47 |
| Gd | 0.29 | 0.49 | 0.75 | 1.34 | 2.74 | 1.26 |
| Tb | 0.05 | 0.08 | 0.11 | 0.2 | 0.46 | 0.24 |
| Dy | 0.32 | 0.52 | 0.58 | 1.09 | 2.74 | 1.54 |
| Ho | 0.07 | 0.11 | 0.11 | 0.21 | 0.54 | 0.32 |
| Er | 0.24 | 0.36 | 0.35 | 0.64 | 1.64 | 0.99 |
| Tm | 0.036 | 0.053 | 0.059 | 0.11 | 0.24 | 0.15 |
| Yb | 0.19 | 0.31 | 0.47 | 0.84 | 1.59 | 0.88 |
| Lu | 0.021 | 0.042 | 0.086 | 0.135 | 0.23 | 0.14 |
| Hf | < 0.1 | 0.9 | 0.5 | 0.6 | 0.491 | 0.525 |
| Ta | < 0.01 | 0.05 | 0.14 | 0.12 | 0.443 | 0.802 |
| W | 1.9 | 1.8 | 1.3 | 1.5 | b.d. | 9.30 |
| Tl | < 0.05 | < 0.05 | 0.29 | 0.42 | 0.08 | b.d. |
| Pb | 6 | < 5 | 8 | < 5 | b.d. | b.d. |
| Bi | < 0.1 | 0.1 | 0.5 | 0.6 | 0.47 | b.d. |
| Th | 0.16 | 0.26 | 0.31 | 0.16 | 0.110 | 1.437 |
| U | 0.22 | 0.38 | 0.95 | 0.38 | 0.155 | 0.055 |

n.d. = not determined
b.d. = below detection
[1] = previously reported in Fedo and Whitehouse (2002)

Table 4.2.
Major element compositions of Isua and Akilia samples

| Oxide wt% | IS-Y | IS-X | 92-197 | AK-33 | AK-38[1] | AK-02[1] |
|---|---|---|---|---|---|---|
| $SiO_2$ | 4.78 | 23.46 | 67.85 | 63.21 | 48.47 | 48.74 |
| $Al_2O_3$ | 0.26 | 0.53 | 0.32 | 0.34 | 4.58 | 7.35 |
| $Fe_2O_3$(T) | 9.07 | 7.51 | 25.84 | 23.28 | 21.75 | 11.68 |
| MnO | 0.812 | 0.708 | 0.314 | 0.333 | 0.355 | 0.177 |
| MgO | 14.26 | 13.88 | 4.5 | 5.53 | 10.12 | 22.35 |
| CaO | 29.27 | 26.82 | 2.34 | 7.33 | 11.64 | 6.46 |
| $Na_2O$ | 0.02 | 0.05 | 0.07 | 0.09 | 0.87 | 1.21 |
| $K_2O$ | < 0.01 | 0.03 | 0.03 | 0.04 | 0.21 | 0.1 |
| $TiO_2$ | 0.008 | 0.016 | 0.025 | 0.005 | 0.274 | 0.283 |
| $P_2O_5$ | 0.02 | 0.02 | 0.05 | 0.01 | 0.05 | 0.04 |
| LOI | 40.65 | 26.37 | b.d. | b.d. | 1.59 | 1.57 |
| Total | 99.13 | 99.39 | 100.1 | 99.99 | 99.89 | 99.95 |

b.d. = below detection
[1] = previously reported in Fedo and Whitehouse (2002)

Table 4.3
Representative microprobe analyses of pyroxene in Akilia samples

| Sample | AK33 | 92-197 | | AK38 | AK42 | AK43 | | AK47 | AK02 |
|---|---|---|---|---|---|---|---|---|---|
| Rock Type | QAP | QAP | | QAP | QAP | QAP | | amphibolite | ultramafic |
| notes[a] | Cpx | Cpx | Opx | Cpx | Cpx | Cpx | Opx | Cpx | Opx |
| Oxide wt% | | | | | | | | | |
| $SiO_2$ | 50.95 | 50.49 | 48.27 | 51.80 | 51.32 | 51.16 | 49.00 | 52.53 | 54.60 |
| $TiO_2$ | 0.00 | 0.00 | 0.00 | 0.02 | 0.00 | 0.00 | 0.00 | 0.11 | 0.04 |
| $Al_2O_3$ | 0.47 | 0.32 | 0.18 | 0.31 | 0.42 | 0.09 | 0.05 | 0.97 | 1.45 |
| $Cr_2O_3$ | 0.00 | 0.00 | 0.01 | 0.16 | 0.01 | 0.02 | 0.00 | 0.05 | 0.09 |
| FeO[b] | 17.5 | 17.7 | 40.3 | 12.7 | 17.6 | 18.06 | 39.93 | 11.15 | 14.2 |
| MnO | 0.46 | 0.38 | 0.67 | 0.54 | 0.46 | 0.28 | 0.72 | 0.41 | 0.26 |
| MgO | 8.42 | 8.73 | 9.70 | 10.8 | 8.36 | 8.71 | 9.76 | 11.26 | 29.47 |
| CaO | 22.0 | 21.3 | 0.58 | 22.6 | 22.1 | 21.6 | 0.69 | 23.6 | 0.13 |
| $Na_2O$ | 0.23 | 0.18 | 0.00 | 0.25 | 0.17 | 0.15 | 0.00 | 0.28 | 0.02 |
| $K_2O$ | - | 0.01 | 0.01 | - | 0.01 | 0.02 | - | 0.01 | - |
| Total | 100.0 | 99.0 | 99.7 | 99.2 | 100.4 | 100.1 | 100.2 | 100.4 | 100.2 |
| | | | | | | | | | |
| Atoms per 6 oxygens | | | | | | | | | |
| Si | 1.98 | 1.98 | 1.98 | 1.99 | 1.99 | 1.99 | 1.99 | 1.98 | 1.95 |
| Ti | 0.00 | 0.00 | 0.00 | 0.00 | 0.00 | 0.00 | 0.00 | 0.00 | 0.00 |
| Al | 0.02 | 0.01 | 0.01 | 0.01 | 0.02 | 0.00 | 0.00 | 0.04 | 0.06 |
| Cr | 0.00 | 0.00 | 0.00 | 0.00 | 0.00 | 0.00 | 0.00 | 0.00 | 0.00 |
| $Fe^{toal}$ | 0.57 | 0.58 | 1.38 | 0.41 | 0.57 | 0.59 | 1.36 | 0.35 | 0.42 |
| Mn | 0.02 | 0.01 | 0.02 | 0.02 | 0.02 | 0.01 | 0.02 | 0.01 | 0.01 |
| Mg | 0.49 | 0.51 | 0.59 | 0.62 | 0.48 | 0.51 | 0.59 | 0.63 | 1.57 |
| Ca | 0.92 | 0.90 | 0.03 | 0.93 | 0.92 | 0.90 | 0.03 | 0.95 | 0.01 |
| Na | 0.02 | 0.01 | 0.00 | 0.02 | 0.01 | 0.01 | 0.00 | 0.02 | 0.00 |
| K | - | <0.01 | <0.01 | - | <0.01 | <0.01 | - | <0.01 | - |
| Total | 4.01 | 4.01 | 4.02 | 4.01 | 4.01 | 4.01 | 4.00 | 4.00 | 4.02 |

[a] Opx = orthopyroxene, Cpx = clinopyroxene.

[b] Total Fe as FeO

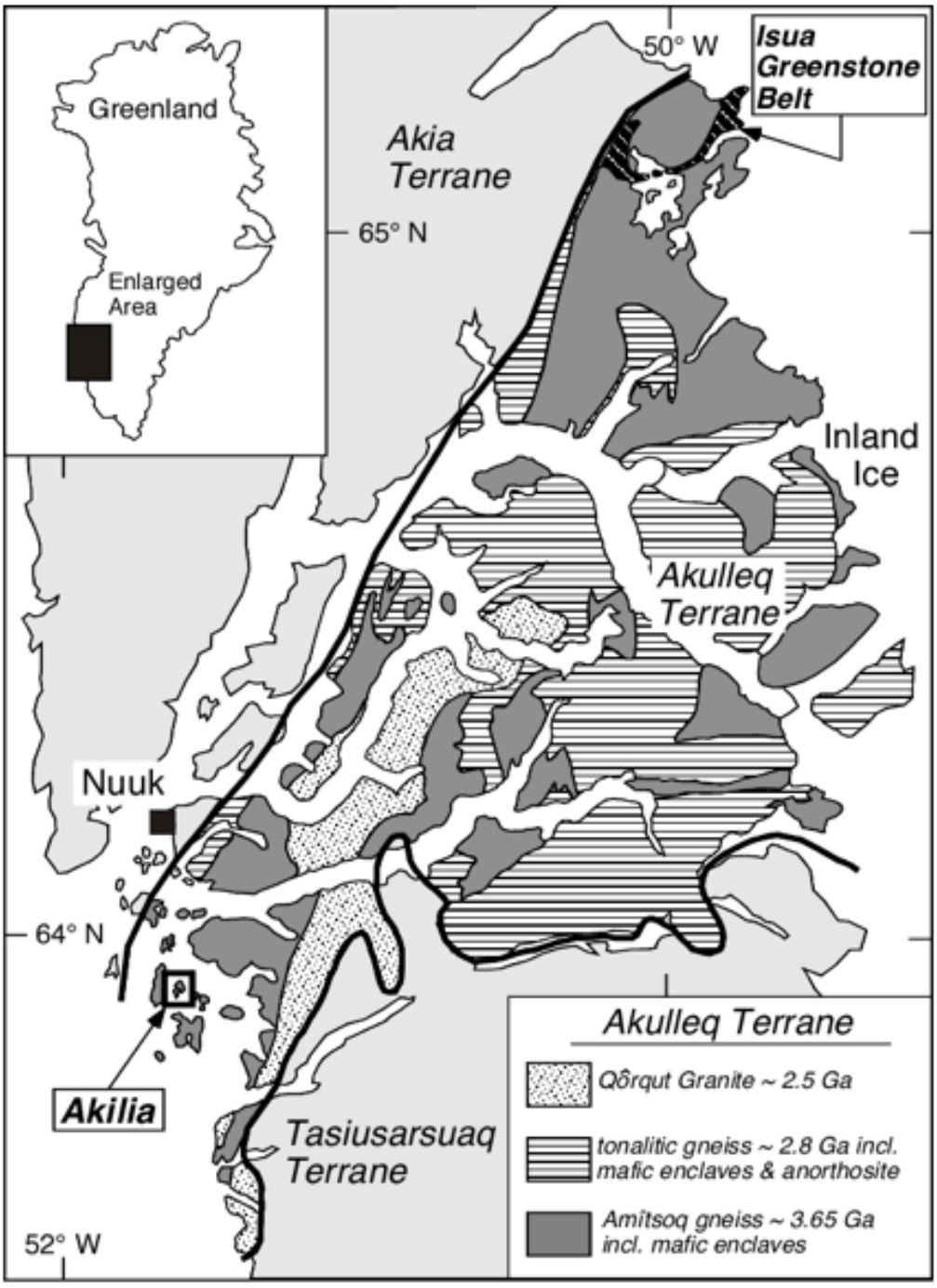
Table 4.4

Representative microprobe analyses of amphibole in Akilia and Isua samples

| Sample | AK30 | | AK33 | | 92-197 | | AK38 | | AK42 | | | AK43 | AK47 | AK48 | | | AK02 | | IS-X | | IS-Y |
|---|---|---|---|---|---|---|---|---|---|---|---|---|---|---|---|---|---|---|---|---|---|
| Rock Type | QAP | | QAP | | QAP | | QAP | | QAP | | | QAP | amphibolite | cross-cutting vein | | | ultramafic | | ultramafic | | ultramafic |
| notes[a] | Hnb | Act | Hnb | Cm | Act | Cm | Act | Cm | Act | Hnb | Cm | Cm | Hnb | Act | Cm | Hnb | Hnb | Cm | Act | Cm | Act |
| Oxide wt% | | | | | | | | | | | | | | | | | | | | | |
| $SiO_2$ | 43.7 | 52.5 | 45.1 | 51.5 | 48.3 | 50.4 | 51.9 | 52.4 | 51.3 | 44.9 | 51.3 | 51.8 | 42.9 | 48.9 | 54.0 | 44.0 | 47.4 | 56.0 | 55.11 | 54.51 | 55.31 |
| $TiO_2$ | 0.87 | 0.24 | 0.06 | 0.02 | 0.00 | 0.01 | 0.16 | 0.01 | 0.00 | 0.07 | 0.00 | 0.00 | 1.14 | 0.38 | 0.02 | 0.16 | 0.41 | 0.06 | 0.02 | 0.00 | 0.04 |
| $Al_2O_3$ | 10.65 | 2.91 | 8.06 | 0.47 | 5.14 | 0.24 | 2.30 | 0.16 | 2.27 | 7.27 | 0.58 | 0.05 | 11.53 | 6.96 | 0.48 | 12.02 | 9.34 | 1.49 | 1.47 | 0.26 | 1.78 |
| $Cr_2O_3$ | 1.52 | 0.01 | 0.00 | 0.01 | 0.00 | 0.03 | 0.38 | 0.00 | 0.02 | 0.00 | 0.04 | 0.00 | 0.17 | 0.00 | 0.00 | 0.00 | 0.37 | 0.02 | 0.02 | 0.00 | 0.00 |
| FeO[b] | 17.0 | 15.6 | 24.4 | 33.4 | 24.3 | 35.17 | 17.25 | 28.4 | 22.8 | 24.95 | 32.64 | 33.49 | 19.24 | 17.00 | 26.15 | 20.00 | 7.3 | 12.8 | 10.22 | 21.50 | 9.43 |
| MnO | 0.29 | 0.28 | 0.23 | 0.70 | 0.29 | 0.55 | 0.35 | 1.13 | 0.30 | 0.24 | 0.77 | 0.44 | 0.36 | 0.23 | 0.69 | 0.20 | 0.13 | 0.30 | 0.19 | 0.81 | 0.32 |
| MgO | 9.80 | 14.36 | 7.25 | 10.9 | 8.85 | 10.00 | 12.90 | 14.08 | 10.36 | 7.28 | 10.10 | 11.17 | 8.25 | 12.36 | 15.81 | 8.98 | 18.61 | 26.17 | 17.91 | 17.88 | 18.78 |
| CaO | 11.6 | 11.6 | 11.22 | 1.3 | 10.9 | 0.7 | 11.87 | 1.3 | 10.3 | 11.2 | 1.3 | 0.6 | 12.0 | 11.3 | 0.9 | 10.5 | 11.33 | 0.3 | 12.20 | 2.11 | 11.99 |
| $Na_2O$ | 1.40 | 0.52 | 0.91 | 0.04 | 0.50 | 0.05 | 0.23 | 0.00 | 0.19 | 0.83 | 0.05 | 0.00 | 1.31 | 0.93 | 0.09 | 1.43 | 1.69 | 0.20 | 0.21 | 0.03 | 0.25 |
| $K_2O$ | 0.44 | 0.08 | 0.40 | 0.01 | 0.11 | 0.01 | 0.09 | 0.00 | 0.05 | 0.47 | 0.03 | 0.00 | 1.05 | 0.28 | 0.00 | 0.54 | 0.16 | 0.01 | 0.03 | 0.01 | 0.05 |
| Total | 97.2 | 98.1 | 97.6 | 98.2 | 98.4 | 97.2 | 97.4 | 97.4 | 97.6 | 97.2 | 96.9 | 97.6 | 98.0 | 98.4 | 98.2 | 97.8 | 96.7 | 97.3 | 97.39 | 97.10 | 97.96 |
| Atoms per 23 oxygens | | | | | | | | | | | | | | | | | | | | | |
| Si | 6.59 | 7.63 | 6.95 | 7.90 | 7.33 | 7.90 | 7.67 | 7.92 | 7.73 | 6.99 | 7.96 | 7.98 | 6.51 | 7.18 | 7.96 | 6.63 | 6.80 | 7.80 | 7.84 | 7.98 | 7.80 |
| Ti | 0.10 | 0.03 | 0.01 | 0.00 | 0.00 | 0.00 | 0.02 | 0.00 | 0.00 | 0.01 | 0.00 | 0.00 | 0.13 | 0.04 | 0.00 | 0.02 | 0.04 | 0.01 | 0.00 | 0.00 | 0.00 |
| Al | 1.89 | 0.50 | 1.47 | 0.09 | 0.92 | 0.04 | 0.40 | 0.03 | 0.40 | 1.33 | 0.11 | 0.01 | 2.06 | 1.20 | 0.08 | 2.13 | 1.58 | 0.24 | 0.25 | 0.04 | 0.30 |
| Cr | 0.03 | 0.00 | 0.00 | 0.00 | 0.00 | 0.00 | 0.01 | 0.00 | 0.00 | 0.00 | 0.00 | 0.00 | 0.00 | 0.00 | 0.00 | 0.00 | 0.02 | 0.00 | 0.00 | 0.00 | 0.00 |
| $Fe^{total}$ | 2.14 | 1.90 | 3.15 | 4.28 | 3.08 | 4.61 | 2.13 | 3.59 | 2.88 | 3.25 | 4.23 | 4.31 | 2.44 | 2.09 | 3.22 | 2.52 | 0.88 | 1.49 | 1.22 | 2.63 | 1.11 |
| Mn | 0.04 | 0.03 | 0.03 | 0.09 | 0.04 | 0.07 | 0.04 | 0.14 | 0.04 | 0.03 | 0.10 | 0.06 | 0.05 | 0.03 | 0.09 | 0.03 | 0.02 | 0.04 | 0.02 | 0.10 | 0.04 |
| Mg | 2.20 | 3.11 | 1.67 | 2.48 | 2.00 | 2.33 | 2.85 | 3.17 | 2.33 | 1.69 | 2.34 | 2.56 | 1.86 | 2.70 | 3.47 | 2.02 | 3.98 | 5.43 | 3.80 | 3.90 | 3.95 |
| Ca | 1.87 | 1.80 | 1.86 | 0.21 | 1.77 | 0.11 | 1.88 | 0.21 | 1.66 | 1.87 | 0.22 | 0.10 | 1.95 | 1.78 | 0.15 | 1.69 | 1.74 | 0.04 | 1.86 | 0.33 | 1.81 |
| Na | 0.41 | 0.15 | 0.27 | 0.01 | 0.15 | 0.01 | 0.07 | 0.00 | 0.05 | 0.25 | 0.01 | 0.00 | 0.38 | 0.26 | 0.02 | 0.42 | 0.47 | 0.05 | 0.06 | 0.01 | 0.07 |
| K | 0.08 | 0.02 | 0.08 | 0.00 | 0.02 | 0.00 | 0.02 | 0.00 | 0.01 | 0.09 | 0.01 | 0.00 | 0.20 | 0.05 | 0.00 | 0.10 | 0.03 | 0.00 | 0.01 | 0.00 | 0.01 |
| Total | 15.4 | 15.2 | 15.5 | 15.1 | 15.3 | 15.1 | 15.1 | 15.1 | 15.1 | 15.5 | 15.0 | 15.0 | 15.6 | 15.3 | 15.0 | 15.6 | 15.6 | 15.1 | 15.06 | 15.00 | 15.09 |

[a] Hnb = hornblende, Act = actinolite Cm = cummingtonite,

[b] Total Fe as FeO.


Greenland
Enlarged Area
50° W
Isua Greenstone Belt
Akia Terrane
65° N
Inland Ice
Akulleq Terrane
Nuuk
64° N
Akilia
Tasiusarsuaq Terrane
52° W
Akulleq Terrane
Qôrqut Granite ~ 2.5 Ga
tonalitic gneiss ~ 2.8 Ga incl. mafic enclaves & anorthosite
Amîtsoq gneiss ~ 3.65 Ga incl. mafic enclaves

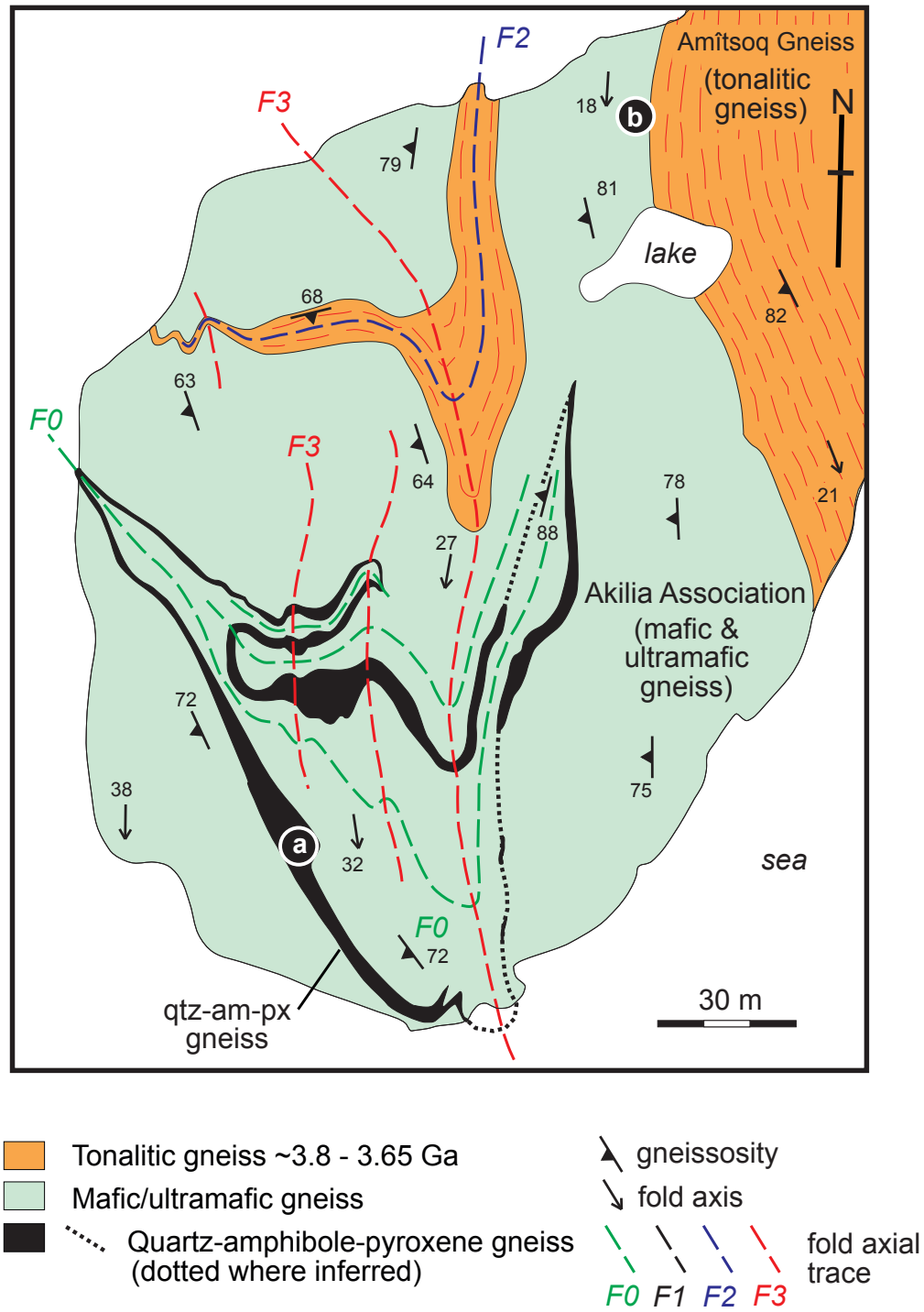



Figure 4.2. Simple structural interpretation of the geology of the southwestern end of Akilia. The location of the main qtz-am-px (QAP) outcrop seen in Fig. 4.3 is marked with (a). The location of the critical contact discussed in this paper between the Amîtsoq Gneiss and Akilia Association is marked with (b). Map modified from Whitehouse et al. (2009).

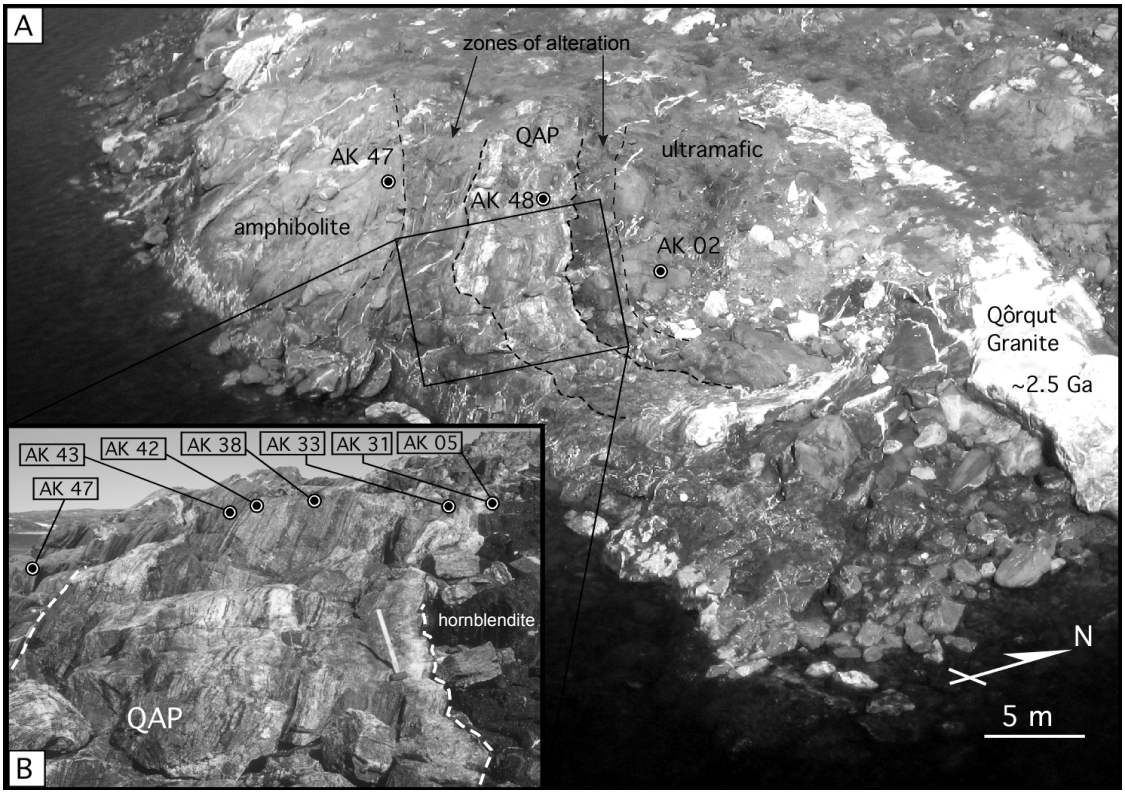



Figure 4.3. (A) Oblique aerial photograph looking NW showing the main 5-m thick QAP outcrop located on the southwestern tip of Akilia. Dashed lines show the contact with the surrounding amphibolite and ultramafic units. Dotted lines show an area of alteration on either side of QAP. The intrusive 2.5 Ga Qôrqut granite can also be seen. (B) The QAP unit, showing the location of samples used in this study. The "banded" nature of the outcrop is evident. Dashed lines show the contact with the surrounding amphibolite (to the south) and hornblendite (to the north).

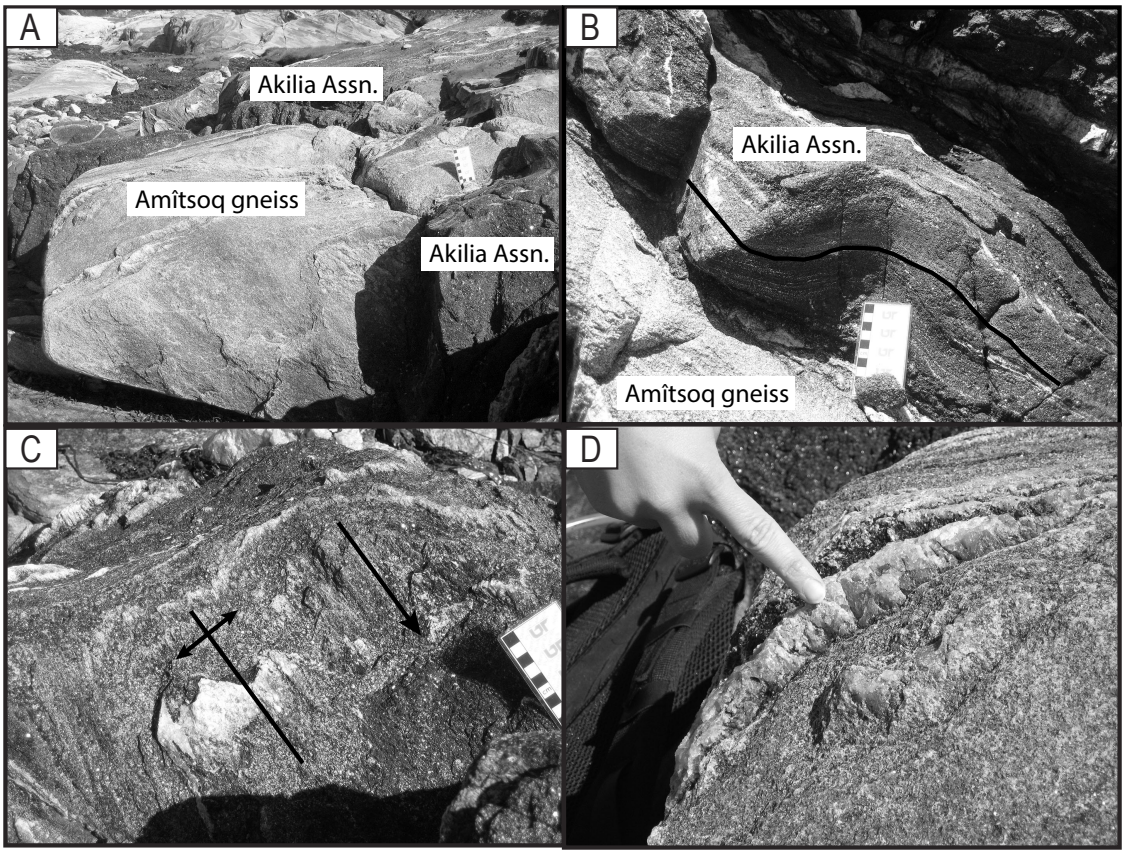



Figure 4.4. Field photographs of the key relationships between the Akilia Association and the Amîtsoq Gneiss. (A) Tectonic interleaving of Akilia Association and the Amîtsoq Gneiss that has been used to date the QAP lithology based on inferred intrusive relationships. (B) Close up of the key contact, where the deformed, tectonically folded nature of the contact can be seen. (C) Foliation surfaces and folded quartz in in the Akilia Association. (D) Close up of quartz stretching lineations in the Akilia Association. Finger in orientation of stretching lineations.

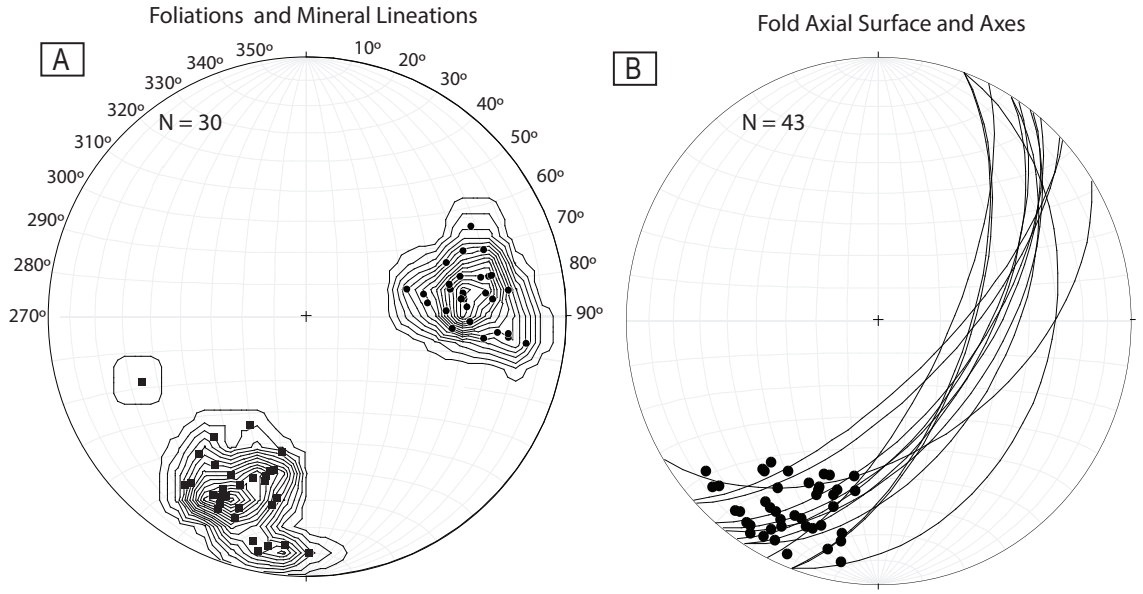



Figure 4.5. Stereographic projections of structural data collected on rocks associated with the contact between the Akilia Association and Amîtsoq Gneisses. (A) All foliations (black circles) consistently strike N and dip W. Mineral lineations (black squares) trend SW and have gentle to moderate plunge towards the SSE. (B) Axial surfaces (great circles) strike NE-SW and dip moderately to the SE. Fold axes (black circles) trend SW and are gently plunging.

Figure 4.6. Photomicrographs and back-scattered electron detection (BSE) images of samples from the QAP unit. (A) Cross-polarized light image of sample AK 33. (B) Plane polarized light image of sample AK 33 showing the presence of garnet surrounded by amphibole and quartz. (C) Plane polarized light image of sample AK 38. (D) BSE image of close-up of sample AK 38 displaying the relationship between amphiboles (amp) and clinopyroxene (cpx). (E) Plane polarized light image of sample AK43. (F) BSE image of close-up of sample AK 43 showing clinopyxroxne (cpx), orthopyroxene (opx), amphibole (amp) and magnetite (mt). (G) Plane polarized light image of sample AK 42. (H) BSE image of close-up of sample AK 42 showing relationship between amphibole (amp) and clinopyroxene (cpx), as well as the presence of calcite.

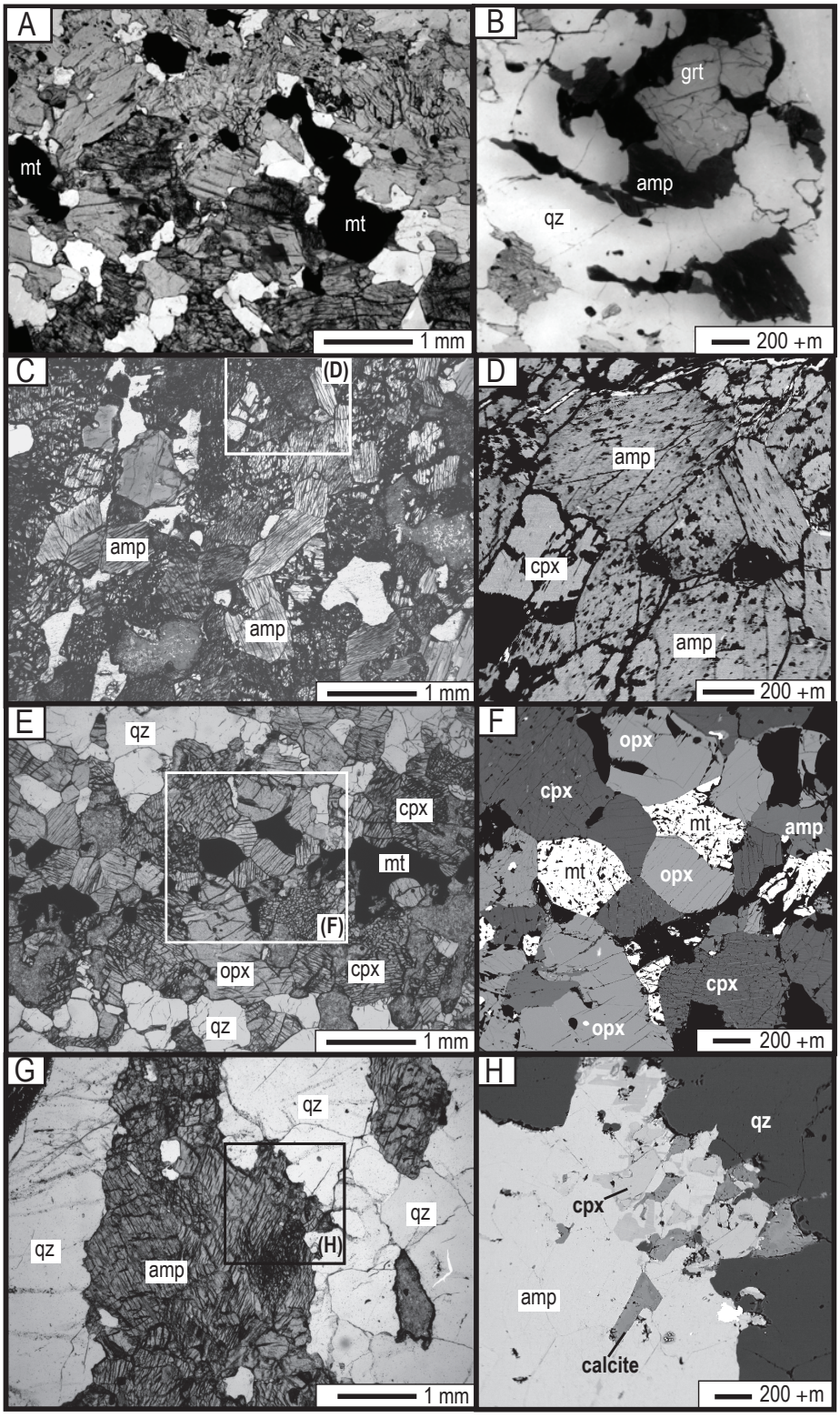



Figure 4.6. continued

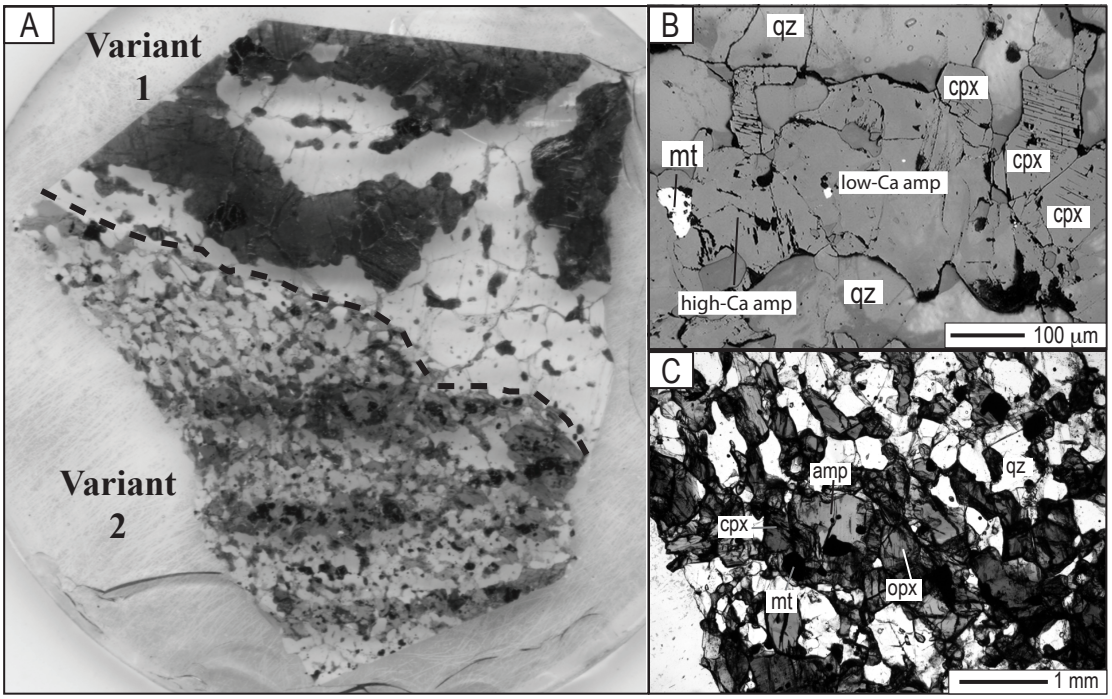



Figure 4.7. Sample 92-197 (A) Incident light image of sample 92-197. The upper half of the thin section is coarsely crystalline, magnetite poor, and dominated by clinopyroxene and quartz. The lower half is finer grained, magnetite is present, and contains dominantly orthopyroxene, quartz, and amphiboles. (B) Reflected light image of clinopyroxene (cpx), high-Ca amphibole, low-Ca amphibole, quartz (qz) and magnetite (mt) from the upper half of sample 92-197. (C) Cross- polarized light image of clinopyroxene (cpx), orthopyroxene (opx), amphibole, quartz (qz) and magnetite (mt) from the lower half of sample 92-197.

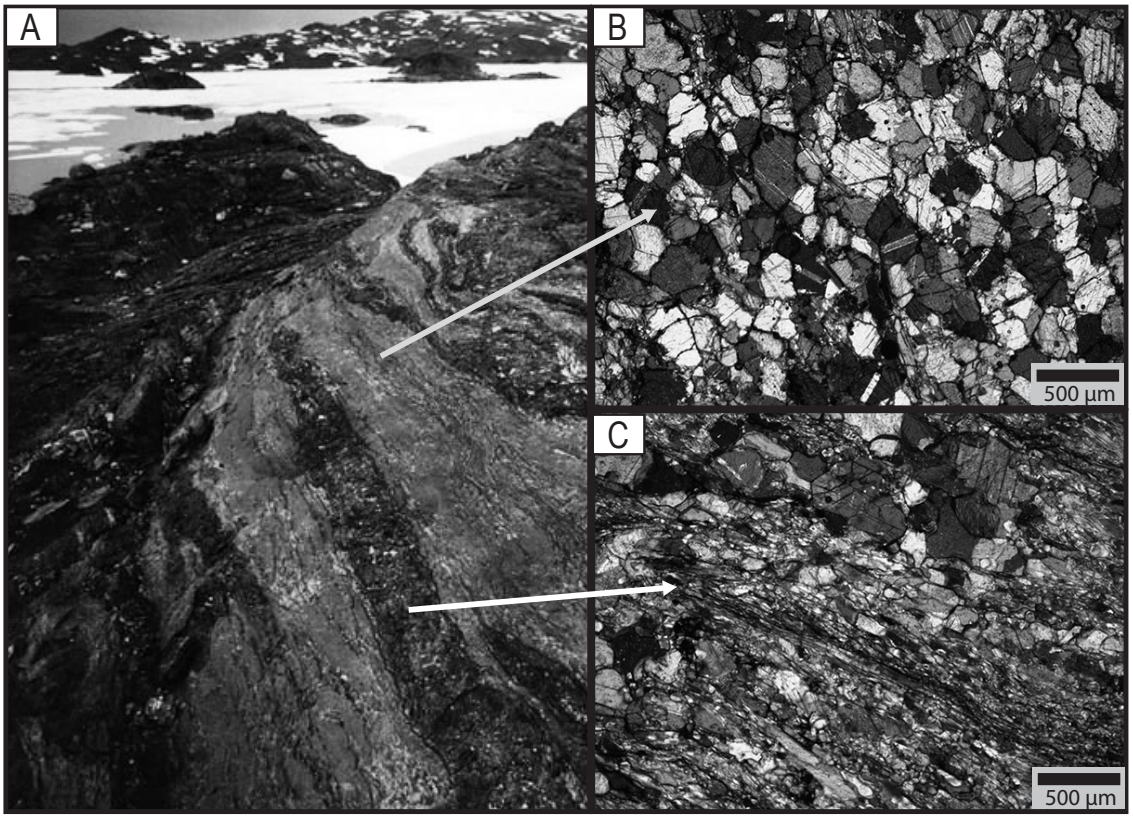



Figure 4.8. (A) Field location of samples IS-X and IS-Y. Photograph by Sarah Simpson (Simpson, 2003). (B) Thin section IS-X. (C) Thin section IS-Y.

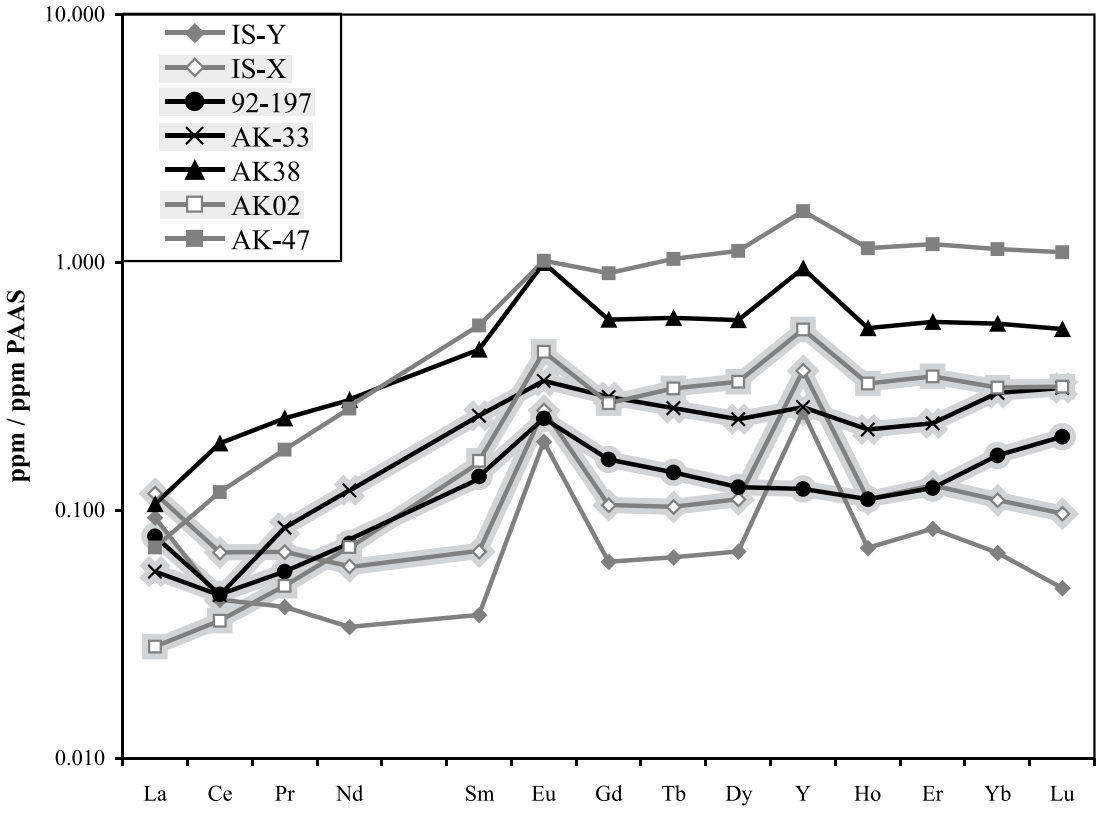



Figure 4.9. REY systematics of a sample from the QAP lithology (AK 38), ultramafic rocks adjacent to the QAP lithology (AK 02), Isua ultramafic sample with disseminated ferroan dolomite (IS- X), Isua ultramafic sample comprised almost entirely of ferroan dolomite (IS-Y), original Akilia life rock (92-197), in-place equivalent of original Akilia life rock from QAP lithology (AK 33) and an amphibolite unit adjacent to the QAP lithology (AK 47). AK 33 and 92-197 have very similar REY patterns, which is why AK 33 is considered the in-place equivalent of 92-197. The REY systematics also show that AK 38 is geochemically more similar to mafic (AK 47) and ultramafic (AK 02) rocks than to other layers in the QAP unit.

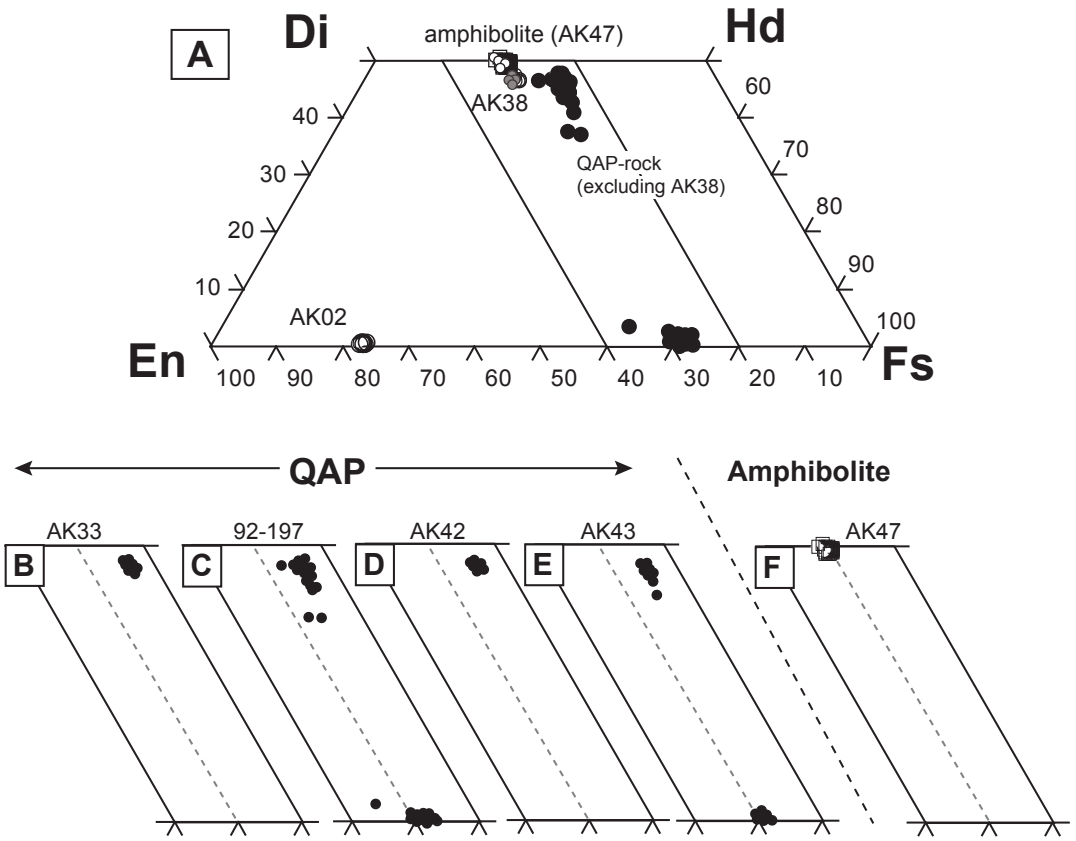



Figure 4.10. (A) Composition of pyroxene from the QAP lithology and the adjacent amphibolite and ultramafic units. Black circle represent samples from QAP, excluding those from AK 38, which are represented by gray circles. Open squares represent amphibolite samples. Open circles represent samples from the ultramafic AK 02. Black squares represent Isua samples. (B) Composition of pyroxene from sample AK 33. (C) Composition of pyroxene from sample 92-197. (D) Composition of pyroxene from sample AK 42. (E) Composition of pyroxene from sample AK 43. (F) Composition of pyroxene from the amphibolite sample AK 47.

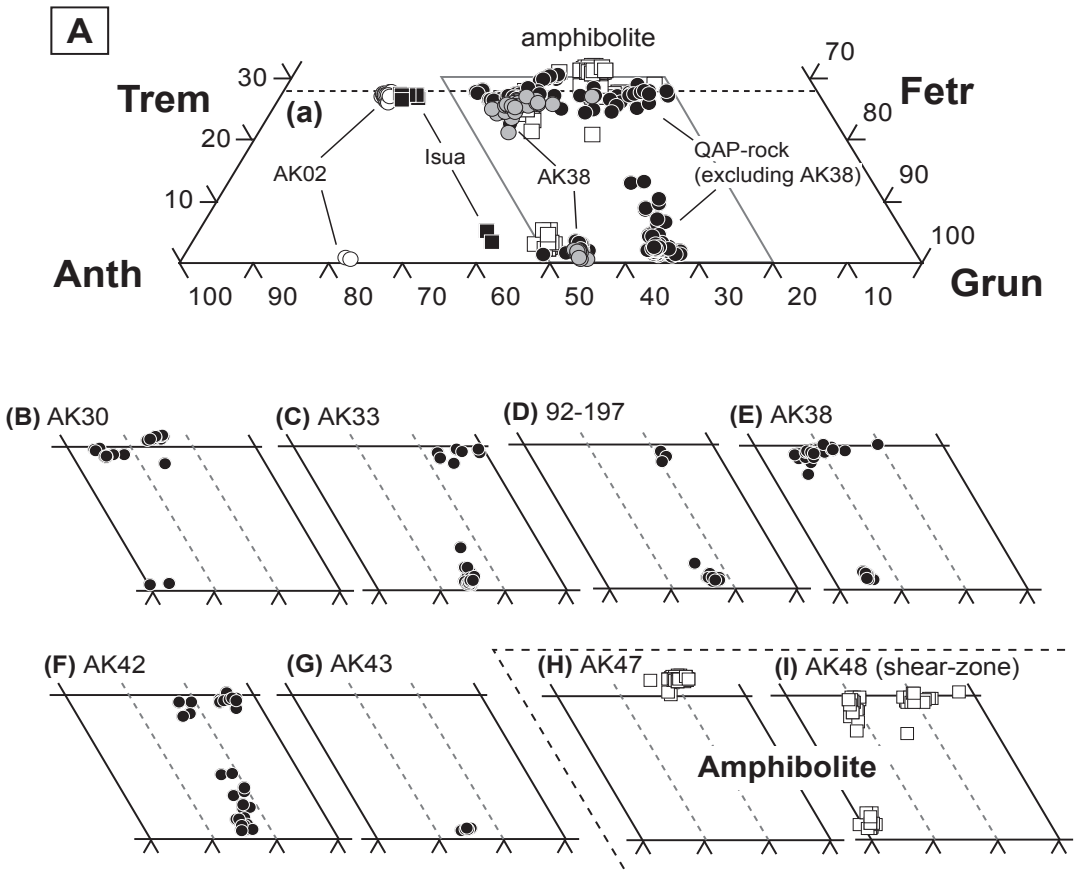



Figure 4.11. (A) Composition of amphibole from the QAP lithology, the adjacent amphibolite and ultramafic units, and the garnet-containing shear zone that cross cuts the QAP rocks, as well as amphibole from Isua. Black circle represent samples from QAP, excluding those from AK 38, which are represented by gray circles. Open squares represent amphibolite samples. Open circles represent samples from the ultramafic AK 02. Black squares represent Isua samples. (B) Composition of amphibole from sample AK 30. (C) Composition of amphibole from sample AK 33. (D) Composition of amphibole from sample 92-197. (E) Composition of amphibole from sample AK 38. (G) Composition of amphibole from sample AK42. (F) Composition of amphibole from sample AK 43. (G) Composition of amphibole from sample AK 47. (H) Composition of amphibole from sample AK 48.

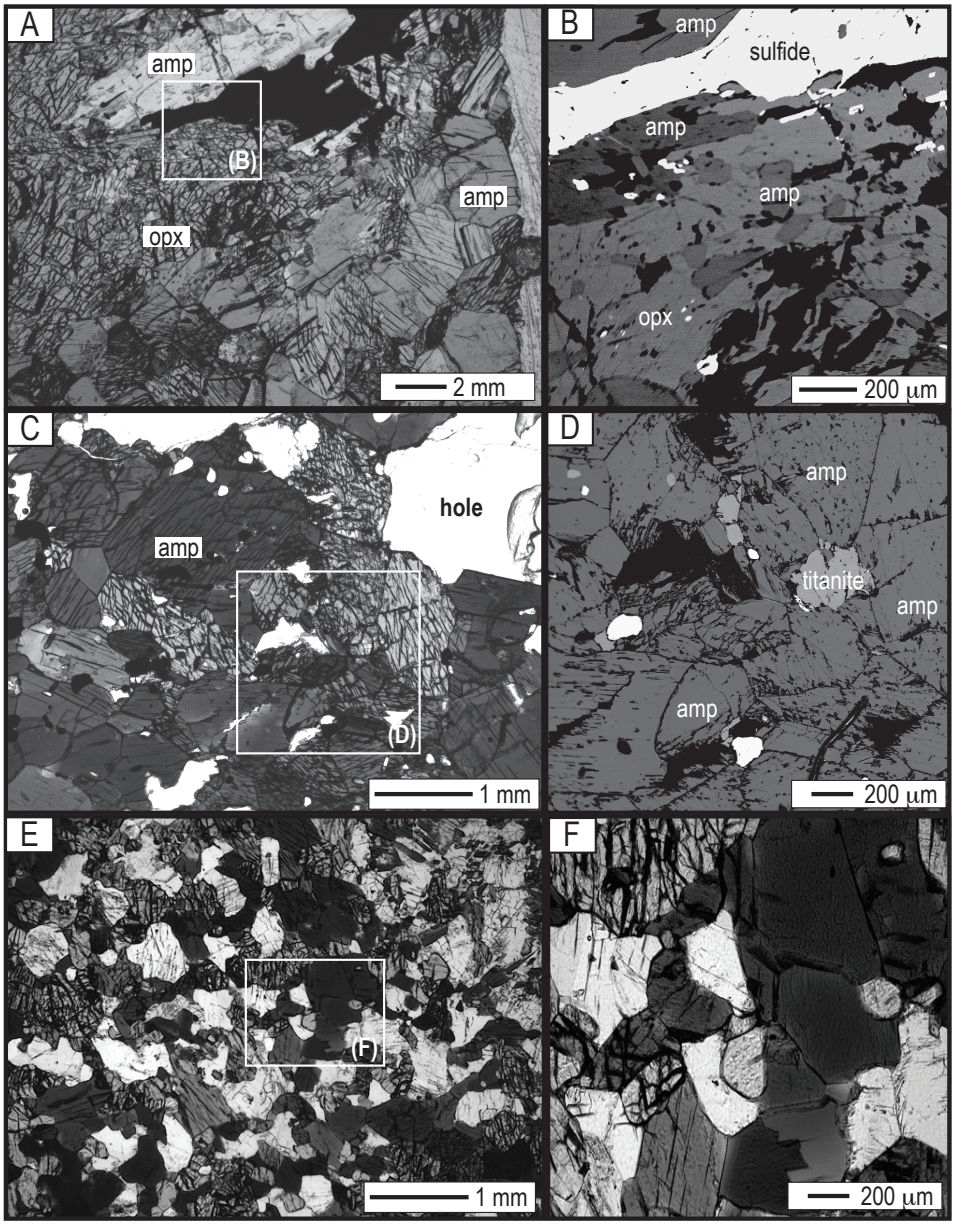



Figure 4.12. Photomicrographs and back-scattered electron detection (BSE) images of ultramafic and amphibolite units on either side of the QAP outcrop. (A) Plane polarized light image of AK 02 from the ultramafic unit, predominantly containing amphibole and orthopyroxene. (B) BSE image of AK 02 highlighting the relationship between the amphibole and orthopyroxene, as well as showing the trace amount of sulfides that can be found in the ultramafic. (C) Plane polarized light image of the ultramafic portion (AK 05) of AK 30, a sample that represents the contact between the ultramafic and QAP units. (D) BSE image of AK 05, which is dominated by amphibole, but contains trace amounts of titanite. (E) Plane polarized light image of sample AK 47 from the amphibolite unit, dominated by hornblende. (F) Close up plane polarized light image of sample AK 47.

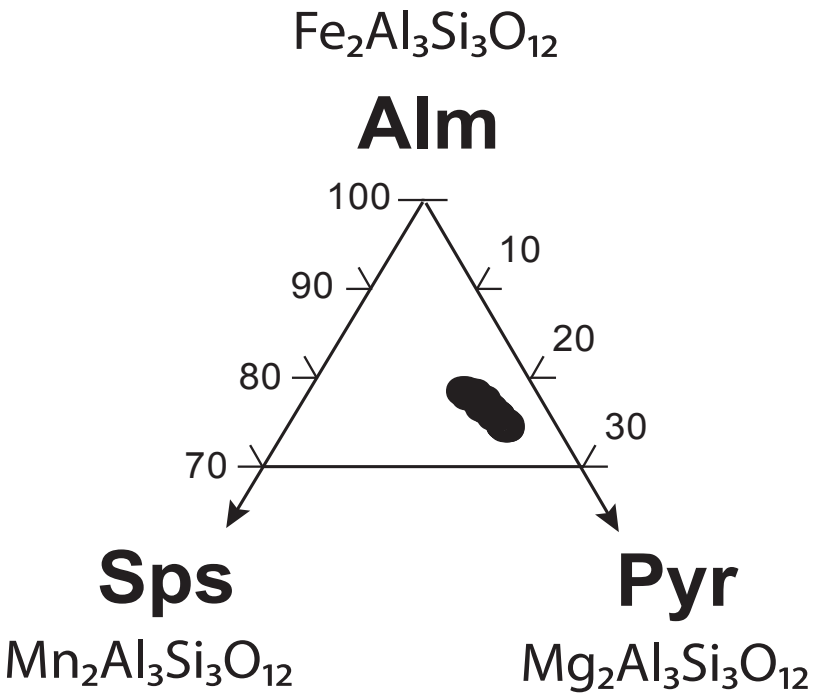



Figure 4.13. Chemistry of garnets found in sample AK 33 and AK 48 from the QAP unit indicates a consistent and homogenous almandine composition, comprised predominantly of FeO (30 wt. %) and $Al_2O_3$ (21 wt. %), with lesser amounts of CaO (8 wt. %) and MgO (2 wt. %). Data points for each sample overlaps each other.

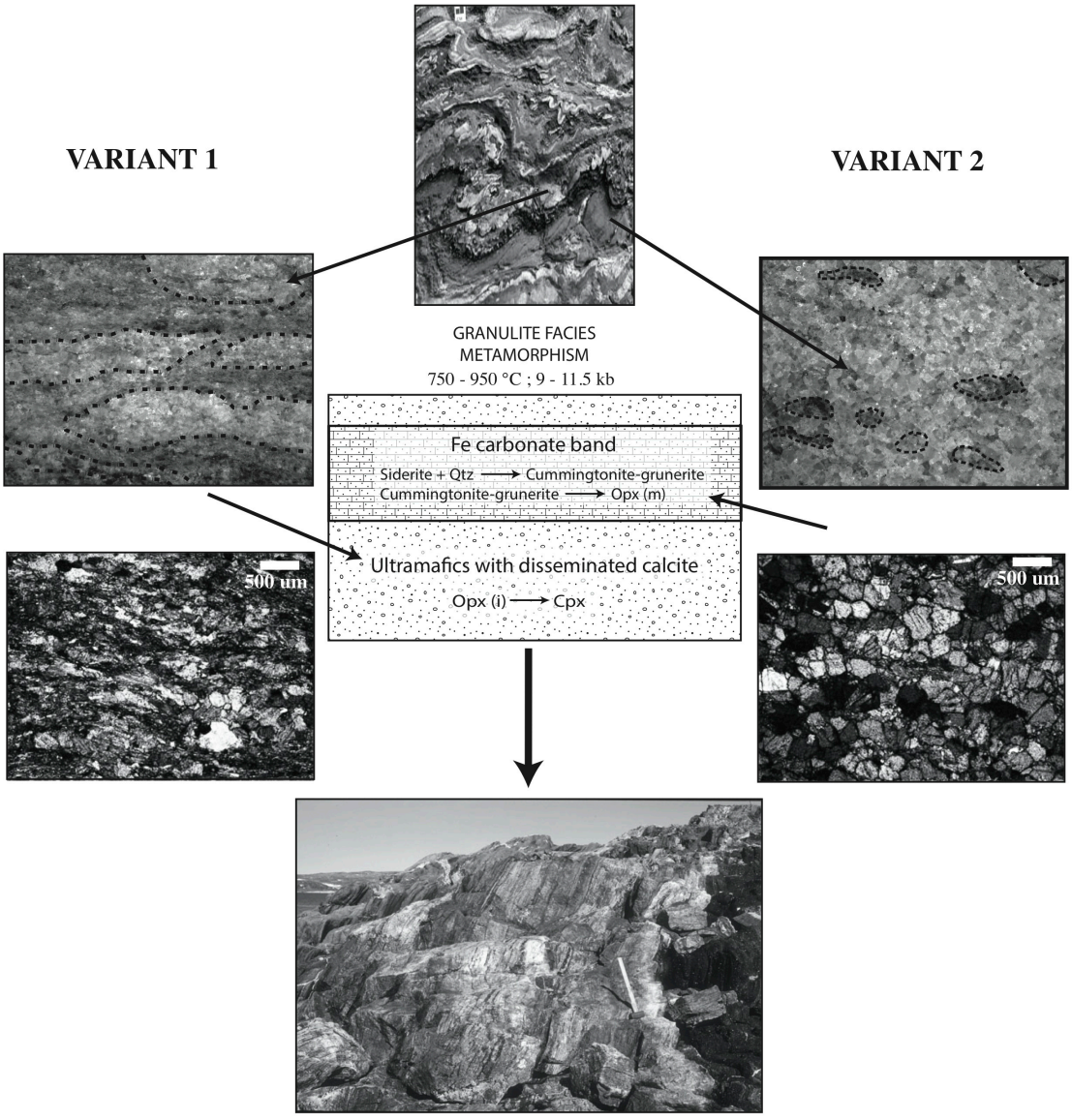



Figure 4.14. Proposed protolith for QAP lithology includes two different intercalated parent rocks. Variant 1 is an ultramafic rock with disseminated carbonate (pods outlined with dashed line) and Variant 2 is a Fe-carbonate band with disseminated ultramafic minerals (pods outlined with dashed lines). Both protoliths were exposed to granulite facies metamorphism, producing the observed pyroxene and amphibole compositions in the QAP.

# Chapter V

# Conclusions

## 5.1 Major Conclusions

### *5.1.1 Evidence For an Oceanic Oxycline and Oxidative Continental Weathering in the Late Paleoproterozoic*

Banded iron formation (BIF) has the potential to preserve important changes in the redox conditions of the Earth's early oceans and atmosphere. The shift from an anoxic to oxic atmosphere occurred during the Great Oxidation Event (GOE) at approximately 2.3 Ga. At 1.9 Ga, the Gunflint Iron Formation was deposited and preserves evidence for the evolving oxidization state of the oceans and atmosphere. When the geochemistry of the 1.9 Ga Gunflint BIF is compared to that of Archean-aged BIF samples, the shift in rare earth and trace element geochemistry from pre- to post-Archean aged samples support the presence of both an oceanic oxycline and oxidative continental weathering in the late Paleoproterozoic.

Evidence for an oceanic oxycline comes from the examination of trace and rare earth element geochemistry from samples deposited before and after the GOE. Pre-GOE BIFs from the > 3.7 Ga Isua Greenstone Belt and the ~ 3.0 Buhwa Greenstone Belt do not display either negative or positive shale-normalized Ce anomalies, indicating trivalent Ce behavior and deposition in a reducing basin. In contrast, post-GOE BIF from the 1.9 Ga Gunflint Iron Formation record both positive and Ce anomalies. This is likely a result of oxidative precipitation of insoluble Ce(IV) above an oxycline in oxygenated shallow water and reductive dissolution to soluble Ce(III) below an oxycline in reducing deep water. An increase in the range of LREE/HREE, calculated as $Pr_{SN}/Yb_{SN}$, is also observed in post-GOE Gunflint BIF when compared to Archean BIF from Greenland and Zimbabwe, which is consistent with the presence of an oxycline in the Gunflint ocean

basin. LREE preferentially adsorb to, and are removed by, Mn- and Fe-oxyhydroxides and other reactive surfaces in oxygenated waters. Reductive dissolution occurs as these particles cross a redox boundary into deep, anoxic waters, where the LREE are released and the ratio of light to heavy REE increases. The decrease in the average $Y_{SN}/Ho_{SN}$ ratio in BIFs from the Archean (Isua = 45, Zimbabwe = 34, Kuruman and Penge = 47) to the Paleoproterozoic (Gunflint = 31) provides further evidence for an ocean oxycline. Because Y is less effectively scavenged than Ho from seawater by Mn- and Fe-oxyhydroxides, there is increased adsorption of Ho. This results in increased Ho in deep anoxic waters as Mn- and Fe-oxyhydroxides dissolve when they cross an oxycline, which in turn results in a decrease in the dissolved seawater $Y_{SN}/Ho_{SN}$ ratio.

Evidence for oxidative continental weathering in the late Paleoproterozoic comes from the examination of terrestrially-sourced, redox-sensitive elements and ratios (Mo, V, Co, Cr and U/Pb). All of these elements and their respective ratios show an increase in concentrations in post-GOE BIFs relative to pre-GOE BIF. Oxidized forms of these elements are more mobile and soluble, compared to reduced forms, and would have been released during oxidative continental weathering and transported to the oceans via rivers.

To determine if samples from the Gunflint Iron Formation preserve primary trace-element signatures or were altered by siliciclastic contamination and/or by modern weathering, a variety of siliciclastic indictors and Pb isotope compositions were measured. As concentrations of $Al_2O_3$ and Zr are indicators of siliciclastic contamination, Gunflint and Zimbabwe samples with greater than 1.7 wt. % $Al_2O_3$ and 30 ppm Zr were considered contaminated. Isua samples with greater than 0.8 wt. % $Al_2O_3$ and 5 ppm Zr were considered contaminated. All samples with a $Pr_{SN}/Yb_{SN}$ ratio of

greater than 1 were also considered contaminated. Examination of the $^{238}U/^{204}Pb$ and $^{206}Pb/^{204}Pb$ ratios indicate that the U/Pb ratios measured today for the Gunflint samples are the same as the original ratios and are not an artifact of modern weathering. Therefore, the REEs provide evidence for fundamental differences in the redox structure of the basins in which pre- and post-GOE BIFs were formed. It was also determined that the Pb was derived from two sources, depleted mantle and continental sediments, suggesting that the Gunflint samples were derived from a complex oceanic geochemical reservoir.

### *5.1.2 Microscale Heterogeneity in the Geochemistry of Algoma and Superior Type Banded Iron Formation*

The microscale heterogeneity of REEs observed in samples from the >3.7 Ga Isua Greenstone Belt, the ~ 3.0 Buhwa Greenstone Belt, and the ~1.9 Ga Gunflint Iron Formation is ubiquitous, regardless of sample age, location, metamorphic grade, BIF type (Algoma vs. Superior), mineralogy (magnetite vs. hematite) and element. The range in the rare earth element (REE) geochemistry observed in individual iron oxide grains only millimeters apart in the same band in the same sample is comparable to the full range in whole rock REE geochemistry observed in all BIFs through time. It is unlikely that this heterogeneity is a reflection of the ocean chemistry conditions during Fe oxyhydroxide precipitation, but rather as a result of inorganic, post-depositional alteration processes. An important implication of this degree of heterogeneity is the possibility that solely examining the whole rock geochemistry of BIF may not provide a complete picture of the paleoenvironmental and/or post-depositional processes being recorded in the sample. When whole rock and mineral geochemistry from the same sample are compared, the

whole rock values rarely plot in the median of the array of mineral chemistry data, suggesting that whole rock geochemistry does not represent the full range of mineral chemistry.

Fine-scale heterogeneity in BIF is also seen in $\delta^{56}Fe$ values in study samples from the >3.7 Ga Isua Greenstone Belt, the ~3.0 Buhwa Greenstone Belt, and the ~1.9 Ga Gunflint Iron Formation. Similarly to the REE geochemistry, the $\delta^{56}Fe$ values within individual bands do not typically coincide with the whole rock $\delta^{56}Fe$ values. This heterogeneity is also likely to represent post-depositional processes related to DIR processes in the sediment porewater prior to lithification as opposed to inorganic processes. Examining the range of $\delta^{56}Fe$ values through time may also provide insight into the timing and extent of DIR. Samples from the IGB have lighter $\delta^{56}Fe$ values in the IGB than have been previously reported may indicate the presence of DIR earlier than previously suggested. In addition, the much smaller range in $\delta^{56}Fe$ values for the 3.0 Ga BGB compared to those previously reported for similarly aged iron formations possibly indicates that DIR was not widespread at this time and might have only been found in specific basins.

### *5.1.3 Origin of > 3.65 Ga Quartz-Amphibole-Pyroxene Rocks from Akilia*

All of the rocks on Akilia, including the Quartz-Amphibole-Pyroxene (QAP) lithology, have been affected by granulite and amphibolite faces metamorphism and intense deformation, resulting in complex field relationships and raising issues about the unit's age and protolith. Examination of the critical cross cutting relationship of the Amîtsoq Gneiss (*Ogn*) and Akilia Association reveals the parallel nature of the foliations,

mineral lineations, and fold axes, which points to a tectonic, rather than igneous relationship between the two units. The intense region deformation makes this contact unable to be used for determining the minimum age of the QAP lithology.

The tectonic nature of the crucial contact Amîtsoq Gneiss and Akilia Association also indicates a broader tectonic overprint on all of the rocks in the area, including the QAP lithology, which adds to the controversy over the unit's origins. In addition, intense deformation has resulted in the rocks of the QAP unit to superficially appear to be comprised of well preserved mm-scale layers, which have been used as a line of evidence supporting the sedimentary BIF protolith of this lithology. The mineral composition of samples from the QAP outcrop and surrounding rocks were examined in relation to the composition of BIF and ultramafic rocks from elsewhere in the Isua Greenstone Belt (IGB) in order to shed light on the QAP's protolith. If the protolith were a sedimentary BIF, it would be expected that the composition of the Fe-Mg minerals present in the unit would also point to this Fe-rich protolith. However, the amphibole in the QAP samples are not Fe-rich, being predominantly actinolite, hornblende and cummingtonite, not grunerite, and the pyroxene are dominantly diopside, hedenbergite and augite, not ferrosilite. We suggest that such amphibole and pyroxene compositions could be derived from an original Mg-rich protolith, consisting of ultramafic rocks with disseminated carbonate combined with a Fe-rich carbonate band brought to granulite facies metamorphism, analogous to rocks on Isua (IS-X and IS-Y). As a result, this renders a BIF protolith for the QAP lithology unnecessary.

## 5.2 Summary

Major, trace, and rare earth element and iron isotopic geochemical analyses of BIFs have the potential to be useful tools for the investigation of paleoenvironmental conditions of early Earth, however, it is key that the data collected be evaluated critically and in the context of relevant local and regional geology. It is important to investigate and understand if the signatures preserved in the rock reflect primary deposition or post depositional alterations, such as metamorphism and diagenesis. It is necessary that investigators look for any evidence of the disruptive effects of modern weathering, tectonic and metamorphic overprinting, and post-depositional alteration processes.

# Appendix 4

Table A.1
Major and trace element geochemisty of samples from the IGB

| | IS-02-08A | IS-02-06 | IS-02-05 | IS-Y | IS-X | ISB-22 |
|---|---|---|---|---|---|---|
| Oxide (wt. %) | | | | | | |
| $SiO_2$ | 49.280 | 43.310 | 55.030 | 4.780 | 23.460 | 72.950 |
| $Al_2O_3$ | 0.070 | 0.150 | 0.190 | 0.260 | 0.530 | 0.500 |
| $Fe_2O_{3(T)}$ | 48.630 | 53.540 | 42.290 | 9.070 | 7.510 | 15.190 |
| MnO | 0.031 | 0.126 | 0.036 | 0.812 | 0.708 | 0.271 |
| MgO | 1.060 | 1.720 | 4.140 | 14.260 | 13.880 | 2.400 |
| CaO | 0.810 | 1.040 | 0.060 | 29.270 | 26.820 | 4.470 |
| $Na_2O$ | 0.040 | 0.060 | 0.060 | 0.020 | 0.050 | 0.020 |
| $K_2O$ | 0.010 | 0.090 | 0.050 | 0.010 | 0.030 | 0.020 |
| $TiO_2$ | 0.001 | 0.004 | 0.004 | 0.008 | 0.016 | 0.015 |
| $P_2O_5$ | 0.080 | 0.070 | 0.040 | 0.020 | 0.020 | 0.020 |
| LOI | -0.060 | -1.600 | -1.270 | 40.650 | 26.370 | 3.580 |
| Total | 99.940 | 98.520 | 100.600 | 99.130 | 99.390 | 99.420 |
| Element (ppm) | | | | | | |
| Sc | 1.000 | 1.000 | 1.000 | < 1 | < 1 | 1.000 |
| Be | 3.000 | 1.000 | 1.000 | < 1 | < 1 | < 1 |
| V | 5.000 | 5.000 | 5.000 | 6.000 | < 5 | 5.000 |
| Cr | 20.000 | 20.000 | 20.000 | 20.000 | 20.000 | 20.000 |
| Co | 4.000 | 2.000 | 2.000 | 1.000 | 1.000 | 3.000 |
| Ni | 20.000 | 20.000 | 20.000 | 20.000 | 20.000 | 20.000 |
| Cu | 10.000 | 10.000 | 10.000 | 10.000 | 10.000 | 20.000 |
| Zn | 30.000 | 30.000 | 30.000 | 50.000 | 40.000 | 90.000 |
| Ga | 1.000 | 1.000 | 1.000 | 1.000 | 2.000 | 2.000 |
| Ge | 15.800 | 9.300 | 5.200 | < 0.5 | 1.000 | 8.200 |
| As | 5.000 | 5.000 | 5.000 | < 5 | < 5 | < 5 |
| Rb | < 1 | 1.000 | 1.000 | < 1 | 1.000 | 2.000 |
| Sr | 4.000 | 2.000 | 2.000 | 30.000 | 20.000 | 8.000 |
| Zr | 3.000 | 1.000 | 1.000 | 3.000 | 40.000 | 8.000 |
| Nb | 0.200 | 0.200 | 0.200 | 0.400 | 1.100 | 0.700 |
| Mo | 2.000 | 2.000 | 2.000 | 2.000 | 2.000 | 2.000 |
| Ag | 0.500 | 0.500 | < 0.5 | < 0.5 | < 0.5 | < 0.5 |
| In | 0.100 | 0.100 | 0.100 | < 0.1 | < 0.1 | < 0.1 |
| Sn | 1.000 | 1.000 | < 1 | < 1 | < 1 | 1.000 |
| Sb | 3.900 | 5.300 | 0.800 | < 0.2 | < 0.2 | 2.500 |
| Cs | < 0.1 | 0.100 | < 0.1 | 0.500 | 0.300 | 0.200 |

Table A.1 continued

| | ISB-7 | ISB-20 | ISB55 | 465942 | 462604 | 462610 | 465940 |
|---|---|---|---|---|---|---|---|
| Oxide (wt. %) | | | | | | | |
| SiO2 | 29.850 | 37.260 | 60.979 | 0.090 | 60.000 | 92.270 | 36.940 |
| Al2O3 | 2.550 | 4.190 | 0.310 | 0.020 | 0.280 | 0.400 | 4.910 |
| Fe2O3(T) | 10.230 | 11.040 | 36.566 | 4.270 | 36.120 | 3.280 | 8.380 |
| MnO | 0.679 | 0.731 | 0.098 | 1.150 | 0.160 | 0.060 | 0.180 |
| MgO | 7.420 | 7.890 | 1.154 | 17.590 | 1.080 | 2.090 | 25.980 |
| CaO | 18.150 | 18.600 | 0.608 | 29.860 | 1.170 | 1.340 | 7.850 |
| Na2O | 0.060 | 0.090 | 0.000 | 0.010 | 0.010 | 0.010 | 0.010 |
| K2O | 0.790 | 2.050 | 0.004 | 0.010 | 0.010 | 0.010 | 0.010 |
| TiO2 | 0.047 | 0.075 | 0.018 | 0.010 | 0.020 | 0.030 | 0.110 |
| P2O5 | 0.020 | 0.030 | 0.036 | 0.200 | 0.030 | 0.020 | 0.010 |
| LOI | 28.090 | 15.870 | < 0.01 | 45.910 | 0.080 | 0.240 | 14.780 |
| Total | 97.900 | 97.830 | 99.772 | 98.930 | 98.870 | 99.640 | 99.120 |
| | | | | | | | |
| Element (ppm) | | | | | | | |
| Sc | 6.000 | 10.000 | 0.150 | 2.710 | 0.095 | 1.686 | 17.836 |
| Be | < 1 | 1.000 | 0.846 | 0.001 | 0.957 | 0.219 | 0.049 |
| V | 32.000 | 42.000 | 0.944 | 0.305 | 0.669 | 6.054 | 76.773 |
| Cr | 80.000 | 80.000 | 10.490 | 7.493 | 4.567 | 3.018 | 2926.559 |
| Co | 5.000 | 4.000 | 2.612 | 15.810 | 1.678 | 8.691 | 82.743 |
| Ni | 50.000 | 30.000 | 14.932 | 58.837 | 9.851 | 26.947 | 1334.075 |
| Cu | 10.000 | 10.000 | 0.579 | 29.070 | 1.233 | 14.834 | 35.348 |
| Zn | 30.000 | 30.000 | 14.381 | 5.795 | 13.968 | 18.216 | 52.927 |
| Ga | 2.000 | 2.000 | 0.329 | 0.044 | 0.369 | 0.990 | 4.470 |
| Ge | 0.700 | 0.700 | 0.000 | 0.000 | 0.000 | 0.000 | 0.000 |
| As | < 5 | < 5 | 0.692 | 0.706 | 0.288 | 0.351 | 0.055 |
| Rb | 15.000 | 33.000 | 0.092 | 0.034 | 0.091 | 1.179 | 0.252 |
| Sr | 60.000 | 79.000 | 0.977 | 856.394 | 3.005 | 0.473 | 133.249 |
| Zr | 7.000 | 6.000 | 0.230 | 0.020 | 0.304 | 0.424 | 0.446 |
| Nb | 0.500 | 0.500 | 0.036 | 0.002 | 0.036 | 0.032 | 0.056 |
| Mo | 2.000 | 2.000 | 0.338 | 0.034 | 0.288 | 0.081 | 0.058 |
| Ag | < 0.5 | < 0.5 | 0.023 | 0.029 | 0.003 | 0.008 | 0.012 |
| In | < 0.1 | < 0.1 | 0.001 | 0.002 | 0.001 | 0.010 | 0.013 |
| Sn | < 1 | < 1 | 0.001 | 0.008 | 0.002 | 0.376 | 0.037 |
| Sb | 0.500 | < 0.2 | 0.356 | 0.038 | 0.359 | 0.032 | 0.075 |
| Cs | 0.400 | 1.100 | 0.017 | 0.012 | 0.014 | 0.285 | 0.094 |

Table A.1 continued

| | IS-02-08A | IS-02-06 | IS-02-05 | IS-Y | IS-X | ISB-22 |
|---|---|---|---|---|---|---|
| Element (ppm) | | | | | | |
| Ba | < 3 | 3.000 | 5.000 | 95.000 | 106.000 | 47.000 |
| La | 3.630 | 1.970 | 1.450 | 3.570 | 4.480 | 1.930 |
| Ce | 5.280 | 3.560 | 2.500 | 3.470 | 5.400 | 1.970 |
| Pr | 0.620 | 0.360 | 0.270 | 0.360 | 0.600 | 0.220 |
| Nd | 2.270 | 1.420 | 1.040 | 1.150 | 2.020 | 0.800 |
| Sm | 0.500 | 0.350 | 0.260 | 0.210 | 0.380 | 0.180 |
| Eu | 0.365 | 0.296 | 0.245 | 0.205 | 0.274 | 0.084 |
| Gd | 0.790 | 0.520 | 0.400 | 0.290 | 0.490 | 0.170 |
| Tb | 0.130 | 0.100 | 0.080 | 0.050 | 0.080 | 0.030 |
| Dy | 0.830 | 0.680 | 0.560 | 0.320 | 0.520 | 0.170 |
| Y | 10.500 | 6.300 | 5.800 | 4.500 | 6.600 | 1.500 |
| Ho | 0.180 | 0.150 | 0.130 | 0.070 | 0.110 | 0.040 |
| Er | 0.540 | 0.490 | 0.410 | 0.240 | 0.360 | 0.130 |
| Yb | 0.560 | 0.510 | 0.410 | 0.190 | 0.310 | 0.120 |
| Lu | 0.097 | 0.083 | 0.061 | 0.021 | 0.042 | 0.016 |
| Tm | 0.084 | 0.077 | 0.064 | 0.036 | 0.053 | 0.020 |
| Hf | 0.100 | 0.100 | 0.100 | 0.100 | 0.900 | 0.200 |
| Ta | < 0.01 | 0.010 | 0.020 | < 0.01 | 0.050 | 0.040 |
| W | 2.200 | 0.500 | < 0.5 | 1.900 | 1.800 | 2.300 |
| Tl | 0.050 | 0.050 | 0.050 | 0.050 | < 0.05 | < 0.05 |
| Pb | 5.000 | 5.000 | 8.000 | 6.000 | 5.000 | 32.000 |
| Th | 0.070 | 0.060 | 0.050 | 0.160 | 0.260 | 0.270 |
| U | 0.080 | 0.010 | 0.070 | 0.220 | 0.380 | 0.150 |

Table A.1 continued

| | ISB-7 | ISB-20 | ISB55 | 465942 | 462604 | 462610 | 465940 |
|---|---|---|---|---|---|---|---|
| Element (ppm) | | | | | | | |
| Ba | 881.000 | 4450.000 | 2.232 | 4.422 | 2.874 | 0.885 | 2.321 |
| La | 1.930 | 3.020 | 0.991 | 1.160 | 0.890 | 0.490 | 0.411 |
| Ce | 2.730 | 3.800 | 1.454 | 2.872 | 1.331 | 0.878 | 0.974 |
| Pr | 0.360 | 0.460 | 0.158 | 0.418 | 0.152 | 0.144 | 0.144 |
| Nd | 1.440 | 1.740 | 0.667 | 1.957 | 0.656 | 0.757 | 0.715 |
| Sm | 0.370 | 0.390 | 0.154 | 0.702 | 0.163 | 0.430 | 0.279 |
| Eu | 0.279 | 0.361 | 0.149 | 0.743 | 0.152 | 0.094 | 0.138 |
| Gd | 0.520 | 0.540 | 0.262 | 1.312 | 0.334 | 0.749 | 0.503 |
| Tb | 0.100 | 0.100 | 0.042 | 0.284 | 0.057 | 0.150 | 0.104 |
| Dy | 0.690 | 0.710 | 0.306 | 2.162 | 0.417 | 0.972 | 0.761 |
| Y | 6.000 | 6.400 | 3.912 | 15.103 | 4.575 | 5.445 | 4.704 |
| Ho | 0.150 | 0.150 | 0.081 | 0.521 | 0.109 | 0.201 | 0.182 |
| Er | 0.440 | 0.480 | 0.251 | 1.568 | 0.333 | 0.572 | 0.551 |
| Yb | 0.450 | 0.440 | 0.227 | 1.520 | 0.316 | 0.610 | 0.593 |
| Lu | 0.063 | 0.064 | 0.036 | 0.218 | 0.050 | 0.084 | 0.096 |
| Tm | 0.070 | 0.071 | 0.037 | 0.237 | 0.049 | 0.091 | 0.087 |
| Hf | 0.300 | 0.200 | 0.007 | 0.001 | 0.008 | 0.013 | 0.023 |
| Ta | 0.010 | 0.030 | 0.002 | 0.001 | 0.002 | 0.004 | 0.003 |
| W | < 0.5 | < 0.5 | 0.219 | 0.012 | 0.121 | 0.142 | 0.042 |
| Tl | < 0.05 | 0.700 | 0.002 | 0.000 | 0.003 | 0.020 | 0.003 |
| Pb | 13.000 | 5.000 | 5.972 | 7.361 | 0.754 | 0.759 | 3.103 |
| Th | 0.170 | 0.140 | 0.026 | 0.005 | 0.037 | 0.019 | 0.021 |
| U | 0.090 | 0.070 | 0.029 | 0.007 | 0.022 | 0.074 | 0.020 |

Table A.2
Major and trace element geochemisty of samples from the BGB

| | **ZB-03** | **ZB-05** | **ZB-07** | **ZB23** | **ZB-27** | **ZB-18** | **ZB-117** |
|---|---|---|---|---|---|---|---|
| Oxide (wt. %) | | | | | | | |
| $SiO_2$ | 99.550 | 49.630 | 97.690 | - | 42.190 | 61.900 | 40.130 |
| $Al_2O_3$ | 0.470 | 0.600 | 1.960 | - | 0.570 | 0.400 | 0.710 |
| $Fe_2O_{3(T)}$ | 0.320 | 46.990 | 0.130 | - | 52.990 | 30.340 | 57.300 |
| MnO | 0.010 | 0.040 | 0.010 | - | 0.281 | 0.470 | 0.550 |
| MgO | 0.100 | 1.680 | 0.080 | - | 1.850 | 0.570 | 0.680 |
| CaO | 0.030 | 1.210 | 0.020 | - | 0.300 | 0.030 | 0.070 |
| $Na_2O$ | 0.010 | 0.010 | 0.010 | - | 0.040 | 0.010 | 0.010 |
| $K_2O$ | 0.010 | 0.040 | 0.490 | - | 0.040 | 0.010 | 0.020 |
| $TiO_2$ | 0.010 | 0.040 | 0.090 | - | 0.023 | 0.010 | 0.010 |
| $P_2O_5$ | 0.010 | 0.090 | 0.010 | - | 0.190 | 0.040 | 0.070 |
| LOI | 0.260 | <0.01 | 0.340 | - | 0.660 | 5.530 | 1.210 |
| Total | 100.640 | 100.320 | 100.740 | - | 99.130 | 99.300 | 100.750 |
| | | | | | | | |
| Element (ppm) | | | | | | | |
| Sc | 0.405 | 1.289 | 1.254 | 0.311 | 2.000 | 0.532 | 0.572 |
| Be | 0.036 | 2.914 | 0.148 | 0.336 | < 1 | 1.208 | 0.629 |
| V | 1.576 | 8.036 | 6.115 | 6.869 | 13.000 | 2.633 | 5.846 |
| Cr | 10.410 | 20.907 | 108.893 | 6.521 | 40.000 | 5.359 | 7.568 |
| Co | 2.371 | 8.749 | 0.947 | 1.983 | 3.000 | 6.453 | 2.737 |
| Ni | 16.240 | 33.384 | 7.296 | 5.138 | 20.000 | 27.607 | 14.898 |
| Cu | 13.967 | 8.820 | 11.010 | 1.381 | 10.000 | 15.978 | 3.930 |
| Zn | 1.840 | 26.662 | 0.968 | 5.387 | 30.000 | 97.479 | 7.311 |
| Ga | 0.332 | 1.331 | 2.490 | 1.043 | 1.000 | 0.344 | 0.841 |
| Ge | 0.000 | 0.000 | 0.000 | | 3.600 | 0.000 | 0.000 |
| As | 1.825 | 0.629 | 1.296 | 1.044 | < 5 | 0.193 | 0.441 |
| Rb | 0.638 | 2.926 | 9.739 | 0.226 | 3.000 | 0.060 | 1.320 |
| Sr | 0.594 | 5.195 | 3.647 | 0.403 | 10.000 | 1.278 | 4.681 |
| Zr | 1.440 | 2.946 | 93.717 | 1.500 | 4.000 | 0.638 | 1.547 |
| Nb | 0.085 | 0.169 | 1.161 | 0.253 | 0.600 | 0.056 | 0.276 |
| Mo | 0.046 | 0.066 | 0.064 | 0.183 | 3.000 | 0.065 | 0.300 |
| Ag | 0.011 | 0.028 | 0.025 | 0.075 | < 0.5 | 0.030 | 0.023 |
| In | 0.001 | 0.010 | 0.004 | 0.002 | < 0.1 | 0.004 | 0.004 |
| Sn | 0.033 | 0.413 | 0.352 | 0.069 | < 1 | 0.426 | 0.489 |
| Sb | 0.027 | 0.095 | 0.041 | 0.580 | 5.400 | 0.116 | 0.214 |
| Cs | 0.009 | 0.363 | 0.042 | 0.020 | < 0.1 | 0.008 | 0.045 |

Table A.2 continued

| | ZB-03 | ZB-05 | ZB-07 | ZB23 | ZB-27 | ZB-18 | ZB-117 |
|---|---|---|---|---|---|---|---|
| Element (ppm) | | | | | | | |
| Ba | 6.170 | 14.063 | 50.576 | 3.110 | 68.000 | 19.502 | 510.209 |
| La | 0.421 | 3.401 | 7.776 | 1.157 | 6.150 | 2.220 | 5.351 |
| Ce | 0.833 | 5.104 | 13.041 | 2.227 | 12.200 | 2.306 | 16.050 |
| Pr | 0.104 | 0.564 | 1.390 | 0.253 | 1.390 | 0.501 | 1.077 |
| Nd | 0.434 | 2.288 | 4.746 | 1.010 | 5.370 | 1.963 | 4.051 |
| Sm | 0.134 | 0.490 | 0.868 | 0.229 | 1.220 | 0.386 | 0.819 |
| Eu | 0.059 | 0.325 | 0.150 | 0.106 | 0.513 | 0.154 | 0.370 |
| Gd | 0.261 | 0.815 | 0.752 | 0.286 | 1.540 | 0.396 | 0.907 |
| Tb | 0.057 | 0.132 | 0.102 | 0.047 | 0.260 | 0.050 | 0.151 |
| Dy | 0.445 | 0.937 | 0.565 | 0.311 | 1.620 | 0.276 | 0.968 |
| Y | 3.291 | 10.906 | 3.179 | 2.206 | 12.300 | 2.228 | 5.772 |
| Ho | 0.113 | 0.245 | 0.113 | 0.073 | 0.340 | 0.063 | 0.220 |
| Er | 0.353 | 0.759 | 0.324 | 0.218 | 1.050 | 0.187 | 0.650 |
| Yb | 0.379 | 0.688 | 0.388 | 0.208 | 1.000 | 0.225 | 0.640 |
| Lu | 0.058 | 0.110 | 0.063 | 0.031 | 0.155 | 0.039 | 0.094 |
| Tm | 0.057 | 0.110 | 0.054 | 0.033 | 0.157 | 0.031 | 0.100 |
| Hf | 0.029 | 0.078 | 2.586 | 0.040 | 0.100 | 0.016 | 0.040 |
| Ta | 0.006 | 0.012 | 0.183 | 0.017 | 0.040 | 0.003 | 0.025 |
| W | 0.067 | 0.205 | 0.497 | 0.312 | < 0.5 | 0.005 | 0.098 |
| Tl | 0.004 | 0.018 | 0.021 | 0.001 | < 0.05 | 0.006 | 0.046 |
| Pb | 0.326 | 0.675 | 2.262 | 3.743 | 5.000 | 0.696 | 0.155 |
| Th | 0.083 | 0.111 | 5.555 | 0.269 | 0.360 | 0.045 | 0.053 |
| U | 0.141 | 0.039 | 1.834 | 0.124 | 0.270 | 0.329 | 0.207 |

Table A.2 continued

| | ZB-105 | ZB-169 | ZB-247 | ZB-294 |
|---|---|---|---|---|
| Oxide (wt. %) | | | | |
| $SiO_2$ | 97.450 | 34.070 | 47.000 | 3.700 |
| $Al_2O_3$ | 0.410 | 0.400 | 1.510 | 2.790 |
| $Fe_2O_{3(T)}$ | 1.270 | 64.870 | 51.320 | 91.710 |
| MnO | 0.006 | 0.010 | 0.010 | 0.031 |
| MgO | 0.210 | 0.110 | 0.070 | 0.020 |
| CaO | 0.060 | 0.030 | 0.030 | 0.030 |
| $Na_2O$ | 0.050 | 0.010 | 0.010 | 0.160 |
| $K_2O$ | 0.030 | 0.010 | 0.030 | 0.150 |
| $TiO_2$ | 0.014 | 0.030 | 0.060 | 0.119 |
| $P_2O_5$ | 0.010 | 0.030 | 0.030 | 0.120 |
| LOI | 0.320 | 0.230 | 0.380 | 0.890 |
| Total | 99.830 | 99.750 | 100.410 | 99.710 |
| | | | | |
| Element (ppm) | | | | |
| Sc | 1.000 | 0.865 | 2.148 | 3.000 |
| Be | 1.000 | 0.521 | 0.809 | < 1 |
| V | 6.000 | 10.160 | 18.673 | 46.000 |
| Cr | 20.000 | 18.776 | 33.162 | 70.000 |
| Co | 2.000 | 3.862 | 3.616 | 4.000 |
| Ni | 20.000 | 9.697 | 26.896 | 20.000 |
| Cu | 10.000 | 1.223 | 2.653 | 10.000 |
| Zn | 30.000 | 4.601 | 9.350 | 30.000 |
| Ga | < 1 | 1.436 | 2.303 | 3.000 |
| Ge | 1.100 | 0.000 | 0.000 | 3.600 |
| As | 7.000 | 0.484 | 0.646 | < 5 |
| Rb | 1.000 | 0.160 | 0.828 | 4.000 |
| Sr | 2.000 | 0.850 | 3.645 | 6.000 |
| Zr | 4.000 | 4.330 | 8.435 | 18.000 |
| Nb | 0.300 | 0.534 | 0.682 | 2.100 |
| Mo | 2.000 | 0.804 | 0.243 | 2.000 |
| Ag | < 0.5 | 0.011 | 0.045 | < 0.5 |
| In | < 0.1 | 0.004 | 0.009 | < 0.1 |
| Sn | < 1 | 0.043 | 0.073 | < 1 |
| Sb | 4.300 | 0.468 | 0.539 | 1.100 |
| Cs | < 0.1 | 0.010 | 0.053 | < 0.1 |

Table A.2 continued

| | ZB-105 | ZB-169 | ZB-247 | ZB-294 |
|---|---|---|---|---|
| Element (ppm) | | | | |
| Ba | 13.000 | 5.731 | 7.647 | 9.000 |
| La | 0.680 | 2.037 | 5.891 | 21.800 |
| Ce | 1.780 | 3.365 | 11.271 | 42.700 |
| Pr | 0.220 | 0.377 | 1.329 | 4.640 |
| Nd | 0.980 | 1.465 | 5.217 | 16.000 |
| Sm | 0.280 | 0.284 | 1.010 | 3.140 |
| Eu | 0.061 | 0.146 | 0.330 | 1.070 |
| Gd | 0.270 | 0.327 | 0.782 | 2.200 |
| Tb | 0.050 | 0.047 | 0.087 | 0.370 |
| Dy | 0.350 | 0.285 | 0.457 | 2.370 |
| Y | 2.300 | 1.891 | 2.469 | 22.000 |
| Ho | 0.080 | 0.062 | 0.094 | 0.550 |
| Er | 0.250 | 0.175 | 0.268 | 1.830 |
| Yb | 0.250 | 0.167 | 0.294 | 1.720 |
| Lu | 0.037 | 0.026 | 0.048 | 0.251 |
| Tm | 0.039 | 0.026 | 0.043 | 0.278 |
| Hf | 0.100 | 0.127 | 0.233 | 0.600 |
| Ta | 0.020 | 0.047 | 0.063 | 0.200 |
| W | < 0.5 | 0.488 | 0.960 | 3.700 |
| Tl | < 0.05 | 0.002 | 0.005 | < 0.05 |
| Pb | 5.000 | 1.978 | 2.583 | 5.000 |
| Th | 0.290 | 0.941 | 0.911 | 3.100 |
| U | 0.150 | 0.179 | 0.241 | 0.880 |

Table A.3
Major and trace element geochemisty of samples from the GF

| | **GF-07-04** | **GF-07-06e** | **GF-07-09** | **GF-07-10** | **GF-07-11** | **GF-07-12** |
|---|---|---|---|---|---|---|
| Oxide (wt. %) | | | | | | |
| $SiO_2$ | 55.780 | 46.110 | 46.650 | 62.380 | 49.040 | 32.754 |
| $Al_2O_3$ | 0.600 | 0.550 | 0.680 | 0.640 | 0.460 | 0.650 |
| $Fe_2O_{3(T)}$ | 38.310 | 47.030 | 46.000 | 33.360 | 36.670 | 57.421 |
| MnO | 0.250 | 0.670 | 0.650 | 0.539 | 0.640 | 0.891 |
| MgO | 4.040 | 3.800 | 3.960 | 2.600 | 3.570 | 5.136 |
| CaO | 0.940 | 1.890 | 2.130 | 3.030 | 10.090 | 3.651 |
| $Na_2O$ | 0.010 | 0.010 | 0.040 | 0.130 | 0.010 | 0.032 |
| $K_2O$ | 0.030 | 0.030 | 0.050 | 0.080 | 0.020 | 0.025 |
| $TiO_2$ | 0.030 | 0.080 | 0.070 | 0.051 | 0.040 | 0.082 |
| $P_2O_5$ | 0.390 | 0.070 | 0.110 | 0.080 | 0.070 | 0.157 |
| LOI | <0.01 | <0.01 | <0.01 | -1.910 | <0.01 | <0.01 |
| Total | 100.370 | 100.240 | 100.340 | 101.000 | 100.600 | 100.799 |
| Element (ppm) | | | | | | |
| Sc | 1.158 | 1.161 | 1.393 | 1.000 | 0.971 | 1.323 |
| Be | 0.944 | 0.942 | 1.232 | 1.000 | 1.006 | 0.977 |
| V | 8.619 | 25.373 | 29.466 | 27.000 | 11.583 | 29.106 |
| Cr | 2.548 | 3.164 | 5.189 | 20.000 | 3.972 | 10.219 |
| Co | 5.884 | 7.849 | 10.994 | 7.000 | 12.145 | 16.761 |
| Ni | 8.565 | 2.674 | 3.482 | 20.000 | 4.047 | 4.547 |
| Cu | 7.128 | 0.744 | 0.261 | 10.000 | 0.765 | 1.084 |
| Zn | 17.427 | 20.890 | 11.695 | 30.000 | 7.785 | 17.444 |
| Ga | 1.785 | 1.213 | 1.439 | 2.000 | 0.819 | 1.402 |
| As | 5.729 | 5.861 | 0.548 | 5.000 | 1.572 | 19.882 |
| Rb | 0.702 | 1.194 | 0.921 | 2.000 | 0.990 | 0.420 |
| Sr | 24.479 | 37.374 | 56.814 | 48.000 | 93.385 | 51.920 |
| Zr | 2.473 | 9.671 | 11.603 | 15.000 | 7.146 | 10.448 |
| Nb | 1.137 | 2.041 | 2.424 | 1.900 | 1.211 | 2.147 |
| Mo | 0.621 | 0.379 | 0.208 | 2.000 | 0.294 | 0.737 |
| Ag | 0.008 | 0.004 | 0.005 | 0.600 | 0.008 | 0.005 |
| In | 0.005 | 0.008 | 0.008 | 0.100 | 0.010 | 0.010 |
| Sn | 0.497 | 0.698 | 0.333 | 1.000 | 1.231 | 0.074 |
| Sb | 0.098 | 2.690 | 0.920 | 1.100 | 0.375 | 1.288 |
| Cs | 0.115 | 0.224 | 0.113 | 0.200 | 0.242 | 0.083 |

Table A.3 continued

| | GF-07-04 | GF-07-06e | GF-07-09 | GF-07-10 | GF-07-11 | GF-07-12 |
|---|---|---|---|---|---|---|
| Element (ppm) | | | | | | |
| Ba | 9.720 | 6.659 | 21.867 | 33.000 | 12.385 | 14.476 |
| La | 5.756 | 2.429 | 6.210 | 4.640 | 4.667 | 7.153 |
| Ce | 11.543 | 6.348 | 14.194 | 11.100 | 9.294 | 15.118 |
| Pr | 1.445 | 0.738 | 1.558 | 1.110 | 0.928 | 1.526 |
| Nd | 6.056 | 3.221 | 6.446 | 3.880 | 3.577 | 6.102 |
| Sm | 1.324 | 0.725 | 1.231 | 0.830 | 0.672 | 1.122 |
| Eu | 0.347 | 0.233 | 0.363 | 0.251 | 0.214 | 0.342 |
| Gd | 1.658 | 0.836 | 1.378 | 0.810 | 0.745 | 1.248 |
| Tb | 0.236 | 0.129 | 0.203 | 0.140 | 0.115 | 0.185 |
| Dy | 1.418 | 0.815 | 1.257 | 0.810 | 0.733 | 1.155 |
| Y | 10.882 | 5.329 | 8.503 | 5.100 | 5.482 | 7.822 |
| Ho | 0.315 | 0.181 | 0.279 | 0.170 | 0.170 | 0.254 |
| Er | 0.873 | 0.515 | 0.774 | 0.480 | 0.513 | 0.702 |
| Yb | 0.730 | 0.410 | 0.589 | 0.370 | 0.483 | 0.532 |
| Lu | 0.107 | 0.054 | 0.079 | 0.049 | 0.069 | 0.069 |
| Tm | 0.122 | 0.072 | 0.107 | 0.067 | 0.079 | 0.097 |
| Hf | 0.055 | 0.182 | 0.214 | 0.200 | 0.142 | 0.206 |
| Ta | 0.033 | 0.062 | 0.071 | 0.060 | 0.042 | 0.071 |
| W | 0.369 | 0.646 | 0.705 | 0.500 | 0.079 | 0.580 |
| Tl | 0.009 | 0.004 | 0.002 | 0.050 | 0.003 | 0.004 |
| Pb | 1.624 | 0.569 | 0.182 | 7.000 | 0.763 | 0.313 |
| Th | 0.246 | 0.258 | 0.303 | 0.370 | 0.201 | 0.348 |
| U | 0.275 | 0.135 | 0.149 | 0.130 | 0.167 | 0.189 |

Table A.3 continued

| | GF-07-13 | GF-07-15 | GF-07-17 | GF-07-18 | GF-07-19 | GF-07-21 |
|---|---|---|---|---|---|---|
| Oxide (wt. %) | | | | | | |
| $SiO_2$ | 82.170 | 38.930 | 35.570 | 72.860 | 41.880 | 25.220 |
| $Al_2O_3$ | 0.260 | 1.150 | 1.620 | 0.450 | 1.540 | 1.229 |
| $Fe_2O_{3(T)}$ | 16.790 | 53.820 | 56.090 | 19.920 | 50.050 | 66.486 |
| MnO | 0.097 | 0.350 | 0.360 | 0.120 | 0.360 | 0.126 |
| MgO | 0.510 | 5.350 | 4.720 | 1.070 | 4.480 | 4.259 |
| CaO | 0.590 | 1.280 | 1.240 | 4.270 | 1.980 | 1.922 |
| $Na_2O$ | 0.070 | 0.080 | 0.080 | 0.010 | 0.100 | 0.051 |
| $K_2O$ | 0.080 | 0.120 | 0.310 | 0.010 | 0.110 | 0.195 |
| $TiO_2$ | 0.016 | 0.120 | 0.150 | 0.030 | 0.180 | 0.161 |
| $P_2O_5$ | 0.040 | 0.050 | 0.130 | 0.020 | 0.070 | 0.956 |
| LOI | -0.150 | <0.01 | <0.01 | 0.280 | <0.01 | <0.01 |
| Total | 100.500 | 101.250 | 100.270 | 98.980 | 100.750 | 100.604 |
| | | | | | | |
| Element (ppm) | | | | | | |
| Sc | 1.000 | 2.593 | 3.507 | 0.421 | 3.205 | 2.721 |
| Be | 1.000 | 1.640 | 1.537 | 0.883 | 2.344 | 1.276 |
| V | 5.000 | 49.598 | 46.261 | 11.561 | 66.953 | 38.923 |
| Cr | 20.000 | 7.624 | 5.674 | 7.750 | 11.252 | 10.806 |
| Co | 2.000 | 22.222 | 18.658 | 10.775 | 17.570 | 12.119 |
| Ni | 20.000 | 7.203 | 5.615 | 1.869 | 6.782 | 5.141 |
| Cu | 10.000 | 0.690 | 10.085 | 92.778 | 3.101 | 0.191 |
| Zn | 30.000 | 30.688 | 43.569 | 14.603 | 40.536 | 20.099 |
| Ga | 1.000 | 2.628 | 2.716 | 0.520 | 2.206 | 2.523 |
| As | 5.000 | 17.222 | 18.753 | 5.273 | 16.687 | 1.601 |
| Rb | 1.000 | 5.188 | 35.649 | 0.311 | 1.411 | 15.965 |
| Sr | 17.000 | 55.680 | 67.069 | 45.031 | 64.084 | 151.205 |
| Zr | 3.000 | 20.789 | 19.828 | 2.772 | 28.007 | 13.933 |
| Nb | 0.600 | 4.050 | 3.383 | 0.673 | 5.003 | 3.854 |
| Mo | 2.000 | 0.368 | 0.450 | 0.250 | 0.356 | 1.085 |
| Ag | 0.500 | 0.007 | 0.019 | 0.147 | 0.012 | 0.007 |
| In | 0.100 | 0.012 | 0.013 | 0.008 | 0.018 | 0.009 |
| Sn | 1.000 | 1.304 | 1.603 | 0.020 | 2.098 | 0.100 |
| Sb | 1.200 | 1.433 | 1.105 | 1.618 | 1.148 | 2.709 |
| Cs | 0.200 | 1.183 | 7.299 | 0.171 | 0.130 | 4.099 |

Table A.3 continued

| | GF-07-13 | GF-07-15 | GF-07-17 | GF-07-18 | GF-07-19 | GF-07-21 |
|---|---|---|---|---|---|---|
| Element (ppm) | | | | | | |
| Ba | 3.000 | 31.354 | 166.726 | 4.010 | 45.480 | 67.995 |
| La | 0.990 | 3.975 | 6.375 | 1.862 | 5.045 | 41.556 |
| Ce | 2.190 | 10.506 | 15.639 | 3.449 | 13.184 | 83.887 |
| Pr | 0.220 | 1.138 | 1.686 | 0.335 | 1.512 | 8.490 |
| Nd | 0.830 | 4.587 | 6.892 | 1.305 | 6.161 | 32.759 |
| Sm | 0.180 | 0.943 | 1.367 | 0.240 | 1.284 | 5.554 |
| Eu | 0.065 | 0.327 | 0.417 | 0.088 | 0.490 | 1.201 |
| Gd | 0.170 | 0.952 | 1.452 | 0.271 | 1.335 | 5.604 |
| Tb | 0.030 | 0.150 | 0.216 | 0.041 | 0.206 | 0.771 |
| Dy | 0.210 | 0.922 | 1.312 | 0.260 | 1.250 | 4.395 |
| Y | 1.600 | 5.543 | 7.959 | 1.801 | 7.486 | 27.970 |
| Ho | 0.040 | 0.205 | 0.285 | 0.058 | 0.271 | 0.888 |
| Er | 0.140 | 0.589 | 0.789 | 0.165 | 0.761 | 2.186 |
| Yb | 0.130 | 0.540 | 0.633 | 0.150 | 0.630 | 1.258 |
| Lu | 0.019 | 0.076 | 0.086 | 0.022 | 0.085 | 0.157 |
| Tm | 0.020 | 0.089 | 0.111 | 0.024 | 0.109 | 0.259 |
| Hf | 0.100 | 0.421 | 0.419 | 0.051 | 0.562 | 0.322 |
| Ta | 0.020 | 0.153 | 0.122 | 0.020 | 0.199 | 0.170 |
| W | 0.500 | 0.651 | 0.728 | 0.359 | 0.309 | 1.664 |
| Tl | 0.050 | 0.027 | 0.168 | 0.003 | 0.010 | 0.096 |
| Pb | 5.000 | 0.553 | 0.518 | 1.322 | 0.609 | 0.779 |
| Th | 0.190 | 0.622 | 0.568 | 0.087 | 0.788 | 0.747 |
| U | 0.020 | 0.166 | 0.170 | 0.035 | 0.244 | 0.250 |

Table A.3 continued

| | GF-07-22 | GF-07-23 | GF-07-26 | GF-07-29 | GF-09-38 | GF-09-39 | GF-09-40 |
|---|---|---|---|---|---|---|---|
| Oxide (wt. %) | | | | | | | |
| SiO2 | 36.100 | 38.720 | 49.320 | 89.560 | 36.160 | 40.100 | 60.310 |
| Al2O3 | 1.670 | 2.799 | 0.130 | 0.200 | 0.270 | 0.200 | 0.970 |
| Fe2O3(T) | 57.380 | 50.903 | 33.750 | 9.890 | 58.510 | 57.670 | 11.960 |
| MnO | 0.267 | 0.133 | 0.460 | 0.120 | 3.410 | 2.060 | 0.260 |
| MgO | 4.930 | 6.081 | 5.000 | 0.280 | 0.800 | 0.540 | 7.200 |
| CaO | 0.880 | 0.947 | 12.200 | 0.120 | 2.270 | 0.720 | 17.200 |
| Na2O | 0.170 | 0.467 | 0.010 | 0.010 | 0.010 | 0.010 | 0.030 |
| K2O | 0.330 | 0.356 | 0.010 | 0.010 | 0.010 | 0.010 | 0.170 |
| TiO2 | 0.184 | 0.276 | 0.010 | 0.010 | 0.010 | 0.010 | 0.070 |
| P2O5 | 0.070 | 0.047 | 0.010 | 0.010 | 0.080 | 0.030 | 0.500 |
| LOI | -2.100 | <0.01 | <0.01 | <0.01 | <0.01 | <0.01 | 2.590 |
| Total | 99.890 | 100.728 | 100.890 | 100.190 | 101.520 | 101.330 | 101.260 |
| | | | | | | | |
| Element (ppm) | | | | | | | |
| Sc | 3.000 | 5.514 | 0.498 | 0.112 | 1.435 | 1.091 | 1.758 |
| Be | 2.000 | 2.679 | 1.859 | 0.385 | 2.670 | 2.642 | 0.508 |
| V | 68.000 | 115.797 | 6.332 | 1.679 | 20.326 | 11.160 | 29.184 |
| Cr | 20.000 | 19.156 | 0.622 | 0.041 | 1.668 | 0.273 | 6.225 |
| Co | 16.000 | 21.422 | 9.881 | 0.923 | 47.647 | 7.989 | 3.643 |
| Ni | 20.000 | 10.146 | 1.642 | 0.155 | 2.970 | 2.200 | 7.996 |
| Cu | 10.000 | 0.027 | 0.547 | 0.423 | 13.729 | 2.680 | 0.650 |
| Zn | 30.000 | 15.991 | 14.985 | 2.001 | 45.327 | 47.050 | 71.428 |
| Ga | 4.000 | 3.226 | 0.355 | 0.339 | 2.390 | 1.801 | 1.490 |
| As | 5.000 | 11.782 | 0.190 | 4.717 | 2.086 | 0.373 | 0.398 |
| Rb | 35.000 | 25.272 | 1.417 | 0.081 | 0.381 | 0.169 | 1.590 |
| Sr | 141.000 | 244.828 | 167.687 | 1.341 | 26.227 | 12.409 | 128.829 |
| Zr | 27.000 | 40.801 | 2.840 | 1.305 | 8.228 | 6.654 | 11.645 |
| Nb | 5.800 | 7.032 | 0.451 | 0.369 | 3.644 | 2.675 | 2.245 |
| Mo | 2.000 | 0.147 | 6.102 | 0.128 | 0.446 | 0.191 | 0.032 |
| Ag | 0.500 | 0.014 | 0.004 | 0.003 | 0.012 | 0.007 | 0.019 |
| In | 0.100 | 0.014 | 0.006 | 0.000 | 0.016 | 0.014 | 0.034 |
| Sn | 1.000 | 0.043 | 0.051 | 0.105 | 1.455 | 1.090 | 0.434 |
| Sb | 6.400 | 0.951 | 0.189 | 1.050 | 0.584 | 0.321 | 0.139 |
| Cs | 11.600 | 9.751 | 0.088 | 0.031 | 0.076 | 0.101 | 0.048 |

Table A.3 continued

| | GF-07-22 | GF-07-23 | GF-07-26 | GF-07-29 | GF-09-38 | GF-09-39 | GF-09-40 |
|---|---|---|---|---|---|---|---|
| Element (ppm) | | | | | | | |
| Ba | 111.000 | 116.668 | 37.352 | 13.379 | 29.116 | 139.845 | 28.348 |
| La | 5.420 | 3.475 | 1.288 | 1.576 | 9.186 | 5.662 | 8.768 |
| Ce | 15.700 | 9.172 | 5.829 | 2.403 | 13.425 | 9.190 | 14.806 |
| Pr | 1.600 | 1.008 | 0.654 | 0.218 | 1.824 | 1.285 | 1.846 |
| Nd | 6.090 | 4.023 | 3.325 | 0.794 | 8.341 | 5.769 | 7.582 |
| Sm | 1.250 | 0.931 | 0.950 | 0.125 | 1.881 | 1.376 | 1.484 |
| Eu | 0.337 | 0.402 | 0.352 | 0.026 | 0.763 | 0.394 | 0.454 |
| Gd | 1.150 | 1.002 | 1.218 | 0.110 | 2.551 | 1.870 | 1.793 |
| Tb | 0.190 | 0.161 | 0.204 | 0.017 | 0.399 | 0.309 | 0.251 |
| Dy | 1.150 | 0.992 | 1.307 | 0.102 | 2.637 | 2.038 | 1.538 |
| Y | 6.700 | 5.317 | 9.263 | 0.557 | 20.249 | 13.062 | 13.782 |
| Ho | 0.240 | 0.210 | 0.293 | 0.023 | 0.615 | 0.472 | 0.351 |
| Er | 0.710 | 0.593 | 0.830 | 0.071 | 1.767 | 1.350 | 0.960 |
| Yb | 0.640 | 0.564 | 0.681 | 0.077 | 1.391 | 1.071 | 0.707 |
| Lu | 0.086 | 0.081 | 0.092 | 0.011 | 0.184 | 0.139 | 0.098 |
| Tm | 0.105 | 0.090 | 0.118 | 0.012 | 0.251 | 0.193 | 0.127 |
| Hf | 0.700 | 0.844 | 0.023 | 0.010 | 0.044 | 0.032 | 0.248 |
| Ta | 0.250 | 0.311 | 0.003 | 0.001 | 0.010 | 0.007 | 0.203 |
| W | 0.800 | 0.447 | 0.074 | 0.068 | 0.103 | 0.058 | 0.061 |
| Tl | 0.200 | 0.168 | 0.010 | 0.001 | 0.005 | 0.001 | 0.003 |
| Pb | 5.000 | 1.205 | 1.268 | 0.145 | 0.235 | 0.103 | 1.781 |
| Th | 1.030 | 1.382 | 0.032 | 0.011 | 0.133 | 0.119 | 0.708 |
| U | 0.260 | 0.207 | 0.035 | 0.044 | 0.149 | 0.104 | 1.832 |

Table A.3 continued

| | GF-09-41 | GF-09-43 | GF-09-45 | GF-09-46 | GF-09-47 | GF-09-48 |
|---|---|---|---|---|---|---|
| Oxide (wt. %) | | | | | | |
| $SiO_2$ | 7.280 | 23.260 | 78.230 | 82.740 | 90.350 | 46.220 |
| $Al_2O_3$ | 0.270 | 0.550 | 0.360 | 0.540 | 0.660 | 2.000 |
| $Fe_2O_{3(T)}$ | 12.030 | 64.460 | 20.170 | 13.430 | 6.120 | 39.620 |
| MnO | 0.680 | 1.490 | 0.090 | 0.210 | 0.040 | 0.350 |
| MgO | 11.890 | 1.340 | 0.190 | 0.250 | 1.130 | 1.890 |
| CaO | 27.330 | 4.450 | 0.370 | 1.650 | 0.280 | 1.890 |
| $Na_2O$ | 0.010 | 0.010 | 0.010 | 0.010 | 0.010 | 0.070 |
| $K_2O$ | 0.010 | 0.040 | 0.030 | 0.060 | 0.020 | 0.200 |
| $TiO_2$ | 0.020 | 0.050 | 0.010 | 0.020 | 0.030 | 0.130 |
| $P_2O_5$ | 0.040 | 0.040 | 0.010 | 0.010 | 0.020 | 0.090 |
| LOI | 40.140 | 5.680 | 0.600 | 1.960 | 1.060 | 7.740 |
| Total | 99.690 | 101.370 | 100.050 | 100.870 | 99.710 | 100.200 |
| | | | | | | |
| Element (ppm) | | | | | | |
| Sc | 0.925 | 0.964 | 0.394 | 0.582 | 0.700 | 4.445 |
| Be | 0.647 | 4.069 | 0.881 | 0.740 | 0.826 | 4.408 |
| V | 5.512 | 24.942 | 11.093 | 6.791 | 3.832 | 30.320 |
| Cr | 4.192 | 5.280 | 0.607 | 1.023 | 1.571 | 17.218 |
| Co | 4.491 | 7.954 | 0.964 | 2.311 | 1.712 | 17.826 |
| Ni | 4.028 | 5.745 | 0.964 | 0.879 | 0.660 | 7.689 |
| Cu | 1.604 | 4.396 | 5.687 | 34.498 | 8.415 | 3.830 |
| Zn | 4.628 | 15.145 | 3.040 | 2.470 | 4.420 | 14.219 |
| Ga | 0.602 | 2.413 | 0.980 | 0.916 | 1.097 | 5.589 |
| As | 2.303 | 0.751 | 1.930 | 1.207 | 0.970 | 3.539 |
| Rb | 0.371 | 6.784 | 2.411 | 6.434 | 1.754 | 28.660 |
| Sr | 146.538 | 71.317 | 8.765 | 20.069 | 8.393 | 57.184 |
| Zr | 5.108 | 21.116 | 4.597 | 9.341 | 3.065 | 54.229 |
| Nb | 0.933 | 4.436 | 1.157 | 1.374 | 0.558 | 8.906 |
| Mo | 0.104 | 4.853 | 0.240 | 0.094 | 0.032 | 0.846 |
| Ag | 0.033 | 0.035 | 0.005 | 0.006 | 0.003 | 0.014 |
| In | 0.003 | 0.024 | 0.002 | 0.003 | 0.002 | 0.011 |
| Sn | 0.203 | 0.593 | 0.112 | 0.122 | 0.184 | 0.633 |
| Sb | 0.160 | 0.135 | 0.082 | 0.213 | 0.032 | 0.161 |
| Cs | 0.047 | 4.110 | 0.578 | 1.659 | 0.682 | 13.549 |

Table A.3 continued

| | GF-09-41 | GF-09-43 | GF-09-45 | GF-09-46 | GF-09-47 | GF-09-48 |
|---|---|---|---|---|---|---|
| Element (ppm) | | | | | | |
| Ba | 9.394 | 6.773 | 7.431 | 27.586 | 4.540 | 62.107 |
| La | 1.788 | 4.715 | 1.550 | 5.667 | 0.713 | 4.780 |
| Ce | 4.515 | 9.938 | 4.220 | 17.921 | 2.082 | 17.198 |
| Pr | 0.361 | 1.058 | 0.363 | 1.028 | 0.159 | 0.980 |
| Nd | 1.424 | 4.461 | 1.442 | 3.797 | 0.638 | 3.647 |
| Sm | 0.291 | 0.932 | 0.273 | 0.660 | 0.132 | 0.678 |
| Eu | 0.105 | 0.380 | 0.071 | 0.169 | 0.039 | 0.210 |
| Gd | 0.345 | 1.136 | 0.282 | 0.561 | 0.160 | 0.684 |
| Tb | 0.049 | 0.184 | 0.049 | 0.092 | 0.025 | 0.108 |
| Dy | 0.294 | 1.202 | 0.332 | 0.555 | 0.171 | 0.684 |
| Y | 2.517 | 8.009 | 1.692 | 2.455 | 1.165 | 4.690 |
| Ho | 0.064 | 0.279 | 0.075 | 0.116 | 0.040 | 0.158 |
| Er | 0.173 | 0.830 | 0.230 | 0.325 | 0.125 | 0.487 |
| Yb | 0.117 | 0.774 | 0.221 | 0.267 | 0.128 | 0.514 |
| Lu | 0.016 | 0.106 | 0.029 | 0.034 | 0.019 | 0.075 |
| Tm | 0.022 | 0.127 | 0.037 | 0.048 | 0.020 | 0.078 |
| Hf | 0.071 | 0.219 | 0.026 | 0.107 | 0.046 | 0.692 |
| Ta | 0.013 | 0.071 | 0.003 | 0.013 | 0.011 | 0.107 |
| W | 0.941 | 5.427 | 0.210 | 0.115 | 0.342 | 6.378 |
| Tl | 0.016 | 0.035 | 0.004 | 0.011 | 0.006 | 0.095 |
| Pb | 1.064 | 2.011 | 0.864 | 1.099 | 0.489 | 1.102 |
| Th | 0.180 | 0.198 | 0.033 | 0.225 | 0.185 | 2.087 |
| U | 0.739 | 0.264 | 0.144 | 0.073 | 0.157 | 0.440 |

Table A.3 continued

| | GF-09-50 | GF-09-52 | GF-09-54 |
|---|---|---|---|
| Oxide (wt. %) | | | |
| $SiO_2$ | 17.190 | 8.530 | 79.420 |
| $Al_2O_3$ | 0.110 | 0.170 | 0.270 |
| $Fe_2O_{3(T)}$ | 9.200 | 28.720 | 4.010 |
| MnO | 2.380 | 0.760 | 0.110 |
| MgO | 8.730 | 11.890 | 3.510 |
| CaO | 27.320 | 19.890 | 5.360 |
| $Na_2O$ | 0.010 | 0.010 | 0.010 |
| $K_2O$ | 0.010 | 0.010 | 0.020 |
| $TiO_2$ | 0.010 | 0.010 | 0.050 |
| $P_2O_5$ | 0.010 | 0.010 | 0.010 |
| LOI | 35.220 | 29.760 | 8.340 |
| Total | 100.160 | 99.740 | 101.100 |
| | | | |
| Element (ppm) | | | |
| Sc | 0.733 | 0.613 | 0.306 |
| Be | 0.479 | 1.218 | 0.548 |
| V | 6.404 | 31.214 | 10.560 |
| Cr | 0.513 | 0.591 | 3.847 |
| Co | 4.242 | 1.969 | 0.804 |
| Ni | 8.864 | 3.920 | 1.561 |
| Cu | 2.468 | 0.732 | 3.883 |
| Zn | 3.848 | 2.306 | 1.697 |
| Ga | 0.809 | 1.005 | 0.707 |
| As | 0.730 | 1.961 | 0.422 |
| Rb | 0.453 | 0.238 | 0.250 |
| Sr | 45.888 | 42.220 | 11.796 |
| Zr | 6.047 | 6.170 | 17.649 |
| Nb | 1.213 | 1.538 | 4.978 |
| Mo | 0.042 | 2.973 | 0.193 |
| Ag | 0.116 | 0.025 | 0.083 |
| In | 0.017 | 0.051 | 0.013 |
| Sn | 0.125 | 0.096 | 0.455 |
| Sb | 0.330 | 0.600 | 0.098 |
| Cs | 0.094 | 0.074 | 0.051 |

Table A.3 continued

| | GF-09-50 | GF-09-52 | GF-09-54 |
|---|---|---|---|
| Element (ppm) | | | |
| Ba | 7.846 | 35.051 | 20.212 |
| La | 9.052 | 7.158 | 22.986 |
| Ce | 12.893 | 15.960 | 42.383 |
| Pr | 1.370 | 1.980 | 4.480 |
| Nd | 5.870 | 8.488 | 16.582 |
| Sm | 1.196 | 2.153 | 2.318 |
| Eu | 0.367 | 0.777 | 0.568 |
| Gd | 1.616 | 2.670 | 1.661 |
| Tb | 0.236 | 0.449 | 0.218 |
| Dy | 1.488 | 2.895 | 1.315 |
| Y | 12.757 | 18.313 | 8.213 |
| Ho | 0.338 | 0.649 | 0.303 |
| Er | 0.951 | 1.816 | 0.932 |
| Yb | 0.768 | 1.409 | 0.894 |
| Lu | 0.108 | 0.185 | 0.122 |
| Tm | 0.133 | 0.252 | 0.146 |
| Hf | 0.027 | 0.027 | 0.171 |
| Ta | 0.002 | 0.005 | 0.023 |
| W | 0.007 | 2.985 | 0.191 |
| Tl | 0.134 | 0.004 | 0.007 |
| Pb | 4.257 | 2.602 | 1.128 |
| Th | 0.024 | 0.076 | 0.268 |
| U | 0.292 | 6.434 | 1.690 |

Table A.4
Major and trace element geochemisty of samples from the Akilia

| | **AK02** | **AK03** | **AK04** | **AK05** | **AK42** | **AK-47** | **AK-33** | **AK38** | **92-197** |
|---|---|---|---|---|---|---|---|---|---|
| Oxide (wt. %) | | | | | | | | | |
| $SiO_2$ | 48.74 | 47.6 | 49.61 | 47.97 | 78.64 | 45.09 | 63.21 | 48.47 | 67.85 |
| $Al_2O_3$ | 7.35 | 7.99 | 6.94 | 8.95 | 0.41 | 15.55 | 0.34 | 4.58 | 0.32 |
| $Fe_2O_{3(T)}$ | 11.68 | 11.95 | 12.19 | 12.92 | 11.15 | 15.57 | 23.28 | 21.75 | 25.84 |
| MnO | 0.177 | 0.186 | 0.179 | 0.219 | 0.202 | 0.316 | 0.333 | 0.355 | 0.314 |
| MgO | 22.35 | 21.67 | 21.53 | 16.55 | 3.67 | 6.42 | 5.53 | 10.12 | 4.5 |
| CaO | 6.46 | 6.67 | 5.34 | 9.59 | 5.58 | 13.89 | 7.33 | 11.64 | 2.34 |
| $Na_2O$ | 1.21 | 1.28 | 1.13 | 1.48 | 0.32 | 1.63 | 0.09 | 0.87 | 0.07 |
| $K_2O$ | 0.1 | 0.14 | 0.47 | 0.11 | 0.06 | 0.64 | 0.04 | 0.21 | 0.03 |
| $TiO_2$ | 0.283 | 0.361 | 0.299 | 0.398 | 0 | 0.804 | 0.005 | 0.274 | 0.025 |
| $P_2O_5$ | 0.04 | 0.03 | 0.03 | 0.03 | 0.03 | 0.04 | 0.01 | 0.05 | 0.05 |
| LOI | 1.57 | 2.22 | 1.91 | 1.37 | -0.085 | 0.27 | -0.16 | 1.59 | -1.29 |
| Total | 99.95 | 100.1 | 99.63 | 99.59 | 99.97 | 100.2 | 99.99 | 99.89 | 100.1 |
| | | | | | | | | | |
| Element (ppm) | | | | | | | | | |
| Sc | n.d. | 34.5 | 28.7 | 33.5 | 0.6 | 55 | 1 | 20.1 | 1 |
| V | 131.17 | 136.12 | 128.06 | 150.81 | 4.00 | 293 | 5 | 118 | 10 |
| Cr | 3600 | 3400 | 3400 | 2100 | 4.6 | 910 | 20 | 2200 | 20 |
| Co | 93 | 103 | 88 | 82 | 5 | 96 | 7 | 35 | 8 |
| Ni | 758.00 | 947.50 | 746.23 | 463.17 | 46.83 | 260 | 90 | 108 | 130 |
| Cu | 106.63 | 165.80 | 176.40 | 12.29 | 47.21 | 80 | 240 | 848 | 210 |
| Zn | 113.95 | 107.56 | 120.49 | 107.94 | 65.45 | 180 | 40 | 131 | 50 |
| Ga | 7.73 | 7.17 | 8.74 | 10.27 | -1.00 | 26 | 3 | 10.17 | 2 |
| Ge | 1.32 | -0.50 | 1.78 | 1.73 | 3.46 | 1.9 | 3.6 | 8.18 | 3.2 |
| Rb | 2.06 | 1.46 | 26.46 | -1.00 | -1.00 | 13 | 2 | 3.82 | 3 |
| Sr | 20.84 | 13.75 | 14.84 | 20.76 | 5.30 | 69 | 7 | 17.69 | 14 |
| Zr | 19.17 | 23.20 | 21.03 | 31.63 | 4.47 | 48 | 2 | 16.02 | 3 |
| Nb | 1.17 | 1.08 | 1.29 | 1.87 | 0.72 | 2.4 | 1.1 | 4.49 | 2.3 |
| Mo | -2.00 | -2.00 | -2.00 | -2.00 | -2.00 | 2 | 3 | 4.38 | 3 |
| In | -0.10 | -0.10 | -0.10 | -0.10 | -0.10 | < 0.1 | 0.1 | 0.11 | 0.1 |
| Sn | -1.00 | -1.00 | 3.34 | 3.16 | 1.71 | < 1 | < 1 | 3.67 | 1 |
| Sb | -0.1 | 0.1 | -0.1 | -0.1 | 0.1 | 7.4 | 0.3 | -0.1 | 0.3 |
| Cs | -1 | -1 | 4 | -1 | -0.10 | 0.2 | 0.3 | -1 | 0.2 |

Table A.4 continued

| | AK02 | AK03 | AK04 | AK05 | AK42 | AK-47 | AK-33 | AK38 | 92-197 |
|---|---|---|---|---|---|---|---|---|---|
| Element (ppm) | | | | | | | | | |
| Ba | 6.13 | -3.00 | 7.54 | -3.00 | -3.00 | 17 | 4 | 4.37 | 36 |
| La | 1.08 | 1.36 | 1.41 | 3.42 | 1.24 | 2.71 | 2.16 | 4.06 | 3 |
| Ce | 2.86 | 3.19 | 3.83 | 8.04 | 3.13 | 9.44 | 3.62 | 14.82 | 3.65 |
| Pr | 0.44 | 0.44 | 0.51 | 0.86 | 0.39 | 1.55 | 0.75 | 2.08 | 0.5 |
| Nd | 2.41 | 2.22 | 2.41 | 3.58 | 1.63 | 8.73 | 4.08 | 9.44 | 2.49 |
| Sm | 0.88 | 0.80 | 0.76 | 1.11 | 0.35 | 3.09 | 1.34 | 2.47 | 0.76 |
| Eu | 0.47 | 0.47 | 0.32 | 0.45 | 0.20 | 1.1 | 0.359 | 1.07 | 0.254 |
| Gd | 1.26 | 1.16 | 1.08 | 1.53 | 0.42 | 4.23 | 1.34 | 2.74 | 0.75 |
| Tb | 0.24 | 0.23 | 0.21 | 0.29 | 0.07 | 0.8 | 0.2 | 0.46 | 0.11 |
| Dy | 1.54 | 1.55 | 1.43 | 1.98 | 0.47 | 5.22 | 1.09 | 2.74 | 0.58 |
| Y | 9.65 | 8.96 | 8.49 | 12.46 | 3.81 | 29 | 4.7 | 17.07 | 2.2 |
| Ho | 0.32 | 0.32 | 0.29 | 0.40 | 0.10 | 1.13 | 0.21 | 0.54 | 0.11 |
| Er | 0.99 | 0.96 | 0.87 | 1.22 | 0.29 | 3.38 | 0.64 | 1.64 | 0.35 |
| Yb | 0.88 | 0.90 | 0.85 | 1.17 | 0.28 | 3.19 | 0.84 | 1.59 | 0.47 |
| Lu | 0.14 | 0.14 | 0.13 | 0.17 | 0.04 | 0.477 | 0.135 | 0.23 | 0.086 |
| Tm | 0.15 | 0.14 | 0.14 | 0.19 | 0.04 | 0.503 | 0.11 | 0.24 | 0.059 |
| Hf | 0.525 | 0.704 | 0.582 | 0.896 | 0.157 | 2 | 0.6 | 0.491 | 0.5 |
| Ta | 0.802 | 0.701 | 1.106 | 1.035 | 0.373 | 0.1 | 0.12 | 0.443 | 0.14 |
| W | 9.30 | -0.50 | 1.83 | 1.01 | -0.50 | < 0.5 | 1.5 | -0.50 | 1.3 |
| Tl | -0.05 | -0.05 | 0.35 | -0.05 | -0.05 | 0.06 | 0.42 | 0.08 | 0.29 |
| Pb | -3.00 | -3.00 | 9.77 | 18.78 | 3.94 | 7 | 5 | -3.00 | 8 |
| Th | 1.437 | 0.625 | 0.276 | 0.385 | 0.125 | 0.06 | 0.16 | 0.110 | 0.31 |
| U | 0.055 | 0.095 | 0.915 | 0.246 | 0.048 | 0.07 | 0.38 | 0.155 | 0.95 |

Table A.5
Lead isotope analyses from samples from the GF

| Sample | 207Pb / 206Pb | ± | 208Pb / 206Pb | ± | 206Pb / 204Pb | ± | 207Pb/204Pb | ± | 204Pb/206Pb | ± | 208Pb/204Pb |
|---|---|---|---|---|---|---|---|---|---|---|---|
| GF-07-04 | 0.7846 | 0.0003 | 1.8580 | 0.0007 | 20.323 | 0.025 | 15.947 | 0.024 | 0.04920 | 0.00007 | 37.76071 |
| GF-07-06e | 0.7948 | 0.0003 | 1.9355 | 0.0007 | 19.574 | 0.024 | 15.557 | 0.023 | 0.05109 | 0.00008 | 37.88544 |
| GF-07-09 | 0.5876 | 0.0002 | 1.5635 | 0.0006 | 27.461 | 0.034 | 16.135 | 0.010 | 0.03642 | 0.00002 | 42.93438 |
| GF-07-11 | 0.8177 | 0.0003 | 1.9440 | 0.0007 | 18.970 | 0.023 | 15.512 | 0.023 | 0.05272 | 0.00008 | 36.87781 |
| GF-07-15 | 0.8087 | 0.0003 | 2.0327 | 0.0007 | 19.028 | 0.023 | 15.387 | 0.023 | 0.05255 | 0.00008 | 38.67681 |
| GF-07-17 | 0.7811 | 0.0003 | 1.9940 | 0.0007 | 19.785 | 0.024 | 15.454 | 0.023 | 0.05054 | 0.00007 | 39.45226 |
| GF-07-26 | 0.8950 | 0.0003 | 2.1042 | 0.0007 | 17.203 | 0.021 | 15.397 | 0.023 | 0.05813 | 0.00009 | 36.19928 |
| GF-09-19 | 0.7558 | 0.0003 | 1.9130 | 0.0007 | 20.521 | 0.025 | 15.509 | 0.023 | 0.04873 | 0.00007 | 39.25673 |
| GF-09-29 | 0.7643 | 0.0003 | 1.7611 | 0.0006 | 20.291 | 0.025 | 15.509 | 0.023 | 0.04928 | 0.00007 | 35.73503 |
| GF-09-38 | 0.7526 | 0.0003 | 1.7825 | 0.0006 | 21.524 | 0.026 | 16.199 | 0.024 | 0.04646 | 0.00007 | 38.36661 |
| GF-09-39 | 0.5830 | 0.0002 | 1.4419 | 0.0005 | 27.617 | 0.034 | 16.101 | 0.024 | 0.03621 | 0.00005 | 39.82187 |
| GF-09-40 | 0.4726 | 0.0002 | 1.0533 | 0.0004 | 35.550 | 0.043 | 16.801 | 0.025 | 0.02813 | 0.00004 | 37.44675 |
| GF-09-41 | 0.5924 | 0.0002 | 1.3577 | 0.0005 | 28.190 | 0.034 | 16.699 | 0.025 | 0.03547 | 0.00005 | 38.27311 |
| GF-09-43 | 0.8015 | 0.0003 | 1.9316 | 0.0007 | 19.862 | 0.024 | 15.920 | 0.023 | 0.05035 | 0.00007 | 38.36598 |
| GF-09-45 | 0.8331 | 0.0003 | 1.9079 | 0.0007 | 19.035 | 0.023 | 15.858 | 0.023 | 0.05254 | 0.00008 | 36.31550 |
| GF-09-46 | 0.8944 | 0.0003 | 2.1184 | 0.0008 | 17.666 | 0.022 | 15.800 | 0.023 | 0.05661 | 0.00008 | 37.42388 |
| GF-09-47 | 0.6685 | 0.0002 | 1.6112 | 0.0006 | 23.644 | 0.029 | 15.805 | 0.023 | 0.04229 | 0.00006 | 38.09472 |
| GF-09-48 | 0.7890 | 0.0003 | 2.1570 | 0.0008 | 20.129 | 0.025 | 15.882 | 0.023 | 0.04968 | 0.00007 | 43.41642 |
| GF-09-50 | 0.8384 | 0.0003 | 1.9884 | 0.0007 | 18.670 | 0.023 | 15.652 | 0.023 | 0.05356 | 0.00008 | 37.12256 |
| GF-09-52 | 0.2350 | 0.0001 | 0.3910 | 0.0001 | 100.109 | 0.122 | 23.527 | 0.035 | 0.00999 | 0.00001 | 39.14571 |
| GF-09-54 | 0.3960 | 0.0001 | 0.8359 | 0.0003 | 47.618 | 0.058 | 18.856 | 0.028 | 0.02100 | 0.00003 | 39.80226 |

Table A.6
Iron isotope analyses from samples from the IGB, BGB, and GF

| Sample | $d^{56/54}Fe$ | 2SE | $d^{57/54}Fe$ | 2SE | $d^{58/54}Fe$ | 2SE | $d^{58/56}Fe$ | 2SE |
|---|---|---|---|---|---|---|---|---|
| 462604 | 0.273 | 0.050 | 0.386 | 0.103 | 0.636 | 0.709 | 0.363 | 0.723 |
| 462610 | 0.470 | 0.056 | 0.706 | 0.101 | 1.133 | 0.832 | 0.662 | 0.839 |
| 465940 | -0.048 | 0.052 | -0.134 | 0.096 | 0.038 | 0.825 | 0.086 | 0.832 |
| 465942 | -0.350 | 0.051 | -0.535 | 0.103 | -0.970 | 0.871 | -0.620 | 0.865 |
| IS-02-05 | 0.698 | 0.044 | 1.054 | 0.085 | 2.134 | 0.870 | 1.434 | 0.871 |
| IS-02-06 | 1.046 | 0.049 | 1.549 | 0.096 | 2.191 | 0.724 | 1.145 | 0.714 |
| IS-02-08 | -0.239 | 0.041 | -0.329 | 0.073 | -0.844 | 0.791 | -0.605 | 0.796 |
| ISB-55 | 0.545 | 0.053 | 0.814 | 0.090 | 1.326 | 0.917 | 0.780 | 0.922 |
| | | | | | | | | |
| ZB-03 | 0.283 | 0.042 | 0.399 | 0.086 | -0.091 | 0.924 | -0.374 | 0.927 |
| ZB-05 | 0.341 | 0.048 | 0.511 | 0.096 | 0.513 | 0.930 | 0.172 | 0.930 |
| ZB-07 | 0.245 | 0.035 | 0.366 | 0.094 | 0.284 | 0.856 | 0.039 | 0.849 |
| ZB-18 | 0.289 | 0.044 | 0.464 | 0.085 | 0.620 | 0.920 | 0.331 | 0.928 |
| ZB-23 | 0.491 | 0.062 | 0.710 | 0.054 | 1.256 | 0.465 | 2.292 | 0.406 |
| ZB-27 | 0.197 | 0.044 | 0.310 | 0.108 | 1.305 | 1.003 | 1.107 | 1.008 |
| ZB-105 | 0.364 | 0.046 | 0.623 | 0.104 | 0.750 | 0.995 | 0.386 | 0.996 |
| ZB-117 | 0.467 | 0.036 | 0.683 | 0.079 | 0.563 | 0.767 | 0.096 | 0.758 |
| ZB-169 | 0.414 | 0.041 | 0.590 | 0.088 | 0.663 | 0.783 | 0.249 | 0.787 |
| ZB-247 | 0.326 | 0.046 | 0.521 | 0.095 | 1.092 | 0.921 | 0.766 | 0.916 |
| ZB-294 | 0.028 | 0.042 | 0.069 | 0.104 | -0.051 | 0.866 | -0.079 | 0.870 |
| | | | | | | | | |
| GF-07-04 | 0.559 | 0.054 | 0.749 | 0.077 | 0.914 | 0.962 | 0.355 | 0.961 |
| GF-07-06e | 0.535 | 0.042 | 0.830 | 0.082 | 1.508 | 0.877 | 0.973 | 0.876 |
| GF-07-09 | 0.673 | 0.043 | 1.025 | 0.082 | 0.542 | 0.894 | -0.131 | 0.890 |
| GF-07-10 | 0.671 | 0.052 | 1.035 | 0.085 | 1.093 | 0.874 | 0.422 | 0.879 |
| GF-07-11 | 0.400 | 0.051 | 0.619 | 0.076 | 0.912 | 0.933 | 0.512 | 0.934 |
| GF-07-12 | 0.449 | 0.048 | 0.654 | 0.080 | 1.036 | 0.972 | 0.587 | 0.973 |
| GF-07-13 | 0.960 | 0.049 | 1.409 | 0.096 | 1.311 | 0.963 | 0.351 | 0.959 |
| GF-07-15 | 0.620 | 0.053 | 0.942 | 0.102 | 1.181 | 0.962 | 0.561 | 0.955 |
| GF-07-17 | 0.671 | 0.056 | 1.049 | 0.105 | 1.251 | 0.902 | 0.580 | 0.886 |
| GF-07-18 | 0.621 | 0.056 | 0.928 | 0.103 | 1.600 | 0.844 | 0.978 | 0.829 |
| GF-07-19 | 0.585 | 0.049 | 0.898 | 0.087 | 1.265 | 0.919 | 0.679 | 0.898 |
| GF-07-21 | 0.871 | 0.046 | 1.228 | 0.091 | 1.978 | 0.787 | 1.105 | 0.775 |
| GF-07-22 | 0.659 | 0.004 | 0.970 | 0.068 | 1.417 | 0.708 | 2.272 | 0.703 |
| GF-07-23 | 0.613 | 0.046 | 0.930 | 0.085 | 1.915 | 0.985 | 1.301 | 0.993 |
| GF-07-26 | -0.027 | 0.042 | -0.011 | 0.085 | -0.001 | 1.058 | 0.025 | 1.059 |
| GF-07-27a | 1.410 | 0.039 | 2.123 | 0.088 | 3.099 | 0.958 | 1.686 | 0.961 |
| GF-09-29 | 0.090 | 0.048 | 0.117 | 0.099 | -0.129 | 0.885 | -0.219 | 0.881 |
| GF-09-38 | -0.108 | 0.037 | -0.089 | 0.077 | -0.304 | 0.980 | -0.196 | 0.985 |
| GF-09-39 | -0.127 | 0.043 | -0.174 | 0.094 | 0.027 | 0.890 | 0.154 | 0.886 |
| GF-09-40 | 0.641 | 0.049 | 0.933 | 0.089 | 1.302 | 0.976 | 0.660 | 0.976 |
| GF-09-41 | 0.080 | 0.057 | 0.142 | 0.093 | -0.052 | 0.860 | -0.132 | 0.842 |
| GF-09-43 | 0.514 | 0.050 | 0.764 | 0.092 | 0.852 | 0.721 | 0.338 | 0.713 |
| GF-09-45 | 0.129 | 0.047 | 0.231 | 0.074 | -0.272 | 0.933 | -0.401 | 0.920 |
| GF-09-46 | -0.205 | 0.043 | -0.284 | 0.083 | -0.048 | 0.777 | 0.157 | 0.778 |
| GF-09-47 | -0.102 | 0.052 | -0.163 | 0.082 | -0.639 | 0.919 | -0.537 | 0.915 |

Table A.6 continued

| Sample | $d^{56/54}Fe$ | 2SE | $d^{57/54}Fe$ | 2SE | $d^{58/54}Fe$ | 2SE | $d^{58/56}Fe$ | 2SE |
|---|---|---|---|---|---|---|---|---|
| GF-09-48 | 0.494 | 0.049 | 0.732 | 0.108 | 1.349 | 0.704 | 0.854 | 0.705 |
| GF-09-50 | 0.045 | 0.048 | 0.109 | 0.079 | -0.251 | 0.821 | -0.296 | 0.821 |
| GF-09-52 | 0.294 | 0.051 | 0.498 | 0.091 | 0.955 | 0.742 | 0.661 | 0.741 |
| GF-09-54 | 0.189 | 0.051 | 0.301 | 0.093 | 0.839 | 0.866 | 0.650 | 0.868 |
| | | | | | | | | |
| IS-02-06/B1 | 0.941 | 0.049 | 1.375 | 0.086 | 2.661 | 0.959 | 1.718 | 0.969 |
| IS-02-06/B2 | 1.012 | 0.048 | 1.491 | 0.078 | 5.186 | 0.966 | 4.170 | 0.966 |
| IS-02-06/B3 | 1.046 | 0.043 | 1.522 | 0.093 | 2.751 | 0.987 | 1.703 | 0.984 |
| | | | | | | | | |
| ISB-55/B1 | 0.549 | 0.039 | 0.822 | 0.093 | 3.286 | 0.883 | 2.735 | 0.882 |
| ISB-55/B2 | 0.482 | 0.037 | 0.815 | 0.093 | 4.785 | 0.836 | 4.300 | 0.832 |
| ISB-55/B3 | 0.528 | 0.041 | 0.808 | 0.090 | 2.758 | 0.618 | 2.229 | 0.614 |
| | | | | | | | | |
| ZB-23/B1 | 0.583 | 0.028 | 0.848 | 0.094 | 1.433 | 0.746 | 0.850 | 0.744 |
| ZB-23/B2 | 0.623 | 0.040 | 0.910 | 0.100 | 1.890 | 0.828 | 1.266 | 0.834 |
| | | | | | | | | |
| ZB-18/B1 | 0.220 | 0.049 | 0.364 | 0.099 | 1.427 | 0.863 | 1.207 | 0.856 |
| ZB-18/B2 | 0.166 | 0.043 | 0.203 | 0.088 | 1.300 | 0.815 | 1.135 | 0.812 |
| | | | | | | | | |
| GF-07-22/B1 | 0.678 | 0.052 | 1.013 | 0.085 | 2.394 | 0.711 | 1.715 | 0.719 |
| GF-07-22/B2 | 0.738 | 0.043 | 1.091 | 0.106 | 2.424 | 0.796 | 1.685 | 0.784 |
| | | | | | | | | |
| GF-07-23/repeat | 0.632 | 0.049 | 0.901 | 0.112 | 2.116 | 0.751 | 1.483 | 0.761 |
| IS-02-06/B1/repeat | 0.993 | 0.054 | 1.431 | 0.121 | 3.392 | 0.770 | 2.397 | 0.778 |

Table A.7
LA-ICP-MS REE analsyses (25μm) from samples from the IGB, BGB, GF

| Sample | Duration(s) | Mineral | Fe57_CPS | Fe57_CPS_2SE | Sr_ppm_m88 |
|---|---|---|---|---|---|
| IS8_1_1 | 16.94 | Hem | 1.56E+07 | 1.26E+06 | 0.129 |
| IS8_1_2 | 16.015 | Mt | 1.29E+07 | 1.04E+06 | 0.719 |
| IS8_3_1 | 18.903 | Hem | 1.46E+07 | 1.15E+06 | 0.028 |
| IS8_3_2 | 14.529 | Mt | 1.28E+07 | 7.53E+05 | 0.048 |
| IS8_5_1 | 16.213 | Hem | 1.49E+07 | 1.19E+06 | 0.245 |
| IS8_5_2 | 16.13 | Mt | 1.35E+07 | 1.14E+06 | 0.046 |
| IS8_5_3 | 18.281 | Mt | 1.38E+07 | 9.08E+05 | 1.041 |
| IS8_5_4 | 17.288 | Hem | 1.43E+07 | 1.52E+06 | 0.025 |
| IS8_7_1 | 16.792 | Mt | 1.33E+07 | 9.85E+05 | 1.739 |
| IS8_8_1 | 16.047 | Mt | 1.44E+07 | 9.71E+05 | 0.235 |
| IS8_8_2 | 16.461 | Hem | 1.48E+07 | 8.58E+05 | 0.066 |
| IS8_10_1 | 17.536 | Mt | 1.26E+07 | 9.90E+05 | 0.052 |
| IS8_11_1 | 19.121 | Mt | 1.14E+07 | 6.30E+05 | 0.002 |
| IS8_13_1 | 15.506 | Mg | 1.37E+07 | 1.54E+06 | 0.042 |
| IS8_13_2 | 5.3741 | Hem | 7.78E+06 | 7.60E+05 | 0.228 |
| IS8_15_1 | 17.785 | Mt | 1.31E+07 | 8.75E+05 | 0.371 |
| IS8_15_2 | 17.123 | Hem | 1.52E+07 | 1.03E+06 | 0.080 |
| IS8_17_1 | 4.5848 | Mt | 1.45E+07 | 1.83E+06 | 0.060 |
| IS8_17_2 | 11.213 | Mt | 1.53E+07 | 8.98E+05 | 0.091 |
| IS8_18_1 | 12.76 | Mt | 1.69E+07 | 1.07E+06 | 1.165 |
| IS8_18_2 | 16.648 | Hem | 1.63E+07 | 1.43E+06 | 0.011 |
| IS8_19_1 | 9.7772 | Mt | 1.56E+07 | 9.31E+05 | 0.076 |
| IS8_19_2 | 14.252 | Mt | 1.37E+07 | 8.11E+05 | 0.060 |
| IS8_20_2 | 6.6839 | Mt | 1.73E+07 | 1.27E+06 | 0.004 |
| | | | | | |
| GF6_16_1 | 10.993 | Mt | 1.72E+07 | 1.48E+06 | 3.207 |
| GF6_16_2 | 13.313 | Mt | 1.74E+07 | 1.08E+06 | 20.481 |
| GF6_3_1 | 18.505 | Mt | 9.50E+06 | 6.29E+05 | 46.677 |
| GF6_3_2 | 18.284 | Mt | 9.73E+06 | 7.09E+05 | 32.794 |
| GF6_1_1 | 18.339 | Mt | 1.01E+07 | 1.48E+06 | 13.698 |
| GF6_2_1 | 16.018 | Mt | 1.18E+07 | 6.44E+05 | 25.644 |
| GF6_2_2 | 14.657 | Mt | 9.78E+06 | 1.45E+06 | 28.870 |
| GF6_5_1 | 16.332 | Mt | 1.02E+07 | 7.31E+05 | 9.792 |
| GF6_4_1 | 17.588 | Mt | 8.69E+06 | 6.15E+05 | 8.757 |
| GF6_6_1 | 17.379 | Mt | 9.01E+06 | 8.67E+05 | 34.027 |
| GF6_17_1 | 6.52 | Mt | 1.22E+07 | 2.57E+05 | 2.024 |
| GF6_11_1 | 14.761 | Mt | 1.11E+07 | 1.13E+06 | 5.214 |
| GF6_8_1 | 14.343 | Mt | 1.14E+07 | 5.88E+05 | 6.755 |
| GF6_7_1 | 15.599 | Mt | 1.16E+07 | 1.18E+06 | 10.351 |
| GF6_9_1 | 14.029 | Mt | 1.13E+07 | 9.36E+05 | 30.796 |

Table A.7 continued

| Sample | Duration(s) | Mineral | Fe57_CPS | Fe57_CPS_2SE | Sr_ppm_m88 |
|---|---|---|---|---|---|
| GF6_10_1 | 17.483 | Mt | 9.96E+06 | 7.75E+05 | 24.769 |
| GF6_18_1 | 17.693 | Mt | 1.27E+07 | 1.06E+06 | 10.671 |
| GF6_13_1 | 14.657 | Mt | 1.18E+07 | 1.09E+06 | 20.303 |
| GF6_12_1 | 18.74 | Mt | 1.28E+07 | 7.56E+05 | 12.430 |
| GF6_15_1 | 18.53 | Mt | 1.07E+07 | 5.81E+05 | 5.178 |
| GF6_19_1 | 16.855 | Mt | 1.10E+07 | 1.20E+06 | 4.844 |
| GF6_20_1 | 17.897 | Mt | 9.94E+06 | 2.07E+06 | 81.052 |
| | | | | | |
| ZB117_1_a | 18.844 | Mt | 2.39E+07 | 1.21E+06 | 0.486 |
| ZB117_2_a | 19.054 | Mt | 1.68E+07 | 6.52E+05 | 0.259 |
| ZB117_4_a | 19.368 | Mt | 2.03E+07 | 1.51E+06 | 0.491 |
| ZB117_7_a | 16.437 | Mt | 1.99E+07 | 1.64E+06 | 1.064 |
| ZB117_14_a | 15.808 | Mt | 1.55E+07 | 7.40E+05 | 0.219 |
| | | Mt | | | |
| GF39_9_1 | 18.635 | Mt | 8.97E+06 | 8.49E+05 | 2.228 |
| GF39_6_1 | 17.274 | Mt | 9.44E+06 | 8.48E+05 | 0.944 |
| GF39_6_2 | 19.444 | Mt | 8.28E+06 | 1.01E+06 | 0.380 |
| GF39_7_1 | 19.057 | Mt | 8.29E+06 | 7.11E+05 | 0.686 |
| GF39_4_1 | 18.229 | Mt | 8.84E+06 | 6.61E+05 | 7.212 |
| GF39_4_2 | 19.891 | Mt | 8.53E+06 | 5.98E+05 | 0.816 |
| GF39_8_1 | 18.426 | Mt | 7.14E+06 | 5.22E+05 | 13.514 |

Table A.7 continued

| Sample | Sr_ppm_m88_2SE | Y_ppm_m89_2SE | Zr_ppm_m90 | Zr_ppm_m90_2SE |
|---|---|---|---|---|
| IS8_1_1 | 0.028 | 0.119 | 0.355 | 0.112 |
| IS8_1_2 | 0.230 | 0.165 | -0.026 | 0.026 |
| IS8_3_1 | 0.020 | 0.036 | 0.331 | 0.029 |
| IS8_3_2 | 0.033 | 0.025 | -0.023 | 0.022 |
| IS8_5_1 | 0.044 | 0.086 | 0.185 | 0.022 |
| IS8_5_2 | 0.028 | 0.020 | -0.010 | 0.030 |
| IS8_5_3 | 0.275 | 0.042 | 0.041 | 0.040 |
| IS8_5_4 | 0.025 | 0.019 | 0.201 | 0.026 |
| IS8_7_1 | 0.218 | 0.103 | -0.013 | 0.027 |
| IS8_8_1 | 0.062 | 0.062 | 0.007 | 0.021 |
| IS8_8_2 | 0.037 | 0.049 | 0.146 | 0.050 |
| IS8_10_1 | 0.039 | 0.019 | 0.007 | 0.039 |
| IS8_11_1 | 0.023 | 0.019 | 0.025 | 0.030 |
| IS8_13_1 | 0.039 | 0.016 | 0.047 | 0.040 |
| IS8_13_2 | 0.107 | 0.273 | 0.016 | 0.044 |
| IS8_15_1 | 0.103 | 0.032 | 0.022 | 0.017 |
| IS8_15_2 | 0.029 | 0.021 | 0.136 | 0.023 |
| IS8_17_1 | 0.030 | 0.035 | 0.077 | 0.026 |
| IS8_17_2 | 0.027 | 0.088 | 0.258 | 0.040 |
| IS8_18_1 | 0.178 | 0.110 | 0.029 | 0.022 |
| IS8_18_2 | 0.026 | 0.021 | 0.132 | 0.034 |
| IS8_19_1 | 0.027 | 0.017 | -0.045 | 0.023 |
| IS8_19_2 | 0.045 | 0.045 | 0.004 | 0.027 |
| IS8_20_2 | 0.027 | 0.002 | 0.472 | 0.103 |
| | | | | |
| GF6_16_1 | 1.834 | 0.029 | -0.033 | 0.033 |
| GF6_16_2 | 9.813 | 1.015 | 0.909 | 0.207 |
| GF6_3_1 | 20.238 | 1.738 | 0.467 | 0.140 |
| GF6_3_2 | 6.088 | 0.492 | 0.385 | 0.058 |
| GF6_1_1 | 3.601 | 0.386 | 0.312 | 0.039 |
| GF6_2_1 | 11.895 | 1.863 | 0.178 | 0.083 |
| GF6_2_2 | 4.758 | 0.926 | 0.321 | 0.066 |
| GF6_5_1 | 3.295 | 0.322 | 0.131 | 0.043 |
| GF6_4_1 | 1.125 | 0.241 | 0.098 | 0.043 |
| GF6_6_1 | 11.830 | 1.300 | 0.243 | 0.086 |
| GF6_17_1 | 0.329 | 0.068 | -0.021 | 0.016 |
| GF6_11_1 | 0.678 | 0.122 | 0.175 | 0.039 |
| GF6_8_1 | 1.183 | 0.199 | 0.169 | 0.032 |
| GF6_7_1 | 1.799 | 0.149 | 0.140 | 0.029 |
| GF6_9_1 | 11.344 | 1.866 | 1.414 | 0.321 |

Table A.7 continued

| Sample | Sr_ppm_m88_2SE | Y_ppm_m89_2SE | Zr_ppm_m90 | Zr_ppm_m90_2SE |
|---|---|---|---|---|
| GF6_10_1 | 7.073 | 0.661 | 0.408 | 0.105 |
| GF6_18_1 | 2.531 | 0.407 | 0.809 | 0.200 |
| GF6_13_1 | 5.394 | 0.838 | 0.164 | 0.052 |
| GF6_12_1 | 2.863 | 0.637 | 1.928 | 0.774 |
| GF6_15_1 | 0.800 | 0.160 | 0.048 | 0.036 |
| GF6_19_1 | 0.794 | 0.430 | 0.076 | 0.032 |
| GF6_20_1 | 34.667 | 3.201 | 2.895 | 0.766 |
| | | | | |
| ZB117_1_a | 0.089 | 0.304 | 0.008 | 0.008 |
| ZB117_2_a | 0.066 | 0.387 | -0.014 | 0.021 |
| ZB117_4_a | 0.057 | 0.302 | -0.002 | 0.009 |
| ZB117_7_a | 0.099 | 0.340 | -0.015 | 0.019 |
| ZB117_14_a | 0.054 | 0.080 | 0.014 | 0.015 |
| | | | | |
| GF39_9_1 | 0.786 | 0.117 | -0.021 | 0.033 |
| GF39_6_1 | 0.124 | 0.182 | 0.016 | 0.041 |
| GF39_6_2 | 0.106 | 0.094 | 0.060 | 0.028 |
| GF39_7_1 | 0.101 | 1.427 | 0.054 | 0.022 |
| GF39_4_1 | 3.394 | 3.505 | 0.267 | 0.112 |
| GF39_4_2 | 0.115 | 0.183 | 0.170 | 0.035 |
| GF39_8_1 | 3.706 | 9.103 | 0.633 | 0.195 |

Table A.7 continued

| Sample | Ba_ppm_m137 | Ba_ppm_m137_2SE | La_ppm_m139 | La_ppm_m139_2SE |
|---|---|---|---|---|
| IS8_1_1 | 1.993 | 0.728 | 0.089 | 0.024 |
| IS8_1_2 | 1.125 | 0.410 | 0.222 | 0.086 |
| IS8_3_1 | 2.031 | 0.579 | 0.115 | 0.015 |
| IS8_3_2 | 0.221 | 0.097 | 0.004 | 0.006 |
| IS8_5_1 | 5.321 | 0.879 | 0.321 | 0.031 |
| IS8_5_2 | -0.002 | 0.000 | 0.000 | 0.000 |
| IS8_5_3 | 1.906 | 0.312 | 0.466 | 0.093 |
| IS8_5_4 | -0.002 | 0.000 | 0.008 | 0.007 |
| IS8_7_1 | 2.304 | 0.318 | 0.782 | 0.167 |
| IS8_8_1 | 0.799 | 0.212 | 0.058 | 0.011 |
| IS8_8_2 | 1.606 | 1.198 | 0.009 | 0.011 |
| IS8_10_1 | -0.002 | 0.000 | 0.000 | 0.000 |
| IS8_11_1 | 0.012 | 0.032 | 0.000 | 0.000 |
| IS8_13_1 | 0.111 | 0.084 | 0.000 | 0.000 |
| IS8_13_2 | 3.579 | 0.706 | 0.160 | 0.018 |
| IS8_15_1 | 0.487 | 0.150 | 0.012 | 0.009 |
| IS8_15_2 | 0.013 | 0.030 | 0.003 | 0.004 |
| IS8_17_1 | 0.242 | 0.157 | 0.000 | 0.000 |
| IS8_17_2 | 2.469 | 0.398 | 0.167 | 0.027 |
| IS8_18_1 | 6.011 | 0.937 | 0.278 | 0.043 |
| IS8_18_2 | -0.003 | 0.000 | 0.009 | 0.007 |
| IS8_19_1 | 0.182 | 0.104 | 0.014 | 0.011 |
| IS8_19_2 | 0.269 | 0.173 | 0.099 | 0.098 |
| IS8_20_2 | 0.143 | 0.116 | 0.025 | 0.011 |
| | | | | |
| GF6_16_1 | 1.704 | 0.220 | 0.016 | 0.010 |
| GF6_16_2 | 6.804 | 2.066 | 5.531 | 2.169 |
| GF6_3_1 | 11.701 | 3.613 | 2.278 | 0.430 |
| GF6_3_2 | 11.959 | 1.359 | 2.196 | 0.305 |
| GF6_1_1 | 4.576 | 1.016 | 2.400 | 0.301 |
| GF6_2_1 | 9.919 | 3.946 | 1.670 | 0.274 |
| GF6_2_2 | 10.975 | 1.564 | 3.311 | 0.615 |
| GF6_5_1 | 5.076 | 0.946 | 1.407 | 0.261 |
| GF6_4_1 | 3.939 | 0.588 | 0.931 | 0.085 |
| GF6_6_1 | 8.992 | 3.171 | 1.187 | 0.222 |
| GF6_17_1 | 1.395 | 0.319 | 0.095 | 0.035 |
| GF6_11_1 | 3.442 | 0.408 | 1.634 | 0.535 |
| GF6_8_1 | 4.721 | 0.675 | 1.643 | 0.324 |
| GF6_7_1 | 4.379 | 0.557 | 1.406 | 0.272 |
| GF6_9_1 | 8.006 | 3.131 | 2.165 | 0.253 |

Table A.7 continued

| Sample | Ba_ppm_m137 | Ba_ppm_m137_2SE | La_ppm_m139 | La_ppm_m139_2SE |
|---|---|---|---|---|
| GF6_10_1 | 6.079 | 1.108 | 1.351 | 0.205 |
| GF6_18_1 | 15.167 | 5.540 | 19.300 | 7.328 |
| GF6_13_1 | 5.687 | 0.628 | 1.891 | 0.782 |
| GF6_12_1 | 14.193 | 2.574 | 1.767 | 0.863 |
| GF6_15_1 | 3.566 | 0.683 | 0.648 | 0.109 |
| GF6_19_1 | 11.577 | 3.063 | 4.597 | 1.896 |
| GF6_20_1 | 22.220 | 8.638 | 1.515 | 0.302 |
| | | | | |
| ZB117_1_a | 3.306 | 0.247 | 1.744 | 0.146 |
| ZB117_2_a | 1.515 | 0.318 | 0.423 | 0.128 |
| ZB117_4_a | 2.474 | 0.224 | 1.176 | 0.081 |
| ZB117_7_a | 37.398 | 5.846 | 3.439 | 0.228 |
| ZB117_14_a | 1.056 | 0.411 | 0.134 | 0.052 |
| | | | | |
| GF39_9_1 | 12.918 | 3.452 | 0.318 | 0.042 |
| GF39_6_1 | 5.565 | 0.874 | 0.235 | 0.053 |
| GF39_6_2 | 3.429 | 0.597 | 0.163 | 0.046 |
| GF39_7_1 | 7.622 | 0.833 | 0.415 | 0.045 |
| GF39_4_1 | 24.290 | 11.625 | 0.235 | 0.094 |
| GF39_4_2 | 16.820 | 1.777 | 0.379 | 0.049 |
| GF39_8_1 | 45.850 | 9.470 | 0.267 | 0.051 |

Table A.7 continued

| Sample | Ce_ppm_m140 | Ce_ppm_m140_2SE | Pr_ppm_m141 | Pr_ppm_m141_2SE |
|---|---|---|---|---|
| IS8_1_1 | 0.139 | 0.035 | 0.008 | 0.005 |
| IS8_1_2 | 0.415 | 0.153 | 0.018 | 0.012 |
| IS8_3_1 | 0.201 | 0.033 | 0.013 | 0.005 |
| IS8_3_2 | 0.021 | 0.010 | 0.000 | 0.000 |
| IS8_5_1 | 0.498 | 0.041 | 0.052 | 0.015 |
| IS8_5_2 | 0.000 | 0.000 | 0.003 | 0.003 |
| IS8_5_3 | 0.659 | 0.118 | 0.047 | 0.009 |
| IS8_5_4 | 0.019 | 0.009 | 0.000 | 0.000 |
| IS8_7_1 | 1.032 | 0.254 | 0.085 | 0.017 |
| IS8_8_1 | 0.123 | 0.033 | 0.005 | 0.005 |
| IS8_8_2 | 0.039 | 0.020 | 0.000 | 0.000 |
| IS8_10_1 | 0.002 | 0.003 | 0.002 | 0.003 |
| IS8_11_1 | 0.004 | 0.005 | 0.000 | 0.000 |
| IS8_13_1 | -0.001 | 0.000 | 0.000 | 0.000 |
| IS8_13_2 | 0.172 | 0.061 | 0.027 | 0.023 |
| IS8_15_1 | 0.033 | 0.013 | 0.002 | 0.003 |
| IS8_15_2 | 0.012 | 0.008 | 0.000 | 0.000 |
| IS8_17_1 | 0.000 | 0.000 | 0.000 | 0.000 |
| IS8_17_2 | 0.220 | 0.040 | 0.031 | 0.008 |
| IS8_18_1 | 0.422 | 0.071 | 0.035 | 0.007 |
| IS8_18_2 | 0.050 | 0.012 | 0.000 | 0.000 |
| IS8_19_1 | 0.072 | 0.023 | 0.000 | 0.000 |
| IS8_19_2 | 0.159 | 0.148 | 0.017 | 0.013 |
| IS8_20_2 | 0.031 | 0.025 | 0.003 | 0.006 |
| | | | | |
| GF6_16_1 | 0.019 | 0.008 | 0.004 | 0.004 |
| GF6_16_2 | 15.946 | 6.522 | 1.634 | 0.581 |
| GF6_3_1 | 7.128 | 1.441 | 0.682 | 0.146 |
| GF6_3_2 | 6.248 | 0.622 | 0.777 | 0.094 |
| GF6_1_1 | 5.520 | 0.753 | 0.563 | 0.082 |
| GF6_2_1 | 4.792 | 0.691 | 0.532 | 0.110 |
| GF6_2_2 | 9.280 | 1.593 | 0.997 | 0.149 |
| GF6_5_1 | 3.580 | 0.623 | 0.387 | 0.087 |
| GF6_4_1 | 2.949 | 0.219 | 0.303 | 0.044 |
| GF6_6_1 | 3.454 | 0.837 | 0.400 | 0.097 |
| GF6_17_1 | 0.194 | 0.102 | 0.028 | 0.014 |
| GF6_11_1 | 4.245 | 1.449 | 0.423 | 0.097 |
| GF6_8_1 | 4.515 | 0.884 | 0.373 | 0.056 |
| GF6_7_1 | 3.764 | 0.597 | 0.347 | 0.042 |
| GF6_9_1 | 6.102 | 0.712 | 0.720 | 0.084 |

Table A.7 continued

| Sample | Ce_ppm_m140 | Ce_ppm_m140_2SE | Pr_ppm_m141 | Pr_ppm_m141_2SE |
|---|---|---|---|---|
| GF6_10_1 | 3.667 | 0.591 | 0.477 | 0.083 |
| GF6_18_1 | 52.199 | 19.820 | 4.724 | 1.734 |
| GF6_13_1 | 4.574 | 1.585 | 0.560 | 0.182 |
| GF6_12_1 | 4.555 | 2.179 | 0.581 | 0.260 |
| GF6_15_1 | 1.495 | 0.255 | 0.224 | 0.044 |
| GF6_19_1 | 13.389 | 6.695 | 1.678 | 0.911 |
| GF6_20_1 | 5.614 | 1.529 | 0.726 | 0.195 |
| | | | | |
| ZB117_1_a | 0.688 | 0.078 | 0.433 | 0.032 |
| ZB117_2_a | 0.081 | 0.025 | 0.105 | 0.037 |
| ZB117_4_a | 0.414 | 0.036 | 0.289 | 0.026 |
| ZB117_7_a | 4.482 | 0.706 | 0.761 | 0.064 |
| ZB117_14_a | 0.064 | 0.016 | 0.034 | 0.010 |
| | | | | |
| GF39_9_1 | 0.422 | 0.064 | 0.050 | 0.014 |
| GF39_6_1 | 0.358 | 0.050 | 0.040 | 0.014 |
| GF39_6_2 | 0.276 | 0.047 | 0.048 | 0.015 |
| GF39_7_1 | 0.811 | 0.112 | 0.161 | 0.024 |
| GF39_4_1 | 0.638 | 0.295 | 0.128 | 0.065 |
| GF39_4_2 | 0.733 | 0.109 | 0.103 | 0.015 |
| GF39_8_1 | 0.579 | 0.095 | 0.092 | 0.017 |

Table A.7 continued

| Sample | Nd_ppm_m146 | Nd_ppm_m146_2SE | Sm_ppm_m147 | Sm_ppm_m147_2SE |
|---|---|---|---|---|
| IS8_1_1 | 0.067 | 0.024 | -0.001 | 0.000 |
| IS8_1_2 | 0.083 | 0.043 | 0.044 | 0.030 |
| IS8_3_1 | 0.058 | 0.019 | 0.011 | 0.014 |
| IS8_3_2 | -0.002 | 0.000 | -0.001 | 0.000 |
| IS8_5_1 | 0.245 | 0.071 | 0.033 | 0.020 |
| IS8_5_2 | -0.002 | 0.000 | -0.001 | 0.000 |
| IS8_5_3 | 0.216 | 0.067 | 0.010 | 0.012 |
| IS8_5_4 | 0.001 | 0.005 | -0.001 | 0.000 |
| IS8_7_1 | 0.428 | 0.101 | 0.048 | 0.025 |
| IS8_8_1 | 0.048 | 0.026 | -0.001 | 0.000 |
| IS8_8_2 | 0.036 | 0.021 | -0.001 | 0.000 |
| IS8_10_1 | 0.002 | 0.007 | -0.001 | 0.000 |
| IS8_11_1 | -0.001 | 0.000 | -0.002 | 0.000 |
| IS8_13_1 | -0.001 | 0.000 | -0.002 | 0.000 |
| IS8_13_2 | 0.251 | 0.104 | 0.045 | 0.064 |
| IS8_15_1 | 0.029 | 0.020 | 0.008 | 0.013 |
| IS8_15_2 | -0.002 | 0.000 | -0.001 | 0.000 |
| IS8_17_1 | -0.002 | 0.000 | -0.001 | 0.000 |
| IS8_17_2 | 0.181 | 0.061 | 0.028 | 0.022 |
| IS8_18_1 | 0.177 | 0.042 | 0.066 | 0.022 |
| IS8_18_2 | 0.005 | 0.009 | -0.001 | 0.000 |
| IS8_19_1 | 0.005 | 0.014 | -0.001 | 0.000 |
| IS8_19_2 | 0.087 | 0.062 | -0.001 | 0.000 |
| IS8_20_2 | 0.050 | 0.047 | -0.001 | 0.000 |
| | | | | |
| GF6_16_1 | 0.032 | 0.020 | -0.001 | 0.000 |
| GF6_16_2 | 6.811 | 2.592 | 1.276 | 0.339 |
| GF6_3_1 | 3.473 | 0.840 | 0.579 | 0.115 |
| GF6_3_2 | 3.604 | 0.395 | 0.767 | 0.131 |
| GF6_1_1 | 2.315 | 0.380 | 0.406 | 0.083 |
| GF6_2_1 | 2.438 | 0.467 | 0.551 | 0.180 |
| GF6_2_2 | 3.931 | 0.488 | 0.667 | 0.092 |
| GF6_5_1 | 1.468 | 0.249 | 0.236 | 0.044 |
| GF6_4_1 | 1.361 | 0.184 | 0.189 | 0.066 |
| GF6_6_1 | 2.324 | 0.546 | 0.449 | 0.175 |
| GF6_17_1 | 0.092 | 0.054 | -0.002 | 0.000 |
| GF6_11_1 | 1.488 | 0.419 | 0.220 | 0.090 |
| GF6_8_1 | 1.629 | 0.180 | 0.299 | 0.054 |
| GF6_7_1 | 1.317 | 0.229 | 0.270 | 0.083 |
| GF6_9_1 | 3.253 | 0.366 | 0.677 | 0.163 |

Table A.7 continued

| Sample | Nd_ppm_m146 | Nd_ppm_m146_2SE | Sm_ppm_m147 | Sm_ppm_m147_2SE |
|---|---|---|---|---|
| GF6_10_1 | 2.137 | 0.441 | 0.546 | 0.092 |
| GF6_18_1 | 16.023 | 6.018 | 1.627 | 0.594 |
| GF6_13_1 | 2.478 | 0.817 | 0.598 | 0.150 |
| GF6_12_1 | 2.480 | 0.974 | 0.530 | 0.200 |
| GF6_15_1 | 0.828 | 0.168 | 0.140 | 0.058 |
| GF6_19_1 | 5.639 | 3.041 | 0.657 | 0.361 |
| GF6_20_1 | 4.290 | 1.403 | 1.035 | 0.357 |
| | | | | |
| ZB117_1_a | 1.741 | 0.094 | 0.465 | 0.035 |
| ZB117_2_a | 0.479 | 0.157 | 0.139 | 0.048 |
| ZB117_4_a | 1.225 | 0.090 | 0.307 | 0.036 |
| ZB117_7_a | 3.122 | 0.196 | 0.729 | 0.067 |
| ZB117_14_a | 0.131 | 0.041 | 0.032 | 0.021 |
| | | | | |
| GF39_9_1 | 0.272 | 0.074 | 0.045 | 0.031 |
| GF39_6_1 | 0.427 | 0.084 | 0.129 | 0.044 |
| GF39_6_2 | 0.263 | 0.058 | -0.002 | 0.000 |
| GF39_7_1 | 1.008 | 0.145 | 0.497 | 0.055 |
| GF39_4_1 | 0.695 | 0.349 | 0.305 | 0.150 |
| GF39_4_2 | 0.406 | 0.079 | 0.102 | 0.046 |
| GF39_8_1 | 0.866 | 0.194 | 0.353 | 0.102 |

Table A.7 continued

| Sample | Eu_ppm_m153 | Eu_ppm_m153_2SE | Gd_ppm_m157 | Gd_ppm_m157_2SE |
|---|---|---|---|---|
| IS8_1_1 | 0.004 | 0.006 | 0.040 | 0.026 |
| IS8_1_2 | 0.015 | 0.011 | 0.036 | 0.026 |
| IS8_3_1 | 0.000 | 0.000 | 0.019 | 0.018 |
| IS8_3_2 | -0.001 | 0.000 | -0.001 | 0.000 |
| IS8_5_1 | 0.021 | 0.010 | 0.070 | 0.027 |
| IS8_5_2 | -0.001 | 0.000 | -0.001 | 0.000 |
| IS8_5_3 | 0.003 | 0.004 | 0.067 | 0.030 |
| IS8_5_4 | -0.001 | 0.000 | 0.006 | 0.010 |
| IS8_7_1 | 0.024 | 0.011 | 0.044 | 0.027 |
| IS8_8_1 | 0.001 | 0.004 | 0.004 | 0.008 |
| IS8_8_2 | 0.000 | 0.000 | -0.001 | 0.000 |
| IS8_10_1 | -0.001 | 0.000 | -0.001 | 0.000 |
| IS8_11_1 | 0.000 | 0.000 | -0.004 | 0.000 |
| IS8_13_1 | 0.000 | 0.000 | 0.008 | 0.016 |
| IS8_13_2 | 0.020 | 0.027 | -0.006 | 0.000 |
| IS8_15_1 | -0.001 | 0.000 | -0.001 | 0.000 |
| IS8_15_2 | 0.000 | 0.000 | -0.001 | 0.000 |
| IS8_17_1 | 0.000 | 0.000 | -0.001 | 0.000 |
| IS8_17_2 | 0.024 | 0.010 | 0.006 | 0.013 |
| IS8_18_1 | 0.012 | 0.009 | 0.085 | 0.028 |
| IS8_18_2 | 0.000 | 0.000 | 0.020 | 0.019 |
| IS8_19_1 | 0.000 | 0.000 | -0.001 | 0.000 |
| IS8_19_2 | 0.000 | 0.000 | -0.001 | 0.000 |
| IS8_20_2 | 0.009 | 0.012 | -0.001 | 0.000 |
| | | | | |
| GF6_16_1 | 0.000 | 0.000 | 0.000 | 0.000 |
| GF6_16_2 | 0.239 | 0.059 | 1.263 | 0.279 |
| GF6_3_1 | 0.297 | 0.108 | 0.866 | 0.274 |
| GF6_3_2 | 0.255 | 0.032 | 1.028 | 0.201 |
| GF6_1_1 | 0.137 | 0.037 | 0.344 | 0.087 |
| GF6_2_1 | 0.144 | 0.055 | 0.708 | 0.260 |
| GF6_2_2 | 0.170 | 0.036 | 0.805 | 0.122 |
| GF6_5_1 | 0.056 | 0.026 | 0.181 | 0.066 |
| GF6_4_1 | 0.035 | 0.021 | 0.182 | 0.052 |
| GF6_6_1 | 0.188 | 0.076 | 0.623 | 0.193 |
| GF6_17_1 | 0.021 | 0.017 | 0.080 | 0.045 |
| GF6_11_1 | 0.040 | 0.018 | 0.139 | 0.055 |
| GF6_8_1 | 0.079 | 0.019 | 0.158 | 0.038 |
| GF6_7_1 | 0.090 | 0.021 | 0.260 | 0.042 |
| GF6_9_1 | 0.186 | 0.058 | 0.749 | 0.227 |

Table A.7 continued

| Sample | Eu_ppm_m153 | Eu_ppm_m153_2SE | Gd_ppm_m157 | Gd_ppm_m157_2SE |
|---|---|---|---|---|
| GF6_10_1 | 0.122 | 0.028 | 0.571 | 0.137 |
| GF6_18_1 | 0.237 | 0.095 | 0.716 | 0.323 |
| GF6_13_1 | 0.166 | 0.050 | 0.460 | 0.112 |
| GF6_12_1 | 0.154 | 0.053 | 0.678 | 0.197 |
| GF6_15_1 | 0.065 | 0.020 | 0.160 | 0.061 |
| GF6_19_1 | 0.159 | 0.111 | 0.524 | 0.228 |
| GF6_20_1 | 0.417 | 0.198 | 1.299 | 0.483 |
| | | | | |
| ZB117_1_a | 0.241 | 0.023 | 0.639 | 0.070 |
| ZB117_2_a | 0.048 | 0.013 | 0.101 | 0.048 |
| ZB117_4_a | 0.151 | 0.017 | 0.508 | 0.063 |
| ZB117_7_a | 0.372 | 0.039 | 0.808 | 0.106 |
| ZB117_14_a | 0.024 | 0.013 | 0.030 | 0.022 |
| | | | | |
| GF39_9_1 | 0.004 | 0.006 | 0.104 | 0.050 |
| GF39_6_1 | 0.037 | 0.016 | 0.233 | 0.066 |
| GF39_6_2 | 0.006 | 0.007 | 0.128 | 0.058 |
| GF39_7_1 | 0.229 | 0.048 | 1.347 | 0.147 |
| GF39_4_1 | 0.064 | 0.029 | 0.510 | 0.231 |
| GF39_4_2 | 0.025 | 0.015 | 0.127 | 0.053 |
| GF39_8_1 | 0.345 | 0.101 | 0.939 | 0.153 |

Table A.7 continued

| Sample | Tb_ppm_m159 | Tb_ppm_m159_2SE | Dy_ppm_m163 | Dy_ppm_m163_2SE |
|---|---|---|---|---|
| IS8_1_1 | 0.000 | 0.000 | -0.001 | 0.000 |
| IS8_1_2 | 0.000 | 0.000 | 0.013 | 0.015 |
| IS8_3_1 | 0.000 | 0.000 | 0.053 | 0.016 |
| IS8_3_2 | 0.000 | 0.000 | -0.002 | 0.000 |
| IS8_5_1 | 0.026 | 0.011 | 0.090 | 0.014 |
| IS8_5_2 | 0.000 | 0.000 | -0.001 | 0.000 |
| IS8_5_3 | 0.001 | 0.002 | 0.028 | 0.017 |
| IS8_5_4 | 0.000 | 0.000 | -0.001 | 0.000 |
| IS8_7_1 | 0.011 | 0.006 | 0.033 | 0.018 |
| IS8_8_1 | 0.002 | 0.003 | -0.001 | 0.000 |
| IS8_8_2 | 0.000 | 0.000 | 0.006 | 0.010 |
| IS8_10_1 | 0.000 | 0.000 | 0.023 | 0.024 |
| IS8_11_1 | 0.000 | 0.000 | -0.001 | 0.000 |
| IS8_13_1 | 0.000 | 0.000 | -0.001 | 0.000 |
| IS8_13_2 | 0.000 | 0.000 | 0.104 | 0.048 |
| IS8_15_1 | 0.000 | 0.000 | -0.001 | 0.000 |
| IS8_15_2 | 0.000 | 0.000 | -0.001 | 0.000 |
| IS8_17_1 | 0.000 | 0.000 | -0.001 | 0.000 |
| IS8_17_2 | 0.011 | 0.007 | 0.052 | 0.029 |
| IS8_18_1 | 0.006 | 0.005 | 0.045 | 0.028 |
| IS8_18_2 | 0.000 | 0.000 | -0.001 | 0.000 |
| IS8_19_1 | 0.000 | 0.000 | -0.001 | 0.000 |
| IS8_19_2 | 0.000 | 0.000 | -0.001 | 0.000 |
| IS8_20_2 | 0.000 | 0.000 | -0.001 | 0.000 |
| | | | | |
| GF6_16_1 | 0.000 | 0.000 | -0.001 | 0.000 |
| GF6_16_2 | 0.125 | 0.028 | 0.744 | 0.154 |
| GF6_3_1 | 0.136 | 0.060 | 0.906 | 0.403 |
| GF6_3_2 | 0.138 | 0.026 | 0.926 | 0.125 |
| GF6_1_1 | 0.067 | 0.019 | 0.329 | 0.083 |
| GF6_2_1 | 0.089 | 0.044 | 0.633 | 0.289 |
| GF6_2_2 | 0.128 | 0.034 | 0.934 | 0.144 |
| GF6_5_1 | 0.019 | 0.013 | 0.159 | 0.035 |
| GF6_4_1 | 0.012 | 0.007 | 0.245 | 0.047 |
| GF6_6_1 | 0.103 | 0.042 | 0.515 | 0.201 |
| GF6_17_1 | 0.000 | 0.000 | 0.031 | 0.026 |
| GF6_11_1 | 0.013 | 0.009 | 0.126 | 0.039 |
| GF6_8_1 | 0.026 | 0.014 | 0.133 | 0.048 |
| GF6_7_1 | 0.027 | 0.014 | 0.247 | 0.055 |
| GF6_9_1 | 0.108 | 0.038 | 0.696 | 0.292 |

Table A.7 continued

| Sample | Tb_ppm_m159 | Tb_ppm_m159_2SE | Dy_ppm_m163 | Dy_ppm_m163_2SE |
|---|---|---|---|---|
| GF6_10_1 | 0.058 | 0.017 | 0.533 | 0.151 |
| GF6_18_1 | 0.073 | 0.029 | 0.219 | 0.080 |
| GF6_13_1 | 0.081 | 0.028 | 0.460 | 0.141 |
| GF6_12_1 | 0.068 | 0.018 | 0.430 | 0.135 |
| GF6_15_1 | 0.018 | 0.007 | 0.169 | 0.035 |
| GF6_19_1 | 0.052 | 0.037 | 0.225 | 0.111 |
| GF6_20_1 | 0.200 | 0.087 | 1.282 | 0.491 |
| | | | | |
| ZB117_1_a | 0.133 | 0.017 | 0.960 | 0.089 |
| ZB117_2_a | 0.012 | 0.005 | 0.179 | 0.079 |
| ZB117_4_a | 0.077 | 0.010 | 0.612 | 0.052 |
| ZB117_7_a | 0.141 | 0.019 | 0.808 | 0.066 |
| ZB117_14_a | 0.003 | 0.004 | 0.051 | 0.018 |
| | | | | |
| GF39_9_1 | 0.017 | 0.010 | 0.129 | 0.037 |
| GF39_6_1 | 0.030 | 0.014 | 0.271 | 0.056 |
| GF39_6_2 | 0.024 | 0.010 | 0.160 | 0.062 |
| GF39_7_1 | 0.295 | 0.053 | 2.389 | 0.276 |
| GF39_4_1 | 0.112 | 0.056 | 1.189 | 0.564 |
| GF39_4_2 | 0.026 | 0.012 | 0.262 | 0.050 |
| GF39_8_1 | 0.261 | 0.076 | 3.383 | 0.840 |

Table A.7 continued

| Sample | Ho_ppm_m165 | Ho_ppm_m165_2SE | Er_ppm_m166 | Er_ppm_m166_2SE |
|---|---|---|---|---|
| IS8_1_1 | 0.005 | 0.003 | 0.032 | 0.014 |
| IS8_1_2 | 0.003 | 0.004 | 0.021 | 0.014 |
| IS8_3_1 | 0.001 | 0.001 | 0.011 | 0.008 |
| IS8_3_2 | 0.006 | 0.004 | 0.000 | 0.000 |
| IS8_5_1 | 0.032 | 0.007 | 0.093 | 0.014 |
| IS8_5_2 | 0.000 | 0.000 | 0.000 | 0.000 |
| IS8_5_3 | 0.010 | 0.005 | 0.047 | 0.017 |
| IS8_5_4 | 0.000 | 0.000 | 0.009 | 0.007 |
| IS8_7_1 | 0.010 | 0.004 | 0.050 | 0.012 |
| IS8_8_1 | 0.000 | 0.000 | 0.021 | 0.014 |
| IS8_8_2 | 0.002 | 0.002 | 0.003 | 0.006 |
| IS8_10_1 | 0.000 | 0.000 | 0.002 | 0.005 |
| IS8_11_1 | 0.000 | 0.000 | -0.001 | 0.000 |
| IS8_13_1 | 0.000 | 0.000 | 0.015 | 0.011 |
| IS8_13_2 | 0.000 | 0.000 | -0.001 | 0.000 |
| IS8_15_1 | 0.000 | 0.000 | 0.010 | 0.009 |
| IS8_15_2 | 0.000 | 0.000 | 0.010 | 0.008 |
| IS8_17_1 | 0.000 | 0.000 | 0.038 | 0.025 |
| IS8_17_2 | 0.020 | 0.002 | 0.078 | 0.024 |
| IS8_18_1 | 0.006 | 0.005 | 0.041 | 0.019 |
| IS8_18_2 | 0.000 | 0.000 | 0.004 | 0.005 |
| IS8_19_1 | 0.000 | 0.000 | 0.000 | 0.000 |
| IS8_19_2 | 0.000 | 0.000 | 0.000 | 0.000 |
| IS8_20_2 | 0.000 | 0.000 | 0.000 | 0.000 |
| | | | | |
| GF6_16_1 | 0.000 | 0.000 | 0.000 | 0.000 |
| GF6_16_2 | 0.153 | 0.027 | 0.439 | 0.076 |
| GF6_3_1 | 0.240 | 0.085 | 0.542 | 0.181 |
| GF6_3_2 | 0.200 | 0.033 | 0.446 | 0.066 |
| GF6_1_1 | 0.097 | 0.026 | 0.287 | 0.054 |
| GF6_2_1 | 0.142 | 0.078 | 0.377 | 0.192 |
| GF6_2_2 | 0.205 | 0.044 | 0.631 | 0.094 |
| GF6_5_1 | 0.030 | 0.009 | 0.140 | 0.049 |
| GF6_4_1 | 0.063 | 0.014 | 0.198 | 0.037 |
| GF6_6_1 | 0.151 | 0.045 | 0.424 | 0.148 |
| GF6_17_1 | 0.006 | 0.007 | 0.050 | 0.025 |
| GF6_11_1 | 0.028 | 0.007 | 0.136 | 0.034 |
| GF6_8_1 | 0.032 | 0.013 | 0.134 | 0.032 |
| GF6_7_1 | 0.044 | 0.008 | 0.171 | 0.042 |
| GF6_9_1 | 0.170 | 0.070 | 0.549 | 0.228 |

Table A.7 continued

| Sample | Ho_ppm_m165 | Ho_ppm_m165_2SE | Er_ppm_m166 | Er_ppm_m166_2SE |
|---|---|---|---|---|
| GF6_10_1 | 0.107 | 0.015 | 0.308 | 0.058 |
| GF6_18_1 | 0.058 | 0.018 | 0.143 | 0.035 |
| GF6_13_1 | 0.110 | 0.046 | 0.357 | 0.090 |
| GF6_12_1 | 0.084 | 0.020 | 0.386 | 0.108 |
| GF6_15_1 | 0.032 | 0.007 | 0.121 | 0.040 |
| GF6_19_1 | 0.041 | 0.025 | 0.170 | 0.078 |
| GF6_20_1 | 0.302 | 0.116 | 1.046 | 0.436 |
| | | | | |
| ZB117_1_a | 0.212 | 0.019 | 0.783 | 0.084 |
| ZB117_2_a | 0.041 | 0.016 | 0.110 | 0.041 |
| ZB117_4_a | 0.153 | 0.015 | 0.510 | 0.042 |
| ZB117_7_a | 0.212 | 0.016 | 0.670 | 0.047 |
| ZB117_14_a | 0.006 | 0.004 | 0.024 | 0.012 |
| | | | | |
| GF39_9_1 | 0.022 | 0.009 | 0.064 | 0.023 |
| GF39_6_1 | 0.077 | 0.021 | 0.212 | 0.042 |
| GF39_6_2 | 0.036 | 0.011 | 0.123 | 0.031 |
| GF39_7_1 | 0.487 | 0.052 | 1.281 | 0.173 |
| GF39_4_1 | 0.283 | 0.117 | 0.887 | 0.379 |
| GF39_4_2 | 0.053 | 0.008 | 0.247 | 0.038 |
| GF39_8_1 | 1.256 | 0.329 | 5.619 | 1.392 |

Table A.7 continued

| Sample | Tm_ppm_m169 | Tm_ppm_m169_2SE | Yb_ppm_m172 | Yb_ppm_m172_2SE |
|---|---|---|---|---|
| IS8_1_1 | 0.004 | 0.003 | 0.076 | 0.024 |
| IS8_1_2 | 0.000 | 0.000 | 0.058 | 0.032 |
| IS8_3_1 | 0.002 | 0.002 | 0.017 | 0.014 |
| IS8_3_2 | 0.000 | 0.000 | 0.000 | 0.000 |
| IS8_5_1 | 0.018 | 0.005 | 0.238 | 0.051 |
| IS8_5_2 | 0.000 | 0.000 | 0.000 | 0.000 |
| IS8_5_3 | 0.004 | 0.003 | 0.102 | 0.034 |
| IS8_5_4 | 0.000 | 0.000 | 0.013 | 0.012 |
| IS8_7_1 | 0.003 | 0.003 | 0.076 | 0.019 |
| IS8_8_1 | 0.004 | 0.003 | 0.026 | 0.017 |
| IS8_8_2 | 0.000 | 0.000 | 0.021 | 0.016 |
| IS8_10_1 | 0.000 | 0.000 | 0.000 | 0.000 |
| IS8_11_1 | 0.000 | 0.001 | -0.001 | 0.000 |
| IS8_13_1 | 0.000 | 0.000 | -0.001 | 0.000 |
| IS8_13_2 | 0.000 | 0.000 | -0.001 | 0.000 |
| IS8_15_1 | 0.000 | 0.000 | 0.013 | 0.013 |
| IS8_15_2 | 0.000 | 0.000 | 0.003 | 0.006 |
| IS8_17_1 | 0.000 | 0.000 | 0.000 | 0.000 |
| IS8_17_2 | 0.014 | 0.007 | 0.132 | 0.048 |
| IS8_18_1 | 0.005 | 0.003 | 0.074 | 0.019 |
| IS8_18_2 | 0.000 | 0.000 | -0.001 | 0.000 |
| IS8_19_1 | 0.000 | 0.000 | 0.000 | 0.000 |
| IS8_19_2 | 0.000 | 0.000 | 0.000 | 0.000 |
| IS8_20_2 | 0.000 | 0.000 | 0.000 | 0.000 |
| | | | | |
| GF6_16_1 | 0.000 | 0.000 | 0.003 | 0.008 |
| GF6_16_2 | 0.070 | 0.016 | 0.467 | 0.126 |
| GF6_3_1 | 0.090 | 0.035 | 0.764 | 0.247 |
| GF6_3_2 | 0.082 | 0.015 | 0.538 | 0.094 |
| GF6_1_1 | 0.030 | 0.011 | 0.412 | 0.088 |
| GF6_2_1 | 0.069 | 0.034 | 0.340 | 0.150 |
| GF6_2_2 | 0.082 | 0.021 | 0.482 | 0.092 |
| GF6_5_1 | 0.020 | 0.009 | 0.083 | 0.026 |
| GF6_4_1 | 0.031 | 0.011 | 0.279 | 0.036 |
| GF6_6_1 | 0.056 | 0.020 | 0.344 | 0.096 |
| GF6_17_1 | 0.000 | 0.000 | -0.001 | 0.000 |
| GF6_11_1 | 0.015 | 0.005 | 0.056 | 0.027 |
| GF6_8_1 | 0.019 | 0.007 | 0.176 | 0.070 |
| GF6_7_1 | 0.019 | 0.008 | 0.109 | 0.039 |
| GF6_9_1 | 0.054 | 0.024 | 0.444 | 0.203 |

Table A.7 continued

| Sample | Tm_ppm_m169 | Tm_ppm_m169_2SE | Yb_ppm_m172 | Yb_ppm_m172_2SE |
|---|---|---|---|---|
| GF6_10_1 | 0.039 | 0.014 | 0.207 | 0.044 |
| GF6_18_1 | 0.017 | 0.008 | 0.115 | 0.054 |
| GF6_13_1 | 0.042 | 0.014 | 0.222 | 0.101 |
| GF6_12_1 | 0.044 | 0.012 | 0.278 | 0.111 |
| GF6_15_1 | 0.018 | 0.004 | 0.117 | 0.039 |
| GF6_19_1 | 0.018 | 0.012 | 0.166 | 0.083 |
| GF6_20_1 | 0.112 | 0.043 | 0.661 | 0.272 |
| | | | | |
| ZB117_1_a | 0.102 | 0.013 | 0.671 | 0.066 |
| ZB117_2_a | 0.014 | 0.006 | 0.107 | 0.037 |
| ZB117_4_a | 0.049 | 0.007 | 0.458 | 0.052 |
| ZB117_7_a | 0.087 | 0.010 | 0.612 | 0.070 |
| ZB117_14_a | 0.003 | 0.003 | 0.030 | 0.024 |
| | | | | |
| GF39_9_1 | 0.010 | 0.006 | 0.041 | 0.022 |
| GF39_6_1 | 0.032 | 0.009 | 0.197 | 0.049 |
| GF39_6_2 | 0.016 | 0.007 | 0.116 | 0.039 |
| GF39_7_1 | 0.103 | 0.019 | 0.324 | 0.076 |
| GF39_4_1 | 0.090 | 0.044 | 0.402 | 0.200 |
| GF39_4_2 | 0.029 | 0.007 | 0.064 | 0.030 |
| GF39_8_1 | 0.905 | 0.258 | 4.246 | 1.139 |

Table A.7 continued

| Sample | Lu_ppm_m175 | Lu_ppm_m175_2SE | Hf_ppm_m178 | Hf_ppm_m178_2SE |
|---|---|---|---|---|
| IS8_1_1 | 0.011 | 0.005 | 0.055 | 0.033 |
| IS8_1_2 | 0.002 | 0.004 | 0.000 | 0.000 |
| IS8_3_1 | 0.000 | 0.000 | 0.059 | 0.028 |
| IS8_3_2 | 0.000 | 0.000 | 0.000 | 0.000 |
| IS8_5_1 | 0.054 | 0.008 | 0.000 | 0.000 |
| IS8_5_2 | 0.000 | 0.000 | 0.000 | 0.000 |
| IS8_5_3 | 0.023 | 0.008 | 0.000 | 0.000 |
| IS8_5_4 | 0.000 | 0.000 | 0.009 | 0.012 |
| IS8_7_1 | 0.012 | 0.005 | 0.000 | 0.000 |
| IS8_8_1 | 0.008 | 0.004 | 0.000 | 0.000 |
| IS8_8_2 | 0.006 | 0.004 | 0.000 | 0.000 |
| IS8_10_1 | 0.000 | 0.000 | 0.000 | 0.000 |
| IS8_11_1 | 0.000 | 0.000 | 0.000 | 0.000 |
| IS8_13_1 | 0.003 | 0.004 | 0.000 | 0.000 |
| IS8_13_2 | 0.008 | 0.010 | 0.000 | 0.000 |
| IS8_15_1 | 0.006 | 0.004 | 0.000 | 0.000 |
| IS8_15_2 | 0.001 | 0.002 | 0.000 | 0.000 |
| IS8_17_1 | 0.000 | 0.000 | 0.000 | 0.000 |
| IS8_17_2 | 0.036 | 0.009 | 0.023 | 0.024 |
| IS8_18_1 | 0.006 | 0.005 | 0.000 | 0.000 |
| IS8_18_2 | 0.000 | 0.000 | 0.000 | 0.000 |
| IS8_19_1 | 0.000 | 0.000 | 0.000 | 0.000 |
| IS8_19_2 | 0.000 | 0.000 | 0.000 | 0.000 |
| IS8_20_2 | 0.000 | 0.000 | 0.098 | 0.074 |
| | | | | |
| GF6_16_1 | 0.000 | 0.000 | 0.000 | 0.000 |
| GF6_16_2 | 0.077 | 0.021 | 0.241 | 0.125 |
| GF6_3_1 | 0.084 | 0.027 | 0.078 | 0.041 |
| GF6_3_2 | 0.072 | 0.011 | 0.000 | 0.000 |
| GF6_1_1 | 0.057 | 0.015 | 0.000 | 0.000 |
| GF6_2_1 | 0.046 | 0.016 | 0.020 | 0.022 |
| GF6_2_2 | 0.087 | 0.018 | 0.111 | 0.061 |
| GF6_5_1 | 0.016 | 0.008 | 0.000 | 0.000 |
| GF6_4_1 | 0.031 | 0.011 | 0.000 | 0.000 |
| GF6_6_1 | 0.061 | 0.016 | 0.000 | 0.000 |
| GF6_17_1 | 0.009 | 0.007 | 0.000 | 0.000 |
| GF6_11_1 | 0.015 | 0.007 | 0.000 | 0.000 |
| GF6_8_1 | 0.012 | 0.007 | 0.000 | 0.000 |
| GF6_7_1 | 0.017 | 0.007 | 0.023 | 0.021 |
| GF6_9_1 | 0.054 | 0.021 | 0.274 | 0.077 |

Table A.7 continued

| Sample | Lu_ppm_m175 | Lu_ppm_m175_2SE | Hf_ppm_m178 | Hf_ppm_m178_2SE |
|---|---|---|---|---|
| GF6_10_1 | 0.043 | 0.009 | 0.026 | 0.030 |
| GF6_18_1 | 0.022 | 0.007 | 0.007 | 0.014 |
| GF6_13_1 | 0.039 | 0.018 | 0.000 | 0.000 |
| GF6_12_1 | 0.049 | 0.017 | 0.230 | 0.152 |
| GF6_15_1 | 0.015 | 0.005 | 0.000 | 0.000 |
| GF6_19_1 | 0.017 | 0.008 | 0.000 | 0.000 |
| GF6_20_1 | 0.105 | 0.040 | 0.121 | 0.079 |
| | | | | |
| ZB117_1_a | 0.105 | 0.009 | 0.000 | 0.000 |
| ZB117_2_a | 0.021 | 0.008 | 0.000 | 0.000 |
| ZB117_4_a | 0.082 | 0.013 | 0.000 | 0.000 |
| ZB117_7_a | 0.084 | 0.012 | 0.000 | 0.000 |
| ZB117_14_a | 0.000 | 0.000 | 0.000 | 0.000 |
| | | | | |
| GF39_9_1 | 0.000 | 0.000 | -0.001 | 0.000 |
| GF39_6_1 | 0.041 | 0.016 | -0.001 | 0.000 |
| GF39_6_2 | 0.013 | 0.008 | -0.001 | 0.000 |
| GF39_7_1 | 0.024 | 0.009 | -0.001 | 0.000 |
| GF39_4_1 | 0.024 | 0.013 | 0.051 | 0.042 |
| GF39_4_2 | 0.011 | 0.006 | -0.001 | 0.000 |
| GF39_8_1 | 0.534 | 0.136 | -0.001 | 0.000 |

Table A.7 continued

| Sample | Pb_ppm_m208 | Pb_ppm_m208_2SE | Th_ppm_m232 | Th_ppm_m232_2SE |
|---|---|---|---|---|
| IS8_1_1 | 0.447 | 0.085 | 0.000 | 0.000 |
| IS8_1_2 | 1.739 | 0.382 | 0.000 | 1.000 |
| IS8_3_1 | 1.300 | 0.188 | 0.000 | 0.000 |
| IS8_3_2 | 0.497 | 0.107 | 0.000 | 0.000 |
| IS8_5_1 | 0.634 | 0.107 | 0.008 | 0.008 |
| IS8_5_2 | 0.078 | 0.032 | 0.000 | 0.000 |
| IS8_5_3 | 1.058 | 0.269 | 0.016 | 0.014 |
| IS8_5_4 | 0.082 | 0.037 | 0.000 | 0.000 |
| IS8_7_1 | 2.172 | 0.189 | 0.024 | 0.011 |
| IS8_8_1 | 1.478 | 0.195 | 0.000 | 0.000 |
| IS8_8_2 | 0.126 | 0.077 | 0.000 | 0.000 |
| IS8_10_1 | 0.105 | 0.055 | 0.000 | 0.000 |
| IS8_11_1 | 0.330 | 0.069 | 0.000 | 1.000 |
| IS8_13_1 | 0.110 | 0.024 | 0.000 | 1.000 |
| IS8_13_2 | 4.604 | 0.718 | 0.000 | 1.000 |
| IS8_15_1 | 0.582 | 0.112 | 0.000 | 0.000 |
| IS8_15_2 | 0.088 | 0.043 | 0.000 | 0.000 |
| IS8_17_1 | 0.381 | 0.087 | 0.000 | 0.000 |
| IS8_17_2 | 0.599 | 0.082 | 0.000 | 0.000 |
| IS8_18_1 | 3.575 | 0.377 | 0.000 | 0.000 |
| IS8_18_2 | 0.226 | 0.065 | 0.000 | 1.000 |
| IS8_19_1 | 0.526 | 0.085 | 0.000 | 0.000 |
| IS8_19_2 | 0.101 | 0.066 | 0.000 | 0.000 |
| IS8_20_2 | 0.136 | 0.035 | 0.000 | 0.000 |
| | | | | |
| GF6_16_1 | 0.510 | 0.132 | 0.010 | 0.009 |
| GF6_16_2 | 1.092 | 0.229 | 0.785 | 0.277 |
| GF6_3_1 | 2.080 | 0.241 | 0.248 | 0.061 |
| GF6_3_2 | 1.927 | 0.155 | 0.165 | 0.032 |
| GF6_1_1 | 1.344 | 0.097 | 0.175 | 0.038 |
| GF6_2_1 | 2.196 | 0.191 | 0.703 | 0.139 |
| GF6_2_2 | 1.723 | 0.178 | 0.703 | 0.107 |
| GF6_5_1 | 1.529 | 0.119 | 0.136 | 0.028 |
| GF6_4_1 | 1.156 | 0.155 | 0.205 | 0.043 |
| GF6_6_1 | 1.258 | 0.083 | 0.275 | 0.044 |
| GF6_17_1 | 0.548 | 0.093 | 0.038 | 0.021 |
| GF6_11_1 | 1.608 | 0.106 | 0.174 | 0.030 |
| GF6_8_1 | 1.693 | 0.170 | 0.249 | 0.043 |
| GF6_7_1 | 1.718 | 0.156 | 0.180 | 0.032 |
| GF6_9_1 | 1.652 | 0.125 | 0.181 | 0.043 |

Table A.7 continued

| Sample | Pb_ppm_m208 | Pb_ppm_m208_2SE | Th_ppm_m232 | Th_ppm_m232_2SE |
|---|---|---|---|---|
| GF6_10_1 | 1.480 | 0.201 | 0.233 | 0.031 |
| GF6_18_1 | 1.758 | 0.503 | 0.248 | 0.067 |
| GF6_13_1 | 2.112 | 0.368 | 0.344 | 0.048 |
| GF6_12_1 | 2.633 | 0.224 | 0.446 | 0.079 |
| GF6_15_1 | 2.429 | 0.216 | 0.299 | 0.036 |
| GF6_19_1 | 2.330 | 0.689 | 0.274 | 0.090 |
| GF6_20_1 | 2.962 | 0.472 | 0.341 | 0.050 |
| | | | | |
| ZB117_1_a | 0.068 | 0.017 | 0.002 | 0.003 |
| ZB117_2_a | 0.015 | 0.019 | 0.003 | 0.005 |
| ZB117_4_a | 0.120 | 0.018 | 0.000 | 0.000 |
| ZB117_7_a | 0.075 | 0.023 | 0.000 | 0.000 |
| ZB117_14_a | 0.013 | 0.020 | 0.000 | 0.000 |
| | | | | |
| GF39_9_1 | 0.166 | 0.063 | 0.000 | 0.000 |
| GF39_6_1 | 0.039 | 0.030 | 0.043 | 0.027 |
| GF39_6_2 | -0.013 | 0.022 | 0.018 | 0.015 |
| GF39_7_1 | 0.281 | 0.040 | 0.290 | 0.048 |
| GF39_4_1 | 0.058 | 0.021 | 0.000 | 0.000 |
| GF39_4_2 | 0.148 | 0.046 | 0.114 | 0.015 |
| GF39_8_1 | 0.520 | 0.098 | 0.064 | 0.028 |

Table A.7 continued

| Sample | U_ppm_m238 | U_ppm_m238_2SE |
|---|---|---|
| IS8_1_1 | 0.000 | 0.000 |
| IS8_1_2 | 0.000 | 1.000 |
| IS8_3_1 | 0.000 | 0.000 |
| IS8_3_2 | 0.004 | 0.006 |
| IS8_5_1 | 0.000 | 0.000 |
| IS8_5_2 | 0.000 | 0.000 |
| IS8_5_3 | 0.000 | 0.000 |
| IS8_5_4 | 0.000 | 0.000 |
| IS8_7_1 | 0.008 | 0.006 |
| IS8_8_1 | 0.008 | 0.007 |
| IS8_8_2 | 0.000 | 0.000 |
| IS8_10_1 | 0.000 | 0.000 |
| IS8_11_1 | 0.000 | 1.000 |
| IS8_13_1 | 0.000 | 1.000 |
| IS8_13_2 | 0.000 | 1.000 |
| IS8_15_1 | 0.002 | 0.004 |
| IS8_15_2 | 0.006 | 0.006 |
| IS8_17_1 | 0.000 | 0.000 |
| IS8_17_2 | 0.002 | 0.004 |
| IS8_18_1 | 0.044 | 0.013 |
| IS8_18_2 | 0.000 | 1.000 |
| IS8_19_1 | 0.000 | 0.000 |
| IS8_19_2 | 0.000 | 0.000 |
| IS8_20_2 | 0.000 | 0.000 |
| | | |
| GF6_16_1 | 0.017 | 0.009 |
| GF6_16_2 | 0.308 | 0.057 |
| GF6_3_1 | 0.317 | 0.048 |
| GF6_3_2 | 0.260 | 0.045 |
| GF6_1_1 | 0.300 | 0.036 |
| GF6_2_1 | 0.383 | 0.051 |
| GF6_2_2 | 0.310 | 0.071 |
| GF6_5_1 | 0.250 | 0.045 |
| GF6_4_1 | 0.230 | 0.032 |
| GF6_6_1 | 0.303 | 0.035 |
| GF6_17_1 | 0.032 | 0.020 |
| GF6_11_1 | 0.327 | 0.037 |
| GF6_8_1 | 0.348 | 0.062 |
| GF6_7_1 | 0.288 | 0.040 |
| GF6_9_1 | 0.399 | 0.051 |

Table A.7 continued

| Sample | U_ppm_m238 | U_ppm_m238_2SE |
|---|---|---|
| GF6_10_1 | 0.287 | 0.024 |
| GF6_18_1 | 0.130 | 0.032 |
| GF6_13_1 | 0.897 | 0.110 |
| GF6_12_1 | 0.851 | 0.069 |
| GF6_15_1 | 0.816 | 0.056 |
| GF6_19_1 | 0.714 | 0.502 |
| GF6_20_1 | 0.569 | 0.102 |
| | | |
| ZB117_1_a | 0.236 | 0.017 |
| ZB117_2_a | 0.044 | 0.018 |
| ZB117_4_a | 0.188 | 0.018 |
| ZB117_7_a | 0.192 | 0.022 |
| ZB117_14_a | 0.012 | 0.008 |
| | | |
| GF39_9_1 | 0.000 | 0.000 |
| GF39_6_1 | 0.058 | 0.015 |
| GF39_6_2 | 0.036 | 0.015 |
| GF39_7_1 | 0.370 | 0.060 |
| GF39_4_1 | 0.042 | 0.020 |
| GF39_4_2 | 0.260 | 0.034 |
| GF39_8_1 | 0.293 | 0.050 |

Table A.8
LA-ICP-MS REE analsyses (40μm) from samples from the IGB, BGB, GF

| Sample | Duration(s) | Mineral | Location | Fe57_CPS | Fe57_CPS_2SE |
|---|---|---|---|---|---|
| ZB117_1_1 | 18.893 | Mt | band 1 | 1.85E+07 | 9.41E+05 |
| ZB117_1_2 | 17.216 | Mt | band 1 | 1.85E+07 | 5.84E+05 |
| ZB117_2_1 | 18.337 | Mt | band 1 | 1.88E+07 | 1.00E+06 |
| ZB117_2_2 | 19.171 | Mt | band 1 | 1.72E+07 | 8.86E+05 |
| ZB117_4_1 | 19.634 | Mt | band 1 | 1.61E+07 | 8.53E+05 |
| ZB117_4_2 | 20.375 | Mt | band 1 | 1.65E+07 | 7.27E+05 |
| ZB117_5_1 | 18.615 | Mt | band 1 | 1.76E+07 | 1.41E+06 |
| ZB117_5_2 | 18.152 | Mt | band 1 | 1.73E+07 | 9.07E+05 |
| ZB117_6_1 | 16.207 | Mt | band 2 | 1.71E+07 | 7.92E+05 |
| ZB117_7_1 | 15.929 | Mt | band 2 | 1.74E+07 | 9.10E+05 |
| ZB117_8_1 | 17.967 | Mt | band 2 | 1.79E+07 | 9.98E+05 |
| ZB117_9_1 | 21.486 | Mt | band 2 | 1.69E+07 | 1.06E+06 |
| ZB117_12_1 | 18.059 | Mt | band 3 | 1.75E+07 | 8.50E+05 |
| ZB117_11_1 | 18.086 | Mt | band 3 | 1.76E+07 | 8.36E+05 |
| ZB117_10_1 | 19.727 | Mt | band 3 | 1.70E+07 | 8.94E+05 |
| ZB117_10_2 | 18.43 | Mt | band 3 | 1.82E+07 | 1.19E+06 |
| ZB117_13_1 | 18.245 | Mt | band 4 | 1.53E+07 | 5.87E+05 |
| ZB117_14_1 | 18.059 | Mt | band 4 | 1.49E+07 | 8.07E+05 |
| ZB117_15_1 | 18.152 | Mt | band 4 | 1.44E+07 | 9.67E+05 |
| | | | | | |
| ZB23_1_1 | 18.708 | Mt | band 1 | 1.50E+07 | 1.14E+06 |
| ZB23_1_2 | 19.39 | Mt | band 1 | 1.52E+07 | 1.11E+06 |
| ZB23_2_1 | 18.43 | Mt | band 1 | 1.59E+07 | 7.95E+05 |
| ZB23_3_1 | 18.986 | Mt | band 1 | 1.62E+07 | 9.68E+05 |
| ZB23_4_1 | 17.133 | Mt | band 2 | 1.60E+07 | 7.16E+05 |
| ZB23_5_1 | 17.504 | Mt | band 2 | 1.62E+07 | 8.55E+05 |
| ZB23_6_1 | 13.181 | Mt | band 2 | 1.68E+07 | 9.96E+05 |
| ZB23_6_2 | 19.022 | Mt | band 2 | 1.67E+07 | 7.63E+05 |
| ZB23_9_1 | 8.3666 | Mt | band 3 | 1.55E+07 | 1.31E+06 |
| ZB23_9_2 | 5.391 | Mt | band 3 | 1.46E+07 | 1.00E+06 |
| ZB23_8_1 | 5.4462 | Mt | band 3 | 1.17E+07 | 2.59E+06 |
| ZB23_8_1 | 18.708 | Mt | band 3 | 1.18E+07 | 5.78E+05 |
| ZB23_10_1 | 16.608 | Mt | band 3 | 1.20E+07 | 5.35E+05 |
| ZB23_10_2 | 17.651 | Mt | band 3 | 1.30E+07 | 8.81E+05 |
| ZB23_11_1 | 11.761 | Mt | band 4 | 1.34E+07 | 9.17E+05 |
| ZB23_13_1 | 16.485 | Mt | band 4 | 1.31E+07 | 8.20E+05 |
| ZB23_14_1 | 3.8897 | Mt | band 4 | 1.91E+07 | 1.73E+06 |

Table A.8 continued

| Sample | Duration(s) | Mineral | Location | Fe57_CPS | Fe57_CPS_2SE |
|---|---|---|---|---|---|
| GF45_1_1 | 18.152 | Mt | | 1.13E+07 | 1.12E+06 |
| GF45_1_2 | 16.782 | Mt | | 1.12E+07 | 8.70E+05 |
| GF45_1_3 | 17.133 | Mt | | 1.33E+07 | 8.08E+05 |
| GF45_2_1 | 19.078 | Mt | | 1.36E+07 | 1.01E+06 |
| GF45_2_2 | 16.97 | Mt | | 1.15E+07 | 8.24E+05 |
| GF45_2_3 | 17.874 | Mt | | 1.24E+07 | 1.00E+06 |
| GF45_2_4 | 18.893 | Mt | | 1.34E+07 | 1.22E+06 |
| | | | | | |
| IS5_1_1 | 18.893 | Mt | band 1 | 1.82E+07 | 1.01E+06 |
| IS5_1_2 | 18.434 | Hem | band 1 | 1.47E+07 | 7.94E+05 |
| IS5_3_1 | 18.615 | Mt | band 2 | 1.31E+07 | 6.72E+05 |
| IS5_3_2 | 16.856 | Hem | band 2 | 1.43E+07 | 8.56E+05 |
| IS5_8_1 | 18.893 | Mt | band 3 | 1.12E+07 | 8.61E+05 |
| IS5_8_2 | 18.523 | Mt | band 3 | 1.10E+07 | 6.77E+05 |
| IS5_8_3 | 18.986 | Hem | band 3 | 1.21E+07 | 1.07E+06 |
| IS5_8_3 | 17.504 | Mt | band 3 | 1.06E+07 | 8.39E+05 |
| IS5_7_1 | 18.608 | Mt | band 3 | 1.04E+07 | 8.59E+05 |
| IS5_7_2 | 18.708 | Mt | band 3 | 1.18E+07 | 7.32E+05 |
| IS5_6_1 | 19.634 | Mt | band 3 | 1.21E+07 | 5.28E+05 |
| IS5_6_2 | 18.43 | Hem | band 3 | 1.32E+07 | 8.71E+05 |
| IS5_5_1 | 17.226 | Mt | band 3 | 1.31E+07 | 6.75E+05 |
| IS5_5_2 | 18.43 | Hem | band 3 | 1.37E+07 | 8.19E+05 |
| IS5_4_1 | 17.133 | Mt | band 3 | 1.09E+07 | 1.08E+06 |
| IS5_9_1 | 16.695 | Mt | band 4 | 1.13E+07 | 8.53E+05 |
| IS5_10_1 | 18.523 | Mt | band 4 | 1.10E+07 | 1.20E+06 |
| IS5_10_2 | 19.078 | Hem | band 4 | 1.42E+07 | 1.08E+06 |
| IS5_11_1 | 17.967 | Mt | band 4 | 9813748 | 6.79E+05 |
| IS5_11_2 | 19.541 | Mt | band 4 | 8556231 | 6.52E+05 |
| IS5_13_1 | 18.523 | Mt | band 4 | 1.06E+07 | 6.34E+05 |
| IS5_13_2 | 18.893 | Hem | band 4 | 1.35E+07 | 8.43E+05 |
| IS5_13_2 | 18.708 | Mt | band 4 | 1.22E+07 | 1.09E+06 |
| IS5_20_1 | 19.216 | Mt | band 5 | 1.23E+07 | 1.06E+06 |
| IS5_20_2 | 18.708 | Hem | band 5 | 1.28E+07 | 1.21E+06 |
| IS5_19_1 | 18.43 | Mt | band 5 | 1.21E+07 | 6.19E+05 |
| IS5_17_1 | 18.523 | Mt | band 5 | 1.13E+07 | 8.38E+05 |
| IS5_17_2 | 18.245 | Hem | band 5 | 1.11E+07 | 8.50E+05 |

Table A.8 continued

| Sample | Sr_ppm_m88 | Sr_ppm_m88_2SE | Y_ppm_m89 | Y_ppm_m89_2SE | Sample |
|---|---|---|---|---|---|
| ZB117_1_1 | 0.328 | 0.033 | 3.517 | 0.320 | ZB117_1_1 |
| ZB117_1_2 | 0.442 | 0.039 | 6.187 | 0.238 | ZB117_1_2 |
| ZB117_2_1 | 0.152 | 0.022 | 0.990 | 0.196 | ZB117_2_1 |
| ZB117_2_2 | 0.244 | 0.034 | 0.325 | 0.027 | ZB117_2_2 |
| ZB117_4_1 | 0.172 | 0.024 | 1.031 | 0.096 | ZB117_4_1 |
| ZB117_4_2 | 0.291 | 0.034 | 0.804 | 0.116 | ZB117_4_2 |
| ZB117_5_1 | 0.495 | 0.049 | 4.110 | 0.358 | ZB117_5_1 |
| ZB117_5_2 | 0.060 | 0.017 | 0.217 | 0.061 | ZB117_5_2 |
| ZB117_6_1 | 11.314 | 0.385 | 18.479 | 0.631 | ZB117_6_1 |
| ZB117_7_1 | 0.778 | 0.048 | 7.356 | 0.194 | ZB117_7_1 |
| ZB117_8_1 | 3.570 | 0.204 | 9.647 | 0.397 | ZB117_8_1 |
| ZB117_9_1 | 4.038 | 0.323 | 10.514 | 0.371 | ZB117_9_1 |
| ZB117_12_1 | 0.866 | 0.044 | 3.563 | 0.109 | ZB117_12_1 |
| ZB117_11_1 | 0.844 | 0.040 | 3.570 | 0.110 | ZB117_11_1 |
| ZB117_10_1 | 0.700 | 0.040 | 5.135 | 0.310 | ZB117_10_1 |
| ZB117_10_2 | 0.692 | 0.064 | 4.178 | 0.152 | ZB117_10_2 |
| ZB117_13_1 | 0.211 | 0.034 | 0.874 | 0.048 | ZB117_13_1 |
| ZB117_14_1 | 0.327 | 0.042 | 1.034 | 0.077 | ZB117_14_1 |
| ZB117_15_1 | 0.642 | 0.118 | 3.530 | 0.145 | ZB117_15_1 |
| | | | | | |
| ZB23_1_1 | 0.368 | 0.060 | 0.689 | 0.075 | ZB23_1_1 |
| ZB23_1_2 | 0.287 | 0.081 | 0.795 | 0.172 | ZB23_1_2 |
| ZB23_2_1 | 0.245 | 0.041 | 0.760 | 0.083 | ZB23_2_1 |
| ZB23_3_1 | 0.233 | 0.021 | 0.472 | 0.059 | ZB23_3_1 |
| ZB23_4_1 | 0.289 | 0.023 | 0.761 | 0.034 | ZB23_4_1 |
| ZB23_5_1 | 0.238 | 0.029 | 0.532 | 0.034 | ZB23_5_1 |
| ZB23_6_1 | 0.158 | 0.054 | 0.279 | 0.037 | ZB23_6_1 |
| ZB23_6_2 | 0.789 | 0.138 | 2.825 | 0.670 | ZB23_6_2 |
| ZB23_9_1 | 0.394 | 0.063 | 0.486 | 0.066 | ZB23_9_1 |
| ZB23_9_2 | 0.275 | 0.093 | 0.764 | 0.051 | ZB23_9_2 |
| ZB23_8_1 | 0.378 | 0.094 | 0.115 | 0.020 | ZB23_8_1 |
| ZB23_8_1 | 0.241 | 0.067 | 0.353 | 0.100 | ZB23_8_1 |
| ZB23_10_1 | 0.252 | 0.070 | 0.391 | 0.103 | ZB23_10_1 |
| ZB23_10_2 | 0.246 | 0.037 | 0.412 | 0.090 | ZB23_10_2 |
| ZB23_11_1 | 0.219 | 0.026 | 0.187 | 0.029 | ZB23_11_1 |
| ZB23_13_1 | 0.223 | 0.030 | 0.772 | 0.084 | ZB23_13_1 |
| ZB23_14_1 | 0.178 | 0.032 | 0.321 | 0.057 | ZB23_14_1 |

Table A.8 continued

| Sample | Sr_ppm_m88 | Sr_ppm_m88_2SE | Y_ppm_m89 | Y_ppm_m89_2SE | Sample |
|---|---|---|---|---|---|
| GF45_1_1 | 4.329 | 0.497 | 1.159 | 0.099 | GF45_1_1 |
| GF45_1_2 | 10.653 | 0.795 | 1.571 | 0.111 | GF45_1_2 |
| GF45_1_3 | 2.601 | 0.147 | 1.386 | 0.084 | GF45_1_3 |
| GF45_2_1 | 7.081 | 0.575 | 1.542 | 0.097 | GF45_2_1 |
| GF45_2_2 | 9.552 | 0.864 | 1.604 | 0.089 | GF45_2_2 |
| GF45_2_3 | 3.039 | 0.313 | 1.580 | 0.084 | GF45_2_3 |
| GF45_2_4 | 2.821 | 0.239 | 1.837 | 0.138 | GF45_2_4 |
| | | | | | |
| IS5_1_1 | 2.158 | 0.134 | 0.307 | 0.023 | IS5_1_1 |
| IS5_1_2 | 0.134 | 0.026 | 0.668 | 0.050 | IS5_1_2 |
| IS5_3_1 | 1.512 | 0.311 | 0.323 | 0.036 | IS5_3_1 |
| IS5_3_2 | 0.050 | 0.013 | 0.146 | 0.036 | IS5_3_2 |
| IS5_8_1 | 0.782 | 0.143 | 0.241 | 0.037 | IS5_8_1 |
| IS5_8_2 | 0.181 | 0.065 | 0.125 | 0.042 | IS5_8_2 |
| IS5_8_3 | 0.019 | 0.012 | 0.328 | 0.030 | IS5_8_3 |
| IS5_8_3 | 2.935 | 0.393 | 1.204 | 0.078 | IS5_8_3 |
| IS5_7_1 | 2.876 | 0.385 | 1.215 | 0.078 | IS5_7_1 |
| IS5_7_2 | 0.112 | 0.076 | 0.038 | 0.019 | IS5_7_2 |
| IS5_6_1 | 1.200 | 0.093 | 1.362 | 0.076 | IS5_6_1 |
| IS5_6_2 | 0.033 | 0.011 | 0.106 | 0.017 | IS5_6_2 |
| IS5_5_1 | 0.363 | 0.072 | 0.264 | 0.037 | IS5_5_1 |
| IS5_5_2 | 0.092 | 0.030 | 0.162 | 0.053 | IS5_5_2 |
| IS5_4_1 | 0.494 | 0.150 | 0.335 | 0.069 | IS5_4_1 |
| IS5_9_1 | 0.023 | 0.019 | 0.027 | 0.012 | IS5_9_1 |
| IS5_10_1 | 1.132 | 0.122 | 2.010 | 0.155 | IS5_10_1 |
| IS5_10_2 | 0.080 | 0.029 | 0.221 | 0.080 | IS5_10_2 |
| IS5_11_1 | 0.072 | 0.015 | 0.095 | 0.020 | IS5_11_1 |
| IS5_11_2 | 0.094 | 0.021 | 0.222 | 0.049 | IS5_11_2 |
| IS5_13_1 | 0.942 | 0.101 | 0.662 | 0.112 | IS5_13_1 |
| IS5_13_2 | 0.018 | 0.014 | 0.073 | 0.041 | IS5_13_2 |
| IS5_13_2 | 0.681 | 0.055 | 0.722 | 0.185 | IS5_13_2 |
| IS5_20_1 | 0.671 | 0.053 | 0.698 | 0.183 | IS5_20_1 |
| IS5_20_2 | 0.017 | 0.011 | 0.034 | 0.012 | IS5_20_2 |
| IS5_19_1 | 0.746 | 0.152 | 0.295 | 0.082 | IS5_19_1 |
| IS5_17_1 | 0.880 | 0.109 | 0.675 | 0.120 | IS5_17_1 |
| IS5_17_2 | 0.015 | 0.011 | 0.070 | 0.036 | IS5_17_2 |

Table A.8 continued

| Zr_ppm_m90 | Zr_ppm_m90_2SE | Ba_ppm_m137 | Ba_ppm_m137_2SE | Sample |
|---|---|---|---|---|
| 0.008 | 0.010 | 3.031 | 0.247 | ZB117_1_1 |
| 0.002 | 0.010 | 1.883 | 0.195 | ZB117_1_2 |
| 0.002 | 0.008 | 1.259 | 0.258 | ZB117_2_1 |
| -0.008 | 0.009 | 1.361 | 0.148 | ZB117_2_2 |
| -0.002 | 0.010 | 1.087 | 0.094 | ZB117_4_1 |
| 0.009 | 0.009 | 0.851 | 0.117 | ZB117_4_2 |
| -0.009 | 0.009 | 2.640 | 0.225 | ZB117_5_1 |
| 0.001 | 0.009 | 0.240 | 0.078 | ZB117_5_2 |
| 0.014 | 0.007 | 3287.246 | 168.602 | ZB117_6_1 |
| 0.003 | 0.006 | 21.560 | 0.502 | ZB117_7_1 |
| 0.015 | 0.007 | 321.051 | 17.745 | ZB117_8_1 |
| 0.005 | 0.009 | 253.277 | 19.730 | ZB117_9_1 |
| 0.015 | 0.005 | 11.582 | 0.664 | ZB117_12_1 |
| 0.022 | 0.006 | 11.542 | 0.630 | ZB117_11_1 |
| 0.024 | 0.013 | 2.705 | 0.226 | ZB117_10_1 |
| 0.014 | 0.007 | 2.095 | 0.135 | ZB117_10_2 |
| 0.002 | 0.008 | 1.468 | 0.148 | ZB117_13_1 |
| -0.015 | 0.007 | 1.873 | 0.145 | ZB117_14_1 |
| -0.005 | 0.011 | 2.021 | 0.212 | ZB117_15_1 |
| | | | | |
| 0.083 | 0.016 | 7.017 | 2.158 | ZB23_1_1 |
| 0.071 | 0.012 | 4.120 | 0.726 | ZB23_1_2 |
| 0.210 | 0.034 | 4.790 | 0.476 | ZB23_2_1 |
| 0.181 | 0.026 | 4.053 | 0.316 | ZB23_3_1 |
| 0.347 | 0.079 | 3.161 | 0.646 | ZB23_4_1 |
| 0.053 | 0.010 | 6.566 | 0.626 | ZB23_5_1 |
| 0.088 | 0.031 | 1.371 | 0.222 | ZB23_6_1 |
| 0.243 | 0.058 | 3.832 | 0.618 | ZB23_6_2 |
| 0.483 | 0.122 | 3.548 | 1.510 | ZB23_9_1 |
| 0.212 | 0.026 | 9.792 | 2.885 | ZB23_9_2 |
| 0.049 | 0.016 | 0.388 | 0.190 | ZB23_8_1 |
| 0.028 | 0.022 | 0.988 | 0.234 | ZB23_8_1 |
| 0.033 | 0.024 | 1.056 | 0.252 | ZB23_10_1 |
| 1.096 | 0.229 | 1.950 | 0.318 | ZB23_10_2 |
| 0.035 | 0.012 | 8.668 | 1.301 | ZB23_11_1 |
| 0.266 | 0.025 | 4.967 | 0.550 | ZB23_13_1 |
| 0.150 | 0.040 | 1.441 | 0.500 | ZB23_14_1 |

Table A.8 continued

| Zr_ppm_m90 | Zr_ppm_m90_2SE | Ba_ppm_m137 | Ba_ppm_m137_2SE | Sample |
|---|---|---|---|---|
| 2.831 | 0.274 | 12.266 | 1.207 | GF45_1_1 |
| 6.786 | 0.312 | 18.407 | 0.935 | GF45_1_2 |
| 3.530 | 0.266 | 23.494 | 1.404 | GF45_1_3 |
| 1.046 | 0.123 | 14.853 | 1.359 | GF45_2_1 |
| 5.159 | 0.273 | 17.572 | 0.952 | GF45_2_2 |
| 7.077 | 0.472 | 14.550 | 0.979 | GF45_2_3 |
| 7.293 | 0.799 | 23.314 | 1.977 | GF45_2_4 |
| | | | | |
| 0.010 | 0.009 | 3.550 | 0.217 | IS5_1_1 |
| 0.140 | 0.017 | 6.747 | 0.692 | IS5_1_2 |
| 0.020 | 0.015 | 3.648 | 0.949 | IS5_3_1 |
| 0.197 | 0.019 | 1.293 | 0.390 | IS5_3_2 |
| 0.006 | 0.014 | 1.252 | 0.194 | IS5_8_1 |
| 0.011 | 0.011 | 0.408 | 0.119 | IS5_8_2 |
| 0.160 | 0.016 | 0.517 | 0.076 | IS5_8_3 |
| 0.010 | 0.009 | 5.691 | 0.533 | IS5_8_3 |
| 0.004 | 0.011 | 5.552 | 0.533 | IS5_7_1 |
| 0.012 | 0.010 | 0.229 | 0.124 | IS5_7_2 |
| 0.011 | 0.014 | 5.142 | 0.582 | IS5_6_1 |
| 0.496 | 0.037 | 0.136 | 0.050 | IS5_6_2 |
| -0.002 | 0.006 | 0.921 | 0.176 | IS5_5_1 |
| 0.181 | 0.020 | 0.046 | 0.040 | IS5_5_2 |
| 0.010 | 0.010 | 3.852 | 0.502 | IS5_4_1 |
| 0.002 | 0.009 | 0.089 | 0.083 | IS5_9_1 |
| 0.016 | 0.012 | 4.813 | 0.520 | IS5_10_1 |
| 0.199 | 0.026 | 8.311 | 3.150 | IS5_10_2 |
| 0.020 | 0.016 | 4.192 | 0.769 | IS5_11_1 |
| -0.009 | 0.015 | 6.344 | 1.134 | IS5_11_2 |
| 0.004 | 0.013 | 1.739 | 0.166 | IS5_13_1 |
| 0.198 | 0.019 | 1.014 | 0.644 | IS5_13_2 |
| 0.016 | 0.010 | 0.818 | 0.111 | IS5_13_2 |
| 0.012 | 0.010 | 0.823 | 0.109 | IS5_20_1 |
| 0.150 | 0.011 | 0.053 | 0.030 | IS5_20_2 |
| -0.002 | 0.010 | 2.594 | 0.206 | IS5_19_1 |
| 0.011 | 0.014 | 1.872 | 0.228 | IS5_17_1 |
| 0.379 | 0.023 | 0.109 | 0.061 | IS5_17_2 |

Table A.8 continued

| La_ppm_m139 | La_ppm_m139_2SE | Ce_ppm_m140 | Ce_ppm_m140_2SE | Pr_ppm_m141 |
|---|---|---|---|---|
| 0.852 | 0.078 | 0.541 | 0.046 | 0.182 |
| 1.871 | 0.093 | 0.154 | 0.011 | 0.317 |
| 0.270 | 0.043 | 0.224 | 0.041 | 0.053 |
| 0.065 | 0.012 | 0.165 | 0.010 | 0.024 |
| 0.235 | 0.027 | 0.225 | 0.021 | 0.047 |
| 0.159 | 0.034 | 0.219 | 0.022 | 0.036 |
| 0.939 | 0.060 | 0.716 | 0.059 | 0.251 |
| 0.063 | 0.020 | 0.024 | 0.007 | 0.014 |
| 26.405 | 1.148 | 118.307 | 4.458 | 4.830 |
| 3.585 | 0.083 | 4.417 | 0.119 | 0.760 |
| 8.058 | 0.305 | 9.459 | 0.432 | 1.674 |
| 7.532 | 0.288 | 9.244 | 0.348 | 1.444 |
| 3.269 | 0.149 | 1.113 | 0.059 | 0.557 |
| 3.261 | 0.144 | 1.114 | 0.061 | 0.548 |
| 1.561 | 0.083 | 0.412 | 0.032 | 0.361 |
| 1.357 | 0.063 | 0.241 | 0.017 | 0.335 |
| 0.299 | 0.019 | 0.125 | 0.009 | 0.077 |
| 0.324 | 0.030 | 0.143 | 0.015 | 0.088 |
| 1.013 | 0.091 | 0.369 | 0.032 | 0.259 |
| | | | | |
| 0.185 | 0.021 | 0.574 | 0.055 | 0.065 |
| 0.553 | 0.238 | 1.175 | 0.499 | 0.128 |
| 0.189 | 0.029 | 0.475 | 0.058 | 0.060 |
| 0.134 | 0.017 | 0.427 | 0.041 | 0.045 |
| 0.142 | 0.022 | 0.472 | 0.045 | 0.057 |
| 0.134 | 0.016 | 0.435 | 0.030 | 0.053 |
| 0.064 | 0.027 | 0.231 | 0.078 | 0.024 |
| 3.695 | 1.433 | 8.116 | 2.583 | 0.601 |
| 0.684 | 0.132 | 1.990 | 0.352 | 0.192 |
| 1.772 | 0.233 | 5.863 | 0.687 | 0.826 |
| 0.090 | 0.019 | 0.352 | 0.061 | 0.027 |
| 0.026 | 0.009 | 0.086 | 0.021 | 0.009 |
| 0.029 | 0.010 | 0.095 | 0.022 | 0.009 |
| 0.353 | 0.032 | 0.998 | 0.093 | 0.098 |
| 0.054 | 0.007 | 0.251 | 0.021 | 0.025 |
| 0.092 | 0.016 | 0.261 | 0.022 | 0.031 |
| 0.027 | 0.020 | 0.108 | 0.013 | 0.014 |

Table A.8 continued

| La_ppm_m139 | La_ppm_m139_2SE | Ce_ppm_m140 | Ce_ppm_m140_2SE | Pr_ppm_m141 |
|---|---|---|---|---|
| 0.273 | 0.038 | 0.660 | 0.071 | 0.055 |
| 0.747 | 0.052 | 1.990 | 0.141 | 0.153 |
| 0.691 | 0.053 | 1.427 | 0.074 | 0.110 |
| 0.602 | 0.043 | 1.237 | 0.100 | 0.108 |
| 0.671 | 0.039 | 1.758 | 0.082 | 0.148 |
| 0.800 | 0.066 | 1.867 | 0.085 | 0.140 |
| 0.729 | 0.063 | 1.385 | 0.110 | 0.104 |
| | | | | |
| 0.468 | 0.091 | 0.716 | 0.164 | 0.057 |
| 2.022 | 0.217 | 128.315 | 15.154 | 0.640 |
| 0.639 | 0.111 | 1.423 | 0.406 | 0.094 |
| 0.250 | 0.081 | 8.766 | 6.450 | 0.045 |
| 0.345 | 0.089 | 0.337 | 0.066 | 0.035 |
| 0.109 | 0.047 | 0.162 | 0.083 | 0.010 |
| 0.644 | 0.031 | 0.354 | 0.033 | 0.118 |
| 0.356 | 0.029 | 0.564 | 0.061 | 0.054 |
| 0.354 | 0.027 | 0.560 | 0.061 | 0.055 |
| 0.029 | 0.016 | 0.017 | 0.011 | 0.000 |
| 0.469 | 0.060 | 0.621 | 0.043 | 0.078 |
| 0.103 | 0.025 | 0.453 | 0.194 | 0.021 |
| 0.099 | 0.023 | 0.111 | 0.021 | 0.019 |
| 0.023 | 0.008 | 0.053 | 0.017 | 0.006 |
| 0.468 | 0.065 | 0.278 | 0.081 | 0.033 |
| 0.003 | 0.003 | 0.010 | 0.008 | 0.000 |
| 0.274 | 0.035 | 0.819 | 0.064 | 0.068 |
| 0.046 | 0.016 | 0.066 | 0.016 | 0.004 |
| 0.051 | 0.008 | 0.124 | 0.020 | 0.006 |
| 0.081 | 0.016 | 0.161 | 0.029 | 0.010 |
| 0.659 | 0.085 | 0.883 | 0.106 | 0.084 |
| 0.026 | 0.014 | 0.034 | 0.018 | 0.001 |
| 0.161 | 0.027 | 0.311 | 0.046 | 0.016 |
| 0.159 | 0.026 | 0.305 | 0.045 | 0.016 |
| 0.009 | 0.006 | 0.014 | 0.003 | 0.000 |
| 0.194 | 0.053 | 0.276 | 0.074 | 0.029 |
| 0.497 | 0.063 | 0.681 | 0.079 | 0.075 |
| 0.013 | 0.007 | 0.028 | 0.007 | 0.002 |

Table A.8 continued

| Sample | Pr_ppm_m141_2SE | Nd_ppm_m146 | Nd_ppm_m146_2SE | Sm_ppm_m147 |
|---|---|---|---|---|
| ZB117_1_1 | 0.021 | 0.989 | 0.100 | 0.281 |
| ZB117_1_2 | 0.021 | 1.596 | 0.069 | 0.364 |
| ZB117_2_1 | 0.007 | 0.321 | 0.062 | 0.089 |
| ZB117_2_2 | 0.005 | 0.115 | 0.021 | 0.046 |
| ZB117_4_1 | 0.006 | 0.285 | 0.032 | 0.073 |
| ZB117_4_2 | 0.006 | 0.138 | 0.026 | 0.060 |
| ZB117_5_1 | 0.033 | 1.148 | 0.088 | 0.348 |
| ZB117_5_2 | 0.006 | 0.072 | 0.028 | 0.013 |
| ZB117_6_1 | 0.237 | 20.123 | 0.723 | 4.403 |
| ZB117_7_1 | 0.028 | 3.467 | 0.097 | 0.851 |
| ZB117_8_1 | 0.069 | 7.470 | 0.261 | 1.581 |
| ZB117_9_1 | 0.068 | 6.802 | 0.334 | 1.447 |
| ZB117_12_1 | 0.027 | 2.502 | 0.127 | 0.415 |
| ZB117_11_1 | 0.023 | 2.526 | 0.132 | 0.419 |
| ZB117_10_1 | 0.020 | 1.562 | 0.104 | 0.355 |
| ZB117_10_2 | 0.022 | 1.473 | 0.073 | 0.391 |
| ZB117_13_1 | 0.007 | 0.375 | 0.039 | 0.094 |
| ZB117_14_1 | 0.010 | 0.424 | 0.032 | 0.123 |
| ZB117_15_1 | 0.014 | 1.080 | 0.051 | 0.286 |
| | | | | |
| ZB23_1_1 | 0.010 | 0.278 | 0.020 | 0.090 |
| ZB23_1_2 | 0.050 | 0.768 | 0.260 | 0.170 |
| ZB23_2_1 | 0.009 | 0.300 | 0.037 | 0.113 |
| ZB23_3_1 | 0.007 | 0.240 | 0.039 | 0.097 |
| ZB23_4_1 | 0.009 | 0.283 | 0.041 | 0.088 |
| ZB23_5_1 | 0.006 | 0.242 | 0.027 | 0.098 |
| ZB23_6_1 | 0.008 | 0.159 | 0.041 | 0.046 |
| ZB23_6_2 | 0.132 | 2.593 | 0.564 | 0.639 |
| ZB23_9_1 | 0.041 | 0.982 | 0.151 | 0.175 |
| ZB23_9_2 | 0.053 | 3.337 | 0.389 | 0.800 |
| ZB23_8_1 | 0.006 | 0.170 | 0.051 | 0.053 |
| ZB23_8_1 | 0.003 | 0.013 | 0.009 | 0.003 |
| ZB23_10_1 | 0.003 | 0.017 | 0.010 | 0.007 |
| ZB23_10_2 | 0.008 | 0.489 | 0.055 | 0.138 |
| ZB23_11_1 | 0.005 | 0.169 | 0.040 | 0.046 |
| ZB23_13_1 | 0.004 | 0.216 | 0.023 | 0.119 |
| ZB23_14_1 | 0.005 | 0.091 | 0.008 | 0.063 |

Table A.8 continued

| Sample | Pr_ppm_m141_2SE | Nd_ppm_m146 | Nd_ppm_m146_2SE | Sm_ppm_m147 |
|---|---|---|---|---|
| GF45_1_1 | 0.008 | 0.300 | 0.043 | 0.106 |
| GF45_1_2 | 0.017 | 0.737 | 0.082 | 0.198 |
| GF45_1_3 | 0.006 | 0.384 | 0.037 | 0.131 |
| GF45_2_1 | 0.010 | 0.384 | 0.031 | 0.085 |
| GF45_2_2 | 0.008 | 0.696 | 0.064 | 0.175 |
| GF45_2_3 | 0.008 | 0.697 | 0.065 | 0.148 |
| GF45_2_4 | 0.007 | 0.369 | 0.053 | 0.071 |
| | | | | |
| IS5_1_1 | 0.011 | 0.227 | 0.048 | 0.018 |
| IS5_1_2 | 0.082 | 1.833 | 0.184 | 0.328 |
| IS5_3_1 | 0.018 | 0.371 | 0.082 | 0.064 |
| IS5_3_2 | 0.016 | 0.210 | 0.084 | 0.043 |
| IS5_8_1 | 0.009 | 0.128 | 0.018 | 0.011 |
| IS5_8_2 | 0.006 | 0.048 | 0.017 | 0.008 |
| IS5_8_3 | 0.017 | 0.326 | 0.035 | 0.067 |
| IS5_8_3 | 0.008 | 0.249 | 0.045 | 0.061 |
| IS5_7_1 | 0.008 | 0.256 | 0.045 | 0.060 |
| IS5_7_2 | 0.000 | 0.012 | 0.009 | -0.003 |
| IS5_6_1 | 0.009 | 0.323 | 0.031 | 0.025 |
| IS5_6_2 | 0.009 | 0.093 | 0.017 | 0.012 |
| IS5_5_1 | 0.008 | 0.056 | 0.016 | 0.009 |
| IS5_5_2 | 0.005 | 0.054 | 0.015 | 0.014 |
| IS5_4_1 | 0.013 | 0.121 | 0.019 | 0.018 |
| IS5_9_1 | 0.001 | -0.001 | 0.000 | -0.001 |
| IS5_10_1 | 0.011 | 0.319 | 0.040 | 0.060 |
| IS5_10_2 | 0.002 | 0.016 | 0.008 | 0.000 |
| IS5_11_1 | 0.003 | 0.008 | 0.009 | -0.004 |
| IS5_11_2 | 0.004 | 0.034 | 0.014 | -0.004 |
| IS5_13_1 | 0.015 | 0.373 | 0.045 | 0.057 |
| IS5_13_2 | 0.001 | 0.025 | 0.013 | -0.003 |
| IS5_13_2 | 0.005 | 0.134 | 0.029 | 0.020 |
| IS5_20_1 | 0.005 | 0.130 | 0.029 | 0.023 |
| IS5_20_2 | 0.000 | -0.002 | 0.000 | -0.003 |
| IS5_19_1 | 0.010 | 0.109 | 0.039 | 0.031 |
| IS5_17_1 | 0.014 | 0.229 | 0.043 | 0.029 |
| IS5_17_2 | 0.002 | 0.008 | 0.008 | -0.003 |

Table A.8 continued

| Sample | Sm_ppm_m147_2SE | Eu_ppm_m153 | Eu_ppm_m153_2SE | Gd_ppm_m157 |
|---|---|---|---|---|
| ZB117_1_1 | 0.038 | 0.163 | 0.018 | 0.414 |
| ZB117_1_2 | 0.039 | 0.165 | 0.015 | 0.567 |
| ZB117_2_1 | 0.018 | 0.045 | 0.009 | 0.149 |
| ZB117_2_2 | 0.011 | 0.015 | 0.005 | 0.056 |
| ZB117_4_1 | 0.015 | 0.035 | 0.007 | 0.103 |
| ZB117_4_2 | 0.013 | 0.033 | 0.007 | 0.098 |
| ZB117_5_1 | 0.025 | 0.167 | 0.015 | 0.546 |
| ZB117_5_2 | 0.008 | 0.008 | 0.003 | 0.017 |
| ZB117_6_1 | 0.141 | 1.770 | 0.071 | 4.471 |
| ZB117_7_1 | 0.046 | 0.339 | 0.025 | 1.148 |
| ZB117_8_1 | 0.063 | 0.699 | 0.030 | 1.905 |
| ZB117_9_1 | 0.079 | 0.685 | 0.031 | 1.917 |
| ZB117_12_1 | 0.024 | 0.198 | 0.014 | 0.561 |
| ZB117_11_1 | 0.025 | 0.195 | 0.012 | 0.568 |
| ZB117_10_1 | 0.033 | 0.175 | 0.013 | 0.469 |
| ZB117_10_2 | 0.024 | 0.148 | 0.008 | 0.432 |
| ZB117_13_1 | 0.015 | 0.032 | 0.006 | 0.120 |
| ZB117_14_1 | 0.018 | 0.053 | 0.007 | 0.155 |
| ZB117_15_1 | 0.028 | 0.148 | 0.019 | 0.473 |
| | | | | |
| ZB23_1_1 | 0.023 | 0.047 | 0.005 | 0.136 |
| ZB23_1_2 | 0.037 | 0.053 | 0.017 | 0.214 |
| ZB23_2_1 | 0.022 | 0.034 | 0.006 | 0.130 |
| ZB23_3_1 | 0.014 | 0.039 | 0.009 | 0.130 |
| ZB23_4_1 | 0.027 | 0.043 | 0.012 | 0.082 |
| ZB23_5_1 | 0.013 | 0.026 | 0.006 | 0.099 |
| ZB23_6_1 | 0.022 | 0.025 | 0.005 | 0.070 |
| ZB23_6_2 | 0.122 | 0.282 | 0.065 | 0.797 |
| ZB23_9_1 | 0.044 | 0.099 | 0.038 | 0.151 |
| ZB23_9_2 | 0.142 | 0.249 | 0.025 | 0.535 |
| ZB23_8_1 | 0.025 | 0.007 | 0.007 | -0.002 |
| ZB23_8_1 | 0.006 | 0.002 | 0.003 | 0.011 |
| ZB23_10_1 | 0.009 | 0.002 | 0.003 | 0.013 |
| ZB23_10_2 | 0.025 | 0.055 | 0.013 | 0.146 |
| ZB23_11_1 | 0.018 | 0.026 | 0.008 | 0.037 |
| ZB23_13_1 | 0.021 | 0.063 | 0.010 | 0.133 |
| ZB23_14_1 | 0.049 | 0.015 | 0.001 | 0.098 |

Table A.8 continued

| Sample | Sm_ppm_m147_2SE | Eu_ppm_m153 | Eu_ppm_m153_2SE | Gd_ppm_m157 |
|---|---|---|---|---|
| GF45_1_1 | 0.027 | 0.027 | 0.008 | 0.121 |
| GF45_1_2 | 0.023 | 0.042 | 0.010 | 0.309 |
| GF45_1_3 | 0.019 | 0.018 | 0.006 | 0.164 |
| GF45_2_1 | 0.017 | 0.029 | 0.007 | 0.156 |
| GF45_2_2 | 0.015 | 0.035 | 0.010 | 0.177 |
| GF45_2_3 | 0.017 | 0.040 | 0.009 | 0.175 |
| GF45_2_4 | 0.017 | 0.035 | 0.007 | 0.186 |
| | | | | |
| IS5_1_1 | 0.010 | 0.017 | 0.004 | 0.036 |
| IS5_1_2 | 0.052 | 0.042 | 0.007 | 0.433 |
| IS5_3_1 | 0.014 | 0.024 | 0.008 | 0.095 |
| IS5_3_2 | 0.018 | 0.000 | 0.000 | 0.062 |
| IS5_8_1 | 0.010 | 0.010 | 0.006 | 0.019 |
| IS5_8_2 | 0.010 | 0.000 | 0.000 | -0.003 |
| IS5_8_3 | 0.020 | 0.013 | 0.005 | 0.083 |
| IS5_8_3 | 0.015 | 0.043 | 0.005 | 0.042 |
| IS5_7_1 | 0.015 | 0.042 | 0.005 | 0.039 |
| IS5_7_2 | 0.000 | 0.000 | 0.000 | -0.003 |
| IS5_6_1 | 0.012 | 0.034 | 0.007 | 0.103 |
| IS5_6_2 | 0.011 | 0.006 | 0.004 | 0.008 |
| IS5_5_1 | 0.008 | 0.012 | 0.004 | 0.023 |
| IS5_5_2 | 0.010 | 0.005 | 0.004 | 0.025 |
| IS5_4_1 | 0.011 | 0.010 | 0.007 | 0.009 |
| IS5_9_1 | 0.000 | 0.000 | 0.000 | 0.011 |
| IS5_10_1 | 0.024 | 0.046 | 0.011 | 0.104 |
| IS5_10_2 | 0.004 | 0.003 | 0.003 | 0.008 |
| IS5_11_1 | 0.000 | 0.000 | 0.000 | -0.004 |
| IS5_11_2 | 0.000 | 0.007 | 0.005 | 0.019 |
| IS5_13_1 | 0.023 | 0.037 | 0.008 | 0.105 |
| IS5_13_2 | 0.000 | 0.000 | 0.000 | 0.001 |
| IS5_13_2 | 0.014 | 0.012 | 0.006 | 0.043 |
| IS5_20_1 | 0.013 | 0.011 | 0.006 | 0.041 |
| IS5_20_2 | 0.000 | 0.000 | 0.000 | -0.003 |
| IS5_19_1 | 0.013 | 0.013 | 0.006 | 0.057 |
| IS5_17_1 | 0.015 | 0.018 | 0.007 | 0.043 |
| IS5_17_2 | 0.000 | 0.000 | 0.000 | -0.004 |

Table A.8 continued

| Sample | Gd_ppm_m157_2SE | Tb_ppm_m159 | Tb_ppm_m159_2SE | Dy_ppm_m163 |
|---|---|---|---|---|
| ZB117_1_1 | 0.061 | 0.086 | 0.012 | 0.580 |
| ZB117_1_2 | 0.036 | 0.089 | 0.006 | 0.690 |
| ZB117_2_1 | 0.036 | 0.025 | 0.006 | 0.187 |
| ZB117_2_2 | 0.015 | 0.010 | 0.002 | 0.062 |
| ZB117_4_1 | 0.022 | 0.021 | 0.004 | 0.155 |
| ZB117_4_2 | 0.018 | 0.016 | 0.003 | 0.134 |
| ZB117_5_1 | 0.039 | 0.093 | 0.011 | 0.683 |
| ZB117_5_2 | 0.009 | 0.000 | 0.000 | 0.022 |
| ZB117_6_1 | 0.221 | 0.696 | 0.030 | 4.194 |
| ZB117_7_1 | 0.069 | 0.196 | 0.010 | 1.233 |
| ZB117_8_1 | 0.098 | 0.299 | 0.016 | 1.974 |
| ZB117_9_1 | 0.103 | 0.299 | 0.013 | 1.933 |
| ZB117_12_1 | 0.043 | 0.106 | 0.007 | 0.577 |
| ZB117_11_1 | 0.045 | 0.107 | 0.007 | 0.569 |
| ZB117_10_1 | 0.041 | 0.106 | 0.008 | 0.725 |
| ZB117_10_2 | 0.032 | 0.078 | 0.008 | 0.638 |
| ZB117_13_1 | 0.020 | 0.021 | 0.004 | 0.138 |
| ZB117_14_1 | 0.029 | 0.021 | 0.007 | 0.186 |
| ZB117_15_1 | 0.067 | 0.072 | 0.008 | 0.566 |
| | | | | |
| ZB23_1_1 | 0.022 | 0.020 | 0.005 | 0.097 |
| ZB23_1_2 | 0.056 | 0.019 | 0.006 | 0.158 |
| ZB23_2_1 | 0.014 | 0.015 | 0.004 | 0.159 |
| ZB23_3_1 | 0.025 | 0.011 | 0.004 | 0.090 |
| ZB23_4_1 | 0.028 | 0.031 | 0.005 | 0.139 |
| ZB23_5_1 | 0.020 | 0.007 | 0.002 | 0.107 |
| ZB23_6_1 | 0.020 | 0.011 | 0.004 | 0.030 |
| ZB23_6_2 | 0.221 | 0.109 | 0.022 | 0.662 |
| ZB23_9_1 | 0.030 | 0.024 | 0.007 | 0.114 |
| ZB23_9_2 | 0.095 | 0.051 | 0.009 | 0.237 |
| ZB23_8_1 | 0.000 | 0.010 | 0.007 | 0.023 |
| ZB23_8_1 | 0.011 | 0.006 | 0.003 | 0.026 |
| ZB23_10_1 | 0.012 | 0.007 | 0.003 | 0.030 |
| ZB23_10_2 | 0.024 | 0.017 | 0.006 | 0.082 |
| ZB23_11_1 | 0.024 | 0.013 | 0.006 | 0.053 |
| ZB23_13_1 | 0.032 | 0.017 | 0.004 | 0.136 |
| ZB23_14_1 | 0.040 | 0.003 | 0.004 | 0.081 |

Table A.8 continued

| Sample | Gd_ppm_m157_2SE | Tb_ppm_m159 | Tb_ppm_m159_2SE | Dy_ppm_m163 |
|---|---|---|---|---|
| GF45_1_1 | 0.018 | 0.035 | 0.003 | 0.264 |
| GF45_1_2 | 0.046 | 0.049 | 0.008 | 0.322 |
| GF45_1_3 | 0.037 | 0.032 | 0.004 | 0.279 |
| GF45_2_1 | 0.030 | 0.040 | 0.004 | 0.280 |
| GF45_2_2 | 0.023 | 0.032 | 0.006 | 0.331 |
| GF45_2_3 | 0.031 | 0.040 | 0.006 | 0.296 |
| GF45_2_4 | 0.024 | 0.039 | 0.006 | 0.313 |
| | | | | |
| IS5_1_1 | 0.014 | 0.002 | 0.002 | 0.041 |
| IS5_1_2 | 0.084 | 0.023 | 0.007 | 0.130 |
| IS5_3_1 | 0.035 | 0.006 | 0.003 | 0.049 |
| IS5_3_2 | 0.043 | 0.000 | 0.000 | 0.013 |
| IS5_8_1 | 0.012 | 0.000 | 0.000 | 0.027 |
| IS5_8_2 | 0.000 | 0.000 | 0.000 | 0.009 |
| IS5_8_3 | 0.010 | 0.007 | 0.004 | 0.038 |
| IS5_8_3 | 0.016 | 0.006 | 0.003 | 0.094 |
| IS5_7_1 | 0.016 | 0.006 | 0.003 | 0.093 |
| IS5_7_2 | 0.000 | 0.000 | 0.000 | 0.000 |
| IS5_6_1 | 0.016 | 0.012 | 0.004 | 0.086 |
| IS5_6_2 | 0.009 | 0.001 | 0.001 | 0.007 |
| IS5_5_1 | 0.012 | 0.000 | 0.000 | 0.013 |
| IS5_5_2 | 0.017 | 0.001 | 0.001 | 0.011 |
| IS5_4_1 | 0.012 | 0.004 | 0.003 | 0.021 |
| IS5_9_1 | 0.012 | 0.000 | 0.000 | -0.001 |
| IS5_10_1 | 0.026 | 0.012 | 0.004 | 0.109 |
| IS5_10_2 | 0.008 | 0.004 | 0.002 | 0.014 |
| IS5_11_1 | 0.000 | 0.000 | 0.000 | 0.001 |
| IS5_11_2 | 0.016 | 0.000 | 0.000 | 0.016 |
| IS5_13_1 | 0.025 | 0.009 | 0.003 | 0.039 |
| IS5_13_2 | 0.006 | 0.000 | 0.000 | 0.002 |
| IS5_13_2 | 0.013 | 0.007 | 0.004 | 0.042 |
| IS5_20_1 | 0.013 | 0.006 | 0.003 | 0.041 |
| IS5_20_2 | 0.000 | 0.000 | 0.000 | 0.000 |
| IS5_19_1 | 0.023 | 0.003 | 0.003 | 0.024 |
| IS5_17_1 | 0.017 | 0.002 | 0.002 | 0.052 |
| IS5_17_2 | 0.000 | 0.000 | 0.000 | 0.000 |

Table A.8 continued

| Sample | Dy_ppm_m163_2SE | Ho_ppm_m165 | Ho_ppm_m165_2SE | Er_ppm_m166 |
|---|---|---|---|---|
| ZB117_1_1 | 0.066 | 0.140 | 0.019 | 0.408 |
| ZB117_1_2 | 0.056 | 0.158 | 0.011 | 0.529 |
| ZB117_2_1 | 0.036 | 0.035 | 0.010 | 0.110 |
| ZB117_2_2 | 0.010 | 0.015 | 0.002 | 0.040 |
| ZB117_4_1 | 0.028 | 0.039 | 0.006 | 0.117 |
| ZB117_4_2 | 0.023 | 0.028 | 0.007 | 0.086 |
| ZB117_5_1 | 0.080 | 0.154 | 0.017 | 0.510 |
| ZB117_5_2 | 0.010 | 0.005 | 0.003 | 0.021 |
| ZB117_6_1 | 0.150 | 0.924 | 0.043 | 2.592 |
| ZB117_7_1 | 0.052 | 0.283 | 0.014 | 0.918 |
| ZB117_8_1 | 0.101 | 0.431 | 0.021 | 1.341 |
| ZB117_9_1 | 0.062 | 0.428 | 0.016 | 1.259 |
| ZB117_12_1 | 0.042 | 0.124 | 0.007 | 0.336 |
| ZB117_11_1 | 0.041 | 0.124 | 0.007 | 0.336 |
| ZB117_10_1 | 0.043 | 0.168 | 0.013 | 0.549 |
| ZB117_10_2 | 0.035 | 0.131 | 0.008 | 0.446 |
| ZB117_13_1 | 0.009 | 0.029 | 0.003 | 0.103 |
| ZB117_14_1 | 0.026 | 0.040 | 0.006 | 0.137 |
| ZB117_15_1 | 0.044 | 0.135 | 0.009 | 0.425 |
| | | | | |
| ZB23_1_1 | 0.020 | 0.024 | 0.003 | 0.073 |
| ZB23_1_2 | 0.027 | 0.029 | 0.004 | 0.082 |
| ZB23_2_1 | 0.013 | 0.035 | 0.004 | 0.075 |
| ZB23_3_1 | 0.015 | 0.020 | 0.004 | 0.063 |
| ZB23_4_1 | 0.023 | 0.027 | 0.003 | 0.076 |
| ZB23_5_1 | 0.017 | 0.021 | 0.004 | 0.059 |
| ZB23_6_1 | 0.013 | 0.010 | 0.002 | 0.025 |
| ZB23_6_2 | 0.173 | 0.124 | 0.032 | 0.389 |
| ZB23_9_1 | 0.016 | 0.017 | 0.004 | 0.083 |
| ZB23_9_2 | 0.043 | 0.029 | 0.005 | 0.138 |
| ZB23_8_1 | 0.014 | 0.008 | 0.007 | 0.000 |
| ZB23_8_1 | 0.013 | 0.010 | 0.004 | 0.050 |
| ZB23_10_1 | 0.015 | 0.011 | 0.004 | 0.055 |
| ZB23_10_2 | 0.012 | 0.016 | 0.004 | 0.048 |
| ZB23_11_1 | 0.010 | 0.006 | 0.003 | 0.015 |
| ZB23_13_1 | 0.016 | 0.023 | 0.004 | 0.075 |
| ZB23_14_1 | 0.022 | 0.014 | 0.004 | 0.032 |

Table A.8 continued

| Sample | Dy_ppm_m163_2SE | Ho_ppm_m165 | Ho_ppm_m165_2SE | Er_ppm_m166 |
|---|---|---|---|---|
| GF45_1_1 | 0.027 | 0.048 | 0.005 | 0.158 |
| GF45_1_2 | 0.024 | 0.067 | 0.006 | 0.198 |
| GF45_1_3 | 0.033 | 0.068 | 0.005 | 0.195 |
| GF45_2_1 | 0.030 | 0.069 | 0.007 | 0.248 |
| GF45_2_2 | 0.035 | 0.065 | 0.007 | 0.238 |
| GF45_2_3 | 0.027 | 0.081 | 0.009 | 0.236 |
| GF45_2_4 | 0.041 | 0.079 | 0.006 | 0.327 |
| | | | | |
| IS5_1_1 | 0.008 | 0.005 | 0.002 | 0.017 |
| IS5_1_2 | 0.020 | 0.016 | 0.003 | 0.039 |
| IS5_3_1 | 0.017 | 0.004 | 0.003 | 0.023 |
| IS5_3_2 | 0.007 | 0.001 | 0.001 | 0.000 |
| IS5_8_1 | 0.010 | 0.005 | 0.002 | 0.010 |
| IS5_8_2 | 0.008 | 0.002 | 0.002 | 0.012 |
| IS5_8_3 | 0.011 | 0.006 | 0.002 | 0.023 |
| IS5_8_3 | 0.015 | 0.016 | 0.003 | 0.067 |
| IS5_7_1 | 0.015 | 0.018 | 0.004 | 0.067 |
| IS5_7_2 | 0.000 | 0.000 | 0.000 | 0.001 |
| IS5_6_1 | 0.010 | 0.025 | 0.003 | 0.091 |
| IS5_6_2 | 0.006 | 0.000 | 0.000 | 0.001 |
| IS5_5_1 | 0.007 | 0.003 | 0.002 | 0.024 |
| IS5_5_2 | 0.006 | 0.003 | 0.002 | 0.011 |
| IS5_4_1 | 0.010 | 0.002 | 0.002 | 0.012 |
| IS5_9_1 | 0.000 | 0.000 | 0.000 | 0.000 |
| IS5_10_1 | 0.022 | 0.035 | 0.005 | 0.132 |
| IS5_10_2 | 0.008 | 0.001 | 0.001 | 0.017 |
| IS5_11_1 | 0.003 | 0.000 | 0.000 | 0.007 |
| IS5_11_2 | 0.009 | 0.000 | 0.000 | 0.013 |
| IS5_13_1 | 0.007 | 0.014 | 0.004 | 0.040 |
| IS5_13_2 | 0.003 | 0.000 | 0.000 | 0.000 |
| IS5_13_2 | 0.013 | 0.016 | 0.004 | 0.042 |
| IS5_20_1 | 0.013 | 0.014 | 0.004 | 0.041 |
| IS5_20_2 | 0.000 | 0.000 | 0.000 | 0.000 |
| IS5_19_1 | 0.014 | 0.010 | 0.004 | 0.032 |
| IS5_17_1 | 0.017 | 0.013 | 0.005 | 0.051 |
| IS5_17_2 | 0.000 | 0.000 | 0.000 | 0.004 |

Table A.8 continued

| Sample | Er_ppm_m166_2SE | Tm_ppm_m169 | Tm_ppm_m169_2SE | Yb_ppm_m172 |
|---|---|---|---|---|
| ZB117_1_1 | 0.054 | 0.066 | 0.009 | 0.376 |
| ZB117_1_2 | 0.056 | 0.063 | 0.006 | 0.492 |
| ZB117_2_1 | 0.023 | 0.016 | 0.005 | 0.084 |
| ZB117_2_2 | 0.008 | 0.007 | 0.001 | 0.049 |
| ZB117_4_1 | 0.017 | 0.013 | 0.002 | 0.098 |
| ZB117_4_2 | 0.013 | 0.008 | 0.002 | 0.072 |
| ZB117_5_1 | 0.044 | 0.084 | 0.010 | 0.441 |
| ZB117_5_2 | 0.008 | 0.002 | 0.002 | 0.013 |
| ZB117_6_1 | 0.147 | 0.373 | 0.019 | 2.229 |
| ZB117_7_1 | 0.033 | 0.125 | 0.006 | 0.893 |
| ZB117_8_1 | 0.065 | 0.189 | 0.005 | 1.102 |
| ZB117_9_1 | 0.064 | 0.174 | 0.014 | 1.100 |
| ZB117_12_1 | 0.029 | 0.051 | 0.003 | 0.348 |
| ZB117_11_1 | 0.030 | 0.052 | 0.003 | 0.358 |
| ZB117_10_1 | 0.027 | 0.085 | 0.007 | 0.571 |
| ZB117_10_2 | 0.039 | 0.059 | 0.005 | 0.407 |
| ZB117_13_1 | 0.020 | 0.012 | 0.003 | 0.086 |
| ZB117_14_1 | 0.013 | 0.020 | 0.004 | 0.156 |
| ZB117_15_1 | 0.029 | 0.061 | 0.007 | 0.426 |
| | | | | |
| ZB23_1_1 | 0.011 | 0.010 | 0.003 | 0.070 |
| ZB23_1_2 | 0.015 | 0.011 | 0.003 | 0.088 |
| ZB23_2_1 | 0.011 | 0.009 | 0.001 | 0.086 |
| ZB23_3_1 | 0.007 | 0.009 | 0.002 | 0.084 |
| ZB23_4_1 | 0.014 | 0.013 | 0.003 | 0.092 |
| ZB23_5_1 | 0.010 | 0.011 | 0.003 | 0.044 |
| ZB23_6_1 | 0.011 | 0.005 | 0.002 | 0.037 |
| ZB23_6_2 | 0.093 | 0.043 | 0.010 | 0.300 |
| ZB23_9_1 | 0.011 | 0.009 | 0.003 | 0.064 |
| ZB23_9_2 | 0.018 | 0.021 | 0.007 | 0.083 |
| ZB23_8_1 | 0.000 | 0.000 | 0.000 | 0.011 |
| ZB23_8_1 | 0.014 | 0.009 | 0.003 | 0.074 |
| ZB23_10_1 | 0.016 | 0.010 | 0.004 | 0.081 |
| ZB23_10_2 | 0.021 | 0.006 | 0.003 | 0.026 |
| ZB23_11_1 | 0.007 | 0.002 | 0.002 | 0.000 |
| ZB23_13_1 | 0.009 | 0.008 | 0.002 | 0.073 |
| ZB23_14_1 | 0.015 | 0.006 | 0.006 | 0.023 |

Table A.8 continued

| Sample | Er_ppm_m166_2SE | Tm_ppm_m169 | Tm_ppm_m169_2SE | Yb_ppm_m172 |
|---|---|---|---|---|
| GF45_1_1 | 0.022 | 0.023 | 0.004 | 0.156 |
| GF45_1_2 | 0.026 | 0.026 | 0.006 | 0.214 |
| GF45_1_3 | 0.027 | 0.039 | 0.002 | 0.205 |
| GF45_2_1 | 0.035 | 0.034 | 0.004 | 0.212 |
| GF45_2_2 | 0.030 | 0.040 | 0.006 | 0.253 |
| GF45_2_3 | 0.025 | 0.040 | 0.006 | 0.248 |
| GF45_2_4 | 0.034 | 0.038 | 0.005 | 0.251 |
| | | | | |
| IS5_1_1 | 0.004 | 0.004 | 0.002 | 0.033 |
| IS5_1_2 | 0.010 | 0.007 | 0.003 | 0.070 |
| IS5_3_1 | 0.009 | 0.007 | 0.003 | 0.027 |
| IS5_3_2 | 0.000 | 0.000 | 0.000 | 0.007 |
| IS5_8_1 | 0.007 | 0.002 | 0.001 | 0.019 |
| IS5_8_2 | 0.007 | 0.000 | 0.000 | 0.004 |
| IS5_8_3 | 0.008 | 0.002 | 0.002 | 0.026 |
| IS5_8_3 | 0.013 | 0.012 | 0.004 | 0.117 |
| IS5_7_1 | 0.013 | 0.012 | 0.003 | 0.114 |
| IS5_7_2 | 0.002 | 0.000 | 0.000 | 0.001 |
| IS5_6_1 | 0.020 | 0.017 | 0.003 | 0.141 |
| IS5_6_2 | 0.003 | 0.003 | 0.001 | 0.000 |
| IS5_5_1 | 0.006 | 0.002 | 0.001 | 0.040 |
| IS5_5_2 | 0.005 | 0.001 | 0.001 | 0.004 |
| IS5_4_1 | 0.008 | 0.001 | 0.001 | 0.021 |
| IS5_9_1 | 0.000 | 0.000 | 0.000 | 0.005 |
| IS5_10_1 | 0.027 | 0.023 | 0.004 | 0.216 |
| IS5_10_2 | 0.007 | 0.002 | 0.001 | 0.031 |
| IS5_11_1 | 0.006 | 0.000 | 0.001 | 0.009 |
| IS5_11_2 | 0.007 | 0.000 | 0.000 | 0.022 |
| IS5_13_1 | 0.006 | 0.009 | 0.003 | 0.055 |
| IS5_13_2 | 0.000 | 0.001 | 0.001 | 0.001 |
| IS5_13_2 | 0.011 | 0.008 | 0.004 | 0.055 |
| IS5_20_1 | 0.011 | 0.007 | 0.004 | 0.053 |
| IS5_20_2 | 0.000 | 0.000 | 0.000 | 0.000 |
| IS5_19_1 | 0.012 | 0.001 | 0.001 | 0.018 |
| IS5_17_1 | 0.017 | 0.004 | 0.003 | 0.055 |
| IS5_17_2 | 0.004 | 0.000 | 0.000 | 0.004 |

Table A.8 continued

| Sample | Yb_ppm_m172_2SE | Lu_ppm_m175 | Lu_ppm_m175_2SE | Hf_ppm_m178 |
|---|---|---|---|---|
| ZB117_1_1 | 0.044 | 0.054 | 0.008 | 0.000 |
| ZB117_1_2 | 0.039 | 0.075 | 0.011 | 0.000 |
| ZB117_2_1 | 0.018 | 0.018 | 0.004 | 0.000 |
| ZB117_2_2 | 0.006 | 0.005 | 0.002 | 0.000 |
| ZB117_4_1 | 0.015 | 0.014 | 0.005 | 0.000 |
| ZB117_4_2 | 0.015 | 0.010 | 0.004 | 0.000 |
| ZB117_5_1 | 0.045 | 0.080 | 0.008 | 0.000 |
| ZB117_5_2 | 0.006 | 0.002 | 0.001 | 0.000 |
| ZB117_6_1 | 0.112 | 0.349 | 0.016 | 0.000 |
| ZB117_7_1 | 0.041 | 0.141 | 0.007 | 0.000 |
| ZB117_8_1 | 0.060 | 0.148 | 0.012 | 0.000 |
| ZB117_9_1 | 0.046 | 0.165 | 0.008 | 0.000 |
| ZB117_12_1 | 0.024 | 0.048 | 0.004 | 0.002 |
| ZB117_11_1 | 0.027 | 0.048 | 0.005 | 0.002 |
| ZB117_10_1 | 0.051 | 0.080 | 0.007 | 0.017 |
| ZB117_10_2 | 0.035 | 0.058 | 0.006 | 0.002 |
| ZB117_13_1 | 0.017 | 0.013 | 0.002 | 0.000 |
| ZB117_14_1 | 0.019 | 0.015 | 0.003 | 0.000 |
| ZB117_15_1 | 0.026 | 0.064 | 0.007 | 0.000 |
| | | | | |
| ZB23_1_1 | 0.010 | 0.012 | 0.003 | 0.012 |
| ZB23_1_2 | 0.022 | 0.011 | 0.003 | 0.000 |
| ZB23_2_1 | 0.015 | 0.013 | 0.003 | 0.017 |
| ZB23_3_1 | 0.020 | 0.015 | 0.004 | 0.008 |
| ZB23_4_1 | 0.021 | 0.013 | 0.003 | 0.029 |
| ZB23_5_1 | 0.011 | 0.007 | 0.002 | 0.000 |
| ZB23_6_1 | 0.012 | 0.004 | 0.002 | 0.000 |
| ZB23_6_2 | 0.082 | 0.045 | 0.010 | 0.014 |
| ZB23_9_1 | 0.019 | 0.015 | 0.003 | 0.026 |
| ZB23_9_2 | 0.014 | 0.009 | 0.008 | 0.000 |
| ZB23_8_1 | 0.015 | 0.001 | 0.002 | 0.000 |
| ZB23_8_1 | 0.022 | 0.014 | 0.006 | 0.000 |
| ZB23_10_1 | 0.023 | 0.016 | 0.007 | 0.000 |
| ZB23_10_2 | 0.017 | 0.009 | 0.007 | 0.110 |
| ZB23_11_1 | 0.000 | 0.000 | 0.000 | 0.000 |
| ZB23_13_1 | 0.011 | 0.009 | 0.003 | 0.028 |
| ZB23_14_1 | 0.022 | 0.007 | 0.001 | 0.000 |

Table A.8 continued

| Sample | Yb_ppm_m172_2SE | Lu_ppm_m175 | Lu_ppm_m175_2SE | Hf_ppm_m178 |
|---|---|---|---|---|
| GF45_1_1 | 0.027 | 0.023 | 0.003 | 0.037 |
| GF45_1_2 | 0.026 | 0.027 | 0.003 | 0.120 |
| GF45_1_3 | 0.017 | 0.025 | 0.004 | 0.073 |
| GF45_2_1 | 0.020 | 0.029 | 0.004 | 0.021 |
| GF45_2_2 | 0.034 | 0.038 | 0.006 | 0.081 |
| GF45_2_3 | 0.025 | 0.036 | 0.004 | 0.114 |
| GF45_2_4 | 0.041 | 0.038 | 0.006 | 0.194 |
| | | | | |
| IS5_1_1 | 0.011 | 0.009 | 0.003 | 0.000 |
| IS5_1_2 | 0.009 | 0.012 | 0.003 | 0.026 |
| IS5_3_1 | 0.009 | 0.008 | 0.003 | 0.000 |
| IS5_3_2 | 0.006 | 0.000 | 0.000 | 0.000 |
| IS5_8_1 | 0.009 | 0.001 | 0.001 | 0.000 |
| IS5_8_2 | 0.005 | 0.000 | 0.000 | 0.000 |
| IS5_8_3 | 0.009 | 0.000 | 0.000 | 0.025 |
| IS5_8_3 | 0.016 | 0.025 | 0.004 | 0.000 |
| IS5_7_1 | 0.016 | 0.024 | 0.004 | 0.000 |
| IS5_7_2 | 0.003 | 0.000 | 0.001 | 0.000 |
| IS5_6_1 | 0.019 | 0.035 | 0.005 | 0.000 |
| IS5_6_2 | 0.000 | 0.004 | 0.002 | 0.028 |
| IS5_5_1 | 0.011 | 0.001 | 0.001 | 0.000 |
| IS5_5_2 | 0.005 | 0.000 | 0.001 | 0.017 |
| IS5_4_1 | 0.010 | 0.006 | 0.003 | 0.000 |
| IS5_9_1 | 0.006 | 0.000 | 0.000 | 0.000 |
| IS5_10_1 | 0.034 | 0.050 | 0.007 | 0.000 |
| IS5_10_2 | 0.010 | 0.005 | 0.002 | 0.021 |
| IS5_11_1 | 0.007 | 0.000 | 0.001 | 0.000 |
| IS5_11_2 | 0.013 | 0.003 | 0.002 | 0.000 |
| IS5_13_1 | 0.023 | 0.017 | 0.003 | 0.000 |
| IS5_13_2 | 0.003 | 0.000 | 0.000 | 0.002 |
| IS5_13_2 | 0.021 | 0.009 | 0.003 | 0.000 |
| IS5_20_1 | 0.021 | 0.009 | 0.003 | 0.000 |
| IS5_20_2 | 0.000 | 0.000 | 0.000 | 0.000 |
| IS5_19_1 | 0.008 | 0.007 | 0.002 | 0.000 |
| IS5_17_1 | 0.014 | 0.011 | 0.004 | 0.000 |
| IS5_17_2 | 0.005 | 0.003 | 0.002 | 0.050 |

Table A.8 continued

| Sample | Hf_ppm_m178_2SE | Pb_ppm_m208 | Pb_ppm_m208_2SE | Th_ppm_m232 |
|---|---|---|---|---|
| ZB117_1_1 | 0.000 | 0.081 | 0.017 | 0.000 |
| ZB117_1_2 | 0.000 | 0.016 | 0.004 | 0.006 |
| ZB117_2_1 | 0.000 | 0.038 | 0.011 | 0.000 |
| ZB117_2_2 | 0.000 | 0.060 | 0.011 | 0.000 |
| ZB117_4_1 | 0.000 | 0.054 | 0.011 | 0.000 |
| ZB117_4_2 | 0.000 | 0.046 | 0.011 | 0.000 |
| ZB117_5_1 | 0.000 | 0.132 | 0.015 | 0.000 |
| ZB117_5_2 | 0.000 | 0.002 | 0.005 | 0.000 |
| ZB117_6_1 | 0.000 | 0.161 | 0.020 | 0.000 |
| ZB117_7_1 | 0.000 | 0.181 | 0.013 | 0.000 |
| ZB117_8_1 | 0.000 | 0.144 | 0.013 | 0.000 |
| ZB117_9_1 | 0.000 | 0.192 | 0.012 | 0.000 |
| ZB117_12_1 | 0.004 | 0.019 | 0.008 | 0.000 |
| ZB117_11_1 | 0.004 | 0.015 | 0.007 | 0.000 |
| ZB117_10_1 | 0.010 | 0.056 | 0.009 | 0.007 |
| ZB117_10_2 | 0.003 | 0.028 | 0.009 | 0.007 |
| ZB117_13_1 | 0.000 | 0.008 | 0.006 | 0.000 |
| ZB117_14_1 | 0.000 | 0.010 | 0.004 | 0.000 |
| ZB117_15_1 | 0.000 | 0.072 | 0.009 | 0.045 |
| | | | | |
| ZB23_1_1 | 0.009 | 1.873 | 0.237 | 0.140 |
| ZB23_1_2 | 0.000 | 1.256 | 0.081 | 0.140 |
| ZB23_2_1 | 0.011 | 1.395 | 0.142 | 0.130 |
| ZB23_3_1 | 0.008 | 1.294 | 0.107 | 0.185 |
| ZB23_4_1 | 0.012 | 1.518 | 0.104 | 0.103 |
| ZB23_5_1 | 0.000 | 1.313 | 0.084 | 0.082 |
| ZB23_6_1 | 0.000 | 0.697 | 0.083 | 0.092 |
| ZB23_6_2 | 0.010 | 2.104 | 0.231 | 0.599 |
| ZB23_9_1 | 0.017 | 1.826 | 0.238 | 0.306 |
| ZB23_9_2 | 0.000 | 1.706 | 0.222 | 0.379 |
| ZB23_8_1 | 0.000 | 0.430 | 0.032 | 0.442 |
| ZB23_8_1 | 0.000 | 0.494 | 0.102 | 0.054 |
| ZB23_10_1 | 0.000 | 0.517 | 0.108 | 0.061 |
| ZB23_10_2 | 0.033 | 2.587 | 0.308 | 0.431 |
| ZB23_11_1 | 0.000 | 1.086 | 0.103 | 0.109 |
| ZB23_13_1 | 0.015 | 2.553 | 0.140 | 0.543 |
| ZB23_14_1 | 0.000 | 1.086 | 0.219 | 0.057 |

Table A.8 continued

| Sample | Hf_ppm_m178_2SE | Pb_ppm_m208 | Pb_ppm_m208_2SE | Th_ppm_m232 |
|---|---|---|---|---|
| GF45_1_1 | 0.017 | 1.430 | 0.088 | 0.007 |
| GF45_1_2 | 0.019 | 2.056 | 0.146 | 0.039 |
| GF45_1_3 | 0.024 | 2.830 | 0.111 | 0.014 |
| GF45_2_1 | 0.015 | 1.543 | 0.107 | 0.000 |
| GF45_2_2 | 0.026 | 1.933 | 0.166 | 0.110 |
| GF45_2_3 | 0.028 | 2.842 | 0.204 | 0.093 |
| GF45_2_4 | 0.020 | 3.467 | 0.242 | 0.056 |
| | | | | |
| IS5_1_1 | 0.000 | 1.441 | 0.083 | 0.007 |
| IS5_1_2 | 0.012 | 4.965 | 0.338 | 0.379 |
| IS5_3_1 | 0.000 | 0.894 | 0.080 | 0.007 |
| IS5_3_2 | 0.000 | 0.259 | 0.048 | 0.038 |
| IS5_8_1 | 0.000 | 0.774 | 0.095 | 0.003 |
| IS5_8_2 | 0.000 | 0.845 | 0.203 | 0.000 |
| IS5_8_3 | 0.015 | 0.319 | 0.031 | 0.000 |
| IS5_8_3 | 0.000 | 4.498 | 0.245 | 0.024 |
| IS5_7_1 | 0.000 | 4.491 | 0.236 | 0.023 |
| IS5_7_2 | 0.000 | 0.143 | 0.042 | 0.000 |
| IS5_6_1 | 0.000 | 5.389 | 0.359 | 0.012 |
| IS5_6_2 | 0.013 | 0.779 | 0.086 | 0.000 |
| IS5_5_1 | 0.000 | 0.698 | 0.090 | 0.000 |
| IS5_5_2 | 0.011 | 0.092 | 0.030 | 0.000 |
| IS5_4_1 | 0.000 | 0.630 | 0.122 | 0.008 |
| IS5_9_1 | 0.000 | 0.138 | 0.038 | 0.000 |
| IS5_10_1 | 0.000 | 5.698 | 0.565 | 0.004 |
| IS5_10_2 | 0.011 | 0.291 | 0.072 | 0.018 |
| IS5_11_1 | 0.000 | 0.157 | 0.043 | 0.000 |
| IS5_11_2 | 0.000 | 0.453 | 0.076 | 0.000 |
| IS5_13_1 | 0.000 | 1.862 | 0.182 | 0.022 |
| IS5_13_2 | 0.004 | 0.063 | 0.011 | 0.000 |
| IS5_13_2 | 0.000 | 1.069 | 0.163 | 0.000 |
| IS5_20_1 | 0.000 | 1.047 | 0.160 | 0.000 |
| IS5_20_2 | 0.000 | 0.241 | 0.050 | 0.000 |
| IS5_19_1 | 0.000 | 1.328 | 0.164 | 0.000 |
| IS5_17_1 | 0.000 | 1.465 | 0.083 | 0.009 |
| IS5_17_2 | 0.019 | 0.143 | 0.029 | 0.000 |

Table A.8 continued

| Sample | Th_ppm_m232_2SE | U_ppm_m238 | U_ppm_m238_2SE |
|---|---|---|---|
| ZB117_1_1 | 0.000 | 0.180 | 0.019 |
| ZB117_1_2 | 0.004 | 0.112 | 0.010 |
| ZB117_2_1 | 0.000 | 0.041 | 0.009 |
| ZB117_2_2 | 0.000 | 0.008 | 0.003 |
| ZB117_4_1 | 0.000 | 0.051 | 0.006 |
| ZB117_4_2 | 0.000 | 0.046 | 0.008 |
| ZB117_5_1 | 0.000 | 0.236 | 0.028 |
| ZB117_5_2 | 0.000 | 0.004 | 0.002 |
| ZB117_6_1 | 0.000 | 0.408 | 0.023 |
| ZB117_7_1 | 0.000 | 0.333 | 0.021 |
| ZB117_8_1 | 0.000 | 0.225 | 0.014 |
| ZB117_9_1 | 0.000 | 0.264 | 0.016 |
| ZB117_12_1 | 0.000 | 0.109 | 0.009 |
| ZB117_11_1 | 1.000 | 0.111 | 0.009 |
| ZB117_10_1 | 0.004 | 0.126 | 0.009 |
| ZB117_10_2 | 0.004 | 0.144 | 0.013 |
| ZB117_13_1 | 0.000 | 0.026 | 0.007 |
| ZB117_14_1 | 0.000 | 0.045 | 0.005 |
| ZB117_15_1 | 0.013 | 0.157 | 0.015 |
| | | | |
| ZB23_1_1 | 0.026 | 0.272 | 0.030 |
| ZB23_1_2 | 0.022 | 0.224 | 0.022 |
| ZB23_2_1 | 0.017 | 0.366 | 0.024 |
| ZB23_3_1 | 0.019 | 0.257 | 0.023 |
| ZB23_4_1 | 0.012 | 0.266 | 0.017 |
| ZB23_5_1 | 0.008 | 0.241 | 0.015 |
| ZB23_6_1 | 0.015 | 0.134 | 0.012 |
| ZB23_6_2 | 0.101 | 0.281 | 0.041 |
| ZB23_9_1 | 0.123 | 0.192 | 0.044 |
| ZB23_9_2 | 0.049 | 0.216 | 0.034 |
| ZB23_8_1 | 0.032 | 0.061 | 0.009 |
| ZB23_8_1 | 0.017 | 0.042 | 0.008 |
| ZB23_10_1 | 0.017 | 0.047 | 0.007 |
| ZB23_10_2 | 0.057 | 0.180 | 0.034 |
| ZB23_11_1 | 0.008 | 0.113 | 0.018 |
| ZB23_13_1 | 0.112 | 0.432 | 0.047 |
| ZB23_14_1 | 0.011 | 0.203 | 0.056 |

Table A.8 continued

| Sample | Th_ppm_m232_2SE | U_ppm_m238 | U_ppm_m238_2SE |
|---|---|---|---|
| GF45_1_1 | 0.005 | 0.083 | 0.014 |
| GF45_1_2 | 0.009 | 0.254 | 0.020 |
| GF45_1_3 | 0.006 | 0.230 | 0.030 |
| GF45_2_1 | 0.000 | 0.360 | 0.037 |
| GF45_2_2 | 0.014 | 0.311 | 0.018 |
| GF45_2_3 | 0.016 | 0.331 | 0.022 |
| GF45_2_4 | 0.013 | 0.946 | 0.052 |
| | | | |
| IS5_1_1 | 0.004 | 0.006 | 0.002 |
| IS5_1_2 | 0.056 | 0.108 | 0.013 |
| IS5_3_1 | 0.005 | 0.007 | 0.004 |
| IS5_3_2 | 0.015 | 0.008 | 0.004 |
| IS5_8_1 | 0.004 | 0.007 | 0.004 |
| IS5_8_2 | 0.000 | 0.000 | 0.000 |
| IS5_8_3 | 0.000 | 0.006 | 0.003 |
| IS5_8_3 | 0.007 | 0.102 | 0.012 |
| IS5_7_1 | 0.007 | 0.101 | 0.012 |
| IS5_7_2 | 0.000 | 0.000 | 0.000 |
| IS5_6_1 | 0.006 | 0.138 | 0.015 |
| IS5_6_2 | 0.000 | 0.010 | 0.004 |
| IS5_5_1 | 0.000 | 0.004 | 0.003 |
| IS5_5_2 | 0.000 | 0.000 | 0.000 |
| IS5_4_1 | 0.005 | 0.004 | 0.003 |
| IS5_9_1 | 1.000 | 0.000 | 1.000 |
| IS5_10_1 | 0.004 | 0.187 | 0.033 |
| IS5_10_2 | 0.007 | 0.001 | 0.001 |
| IS5_11_1 | 0.000 | 0.000 | 0.000 |
| IS5_11_2 | 0.000 | 0.002 | 0.002 |
| IS5_13_1 | 0.006 | 0.014 | 0.004 |
| IS5_13_2 | 0.000 | 0.000 | 0.000 |
| IS5_13_2 | 0.000 | 0.005 | 0.003 |
| IS5_20_1 | 1.000 | 0.005 | 0.003 |
| IS5_20_2 | 0.000 | 0.000 | 0.000 |
| IS5_19_1 | 0.000 | 0.004 | 0.003 |
| IS5_17_1 | 0.006 | 0.001 | 0.002 |
| IS5_17_2 | 0.000 | 0.001 | 0.001 |

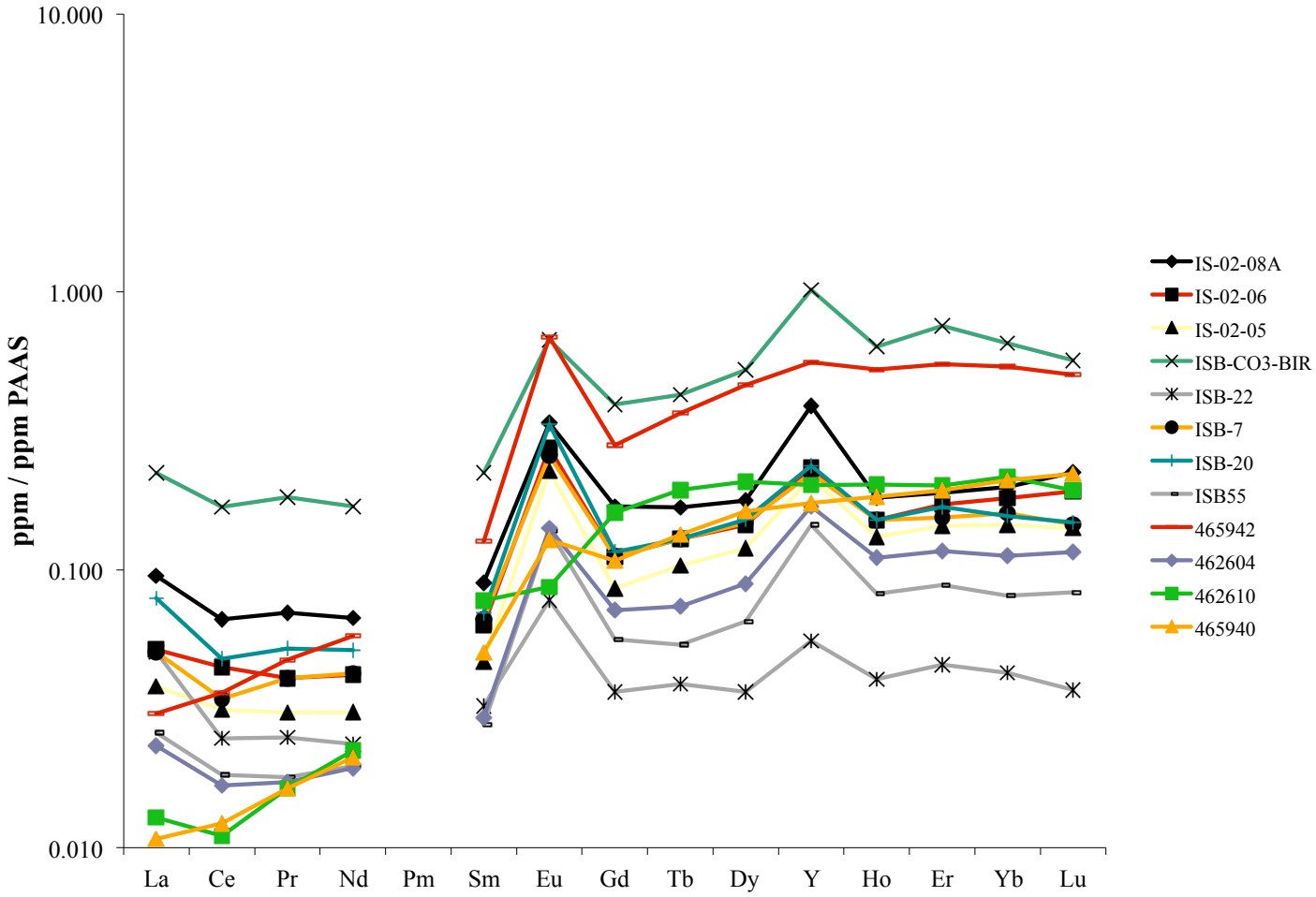



Figure A4.1 Shale-normalized REY patterns for BIFs from the IGB used in this study.

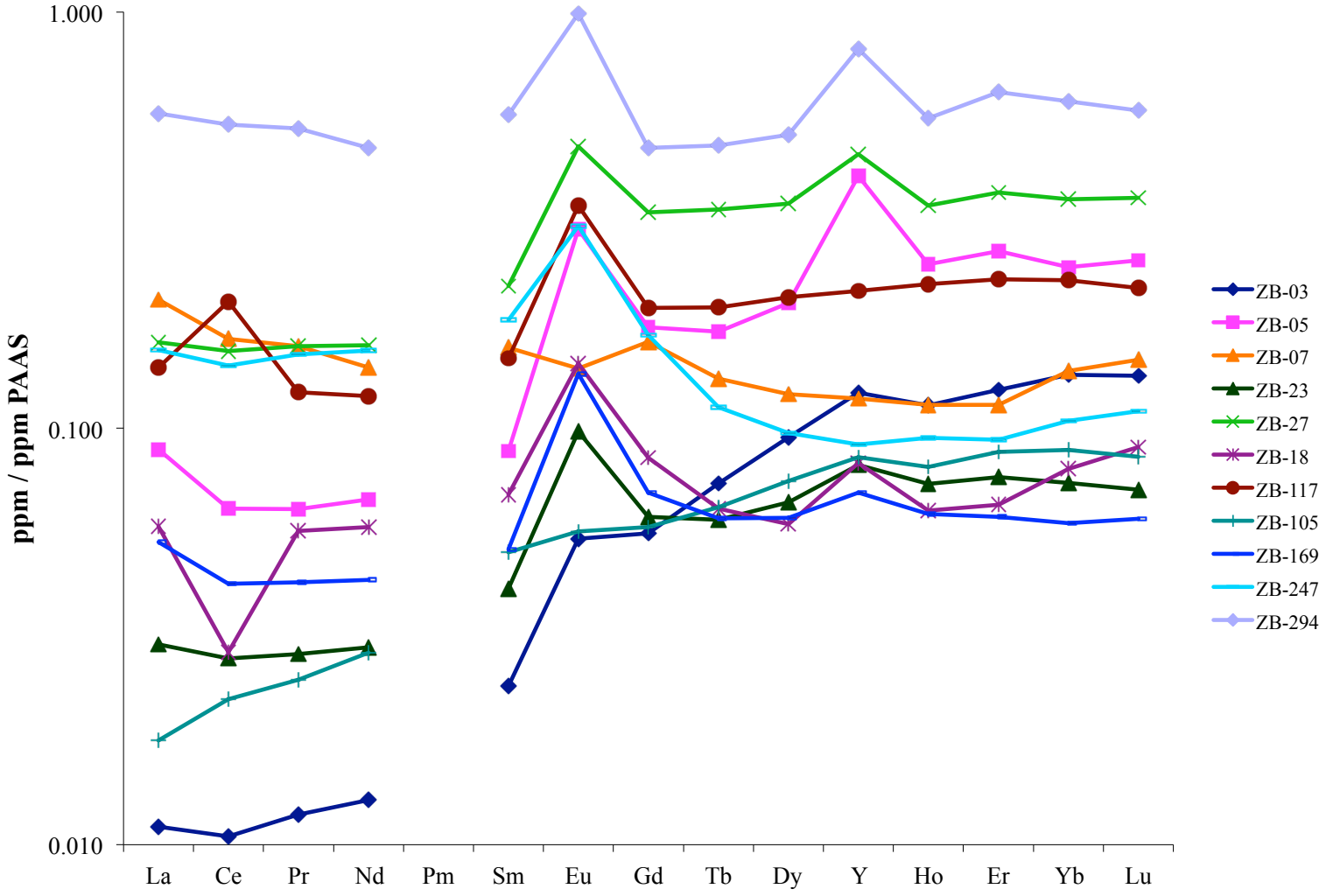



Figure A4.2 Shale-normalized REY patterns for BIFs from the BGB used in this study.

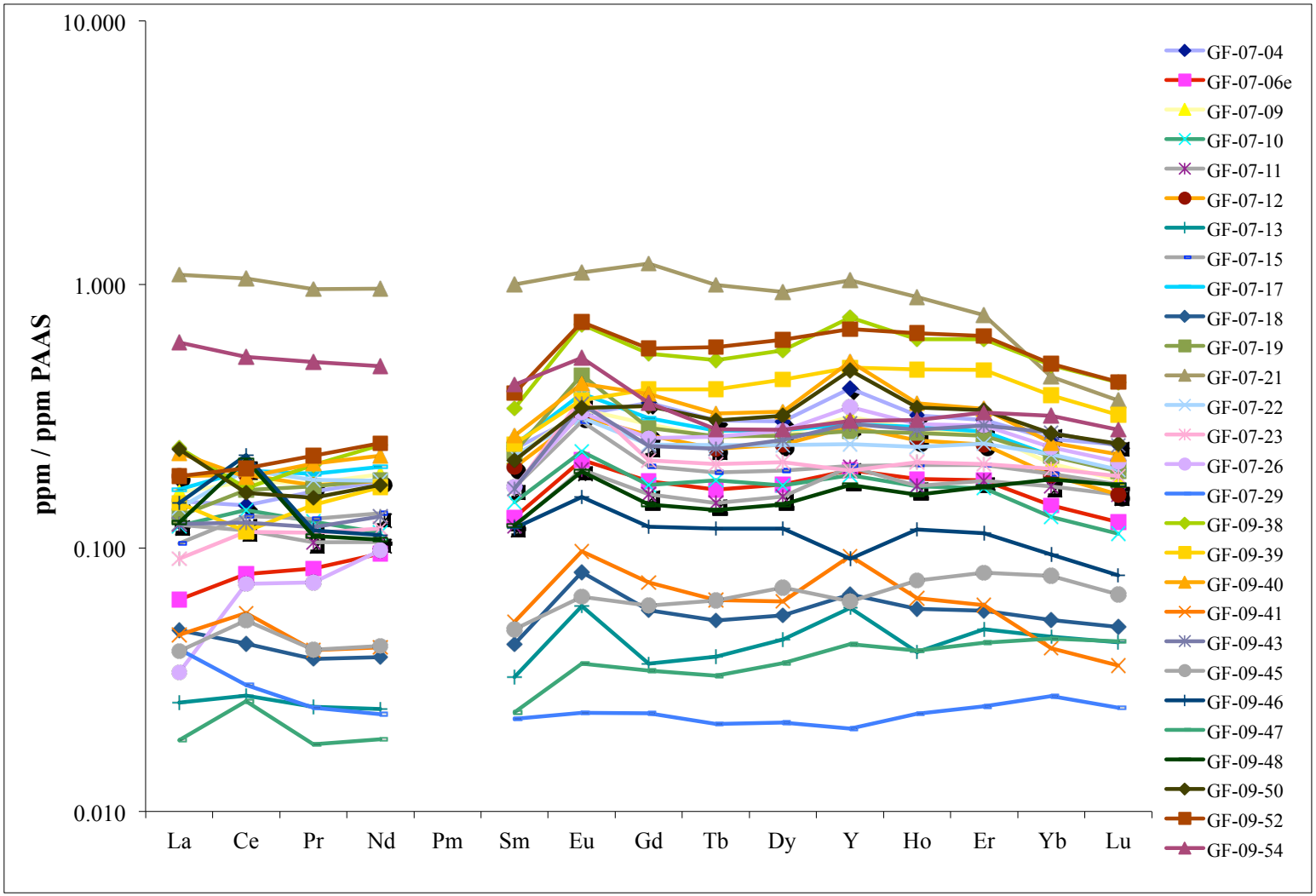



Figure A4.3 Shale-normalized REY patterns for BIFs from the GF used in this study.

# Vita

Melissa Margaret Hage was born on December 4, 1979 in Langhorne, Pennsylvania to Robert and Marie Hage. She grew up in Lawrenceville, NJ and graduated from Notre Dame High School in 1998. From there, Melissa graduated with honors from Franklin and Marshall College in Lancaster, PA and received a B.A. in geology/biology with a minor in environmental public policy. While attending F&M, she completed an undergraduate thesis entitled "Landscape scale impacts of a waterfowl refuge on nutrient dynamics of the Middle Creek watershed, Lancaster, PA". Melissa then moved south and attended the University of Tennessee in Knoxville, TN. She graduated with a M.S. degree in Earth and Planetary Sciences in August 2006 with a thesis entitled "Biomarker and stable isotope characterization of coastal pond organic matter, McMurdo Dry Valleys, Antarctica". After deciding that she still did not have enough schooling, Melissa stayed in the Earth and Planetary Sciences Department at the University of Tennessee, Knoxville to pursue her doctoral degree. In June 2011, Melissa moved to Salem, Oregon to take a position as a Visiting Lecturer in the Environmental and Earth Sciences Department at Willamette University while continuing to write her dissertation. In June, 2014, Melissa moved to Baraboo, WI to take a tenure-track position as an assistant professor in the Geography-Geology Department at the University of Wisconsin-Baraboo/Sauk County while finishing the writing of her dissertation. Just when everyone thought it would never happen, Melissa finally graduated with a PhD in August 2015.